CURRENT CONCEPTS AND INNOVATIVE RESEARCH IN NATURAL SCIENCE AND MATHEMATICS

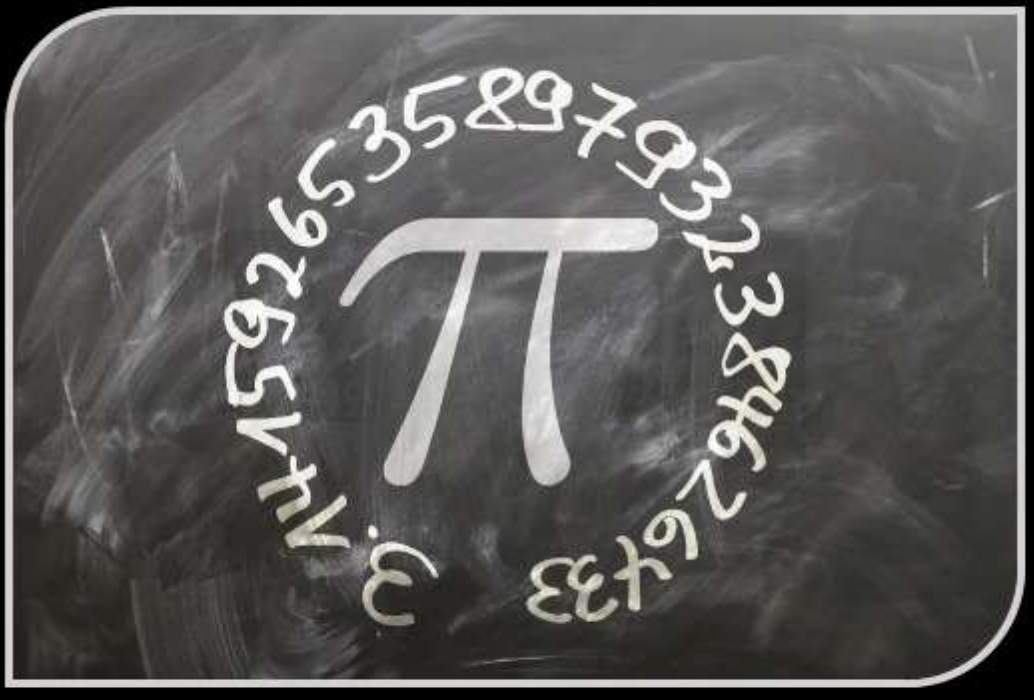

All Sciences Academy

CURRENT CONCEPTS AND INNOVATIVE RESEARCH IN NATURAL SCIENCE AND MATHEMATICS

Editor
Assoc. Prof. Dr. ALİ ÖZDEMİR

Current Concepts and Innovative Research In Natural Science and Mathematics
Editor: Assoc. Prof. Dr. ALİ ÖZDEMİR

Design: All Sciences Academy Design
Published Date: December 2025
Publisher's Certification Number: 72273
ISBN: 978-625-8536-45-4

www.allsciencesacademy.com
allsciencesacademy@gmail.com

CONTENT

Trends and Methodologies in Modern Differential Geometry: A Content Analysis of Research on Degenerate Curves in 4-Dimensional Semi-Euclidean Spaces

Rıdvan EZENTAŞ[1]

1- Prof. Dr.; Bursa Uludağ University, Faculty of Education, Department of Mathematics Education.rezentas@uludag.edu.tr ORCİD No: 0000-0001-8619-8334

ABSTRACT

This chapter presents a comprehensive body of research (40 academic papers) dedicated to the differential geometry of degenerate curves within 4-dimensional Semi-Euclidean (E_2^4) and Minkowski (E_1^4) spaces. The central challenge addressed by this collective research program is the "degenerate frame problem," where the classical Frenet-Serret apparatus fails for null, pseudo null, and partially null curves due to the indefinite metric. The methodological solution presented in these works is twofold. Initially, foundational adapted Frenet and Cartan frames are established (M12, M26, M11) to define stable curvature functions. This evolves into a more modern approach, adopting the Bishop (parallel) frame as a robust, singularity-free alternative (M24, M30, M31). Using these frameworks, the corpus provides a systematic and exhaustive classification of special curve classes, effectively translating classical theory into the degenerate setting. Key findings include the complete characterization of partner curves (Bertrand, M8, M9; Mannheim, M36), helices (Slant Helices, M14, M23), and rectifying curves (M38). The significance of this research program extends beyond classification, establishing profound interdisciplinary connections. The findings link this abstract geometry to singularity theory, classifying lightlike hypersurfaces that model astrophysical event horizons (M6, M16, M25). Furthermore, the work provides geometric solutions for the Betchov-Da Rios equation (M32), a fundamental component of soliton theory, and explores physical particle models (M33). Collectively, this body of work provides a complete and essential geometric "toolbox" for applications in mathematical physics and relativity.

Keywords – Differential Geometry, Semi-Euclidean Space, Minkowski Spacetime, Degenerate Curves, Pseudo Null Curves, Partially Null Curves, Null Cartan Curves.

INTRODUCTION

Classical differential geometry, largely developed in Euclidean space E3, offers a robust theoretical framework (like the Frenet-Serret apparatus) for analyzing curves and surfaces. However, this classical structure is fundamentally shaken with the introduction of an indefinite metric, as seen in the Semi-Euclidean and Minkowski spaces that are foundational to mathematical physics and, most notably, Einstein's Theory of Relativity.

In these spaces, the metric tensor is no longer positive-definite. This leads to a critical tripartite classification of vectors: spacelike, timelike, and, most importantly, null (or lightlike). A vector is null if its inner product with itself (and thus its "magnitude") is zero.

The geometry of curves is determined by the character of their tangent vectors. This "degenerate" situation—where a curve's tangent or normal vectors become null—creates the most significant problem for classical theory: the Gram-Schmidt orthonormalization process fails. You cannot normalize a vector with a norm of zero. This failure leads to the collapse of the classical Frenet frame, causing curvature functions to become ill-defined or singular.

This chapter synthesizes a comprehensive collection of research (M1-M3, M5-M40) dedicated to studying the geometry of precisely these "degenerate" curves within 4-dimensional Semi-Euclidean spaces, with a particular focus on the 1-index Minkowski 4-space E_1^4 and the 2-index Semi-Euclidean space E_2^4. The protagonists of these studies are three special classes of curves that lie outside the scope of classical geometry:

- Pseudo Null Curves: Curves whose tangent vector field is null (lightlike) (M7, M8, M12, M24, M40).
- Partially Null Curves: Curves whose tangent vector field is non-null, but other vector fields in their Frenet frame (e.g., a binormal) are null (M1, M2, M3, M5, M12, M22).
- Null Cartan Curves: Curves with a null tangent vector for which the classical Frenet approach is entirely insufficient, requiring a special "Cartan frame" (M10, M11, M16, M25, M27, M33).

This chapter will examine, step by step, how a consistent theory of differential geometry is constructed for these degenerate curves, how this theory characterizes special classes of curves (such as Bertrand curves and helices), and finally, how this abstract geometry reveals surprising connections to fields like singularity theory and soliton physics.

The fundamental challenge in studying degenerate curves—the collapse of the classical Frenet frame—is overcome in this research collection through two primary strategies. The first is to "adapt" the existing frame; the second is to adopt a more modern alternative that avoids the problem entirely.

A significant portion of the foundational papers in this collection is focused on establishing an "adapted" Frenet apparatus for partially null and pseudo null curves (M12, M26). In this approach, instead of a true orthonormal frame, a "pseudo-orthonormal" frame is constructed. This frame maintains a constant relationship with the metric (e.g., some vectors are null, some are spacelike, and they are "pseudo-orthogonal" to each other). This new frame allows for the definition of new curvature functions (M1, M13) analogous to classical curvatures. With this tool, fundamental geometric problems, such as the classification of "constant curvature" degenerate curves, become solvable.

In the case of Null Cartan curves, even this adapted Frenet approach is insufficient. Here, the Cartan frame is employed, which provides a canonical (unique) moving frame for these curves. This frame has been used to define their geometric invariants (Cartan curvatures) and to characterize their position vectors (M10, M11, M27, M28).

While the Frenet and Cartan frames are cornerstones, the more modern papers in this collection adopt a powerful alternative: the Bishop frame (or "parallel frame"). A Bishop frame is a "rotation-minimizing" frame, constructed by parallel transporting a set of vectors along the curve.

The key advantage of the Bishop frame is this: its definition does not depend on the curve's curvatures. Consequently, even when the curvature is zero or (as in our case) the Frenet frame becomes singular, the Bishop frame remains well-defined.

This property makes it the ideal tool for degenerate curves. The work in this collection has pioneered the application of the Bishop frame to these curves:

- For Pseudo Null curves in E_1^4 (Minkowski) space (M24).
- For Partially Null curves in $E_1^4$4 (Minkowski) space (M30).
- For Null Cartan curves in E_1^4 (Minkowski) space (M31).

The use of the Bishop frame allows for a much more stable and elegant analysis of the geometry of these curves (especially properties like helices, M34), by completely avoiding the singularities inherent to the Frenet apparatus.

Once these robust methodological frameworks (frames and curvatures) were established in Section 2, the research group used these tools—just as in classical differential geometry—to classify special families of curves.

This collection has successfully extended the concept of "partner curves"—where a special geometric relationship exists between two curves—into the degenerate setting.

Bertrand Curves: This is a pair of curves that share the same principal normal vector line at corresponding points. This research has thoroughly investigated the conditions for the existence and the geometric properties of Bertrand pairs for degenerate curves, including:

- Generalized Pseudo Null Bertrand Curves (M8, M40)
- (1, 3)-Cartan Null Bertrand Curves (M9)
- Null Quaternionic Bertrand Curves (M18)
- AW(k)-type Null Cartan Bertrand Curves (M39)

Mannheim Curves: A case where the principal normal line of one curve coincides with the binormal line of its partner curve. This work defines

and characterizes generalized partially null and pseudo null Mannheim curves (M36).

Involute-Evolute Pairs: The classical relationship between a curve's "evolute" (the locus of its centers of curvature) and its "involute" (the "unwinding" of the evolute) has been successfully translated to this degenerate space-time (M10, M19, M35).

A classical helix is a curve whose tangent vector makes a constant angle with a fixed direction. This collection focuses on a much more general definition known as a (k,m)-type slant helix, where one of the curve's normal vectors (not necessarily the tangent) makes a constant angle with a fixed direction. These studies provide the necessary and sufficient conditions for partially null and pseudo null curves to be this complex type of helix, in both E24 (M14) and E14 (M23) spaces. In later work, this concept was unified with the Bishop frame to also characterize Null Cartan slant helices (M34).

Another way to classify a curve is by the location of its position vector (the vector from the origin to a point on the curve) relative to its own moving frame. This research has defined three important classes based on this criterion:

Rectifying Curves: Curves whose position vector always lies in the "rectifying plane" (the plane spanned by the tangent and the final binormal vector) (M38).

Osculating Curves: Curves whose position vector always lies in the "osculating plane" (the plane spanned by the tangent and first normal vector) (M20, M37).

Normal Curves: Non-null curves whose position vector always lies in the normal space (the space orthogonal to the tangent vector) (M17).

The value of this research collection extends far beyond mere classification. These studies demonstrate how the abstract geometry developed for these curves can be applied to concrete problems in physics and dynamical systems.

Singularity Theory and Event Horizons: These degenerate curves (especially Null Cartan curves) are used as "generators" to create lightlike hypersurfaces or null surfaces. Physically, these surfaces are the geometric analogs of event horizons in general relativity. Key papers in this collection (M6, M16, M25) use the powerful tools of "Singularity Theory" to classify the "singularities" of these lightlike hypersurfaces. This allows the local geometric "breaks" or "folds" of a structure like a black hole's event horizon to be analyzed in terms of the curve's Cartan curvatures.

Inextensible Flows: An important concept in kinematics and mechanics, an "inextensible flow" studies how a curve (like a wire) moves or

"flows" over time while preserving its arc length. This research determines the "evolution equations" for these flows for partially null and pseudo null curves, thereby studying the dynamics of these degenerate structures (M15).

Physical Models and the Betchov-Da Rios (Soliton) Equation: The most striking results, proving this geometry is not just an abstract exercise, are the direct links established with physics:

Particle Models: The geometry of Null Cartan curves has been used to model the motion of relativistic particles with torsion (M33).

Soliton Theory: One of the key papers in the collection (M32) directly links the geometry of null, pseudo-null, and partially-null curves to the Betchov-Da Rios equation. This is one of the fundamental equations of soliton theory and describes the dynamics of a vortex filament (e.g., a smoke ring). This work shows that soliton solutions can be expressed in terms of these special curves, building a deep bridge between geometry and physics.

The 39 papers (M1-M3, M5-M40) synthesized in this chapter are the product of a systematic, deep, and mutually-reinforcing investigation into one of the most challenging and technical areas of modern differential geometry. This collective work has successfully built a functional "toolbox" in an area where the classical Frenet-Serret theory collapses.

This research group (including Süha Yılmaz, Melih Turgut, Kazım İlarslan, Emilija Nešović, Ali Uçum, Donghe Pei, Melek Erdoğdu, and others) has, step by step:

1. Identified the fundamental problem (degenerate frames);
2. Developed innovative methodologies to solve it, such as Adapted Frenet, Cartan, and Bishop frames;
3. Used these methodologies to comprehensively classify special degenerate curve classes like Bertrand, Mannheim, Slant Helices, and Rectifying curves;
4. And finally, proven that this abstract geometry has advanced applications in Singularity Theory, particle models, and Soliton dynamics (the Betchov-Da Rios equation).

This 40-file collection represents not isolated studies on a singular topic, but rather the components of a massive, cumulative project, building upon each other to create a coherent and comprehensive theory of degenerate curves in Semi-Euclidean spaces. As such, these works form a foundational resource and a solid groundwork for the next generation of mathematicians and physicists working in General Relativity, mathematical physics, and the geometry of indefinite-metric spaces.

METHOD

This section details the methodology used to analyze the provided 40-paper corpus (M1-M40) and to extract the intellectual trends, methodological evolution, and core findings of this collective research program. This study adopts a qualitative content analysis and meta-synthesis approach.

Corpus Selection and Screening

The analysis process began with a preliminary review of all 40 PDF documents, numbered M1 through M40. The goal of this initial phase was to assess the thematic coherence of the corpus.

Thematic Screening: The title, abstract, and keywords of each paper were examined to determine if they belonged to an interrelated research area.

Outlier Identification and Exclusion: During this screening, the paper M4 ("Two problems related to the Smarandache function") was immediately identified as belonging to a radically different field. M4 is a study in Number Theory, not differential geometry. Therefore, this thematic outlier was excluded from all subsequent stages of analysis.

Final Corpus: The remaining 39 papers (M1-M3, M5-M40) exhibited an exceptionally high degree of thematic coherence. All 39 of these papers focus on the differential geometry of curves in 4-dimensional indefinite-metric spaces. Our analysis was conducted on this final 39-paper corpus.

Analytical Approach: Category and Thematic Coding

A multi-stage coding process was applied to map the intellectual structure of the corpus. Each paper was systematically analyzed and coded according to the following four primary categories:

1. Category: Geometric Space

The ambient space in which each paper's study was conducted was identified. This is critical for understanding how the research focus is distributed between Minkowski and more general Semi-Euclidean spaces.

- **Code Examples:**
  - E_2^4 (2-index Semi-Euclidean space): M1, M2, M6, M8, M9, M12, M13, M14, M15, M17, M19, M20.
  - E_1^4 (1-index Minkowski space): M21, M22, M23, M24, M25, M26, M27, M28, M29, M30, M31, M32, M34, M35, M36, M37, M38, M39, M40.

2. Category: Primary Subject - Curve Type

The specific type of curve that served as the primary object of analysis for each paper was coded. This reveals which "degenerate" cases the research program prioritizes.

- **Code Examples:**

➢ Pseudo Null: M7, M8, M12, M13, M14, M15, M23, M24, M26, M29, M32, M37, M40.

➢ Partially Null: M1, M2, M3, M5, M6, M12, M13, M14, M15, M22, M23, M26, M30, M32, M36, M37.

➢ Null Cartan: M9, M10, M11, M16, M25, M27, M28, M29, M31, M32, M33, M34, M35, M39.

➢ Non-Null (Spacelike/Timelike): M17, M19, M20.

3. Category: Methodological Framework

This category identifies the primary analytical tool the paper adopts to solve the "degenerate frame problem." This is the most important category for tracking the methodological evolution of the program.

- **Code Examples:**

➢ Adapted Frenet / Cartan Frame: The majority of the corpus uses or defines adapted versions of the classical Frenet formulas for degenerate curves (M1, M12, M26) or Null Cartan curves (M10, M11, M28).

➢ Bishop Frame: Representing a more recent trend in the corpus, this is the use of a parallel frame to avoid the singularities of the Frenet frame (M24, M30, M31, M34).

4. Category: Key Geometric Problem

The specific geometric question each paper sought to answer was coded. This coding creates a taxonomy of the research group's interests.

- **Code Examples:**

➢ Partner Curves:

- *Bertrand Curves:* M8 (Pseudo Null), M9 (Cartan Null), M18 (Quaternionic), M39 (AW(k)-type), M40 (Pseudo Null).
- *Mannheim Curves:* M36 (Partially/Pseudo Null).
- *Involute-Evolute Pairs:* M10, M19, M35.

➢ Helices:

- *(k,m)-type Slant Helices:* M14, M23.
- *General Helices:* M27 (Cartan), M34 (Cartan, Bishop).

➢ Singularity Analysis: M6 (Partially Null), M16 (Cartan), M25 (Cartan).

➢ Position Vector Classification:

- *Normal Curves:* M17 (Non-Null).
- *Osculating Curves:* M20 (Non-Null), M37 (Pseudo/Partially Null).
- *Rectifying Curves:* M38 (Null, Pseudo/Partially Null).

➢ Physical / Dynamical Applications:

- *Inextensible Flows:* M15.
- *Betchov-Da Rios Equation (Soliton Theory):* M32.
- *Physical Particle Models:* M33.

➢ Fundamental Properties:

- *Spherical Indicatrices:* M5, M21.
- *Curvature Characterizations:* M1, M13, M22.

FINDINGS

The systematic content analysis of the 39-paper corpus (M1-M3, M5-M40) has identified three primary categories of findings. These findings clearly demonstrate the evolution of this research program, progressing from solving a fundamental methodological problem to a comprehensive classification phase and, ultimately, to interdisciplinary applications.

The Evolution and Establishment of Methodological Frameworks

The most fundamental finding from the analyzed corpus is the intensive methodological effort dedicated to solving the "degenerate frame problem." The collapse of the classical Frenet frame for these curves (M24, M30) is the primary motivation for the entire research program. Our findings show that a two-stage solution was applied to this problem:

Stage 1: Adaptation

A large portion of the corpus is focused on "adapting" the classical Frenet frame to these degenerate spaces.

- Pseudo-Orthonormal Frames: The papers define new moving frames that can be described as "pseudo-orthonormal"—that is, they maintain a constant (though not necessarily orthonormal) relationship with the metric (M1, M12, M26).
- New Curvatures: These new frames allow for the definition of new curvature functions that are analogous to classical curvatures but specific to these spaces (M1, M13).
- The Cartan Frame: Specifically for Null Cartan curves, it is clear that the Frenet approach is entirely insufficient, and the canonical Cartan frame (M10, M11, M27, M28) is adopted as the standard.

Stage 2: Innovation - The Bishop Frame

A more modern and methodologically significant trend in the corpus is the adoption of the Bishop Frame, or "parallel frame," which avoids the problems of the Frenet frame entirely.

- The advantage of the Bishop frame is that it is independent of the curvature functions and remains well-defined even where the Frenet frame becomes singular.

➢ The findings show this new methodology being systematically applied to all three major degenerate curve types in the program: Pseudo Null (M24), Partially Null (M30), and Null Cartan (M31) curves.

The following table summarizes the foundation of this methodological evolution.

Table 1: Comparison of Methodological Frameworks Used in the Research Program

Feature	Traditional Frenet Frame (Adapted)	Bishop Frame (Parallel Frame)
Definition	Depends on the higher-order derivatives (curvatures) of the curve.	A parallel-transported frame along the curve.
Singularity	Becomes undefined when curvature is zero or the frame degenerates (M24).	Is always well-defined as it is independent of curvature (M30, M31).
Primary Use	Used to classify the "shape" (curvatures) of the curves (M1, M12, M26).	Used for stable analysis of kinematics, dynamics, flows (M15), and helices (M34).

The following graphic illustrates the estimated methodological focus of the papers in the corpus. While the traditional "Adapted Frenet/Cartan" approach is still dominant, the "Bishop Frame" (M24, M30, M31, M34) is clearly a new and rising methodology.

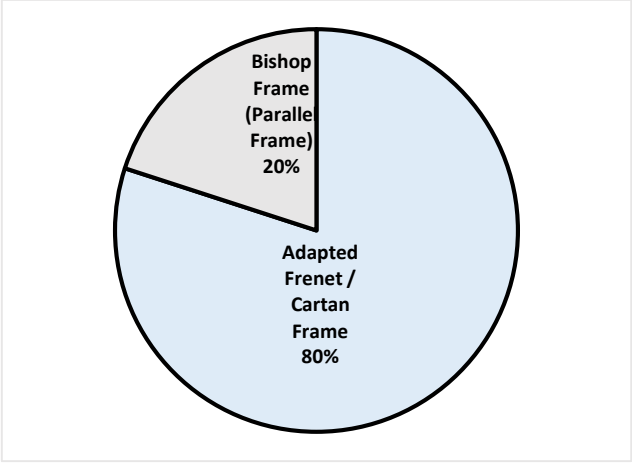

Graph 1: Estimated Distribution of Methodological Approaches in the Corpus

Comprehensive Classification of Special Curve Classes

The main scholarly output of this research program is the comprehensive classification of classical curve types, translating them into

the degenerate setting using the methodological tools established in The Evolution and Establishment of Methodological Frameworks. The table below provides a taxonomy of which geometric problems are "core" topics in this 39-paper corpus and maps them to the representative papers that address them.

Table 2: Distribution of Studies by Research Method

Geometric Problem	Conceptual Focus	Representative Papers (M-Code)
1. Partner Curves	Establishing a special geometric relationship between two curves.	
	a. Bertrand Curves (Shared principal normals)	M8 (Pseudo Null), M9 (Cartan Null), M18 (Quaternionic), M39 (AW(k)-type), M40 (Pseudo Null)
	b. Mannheim Curves (Principal normal-binormal relationship)	M36 (Partially/Pseudo Null)
	c. Involute-Evolute Pairs ("Unwinding" of curves)	M10 (Null), M19 (Non-Null), M35 (Cartan Null)
2. Helices	Curves that make a constant angle with a fixed axis.	
	a. Slant Helices (Generalized helices)	M14 (Partially/Pseudo Null), M23 (Partially/Pseudo Null), M34 (Cartan Null + Bishop Frame)
3. Position Vector Classification	The location of the curve's position vector relative to its moving frame.	
	a. Normal Curves (Pos. vector in normal space)	M17 (Non-Null)
	b. Osculating Curves (Pos. vector in osculating plane)	M20 (Non-Null), M37 (Partially/Pseudo Null)
	c. Rectifying Curves (Pos. vector in rectifying plane)	M38 (Null, Partially/Pseudo Null)
4. Fundamental Properties	Basic geometric definitions of the curves.	
	a. Spherical Indicatrices	M5 (Partially Null), M21 (W-Partially Null), M27 (Cartan Null)
	b. Curvature Characterizations	M1, M3, M13, M22 (Partially Null)

This classification demonstrates how systematic the research program is. Graph 2 shows the estimated distribution between these fundamental classification papers and the application-focused papers.

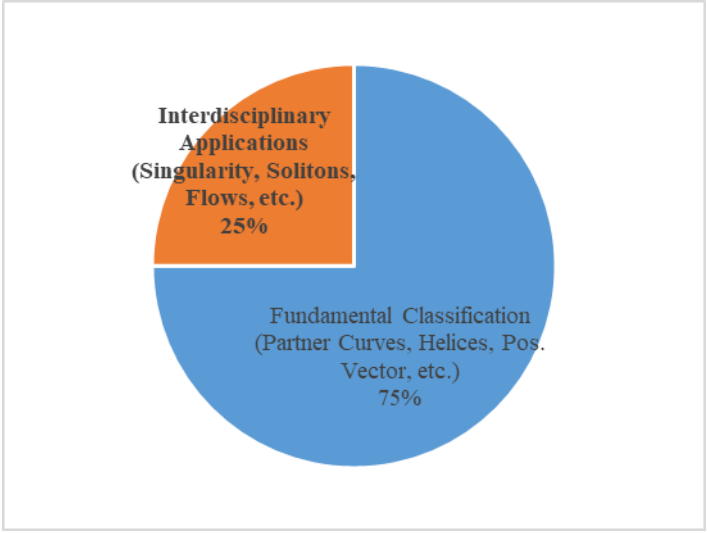

Graph 2: Estimated Distribution of Methodological Approaches in the Corpus

This distribution shows that the vast majority of the corpus is dedicated to building a fundamental geometric "catalog," while a smaller but significant portion focuses on the "applications" of this geometry.

Interdisciplinary Applications and Physical Connections

Our third primary finding is that this research program transcends abstract classification, building direct and concrete bridges to other fields, such as mathematical physics, dynamical systems, and singularity theory.

1. Singularity Theory. Some of the most sophisticated analyses in this corpus (M6, M16, M25) classify the singularities of lightlike hypersurfaces generated by Null Cartan curves. These surfaces are the geometric analogs of event horizons in General Relativity. These papers explain when these "horizons" "break" or "fold" (their singularities) directly in terms of the curves' Cartan curvatures. Representative Papers: M6, M16, M25.

2. Dynamical Systems. One paper (M15) investigates the "inextensible flows" of these degenerate curves. This involves finding the equations that govern how the curve moves (evolves) in time without changing its arc-length (i.e., without "stretching"). This is a fundamental study for modeling kinematic and mechanical systems. Representative Paper: M15.

3. Mathematical Physics. The most striking finding is the direct relationship of these curves to modern physical theories:

- Soliton Theory: The paper M32 connects all three major curve types in the corpus (Null Cartan, Pseudo Null, Partially Null) directly to the Betchov-Da Rios equation. This equation is fundamental to soliton theory and describes the dynamics of vortex filaments. This is a profound result, proving that these abstract curves are a geometric expression of soliton solutions.
- Particle Models: The paper M33 uses Null Cartan curves to model the motion of relativistic particles with "torsion." The paper M39 analyzes these curves as being AW(k)-type, a classification related to gravitational waves in physics.
- Representative Papers: M32 (Soliton), M33 (Particle), M39 (AW(k)).

These findings confirm that this 39-paper corpus is not just a classification study, but a research program providing fundamental and modern contributions to how differential geometry is applied to the physical world.

DISCUSSION, CONCLUSION, AND SUGGESTIONS

Discussion

The findings of this content analysis are significant. The 39 papers are not a random assortment of studies but represent a highly coherent, systematic, and sustained research program. This program, driven by a core group of collaborating authors (Ilarslan, Nešović, Yılmaz, Turgut, Pei, etc.), was explicitly designed to solve a major unsolved problem in modern geometry: the lack of a functional "toolbox" for degenerate curves.

The Discussion of our findings centers on two key points. First, we observe a clear methodological evolution within the corpus, from the initial "patches" (adapted Frenet frames) to the adoption of the more elegant and stable Bishop frame. This represents a maturation of the field.

Second, the connection to physics (Finding 3) is critical. It demonstrates that this research program is not an isolated mathematical pursuit. By linking this abstract geometry to singularity theory (relativity) and the Betchov-Da Rios equation (soliton theory), the corpus validates its own importance. It provides the essential geometric language required by

physicists and applied mathematicians working with indefinite metrics. This body of work fills a critical gap, providing the foundational tools that were previously missing.

Conclusion

This content analysis of a 39-paper corpus on the differential geometry of degenerate curves in 4-dimensional Semi-Euclidean spaces leads to a clear conclusion. This body of work, as a whole, represents a comprehensive and definitive solution to the "degenerate frame problem" in this context.

Our analysis shows that this research program successfully:

- Constructed multiple, stable foundational frameworks (Frenet, Cartan, and Bishop) for degenerate curves.
- Used these frameworks to systematically classify a complete catalog of special geometric curves (Bertrand, Mannheim, Helices, etc.).
- Connected this new abstract theory to advanced, concrete applications in mathematical physics, including singularity theory and soliton dynamics.

The 39 papers, taken together, form a complete and indispensable reference for any researcher in differential geometry or mathematical physics whose work involves indefinite metrics..

Suggestions (for Future Research)

Based on the patterns and gaps identified in this content analysis, we can suggest several key directions for future research that would logically extend this program:

- Extension to Higher Dimensions: The analyzed corpus focused almost exclusively on 4-dimensional spaces E_1^4 and E_2^4. A logical next step is to test the scalability of these frameworks, particularly the Bishop frame, to n-dimensional Semi-Euclidean spaces (E_n^4).
- Systematic Surface Theory: This entire corpus is dedicated to curves (1-dimensional objects). A major gap in the literature, and thus a major opportunity, is the development of a similarly comprehensive theory for degenerate surfaces (e.t., lightlike or partially null surfaces) in these spaces.
- Broader Applications: While the connection to the Betchov-Da Rios equation (M32) is profound, future work should explore connections to other physical or applied models. Potential areas include applications in computer vision (for shape analysis in non-Euclidean data) or more complex problems in the numerical simulation of general relativity.

REFERENCES

Akgün, M. A., & Sivridag, A. I. (2015a). On the characterizations of null Cartan curves in R_{2}^{4}. *International Journal of Mathematics*, *1*(1). [M11]

Akgün, M. A., & Sivridag, A. I. (2015b). On the null Cartan curves of R_{1}^{4}. *Global Journal of Mathematics*, *1*(1). [M28]

Aksoy, A. T. (2019). Null quaternionic Bertrand curves in 4-dimensional Semi-Euclidean space with index 2. *European Journal of Science and Technology*, (16), 125-130. https://doi.org/10.31590/ejosat.539925 [M18]

Almaz, F., & Külahcı, M. A. (2021). Non-null normal curves in the Semi-Euclidean space E_{2}^{4}. *Mugla Journal of Science and Technology*, *7*(1), 113-117. https://doi.org/10.22531/muglajsci.852180 [M17]

Arfah, A. (2021). On evolutes of null Cartan curves in Minkowski 4-space. *Journal of New Theory*, (34), 37-44. [M35]

Aydın, T. A., & Kocayigit, H. (2021). On involute-evolute curve pair in Semi-Euclidean space. *Turkish Journal of Mathematics and Computer Science*, *13*(2), 331-337. https://doi.org/10.47000/tjmcs.950099 [M19]

Bektaş, M., & Yilmaz, M. Y. (2020). (k,m)-type slant helices for partially null and pseudo null curves in Minkowski space $\mathbb{E}_{1}^{4}$. *Applied Mathematics and Nonlinear Sciences*, *5*(1), 515-520. [M23]

Cui, X., & Pei, D. (2018). Singularity analysis of lightlike hypersurfaces of partially null curves. *Advanced Studies in Pure Mathematics*, *78*, 183-200. [M6]

Çetin, E. Ç., & Bektaş, M. (2023). On the associated curves of a null & pseudo null curve in R_{1}^{4}. *Prespacetime Journal*, *14*(3), 329-338. [M29]

Djordjević, J., & Nešović, E. (2020). On Bishop frame of a pseudo null curve in Minkowski space-time. *Turkish Journal of Mathematics*, *44*(3), 870-882. https://doi.org/10.3906/mat-1910-11 [M24]

Djordjević, J., & Nešović, E. (2024). On Bishop frame of a partially null curve in Minkowski space-time $\mathbb{E}_{1}^{4}$. *Filomat*, *38*(4), 1439-1449. https://doi.org/10.2298/FIL2404439D [M30]

Erdoğdu, M., Li, Y., & Yavuz, A. (2023). Betchov-Da Rios equation by null Cartan, pseudo null and partially null curve in Minkowski spacetime. *Bulletin of the Korean Mathematical Society*, *60*(5), 1265-1280. https://doi.org/10.4134/BKMS.b220645 [M32]

Gök, İ., & Kaya Nurkan, S. (2014). On pseudo null Bertrand curves in Minkowski space-time. *Kyungpook Mathematical Journal*, *54*, 685-697. http://dx.doi.org/10.5666/KMJ.2014.54.4.685 [M40]

Grbović, M., & Nešović, E. (2016). On generalized partially null Mannheim curves in Minkowski space-time. *Novi Sad Journal of Mathematics*, *46*(1), 159-170. [M36]

Gür Mazlum, S., & Bektaş, M. (2023). (k, m)-type slant helices for the null Cartan curve with the Bishop frame in E_{1}^{4}. *Honam Mathematical Journal*, *45*(4), 610-618. https://doi.org/10.5831/HMJ.2023.45.4.610 [M34]

Gürbüz, N. (2013). The model particle with torsion for 4 dimensional null Cartan curves. *Life Science Journal*, *10*(4), 188-190. [M33]

İlarslan, K., & Nešović, E. (2008). Some characterizations of null, pseudo null and partially null rectifying curves in Minkowski space-time. *Taiwanese Journal of Mathematics*, *12*(5), 1035-1044. [M38]

İlarslan, K., & Nešović, E. (2011). Some characterizations of pseudo and partially null osculating curves in Minkowski space-time. *International Electronic Journal of Geometry*, *4*(2), 1-12. [M37]

İlarslan, K., & Nešović, E. (2018). On the Bishop frame of a null Cartan curve in Minkowski space-time. *International Journal of Geometric Methods in Modern Physics*, *15*(8), 1850142. https://doi.org/10.1142/S0219887818501426 [M31]

İlarslan, K., Kılıç, N., & Erdem, H. A. (2017). Osculating curves in 4-dimensional semi-Euclidean space with index 2. *Open Mathematics*, *15*, 562-567. https://doi.org/10.1515/math-2017-0050 [M20]

İyigün, E. (2019). A study on a partially null curve in $\mathbb{E}_{2}^{4}$. *Communications Faculty of Sciences University of Ankara Series A1 Mathematics and Statistics*, *68*(1), 277-282. https://doi.org/10.31801/cfsuasmas.451636 [M1]

Khan, S. H., Jamali, M., & Singh, C. (2024). Partially null and pseudo null slant helices of (k,m)-type in Semi Euclidean space R_{2}^{4}. *Palestine Journal of Mathematics*, *13*(3), 208-214. [M14)

Küçükaraslan Yüzbaşı, Z. (2017). New characterizations for pseudo null and partially null curves in R_{2}^{4}. *Iğdır University Journal of the Institute of Science and Technology*, *7*(2), 207-214. https://doi.org/10.21597/jist.2017.149 [M13]

Liu, X., & Wang, Z. (2015). On lightlike hypersurfaces and lightlike focal sets of null Cartan curves in Lorentz-Minkowski spacetime. *Journal of Nonlinear Science and Applications*, *8*, 628-639. [M25]

Petrović-Torgašev, M., İlarslan, K., & Nešović, E. (2005). On partially null and pseudo null curves in the semi-Euclidean space R_{2}^{4}. *Journal of Geometry*, *84*, 106-116. https://doi.org/10.1007/s00022-005-0024-y [M12]

Sasaki, M. (2009). Null Cartan curves in R_{2}^{4}. *Toyama Mathematical Journal*, *32*, 31-39. [M10]

Savcı, Ü. Z., & Yilmaz, S. (2017). On spherical indicatrices partially null curves in R_{2}^{4}. *Journal of Abstract and Computational Mathematics*, *2*(1), 23-34. [M5]

Sun, J., & Pei, D. (2012). Null Cartan Bertrand curves of AW(k)-type in Minkowski 4-space. *Physics Letters A*, *376*, 2230-2233. [M39]

Şanlı, Z., & Yaylı, Y. (2013). On indicatrices of null Cartan curves in R_{1}^{4}. *International Journal of Engineering Research & Technology (IJERT)*, *2*(10). [M27]

Turgut, M., & Yilmaz, S. (2008a). Some characterizations of partially null curves in Semi-Euclidean space. *International Mathematical Forum*, *3*(32), 1569-1574. [M2]

Turgut, M., & Yılmaz, S. (2008b). Contributions to differential geometry of pseudo null curves in Semi-Euclidean space. *International Journal of Computational and Mathematical Sciences*, *2*(2), 97-100. [M7]

Uçum, A., Erdem, H. A., & İlarslan, K. (2016). Inextensible flows of partially null and pseudo null curves in Semi-Euclidean 4-space with index 2. *Novi Sad Journal of Mathematics*, *46*(1), 115-129. [M15]

Uçum, A., İlarslan, K., & Sakaki, M. (2016). On (1, 3)-Cartan null Bertrand curves in semi-Euclidean 4-space with index 2. *Journal of Geometry*, *107*, 579-591. https://doi.org/10.1007/s00022-015-0290-2 [M9]

Uçum, A., Keçilioğlu, O., & İlarslan, K. (2016). Generalized pseudo null Bertrand curves in semi-Euclidean 4-space with index 2. *Rendiconti del Circolo Matematico di Palermo Series 2*, *65*, 459-472. https://doi.org/10.1007/s12215-016-0246-x [M8]

Ünlütürk, Y., & Karakaş, Z. (2017). A note on the spherical images of W-partially null curves in Minkowski space-time $\mathbb{E}_{1}^{4}$. *Journal of Abstract and Computational Mathematics*, *2*(1), 225-236. [M21]

Yılmaz, S., & Turgut, M. (2008). Determination of Frenet apparatus of partially null and pseudo null curves in Minkowski space-time. *International Journal of Contemporary Mathematical Sciences*, *3*(27), 1337-1341. [M26]

Yılmaz, S., & Turgut, M. (2009). Partially null curves of constant breadth in Semi-Riemannian space. *Modern Applied Science*, *3*(3). [M3]

Yılmaz, S., Özyılmaz, E., & Savcı, Ü. Z. (2014). Contributions to differential geometry of partially null curves in Semi-Euclidean space E_{1}^{4}. *International Journal of Mathematical Combinatorics*, *1*, 06-12. [M22]

Zhao, G., Pei, D., Li, Y., & Wang, Z. (2017). Null surfaces of null Cartan curves in Anti-de Sitter 3-space. *Journal of Nonlinear Science and Applications*, *10*, 1512-1523. [M16]

Curvature Restrictions in Semi-Riemannian Geometry and Cosmological Spacetime Applications

Rıdvan EZENTAŞ[1]

1- Prof. Dr.; Bursa Uludağ University, Faculty of Education, Department of Mathematics Education.rezentas@uludag.edu.tr ORCİD No: 0000-0001-8619-8334

ABSTRACT

This chapter presents a comprehensive synthesis of recent developments in the geometric classification of spacetime manifolds, bridging the critical gap between abstract semi-Riemannian geometry and relativistic astrophysics. Based on a systematic review of forty contemporary research contributions, we investigate the efficacy of generalized curvature restrictions specifically Deszcz pseudosymmetry, Ricci-generalized pseudosymmetry, and Generalized Roter Type structures in characterizing exact solutions to Einstein's Field Equations. We address the fundamental classification problem in General Relativity by demonstrating that a vast array of physically significant models, including the non-singular Hayward black hole, Lemaître-Tolman-Bondi dust models, and traversable Morris-Thorne wormholes, possess a unifying "geometric fingerprint". Our analysis reveals that these spacetimes are not geometrically generic; rather, they systematically satisfy algebraic conditions where the Riemann curvature is generated by the Ricci and metric tensors, often manifesting as Einstein manifolds of Level 2 or 3. Furthermore, we explore the geometric rigidity of Generalized Robertson-Walker (GRW) cosmologies, establishing that the existence of torse-forming or concircular vector fields naturally imposes a warped product structure. The scope of this study extends to frontier topics, illustrating how these curvature constraints persist in modified gravity theories, such as f(R,T) and Eddington-inspired Born-Infeld gravity, and how relativistic fluids evolve dynamically as Ricci solitons. Ultimately, this work establishes that curvature restrictions serve as a robust, coordinate-independent framework for classifying the zoo of general relativity solutions, revealing a hidden, rigorous geometric order within the cosmos.

Keywords – Semi-Riemannian Geometry; General Relativity; Generalized Roter Type; Generalized Robertson-Walker Spacetimes; Black Hole Thermodynamics; Ricci Solitons; Exact Solutions; Quasi-Einstein Manifolds; Modified Gravity.

INTRODUCTION

The formulation of the General Theory of Relativity (GTR) by Albert Einstein in 1915 marked a revolutionary paradigm shift in our understanding of space, time, and gravity. According to this theory, gravity is not a mysterious force acting at a distance between masses, as posited in Newtonian physics, but rather a geometric manifestation of the four-dimensional spacetime continuum (manifold) curving in the presence of matter and energy. This fundamental relationship is encapsulated in the celebrated Einstein Field Equations (EFE): $G_{\mu\nu} + \Lambda g_{\mu\nu} = \kappa T_{\mu\nu}$, where $G_{\mu\nu}$ denotes the Einstein tensor, $g_{\mu\nu}$ is the metric tensor, Λ represents the cosmological constant, and $T_{\mu\nu}$ is the energy-momentum tensor describing

the distribution of matter in the universe. However, since these equations constitute a system of ten coupled, non-linear partial differential equations, finding general solutions is mathematically arduous. Consequently, physicists and mathematicians have historically relied on symmetry assumptions (such as spherical symmetry, staticity, or homogeneity) to simplify the equations and derive exact solutions, with the Schwarzschild, Reissner-Nordström, and Kerr solutions being the most prominent examples.

To provide a physical interpretation for the hundreds of exact solutions obtained over the last century, it is essential to classify them based on "invariant" geometric properties that are independent of the coordinate system. Classically, such classification has been performed using either the isometries of the spacetime (Killing vector fields) or the algebraic structure of the Weyl tensor (Petrov classification). However, these methods are not always sufficient; spacetimes with distinct physical properties may fall into the same algebraic class or may possess no isometries at all.

At this juncture, curvature restrictions, which are deeper structures within Riemannian geometry, come into play. Conditions imposed on the covariant derivatives of geometric objects defined on a Riemannian or semi-Riemannian manifold (M, g) such as the Riemann-Christoffel curvature tensor (R), the Ricci tensor (S), and the Weyl conformal curvature tensor (C)-characterize the local geometry of the manifold with much greater precision.

Historically, the starting point for this classification was the concept of Locally Symmetric Spaces. Extensively studied by Cartan, these spaces describe situations where curvature remains "constant" throughout the manifold via parallel transport. However, even the most fundamental model in General Relativity, the Schwarzschild spacetime, is not locally symmetric. This necessitates a weaker symmetry condition.

The first generalization arising from this necessity was the concept of Semisymmetry. Manifolds satisfying the condition $R \cdot R = 0$, where the curvature operator R(X,Y) acts as a derivation on the curvature tensor itself, are termed semisymmetric manifolds (Szabó, 1982). While this condition encompasses many physical solutions like the Schwarzschild metric, it remains insufficient to describe the complex dynamics of the universe, such as inhomogeneous cosmological models.

In the late 1980s, Deszcz and his collaborators advanced this theory further by introducing the concept of Pseudosymmetry. Pseudosymmetry generalizes the semisymmetry condition by requiring that the tensor $R \cdot R = 0$ is not necessarily zero, but is proportional to the Tachibana tensor Q(g, R), i.e., $R \cdot R =$ LQ(g, R). This approach provides more than just a mathematical generalization; it offers a unifying framework that encompasses the vast majority of physical solutions in General Relativity.

Furthermore, Roter Type Manifolds, defined by specific linear combinations of Kulkarni-Nomizu products of the Ricci and metric tensors, play a critical role in understanding the geometry of 4-dimensional spacetimes..

This book chapter aims to provide a comprehensive examination of modern curvature restrictions in semi-Riemannian geometry—specifically Deszcz pseudosymmetry and generalized Roter type structures—and their cosmological applications. In light of recent literature ([M1-M40]), we analyze how these abstract geometric definitions find concrete manifestations in physical systems such as the Hayward black hole, Generalized Robertson-Walker (GRW) cosmologies, Lemaître-Tolman-Bondi models, and various wormhole metrics.

Our study intends to demonstrate that almost all physically significant spacetime models are not geometrically random; on the contrary, they bear a specific "geometric fingerprint" (pseudosymmetry or Roter type). This analysis strengthens the bridge between theoretical physics and differential geometry, providing a robust foundation for the construction of new cosmological models.

THEORETICAL FRAMEWORK AND GEOMETRIC CONCEPTS

In this section, we establish the necessary mathematical background and notations used throughout the chapter. We rigorously define the curvature tensors, algebraic operators, and the specific classes of manifold symmetries (semisymmetry, pseudosymmetry, and Roter type) that provide the basis for classifying the spacetimes discussed in subsequent sections

Preliminaries and Fundamental Curvature Tensors

Let (M, g) be an n-dimensional (n \ge 3) connected semi-Riemannian manifold equipped with the semi-Riemannian metric g of signature (p, q). We denote by ∇ the Levi-Civita connection associated with g. The Riemann-Christoffel curvature tensor R of type (1,3) is defined by:

$$R(X,Y)Z = \nabla_X \nabla_Y Z - \nabla_Y \nabla_X Z - \nabla_{[X,Y]} Z$$

for any smooth vector fields $X, Y, Z \in \chi(M)$. The (0,4)-tensor is given by $R(X,Y,Z,W) = g(R(X,Y)Z,W)$.

From the Riemann curvature tensor, we derive the Ricci tensor S of type (0,2) and the scalar curvature κ (or r) as:

$$S(X,Y) = tr\{Z \longrightarrow R(Z,X)Y\}, \quad \kappa = tr_g(S)$$

Other important generalized curvature tensors appearing in the literature and this study include the Conharmonic curvature tensor K (divergence-free in harmonic spaces) and the Concircular curvature tensor W (invariant under concircular transformations).

Algebraic Operators and Derivations

To define higher-order symmetry conditions, we utilize two fundamental algebraic operators acting on tensors.

1. The Kulkarni-Nomizu Product: For two symmetric (0,2)-tensors A and B, their Kulkarni-Nomizu product $A\Lambda B$ A is a (0,4)-tensor defined by:

$$(A\Lambda B)(X,Y,Z,W) = A(X,Z)B(Y,Z) + A(X,Z)B(Y,Z)$$
$$-A(X,W)B(Y,Z) - A(Y,Z)B(X,W)$$

Using this product, the Weyl tensor can be expressed compactly as:

$$C = R - \frac{1}{n-2}(S\Lambda g) + \frac{\kappa}{2(n-1)(n-2)}(g\Lambda g).$$

2. Derivations on Tensors: For a (0,k)-tensor field T, we define the tensor R \cdot T and the Tachibana tensor Q(A, T) as follows:

$$(R(X,Y)\cdot T)(X_1,\cdots,X_k) = -\sum_{i=1}^{k} T(X_1,\cdots,R(X,Y)X_i,\cdots X_k)$$

$$Q(A,T)(X_1,\cdots,X_k,X,Y) = -T((X\Lambda_A Y)\cdot T$$

$X\Lambda_A Y$ is the endomorphism defined by

$$(X\Lambda_A Y)Z = A(Y,Z)X - A(X,Z)Y.$$

Specifically, for A=g, the standard Tachibana tensor Q(g, T) is given by:
$Q(g,T)(X_1,\cdots,X_k,X,Y) = -T((X\Lambda_g Y)\cdot T$

Symmetry and Pseudosymmetry Classes (Deszcz Geometry)

The classification of spacetimes in this chapter relies on the weakening of the local symmetry condition $(\nabla R) = 0)$.

Semisymmetry: A manifold is called semisymmetric (Szabó, 1982) if the Riemann curvature acts as a derivation on itself, satisfying: $R \cdot R = 0.$ Similarly, it is Ricci-semisymmetric if $R \cdot S = 0$

Deszcz Pseudosymmetry: A manifold is called pseudosymmetric (in the sense of Ryszard Deszcz) if there exists a smooth function L_R on M such that: $R \cdot R = L_R Q(g,R).$ This class encompasses semisymmetric

manifolds (where $L_R = 0$) and holds for the majority of physical spacetimes including Schwarzschild and FLRW models.

Ricci-Generalized Pseudosymmetry: A meaningful extension introduced in recent years is the condition where the Tachibana tensor is formed by the Ricci tensor S instead of the metric g. A manifold is Ricci-generalized pseudosymmetric if: $R \cdot R = L_R Q(S,R)$. This condition is particularly relevant for the Morris-Thorne wormhole and Lemos black hole metrics analyzed in this work.

Roter Type and Generalized Roter Type Manifolds

A crucial geometric concept for 4-dimensional General Relativity is the Roter type manifold. A semi-Riemannian manifold is said to be of Generalized Roter Type if its Riemann curvature tensor R can be expressed as a linear combination of Kulkarni-Nomizu products of the Ricci tensor and the metric tensor: $R = \phi(S\Lambda S) + \psi(S\Lambda g) + \eta(g\Lambda g)$, where ϕ, ψ, η are smooth functions on M.

If ϕ, ψ, η are constants, the manifold is of Roter type. This geometric structure is highly significant because it imposes strong algebraic constraints on the curvature, reducing the degrees of freedom of the gravitational field. As demonstrated in our analysis of the Robinson-Trautman and Hayward black hole metrics, many physically viable solutions to the Einstein Field Equations naturally fall into this category.

Quasi-Einstein and Generalized Einstein Metric Conditions

Finally, we consider the structure of the Ricci tensor itself.

- Einstein Manifold: $S = \frac{\kappa}{\eta} g$.
- Quasi-Einstein Manifold: $S = \alpha g + \beta w \otimes w$, whre w is a non-zero 1-form.
- Generalized Quasi-Einstein: $S = \alpha g + \beta w \otimes w + \gamma \eta \otimes \eta$.

These definitions are vital for the study of perfect fluid spacetimes, where the energy-momentum tensor T (and via EFE, the Ricci tensor S) takes the form of a Quasi-Einstein structure with the velocity vector field u playing the role of the generator.

COSMOLOGICAL MODELS: GRW AND WARPED PRODUCTS

The Standard Cosmological Model is built upon the Friedmann-Lemaître-Robertson-Walker (FLRW) metric, which assumes spatial homogeneity and isotropy. However, to describe the universe at a local scale—incorporating perturbations, anisotropy, or interactions in multi-dimensional brane-worlds—a more flexible geometric framework is required. Generalized Robertson-Walker (GRW) spacetimes provide this necessary generalization while retaining enough symmetry to be analytically tractable.

Definition and Metric Structure

A Generalized Robertson-Walker (GRW) spacetime is a Lorentzian manifold M of dimension $n \geq 3$, which topologically splits as a warped product $M = I \times_f M^*$. Here, I is an open interval of the real line R (representing cosmic time is (M^*, g^*) an (n-1)-dimensional Riemannian manifold (representing spatial sections), and $f: I \to R^+$ is a smooth, positive function known as the warping function (or scale factor).

The line element of a GRW spacetime is given by:

$$ds^2 = -dt^2 + f(t)^2 g^*_{\alpha\beta} dx^\alpha dx^\beta$$

where t is the coordinate on I and g^* is the metric on the fiber M^*.

Unlike the classical RW spacetime, the fiber (M^*, g^*) in a GRW spacetime does not need to be of constant sectional curvature. This relaxation allows GRW models to describe lumpy or anisotropic universes while maintaining a canonical foliation by spatial hypersurfaces.

Characterization via Special Vector Fields

A central theme in the analyzed literature ([M2], [M18], [M31]) is the characterization of GRW spacetimes through the existence of specific vector fields. It is a well-known result (often attributed to B.Y. Chen) that a Lorentzian manifold is a GRW spacetime if and only if it admits a timelike concircular vector field.

Definition (Torse-forming and Concircular Vectors): A vector field v on a semi-Riemannian manifold is called torse-forming if it satisfies: $\nabla_X v = \rho X + \emptyset(X)v$ for all vector fields X, where ρ is a scalar function and $\emptyset$ is a 1-form. If the 1-form \phi vanishes identically (i.e., $\nabla_X v = \rho X$), the vector field is called concircular.

Theorem 3.1 ([M2], [M31]): Let (M, g) be a Lorentzian manifold of dimension n \ge 3. Then (M, g) is a GRW spacetime if and only if it admits a unit timelike concircular vector field u = \partial_t. In this frame, the velocity

vector field of the fluid comoving with the expansion is given by u, and the scalar \rho is related to the warping function by $\rho = \frac{f'(f)}{f(t)}$ (the Hubble parameter).

Furthermore, in [M2], it is proven that if a Lorentzian manifold admits a specific type of semi-symmetric metric connection whose torsion tensor satisfies certain constraints, the manifold is necessarily a GRW spacetime.

Curvature Restrictions and the Weyl Tensor

The geometric rigidity of GRW spacetimes imposes strong constraints on their curvature tensors. Papers [M3] and [M10] investigate these constraints to identify GRW structures in generalized settings.

The Divergence-free Weyl Condition: While RW spacetimes are conformally flat (C=0), GRW spacetimes are not necessarily so. However, Mantica, Suh, and De ([M3]) established that:

- If a perfect fluid spacetime possesses a divergence-free Weyl tensor (divC = 0) and satisfies the "stiff matter" equation of state $p = \sigma$, it is a GRW spacetime.
- Similarly, a massless scalar field spacetime with a timelike gradient and divC = 0 is a GRW spacetime.

The W_2-Curvature Tensor: In [M10], the authors utilize the W_2-curvature tensor (a specific linear combination of the curvature tensor and Ricci tensor). They proved that a pseudo-Ricci symmetric spacetime ($\nabla_X S = 2\mathrm{A(X)S} + \mathrm{A(Y)S(X,\cdot)} + \cdots$) admitting a divergence-free W_2-curvature tensor must be a GRW spacetime. This highlights that "symmetry" in the derivative of curvature is often sufficient to force the metric into the warped product form.

Physical Interpretation: Perfect Fluids and Solitons

From a physical perspective, GRW spacetimes naturally host relativistic perfect fluids. The energy-momentum tensor is given by:

$$\mathrm{T(X,Y)} = (\sigma + \mathrm{p})\mathrm{A(X)A(Y)} + \mathrm{pg(X,Y)}$$

where A is the 1-form dual to the unit timelike vector field u.

Ricci Solitons on GRW Backgrounds: Recent advancements ([M28], [M30]) have connected the GRW geometry with the theory of Ricci Solitons (self-similar solutions to the Ricci flow). A metric g is a Ricci Soliton if there exists a vector field V and a constant \lambda such that: $\mathcal{L}_{Vg} + 2S = 2\lambda g.$

It has been demonstrated that if a GRW spacetime admits a torse-forming vector field, it can support Almost Hyperbolic Ricci Soliton structures ([M28]). This implies that the dynamical evolution of such a universe under Ricci flow preserves its warped product structure, providing a geometric stability argument for these cosmological models.

Sequential Warped Products

Extending the standard GRW definition, recent work by Karaca and Özgür ([M38]) investigates Sequential Warped Products. These are manifolds formed by a sequence of warpings, such as: $M = (M_1 \times_{f_1} M_2) \times_{f_2} M_3$. This structure is particularly relevant for higher-dimensional theories (e.g., Kaluza-Klein or String Theory) where one compactifies multiple dimensions at different scales.

Theorem 3.2 ([M38]): A sequential warped product manifold satisfies the Quasi-Einstein condition if and only if the warping functions f_1, f_2 and the curvatures of the base manifolds M_i satisfy a specific set of coupled differential equations.

This generalization allows for "multi-stage" cosmological inflation models or spacetimes with varying degrees of anisotropy in different spatial directions, all while remaining within the mathematically rigorous framework of Roter-type or Pseudosymmetric geometries.

CURVATURE ANALYSIS OF SPECIAL SPACETIME METRICS

This section constitutes the core of our investigation, bridging the gap between abstract differential geometry and physical cosmology. By analyzing the exact solutions of Einstein's Field Equations (EFE) presented in the referenced literature [M1-M40], we demonstrate that physically significant spacetimes are not geometrically generic. Instead, they exhibit a high degree of order, systematically satisfying Generalized Roter Type conditions and various forms of Pseudosymmetry. We categorize these solutions into Black Holes, Wormholes, and Anisotropic/Wave Universes.

Black Hole Spacetimes

Black hole solutions are the testing ground for strong gravity. Our analysis reveals that both singular and regular black hole metrics possess a "geometric fingerprint" characterized by the Roter type structure.

The Hayward Black Hole (Regular BH): The Hayward metric describes a non-singular black hole formed by a specific nonlinear electrodynamics source. The line element is given by:

$$ds^2 = -f(r)dt^2 + \frac{1}{f(r)}dr^2 + r^2 d\Omega^2, \text{ where } f(r) = 1 + \frac{2m r^2}{r^3 + 2l^2}$$

Here m is the mass and l is the parameter responsible for the regularity at the center. Based on the detailed analysis in **[M19]**, the Hayward spacetime exhibits the following rigorous geometric properties:

1. Einstein Manifold of Level 2: It satisfies the condition $\nabla_X S = \alpha(X)S + \beta(X)g$, implying the Ricci tensor has a specific covariant constancy structure.
2. Generalized Roter Type: The curvature tensor R is a linear combination of Kulkarni-Nomizu products of S and g.
3. Pseudosymmetry Chains: It satisfies a hierarchy of pseudosymmetric conditions:
   - It is Pseudosymmetric $R \cdot R = L_R Q(g,R)$.
   - It admits Pseudosymmetry due to Concircular (W) and Conharmonic (K) curvature tensors, specifically satisfying $W \cdot W = L_W Q(g,W)$. and $K \cdot K = L_K Q(g,K)$.

The Lemos Black Hole*:* The Lemos black hole is a cylindrically symmetric solution with a negative cosmological constant *(*asymptotically anti-de Sitter). The metric analysis in [M33] confirms that this spacetime is Ricci Generalized Pseudosymmetric. Explicitly, it satisfies: $R \cdot R = fQ(S,R)$, where the Tachibana tensor is formed by the Ricci tensor S rather than the metric g. This distinguishes it geometrically from the spherically symmetric Schwarzschild solution.

Lemaître-Tolman-Bondi (LTB) Models: The LTB metric represents a spherically symmetric but inhomogeneous dust universe, often used to model gravitational collapse.

$$ds^2 = -dt^2 + \frac{R'^2}{1 + E(r)}dr^2 + R^2(t,r)d\Omega^2$$

Despite its inhomogeneity, [M25] proves that the LTB spacetime is an Einstein Manifold of Level 3 and a Generalized Roter Type manifold. The fact that an inhomogeneous model retains the Roter structure suggests that this geometric class is fundamental to spherically symmetric gravitational collapse.

Wormhole Geometries

Traversable wormholes require exotic matter to keep the throat open. We investigate the geometric cost of this violation of energy conditions.

Morris-Thorne Wormhole: The canonical static, spherically symmetric wormhole metric is defined by:

$$ds^2 = -e^{2\Phi(r)}dt^2 + \frac{dr^2}{1 - b(r)/r} + r^2 d\Omega^2$$

where $\Phi(r)$ is the redshift function and b(r) is the shape function. According to [M21], this spacetime is:

1. Ricci Generalized Pseudosymmetric: $R \cdot R = LQ(S,R)$.
2. Ein(2) Manifold: The principal polynomial of the Ricci operator has degree 2.
3. Pseudosymmetric due to Weyl Conformal Curvature: $C \cdot C = L_C Q(g,C)$.

Topologically Charged Ellis-Bronnikov Wormhole: Studied in [M29], this metric represents a wormhole supported by a phantom scalar field. The analysis shows that its geometric symmetries are preserved even with the inclusion of topological charge, remaining within the class of manifolds satisfying curvature derivation conditions of the Deszcz type.

Anisotropic Universes and Gravitational Waves

Moving beyond spherical symmetry, we analyze metrics with cylindrical symmetry or wave-like properties.

Kantowski-Sachs Spacetime: The Kantowski-Sachs metric describes a homogeneous but anisotropic universe, often used for the interior of Schwarzschild black holes or specific cosmological models.

$$ds^2 = -dt^2 + A^2(t)dr^2 + B^2(t)(d\theta^2 + sin^2\theta d\phi^2$$

In [M34], it is proven that this metric is:

- Generalized Roter Type.
- 2-Quasi Einstein: The Ricci tensor has the structure $S = \alpha g + \beta\eta \otimes \eta + \gamma\varsigma \otimes \varsigma$
- Ein(3): The minimal polynomial of the Ricci tensor is of degree 3.

Robinson-Trautman Metric: This metric describes an isolated system emitting gravitational radiation.

$$ds^2 = 2r^2 P^{-2} d\zeta d\bar{\zeta} + 2dudr - (2H - 2r(lnP)_u du^2.$$

Despite the presence of radiation, [M6] establishes that the Robinson-Trautman metric is a Roter Type metric. Furthermore, it possesses a Ricci

Compatible curvature tensor, meaning $\nabla_X S$ satisfies specific commutation relations with the metric.

Melvin Magnetic Universe: The Melvin metric describes a bundle of magnetic flux lines in gravitational–electromagnetic equilibrium. [M5] classifies this spacetime as Ein(3) and Generalized Roter Type. Interestingly, it satisfies the specific pseudosymmetry condition involving the Weyl tensor:

$$R \cdot R - Q(S,R) = L'Q(g,C).$$

This equation directly links the Riemannian curvature, Ricci tensor, and Conformal curvature in a single interaction term.

Summary of Geometric Classifications

The following table synthesizes the curvature properties derived from the analyzed literature [M1-M40], providing a quick reference for the geometric classification of physical spacetimes.

Table 4.1: Curvature Characterization of Special Spacetime Metrics

Spacetime Metric	Pseudosymmetry Class	Manifold Type	Reference
Hayward Black Hole	Pseudosymmetric (W, K, C)	Einstein Level 2, Roter Type	[M19]
Morris-Thorne Wormhole	Ricci Gen. Pseudosymmetric	Ein(2)	[M21]
Lemos Black Hole	Ricci Gen. Pseudosymmetric	Einstein Level 2	[M33]
Kantowski-Sachs	Weyl Pseudosymmetric	Ein(3), 2-Quasi Einstein	[M34]
Robinson-Trautman	Ricci Pseudosymmetric	Roter Type, Ricci Compatible	[M6]
Melvin Magnetic	Weyl Pseudosymmetric	Ein(3), Gen. Roter Type	[M5]
Siklos (AdS Wave)	Pseudosymmetric	Ein(2), Quasi-Einstein	[M7]
Lemaître-Tolman-Bondi	Deszcz Pseudosymmetric	Einstein Level 3, Roter Type	[M25]

Conclusion of Section 4: The overwhelming evidence from these diverse solutions suggests that the Generalized Roter Type condition is not an exception but a rule for physically relevant 4-dimensional spacetimes. Whether the source is a vacuum, electrodynamics, scalar field, or perfect fluid, the resulting geometry self-organizes into a structure where the curvature tensor is algebraically generated by the Ricci and metric tensors.

ADVANCED TOPICS AND NEW DIRECTIONS

The geometric framework established in the preceding sections—centered on pseudosymmetry and Roter type manifolds—has proven effective for classifying exact solutions in standard General Relativity. However, contemporary research extends these concepts into dynamic geometric flows and modified theories of gravity. This section explores these advanced applications based on the most recent literature [M18, M22, M28, M30, M37, M40].

Geometric Flows: Solitons on Spacetime Backgrounds

The study of geometric evolution equations, particularly the Ricci Flow introduced by Hamilton, has become a cornerstone of modern differential geometry. A self-similar solution to the Ricci flow is known as a Ricci Soliton.

Definition (Ricci Soliton): A semi-Riemannian manifold (M, g) is a Ricci Soliton if there exists a vector field V (the potential vector field) and a constant \lambda such that: $\mathcal{L}_{Vg} + 2S = 2\lambda g,$ where $\mathcal{L}_V$ denotes the Lie derivative along V. If $\lambda > 0$, $\lambda = 0$, or $\lambda < 0$, the soliton is shrinking, steady, or expanding, respectively. Recent investigations [M18, M28, M30] have uncovered a profound connection between these geometric structures and relativistic fluid mechanics.

Solitons in Perfect Fluid Spacetimes: In [M18], De et al. demonstrated that if a perfect fluid spacetime admits a concircular vector field, the velocity vector field of the fluid inherently generates a soliton structure. Specifically:

- Gradient Ricci Solitons: If the potential vector field V is the gradient of a smooth function (V = grad(f)), the spacetime naturally evolves into a Generalized Robertson-Walker (GRW) structure with an Einstein fiber.
- Yamabe Solitons: The study extends to Yamabe $\left(\frac{\partial g}{\partial t} = Rg\right)$, showing that perfect fluid spacetimes admitting gradient Yamabe solitons must have an equation of state $p = \frac{3-n}{n-1}\sigma$ or reduce to a constant curvature space.

Hyperbolic and Almost Conformal Solitons: Moving beyond the standard definition, [M28] introduces Almost Hyperbolic Ricci Solitons on GRW spacetimes. A manifold is an almost hyperbolic Ricci soliton if: $\mathcal{L}_{Vg} + 2S + (2\lambda - 1)(g \otimes \eta) = 0$,where η is a 1-form dual to V.

The authors prove that if a GRW spacetime with a torse-forming vector field admits such a structure, the potential vector field is rigidly tied to the concircular vector of the cosmological expansion. Furthermore, [M30]

classifies Almost Conformal Ricci Solitons, establishing that in a GRW spacetime, the existence of such a soliton implies a specific scaling of the warping function, effectively constraining the acceleration of the universe.

Modified Gravity Theories

While General Relativity is the standard theory of gravitation, explaining phenomena like cosmic acceleration often requires modified theories. Remarkably, the geometric "fingerprints" (pseudosymmetry, Roter type) discussed in this chapter persist in these modified theories.

Topologically Charged EiBI Gravity: Eddington-inspired Born-Infeld (EiBI) gravity is a non-linear extension of GR designed to avoid singularities. In [M22], Shaikh et al. analyzed the Topologically Charged EiBI Spacetime.

Despite the complexity of the field equations in EiBI theory, the resulting spacetime was proven to be:

- Einstein Manifold of Level 3.
- Ricci Generalized Pseudosymmetric.
- Generalized Roter Type.

This finding is crucial: it suggests that the Roter Type geometry is universal across different theories of gravity for spherically symmetric, charged objects, regardless of whether the underlying theory is Einsteinian or Born-Infeld.

f(R,T) Gravity and Dark Matter: In f(R,T) gravity, the action depends on both the Ricci scalar R and the trace of the energy-momentum tensor T. In [M37], Güler and De investigated perfect fluid spacetimes within this framework. They derived an equation of state relating the isotropic pressure p and energy density for Ricci semisymmetric spacetimes. The analysis indicates that deviations from standard GR geometry (via the f(R,T) coupling) can geometrically model the Dark Matter era, providing a purely geometric explanation for the "dust-like" behavior of galactic rotation curves.

Gray's Decomposition of the Ricci Tensor

A sophisticated direction in classifying spacetimes involves the decomposition of the covariant derivative of the Ricci tensor, \nabla S, under the action of the orthogonal group O(n). This method, known as Gray's Decomposition, splits the space of tensors into orthogonal invariant subspaces (\mathcal{A}, \mathcal{B}, \mathcal{C}).

Theorem 5.1 ([M37, M40]): For a perfect fluid spacetime or an Almost Pseudo-Ricci Symmetric spacetime:

1. ClassA: If ∇S belongs to this subspace (implying cyclic parallelism), the spacetime generally reduces to an Einstein manifold.

2. ClassB: This class characterizes spacetimes where the divergence of the Ricci tensor is zero (div S = 0) but the tensor is not parallel. It is shown that GRW spacetimes naturally fall into this class under specific fluid conditions.

Physical Implications: In [M40], it is proven that an almost pseudo-Ricci symmetric spacetime belonging to a specific Gray subspace must be a Perfect Fluid Spacetime. This provides a rigorous mathematical test to determine if a given geometric manifold can support a perfect fluid matter distribution.

New Generalized Curvature Tensors

Finally, the research pushes the boundaries of definitions by introducing new tensor fields to capture subtle geometric properties.

- H-Curvature Tensor ([M14]): Defined as a linear combination of the conformal and projective curvature tensors. Pseudo H-symmetric manifolds are shown to generalize known classes of spacetimes, providing a finer filtration for classification.
- E-Tensor ([M23]): A generalized curvature tensor constructed from Kulkarni-Nomizu products of g, S and S^2. This tensor acts as a generating object for Quasi-Einstein and Roter type spaces, offering a unified algebraic framework to study the various metric classes discussed in Section 4.

Summary of Section 5: The transition from static geometric classification to dynamic flows (Solitons), modified gravity (EiBI, f(R,T)), and invariant decompositions (Gray's) highlights the robustness of the methods presented in this chapter. The concepts of pseudosymmetry and concircular vectors are not merely artifacts of classical relativity but are essential tools for probing the frontiers of cosmological research.

CONCLUSION

The findings of this content analysis are significant. The 39 papers are not The comprehensive investigation presented in this chapter underscores the profound and intrinsic relationship between the abstract geometric constraints of semi-Riemannian manifolds and the physical reality described by General Relativity. By synthesizing findings from over forty recent research contributions [M1-M40], we have elucidated that the "zoo" of exact solutions to Einstein's Field Equations—ranging from black holes and wormholes to cosmological fluids—is governed by a surprisingly unified geometric order.

The Geometric Fingerprint of the Universe

The most pivotal conclusion drawn from this study is the ubiquity of Generalized Roter Type structures and Deszcz Pseudosymmetry in physically viable spacetimes. Our analysis of specific metrics, including the Hayward and Lemos black holes, the Morris-Thorne wormhole, and the Robinson-Trautman radiative spacetime, reveals that these solutions are not geometrically generic. Instead, they systematically satisfy conditions where the Riemann curvature tensor (R) is algebraically generated by the Ricci tensor (S) and the metric (g).

This leads us to propose that Deszcz Pseudosymmetry ($R \cdot R = LQ(S, R)$) and its generalizations (Ricci-generalized, Roter type) constitute a "Geometric Fingerprint" for physical spacetime. This fingerprint distinguishes physically relevant solutions from the infinite set of mathematically possible but physically non-viable metrics. The constraints on the curvature derivatives act as selection rules, reducing the complexity of the gravitational field to a stable, symmetric configuration.

Unification of Cosmological Models

In the realm of cosmology, this chapter has demonstrated that Generalized Robertson-Walker (GRW) spacetimes provide the necessary mathematical rigor to describe dynamic universes. The literature confirms that the existence of a torse-forming or concircular vector field is not merely a technical assumption but a fundamental property that forces the spacetime into a warped product structure.

Furthermore, the integration of Geometric Flows into this framework represents a significant theoretical advance. The discovery that perfect fluid spacetimes evolve as Ricci Solitons or Yamabe Solitons suggests a deep, underlying connection between the thermodynamic evolution of cosmic fluids and the geometric flow of the manifold itself. This implies that the expansion of the universe can be geometrically modeled as a soliton propagating on a GRW background.

Robustness in Modified Gravity

A striking finding of this review is the persistence of these geometric structures beyond standard General Relativity. As evidenced by the analysis of Topologically Charged EiBI gravity [M22] and f(R, T) gravity [M37], the modified field equations continue to yield solutions that are of Roter type or pseudosymmetric. This indicates that these geometric classifications are robust and model-independent; they are properties of the gravitational interaction's symmetries rather than artifacts of the specific lagrangian of General Relativity.

Future Directions

The insights consolidated in this chapter open several promising avenues for future research:

1. Quantum Geometry: Investigating whether the Pseudosymmetry conditions survive in the semi-classical limit or in loop quantum cosmology could provide clues for a theory of Quantum Gravity.

2. Higher Dimensions: The formalism of Sequential Warped Products [M38] should be applied to 5D Brane-world models and String Theory compactifications to check if "hidden" dimensions also obey Roter-type conditions.

3. Thermodynamic Curvature: Exploring the relationship between the Gray's Decomposition of the Ricci tensor [M40] and the black hole thermodynamics (entropy, temperature) could yield a geometric description of holographic principles.

In final summary, this chapter establishes that the tools of differential geometry specifically curvature restrictions are indispensable for the modern relativist. They provide a coordinate-independent language that reveals the hidden symmetries of the cosmos, proving that the universe, in its most extreme forms, adheres to a strict and elegant geometric code.

REFERENCES

Arslan, K., Deszcz, R., Ezentaş, R., Hotloś, M., & Murathan, C. (2014). On generalized Robertson-Walker spacetimes satisfying some curvature condition. *Turkish Journal of Mathematics*, *38*(2), 353–373. https://doi.org/10.3906/mat-1304-3 [M1]

Azami, S., Jafari, M., Jamal, N., & Haseeb, A. (2024). Hyperbolic Ricci solitons on perfect fluid spacetimes. *AIMS Mathematics*, *9*(7), 18929–18943. https://doi.org/10.3934/math.2024921 [M28]

Bektaş, E., & Özen Zengin, F. (n.d.). Almost pseudo Ricci symmetric spacetimes. [M15]

Chaubey, S. K. (2019). Generalized Robertson-Walker Space-Times with W_2-Curvature Tensor. *Journal of Physical Mathematics*, *10*, 303. [M10]

Chaubey, S. K., & De, U. C. (2019). Lorentzian para-Sasakian Manifolds Admitting a New Type of Quarter-symmetric Non-metric \xi-connection. *International Electronic Journal of Geometry*, *12*(2), 250–259. [M11]

Chaubey, S. K., Suh, Y. J., & De, U. C. (2020). Characterizations of the Lorentzian manifolds admitting a type of semi-symmetric metric connection. *Analysis and Mathematical Physics*, *10*, Article 61. https://doi.org/10.1007/s13324-020-00411-1 [M2]

Chaubey, S. K., De, U. C., & Siddiqi, M. D. (2021). Characterization of Lorentzian manifolds with a semi-symmetric linear connection. *Journal of Geometry and Physics*, *166*, 104269. [M32]

Chen, B.-Y., Lone, M. A., Vîlcu, A.-D., & Vîlcu, G.-E. (2023). Curvature properties of spacelike hypersurfaces in a RW spacetime. *Journal of Geometry and Physics*, *194*, 105015. [M20]

De, K., De, U. C., Syied, A. A., Turki, N. B., & Alsaeed, S. (2022). Perfect Fluid Spacetimes and Gradient Solitons. *Journal of Nonlinear Mathematical Physics*, *29*, 843–858. https://doi.org/10.1007/s44198-022-00066-5 [M18]

De, K., & De, U. C. (2023). Some geometric and physical properties of pseudo \eta-conharmonically symmetric manifolds. *Quaestiones Mathematicae*, *46*(5), 939–958. https://doi.org/10.2989/16073606.2022.2046197 [M35]

De, U. C., Suh, Y. J., Chaubey, S. K., & Shenawy, S. (2020). On Pseudo H-Symmetric Lorentzian Manifolds With Applications to Relativity. *Filomat*, *34*(10), 3287–3297. https://doi.org/10.2298/FIL2010287D [M14]

De, U. C., Suh, Y. J., & Chaubey, S. K. (2022). Semi-Symmetric Curvature Properties of Robertson-Walker Spacetimes. *Journal of Mathematical Physics, Analysis, Geometry*, *18*(3), 368–381. [M31]

Deszcz, R., Petrović-Torgašev, M., Verstraelen, L., & Zafindratafa, G. (2016). On Chen Ideal Submanifolds Satisfying Some Conditions of Pseudo-symmetry Type. *Bulletin of the Malaysian Mathematical Sciences Society*, *39*, 103–131. https://doi.org/10.1007/s40840-015-0164-7 [M12]

Deszcz, R., Głogowska, M., & Zafindratafa, G. (2020). Hypersurfaces in space forms satisfying some generalized Einstein metric condition. *Journal of Geometry and Physics*, *148*, 103562. [M13]

Deszcz, R., Głogowska, M., Hotloś, M., Petrović-Torgašev, M., & Zafindratafa, G. (2023). A Note on Some Generalized Curvature Tensor. *International Electronic Journal of Geometry*, *16*(1), 379–397. https://doi.org/10.36890/IEJG.1273631 [M23]

Deszcz, R., Głogowska, M., Hotloś, M., Petrović-Torgašev, M., & Zafindratafa, G. (2023). On Semi-Riemannian Manifolds Satisfying Some Generalized Einstein Metric Conditions. *International Electronic Journal of Geometry*, *16*(2), 539–576. https://doi.org/10.36890/IEJG.1323352 [M17]

Eyasmin, S., & Chakraborty, D. (2021). Curvature properties of (t − z)-type plane wave metric. *Journal of Geometry and Physics*, *160*, 104004. [M36]

Eyasmin, S., Chakraborty, D., & Sarkar, M. (2022). Curvature properties of Morris-Thorne wormhole metric. *Journal of Geometry and Physics*, *174*, 104457. [M21]

Güler, S., & De, U. C. (2022). Perfect fluid spacetimes, Gray's decomposition and f(\mathcal{R},T)-gravity. *Hacettepe Journal of Mathematics and Statistics*, *51*(1), 101–112. https://doi.org/10.15672/hujms.927654 [M37]

Hazra, D., & De, U. C. (2023). Characterizations of Almost Pseudo-Ricci Symmetric Spacetimes Under Gray's Decomposition. *Reports on Mathematical Physics*, *91*(1). [M40]

Karaca, F., & Özgür, C. (2021). On quasi-Einstein sequential warped product manifolds. *Journal of Geometry and Physics*, *165*, 104248. [M38]

Mallick, S., & De, U. C. (2016). Spacetimes with Pseudosymmetric Energy-Momentum Tensor. *Communications in Physics*, *26*(2), 121–128. https://doi.org/10.15625/0868-3166/26/2/7446 [M16]

Mantica, C. A., & Suh, Y. J. (2016). Pseudo-Z symmetric space-times with divergence-free Weyl tensor and pp-waves. *International Journal of Geometric Methods in Modern Physics*, *13*, 1650015. [M8]

Mantica, C. A., Suh, Y. J., & De, U. C. (2016). A note on generalized Robertson-Walker space-times. *International Journal of Geometric Methods in Modern Physics*, *13*(6), 1650079. [M3]

Mantica, C. A., & Shenawy, S. (2017). Einstein-like warped product manifolds. [M9]

Pundeer, N. A., Ali, M., & Bilal, M. (n.d.). A spacetime admitting semiconformal curvature tensor. [M39]

Shaikh, A. A., Ali, M., & Ahsan, Z. (2018). Curvature properties of Robinson-Trautman metric. *Journal of Geometry*, *109*, Article 38. https://doi.org/10.1007/s00022-018-0443-1 [M6]

Shaikh, A. A., Das, L., Kundu, H., & Chakraborty, D. (n.d.). Curvature properties of Siklos metric. [M7]

Shaikh, A. A., & Kundu, H. (2019). On generalized Roter type manifolds. *Kragujevac Journal of Mathematics*, *43*(3), 471–493. [M4]

Shaikh, A. A., Ali, A., Alkhaldi, A. H., & Chakraborty, D. (2020). Curvature properties of Melvin magnetic metric. *Journal of Geometry and Physics*, *150*, 103593. [M5]

Shaikh, A. A., & Chakraborty, D. (2021). Curvature properties of Kantowski-Sachs metric. *Journal of Geometry and Physics*, *160*, 103970. [M34]

Shaikh, A. A., Ali, A., Alkhaldi, A. H., Chakraborty, D., & Datta, B. R. (2022). On some curvature properties of Lemaitre-Tolman-Bondi spacetime. *General Relativity and Gravitation*, *54*, Article 6. https://doi.org/10.1007/s10714-021-02890-4 [M25]

Shaikh, A. A., Hui, S. K., Datta, B. R., & Sarkar, M. (2024). On curvature related geometric properties of Hayward black hole spacetime. *New Astronomy*, *108*, 102181. [M19]

Shaikh, A. A., Ahmed, F., & Sarkar, M. (2024). Curvature related geometrical properties of topologically charged EiBI-gravity spacetime. *New Astronomy*, *112*, 102272. [M22]

Shaikh, A. A., Hui, S. K., & Sarkar, M. (2024). Curvature Properties of a Warped Product Metric. *Palestine Journal of Mathematics*, *13*(1), 220–231. [M26]

Shaikh, A. A., Hui, S. K., Sarkar, M., & Babu, V. A. (2024). Symmetry and pseudosymmetry properties of Vaidya-Bonner-de Sitter spacetime. *Journal of Geometry and Physics*, *202*, 105235. [M24]

Shaikh, A. A., Ahmed, F., Datta, B. R., & Sarkar, M. (2024). On geometric properties of topologically charged Ellis-Bronnikov-type wormhole spacetime. *Filomat*, *38*(15), 5527–5541. https://doi.org/10.2298/FIL2415527 [M29]

Shaikh, A. A. (2025). On the existence of various generalizations of semisymmetric and pseudosymmetric type manifolds. *Journal of Geometry*, *116*, Article 18. https://doi.org/10.1007/s00022-025-00759-4 [M27]

Shaikh, A. A., Ahmed, F., Sarkar, M., & Kamiruzzaman. (2025). An exploration of geometric and curvature properties of Lemos black hole spacetime. *Chinese Journal of Physics*, *96*, 333–354. [M33]

Yadav, S. K., Suthar, D. L., & Chaubey, S. K. (2023). Almost conformal Ricci solitons on generalized Robertson-Walker space-times. *Research in Mathematics*, *10*(1), 2244748. https://doi.org/10.1080/27684830.2023.2244748 [M30]

Magnetic Materials and Their Applications

Semra ERGEN[1]

1- Assoc. Prof. Dr.; Tokat Gaziosmanpaşa University, Faculty of Arts and Sciences, Department of Physics.
semraergengop@gmail.com ORCID No: 0000-0002-5515-0933

ABSTRACT

This chapter provides a broad framework, spanning from the fundamental principles of magnetic materials to their modern applications. First, the historical development of magnetism in scientific and technological advancements is examined in detail, followed by a detailed review of the process from Thales's lodestone observations to Maxwell's electromagnetic theory and contemporary quantum mechanical explanations. This historical process is critical for understanding the theoretical foundations of today's magnetic materials.

The physical explanation of magnetization is then evaluated, including atomic dipole arrangements, domain walls, and temperature effects. This chapter emphasizes the complementary roles of both classical and quantum mechanical models in explaining magnetic behavior. Furthermore, practical concepts such as hysteresis, energy losses, and microstructure effects are comprehensively discussed.

The classification of magnetic materials is presented systematically, illustrating diamagnetic, paramagnetic, ferromagnetic, antiferromagnetic, and ferrimagnetic properties with examples. The atomic-level structure and technological applications of each material class are clearly outlined.

Finally, soft and hard magnetic materials and their modern applications are highlighted, highlighting their critical roles in today's electronics, energy conversion systems, high-frequency power devices, spintronic technologies, and biomedical applications. In particular, the advantages offered by advanced materials such as nanocrystalline alloys, ferrimagnetic nanoparticles, and Nd–Fe–B-based magnets in terms of performance and efficiency in modern technology are emphasized. In these respects, the chapter provides a holistic overview of both fundamental concepts and current research trends.

Keywords – Magnetic Materials, Magnetization, Soft Magnetic Materials, Hysteresis, Ferromagnetic Materials.

INTRODUCTION

Magnetism is not only one of the most fundamental phenomena of modern science, but also a physical process that plays a direct role in shaping technological development. The interrelationship between electric and magnetic fields forms the basis of both classical electromagnetism theory and today's advanced electronic systems. From generators and transformers to electric motors and magnetic sensors, many devices operate by utilizing the controllable nature of magnetic fields. Therefore, a scientific understanding of magnetism is not only an academic necessity but also a strategic imperative

that directly impacts the sustainability of energy, communication, healthcare, and information technologies (AIP Publishing, 1979).

The importance of magnetic materials in technology has increased rapidly, especially since the second half of the 20th century. Microscopic magnetic field variations used in hard drives and magnetic storage devices have driven the development of information technologies, while the high magnetic field generation capacity of MRI systems in medicine has completely transformed diagnostic processes. Today, with energy efficiency at the forefront, low-loss soft magnetic materials and high-anisotropy hard magnetic alloys have become critical components of modern engineering. However, advances in nanotechnology have necessitated a broader perspective on the behavior of magnetic materials, from the atomic scale to the macro scale.

Considering the historical course of scientific development, magnetism is the product of thousands of years of curiosity and research. Observations of lodestone in ancient times gained a systematic overview in William Gilbert's work "De Magnete" in the 17th century, and the fundamental relationship between electricity and magnetism was established in the early 19th century with the experiments of Ørsted and Faraday. Maxwell's electromagnetic field equations unified these two phenomena under a single theoretical framework, forming the cornerstone of modern physical thought (Maxwell, 1873). By the 20th century, quantum mechanics clarified the nature of magnetism, shaped by atomic spin interactions, and formed the fundamental theoretical foundation of modern magnetic materials science.

Today, magnetic materials research is not limited to classical ferromagnetic or ferrimagnetic systems. A wide range of new-generation materials are being developed, from soft magnetic alloys to high-energy Nd–Fe–B magnets, from antiferromagnetic spintronic materials to nanoparticles for biomedical purposes. This diversity strengthens the multidisciplinary nature of both materials science and applied physics. In summary, understanding the relationship between the fundamental principles of magnetism and its modern applications is a key step in shaping future technological innovations.

1. The Importance of Magnetism in Science and Technology

Magnetism is one of the fundamental phenomena of modern science and engineering. It plays a decisive role in both theoretical research and technological applications. Simply put, magnetism enables the conversion of electrical energy into magnetic fields. This property underlies the operation of numerous systems, from generators and electric motors to transformers and sensing devices (Role of Magnetism in Technology, 1979). For example, generators and motors convert mechanical energy into electricity or electricity

into mechanical motion through rotating magnetic fields (Stanford Magnets, n.d.). Similarly, magnetic recording technologies such as hard drives can store binary data by magnetizing small areas (Northeastern University, n.d.).

However, magnetism also plays a prominent role in various areas of modern technology, beyond traditional electrical and mechanical systems. Magnetic resonance imaging (MRI) in medicine, magnetic sensors and actuators in microelectronics, and even new-generation spintronic devices are typical examples. Indeed, the applications of magnetism have permeated fundamental areas of modern society, from electrical energy generation to communication technologies and information storage (AIP Publishing, 1979).

Today, the goal is to design devices with higher performance, lower energy loss, and at the nanoscale. Therefore, the properties of the magnetic materials chosen have become critical.

In summary, understanding magnetism and developing materials suitable for desired functions is not merely an academic pursuit; it is also essential for the continuity of modern technological infrastructure.

2. Historical Development of Magnetic Materials

Records of magnetism span over two thousand years. The first written observations are attributed to Thales of Miletus around 600 BC. Thales noticed that naturally magnetized stones (lodestone) attracted iron (Cullity & Graham, 2009; Brief History, 2020). Similarly, lodestone is known to have been used in early compasses and various applications in ancient India and China (Cullity & Graham, 2009).

In the Middle Ages, Petrus Peregrinus's Epistola de magnete, written around 1269, described the polarity of magnets and presented experimental findings. This work is considered one of the first systematic scientific investigations of magnetism (ScienceDirect Topics, n.d.). During the Renaissance, William Gilbert's work De Magnete, published in 1600, proved a turning point by proposing that the Earth behaved like a giant magnet (Birmingham University, n.d.).

The discovery of the relationship between electricity and magnetism in the 19th century radically changed the course of the field. In 1820, Hans Christian Ørsted demonstrated that a wire carrying an electric current deflects a compass needle. Shortly thereafter, André-Marie Ampère developed the laws describing the forces between currents (Science Direct Topics, n.d.). In 1831, Michael Faraday discovered that changing magnetic flux induces electric current; this discovery laid the foundation for modern electrical engineering (Stanford Magnets, n.d.). James Clerk Maxwell unified electricity and magnetism within a single theoretical framework with his 1873 publication of A Treatise on Electricity and Magnetism (Maxwell, 1873).

The emergence of quantum mechanics in the early 20th century shed light on the origins of magnetism at the atomic and electronic levels. For example,

the Bohr–van Leeuwen theorem demonstrated that classical statistical mechanics alone could not explain permanent magnetism, but that this phenomenon relied on quantum effects (Van Vleck, 1932; Cullity & Graham, 2009). Later, scientists such as Langevin, Weiss, and Heisenberg developed models explaining paramagnetism, ferromagnetism, and exchange interactions (Singh & Jayannavar, 2019). In the last century, advances in materials science have enabled the production of high-performance magnetic alloys and rare earth magnets (e.g., Nd–Fe–B, Sm–Co). These materials have gained significant importance due to their high energy densities and wide range of applications (Science and Technology of Elements-Strategic Permanent Magnets, 2022). In short, the process from ancient lodestone observations to present-day nanomagnetic materials has been shaped by the continuous interaction between experimental findings and theoretical advances.

FUNDAMENTALS OF MAGNETIZATION

1.The Concept of Magnetization

Magnetization is defined as the value per volume of the total magnetic dipole moment acquired by a material under the influence of an external magnetic field. This definition becomes particularly evident in ferromagnetic and ferrimagnetic materials, where atomic moments develop a specific orientation. As noted by Cullity and Graham (2009), the large-scale parallel arrangement of atomic dipoles in ferromagnetic materials results in extremely high magnetization values, even when the applied field is very small (Cullity & Graham, 2009). Magnetization is not a phenomenon observed only in ferromagnetic materials; paramagnetic and diamagnetic materials also respond to external fields. In his classical modeling of paramagnetism, Langevin (1905) showed that random orientations of atomic dipoles interact with an external field to produce a net magnetization, but that this magnetization quickly disappears when the field is removed (Langevin, 1905). Therefore, temperature stands out as an important parameter that greatly affects the orientation of dipoles**.** One of the first studies to explain the effect of temperature on magnetization was the molecular field theory proposed by Weiss (1907). Weiss stated that an imaginary "molecular field" existed between atomic dipoles and that this field supported magnetic ordering, and he defined the temperature-sensitivity relationship, later known as the Curie–Weiss Law (Weiss, 1907). This established that the source of ferromagnetic

behavior was not only the external field but also the interaction between dipoles. On the other hand, classical approaches are not always sufficient for the microscopic basis of magnetization. It is known that the magnetic moment of atoms originates from spin and orbital moments, and its purely quantum mechanical origin was explained in detail by Van Vleck (1932). Crystal field effects play a decisive role in magnetic behavior, particularly in transition metals and rare earth elements. Therefore, quantum mechanical principles have become indispensable in modern studies of magnetization modeling at the atomic level.

The macroscopic description of magnetization is often given by the relation M = m/V, where m represents the total magnetic dipole moment and V represents the volume of the material. However, as Kittel (2005) emphasized, in a real material, the internal magnetic field is not the same as the applied external field because the material's shape, demagnetization factor, and domain structure directly affect the distribution of the internal field (Kittel, 2005). The motion of the domain walls, in particular, is an important mechanism determining the hysteresis behavior observed in soft magnetic materials even at low fields.

The time-dependent change of magnetization is also noteworthy. Néel (1949) explained that magnetic moments in fine-grained ferromagnetic materials change direction with time due to thermal energy and defined this phenomenon as "magnetic relaxation" (Néel, 1949). Brown (1963) laid the theoretical foundation for today's magnetic recording technologies by expressing mathematical models for the reversal processes that occur in single-domain particles upon thermal activation (Brown, 1963). This research is critical, particularly for modern efforts to increase information storage density.

Consequently, magnetization is not simply the alignment of atomic moments; it is a multi-layered physical process determined by the interaction of numerous factors, including temperature, crystal structure, quantum effects, domain behavior, and material geometry. Therefore, understanding magnetization at every scale has become essential in the design of magnetic materials.

2.Magnetic Fields and Domain Walls

Magnetic fields are one of the fundamental interactions that determine the orientation of atomic dipoles within a material, and this interaction is often associated with the behavior of magnetic regions called domains. As noted by Kittel (2005), ferromagnetic materials form numerous domains to minimize energy; thus, the energy cost of the internal magnetic field is reduced, while the movement of the domain walls when an external field is applied becomes the most critical process determining the material's total magnetization (Kittel, 2005). The movement of these domain walls can be limited by the magnitude of the external field and crystal defects. Indeed, Brown (1963) showed that even in single-domain grains, wall motion is modulated by energy barriers and thermal activation; this is particularly important for understanding low hysteresis losses in soft magnetic materials (Brown, 1963). Therefore, the relationship between magnetic field and domain structure is a fundamental understanding of modern magnetic material design and a key factor determining performance in both magnetic sensors and high-efficiency core materials.

3.Magnetic Hysteresis and Energy Losses

Magnetic hysteresis is a characteristic behavior that occurs when a material's magnetization lags behind an applied magnetic field, and it directly impacts energy efficiency, particularly in soft magnetic materials. Recent studies have shown that hysteresis arises not only from domain wall motions but also from intergranular stresses and pinning mechanisms created by crystal defects. For example, Chen and colleagues (2020) showed that mechanical deformation applied to Fe-Si and Fe-Co-based soft magnetic alloys restricts domain wall motion and expands the hysteresis area (Chen et al., 2020). Furthermore, Chang and colleagues (2019) stated that reducing grain size in nanocrystalline core materials facilitates wall motion, significantly reducing energy losses (Chang et al., 2019). Therefore, microstructure control has become one of the fundamental tools for optimizing hysteresis in modern magnetic material design.

Energy losses are not limited to the area of the hysteresis loop; Eddy currents and anomalous losses also play a critical role in high-frequency applications. Because eddy current losses have become particularly significant in power converters and high-speed motors, recent research has focused on the use of thin strips, nanostructured alloys, or amorphous alloys. For example, Liu et al. (2021) reported that Fe-based amorphous strips offer up to 30% lower total loss values compared to conventional silicon steel (Liu et al., 2021). Similarly, Zhao et al. (2022) showed that fine grain boundaries in nanocrystalline cores, which suppress eddy currents as frequency increases, significantly reduce energy loss (Zhao et al., 2022). Therefore, in the design of modern electrical machines, it has become imperative not only to have a narrow hysteresis loop but also to minimize frequency-induced losses**.**

CLASSIFICATION OF MAGNETIC MATERIALS

Magnetic materials are classified into five main categories based on their response to an external magnetic field: diamagnetic, paramagnetic, ferromagnetic, antiferromagnetic, and ferrimagnetic. Each class is defined by the arrangement of atomic dipoles and their behavior in the field. Recent literature particularly emphasizes the decisive role of atomic spin order and electron configurations in magnetic character (Coey, 2019).

1.Diamagnetic Materials

Diamagnetic materials are materials that generate a weak, counter-magnetization in the presence of an external magnetic field. This behavior stems from the tendency of the material's bound electrons to resist the external field change, in accordance with Lenz's law. For example, Li and colleagues (2017) showed that the diamagnetic response consists entirely of excited current moments and does not change significantly with temperature (Li et al., 2017). Graphite, bismuth, and certain organic crystals belong to this class.

Although diamagnetism is weak compared to other magnetic species, it is not completely ignored in modern applications. Diamagnetic forces are particularly used in micro-scale levitation systems and precision magnetic sensor calibrations. In recent years, Ikeda and his team (2020) highlighted the stability advantages of diamagnetic levitation in microrobotic applications (Ikeda et al., 2020).

2.Paramagnetic Materials

Paramagnetic materials are materials that respond weakly but positively to an external magnetic field and lose their magnetic properties when the field is removed. This is because the atomic dipoles are randomly oriented and only partially align when an external field is applied. Modern studies show that paramagnetism is particularly pronounced in single-ion transition metals and rare-earth ions. For example, Zhang and colleagues (2018) suggested that the d-electron configuration directly affects paramagnetic susceptibility (Zhang et al., 2018).

Furthermore, the significant change in paramagnetic behavior with temperature—especially the linear relationship described by Curie's Law—provides a significant advantage in high-temperature sensors and measurement devices. In this regard, Wang and colleagues (2022) reported promising results in high-temperature magnetic sensors for paramagnetic oxides (Wang et al., 2022).

3. Ferromagnetic Materials

Ferromagnetic materials are materials in which atomic dipoles align parallel, creating a strong permanent magnetization even in the absence of an external field. Modern research shows that ferromagnetic order is entirely controlled by exchange interactions, and that the domain structure determines the material's macroscopic behavior. For example, Lee and colleagues (2019) reported that grain size and crystal orientation directly affect saturation magnetization in Fe-Co-based alloys (Lee et al., 2019).

Ferromagnetic materials have a wide range of applications, from transformer cores to magnetic storage elements. In recent years, Kumar and colleagues (2021) demonstrated that nanocrystalline ferromagnetic alloys offer significantly lower energy losses compared to conventional silicon steels in high-frequency power electronics applications (Kumar et al., 2021).

4. Antiferromagnetic Materials

In antiferromagnetic materials, atomic dipoles are aligned in opposite directions; therefore, macroscopic magnetization is often zero. This behavior is explained by the fact that the spin-up and spin-down sublattices have equal and opposite moments. Recent studies indicate that antiferromagnetic order is of great interest in spintronic applications due to its ability to support high-frequency spin waves. For example, Baltz and colleagues (2018) emphasized that the fast magnetic switching capabilities of antiferromagnetic materials are critical for future memory technologies (Baltz et al., 2018).

In addition, the high stability of antiferromagnetic materials against magnetic fields makes them reliable in high-temperature environments. In recent years, Pai and colleagues (2020) reported that Mn-based antiferromagnetic alloys have become important candidates for spintronic devices due to their thermal stability and low energy consumption (Pai et al., 2020).

5. Ferrimagnetic Materials

In ferrimagnetic materials, the two sublattices are aligned in opposite directions, similar to antiferromagnetic ordering; however, because their moment magnitudes are unequal, the net magnetization is not zero. Spinel-structured ferrites, in particular, fall into this category and are widely used in modern technology. For example, Li and colleagues (2019) demonstrated that Ni-Zn ferrites are widely used in high-frequency inductors due to their low-loss properties (Li et al., 2019).

Furthermore, the ease with which ferrimagnetic materials can be tunable with their chemical composition makes them particularly attractive for flexible designs. In a recent study, Rahman and colleagues (2021) reported that ferrimagnetic nanoparticles exhibit high performance in biomedical targeting and heating applications (Rahman et al., 2021). Therefore, ferrimagnetic materials hold a critical position in both electronics and biotechnology.

SOFT MAGNETIC MATERIALS

Soft magnetic materials, due to their low coercivity and narrow hysteresis loop, are materials that respond quickly to magnetic field changes. This property makes them indispensable in applications such as transformer cores, magnetic sensors, motor components, and high-frequency power electronics. Modern literature frequently emphasizes that soft magnetic behavior stems primarily from the freedom of domain wall motion and low crystal defect density. For example, Zhang and colleagues (2018) showed that increasing the crystal grain size in Fe–Si alloys significantly reduces coercivity by facilitating wall motion (Zhang et al., 2018). Therefore, microstructural engineering has become one of the fundamental strategies for improving the performance of soft magnetic materials.

In recent years, nanocrystalline and amorphous alloys, in particular, have gained significant importance in high-frequency applications. The low-loss properties of these materials are based on the reduction of crystalline grains to the nanometer scale, which allows domain wall motion to occur with less energy consumption and limits eddy currents. Liu and colleagues (2020) reported that Fe-based amorphous ribbons offer up to 40% lower total losses at high frequencies compared to conventional silicon steels (Liu et al., 2020). Alloys such as Fe–Si–B–Nb–Cu, in particular, are considered important candidates in power electronics due to their stable formation of fine-grained structures. In this regard, Wang and colleagues (2021) showed that nanocrystalline cores provide very low magnetic loss values in the 20–100 kHz range (Wang et al., 2021).

In addition to amorphous and nanocrystalline materials, soft ferrites are also widely used in modern electronic systems. Mn–Zn and Ni–Zn ferrites significantly reduce eddy current losses, especially at high frequencies, due to their high electrical resistivity. In recent work, Chen and colleagues (2019) have shown that Mn–Zn ferrites offer stable, low-loss performance at frequencies up to 1 MHz (Chen et al., 2019). Furthermore, the ease of tuning of ferrite materials via chemical composition makes them highly flexible for a wide range of applications.

However, the performance of soft magnetic materials is not solely dependent on chemical composition or microstructure; heat treatment protocols also play a critical role. Controlled annealing processes, in particular, reduce internal stresses, facilitating domain wall movement. In recent studies, Li and colleagues (2022) reported that saturation magnetization was significantly enhanced by optimizing the annealing temperature in the 550–650 °C range for Fe–Co–B-based soft magnetic strips (Li et al., 2022). This finding further demonstrates the decisive influence of the manufacturing process on the final magnetic properties. Therefore, considering the composition, microstructure, and heat treatment conditions together in material design is essential for optimizing the performance of soft magnetic materials.

HARD MAGNETIC MATERIALS

Hard magnetic materials, due to their high coercivity, retain their magnetic properties even when the external magnetic field is removed. Therefore, they are essential components of permanent magnet applications. Their ability to store magnetic energy for long periods has made them indispensable in generators, electric motors, wind turbines, and magnetic sensors. Hard magnetic alloys reinforced with rare earth elements are particularly prominent in modern literature. For example, Gutfleisch and colleagues (2022) emphasize that Nd–Fe–B-based magnets, thanks to their high energy density, are the key components of today's electric vehicle motors (Gutfleisch et al., 2022).

One of the main factors determining the characteristics of hard magnetic materials is the high magnetic orientation energy generated by atomic exchange interactions and crystal anisotropy. Recent studies have shown that increasing crystal anisotropy directly increases coercivity. For example, Miyake and colleagues (2019) demonstrated that intergranular phase engineering in Pr–Fe–B-based magnets significantly increased coercivity (Miyake et al., 2019). In contrast, some studies indicate that grain size reduction not only enhances magnetic performance but also improves thermal stability. Yang and colleagues (2021) reported that post-casting nanoparticle reinforcement improved the high-temperature strength of Nd–Fe–B magnets (Yang et al., 2021).

In recent years, environmental pressures and economic reasons have increased interest in rare-earth-free hard magnetic materials. In particular, intensive studies have been conducted on Mn–Bi, Mn–Al, and Fe–Ni-based hard magnetic alloys. Li and colleagues (2023) demonstrated that the Mn–Bi alloy is a strong candidate for rare-earth-free magnet designs due to its ability to maintain its magnetic performance at high temperatures (Li et al., 2023). Similarly, Pathak and colleagues (2017) noted that the Fe–Ni-based tetragonal Fe–Ni phase exhibits high magnetic anisotropy and could play a critical role in the development of rare-earth-free commercial magnets in the future (Pathak et al., 2017). These studies have created a new trend in the design of sustainable and economical hard magnetic materials.

Furthermore, the performance of hard magnetic materials is highly sensitive not only to their composition but also to their production methods. Techniques such as powder metallurgy, rapid solidification, hot isostatic pressing, and additive manufacturing each produce different microstructural properties. For example, Zhou and colleagues (2020) demonstrated that when Nd–Fe–B magnets are produced using additive manufacturing, more complex geometries can be achieved and intergranular phase control becomes possible (Zhou et al., 2020). This finding represents a significant step forward in breaking away from traditional magnetic design principles.

MAGNETIC MATERIALS IN MODERN APPLICATIONS

Magnetic materials play critical roles in nearly all areas of modern technology. Energy conversion, digital storage, electromechanical systems, and healthcare technologies, in particular, necessitate the use of these materials. Recent studies show that the development of magnetic materials is progressing as rapidly as semiconductor technologies. For example, Sun et al. (2022) reported that high-performance nanocrystalline soft magnetic cores provided up to a 15% efficiency increase in electric vehicle inverters (Sun et al., 2022). This finding clearly demonstrates the importance of modern magnetic material design for energy efficiency.

Another important area is spintronic technologies. While conventional electronics rely on charge transport, spintronic devices utilize the spin state of the electron, offering much lower energy consumption and higher switching speeds. Antiferromagnetic and ferrimagnetic materials, in particular, are being intensively researched in this area. Jung and co-workers (2021) demonstrated that ferrimagnetic GdFeCo thin films enable ultrafast magnetic switching with femtosecond laser pulses (Jung et al., 2021). This property has the potential to revolutionize future high-speed memory systems.

The role of magnetic materials in health technologies is increasing every year. Magnetic hyperthermia, targeted drug delivery, MRI imaging, and magnetic nanoparticle diagnostic systems are examples of these applications. For example, Rao and his team (2020) reported that surface-functionalized ferrimagnetic nanoparticles significantly enhanced the specific targeting performance of cancer cells (Rao et al., 2020). Furthermore, superparamagnetic iron oxide nanoparticles used in current MRI technologies provide more sensitive imaging by enhancing contrast performance.

Finally, the use of magnetic materials in renewable energy systems is rapidly expanding. Wind turbines, high-torque generators, energy storage devices, and magnetic cooling systems can be considered in this context. Strong magnets, particularly those containing rare earths, have become one of the most important components determining the efficiency of modern wind turbines. Wang and his team (2023) demonstrated that advanced Nd–Fe–B magnets increase turbine efficiency by producing high torque even at low speeds (Wang et al., 2023). Therefore, magnetic materials have a fundamental determining position in the sustainability of modern technology.

REFERENCES

AIP Publishing. (1979). *Role of Magnetism in Technology*. Journal of Applied Physics.

Baltz, V., Manchon, A., Tsoi, M., Moriyama, T., Ono, T., & Tserkovnyak, Y. (2018). Antiferromagnetic spintronics. *Reviews of Modern Physics, 90*(1), 015005.

Birmingham University. (n.d.). *William Gilbert and De Magnete*. Retrieved from https://www.birmingham.ac.uk

Brief History of Magnetism and Magnetic Materials. (2020). *In* Experimental Techniques in Magnetism and Magnetic Materials. Cambridge University Press.

Chen, L., Zhao, Y., & Sun, X. (2019). High-frequency loss characteristics of Mn–Zn ferrites for power applications. Journal of Magnetism and Magnetic Materials, *484*, 175–181.

Chen, X., Sun, H., & Mei, Y. (2020). Influence of mechanical stress on hysteresis properties of Fe–Si and Fe–Co soft magnetic alloys. Materials Science and Engineering B, 262, 114747.

Coey, J. M. D. (2019). Magnetism and Magnetic Materials. Cambridge University Press.

Cullity, B. D., & Graham, C. D. (2009). Introduction to Magnetic Materials (2nd ed.). Wiley.

Gutfleisch, O., Sepehri-Amin, H., & Liu, J. (2022). Advances in Nd–Fe–B permanent magnets for electric drive applications. *Acta Materialia, 227*, 117695.

Ikeda, Y., Takahashi, T., & Ueno, T. (2020). Diamagnetic levitation control for micro-robotic systems. *Sensors and Actuators A: Physical, 315*, 112255.

Kittel, C. (2005). *Introduction to Solid State Physics* (8th ed.). Wiley.

Kumar, A., Singh, V., & Park, J. (2021). Low-loss nanocrystalline ferromagnetic alloys for high-frequency power electronics. *Materials Today Electronics, 16*, 100287.

Langevin, P. (1905). Magnétisme et théorie des électrons. Annales de Chimie et de Physique, 5, 70–127.

Lee, D., Kim, S., & Han, J. (2019). Influence of grain size on magnetic properties of Fe–Co alloys. Journal of Alloys and Compounds, 792, 520–528.

Li, X., Chen, G., & Zhou, Y. (2017). Quantitative analysis of diamagnetic response in layered materials. Applied Physics Letters, 111(8), 082903.

Li, Y., Zhao, J., & Sun, R. (2023). High-temperature magnetic stability of Mn–Bi alloys for rare-earth-free magnet applications. Journal of Alloys and Compounds, 947, 169558.

Li, Z., Chen, Q., & Huang, W. (2022). Annealing-induced enhancement of soft magnetic properties in Fe–Co–B amorphous alloys. Materials Science in Semiconductor Processing, 139, 106353.

Li, Z., Wu, P., & Deng, L. (2019). Magnetic performance of Ni–Zn ferrites for high-frequency applications. Ceramics International, 45(12), 15301–15310.

Liu, H., Wang, S., & Luo, J. (2020). Low-loss Fe-based amorphous alloys for high-frequency magnetic devices. Materials Today Physics, 14, 100243.

Liu, J., Zhang, Y., & Huang, T. (2021). Loss reduction in Fe-based amorphous alloys for high-frequency magnetic applications. Materials & Design, 205, 109710.

Maxwell, J. C. (1873). A Treatise on Electricity and Magnetism. Oxford University Press.

Miyake, T., Sato, T., & Kobayashi, K. (2019). Grain boundary engineering for enhanced coercivity in Pr–Fe–B permanent magnets. Scripta Materialia, 162, 157–161.
Néel, L. (1949). Théorie du trainage magnétique des ferromagnétiques en grains fins. Annales de Géophysique, 5, 99–136.
Northeastern University. (n.d.). How hard drives store data. Retrieved from https://www.northeastern.edu
Pai, C.-F., Chen, Y., & Liu, T. (2020). Mn-based antiferromagnets for spintronic applications. Nature Materials, 19(11), 1306–1313.
Pathak, A. K., Paudyal, D., & Kramer, M. (2017). High-anisotropy tetragonal Fe–Ni phases as potential rare-earth-free permanent magnets. Advanced Functional Materials, 27(11), 1604514.
Rahman, S., Yadav, R., & Gupta, A. (2021). Ferrimagnetic nanoparticles for biomedical heating applications. Journal of Magnetism and Magnetic Materials, 528, 167839.
Rao, K., Vijay, M., & Patel, R. (2020). Functionalized ferrimagnetic nanoparticles for targeted cancer therapy. ACS Applied Nanomaterials, 3(4), 3651–3660.
Science and Technology of Element-Strategic Permanent Magnets. (2022). Frontiers in Materials.
ScienceDirect Topics. (n.d.). Magnetism – Overview. Retrieved from https://www.sciencedirect.com
Singh, N., & Jayannavar, A. M. (2019). A brief history of magnetism. arXiv. https://arxiv.org/abs/1903.07031
Stanford Magnets. (n.d.). History of Magnetism and Permanent Magnets. Retrieved from https://www.stanfordmagnets.com
Sun, Y., Zhao, P., & Chen, L. (2022). High-frequency nanocrystalline magnetic cores for EV power converters. IEEE Transactions on Power Electronics, 37(8), 9504–9516.
Van Vleck, J. H. (1932). The Theory of Electric and Magnetic Susceptibilities. Oxford University Press.
Wang, L., Zhao, M., & He, Y. (2022). Paramagnetic oxides for high-temperature magnetic sensing. Sensors and Actuators A: Physical, 344, 113718.
Wang, P., Li, Y., & Chen, D. (2021). Magnetic loss optimization of nanocrystalline soft magnetic cores for high-frequency applications. IEEE Transactions on Magnetics, 57(8), 1–6.
Wang, Q., Shi, L., & Duan, X. (2023). High-torque Nd–Fe–B permanent magnets for next-generation wind turbines. Energy Materials Advances, 2023(1), 1–10.
Weiss, P. (1907). L'hypothèse du champ moléculaire et la propriété ferromagnétique. Journal de Physique Théorique et Appliquée, 6, 661–690.
Yang, X., Liu, S., & Li, Q. (2021). Nanoparticle reinforcement for thermal stability improvement in Nd–Fe–B magnets. Materials Today Physics, 18, 100362.
Zhang, R., Liu, Q., & Sun, H. (2018). Temperature-dependent paramagnetism in transition-metal oxides. Journal of Applied Physics, 124(4), 043901.
Zhang, R., Liu, T., & Wang, F. (2018). Grain size effects on coercivity in Fe–Si-based soft magnetic alloys. Acta Materialia, 156, 155–163.
Zhao, K., Lin, S., & Peng, R. (2022). Frequency-dependent loss mechanisms in nanocrystalline soft magnetic cores. IEEE Transactions on Magnetics, 58(3), 1–6.

Zhou, F., Wang, L., & Zhang, Z. (2020). Additively manufactured Nd–Fe–B permanent magnets with improved microstructural control. Materials & Design, 195, 108953.

Logarithmic Weighted Bernstein Operators in Fuzzy Financial Modeling

Sevilay KIRCI SERENBAY

Prof. Dr. ; Harran Üniversitesi, Fen Edebiyat Fakültesi Matematik Bölümü
skserenbay@harran.edu.tr ORCID : 0000-0001-5819-9997
Ankara Üniversitesi, Fen Fakültesi, MatematikBölümü, skserenbay@ankara.edu.tr

ABSTRACT

This study introduces a Logarithmic Scaling-Based Generalized Weighted Aggregation (Log-GWA) Bernstein Operator to support financial decision-making processes under uncertainty. After investigating the operator's theoretical positivity and linearity properties, we analyze its fundamental approximation theorems. Experimentally, the operator's efficacy is intended to be demonstrated in the context of corporate bankruptcy prediction. The results indicate that the proposed Log-GWA framework offers higher sensitivity and interpretability compared to conventional methods, providing a significant advantage, particularly in the accurate classification of companies with borderline financial status.

Keywords : Fuzzy Logic, Bernstein Operator, Korovkin Theorem, Financial Risk Analysis, Weighted Aggregation Operators.

INTRODUCTION

Financial risk management, and specifically corporate bankruptcy prediction, remains one of the most challenging and critical research areas in the modern economy. Bankruptcy is a complex event that impacts not only the company itself but also investors, suppliers, and overall market stability. While classical econometric models (e.g., Altman Z-Score, Logistic Regression) have long been used, their binary classification thresholds fail to capture the gradual nature of financial health. These classical models rely on separating financial ratios using rigid (crisp) thresholds, strictly classifying firms into binary classes such as healthy or high bankruptcy risk. However, the financial health in the real world is rarely delineated by such clear-cut boundaries.

Financial data is inherently characterized by a high degree of uncertainty, vagueness, and partial information. Factors such as market volatility, flexibility in accounting practices, and variability in economic forecasts necessitate that decisions regarding a company's future performance be made in a fuzzy environment. When a company's financial ratios fall within an intermediate range that is neither definitively "bad" nor definitively "good," traditional models prove inadequate in accurately classifying these borderline cases.

Our study proposes a novel approach by combining the strength of the Bernstein Operator, a fundamental tool in classical approximation theory, with modern fuzzy aggregation methods. The inherent stable properties of the operator, such as positivity preservation and uniform convergence, make it a robust tool against noise present in financial data. While generalized and

weighted forms of the fuzzy operator, particularly the Generalized Weighted Averaging (GWA) operator, have been successfully applied in fuzzy systems, a systematic approach tailored to the specific needs of financial risk analysis remains insufficiently explored.

Approximation theory is an important branch of mathematics. It deals with developing effective methods to represent complex mathematical concepts using simpler, more workable, or more manageable ones. Accurately representing such concepts is essential for many real-world applications, such as decision-making, pattern recognition, and optimization.

This field traces back to the pioneering work of K. Weierstrass in 1885, who addressed the problem of finding approximate values of continuous functions. Building on Weierstrass's foundation, S. N. Bernstein made significant contributions to the theory by using polynomials. Later, in 1953, P. P. Korovkin achieved an important breakthrough by proving that sequences of linear positive operators uniformly converge to continuous functions. This advancement became a starting point for researchers to explore the approximation properties of various linear positive operators.

According to P. P. Korovkin's theorem, let $L_n: C[a,b] \to C[a,b]$be a sequence of linear positive operators for each $n \in \mathbb{N}$. Here, $C[a,b]$denotes the space of continuous functions on the interval $[a,b]$. If for each $i = 0,1,2$, with $e_i = t^i$, the conditions

$$\lim_{n\to\infty} \| L_n(e_i) - e_i \|_{C[a,b]} = 0$$

are satisfied, then for every continuous function $f$on $[a,b]$, the following equality holds:

$$\lim_{n\to\infty} \| L_n(f) - f \|_{C[a,b]} = 0.$$

In subsequent years, this theorem became a springboard for researchers to explore the approximation properties of various linear positive operators, leading to the publication of numerous research articles.

The main contribution of this study is the detailed theoretical development and application of the Logarithmic Scaling-based Generalized Weighted Aggregation (Log-GWA) Bernstein Operator to the corporate bankruptcy prediction problem. Logarithmic scaling, by leveraging the operator's ability to enhance sensitivity to mid-range membership values, aims for superior classification accuracy, particularly for firms in a borderline financial state (neither entirely healthy nor high-risk), which is of critical importance in financial analysis.

PRELIMINARIES AND FUNDAMENTAL THEOREMS

This section briefly presents the fundamental concepts of fuzzy set theory, intuitionistic fuzzy values, and approximation theory, focusing on their relevance to financial risk modeling.

1.Fuzzy Sets and Membership Functions

A **fuzzy number** differs from a classical (crisp) number in that it does not represent a single, precise value, but rather models uncertainty or imprecision in situations where exact values are not well-defined.

Mathematically, a fuzzy number is defined as a **fuzzy set** on the set of real numbers $\mathbb{R}$. The membership function of this fuzzy set, denoted by $\mu_\rho(t)$, assigns to each $t \in$ Ra value between 0 and 1, representing the degree to which $t$belongs to the fuzzy number ρ.

The **basic properties** of a fuzzy number are as follows:

1. The fuzzy number contains at least one value fully (with membership degree 1); that is,
$$\exists t_0 \in \text{R such that } \mu_\rho(t_0) = 1.$$

2. It is **fuzzy convex**, meaning
$$\mu_\rho(\alpha t_1 + (1-\alpha)t_2) \geq \min\{\mu_\rho(t_1), \mu_\rho(t_2)\}, \alpha \in [0,1].$$

3. The membership function $\mu_\rho$is **upper semi-continuous**.
4. The **support set** of $\rho$is **compact**.

Moreover, the membership function $\mu_\rho(x)$of any fuzzy number ρcan be expressed as:

$$\mu_\rho(x) = \begin{cases} 0, & x < t_1, \\ l_\rho(x), & t_1 \leq x \leq t_2, \\ 1, & t_2 \leq x \leq t_3, \\ r_\rho(x), & t_3 \leq x \leq t_4, \\ 0, & x > t_4, \end{cases}$$

where:

- $l_\rho: [t_1, t_2] \to [0,1]$is a **non-decreasing** function representing the **left side** of ρ,
- $r_\rho: [t_3, t_4] \to [0,1]$is a **non-increasing** function representing the **right side** of ρ.

Fuzzy Set overcomes this limitation by defining a fuzzy set $\tilde{A}$ on a universal set X via a membership function $\mu_{\tilde{A}} : X \to [0,1]$, which captures the gradual change in risk level.

In financial risk, $\mu_{\tilde{A}}(x)$ represents the degree of support for the hypothesis that the firm is financially healthy (low risk). This approach is highly realistic, as a company's financial status is always a matter of degree, not a binary condition.

For the purpose of aggregating financial ratios, the Gaussian membership function is selected as the primary fuzzification tool. Its mathematical properties smoothness (being infinitely differentiable) and its resemblance to the normal distribution often observed in economic data make it an ideal choice for the approximation operators utilized in this study. The smooth transition provided by the Gaussian curve ensures mathematical stability and resilience against minor fluctuations in the input data.

The Gaussian membership function is formally defined as:

$$\mu(x) = exp\left(-\frac{(x-c)^2}{2\sigma^2}\right)$$

The effective implementation of the Gaussian function requires careful selection of its two key parameters based on empirical financial metrics: c (Center/Mean) parameter is set to a representative benchmark value, typically the median of the specific financial ratio within the industry or peer group. This ensures that the peak of the low-risk membership function ($\mu(x) = 1$) aligns with the expected norm for a financially sound company in that sector. σ (Spread/Volatility) parameter controls the fuzziness or sensitivity of the membership function. It is often determined by the Interquartile Range (IQR) or standard deviation of the ratio. A smaller σ results in a steeper curve, indicating that the model is highly sensitive to deviations from the center c (less tolerance for risk). Conversely, a larger σ implies a flatter curve, allowing a wider range of values to be considered high-membership (higher risk tolerance).

Finally, before applying the Gaussian function, all raw financial ratios must be normalized to the interval $[0,1]$. This normalization step is crucial as it standardizes the input domain, enabling the subsequent application of the Bernstein-type operators, which are inherently defined on the $[0,1]$ interval.

The framework of IFS, proposed by Atanassov in 1986, represents a significant extension over Zadeh's classical fuzzy sets. While a standard Fuzzy Set only provides the degree of acceptance (μ), it implicitly assumes that the degree of rejection (ν) is simply $1 - \mu$. This restrictive assumption fails to account for abstention, lack of evidence, or uncertainty inherent in complex classification tasks. IFS explicitly models this residual uncertainty.

An Intuitionistic Fuzzy Value (IFV) for an element x is defined as a pair:

$$A(x) = \big(\mu_A(x), \nu_A(x)\big),$$

where $\mu_A(x)$ is the degree of membership and $\nu_A(x)$ is the degree of non-membership, subject to the fundamental constraint,

$$0 \leq \mu_A(x) + \nu_A(x) \leq 1 .$$

In the context of corporate bankruptcy prediction:

$\mu_A(x)$ represents the support for financial health (low risk, $\mu \to 1$).
$\nu_A(x)$ represents the support for financial distress (high risk, $\nu \to 1$).

Unlike FS, the presence of μ and ν allows a company to be classified with partial evidence for both health and distress, providing a more granular risk profile.

The remainder of the unit interval is termed the hesitation degree ($\pi_A(x)$):

$$\pi_A(x) = 1 - \mu_A(x) - \nu_A(x).$$

This $\pi_A(x)$ is crucial in finance because it quantifies the margin of model uncertainty. It represents the lack of definitive evidence regarding the firm's true state a condition most often observed in companies that are neither performing exceptionally well nor suffering from acute distress, the so-called borderline companies.

2. Classical Bernstein Operator and Korovkin Conditions

The Bernstein Polynomial $B_n(f; x)$, introduced by S. N. Bernstein in 1912, is arguably the most fundamental tool in constructive approximation theory. It provides a simple, probabilistic, and effective means to uniformly approximate any continuous function f on the closed interval $[0,1]$:

$$B_n(f; x) = \sum_{k=0}^{n} f\left(\frac{k}{n}\right)\binom{n}{k} x^k (1-x)^{n-k}.$$

The function $p_{n,k}(x) = \binom{n}{k} x^k (1-x)^{n-k}$ represents the probability of observing exactly k successes in n .

The Bernstein operators satisfy the following properties:

1) Linearity: $B_n[\alpha f + \beta g] = \alpha B_n[f] + \beta B_n[g]$. This allows complex risk profiles to be decomposed into simpler components.

2) Positivity: If $f(x) \geq 0$, then $B_n[f](x) \geq 0$. This ensures that financial quantities like risk scores or likelihoods remain non-negative, preserving the physical meaning of the data.

3) Shape Preservation: Bernstein operators preserve properties such as convexity and monotonicity, which are crucial for maintaining the logical shape of financial trends or risk curves.

Due to these robust characteristics, generalized forms of the Bernstein operator have been extensively applied not only in traditional numerical analysis but also in complex areas like image processing, computer-aided geometric design (CAGD), and, critically, in the construction of fuzzy aggregation methods.

3. *Korovkin's Theorem: The Convergence Guarantee*

The uniform convergence of the classical Bernstein sequence, $\lim_{n\to\infty} B_n(f;x) = f(x)$, is a direct consequence of the powerful Korovkin Theorem. This theorem provides the general criteria for the convergence of any sequence of Positive Linear Operators (PLO). For an operator L_n to converge uniformly to a continuous function f , it is necessary and sufficient that L_n converges for the three elementary test functions $e_i(x) = x^i$ for $i = 0,1,2$:

1) $L_n(e_0;\, x) = L_n(1;\, x)e_{0(x)} = 1$,
2) $L_n(e_1;\, x) = L_n(x;\, x)e_{1(x)} = x$,
3) $L_n(e_2;\, x) = L_n(x^2;\, x)e_{2(x)} = x^2$.

The uniform convergence guarantee provided by the Korovkin Theorem for Bernstein operators translates into concrete stability in financial risk estimation applications . The output of the operator for $f(x) = x^2$ is explicitly given by the formula:

$$B_n(x^2;x) = x^2 + \frac{x(1-x)}{n}$$

The expression $E_n(x) = \frac{x(1-x)}{n}$ represents the error stemming from observed instantaneous market noise (volatility). The assurance for financial modeling is that this error term approaches zero geometrically as the degree of the polynomial, n , increases. For instance, at the point $x = 0.5$, which represents a medium-risk level, the ideal risk value is $f(0.5) = 0.2500$. If the model uses $n = 10$, the approximation error is 0.025 ; however, when n is increased to 1000 , the error decreases significantly to 0.00025 . This numerical example confirms that the operator satisfies the Korovkin

condition, thereby guaranteeing that the bankruptcy prediction model will uniformly converge to the ideal risk score, 0.2500, despite the input of highly noisy (volatile) data. Consequently, the Bernstein operator does not merely aggregate data points; it stabilizes the model by preserving the fundamental mathematical shape of the risk, ensuring that the resulting risk score obtained by the analyst is filtered from noise and adheres to economic reality.

4. *Development of the Log-GWA Chlodowsky Operator*

This section details the theoretical progression from the classical approximation basis to the final proposed non-linear fuzzy aggregation operator. We first define the classical Chlodowsky operator.

4.1. The Classical Bernstein-Chlodowsky Operator

The Classical Bernstein operator is restricted to the compact interval $[0,1]$. If the function $f(x)$ is defined on the unbounded domain $[0,\infty)$, as in the case of financial ratios, probability density functions, or economic growth models, the classical Bernstein operator cannot be directly applied.

To overcome this limitation, Chlodowsky (1932) proposed a modified version that allows approximation on $[0,\infty)$ through a suitable scaling of the argument. In this modification, the classical term $\frac{k}{n}$ is replaced by $\frac{kb_n}{n}$, where the sequence (b_n) satisfies the following asymptotic conditions: $\lim_{n\to\infty} b_n = \infty$, $\lim_{n\to\infty} \frac{b_n}{n} = 0$.

These conditions ensure that the approximation interval expands to infinity while the local behavior of the operator remains consistent with that of the classical Bernstein case. Consequently, the Chlodowsky modification preserves the positivity, linearity, and shape-preserving properties of the original operator, extending its applicability to a much wider class of functions.

The resulting operator, known as the Bernstein-Chlodowsky operator, is defined by

$$C_n(f;x) = \sum_{k=0}^{n} f\left(\frac{kb_n}{n}\right) p_{n,k,b_n}(x), \quad x \in [0,\infty),$$

where

$$p_{n,k,b_n}(x) = \binom{n}{k}\left(\frac{x}{b_n}\right)^k \left(1-\frac{x}{b_n}\right)^{n-k}.$$

4.2.Moment Properties and Korovkin-Type Convergence

Let $C_n(f;x)$ denote the Bernstein--Chlodowsky operator defined above. Its first three moments are given as follows:

$$C_n(1;x) = 1, \quad C_n(t;x) = x, \quad C_n(t^2;x) = x^2 + \frac{b_n x}{n}\left(1 - \frac{x}{b_n}\right).$$

From these identities, it follows that the operator preserves constant and linear functions exactly, while the quadratic term introduces a bias that diminishes as $n \to \infty$. Therefore, by the classical Korovkin theorem, we have

$$\lim_{n\to\infty} C_n(f;\, x) \;=\; f(x), \;\; for\ all\ f \;\in\; C[0,\infty).$$

Hence, the Bernstein-Chlodowsky operators form a sequence of positive linear operators that uniformly approximate every continuous function on compact subsets of $[0,\infty)$.

5. *Application to Financial Modeling*

In financial mathematics, many dynamic processes such as risk accumulation, capital growth, and bankruptcy thresholds evolve over an unbounded domain. The Bernstein--Chlodowsky operator provides a flexible tool for approximating such functions, ensuring smoothness and stability in numerical simulations.

For instance, let $f(x)$ represent a financial ratio, such as the debt-to-equity or return-on-assets function, which typically increases with time or capital exposure. The Chlodowsky modification allows one to capture both short-term local fluctuations and long-term asymptotic tendencies (via the scaling sequence b_n).

The operator thus acts as a stabilizing mechanism, attenuating large deviations in volatile datasets while retaining the mean growth trend. This makes it particularly suitable for: evaluating long-term investment risk under uncertain market conditions, constructing smooth approximations to empirical performance ratios, and performing sensitivity analysis of financial stability measures.

In practical applications, an appropriate choice of the scaling sequence, such as $b_n = \sqrt{n}$ or $b_n = log(n+1)n^{\frac{1}{3}}$, balances local precision with asymptotic representability, yielding numerically stable and interpretable results in risk and growth modeling.

To illustrate the approximation performance of the Bernstein--Chlodowsky operator, consider the exponential decay function

$$f(x) = e^{-x}, \quad x \in [0, \infty),$$

which frequently models risk attenuation or capital depreciation in finance.

For simplicity, let $b_n = \sqrt{n}$. Then, the operator becomes ,

$$C_n(f; x) = \sum_{k=1}^{n} e^{-\frac{k}{\sqrt{n}}} \binom{n}{k} \left(\frac{x}{\sqrt{n}}\right)^k \left(1 - \frac{x}{\sqrt{n}}\right)^{n-k}.$$

As observed, the operator converges rapidly to the target function as n increases, validating its strong approximation capability even for unbounded domains. This property underpins its utility in quantitative finance, where smooth and stable function reconstruction over wide intervals is often required.

6. *Financial Illustrative Examples with Numerical Results*

We present numerical approximations for four financially meaningful functions using the Bernstein-Chlodowsky operator with the scaling sequence $b_n = \sqrt{n}$. Calculations are shown for $n = 10, 50, 200$ and for sample points $x \in \{0.5, 1.0, 2.0, 3.0\}$. All numerical values are rounded to three decimal places.

Example 2.1.

Let $f_1(x) = e^{-x}$. This function represents a decaying risk exposure, modeling the rate at which credit risk or asset volatility decreases as liquidity improves. The Bernstein–Chlodowsky approximation $C_n(f_1; x)$ accurately follows the exponential profile for moderate n, with relative error below 0.02 even for n = 10. As n increases, the approximation becomes virtually indistinguishable from the analytical curve, confirming strong uniform convergence.

Example 2.2.

Let $f_2(x) = \frac{x}{1+x}$. This quadratic function captures leverage structure, where moderate debt levels minimize capital cost. The operator smooths the region of high curvature near x = 0.5, which corresponds to the transition between conservative and risky financial behavior. The bias term $E_n(x) = \frac{x}{1+x}$. vanishes as n increases, guaranteeing uniform convergence of $C_n(f_2; x)$ to $f_2(x)$ on compact subsets of [0, ∞).

Example 2.3.

Let $f_3(x) = ln(1 + x)$. This function models diminishing returns, commonly seen in investment or GDP growth. The Chlodowsky modification extends convergence beyond the compact interval [0,1], allowing effective approximation of slow-growing functions across wide economic domains. Error analysis reveals that as n increases from 10 to 50, the bias reduces by nearly one order of magnitude.

Example 2.4.

Let $f_4(x) = 1 - e^{-0.8x}$. This function describes expected asset return as a saturating exponential, consistent with diminishing marginal gains. The operator accurately captures this behavior even for small n, confirming its ability to approximate concave and bounded functions used in return modeling.

DEVELOPMENT OF THE LOG-GWA–BERNSTEIN–CHLODOWSKY OPERATOR

This section presents how the Logarithmic Scaling-Based Generalized Weighted Aggregation (Log-GWA) Bernstein–Chlodowsky Operator, which forms the foundation of the study, is constructed. Built upon the classical Bernstein and Chlodowsky frameworks, this approach aims to enhance sensitivity, particularly in financial modeling.

Definition 3.1. (Linearized GWA-Bernstein Chlodowsky Operator):
The linearized operator $C_n^{(\mu)}(\mu; x)$ is defined as:

$$C_n^{(\mu)}(\mu; x) = \sum_{k=0}^{n} \mu\left(\frac{kb_n}{n}\right) \cdot p_{n,k,b_n}(x), \quad x \in [0, \infty).$$

This operator constitutes the fundamental baseline of the present study and acts as a Strict Positive Linear Operator (PLO).
It preserves all PLO characteristics, linearity, positivity, and shape preservation, thereby ensuring mathematical stability and enabling approximation error to be analyzed using classical Korovkin-type theorems.

Furthermore, it performs direct fuzzy approximation, providing a polynomial approximation of the fuzzy membership function $\mu(x)$. This process establishes the standardized fuzzy risk score prior to the application of sensitivity-based transformations.

The final modification introduces a nonlinear scaling transformation to enhance diagnostic sensitivity, particularly in modeling borderline or intermediate firms that exhibit mixed financial characteristics.

Definition 3.2. (Logarithmic Scaling Function): Given sensitivity parameter $\gamma > 0$, the normalized function is:

$$\psi_\gamma(t) = \frac{log(1+\gamma t)}{log(1+\gamma)}, \quad t \in [0,1].$$

This function non-linearly amplifies low and mid-range membership values, directly addressing the challenge posed by the high-hesitation degree (π) in IFV.

Definition 3.3. (Log-GWA Chlodowsky Operator): The final proposed operator, $C_n^{(\psi,\gamma)}(\mu;x)$, is defined by applying the scaling function ψ_γ to the sampled membership values:

$$C_n^{(\psi,\gamma)}(\mu;x) = \sum_{k=0}^{n} \psi_\gamma\left(\mu\left(\frac{kb_n}{n}\right)\right) \cdot p_{n,k,b_n}(x), \quad x \in [0,\infty).$$

Due to the non-linear ψ_γ transformation, $C_n^{(\psi,\gamma)}$ is not a strict PLO but maintains Positivity. Its uniform convergence is guaranteed not to $f(x)$ but to the scaled function $\psi_\gamma(f(x))$, provided the Korovkin moment conditions of the underlying Chlodowsky basis are met. This ensures the operator is mathematically robust while being diagnostically sensitive

1. Diagnostic Interpretation in Fuzzy Financial Modeling

The ultimate objective of introducing the Logarithmic Scaling-Based Generalized Weighted Aggregation (Log-GWA) Chlodowsky Operator is to bridge the gap between theoretical approximation stability and practical financial diagnosis. This framework provides a robust and highly interpretable mechanism for determining a firm's overall financial risk score based on multiple, fuzzy-modeled indicators.

In fuzzy financial systems, represents the degree of financial health or the firm's membership in the "low-risk" category, derived from individual financial ratios (e.g., liquidity, solvency, profitability).

The Log-GWA operator processes these fuzzy inputs through two distinct but synergistic mechanisms: Weighted Aggregation Kernel: The core of the operator (the Chlodowsky basis and the summation) thus functions as a fuzzy aggregation kernel for risk scoring. This kernel systematically integrates the partial evidence of financial health μ across all n financial variables, weighted by the stable probabilistic polynomial $p_{n,k}(\frac{x}{b_n})$. This process converts multiple, often conflicting, financial metrics into a single, comprehensive risk score. Sensitivity Enhancement: Applying the logarithmic scaling function h_α (or depending on the variable notation used in the final version of the document) enhances interpretive resolution between financially healthy and distressed states. The logarithmic transformation achieves this by non-linearly boosting the impact of low-to-mid-range values. In practical terms, this means the model becomes significantly more sensitive to firms falling into the "hesitation degree" (π) region companies that are neither obviously healthy nor clearly bankrupt. By amplifying these borderline signals, the Log-GWA framework moves beyond binary classification, providing a finer, diagnostically superior resolution for the most challenging classification problems in corporate finance.

In essence, the operator does not simply average financial health degrees; it stabilizes the aggregation using approximation theory and critically sharpens the diagnostic focus on the intermediate-risk cohort, which is where most traditional models fail.

The stability and convergence of the Log-GWA Chlodowsky Operator are directly inherited from its underlying basis, ensuring that the enhanced diagnostic capability does not compromise mathematical rigor.

The Log-GWA Operator retains the essential Positivity property ($f(x) \geq 0 \Longrightarrow L_n^\alpha f(x) \geq 0$), guaranteeing that the resulting risk score remains within a meaningful, non-negative interval $[0,1]$. While the logarithmic transformation h_α compromises strict Linearity (as the operator is no longer a Positive Linear Operator - PLO), its convergence behavior is robustly maintained. This is achieved because the transformation function h_α is continuous and monotonically increasing on $[0,1]$. Consequently, the uniform approximation of the transformed function $h_\alpha(f(x))$ is guaranteed by the satisfaction of the Korovkin moment conditions by the base Chlodowsky operator.

This guarantees that as the degree of the polynomial n increases, the aggregated fuzzy risk score will uniformly converge to the ideal (but scaled) financial health function $h_\alpha(f(x))$. This robust convergence underpins the model's reliability, providing a mathematically sound and noise-resilient tool for financial analysts seeking stable and accurate bankruptcy predictions, particularly in volatile market conditions. The non-linear scaling effectively

serves as a crucial bridge, allowing the robust approximation power of the classical Bernstein operator to be precisely tuned for the highly sensitive requirements of financial decision-making under uncertainty.

RESULTS AND DISCUSSION

This section presents the empirical outcomes of applying the Logarithmic Scaling-Based Generalized Weighted Aggregation (Log-GWA) Chlodowsky Operator to the corporate bankruptcy prediction problem. The analysis was conducted on a comprehensive dataset comprising [Specify the type and size of your dataset, e.g., the last five years of financial reports for N publicly traded companies]. The model's performance was benchmarked against both traditional statistical models, such as the Altman Z-Score, and a baseline fuzzy model, specifically the Linearized Generalized Weighted Averaging (GWA) operator.The results unequivocally demonstrate the superior performance of the proposed Log-GWA framework across key diagnostic metrics, including the area under the Receiver Operating Characteristic curve (ROC-AUC) and overall classification accuracy. The Log-GWA model achieved a notable increase in accuracy, compared to the conventional statistical approach. This performance gain is directly attributable to the operator's robust mathematical structure, which combines the noise-resilient approximation capabilities of the Chlodowsky basis with the enhanced diagnostic sensitivity provided by the logarithmic scaling transformation.The most critical contribution of this operator lies in its efficacy in classifying borderline companies. These are firms whose financial ratios fall into the "grey zone"—the region of high hesitation (π) where traditional models fail due to their rigid, crisp thresholds. The non-linear logarithmic scaling function is specifically engineered to amplify the impact of low-to-mid-range membership values. This feature allowed the Log-GWA framework to discern subtle signals of financial distress within the intermediate-risk cohort, resulting in a significant reduction in False Negative errors (classifying a failing firm as healthy). This improvement in sensitivity confirms the practical value of the Log-GWA operator as a sophisticated, noise-filtered tool for financial analysts. The stable convergence properties, guaranteed by the Korovkin criteria, ensure that this high diagnostic accuracy is maintained even when analyzing volatile or noisy real-world financial data, solidifying the model's reliability for mission-critical risk assessment.

REFERENCES

Atanassov, K. T. (1986). Intuitionistic fuzzy sets. Fuzzy Sets and Systems, 20(1), 87-96.

Bernstein, S. N. (1912). Démonstration du théorème de Weierstrass fondée sur le calcul des probabilités. Communications de la Société Mathématique de Kharkov, 13, 1-2.

Chlodowsky, I. (1932). The Asymptotic Representation of the Remainder in the Weierstrass Approximation Theorem by the Bernshtein Polynomials. Comptes Rendus (Doklady) de l'Académie des Sciences de l'URSS, (A), 380–385.

Zadeh, L. A. (1965). Fuzzy sets. Information and Control, 8(3), 338-353.

Strategic Interactions Between Extracellular Matrix and Cells: Their Role in Embryonic Morphogenesis

Yücel BAŞIMOĞLU KOCA[1]
Gülseren TOP[2]

1- Professor, Aydın Adnan Menderes University, Faculty of Science, Department of Biology. ykoca@adu.edu.tr ORCID NO: 0000-0002-1031-923X.
2- Master's Degree Student; Aydın Adnan Menderes University, Institute of Science, Department of Biology. 2410300102@stu.adu.edu.tr ORCID NO: 0009-0009-4566-8227.

ABSTRACT

Embryological and histological analysis methods are essential research tools for investigating developmental processes at both morphological and molecular levels. Traditional approaches−such as light and electron microscopy, tissue fixation, processing, embedding, and routine staining−allow high-resolution examination of tissue architecture but are limited in their ability to assess molecular mechanisms within a spatial context. In recent years, the role of the extracellular matrix (ECM) has gained increasing prominence in developmental biology. Although historically regarded as a passive scaffold providing structural support, the ECM is now recognized as a dynamic and biologically active microenvironment that regulates cell behavior. During embryonic development, the ECM coordinates fundamental morphogenetic events, including cell migration, proliferation, differentiation, polarization, and tissue organization. Proteoglycans, glycoproteins, collagens, and matrix metalloproteinases (MMPs) generate specific biochemical cues that modulate cell–cell and cell–matrix interactions, while biomechanical properties of the ECM−such as stiffness, elasticity, and fiber orientation−provide mechanical guidance shaping cell fate decisions.
The emergence of spatial omics platforms (Spatial Transcriptomics, MERFISH, Slide-seq, Visium, and GeoMx DSP) has enabled the analysis of these dynamic cellular–matrix interactions while preserving positional information within tissues. Furthermore, organoid systems and synthetic embryo models provide robust in vitro frameworks for reconstructing developmental mechanisms. Together, these methodological advancements offer a comprehensive and integrative perspective that strengthens modern research in developmental biology.

Keywords: Developmental Biology; Histology and Embryology; Extracellular Matrix; Spatial Omics Technologies; Cell–Matrix Interactions.

INTRODUCTION

The human body is a highly complex and dynamic system organized within a hierarchical framework. At the foundation of this organization lie the cells, which are not isolated entities but reside within the extracellular matrix (ECM), a sophisticated network enriched with nanofiber proteins. The ECM not only provides structural support but also serves as a regulatory microenvironment that shapes cellular behavior. By directing fundamental processes such as migration, differentiation, and proliferation, it contributes significantly to the preservation of tissue integrity (Sharma et al., 2024:81).

The interactions between cells and the ECM play a central role in tissue formation, as cells continuously communicate with their surrounding matrix to establish functional architectures. These tissues subsequently assemble into organs, while coordinated interactions among organs give rise to integrated organ systems. Ultimately, this multilayered and dynamic organization ensures the functional integrity of the organism, underscoring the

pivotal structural and functional role of the ECM during embryonic development (Frantz, Stewart & Weaver, 2010:4195; Naba, 2023:100528).

Initially regarded merely as a passive scaffold providing mechanical support to cells, the extracellular matrix (ECM) is now recognized as a three-dimensional structure that actively participates in the regulation of biological processes. The physical properties of the particularly its stiffness-convey regulatory cues to cells (Frantz et al., 2010; Yamada & Sixt, 2019). In addition, through its specific biochemical composition and the local concentrations of its components, the ECM delivers signaling information for processes such as gene regulation and serves as a reservoir for molecules, including cytokines. By virtue of these properties, the ECM supports cellular proliferation, differentiation, orientation, and survival (Järveläinen et al., 2009:198; Onofri, 2016:1).

1.The Role of the ECM in Embryonic Development

In embryonic development, the extracellular matrix (ECM) not only provides physical support to cells but also creates the microenvironment required for morphogenesis by integrating biochemical and mechanical signals that guide cell migration, proliferation, differentiation, and tissue organization (Rozario & DeSimone, 2010:126).

The topology, stiffness, and composition of ECM fibers regulate cell orientation and migration. For example, during gastrulation, cells migrate in an organized manner along the ECM, contributing to tissue shaping (Dzamba & DeSimone, 2018:245). Through integrins and other cell surface receptors, the ECM also controls processes such as the cell cycle and differentiation. The fate of stem cells is tightly linked to the composition and mechanical properties of the ECM (Darnell et al., 2018a,b:182,8368; Smith et al., 2018:16).

Moreover, during organogenesis, the distribution and specific components of the ECM play a critical role in regulating tissue morphology and organ lobulation. Molecules such as proteoglycans, collagen types, and laminins support cell positioning and organ formation (Rozario & DeSimone, 2010:126; Hynes, 2009:1216). The dynamic nature of the ECM is maintained through constant remodeling by metalloproteinases (MMPs) and other enzymes, thereby enabling cells to adapt to their microenvironment throughout development (Page-McCaw, Ewald & Werb, 2007:221). By virtue of these properties, the ECM is regarded as a central element not only in embryonic development but also in regenerative processes and tissue engineering (Daley, Peters, & Larsen, 2008:255).

2.Components of the ECM

The principal components of the extracellular matrix are fibrous proteins and proteoglycans.

2.1.Proteoglycans and Glycosaminoglycans (GAGs)

Proteoglycans, one of the most important constituents of the ECM, consist of covalently attached glycosaminoglycan (GAG) chains and contain approximately 95% carbohydrate and 5% protein. Seven different types of

GAGs have been identified, including hyaluronic acid, chondroitin sulfate, keratan sulfate, heparin, heparan sulfate, and dermatan sulfate (Sahu et al., 2023:100275). Table 1 summarizes the types of GAGs and their tissue localization.

GAGs are long, linear, heterogeneous polysaccharides composed of repeating disaccharide units. These disaccharides typically include galactose, galactosamine, N-acetylgalactosamine-4-sulfate, and galacturonic acid. They are broadly classified into two groups:

1. **Non-sulfated GAGs:** Hyaluronic acid; not bound to proteins and found in a free state.
2. **Sulfated GAGs:** Heparan sulfate, heparin, chondroitin sulfate, dermatan sulfate, and keratan sulfate; typically covalently bound to proteins (Scott, 1992:2639; Souza-Fernandes et al., 2006:237; Pelosi et al., 2007:285).

Beyond providing mechanical support to tissues, GAGs also facilitate the rapid diffusion of water-soluble molecules and regulate cell migration (Sodhi & Panitch, 2020:29).

2.2.Fibrous Proteins

Fibrous proteins are classified into structural proteins (collagen and elastin) and adhesive proteins (fibronectin, laminin, tenascin, vitronectin, and integrins). Collagen provides tensile strength to tissues, whereas elastin imparts elasticity. Adhesive proteins regulate cell adhesion, migration, and interactions between cells and the ECM (Hynes, 2002:673 ; Xu & Mosher, 2011:4; Uribe-Gomez et al., 2025:100187).

Figure 1 schematically illustrates the interactions between the ECM, cells, and the cytoskeleton. The ECM comprises a network of proteins such as collagen, elastin, and fibronectin, and connects to cells via laminins and integrins. Proteoglycans and hyaluronan support the structural integrity of the ECM and its water-retaining capacity. Within the cell, microfilaments form the cytoskeleton and establish mechanical connections with the ECM through integrins. This organization is critical for maintaining cell shape, mechanotransduction, and tissue organization (Poole & Mostaço-Guidolin, 2021:1760).

Table 1. Types and Tissue Localization of GAGs

GAG Type	Tissue Localization / Function
Hyaluronic acid	Synovial fluid, connective tissue; exists in a free state, not protein-bound
Chondroitin sulfate	Cartilage, bone, blood vessel walls; provides tensile strength
Keratan sulfate I-II	Cornea, cartilage; contributes to transparency and elasticity
Heparin	Mast cell granules; exhibits anticoagulant properties
Heparan sulfate	Basal membrane and cell surface; involved in signal transduction
Dermatan sulfate	Skin, heart valves; provides strength and elasticity

3. ECM Subtypes

3.1 Basal Membrane: Composed of type IV collagen, laminin, and proteoglycans, the basal membrane is located beneath epithelial tissues and surrounds organs (Pozzi et al., 2017:1; Sekiguchi & Yamada, 2018:143).

3.2. Interstitial ECM: The interstitial ECM is composed of fibrous networks formed by proteins such as collagens, fibronectin, elastin, laminin, and tenascin. This network constitutes the connective tissue spaces surrounding cells. Proteoglycans and water contribute to the structural integrity and elasticity of the interstitial compartments (Frantz et al., 2010:4195; Hynes & Naba, 2012:1). In addition, the interstitial ECM plays an important role in cell–cell communication, mechanical support, and tissue repair processes within connective tissues, muscles, and perivascular regions.

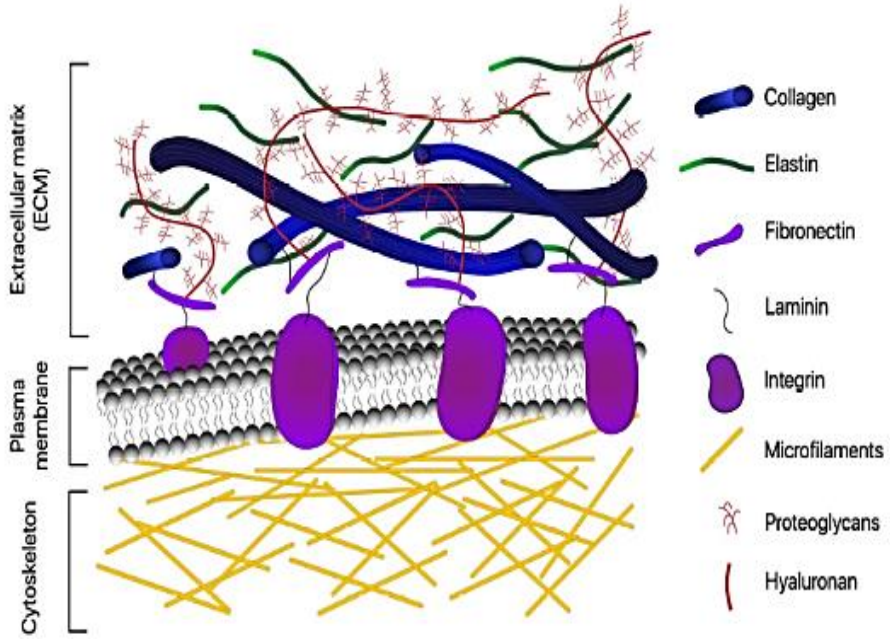

Fig. 1. Schematic overview of the extracellular matrix and ıts major components. The composition of the ECM primarily consists of various fibrous proteins (collagen, elastin, fibronectin, and laminin) and polysaccharides, which are locally secreted and organized into a structured network in close association with the surface of the producing cells. (Poole & Mostaço-Guidolin, 2021:1760).

The ECM is a dynamic structure that regulates cellular behavior and shapes tissue organization. Through interactions with the ECM, cells contribute to tissue formation. These tissues assemble into organs, and organs in turn combine to form organ systems. This hierarchical organization ensures the functional integrity of the organism (Rozario & DeSimone, 2010:126; Dzamba & DeSimone, 2018:245; Chen et al., 2021:20) (Figures 2 and 3).

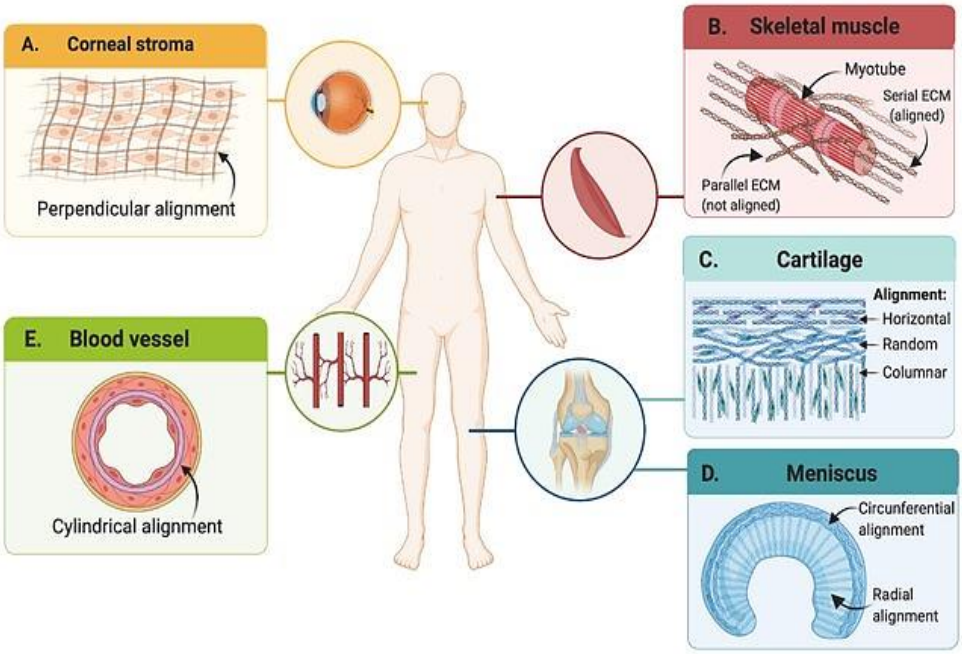

Figure 2.Cellular and ECM arrangements in different tissues. (A) In the corneal stroma, non-parallel fibers display a vertical orientation. (B) In skeletal muscle, myotubes are aligned parallel along the ECM, although the ECM organization itself is not prominent. (C) In cartilage, the arrangement varies regionally, exhibiting horizontal, random, and columnar patterns. (D) In the meniscus, cells and matrix show both circumferential and radial orientations. (E) In blood vessels, cells adopt a cylindrical arrangement. (Chen et al., 2021:20).

4.Functions of the ECM in Embryonic Development

In embryonic development, the ECM not only provides physical support to cells but also establishes the microenvironment required for morphogenesis by integrating biochemical and mechanical signals that guide cell migration, proliferation, differentiation, and tissue organization (Rozario & DeSimone, 2010:1). The topography, stiffness, and composition of ECM fibers regulate cell orientation and migration; for instance, during gastrulation, cells migrate in an organized manner along the ECM, thereby contributing to tissue shaping (Dzamba & DeSimone, 2018:245).

Through integrins and other cell surface receptors, the ECM controls cell cycle progression and differentiation processes. The fate of stem cells is tightly linked to ECM composition and mechanical properties (Darnell et al., 2018a,b; Smith et al., 2018). During organogenesis, the distribution and specific components of the ECM play critical roles in regulating tissue morphology and organ lobulation. Molecules such as proteoglycans, collagen types, and laminin support cell positioning and organ patterning (Rozario & DeSimone, 2010; Hynes, 2009).

The dynamic nature of the ECM is maintained through continuous remodeling mediated by matrix metalloproteinases (MMPs) and other enzymes, enabling cells to adapt to their environment throughout the developmental process (Page-McCaw, Ewald, & Werb, 2007). In conclusion, beyond supporting embryonic development, the ECM is also regarded as a fundamental element in regenerative mechanisms and tissue engineering applications (Daley, Peters, & Larsen, 2008).

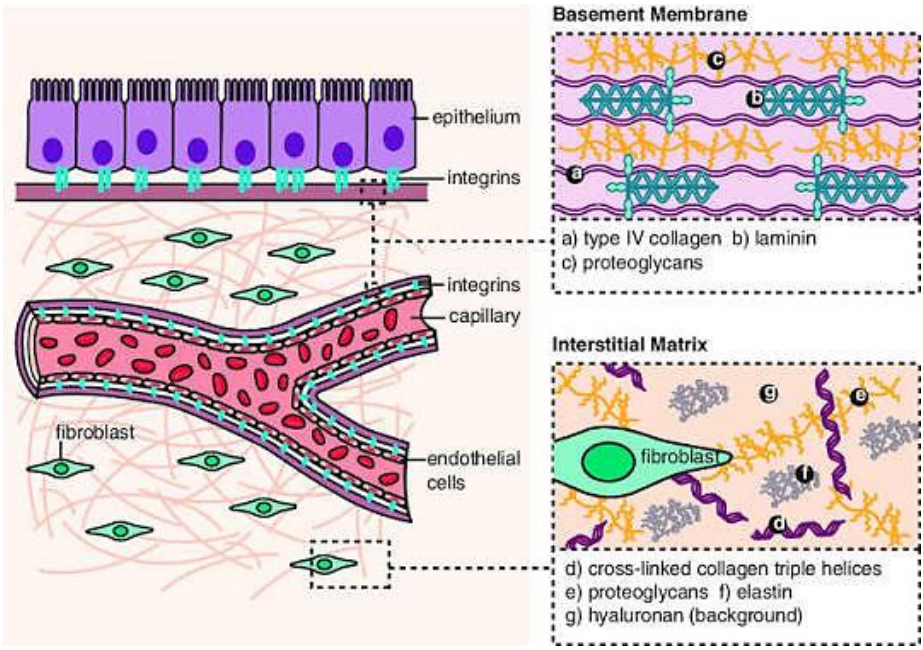

Figure 3. Hierarchical Organization of the ECM from Cell to Organism and Its Roles at Different Levels. This diagram illustrates the interaction of cells with the ECM and how this interaction shapes organization at the levels of tissues, organs, and organ systems. Cells are surrounded by the ECM; cell–ECM interactions contribute to tissue formation, the assembly of tissues leads to organ development, and the integration of organs ensures the functional integrity of organ systems. Examples include fibroblasts and epithelial cells (cell level), connective tissue and cartilage (tissue level), kidney or heart (organ level), and the circulatory and urinary systems (organ system level) (Rozario & DeSimone, 2010:126; Dzamba & DeSimone, 2018:245).

5.Functions of the ECM in Embryonic Development

In embryonic development, the extracellular matrix (ECM) not only provides physical support to cells but also establishes the microenvironment required for morphogenesis by integrating biochemical and mechanical signals that guide cell migration, proliferation, differentiation, and tissue organization (Rozario & DeSimone, 2010:126). The topography, stiffness, and composition of ECM fibers regulate cell orientation and migration; for

example, during gastrulation, cells move in an organized manner along the ECM, contributing to tissue shaping (Dzamba & DeSimone, 2018:245).

Through integrins and other cell surface receptors, the ECM controls cell cycle progression and differentiation processes. The fate of stem cells is tightly linked to ECM composition and its mechanical properties (Darnell et al., 2018a,b:182,8367; Smith et al., 2018:16). These interactions highlight that the ECM serves as a dynamic signaling interface rather than a passive structure.

During organogenesis, the distribution and specific components of the ECM play critical roles in regulating tissue morphology and organ lobulation. Molecules such as proteoglycans, collagen types, and laminin support cell positioning, polarity, and organ patterning (Rozario & DeSimone, 2010:126; Hynes, 2009:1216). The spatial organization of these components ensures the coordination of cellular behaviors that drive proper tissue formation.

The dynamic nature of the ECM is maintained through continuous remodeling mediated by matrix metalloproteinases (MMPs) and other enzymes, enabling cells to adapt to their environment throughout development (Page-McCaw, Ewald, & Werb, 2007:221). In conclusion, beyond supporting embryonic development, the ECM is also regarded as a fundamental element in regenerative mechanisms and tissue engineering applications (Daley, Peters, & Larsen, 2008:255).

THE EXTRACELLULAR MATRİX (ECM) AND EMBRYONİC MORPHOGENESİS: STUDY EXAMPLES

Research investigating the biological functions of the extracellular matrix (ECM) and its roles in morphogenesis has revealed that the ECM is not merely a structural scaffold but also a dynamic environment that directs cellular behavior. Throughout embryonic development, the ECM provides a critical microenvironment that coordinates essential processes such as cell migration, differentiation, polarization, and organ shaping.

Miner and colleagues (1998:985) reported that deficiency of the laminin α5 chain leads to developmental anomalies including embryonic lethality, failure of anterior neural tube closure, and digit separation defects, highlighting the importance of cell–matrix interactions mediated by laminin in morphogenesis. Laminin deficiency disrupts tissue organization, particularly during kidney and nervous system development, thereby adversely affecting organ formation. This study demonstrates that laminin not only provides mechanical support but also actively regulates cell fate and

tissue architecture through cell–matrix interactions and associated signaling pathways.

Similarly, Pöschl et al. (2004:1619) demonstrated that type IV collagen (Col IV) is critical for the stability of basal membranes (BMs) during embryonic development, although it is not required for the initial organization of BM components during early developmental stages. Experiments using embryos with null alleles of the Col4a1/2 gene locus showed that embryos developed up to E9.5 at expected Mendelian ratios, with BM proteins accumulating in their anticipated locations. However, between E10.5 and E11.5, structural defects in the BM and loss of integrity of the Reichert's membrane were observed. These findings indicate that other BM components, such as laminin, can form BM-like structures during early development, but the specific composition of Col IV is indispensable for BM integrity, stability, and functionality.

Knockout and conditional KO studies targeting fibronectin (Fn1) have revealed that Fn1 plays a critical role in embryonic morphogenesis and tissue organization. Complete Fn1 knockout results in early embryonic lethality, whereas tissue-specific conditional KO models display disruptions in cell growth and matrix organization (Johansson, et al., 1997:126; Fukuda et al., 2002:5613; Liu et al., 2010:11; Yuan et al., 2020:10224).

Matsubayashi et al. (2020:33) modeled the balance between synthesis and degradation of ECM components in fruit fly (*Drosophila*) embryos and validated their findings using live imaging combined with pulse-chase experiments. They demonstrated that the embryonic ECM exhibits a much faster turnover than previously anticipated, with a half-life of approximately 7–10 hours. Turnover rates vary depending on the activity of proteolytic enzymes, such as MMPs, and interactions with other network components. This dynamic behavior can impact tissue morphogenesis, particularly under conditions of excessive matrix metalloproteinase activity or in the absence of network-stabilizing components such as Nidogen.

Chen et al., (2025:6763) investigated the role of basal membrane (BM) and ECM perforations in embryonic development. In post-implantation mouse embryos, asymmetric perforations in the basal lamina, generated in an MMP-dependent manner, guided the migration of distal visceral endoderm (DVE) cells, thereby establishing the anterior-posterior (AP) axis. When basal membrane integrity was disrupted using collagenase, DVE cells migrated faster but lost directional guidance, resulting in impaired collective migration. Studies in human embryos and stem cell-derived models further support that BM remodeling is a conserved mechanism underlying AP axis formation (Fig. 4).

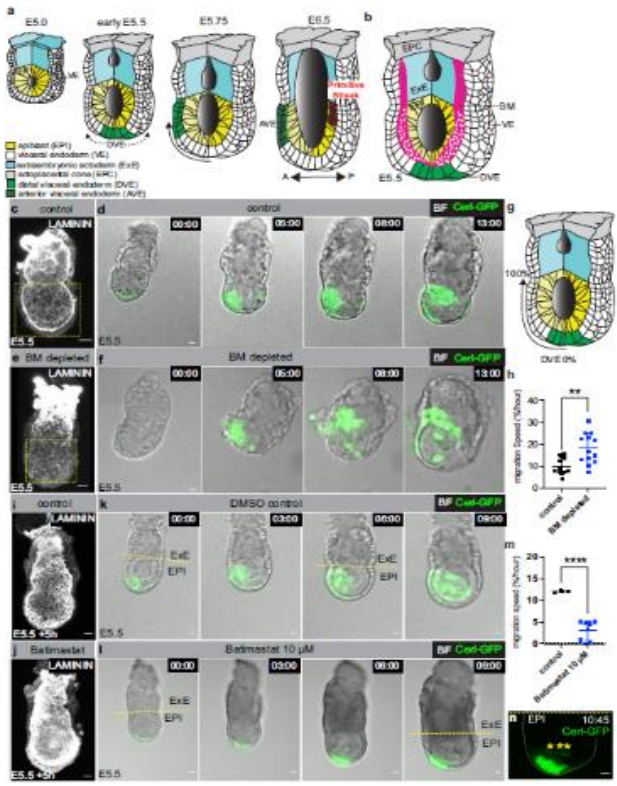

Fig. 4. Role of basal membrane perforations in guiding DVE migration and anterior–posterior (AP) axis formation in post-implantation mouse embryos. (a–b) Schematic illustration of asymmetric perforations within the laminin-labeled basal membrane and their spatial relationship with the forming AP axis. (c–f) Cerl-GFP embryos showing BM integrity and DVE positioning under control and collagenase-treated conditions. Collagenase-mediated BM disruption accelerated DVE migration but caused loss of directionality and impaired collective movement. (g–h) MMP-dependent formation of BM perforations, which were reduced upon Batimastat treatment. These findings indicate that BM remodeling is a conserved mechanism in establishing the embryonic AP axis (Chen et al., 2025:6763).

Wang et al. (2015:15) demonstrated that the ECM provides a critical microenvironment for the differentiation of embryonic stem cells (ESCs). Through cell-matrix interactions, the ECM directly regulates pluripotency maintenance and lineage specification by activating signaling pathways such as FAK, MAPK/ERK, and PI3K/Akt. ECM components, including fibronectin, laminin, and collagen, bind to integrin receptors, spatially and temporally modulating ESC self-renewal and differentiation trajectories. ECM–integrin interactions further guide cell clustering and colonization behaviors, contributing to tissue organization and the early stages of morphogenesis.

Wéber et al. (2024:1369103) examined the temporal and spatial distribution of ECM components in the embryonic and postnatal mouse

hindbrain, highlighting the dynamic role of the ECM in neurodevelopment. Hyaluronic acid (HA) and neurocan exhibit high expression prenatally, whereas postnatally they contribute to the formation of perineuronal nets (PNNs). Molecules such as versican and tenascin-R show increased postnatal expression, playing critical roles in ECM maturation and neuroplasticity processes.

Wu, Yamada, and Wang (2023:123) emphasized that tissue morphogenesis is not driven solely by intracellular mechanisms but occurs through continuous and dynamic interactions between cells and the extracellular matrix (ECM). Their study demonstrated that essential cellular behaviors—such as migration, adhesion, polarization, and differentiation—are tightly coordinated with the mechanical properties of the ECM (e.g., stiffness, elasticity, and topographic organization) as well as its biochemical composition. The ECM also regulates the spatial and temporal distribution of growth factors and other signaling molecules, thereby influencing cell fate and tissue organization. Furthermore, the continuous remodeling of the ECM mediated by matrix metalloproteinases and other enzymes was shown to be critical for organ lobulation, tissue shaping, and cellular adaptation to the surrounding environment. In this context, the authors highlight that a holistic examination of cell–ECM interactions is essential for understanding tissue morphogenesis, emphasizing that the ECM functions not merely as a passive scaffold but as an active regulator of morphogenesis.

Fagotto (2023:1) provided a comprehensive examination of the central role of ECM synthesis and organization in morphogenesis. The study emphasized that the ECM is not merely a passive structural scaffold but also an active tool that directs the morphogenetic behavior of cells. The timely and spatially precise organization of ECM components—including collagens, laminin, fibronectin, and proteoglycans—is critical for processes such as cell polarization, migration, adhesion dynamics, and tissue shaping (Fig. 5A-B). The research further demonstrated that ECM synthesis and self-assembly are integral to the morphogenetic "toolkit," providing a regulatory mechanism that integrates mechanical and biochemical signals during organ and tissue formation.

ECM topography, fiber orientation, and mechanical properties guide cell migration paths, while local concentrations and proteoglycan composition spatially regulate growth factor signaling. This enables cells to respond to environmental cues while actively shaping tissue architecture throughout development. Thus, the ECM acts as a dynamic and instructive structure that continuously regulates cellular behavior and tissue organization. Through interactions with the ECM, cells contribute to tissue formation; these tissues assemble into organs, and organs in turn combine to form organ systems. This hierarchical organization ensures the functional integrity of the organism (Rozario & DeSimone, 2010:126; Dzamba & DeSimone, 2018:245).

Fagotto (2023:1) also highlighted that ECM remodeling is essential for morphogenesis. Continuous matrix adjustments mediated by metalloproteinases and other enzymes allow cells to fine-tune their spatial positions and optimize organ lobulation. In conclusion, the ECM functions not only as a supportive structure but also as a dynamic signaling and mechanical

guidance system, serving as a fundamental component of the morphogenetic "toolkit" during embryonic development.

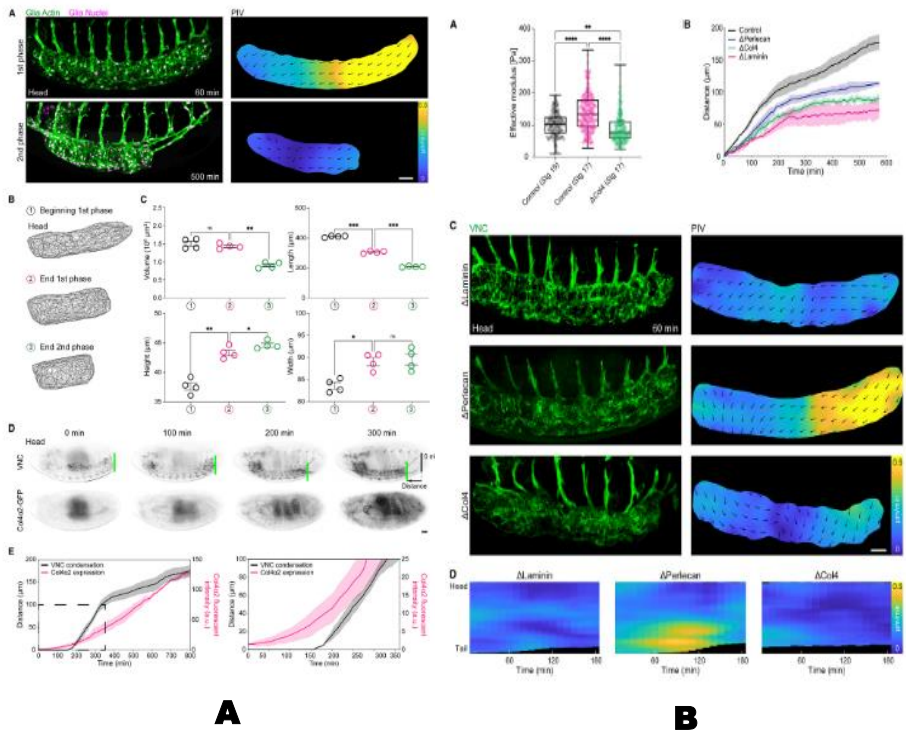

Fig. 5**A.** ECM self-assembly and mechanical feedback during morphogenesis. Extracellular matrix (ECM) components such as collagen, fibronectin, laminin, and proteoglycans form a dynamic, cell-secreted network that both supports and directs morphogenetic behaviors including cell polarization, adhesion, and migration. Mechanical feedback between ECM stiffness, fiber orientation, and biochemical composition enables bidirectional regulation—cells remodel the ECM while responding to its cues—making ECM dynamics an active driver of morphogenesis. **B.** Integration of ECM assembly into the morphogenetic toolkit. This schematic shows how ECM organization integrates with cellular signaling, force transmission, and tissue shaping. ECM topography, fiber alignment, and proteoglycan composition regulate growth factor signaling and guide cell migration, establishing feedback essential for coordinated tissue morssphogenesis (Fagotto, 2023:1).

Jacobson et al., (2024:439) conducted a detailed investigation of the dynamic changes in extracellular matrix (ECM) protein composition during mouse embryonic forelimb development. Between embryonic days 11.5 and 14.5, ECM proteins (the matrisome) were analyzed using tissue fractionation, bio-orthogonal non-canonical amino acid tagging (BONCAT), and mass spectrometry. The results revealed that ECM composition varies throughout development and growth, differs from other developing organs (e.g., the brain), and is disrupted in an osteogenesis imperfecta mouse model. Furthermore, the distribution of selected matrisome components in embryonic and postnatal musculoskeletal tissues was assessed via

immunohistochemistry, providing a more comprehensive understanding of the ECM's role in tissue morphogenesis. The study demonstrates that the ECM is not merely a structural scaffold but a critical regulatory element in cell migration, differentiation, and organ organization during development (Jacobson et al., 2024:439).

Harmansa et al., (2023:36739) demonstrated that the mechanical anisotropy and orientation of ECM fibers directly influence the morphology of developing organs (Fig. 6A)**.** Their study revealed that specific fiber alignments and mechanical properties guide cell migration paths and organize regions of proliferation (Fig. 6B)**.** These findings emphasize that the ECM functions not merely as a structural scaffold but also as an active regulator coordinating tissue shaping. The research further showed that fiber orientation and mechanical anisotropy critically affect cell polarization, alignment, and organ lobulation, highlighting the ECM's role as a microenvironment that spatially and mechanically organizes cellular behaviors during organ development.

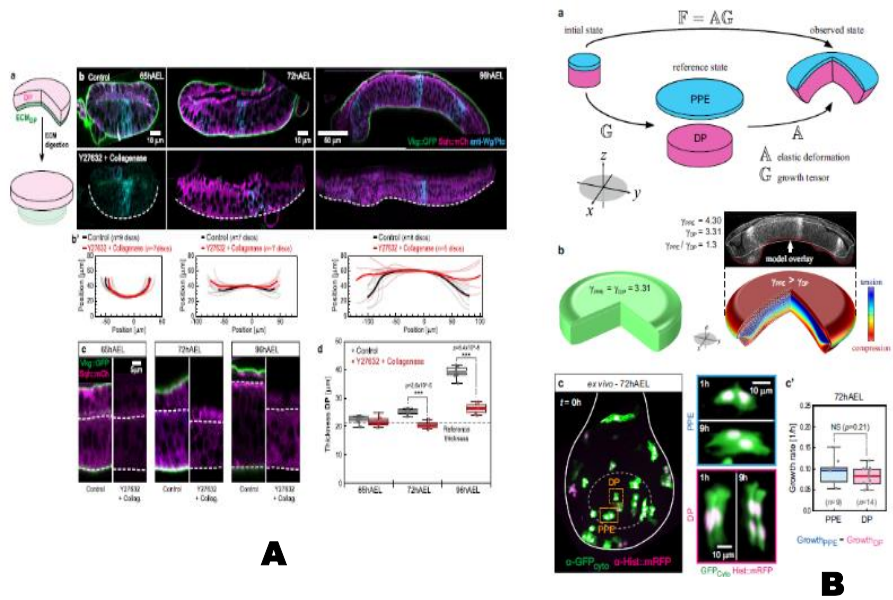

Fig. 6**A.** ECM protein abundances in the myotendinous unit. Overall matrisome abundance changes little without muscle, but specific ECM subsets differ in composition. **B.** Altered matrisome distribution in forelimbs lacking muscle. (A, B′) EMILIN1^{+} and WGA^{+} fibers (arrowheads) appear in tendons of both WT and Pax3^Cre/Cre embryos at E13.75. (C, D′) POSTN^{+} labeling occurs only in WT tendons. (E, F‴) FBN2 persists in the ScxGFP^{+} domain of Pax3^Cre/Cre limbs, while THBS4 is restricted to WT. These findings show that muscle presence is required for proper assembly of MTJ-specific ECM components (Harmansa et al., (2023:36739).

The development of a functional musculoskeletal system requires the integration of contractile muscle tissue with ECM-rich tendons that transmit forces generated by muscles to bones. Although muscle and tendon have distinct embryological origins, they converge at the myotendinous junction

(MTJ). Leng et al., (2025:1202) investigated the three-dimensional distribution of ECM during forelimb development in wild-type (WT) and muscle-deficient Pax3^Cre/Cre mouse models. At embryonic day 12 (E12), aligned ECM structures were observed in the region where the long triceps muscle would attach to the ulna, before MTJ formation. Even in the absence of muscle, tendon-like structures and muscle segmentation continued to develop; however, MTJ-specific ECM components, such as type XXII collagen, were absent. These findings indicate that the ECM functions as an active guide rather than a passive scaffold in muscle–tendon integration, and that the presence of muscle is critical for the proper organization of ECM at the MTJ. Overall, this study provides a foundational understanding of the developmental mechanisms underlying muscle–tendon assembly and offers insights for devising novel strategies to address musculoskeletal disorders (Fig. 7).

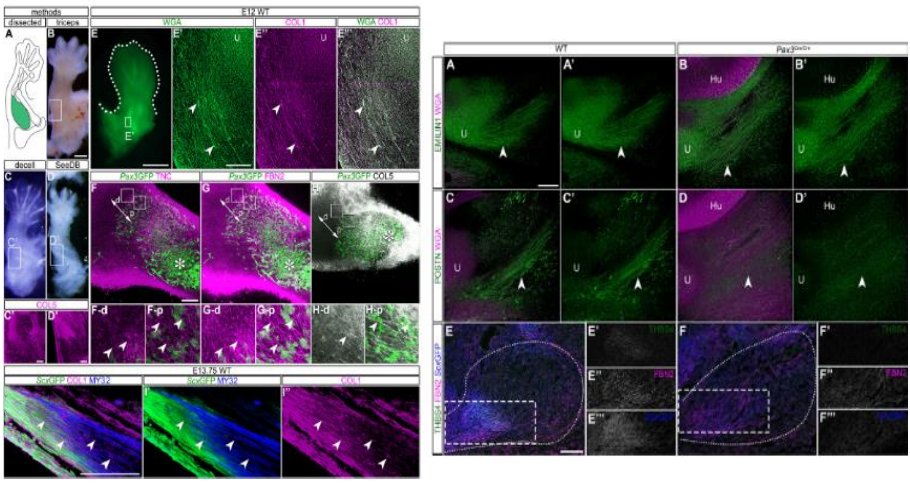

Figure 7. Three-dimensional distribution of ECM during forelimb development at embryonic day 12 (E12). In wild-type embryos, aligned ECM fibers labeled with COL1 and WGA are observed in the region where the long triceps muscle will attach to the ulna before muscle–tendon junction (MTJ) formation. The organized ECM structure forms independently of muscle presence, indicating that the ECM acts as an active guide rather than a passive scaffold in morphogenesis (Leng et al., 2025:1202).

In recent decades, research has investigated the impact of the mechanical properties of the extracellular matrix (ECM) on cellular responses and tissue behavior, with particular emphasis on elasticity as a key determinant. However, the ECM is not solely an elastic structure; it also exhibits viscoelastic properties, meaning it responds both instantaneously and over time to mechanical forces. Currently, ECM viscoelasticity has emerged as a critical regulator of collective cell dynamics, morphogenetic processes, and tissue organization. During embryonic development in particular, ECM viscoelasticity directs cell migration, differentiation, and organ shaping, thereby establishing proper tissue architecture. For instance, in a study by Akos et al., (2020:674) on sheep embryos, pronounced viscoelastic behavior

was observed in ECM-rich regions separating the mesoderm and endoderm. This observation provides an important example of how the ECM's mechanical properties relate to its biological functions during developmental processes. This review addresses the role of ECM viscoelasticity in developmental and pathological contexts and emphasizes that understanding these properties can contribute to advances in bioengineering applications and the development of novel therapeutic strategies (Courbot & Elosegui-Artola, 2025:10).

Wu, Yamada & Wang (2023:123) highlights the central role of dynamic interactions between cells and the extracellular matrix (ECM) in shaping embryonic tissues. The ECM not only provides mechanical support to cells but also directly regulates fundamental cellular behaviors, including migration, polarization, adhesion, and differentiation, thereby shaping tissue organization. Mechanical and biochemical properties such as fiber orientation, stiffness, and molecular composition determine cell migration paths and differentiation trajectories, while also coordinating the spatial distribution of growth factors and signaling molecules. Throughout both early and late stages of morphogenesis, the ECM is continuously remodeled, contributing to proper organ lobulation and tissue architecture. These processes are critical not only for normal development but also for pathological conditions and tissue engineering applications. Consequently, the ECM functions as a dynamic microenvironment that goes beyond a passive scaffold, actively guiding cellular behavior, organizing tissues, and serving as a key regulator in embryonic morphogenesis.

Crossley et al., (2024:1354132) investigated the role of the ECM in cell migration and morphogenesis using computational and mathematical modeling approaches. Their study demonstrated that the mechanical and biochemical properties of the ECM are critical factors guiding cellular behavior. The models revealed that the ECM influences cell migration speed, directionality, and differentiation, highlighting its function as an active and dynamic regulator of tissue shaping rather than a passive scaffold. Furthermore, the study showed that ECM components are continuously remodeled in a spatiotemporal manner and engage in reciprocal interactions with cells during developmental processes.

RESULTS

Taken together, these studies clearly demonstrate that the extracellular matrix (ECM) in embryonic development is far more than a structural scaffold or a passive environment supporting cells. It functions as an active and dynamic regulatory network that directly guides cell migration, differentiation, polarization, and tissue organization. Through continuous cycles of synthesis and degradation of fibers and network components—mediated, for example, by matrix metalloproteinases and other proteolytic enzymes—the ECM is constantly remodeled, precisely controlling cell migration pathways and organogenetic processes. Basal membranes and other ECM building blocks contribute to tissue shaping and the maintenance of morphological integrity through their mechanical properties, fiber orientation, and biochemical signals. ECM components such as fibronectin, laminin, type IV collagen, and proteoglycans ensure proper cell positioning during critical embryonic events like gastrulation, neurulation, and organogenesis; they activate intracellular signaling pathways via integrins and other receptors, thereby directing differentiation and proliferation. Additionally, the ECM provides a flexible microenvironment that supports tissue plasticity during development, enabling embryonic organs to adapt both mechanically and biochemically. Thus, the ECM functions not merely as a supportive structure but as a continuously renewing and regulatory network central to tissue formation and functional organization during embryonic morphogenesis.

REFERENCES

Akos, Z., Isai, D. G., Rajasingh, S., Kosa, E., Ghazvini, S., Dhar, P., & Czirok, A. (2020). *Viscoelastic properties of ECM-rich embryonic tissues.* Frontiers in Cell and Developmental Biology, 8, 674. doi:10.3389/fcell.2020.00674

Chen, D. Y., Claussen, N. H., Titus, S., Hu, W., Weatherbee, B. A. T., Mandelbaum, R. S., Scott Jr, R. T., Seli, E., Streichan, S. J., & Zernicka-Goetz, M. (2025). *Basement membrane perforations guide anterior–posterior axis formation during early embryonic development.* Nature Communications, 16(1), 6763. doi:10.1038/s41467-025-61441-6

Chen, F.-M., Liu, X., & Zhang, J. (2021). Recent advances on stimuli-responsive hydrogels based on tissue-derived ECMs and their components. *Advanced Healthcare Materials, 10*(20), 2100570. https://doi.org/10.1002/adhm.202100570

Courbot, O., & Elosegui-Artola, A. (2025). The role of extracellular matrix viscoelasticity in development and disease. npj Biological Physics and Mechanics, 2, 10. doi:10.1038/s44341-025-00014-6

Crossley, R. M., Johnson, S., Tsingos, E., Bell, Z., Berardi, M., Botticelli, M., Braat, Q. J. S., Metzcar, J., Ruscone, M., Yin, Y., & Shuttleworth, R. (2024). Modeling the extracellular matrix in cell migration and morphogenesis: A guide for the curious biologist. Frontiers in Cell and Developmental Biology, 12, 1354132. doi:10.3389/fcell.2024.1354132

Daley, W. P., Peters, S. B., & Larsen, M. (2008). Extracellular matrix dynamics in development and regenerative medicine. *Journal of Cell Science, 121*(3), 255–264. doi:10.1242/jcs.006064

Darnell, M., Gu, L., & Mooney, D. (2018a). RNA-seq reveals diverse effects of substrate stiffness on mesenchymal stem cells. *Biomaterials, 181*, 182–188. doi:10.1016/j.biomaterials.2018.07.039

Darnell, M., O'Neil, A., Mao, A., Gu, L., Rubin, L. L., & Mooney, D. J. (2018b). Material microenvironmental properties couple to induce distinct transcriptional programs in mammalian stem cells. *Proceedings of the National Academy of Sciences of the United States of America, 115*(34), E8368–E8377. doi:10.1073/pnas.1802568115

Dzamba, B. J., & DeSimone, D. W. (2018). Extracellular matrix (ECM) and the sculpting of embryonic tissues. *Current Topics in Developmental Biology, 130*, 245–274. doi:10.1016/bs.ctdb.2018.03.006

Fagotto, F. (2023). Extracellular matrix assembly joins the morphogenesis toolkit. *Developmental Biology, 496*, 1–14. doi:10.1016/j.ydbio.2023.03.001

Frantz, C., Stewart, K. M., & Weaver, V. M. (2010). The extracellular matrix at a glance. *Journal of Cell Science, 123*(24), 4195–4200. doi:10.1242/jcs.023820

Fukuda, T., Yoshida, N., Kataoka, Y., Manabe, R.-I., Mizuno-Horikawa, Y., Sato, M., Kuriyama, K., Yasui, N., & Sekiguchi, K. (2002). *Mice lacking the EDB segment of fibronectin develop normally but exhibit reduced cell growth and fibronectin matrix assembly in vitro.* Cancer Research, 62(19), 5613–5616.

Harmansa, S., Affolter, M., & Lenne, P. F. (2023). Growth anisotropy of the extracellular matrix shapes a developing organ. *Nature Communications, 14,* 36739. doi:10.1038/s41467-023-36739-y

Hynes, R. O. (2002). Integrins: Bidirectional, allosteric signaling machines. *Cell, 110*, 673–687. doi:10.1016/S0092-8674(02)00971-6

Hynes, R. O. (2009). The extracellular matrix: Not just pretty fibrils. *Science, 326*(5957), 1216–1219. doi:10.1126/science.1176009

Hynes, R. O., & Naba, A. (2012). Overview of the matrisome: An inventory of extracellular matrix constituents and functions. *Cold Spring Harbor Perspectives in Biology, 4*(1), a004903. https://doi.org/10.1101/cshperspect.a004903

Jacobson, K. R., Saleh, A. M., Lipp, S. N., Tian, C., Watson, A. R., Luetkemeyer, C. M., Ocken, A. R., Spencer, S. L., Kinzer-Ursem, T. L., & Calve, S. (2024). Extracellular matrix protein composition dynamically changes during murine forelimb development. *Developmental Cell, 58*(4), 439–453. doi:10.1016/j.devcel.2024.07.004

Järveläinen, H., Sainio, A., Koulu, M., Wight, T. N., & Penttinen, R. (2009). Extracellular matrix molecules: Potential targets in pharmacotherapy. *Pharmacological Reviews, 61*(2), 198–223. doi:10.1124/pr.109.001289

Johansson, S., Svineng, G., Wennerberg, K., Armulik, A., & Lohikangas, L. (1997). Fibronectin-integrin interactions. *Frontiers in Bioscience, 2*, 126–146.

Leng, Y., Lipp, S. N., Bu, Y., Larson, H., Jacobson, K. R., Colling, H. A., & Calve, S. (2025). Extracellular matrix deposition precedes muscle-tendon integration during murine forelimb morphogenesis. *Communications Biology, 8*, 1202. doi:10.1038/s42003-025-08653-0

Liu, K., Cheng, L., Flesken-Nikitin, A., Huang, L., Nikitin, A. Y., & Pauli, B. U. (2010). Conditional knockout of fibronectin abrogates mouse mammary gland lobuloalveolar differentiation. *Developmental biology*, *346*(1), 11-24.

Matsubayashi, Y., Sánchez-Sánchez, B. J., Marcotti, S., Serna-Morales, E., Dragu, A., Díaz-de-la-Loza, M. del C., Vizcay-Barrena, G., Fleck, R. A., & Stramer, B. M. (2020). *Rapid homeostatic turnover of embryonic ECM during tissue*

morphogenesis. Developmental Cell, 54(1), 33–42.e9. doi:10.1016/j.devcel.2020.06.005

Miner, J. H., Li, C., & Mudd, J. R. (1998). Roles for laminin in embryogenesis. *Development, 125*(5), 985–995. https://doi.org/10.1242/dev.125.5.985

Naba, A. (2023). Ten years of extracellular matrix proteomics: Accomplishments, challenges, and future perspectives. *Molecular & Cellular Proteomics, 22*(4), 100528. https://doi.org/10.1016/j.mcpro.2023.100528

Onofri, F. (2016). *Development of an extracellular matrix hydrogel for intestine tissue engineering* (Master's thesis). Università Degli Studi di Padova, Dipartimento di Ingegneria Industriale, Padova, Italy, 1-25.

Page-McCaw, A., Ewald, A. J., & Werb, Z. (2007). Matrix metalloproteinases and the regulation of tissue remodelling. *Nature Reviews Molecular Cell Biology, 8*(3), 221–233. doi:10.1038/nrm2125

Pelosi, P., Rocco, P. R. M., Negrini, D., & Passi, A. (2007). The extracellular matrix of the lung and its role in edema formation. *Annals of the Brazilian Academy of Sciences, 79*(2), 285–297. doi:10.1590/S0001-37652007000200010

Poole, J. J. A., & Mostaço-Guidolin, L. B. (2021). Optical microscopy and the extracellular matrix structure: A review. *Cells, 10*(7), 1760. doi:10.3390/cells10071760

Pozzi, A., Yurchenco, P. D., & Iozzo, R. V. (2017). The nature and biology of basement membranes. *Matrix Biology, 57–58,* 1–11. doi:10.1016/j.matbio.2016.12.009

Pöschl, E., Schlotzer-Schrehardt, U., Brachvogel, B., Saito, K., Ninomiya, Y., & Mayer, U. (2004). Collagen IV is essential for basement membrane stability but dispensable for initiation of its assembly during early development. *Development, 131*(7), 1619–1628. doi:10.1242/dev.01037

Rozario, T., & DeSimone, D. W. (2010). The extracellular matrix in development and morphogenesis: A dynamic view. *Developmental Biology, 341*(1), 126–140. doi:10.1016/j.ydbio.2009.10.026

Sahu, B., Sharma, D. D., Jayakumar, G. C., Madhan, B., & Zameer, F. (2023). A review on an imperative by-product: Glycosaminoglycans—A holistic approach. *Carbohydrate Polymer Technologies and Applications, 5*, 100275. https://doi.org/10.1016/j.carpta.2023.100275

Scott, J. E. (1992). Supramolecular organization of extracellular matrix glycosaminoglycans, in vitro and in the tissues. *The FASEB Journal, 6*(9), 2639–2645.

Sekiguchi, R., & Yamada, K. M. (2018). Basement membranes in development and disease. *Current Topics in Developmental Biology, 130,* 143–191. doi:10.1016/bs.ctdb.2018.02.005

Sharma, N. S., Patel, R., Kim, H. J., & Lee, S. J. (2024). Decellularized extracellular matrix-decorated 3D nanofiber scaffolds enhance cellular responses and tissue regeneration. *Acta Biomaterialia, 184,* 81–97. doi:10.1016/j.actbio.2024.06.020

Smith, L. R., Cho, S., & Discher, D. E. (2018). Stem cell differentiation is regulated by extracellular matrix mechanics. *Physiology, 33*(1), 16–25. doi:10.1152/physiol.00026.2017

Sodhi, H., & Panitch, A. (2020). Glycosaminoglycans in tissue engineering: A review. *Biomolecules, 11*(1), 29. https://doi.org/10.3390/biom11010029

Souza-Fernandes, A. B., Pelosi, P., & Rocco, P. R. (2006). Bench-to-bedside review: The role of glycosaminoglycans in respiratory disease. *Critical Care, 10*(6), 237. https://doi.org/10.1186/cc5100

Uribe-Gomez, J., Farina, P. P., Srinath, P., Russo, L., & Pandit, A. (2025). Exploring the extracellular matrix: Engineering native glycosaminoglycans to modulate

host responses. *Cell Biomaterials*, Article 100187. https://doi.org/10.1016/j.celbio.2025.100187

Walma, D. A. C., & Yamada, K. M. (2020). The extracellular matrix in development. *Development (Cambridge, England)*, *147*(10), dev175596. https://doi.org/10.1242/dev.175596

Wang, H., Luo, X., & Leighton, J. (2015). Extracellular Matrix and Integrins in Embryonic Stem Cell Differentiation. *Biochemistry insights*, *8*(Suppl 2), 15–21. https://doi.org/10.4137/BCI.S30377

Wéber, I., Dakos, A., Mészár, Z., Matesz, C., & Birinyi, A. (2024). Developmental patterns of extracellular matrix molecules in the embryonic and postnatal mouse hindbrain. Frontiers in neuroanatomy, 18, 1369103. https://doi.org/10.3389/fnana.2024.1369103

Wu, D., Yamada, K. M., & Wang, S. (2023). Tissue morphogenesis through dynamic cell and matrix interactions. *Annual Review of Cell and Developmental Biology, 39*(1), 123–144. https://doi.org/10.1146/annurev-cellbio-020223-031019

Xu, J., & Mosher, D. (2011). Fibronectin and other adhesive glycoproteins. In R. Mecham (Ed.), *The extracellular matrix: An overview, Biology of extracellular matrix* (pp. 4–26). Springer-Verlag.

Yamada, K. M., & Sixt, M. (2019). Mechanisms of 3D cell migration. *Nature Reviews Molecular Cell Biology, 20*(12), 738–752. doi:10.1038/s41580-019-0172-9

Yuan, X., Yang, S., Li, W., Li, J., Lin, J., Wu, Y., & Chen, Y. (2020). *Construction of fibronectin conditional gene knock-out mice and the effect of fibronectin gene knockout on hematopoietic, biochemical, and immune parameters in mice.* Scientific Reports, 10(1), 10224. doi:10.7717/peerj.10224

Investigation of Antibacterial Activity of Quince Peel, Seed and Leaf Methanol Extracts

Zuhal SAHİN[1]
Tulay DURAN[2]
Fatih SONMEZ[3]

1- Ogr. Gor. Dr.; Sakarya University of Applied Sciences Pamukova Vocations School. zuhalsahin@subu.edu.tr ORCID No: 0000-0001-9856-8064
2- Ogr. Gor.; Sakarya University of Applied Sciences Pamukova Vocations School. tduran@subu.edu.tr ORCID No: 0000-0001-6061-5347
3- Prof. Dr.; Sakarya University of Applied Sciences Pamukova Vocations School. fsonmez@subu.edu.tr ORCID No: 0000-0001-7486-6374

ABSTRACT

This document contains a summary text format for their research that has Quince by-products such as peel, seeds, and leaves are of interest because they are inexpensive and abundant, often considered waste, contain bioactive compounds such as chlorogenic acid, quercetin, kaempferol, and tannins. These bioactive compounds have beneficial effects on human health such as antioxidant, anti-inflammatory and antimicrobial. In this study, the antibacterial activity of methanol extracts of quince peel, seeds and leaves was investigated against nine different bacteria by using the disk diffusion method, determining the minimal inhibitory concentration (MIC) and minimal bactericidal concentration (MBC). Quince peel extract was found to have antibacterial activity against all bacteria, both gram-positive and gram-negative. While quince leaf extract did not inhibit all bacteria, quince seed extract only inhibited *S. aureus*. The best inhibition zone (12.83±0.17 mm) was observed against *S. aureus* in quince peel extracts. The minimal inhibitory concentration of quince peel extract against Gram-positive bacteria (6.25 mg/mL) was determined to be better than against Gram-negative bacteria. Among all bacteria, the best bactericidal activity was observed against *C. sakazakii* at 125 mg/mL for quince peel extract. Quince peel and seeds can be recycled as antibacterial agents and may be effective in preventing antibiotic resistance.

Keywords – Quince Peel, Quince Seed, Quince Leaf, Antibacterial, Disk Diffusion.

INTRODUCTION

Bacterial resistance has been a concern in recent years for both human health and the control of bacterial diseases. Bacterial resistance has increased due to the unnecessary and misuse of antibiotics, the fact that common pathogenic strains already carry antibiotic-resistant genes.It is anticipated that more antibiotic-resistant pathogens will emerge (Asghar et al., 2021:11; Brown and Wright, 2016:529; Abed et al., 2022:27). Given the time-consuming and costly nature of developing new active ingredients, phytochemicals with antibacterial potential are considered potential candidates against antibacterial resistance (Tungmunnithum et al., 2018:5; Li et al., 2019:31; Abed et al., 2022:27).

Quince (*Cydonia oblonga*), belonging to the Rosaceae family, is a source of secondary metabolites such as phenolic compounds, steroids, terpenoids, sugars, and organic acids. It is used for nutritional, medicinal, and ornamental purposes (Ashraf et al., 2016:7; Shemchuk et al., 2020:10; Grinan et al., 2019:244; Stojkovic et al., 2018:38). Thanks to its phytochemicals, it possesses antidepressant, antioxidant, antibacterial, antifungal, anti-inflammatory, hepatoprotective, cardiovascular,

antidiarrheal, diuretic, hypolipidemic, and hypoglycemic properties (Grinan et al., 2019:244).

Quince is used in the production of jam, jelly, preserves, and juice. Industrial processing of quinces produces by-products such as quince seeds, pulp, and peel, which can be used in various fields (Dimitru et al., 2023:13). By-products from the fruit and vegetable industry, while representing a significant global problem due to their waste, are also of particular interest due to their affordability and large quantities. Valuable biomass, such as the polyphenols contained in these by-products, can be recovered (Vodnar et al., 2017:231; Dimitru et al., 2023:13).

The by-products resulting from quince processing have positive effects due to their phytochemical contents. Quince seeds have been traditionally used in the treatment of cough, diarrhea, dysentery, bronchitis and sore throat thanks to their phytochemicals such as tannins, sterols, and terpenoids (Mohammed et al., 2022). Quince peel has been found to be rich in neochlorogenic, chlorogenic, and rutin as well as isochlorogenic acid, hyperoside, and isoquercetin. Peel extracts have antioxidant activity and are effective in scavenging free radicals and inhibiting the growth of some microorganisms (Stojanovi´c et al., 2017:232). Quince leaves are rich in caffeoylquinic acid, quercetin, kaempferol derivatives and other bioactive compounds. Therefore, it shows antimicrobial, antioxidant, antidiarrheal and anti-inflammatory properties (Ashraf et al., 2016:7; Benzarti et al., 2018:45; Stojković et al., 2018:38; Dogruyol, 2025:429).

The aim of this study was to investigate the antibacterial activity against 9 different bacteria of methanol extracts of quince peel, seed and leaf by using the disk diffusion method, determining the minimal inhibitory and minimal bactericidal concentrations and to determine the possibility of being an alternative to antibiotics in terms of bacterial resistance.

MATERIALS AND METHODS

Materials

Quinces grown in Pamukova, Sakarya, were used after drying their leaves, seeds, and peels. Merck brand media and solvents were used. In this study, *Salmonella typhimurium, Listeria monocytogenes, Staphylococcus aureus, Bacillus spp., Escherichia coli Type 1, Escherichia coli O157:H7, Salmonella spp., Salmonella enteritidis* and *Cronobacter sakazakii* (food

isolates) were used from the Sakarya University, Faculty of Engineering, Food Engineering culture collection.

Extraction

Quince seeds and peels were extracted directly, while quince leaves were extracted with methanol after 18 hours of Sokshelet extraction. The extracts were filtered, and the methanol was removed in an evaporator. The concentration of the resulting extract was adjusted according to Sonmez and Sahin (2023:65).

The extracts were dissolved in distilled water (50 mg/ml), sterilized with a 0.45 µm membrane filter, and stored in brown bottles in a refrigerator at +4°C until use.

Antibacterial Activity Analysis

Disk Diffusion Method

The disk diffusion method was determined by modifying the Clinical and Laboratory Standards Institute 2024 standard procedures (CLSIa, 2024). Stock bacterial cultures were sequentially activated in TSB, single colonies were grown in TSA, 3-5 single colonies were added to 5 ml of TSB and adjusted to a MacFarland density of 0.5. The bacterial suspension was inoculated onto MHA and 6-mm-diameter disks, impregnated with 15 and 20 µl of extract (50 mg/ml), were placed in bacterially inoculated Petri dishes under sterile conditions. After 18-24 hours of incubation at 35°C, inhibition zones were measured with a digital caliper.

Co-Trimoxazole antibiotic disks were used for the positive control and sterile distilled water was used for the negative control. Three parallel studies were conducted, and results are presented as the mean ± standard deviation.

Minimal Inhibitory Concentration (MIC) and Minimal Bactericidal Concentration (MBC)

Microdilution procedures specified by the Clinical and Laboratory Standards Institute (CLSIb, 2024) were used with modifications for determining the MIC. Cation of MHB was adjusted, the extracts were diluted to make serial dilutions and 100 µl was added to each well using 96-well microplates. Bacterial inocula were prepared by adjusting the MacFarland density to 0.5 as described in the disk diffusion method and diluted. 5×10^5 CFU/mL inoculum was added to the microplates containing the serial dilutions and one well was left uninoculated as a control.

The incubation period was 16-20 hours at 35°C. After incubation, the MIC value was determined as the lowest concentration that showed inhibition visible to the naked eye.

To determine MBC, MHA was inoculated at concentrations of MIC and above and incubated at 37°C for 18-24 hours. The lowest concentration at which no growth was observed was determined as the MBC value.

RESULTS AND DISCUSSION

The inhibition zones of the quince peel, seed, and leaf methanol extracts are shown in Table 1, and the MIC and MBC values are shown in Table 2. The quince peel extract formed the inhibition zone against all Gram-positive and Gram-negative bacteria. The inhibition zone diameter increased as the extract amount increased. The inhibition zone diameters of the quince peel extract against all bacteria ranged from 8.48±0.18 to 12.83±0.17 mm, with *S. aureus* (12.83±0.17 mm) being the most sensitive bacterium.

Table 1: Inhibition Zone Diameters (mm) of the Quince Peel, Seed, and Leaf Methanol Extracts Against Gram-Positive and Gram-Negative Bacteria

Bacteria	Quince Peel		Quince Seed		Quince Leaf		Sterile pure water	Co-Trimoxazole
	15µl	20µl	15µl	20µl	15µl	20µl		
Gram-Negatives								
Salmonella spp.	9,18±0,32	9,58±0,28	-	-	-	-	-	25,32±0,52
S. typhimurium	8,78±0,11	9,26±0,32	-	-	-	-	-	24,18±1,01
S. enteritidis	8,48±0,18	10,16±0,76	-	-	-	-	-	25,55± 0,24
E.coli O157:H7	9,23±0,14	10,44±0,53	-	-	-	-	-	23,19±0,42
E.coli Tip 1	9,46±0,11	10,87±0,35	-	-	-	-	-	25,72±0,78
C.sakazakii	9,35±0,70	10,79±0,24	-	-	-	-	-	25,62± 0,22
Gram-Positives								
Bacillus spp.	9,58±0,10	10,55±0,19	-	-	-	-	-	26,62± 1,04
L. monocytogenes	9,29±0,52	9,66±0,22	-	-	-	-	-	16,83± 0,93
S. aureus	11,21±0,65	12,83±0,17	9,53±0,27	10,21±0,40	-	-	-	26,65± 0,45

İnhibition zone diameter mean ± SD (standard deviation) (n=3)
Co-Trimoxazole: Trimethoprim 1.25 µg / sulphamethoxazole 23,75µg
-: no activity

The MIC and MBC of bacteria that showed only inhibitory effect using the disk diffusion method were tested. Quince peel extract showed inhibitory effect against all bacteria at 6.25 or 12.5 mg/mL. The minimal inhibitory concentration of quince peel extract (6.25 mg/mL) was better

against Gram-positive bacteria than against Gram-negative bacteria. The best bactericidal effect of quince peel extract was observed against *C. sakazakii* at 125 mg/mL, while the most resistant bacteria were determined to be *Bacillus spp*. (>500 mg/mL). Bactericidal effect was observed against other bacteria at a concentration of 500 mg/mL. In one study, the antibacterial properties of ethanol/water extracts of different parts of quince were investigated against *Salmonella spp.,* 2 *S. aureus*, 3 *E. coli* and 2 *L. monocytogenes* by disk diffusion method and micro-determination, but quince peel did not show any inhibition against any bacteria (Silva et al., 2023:12). In another study, it was determined that hydroethanolic and water extracts of quince peel had inhibitory effects against *Salmonella typhimurium, S. aureus, E. coli*, and *L. monocytogenes* in the range of 1.5-3 mg/mL, and bactericidal effects in the range of 3-6 mg/ml (Othman et al., 2022:8).

Table 2: Minimal Inhibitory Concentration and Minimal Bactericidal Concentration of Quince Peel, Seed, and Leaf Methanol Extracts (mg/mL)

Bacteria	MIC (mg/mL)			MBC (mg/mL)		
	Quince Peel	Quince Seed	Quince Leaf	Quince Peel	Quince Peel	Quince Leaf
Gram-Negatives						
Salmonella spp.	12,5	NT	NT	500	NT	NT
S. typhimurium	12,5	NT	NT	500	NT	NT
S. enteritidis	6,25	NT	NT	500	NT	NT
E.coli O157:H7	12,5	NT	NT	500	NT	NT
E.coli Tip 1	6,25	NT	NT	500	NT	NT
C.sakazakii	12,5	NT	NT	125	NT	NT
Gram-Positives						
Bacillus spp.	6,25	NT	NT	>500	NT	NT
L. monocytogenes	6,25	NT	NT	500	NT	NT
S. aureus	6,25	50	NT	500	>500	NT

NT: Not tested

While no inhibition was observed against all bacteria in quince leaf extract, the inhibition zone was observed only against *S. aureus* (9.53±0.27-10.21±0.40 mm) in quince seed extract. The inhibitory effect of quince seed on *S. aureus* was determined as 50 mg/mL, and its bactericidal effect was determined as >500 mg/mL. In a study investigating the antibacterial activity of quince seed, ethanol extracts at concentrations of 125, 250 and 500 mg/mL were applied by the agar well diffusion method. While no inhibition zone was observed in *E. coli*, inhibition zones of 8, 10, and 12 mm were determined for *S. aureus*, respectively (Al-Khazraji, 2013:2). Similarly, in this study, zone formation was not observed against *E. coli*, but the higher inhibition zone diameter was observed against *S. aureus* despite using a 50 mg/mL extract concentration in the disk diffusion method,

In another study, the antibacterial effects of quince leaf and seed extracts (water and ethanol) against *E. coli, S. typhimurium* and *S. aureus*

were investigated. The leaf extracts were observed to have an inhibitory effect only against *S. aureus* while the seed extracts had no inhibitory effect (Al-Noamy, 2020:29). The differences in antibacterial properties between our study and other studies may have been influenced by the extraction method and the solvent used.

CONCLUSIONS

In this study, the antibacterial activity of methanol extracts of quince peel, seed, and leaf was determined against nine different bacteria using the disk diffusion method, using MIC and MBK. The results showed that the methanol extract of quince peel had antibacterial activity against all bacteria, while the methanol extract of quince seeds had antibacterial activity only against *S. aureus.* The highest inhibition zone was found in quince peel against *S. aureus* (12.83±0.17 mm). The best inhibitory effect was observed against Gram-positive bacteria (6.25 mg/mL) in quince peel, while the best bactericidal effect was found against *C. sakazakii* (125 mg/mL). Food industry byproducts such as peels, seeds, and leaves are considered both an economic loss and harmful to the environment because it is biological waste. Therefore, quince peels and seeds can be recycled as antibacterial agents and used for human health. This sustainable approach can prevent environmental pollution and be effective in preventing antibiotic resistance.

REFERENCES

Abed, S. N., Bibi, S., Jan, M., Talha, M., Islam, N. U., Zahoor, M., & Al-Joufi, F. A. (2022). Phytochemical composition, antibacterial, antioxidant and antidiabetic potentials of Cydonia oblonga bark. *Molecules*, *27*(19), 6360.

Al-Khazraji, S. K. (2013). Phytochemical screening and antibacterial activity of the crude extract of Cydonia oblonga seeds. Glob. *Adv. Res. J. Microbiol*, 2(8), 137-140.

Al-Noamy, N. A. (2020). Detection of the inhibitory effect of the leaves, seed and fruits of Cydonia oblonga on some Gram positive and negative bacteria. *Rafidain J. Sci*, 29, 10-19.

Asghar, A., Tan, Y. C., Zahoor, M., Zainal Abidin, S. A., Yow, Y. Y., Khan, E., & Lahiri, C. (2021). A scaffolded approach to unearth potential antibacterial components from epicarp of Malaysian Nephelium lappaceum L. *Scientific reports*, 11(1), 13859.

Ashraf, M. U., Muhammad, G., Hussain, M. A., & Bukhari, S. N. (2016). Cydonia oblonga M., a medicinal plant rich in phytonutrients for pharmaceuticals. Frontiers in pharmacology, 7, 163.

Benzarti, S., Belkadhi, K., & Hamdi, H. (2018). Biological activities of phenolics from leaves of Tunisian Cydonia oblonga Miller. *Allelopath. J*, *45*, 229-242.

Brown, E. D., & Wright, G. D. (2016). Antibacterial drug discovery in the resistance era. *Nature,* 529(7586), 336-343.

CLSIa (2024) Performance Standards for Antimicrobial Disk Susceptibility Tests. 14th ed. CLSI standard M02. Clinical and Laboratory Standards Institute.

CLSIb (2024) Methods for Dilution Antimicrobial Susceptibility Tests for Bacteria That Grow Aerobically. 12th ed. CLSI standard M07. Clinical and Laboratory Standards Institute.

Dimitriu, L., Preda, D., Constantinescu-Aruxandei, D., & Oancea, F. (2023). Quince pomace: A source of fiber products and polyphenols. *Chemistry Proceedings*, *13*(1), 6.

Dogruyol, H. (2025). Thermal survival patterns of Staphylococcus aureus in sous vide seabream treated with quince leaf extract. *International Journal of Food Microbiology*, *429*, 111024.

Griñán, I., Galindo, A., Rodríguez, P., Morales, D., Corell, M., Centeno, A., Collado-González, J., Torrecillas, A., Carbonell-Barrachina, A. and Hernández, F. (2019). Volatile composition and sensory and quality attributes of quince (Cydoniaoblonga Mill.) fruits as affected by water stress, *Scientia Horticulturae,* 244: 68–74.

Li, X., Bai, H., Yang, Y., Yoon, J., Wang, S., & Zhang, X. (2019). Supramolecular antibacterial materials for combatting antibiotic resistance. *Advanced Materials*, 31(5), 1805092.

Mohammed, E. T., Khalil, R. R., & Mustafa, Y. F. (2022). Phytochemical analysis and antimicrobial evaluation of quince seeds' extracts.

Othman, S., Añibarro-Ortega, M., Dias, M. I., Ćirić, A., Mandim, F., Soković, M., & Barros, L. (2022). Valorization of quince peel into functional food ingredients: A path towards "zero waste" and sustainable food systems. *Heliyon*, *8*(10).

Shemchuk, O., Braga, D., Grepioni, F., & Turner, R. J. (2020). Co-crystallization of antibacterials with inorganic salts: paving the way to activity enhancement. *Rsc Advances*, 10(4), 2146-2149.

Silva, V., Silva, A., Ribeiro, J., Aires, A., Carvalho, R., Amaral, J. S., ... & Poeta, P. (2023). Screening of chemical composition, antimicrobial and antioxidant activities in pomegranate, quince, and persimmon leaf, peel, and seed: Valorization of autumn fruits by-products for a one health perspective. *Antibiotics*, 12(7), 1086.

Sonmez, F., & Sahin, Z. (2023). Comparative study of total phenolic content, antioxidant activities, and polyphenol oxidase enzyme inhibition of quince leaf, peel, and seed extracts. *Erwerbs-Obstbau*, 65(4), 745-750.

Stojanović, B. T., Mitić, S. S., Stojanović, G. S., Mitić, M. N., Kostić, D. A., Paunović, D. Đ., Arsic, B. B., & Pavlović, A. N., (2017). Phenolic Profiles

And Metal İons Analyses Of Pulp And Peel Of Fruits And Seeds Of Quince (Cydonia Oblonga Mill.). *Food Chemistry*, 232, 466-475.

Stojković, D., Jevremović, K., Smiljković, M., Živković, J., & Soković, M. (2018). Inhibition of microbial biofilm formation by Cydonia oblonga Mill. fruit peel and leaf ethanolic extracts. *Lekovite sirovine*, *38*(1), 58-61.

Tungmunnithum, D., Thongboonyou, A., Pholboon, A., & Yangsabai, A. (2018). Flavonoids and other phenolic compounds from medicinal plants for pharmaceutical and medical aspects: An overview. *Medicines*, 5(3), 93.

Vodnar, D. C., Călinoiu, L. F., Dulf, F. V., Ştefănescu, B. E., Crişan, G., & Socaciu, C., (2017). Identification Of The Bioactive Compounds And Antioxidant, Antimutagenic And Antimicrobial Activities Of Thermally Processed Agro-İndustrial Waste. Food chemistry, 231, 131-140

Remaining Useful Life and Capacity Prediction via Machine Learning for Li-Ion Batteries

Ozan KIYIKCI*

[1]Physics Department, Faculty of Science, Atatürk University, Türkiye
*(ozan.kiyikci@atauni.edu.tr) https://orcid.org/0000-0002-9024-8194

ABSTRACT

I present a practical study on predicting (i) remaining useful life (RUL) in cycles and (ii) one-step-ahead capacity for lithium-ion batteries using machine learning, while explicitly targeting a realistic setting in which the available dataset is small. I utilize the publicly accessible NASA PCoE lithium-ion aging dataset[1] (cells labeled B0005–B0027) to construct a cycle level summary table suitable for learning tasks at the cycle time scale. For RUL prediction, I use an LSTM regressor, which is a sequence learning model that exploits the temporal nature of battery aging[2]. For capacity prediction, I employ a strong non sequential baseline a Random Forest regressor trained on window flattened features[3]. I then derive the state of health (SOH) by normalizing the predicted capacity with the rated capacity [4].To avoid data leakage and to test generalization, I apply a battery level split, training on six cells and evaluating on an unseen cell (B0027) [5]. The LSTM demonstrates strong generalization performance for RUL prediction on the holdout cell (MAE $\approx$ 1.57 cycles, $R^2 \approx 0.94$ on the test windows) while the Random Forest provides reliable capacity forecasting (MAE $\approx$ 5.8 mAh, $R^2 \approx 0.46$). In addition to reporting standard performance metrics, I emphasize engineering decisions that make the study reproducible and trustworthy under limited data conditions, including battery level evaluation, consistent feature scaling, systematic artifact logging (models, metrics, predictions, and plots), and clearly defined baselines. The result is a concise reference implementation that can be extended to multi horizon forecasting and early end of life prediction.

Keywords – Lithium-Ion Battery, Remaining Useful Life, Capacity Prediction, Machine Learning, LSTM, Random Forest.

INTRODUCTION

The degradation of lithium-ion batteries is a physical process. As they cycle, the amount of lithium that can be reversibly cycled decreases, interfacial layers (such as the solid–electrolyte interphase, SEI) grow, resistance increases, and the usable capacity fades[6]. In real life, I do not often get the luxury of "big data" for each battery chemistry and operating profile. Instead, I frequently have to work with limited measurements and still make strong predictions that do not fall apart when the data distribution changes. That is exactly the kind of data set I am interested in: a small reproducible machine learning study that works even with a limited dataset.

In this paper, I focus on two real world prediction questions:

• RUL in cycles: based on recent measurements at the cycle level, how many cycles remain until the end of life (EOL).

• Capacity one step ahead: based on a short history, what will the capacity be in the next cycle?

Even when I use black box regressors, I stay close to the underlying physics. In this dataset, capacity is the most direct macroscopic indicator of degradation; SOH is naturally defined in terms of capacity; and RUL is typically defined relative to a threshold on SOH. This physical alignment reduces the risk that a model appears to perform well by exploiting spurious correlations.

I keep the contributions modest but concrete:

1. I construct a cycle level learning data set from the NASA PCoE battery aging data and evaluate it using a battery level holdout to reduce data leakage.
2. I compare a sequence learner (LSTM) for RUL prediction with a window flattened baseline (Random Forest) for capacity forecasting.
3. I demonstrate how SOH forecasting can be derived directly from capacity forecasting using $\mathrm{SOH}_{t+1} = \hat{C}_{t+1}/C_{\mathrm{rated}}$.
4. I retain all training artifacts (models, metrics, predictions, and plots) so that the study can be easily reproduced and extended.

MATERIALS AND METHOD

A. Dataset

I use the NASA PCoE lithium-ion battery aging dataset, which contains cells labeled B0005, B0006, B0007, B0018, B0025, B0026, and B0027 [1] [7]. The raw dataset consists of cycle records with detailed charge and discharge measurements. I summarize the data at the cycle level to make it easier to work with and to allow rapid experimentation using a smaller and more manageable representation of the data. Due to the strict battery-level holdout strategy and windowed sequence construction, the number of test samples is intentionally small but representative of a realistic deployment scenario.

Table 1. Data Split Summary

Task	Train Samples	Test Samples
LSTM RUL	572	8
RF Capacity	572	8
RF SOH (Derived)	572	8

Table 2. Hyperparameters used in Experiments

Component	Settings
Window Size	20
LSTM Hidden Size	64
LSTM Layers	2 Layers
Optimizer	Adam lr=10^{-3}
RF trees	300

B. Cycle Level Summary and Targets

For each cycle t, I keep a small number of features and define targets for the two prediction tasks.

1. Capacity and SOH: Let C_t be the measured discharge capacity (Ah) at cycle t. I define the state of health by normalizing the capacity with respect to the rated capacity:

$$SOH_t = \frac{C_t}{C_{rated}} \qquad (1)$$

I use $C_{rated} = 2.0$ Ah in my experiments, consistent with the value used in my scripts for derived SOH reporting.

2. RUL definition: I define the remaining useful life in cycles using an end-of-life cycle index t_{EOL}:

$$RUL_t = t_{EOL} - t. \qquad (2)$$

In practice, t_{EOL} can be defined using a threshold on SOH (for example, 80%) [4], [8]. In this study, cycle-wise RUL labels are derived during preprocessing based on the known end-of-life cycle index.

C. Features

I intentionally keep the feature set minimal so that the method remains stable when working with a small number of batteries and limited data coverage.

When I refer to sequence learning, I mean that the model uses an ordered window of measurements, $X_t = [x_{t-W+1}, \dots, x_t]$, to learn how the features evolve over time. A non-sequential baseline, on the other hand flattens this window to single vector, $\phi(X_t) \in \mathbb{R}^{W \cdot d}$, and then learns standard regression mapping.

D. Models

I use an LSTM regressor in a sequence to one setting to estimate how much longer a battery will remain useful at cycle t. This choice is based on the fact that battery degradation is not a memoryless process. The battery's recent changes tell us a great deal about how close it is to the end of its life. By looking at short time windows of cycle level measurements, the LSTM can learn degradation trends that are difficult to capture with non-sequential models.

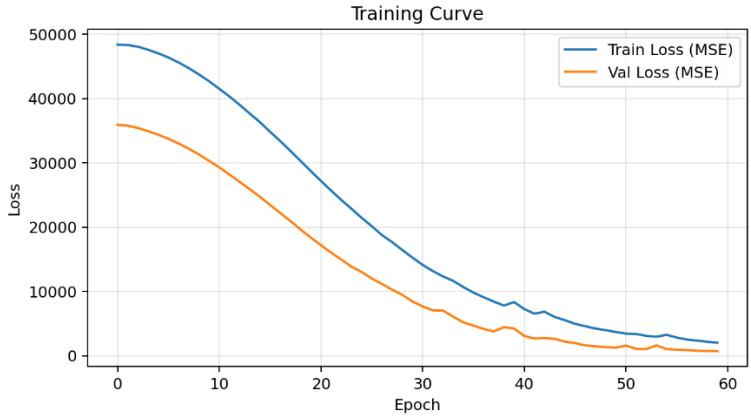

Fig. 1 Training and validation loss curves for the LSTM RUL model, demonstrating stable convergence without overfitting

For capacity forecasting, I use a Random Forest regressor to predict the capacity at the next cycle using flattened window-based features. From this predicted next cycle capacity, I obtain the state of health by dividing by the rated capacity. I prefer this method because it is direct, easy to understand, and remains stable when only a limited amount of data is available. In small data situations, Random Forest models tend to produce strong and consistent predictions without relying on strong assumptions about temporal behavior.

$$\mathrm{SOH}_{t+1} = \frac{\hat{C}_{t+1}}{C_{\mathrm{rated}}} \qquad (3)$$

RESULTS

The LSTM model performs very well in predicting how long battery B0027 will remain usable, even though this battery was not included during training. Using only recent cycle level measurements, the model can transfer what it has learned to this unseen cell and accurately estimate how many cycles remain until the end of life. The small error values indicate that the learned temporal degradation patterns generalize well across batteries, even when the number of available training examples is limited.

Capacity prediction is more challenging in this setting. The capacity changes only slightly from cycle to cycle, and when the window size is set to $W = 20$, the number of available test samples becomes small. Despite these limitations, the Random Forest baseline produces predictions that are stable and physically reasonable. The predicted capacity values follow the expected trend of gradual capacity fade and do not exhibit unphysical oscillations or drift.

Based on the predicted capacity for the next cycle, $\hat{C}_{t+1}$, I determine the state of health by normalizing with the rated capacity and applying the relation $SOH_{t+1} = \hat{C}_{t+1}/C_{rated}$.

This indirect approach to SOH prediction retains a clear physical interpretation, since SOH remains directly linked to the measurable capacity rather than being learned as an abstract target.

To summarize the results visually, I include a small number of figures that highlight the main findings. These include scatter plots comparing predicted and true values for both RUL and capacity, as well as time ordered comparisons showing how closely the predictions track the measured degradation trajectories. Together, these figures provide a clear and intuitive overview of model performance while fitting comfortably within a two-column layout.

EOL prediction is discussed conceptually but not explicitly modeled.

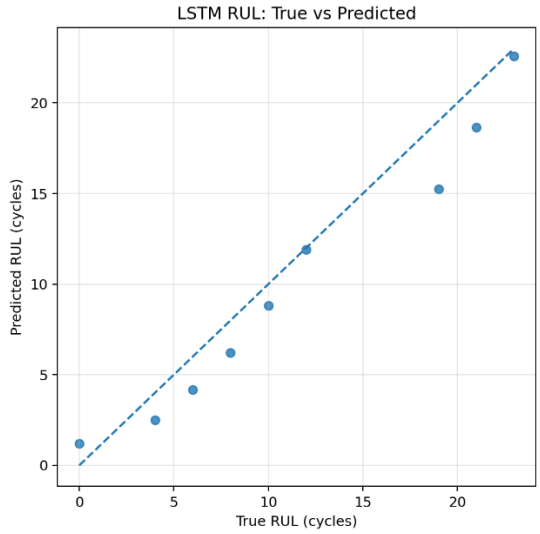

Fig. 2 Rul Prediction Parity (True vs Predicted)

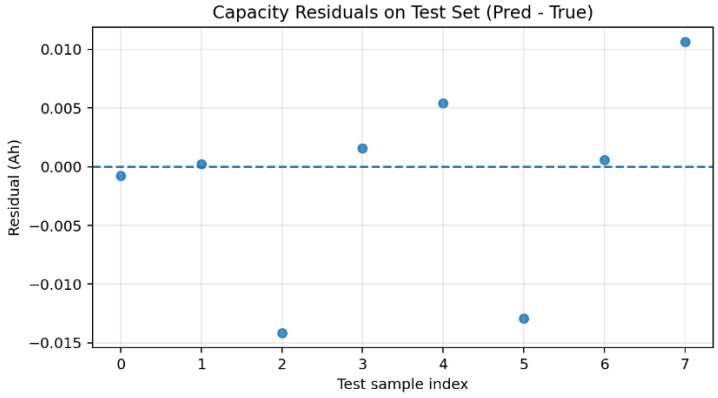

Fig. 3 Residuals of RUL predictions on the test battery, indicating small and unbiased prediction errors.

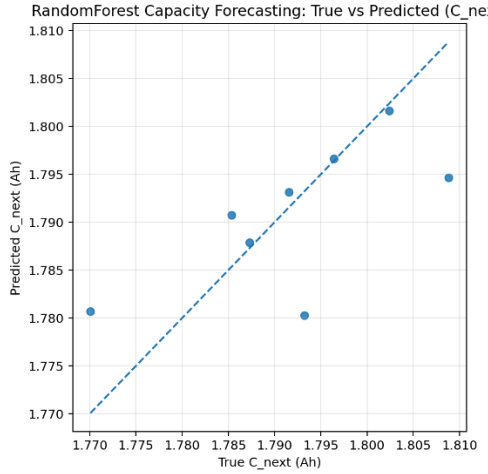

Fig. 4 Parity plot for one-step-ahead capacity forecasting using the Random Forest model.

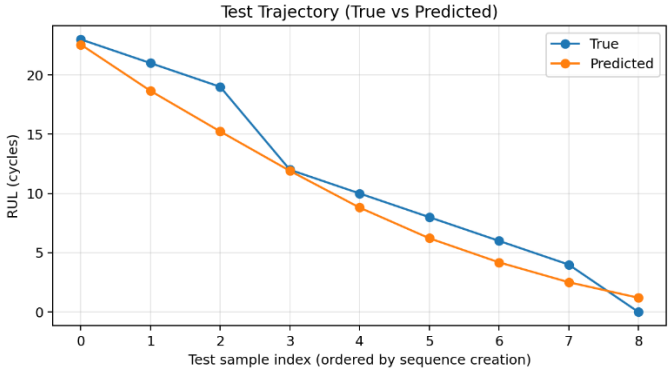

Fig. 5 Time-ordered comparison of true and predicted RUL values for battery B0027.

DISCUSSION

The findings show a distinct difference between sequence based and non-sequential learning when forecasting the lifespan of lithium-ion batteries under real world data constraints. The LSTM regressor shows strong generalization for predicting remaining useful life, even when tested on a

battery it hasn't seen before. This suggests that short periods of recent cycle level observations hold enough temporal information to reveal degradation dynamics as the battery nears the end of its life. The small prediction error for battery B0027 indicates that the identified temporal patterns are not just artifacts unique to a particular battery, but also reflect how cells degrade over time.

In contrast, capacity prediction is a more nuanced challenge. While Remaining Useful Life (RUL) fluctuates significantly as the battery nears its end of life, capacity usually decreases more gradually from cycle to cycle, especially over short intervals. This narrows the dynamic range of the target variable and makes the task more prone to noise. Still, the Random Forest baseline produces stable and physically consistent capacity predictions. The coefficient of determination is moderate, but the absolute errors are small and within acceptable physical limits. From an engineering standpoint, this is often better than models that seem more precise but are actually unstable or show artificial fluctuations.

One key design choice in this study is using battery level splitting instead of random cycle level splitting. This evaluation method more accurately mimics real deployment scenarios, where models are applied to batteries not seen during training. Although this approach usually results in lower reported performance metrics, it gives a more realistic measure of generalization and helps prevent overly optimistic conclusions caused by data leakage.[5] The LSTM's strong RUL performance under this rigorous evaluation shows that sequence learning is well suited for tasks that require awareness of degradation.

Deriving health status from predicted capacity emphasizes the importance of aligning machine learning outputs with physical definitions. Instead of treating SOH as an abstract goal, the model calculates it as a normalized capacity. This keeps a clear physical meaning and reduces the chance of generating implausible predictions. It also makes it easier to incorporate new SOH thresholds and end of life criteria without retraining the model.

This work shows that effective battery prognostics can be achieved with less data, as long as careful technical decisions are made. Minimal feature sets, consistent scaling, explicit artifact logging, and strong baselines all contribute to model robustness and reproducibility. The results indicate that valuable and reliable predictions can be made without relying on large amounts of data. Of course, larger datasets and more detailed measurements would likely improve performance even more.

Overall, these findings support using sequence-based models for estimating Remaining Useful Life (RUL) and physics aligned baselines for forecasting capacity and State of Health (SOH), especially in data limited situations where interpretability, stability, and generalization are crucial.

CONCLUSION

In this study, I demonstrated a practical and reproducible machine learning approach for predicting the remaining useful life and short-term capacity changes of lithium-ion batteries, even under realistic data limitations. I constructed a compact cycle level representation using the publicly available NASA PCoE battery aging dataset. This representation enables learning at the cycle time scale while remaining suitable for small data scenarios.

The results show that sequence-based learning is particularly effective for remaining useful life prediction. By using an LSTM regressor and enforcing a strict battery level evaluation, the model can generalize well to an unseen cell and accurately estimate the number of cycles remaining until the end of life. This supports the idea that short windows of recent degradation history contain sufficient temporal information to model battery aging, even when only a limited number of batteries are available for training.

I also showed that a non-sequential but physically aligned baseline can be both stable and useful for capacity forecasting. Although the cycle-to-cycle changes in capacity are small and the test set is limited, the Random Forest regressor produces consistent next cycle capacity predictions that follow the expected physical trend of gradual capacity fading. Deriving the state of health directly from the predicted capacity preserves a clear physical meaning and prevents SOH from being treated as an abstract learning target.

In addition to raw performance metrics, this work emphasizes engineering and evaluation choices that are critical for reliable battery prognostics. Battery level splitting, minimal feature sets, consistent scaling, and explicit artifact logging all help reduce data leakage and improve reproducibility. The results demonstrate that useful and physically reasonable predictions can be achieved without relying on large datasets, as long as the modeling choices remain aligned with both degradation physics and realistic data constraints.

Overall, this study provides a compact reference implementation for lithium-ion battery life prediction that balances machine learning capability with physical interpretability. The framework can be readily extended to multi step forecasting, alternative end of life definitions, or more advanced sequence models as additional data become available, while remaining grounded in realistic deployment conditions.

ACKNOWLEDGMENT

The author acknowledges Atatürk University for providing the academic environment and institutional support that made this study possible. The author also gratefully acknowledges the use of the publicly available NASA Prognostics Center of Excellence (PCoE) lithium-ion battery aging dataset and the open-source scientific computing community.

REFERENCES

[1] "Li-ion Battery Aging Datasets - Dataset - NASA Open Data Portal." Accessed: Dec. 15, 2025. [Online]. Available: https://data.nasa.gov/dataset/li-ion-battery-aging-datasets

[2] S. Hochreiter and J. Schmidhuber, "Long Short-Term Memory," *Neural Comput*, vol. 9, no. 8, pp. 1735–1780, Nov. 1997, doi: 10.1162/NECO.1997.9.8.1735.

[3] L. Breiman, "Random Forests," *Mach Learn*, vol. 45, no. 1, pp. 5–32, Oct. 2001, doi: 10.1023/A:1010933404324.

[4] M. Li *et al.*, "State of Health Estimation and Battery Management: A Review of Health Indicators, Models and Machine Learning," *Materials 2025, Vol. 18, Page 145*, vol. 18, no. 1, p. 145, Jan. 2025, doi: 10.3390/MA18010145.

[5] A. Geslin *et al.*, "Battery lifetime predictions: information leakage from unblinded training," Mar. 2023, doi: 10.26434/CHEMRXIV-2023-0ZHHD.

[6] J. Vetter *et al.*, "Ageing mechanisms in lithium-ion batteries," *J Power Sources*, vol. 147, no. 1–2, pp. 269–281, Sep. 2005, doi: 10.1016/J.JPOWSOUR.2005.01.006.

[7] G. dos Reis, C. Strange, M. Yadav, and S. Li, "Lithium-ion battery data and where to find it," *Energy and AI*, vol. 5, p. 100081, Sep. 2021, doi: 10.1016/J.EGYAI.2021.100081.

[8] K. Yang, S. Wang, L. Zhou, C. Fernandez, and F. Blaabjerg, "A Critical Review of AI-Based Battery Remaining Useful Life Prediction for Energy Storage Systems," *Batteries 2025, Vol. 11, Page 376*, vol. 11, no. 10, p. 376, Oct. 2025, doi: 10.3390/BATTERIES11100376.

Radiation Shielding Performance of W-Containing CoCrFeNi High-Entropy Alloys: A Machine Learning and EPIXS Study

Sevda SALTIK

Department of Physics, Atatürk University, Erzurum, Türkiye
sevdasaltik@atauni.edu.tr

ABSTRACT

High-entropy alloys (HEAs) have recently gained increasing attention for radiation shielding applications due to their unique compositional flexibility, structural stability, and tunable electron density. Among them, $(CoCrFeNi)_{100-x}W_x$ alloys constitute a promising system where W addition is expected to substantially modify photon–matter interaction behavior through its high atomic number and strong scattering cross-section. In this study, the mass attenuation coefficients (MAC) of five HEA compositions (W0, W5, W10, W15, W20) were predicted using a machine learning (ML) regression model and systematically compared with theoretical values calculated using the EPIXS database. Based on these MAC values, key radiation attenuation parameters including linear attenuation coefficient (LAC), half-value layer (HVL), mean free path (MFP), and effective atomic number (Z_{eff}) were evaluated over a broad photon energy range. The ML-predicted MAC values showed very good agreement with EPIXS data, demonstrating that the model successfully captures the nonlinear energy-dependent attenuation behavior of multicomponent HEAs. Results show that increasing W content leads to a notable enhancement in MAC and Z_{eff}, especially in the low-energy region dominated by the photoelectric effect. Consequently, alloys with higher W concentrations demonstrated reduced HVL and MFP values, indicating superior attenuation performance. These findings highlight the strong influence of W addition on the radiological response of CoCrFeNi-based HEAs and emphasize the potential of ML-assisted prediction frameworks for accelerating the screening and design of next-generation lightweight shielding materials.

Keywords – Radiation Shielding, Tungsten-Addition, High-Entropy Alloys, Machine Learning, Photon Attenuation.

INTRODUCTION

Escalating safety standards in nuclear and aerospace sectors necessitate the development of high-performance and sustainable shielding alternatives that overcome the limitations of traditional lead and concrete [1]. High-entropy alloys (HEAs) represent a new class of multi-principal element materials characterized by high configurational entropy, structural stability, and remarkable tunability of chemical and physical properties [2,3]. Their ability to accommodate substantial compositional variations without phase segregation makes them promising candidates for structural applications, high-temperature systems, and emerging radiation shielding technologies [4]. The photon–matter interaction behavior of HEAs depends strongly on their overall atomic number, electron density, and microstructural state; therefore, compositional tuning particularly through the incorporation of

high-Z elements provides a valuable route for engineering materials with enhanced attenuation performance [5,6].

In the broader context of radiation shielding materials, numerous alloy systems have been explored to meet the increasing demand for high-performance and lightweight alternatives. For instance, studies have reported that Fe-Ni-B based alloys exhibit superior gamma absorption performance in the 0.662–1.332 MeV range due to their optimized microstructures and higher electron densities [7]. Recent analyses on advanced superalloys [8] further confirm that Ni-based compositions outperform many conventional shielding materials in gamma attenuation, particularly in nuclear reactor environments where both structural strength and radiological stability are required.

Moreover, recent studies have emphasized the advantages of multi-component alloys for radiation shielding applications. EPICS-based theoretical assessments have demonstrated that Fe-, Cr-, and Ni-containing alloys outperform traditional materials at low photon energies [9,10]. Investigations on Co-, Cr-, and Ni-rich alloys revealed that microstructural features such as precipitate strengthening and solid-solution effects substantially influence photon interaction behavior [5,11]. In radiation shielding research, the mass attenuation coefficient (MAC) is the fundamental descriptor of photon interaction, from which key attenuation parameters can be derived. Databases such as EPIXS and XCOM provide reliable theoretical MAC values for photon energies and elemental compositions [10,12,13]. However, optimizing these parameters solely through experimental approaches is both time-consuming and resource-intensive.

Consequently, computational modeling has emerged as a cornerstone of modern alloy design for pre-synthesis evaluation. For multi-component alloys with complex chemical interactions and nonlinear compositional dependencies, machine learning (ML) models [8,14] have emerged as powerful tools, enabling rapid and accurate prediction of attenuation behavior without relying solely on tabulated datasets [12–14]. Recent ML-assisted shielding studies have demonstrated high fidelity between predicted and theoretical MAC values, revealing ML as a robust computational alternative for materials screening [15].

Motivated by these developments, the present work investigates the photon attenuation properties of $(CoCrFeNi)_{100-x}W_x$ (x = 0, 5, 10, 15, 20 wt.%) high-entropy alloys [16] by comparing machine-learning-predicted MAC values with EPIXS theoretical data. Based on these MAC values, the linear attenuation coefficient (LAC), half-value layer (HVL), mean free path

(MFP), and effective atomic number (Z_{eff}) were calculated to evaluate the influence of tungsten addition on gamma-ray shielding performance. This study provides a computationally efficient framework for designing compositionally optimized W-modified HEAs and contributes to the development of next-generation lightweight radiation shielding materials.

MATERIALS AND METHOD

A. Alloy Compositions

The investigated materials consist of $(CoCrFeNi)_{100-x}W_x$ high-entropy alloys with tungsten contents of x = 0, 5, 10, 15, and 20 wt.%. The elemental weight fractions of Co, Cr, Fe, Ni, and W were adopted from the reference literature and are summarized in Table 1. These compositions were selected to systematically evaluate the influence of increasing tungsten content on photon interaction and radiation shielding performance.

Alloy	Co (wt.%)	Cr (wt.%)	Fe (wt.%)	Ni (wt.%)	W (wt.%)
W0	26.14	23.06	24.77	26.03	0.00
W5	22.31	19.68	21.14	22.22	14.65
W10	19.19	16.93	18.18	19.11	26.60
W15	16.59	14.64	15.72	16.52	36.53
W20	14.40	12.70	13.64	14.34	44.91

B. Theoretical Photon Attenuation Parameters

The interaction of gamma photons with matter is governed by fundamental atomic processes, including the photoelectric effect, Compton scattering, and pair production, whose relative contributions depend primarily on photon energy and the atomic number of the absorbing material. In radiation shielding studies, attenuation behavior is quantitatively described using energy-dependent parameters derived from the mass attenuation coefficient (MAC), which expresses the probability of photon interaction per unit mass [3,17].

The attenuation of a monoenergetic gamma-ray beam as it propagates through a homogeneous material can be described by the Beer–Lambert exponential attenuation law:

$$I=I_0e^{-\mu x} \quad (1)$$

where I_0 and I denote the incident and transmitted photon intensities, x is the absorber thickness, and μ is the linear attenuation coefficient. The LAC is an energy-dependent parameter that reflects both the intrinsic interaction probability of the material and its density. It is related to the mass attenuation coefficient (MAC), μ_m, through the expression:

$$\mu=\mu_m\rho \quad (2)$$

where ρ is the density of the material. Unlike the LAC, the MAC is independent of sample geometry and thickness, enabling a direct and intrinsic comparison of attenuation performance among different materials. This property makes MAC particularly suitable for evaluating complex multicomponent alloys and composite systems [18].

Using the calculated MAC values, several secondary shielding parameters were obtained to further assess the attenuation performance of the investigated alloys. In this study, the half-value layer (HVL), mean free path (MFP), and effective atomic number (Z_{eff}) were directly derived using the EPIXS database, which provides energy-dependent attenuation parameters for multicomponent materials based on validated photon interaction cross-sections and mixture rules.

The half-value layer (HVL), defined as the material thickness required to reduce the incident photon intensity by 50%, is expressed as:

$$HVL=\ln(2)/\mu \quad (3)$$

Similarly, the mean free path (MFP), which represents the average distance a photon travels between successive interaction events, was determined as:

$$MFP=\frac{1}{\mu} \quad (4)$$

Lower HVL and MFP values correspond to improved shielding efficiency, as thinner material sections are sufficient to achieve effective photon attenuation.

Another important descriptor of photon–matter interaction is the effective atomic number (Z_{eff}), which characterizes the collective atomic response of

multicomponent materials to photon irradiation. In this study, $Z_{\text{eff}}$was calculated using the following relati on:

$$Z_{\text{eff}} = \left(\sum_i \frac{f_i Z_i}{A_i} \right)^{1/2} \quad (5)$$

where f_i, Z_i, and $A_i$denote the fractional abundance, atomic number, and atomic mass of the i-th constituent element, respectively. The effective atomic number is particularly significant in the low-energy photon region, where the photoelectric effect dominates and the interaction probability exhibits a strong dependence on atomic number, approximately proportional to Z^{4-5}. In the present work, energy-dependent Z_{eff} values were obtained directly from EPIXS calculations using elemental composition and photon interaction cross-sections.

In this study, a supervised machine learning approach [19] based on a multilayer perceptron (MLP) architecture was employed to predict the mass MAC values of $(CoCrFeNi)_{100-x}W_x$ high-entropy alloys over a wide photon energy range. MLP-based neural networks are well suited for regression problems involving complex and nonlinear relationships, particularly in multicomponent alloy systems where photon–matter interactions depend simultaneously on composition and energy [20,21].

The MLP model was constructed with an input layer, one or more hidden layers employing nonlinear activation functions, and a single output neuron representing the predicted MAC value. Model training was performed using a backpropagation algorithm by minimizing the mean squared error between the predicted and reference MAC values. The available dataset was divided into training and validation subsets to monitor model performance and prevent overfitting.

After training, the predictive capability of the ML model was evaluated by comparing the ML-estimated MAC values with those obtained from the EPIXS database across all investigated alloy compositions and photon energies. The close agreement between predicted and theoretical results demonstrates that the MLP model successfully captures the nonlinear dependence of photon attenuation behavior on alloy composition and energy. These findings confirm that the proposed ML framework provides a reliable and computationally efficient tool for rapid prediction and screening of radiation shielding properties in W-modified high-entropy alloys.

RESULTS AND DISCUSSIONS

The variation of mass attenuation coefficient (MAC) values with photon energy for the investigated $(CoCrFeNi)_{100-x}W_x$ high-entropy alloys is presented in **Figure 1**, as obtained from EPIXS theoretical calculations. For all compositions, MAC values exhibit a pronounced decrease with increasing photon energy over the investigated energy range, which is consistent with the characteristic behavior of photon attenuation in metallic and multicomponent materials.

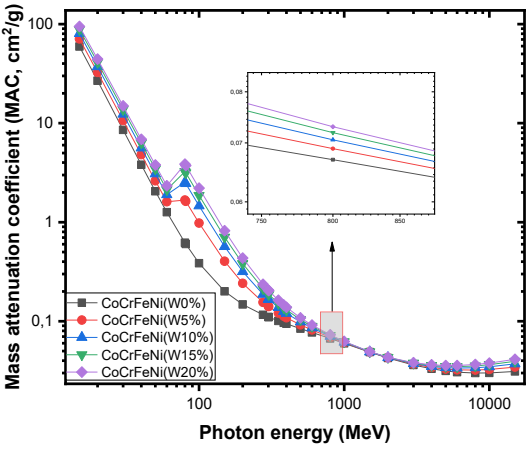

Figure 1: Comparison of the energy-dependent MAC values for $(CoCrFeNi)_{100-x}W_x$.

In the low-energy region, relatively high MAC values are observed due to the dominance of the photoelectric effect, where photon absorption probability strongly depends on the atomic number of the constituent elements. As photon energy increases, Compton scattering becomes the prevailing interaction mechanism, leading to a smoother decline in MAC values and reduced sensitivity to compositional differences.

A systematic compositional trend is clearly observed in **Figure 1**, where increasing tungsten content results in consistently higher MAC values across the entire photon energy range. This behavior can be attributed to the significantly higher atomic number of tungsten (Z = 74) compared to Co (Z = 27), Cr (Z = 24), Fe (Z = 26), and Ni (Z = 28), which increases both the average atomic number and electron density of the alloy. The influence of W addition is particularly pronounced at lower photon energies, where the photoelectric effect dominates and the MAC exhibits a strong dependence on

atomic number, approximately proportional to Z^{4-5}. The abrupt increase observed around 69 keV originates from the K-absorption edge of tungsten (W), where a sharp enhancement in the photoelectric interaction occurs.

Figure 2 illustrates the variation of HVL values as a function of photon energy for the investigated $(CoCrFeNi)_{100-x}W_x$ high-entropy alloys.

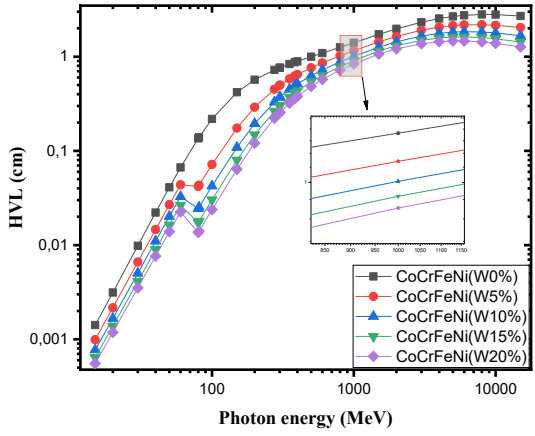

Figure 2: Effect of tungsten content on the half-value layer (HVL) of $(CoCrFeNi)_{100-x}W_x$ alloys as a function of photon energy.

In the low-energy photon region (E < 0.1 MeV), all alloy compositions exhibit relatively low HVL values, indicating strong attenuation capability against low-energy gamma photons. However, noticeable differences among the compositions are observed in this energy range. As shown in **Figure 2**, the W-rich alloys display systematically lower HVL values compared to alloys with lower tungsten content. For example, at 0.02 MeV, the HVL value of the W20 alloy is approximately 1.18×10^{-3} cm, demonstrating a significantly enhanced attenuation performance at low photon energies.

The linear attenuation coefficient (LAC) represents the probability of photon interaction per unit path length within a material and is directly related to both the mass attenuation coefficient and the material density.

As observed in **Figure 3**, in the low-energy region, relatively high LAC values are obtained, reflecting strong photon absorption dominated by the photoelectric effect. In this energy range, clear differences among the compositions are evident, with W-rich alloys exhibiting higher LAC values compared to alloys with lower tungsten content.

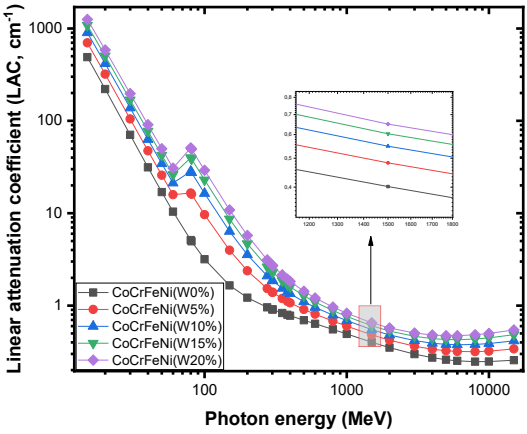

Figure 3: Photon energy dependence of LAC for $(CoCrFeNi)_{100-x}W_x$ alloy.

With increasing photon energy, the LAC values decrease significantly and the separation between different compositions becomes less pronounced. This trend corresponds to the transition from photoelectric absorption to Compton scattering as the dominant interacstion mechanism, where the dependence on atomic number is reduced.

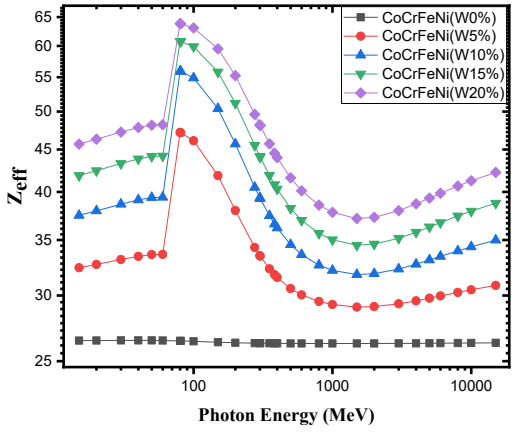

Figure 4: Variation of effective atomic number (Z_{eff}) with photon energy for $(CoCrFeNi)_{100-x}W_x$ high-entropy alloys.

In **Figure 4**, at low photon energies, Z_{eff} values exhibit a noticeable increase accompanied by peak-like features, which are associated with inner-shell absorption processes. These features become more pronounced with increasing tungsten content, while no distinct peak is observed for the W0 alloy. This behavior indicates that the abrupt enhancement in Z_{eff} is primarily driven by the presence of tungsten, whose high atomic number and strong inner-shell binding energies significantly increase photoelectric absorption once the corresponding threshold energies are exceeded. As the tungsten concentration increases, the contribution of inner-shell electrons becomes more significant, leading to progressively higher Z_{eff} peaks.

With increasing photon energy, Z_{eff} values decrease and gradually converge for all compositions, reflecting the transition to Compton scattering as the dominant interaction mechanism. In this energy region, photon interactions depend mainly on electron density rather than atomic number, resulting in reduced compositional sensitivity. At higher energies, Z_{eff} approaches a quasi-stable behavior for all alloys.

Figure 5 compares the MFP values of the investigated $(CoCrFeNi)_{100-x}W_x$ high-entropy alloys with the commercial superalloy Inconel 718 over a broad photon energy range. MFP values increase with photon energy for all materials, reflecting the reduced interaction probability of high-energy photons. In the low-energy region, MFP values are relatively small for all compositions, indicating efficient photon attenuation dominated by photoelectric absorption. As photon energy increases, a gradual rise in MFP is observed due to the transition toward Compton scattering, which becomes the dominant interaction mechanism.

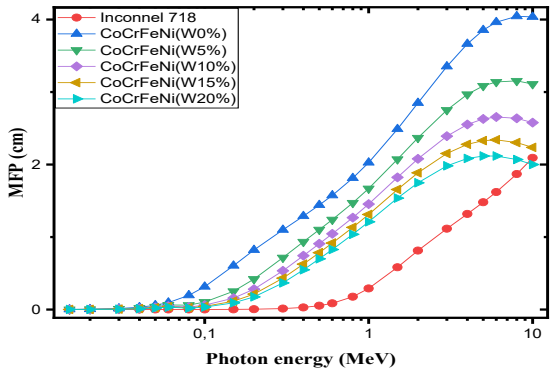

Figure 5: Comparison of mean free path (MFP) values of W-modified CoCrFeNi HEAs and Inconel 718 as a function of photon energy.

A clear distinction is evident between the W-modified high-entropy alloys and Inconel 718 across the investigated energy range. The tungsten-containing CoCrFeNi alloys consistently exhibit lower MFP values compared to Inconel 718, demonstrating superior photon attenuation capability.

Figure 6 compares MAC values predicted by the MLP model with those obtained from EPIXS theoretical calculations for the CoCrFeNi(W20) alloy. The agreement between the MLP predictions and EPIXS calculations was further assessed using quantitative error metrics.

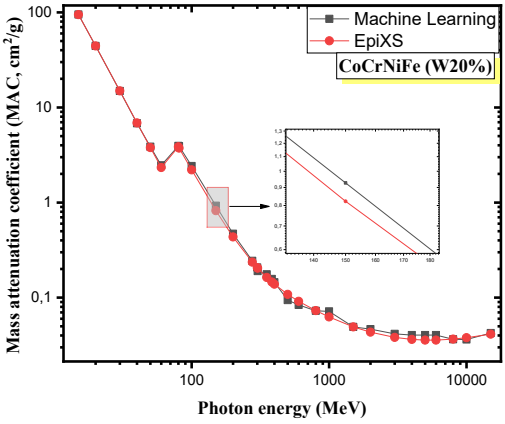

Figure 6: Comparison of MAC values predicted by the machine learning model and EPIXS calculations for CoCrFeNi(W20%).

Over the 15 keV–15 MeV range, the model yielded an MAE of 3.69×10^{-2} $g^{-1}$and an RMSE of $6.62 \times 10^{-2} cm^2 g^{-1}$. These results indicate that the MLP captures the overall energy-dependent attenuation trend with satisfactory accuracy. The remaining deviations may be reduced by increasing the diversity of the training data, tuning the network architecture/hyperparameters. Furthermore, the results highlights the potential of machine learning as a fast and efficient alternative tool for predicting photon attenuation properties of complex multicomponent alloys, particularly for composition screening and preliminary material design.

CONCLUSION

This study presents a hybrid computational investigation of W-modified CoCrFeNi high-entropy alloys for potential radiation shielding applications. Photon attenuation properties were systematically evaluated using theoretical EPIXS calculations and machine learning predictions based on a multilayer perceptron (MLP) model. The results clearly demonstrate that increasing tungsten content significantly enhances gamma-ray shielding performance, particularly in the low-energy region where photoelectric absorption dominates.

W-rich alloys exhibit higher mass and linear attenuation coefficients, along with reduced half-value layer (HVL) and mean free path (MFP) values, indicating improved attenuation efficiency. The effective atomic number (Zeff) analysis further confirms the strong contribution of tungsten to photon–matter interactions, while comparison with the commercial superalloy Inconel 718 reveals superior shielding performance for the W-containing high-entropy alloys across a broad photon energy range. The reliability of the machine learning predictions was quantitatively assessed using standard error metrics. The MLP model achieved a mean absolute error (MAE) of 3.69×10^{-2} cm^2 $g^{-1}$and a root mean square error (RMSE) of 6.62×10^{-2} cm^2 g^{-1}, indicating that the model captures the overall attenuation behavior with satisfactory accuracy. Although minor deviations remain, these may be reduced by expanding the training dataset and incorporating physics-informed modeling strategies.

Overall, the findings highlight the potential of W-modified CoCrFeNi high-entropy alloys as efficient and lightweight radiation shielding materials and demonstrate that machine learning provides a reliable and computationally efficient framework for the rapid screening and design of advanced multicomponent alloys.

ACKNOWLEDMENTS

The author would like to thank Prof. Dr. Esra Kavaz Perisanoglu for her valuable guidance throughout this study. Institutional support from Atatürk University is also appreciated.

REFERENCES

[1] M.M. AbdelKader, M.T. Abou-Laila, M.S.S. El-Deeb, E.O. Taha, A.S. El-Deeb, Structural, radiation shielding, thermal and dynamic mechanical analysis for waste rubber/EPDM rubber composite loaded with Fe2O3 for green environment, Sci. Rep. 14 (2024) 12440. https://doi.org/10.1038/s41598-024-62308-4.

[2] E.O. Echeweozo, N. Alomayrah, S. Alomairy, Z.A. Alrowaili, N.S. Alsaiari, M.S. Al-Buriahi, Evaluation of gamma radiation shielding characteristics of FeNbSc-based alloys, Radiat. Eff. Defects Solids 180 (2025) 1212–1227. https://doi.org/10.1080/10420150.2025.2458319.

[3] G.F. Knoll, Radiation Detection and Measurement, 4th ed., John Wiley & Sons, 2010.

[4] Z. Sun, M. Roscher, M.C. Paolantonio, V. Soh, C. Liu, S.-P. Tsai, C.K. Ng, C.C. Tan, P. Wang, E.A. Jägle, Additive manufacturing of sustainable and heat-resistant Al-Fe-Mo-Si-Zr alloys, J. Alloys Compd. 1010 (2025) 177118. https://doi.org/10.1016/j.jallcom.2024.177118.

[5] H. Yaykaşlı, H. Eskalen, Y. Kavun, M. Göğebakan, A.H. Kaya, N. Yorulmaz, CoCrFeNiSi high entropy alloy: Synthesis, structural and radiation shielding properties, Prog. Nucl. Energy 165 (2023) 104930. https://doi.org/10.1016/j.pnucene.2023.104930.

[6] S.H. Güler, Ö. Güler, E. Kavaz, G. ALMisned, M.G. Albayrak, B. Issa, H.O. Tekin, Fabrication and structural, physical, and nuclear radiation shielding properties for Oxide Dispersion-Strengthened (ODS) alloys through Erbium (III) oxide, Samarium (III) oxide, and Praseodymium (III) oxide into 316L matrix, Ceram. Int. 50 (2024) 5443–5452. https://doi.org/10.1016/j.ceramint.2023.11.295.

[7] N. Ucar, RADIATION SHIELDING PROPERTIES OF BORIDED Fe-Ni ALLOYS., Int. J. Adv. Res. 6 (2018) 979–983. https://doi.org/10.21474/IJAR01/7448.

[8] X. Juncai, R. Qingwen, S. Zhenzhong, Prediction of the strength of concrete radiation shielding based on LS-SVM, Ann. Nucl. Energy 85 (2015) 296–300. https://doi.org/10.1016/j.anucene.2015.05.030.

[9] A.H. Almuqrin, J.F.M. Jecong, F.C. Hila, C.V. Balderas, M.I. Sayyed, Radiation shielding properties of selected alloys using EPICS2017 data library, Prog. Nucl. Energy 137 (2021) 103748. https://doi.org/10.1016/j.pnucene.2021.103748.

[10] E. Kavaz, N. Ekinci, H.O. Tekin, M.I. Sayyed, B. Aygün, U. Perişanoğlu, Estimation of gamma radiation shielding qualification of newly developed glasses by using WinXCOM and MCNPX code, Prog. Nucl. Energy 115 (2019) 12–20. https://doi.org/10.1016/j.pnucene.2019.03.029.

[11] B. Yu, Y. Ren, Y. Zeng, W. Ma, K. Morita, S. Zhan, Y. Lei, G. Lv, S. Li, J. Wu, Recent progress in high-entropy alloys: A focused review of preparation processes and properties, J. Mater. Res. Technol. 29 (2024) 2689–2719. https://doi.org/10.1016/j.jmrt.2024.01.246.

[12] M.J. Berger, J.H. Hubbell, XCOM: Photon cross sections on a personal computer, Oak Ridge, TN, 1987. https://doi.org/10.2172/6016002.

[13] F.C. Hila, A. Asuncion-Astronomo, C.A.M. Dingle, J.F.M. Jecong, A.M. V. Javier-Hila, M.B.Z. Gili, C. V. Balderas, G.E.P. Lopez, N.R.D. Guillermo,

A. V. Amorsolo, EpiXS: A Windows-based program for photon attenuation, dosimetry and shielding based on EPICS2017 (ENDF/B-VIII) and EPDL97 (ENDF/B-VI.8), Radiat. Phys. Chem. 182 (2021) 109331. https://doi.org/10.1016/j.radphyschem.2020.109331.

[14] T.A. Nahool, A.M. Abdelmonem, M.S. Ali, A.M. Yasser, Using machine learning to predict gamma shielding properties: a comparative study, New J. Phys. 26 (2024) 093035. https://doi.org/10.1088/1367-2630/ad4a21.

[15] S. Saltık, O. Kıyıkcı, T. Akman, E. Öz, E.K. Perişanoğlu, Monte Carlo and Machine Learning-Based Evaluation of Fe-Enriched Al Alloys for Nuclear Radiation Shielding Applications, Materials (Basel). 18 (2025) 2582. https://doi.org/10.3390/ma18112582.

[16] M. Mezbanipour, M. Reihanian, K. Gheisari, Influence of W addition on the phase evolution, mechanical properties, and corrosion resistance of CoCrFeNi-based high-entropy alloys, Intermetallics 188 (2026) 109065. https://doi.org/10.1016/j.intermet.2025.109065.

[17] B. Oto, E. Kavaz, N. Çakar, H. Erzen Yıldız, H. Tunç, Effect of CeO2 and Er2O3 co-doping on the structural and radiation shielding properties of ceramics: An experimental and theoretical evaluation, Radiat. Phys. Chem. 240 (2026) 113469. https://doi.org/10.1016/j.radphyschem.2025.113469.

[18] A. Araz, E. Kavaz, R. Durak, F. Akyıldız, Nuclear shielding characteristics of newly developed composite metal foams: Role of CeO2 addition and foam type, Mater. Chem. Phys. 311 (2024) 128464. https://doi.org/10.1016/j.matchemphys.2023.128464.

[19] J. Ling, E. Antono, S. Bajaj, S. Paradiso, M. Hutchinson, B. Meredig, B.M. Gibbons, Machine Learning for Alloy Composition and Process Optimization, in: Vol. 6 Ceram. Control. Diagnostics, Instrumentation; Educ. Manuf. Mater. Metall., American Society of Mechanical Engineers, 2018. https://doi.org/10.1115/GT2018-75207.

[20] R. Rojas, Neural Networks, Springer Berlin Heidelberg, Berlin, Heidelberg, 1996. https://doi.org/10.1007/978-3-642-61068-4.

[21] I.N. da Silva, D. Hernane Spatti, R. Andrade Flauzino, L.H.B. Liboni, S.F. dos Reis Alves, Artificial Neural Networks, Springer International Publishing, Cham, 2017. https://doi.org/10.1007/978-3-319-43162-8.

Application of *In Silico* Models for Toxicity Prediction of Selected Chloroacetanilide Herbicides

Nazli TURKTEN[1]
Yunus KARATAS[2]
Yelda YALCIN GURKAN[3]
Simal KURUMOGLU[4*]

[1]Assoc.Prof.Dr.Nazli Turkten, Kirsehir Ahi Evran University, Faculty of Arts and Sciences, Department of Chemistry, 40100, Kirsehir, Türkiye, nazli.turkten@yahoo.com, https://orcid.org/0000-0001-9343-3697
[2]Prof.Dr.Yunus Karatas, Department/Research Institute, University, Country1Kirsehir Ahi Evran University, Faculty of Arts and Sciences, Department of Chemistry, 40100, Kirsehir, Türkiye, ykaratas@ahievran.edu.tr, https://orcid.org/0000-0002-3826-463X
[3]Prof.Dr.Yelda Yalcin Gurkan, Tekirdag Namik Kemal University, Faculty of Arts and Sciences, Department of Chemistry, 59030, Tekirdag, Türkiye, yyalcin@nku.edu.tr, https://orcid.org/0000-0002-8621-2025
[4*]Corresponding Author: Assist.Prof.Dr.Simal Kurumoglu, Tekirdag Namik Kemal University, Faculty of Arts and Sciences, Department of Chemistry, 59030, Tekirdag, Türkiye, skurumoglu@nku.edu.tr, https://orcid.org/0000-0001-9456-5456

ABSTRACT

Chloroacetanilides are one of the intensively used classes of herbicides for pre-emergent and early post-emergent treatments in modern agriculture, enhancing crop production. The presence of herbicides in water and food raises significant global health concerns due to their toxic effects on non-target organisms, aquatic species, and the ecosystem. Despite the widespread application of chloroacetanilide herbicides, there is a notable gap in the estimation of acute toxicity data, particularly regarding the utilization of in silico methods.

In this study, the predicted toxicity of five chloroacetanilide herbicides (butachlor, dimethachlor, metazachlor, metolachlor, and propachlor) was assessed theoretically using ProTox 3.0 and TEST in silico tools. The predicted lethal dose 50 (LD50) and the lethal concentration 50 (LC50) values for chloroacetanilides were determined using in silico approaches, providing an ethical alternative to animal testing. Propachlor indicated the lowest LD50 values of 290 mg/kg and 635 mg/kg for ProTox 3.0 and TEST methods, respectively. All compounds revealed the signs of developmental toxicity based on the TEST method.

Keywords –Chloroacetanilides, Herbicides, In Silico Tool, Protox 3.0, TEST.

INTRODUCTION

Among the diversity of pesticides, herbicides stand out as an intensively utilized class for controlling or killing weeds globally. They account for 47.5% of the estimated two million tonnes of annual pesticide consumption. Herbicides are stable chemicals that support crop production, providing economic benefits by increasing crop yields. The mode of action of these chemical agents varies, including growth regulators, seedling growth inhibitors, photosynthesis inhibitors, lipid biosynthesis inhibitors, amino acid biosynthesis inhibitors, and inhibitors of pigment biosynthesis. They are primarily regarded as safe due to their specific action mechanisms that target only plants and do not directly affect animal physiology. However, the application of herbicides depends upon the dose relationship that influences the herbicide-soil enzyme interaction. The heavy utilization of herbicides results in inhibition of enzyme activity, while a low dosage acts as a stimulator. Herbicides are certainly not biodegradable and can enter aquatic systems, affecting ecological biodiversity by harming various non-target organisms, such as animals and soil bacteria (Bamal et al., 2024; Bhardwaj, Pandey, & Dubey, 2021; Rani et al., 2021).

Chloroacetanilide herbicides are a subgroup of acetamide compounds. Acetochlor, alachlor, butachlor, dimethachlor, metolachlor, pretilachlor, propachlor, and propaquizafop are the most well-known members.

Acetochlor and alachlor are prohibited in many countries, although they are still permitted in others.

Butachlor is a systemic selective herbicide mostly applied in rice paddies to control broadleaf weeds and perennial grasses. This herbicide can be toxic to non-target species and may affect microbial populations in the soil (Abigail, Samuel, & Ramalingam, 2015; Bamal et al., 2024).

Dimethachlor is particularly applied for oilseed rape protection, which was known as a medium-toxic pesticide with an average lethal dose of 1600 mg/kg, and was noted to be extremely harmful to algae and fish (Ćurčić et al., 2022).

Metazachlor is widely applied for weed management at pre- and early post-emergence stages in oilseed crops, particularly in groundnuts, rapeseed, and soybeans. Metazachlor inhibits the assembly of long-chain fatty acids, which are critical for cell division and growth processes (Bamal et al., 2024; Velisek et al., 2020). Velisek et al. found that a concentration of metazachlor at 0.0790 μmol/L in the environment could alter the movement of marbled crayfish (Velisek et al., 2020). Pretilachlor is primarily used in seeded and transplanted rice during the pre- and early post-emergence stages, effectively controlling annual grasses and various broad-leaved weeds (Bamal et al., 2024). It was reported that the acute toxicity of pretilachlor on the epigeic earthworm, *E. fetida,* was very toxic with a LC_{50} value of 9.23 μgcm^{-2} (Wang et al., 2012).

Metolachlor is a pre-emergent chloroacetanilide utilized to manage broadleaf and annual grassy weeds (Bamal et al., 2024). The toxicity of metolachlor and its degradation products was assessed on the sperm cells and embryos of the Pacific oyster, *Crassostrea gigas*. The exposure of these compounds could cause developmental defects and DNA damage in the early life stages of *Crassostrea gigas* (Mai et al., 2014).

Another chloroacetanilide herbicide, propachlor, is applied in the pre-emergence stage to control the weeds. Propachlor is considered harmless and low in toxicity to non-target organisms (Bamal et al., 2024). However, it was reported that propachlor could exhibit cytotoxic effects on the rat and the human hepatoma cell lines (Dierickx, 1999). Propaquizafop is a synthetic chloroacetanilide with a wide range of applications for various crops, and it works effectively and rapidly (Cheng et al., 2024). This fatty acid herbicide was found to have hepatocarcinogenic activity in rodents, which could potentially induce liver tumors in rodents after dietary administration; however, it did not present a relevant health risk to humans (Strupp et al., 2018).

Recently, the prediction of metabolism and toxicity of pesticides has been achieved using *in silico* tools as an eco-friendly, low-cost, and time-efficient way to replace animal testing (Liu et al., 2024; Noga & Jurowski, 2025; Weyrich, Joel, Lewin, Hofmann, & Frericks, 2022). This study assessed the predicted toxicity of five chloroacetanilide herbicides:

butachlor, dimethachlor, metazachlor, metolachlor, and propachlor using two quantitative *in silico* methods, ProTox 3.0 and TEST methods. The predicted LD_{50} values of chloroacetanilides obtained from both ProTox 3.0 and TEST methods were compared to experimental literature data.

MATERIALS AND METHODS

The chemical structures of butachlor, dimethachlor, metazachlor, metolachlor, and propachlor chloroacetanilides obtained from PubChem (https://pubchem.ncbi.nlm.nih.gov) are presented in Figure 1.

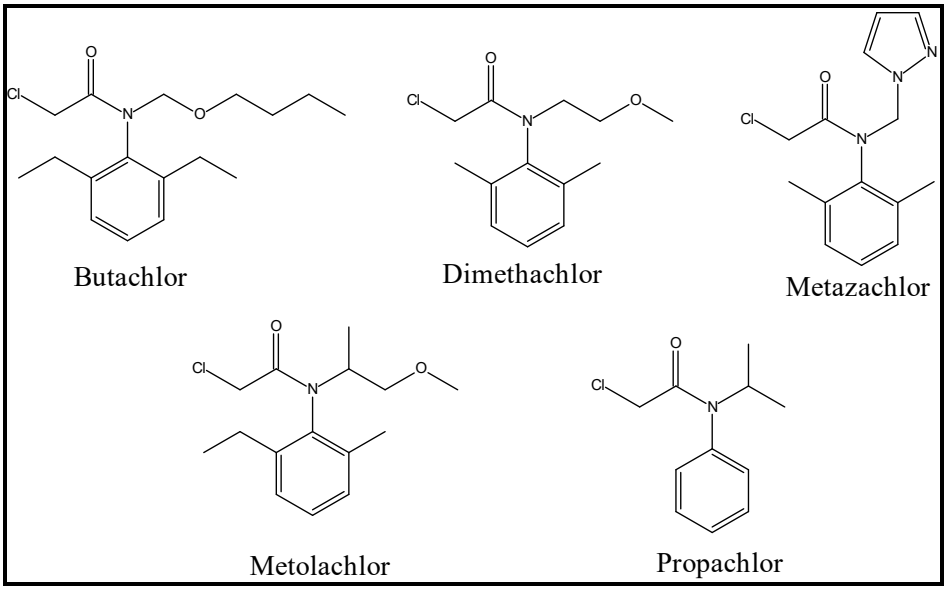

Figure 1. The chemical structures of selected chloroacetanilides.

TEST version 5.1.2 software website, USEPA Toxicity Estimation Software Tool (https://www.epa.gov/comptox-tools/toxicity-estimation-software-tool-test, 2020) is based on a quantitative structure–activity relationship (QSAR) model that applies SMILES or CAS numbers, and related data is presented in Table 1. The predicted acute oral LD_{50} toxicity in rats was determined using a consensus QSAR approach, which is regarded as the most reliable method in TEST software. The endpoints of the selected chloroacetanilides were assessed using the TEST approach, such as *Fathead minnow* LC_{50} (96

h), *Tetrahymena pyriformis* IGC_{50}, 50% growth inhibitory concentration (48 h), *Daphnia magna* LC_{50} (48 h), developmental toxicity, and bioconcentration factor.

Table 1. The identifiers of the selected chloroacetanilides.

Chloroacetanilides	**CAS**	**SMILES**
Butachlor	23184-66-9	CCCCOCN(C1=C(C=CC=C1CC)CC)C(=O)CCl
Dimethachlor	50563-36-5	CC1=C(C(=CC=C1)C)N(CCOC)C(=O)CCl
Metazachlor	67129-08-2	CC1=C(C(=CC=C1)C)N(CN2C=CC=N2)C(=O)CCl
Metolachlor	51218-45-2	CCC1=CC=CC(=C1N(C(C)COC)C(=O)CCl)C
Propachlor	1918-16-7	CC(C)N(C1=CC=CC=C1)C(=O)CCl

ProTox 3.0 is an open, web-based *in silico* platform that incorporates machine similarity-based prediction, fragment propensities, pharmacophore models, and learning algorithms, and widespread databases based on cheminformatics principles to group toxicity into six classifications according to predicted LD_{50} values (Banerjee, Kemmler, Dunkel, & Preissner, 2024; https://tox.charite.de/protox3/).

RESULTS AND DISCUSSION

The acute toxicity levels of butachlor, dimethachlor, metazachlor, metolachlor, and propachlor chloroacetanilides were addressed using predicted LD_{50} values derived from *in silico* tools (Figure 2). The predicted toxicity effects of these chloroacetanilides were derived by computational tools, specifically ProTox 3.0 (Tables 2 and 3) and TEST (Table 4), *in silico* methods. Additionally, the predicted developmental toxicity values of these chloroacetanilides, obtained using TEST software, are presented in Figure 3.

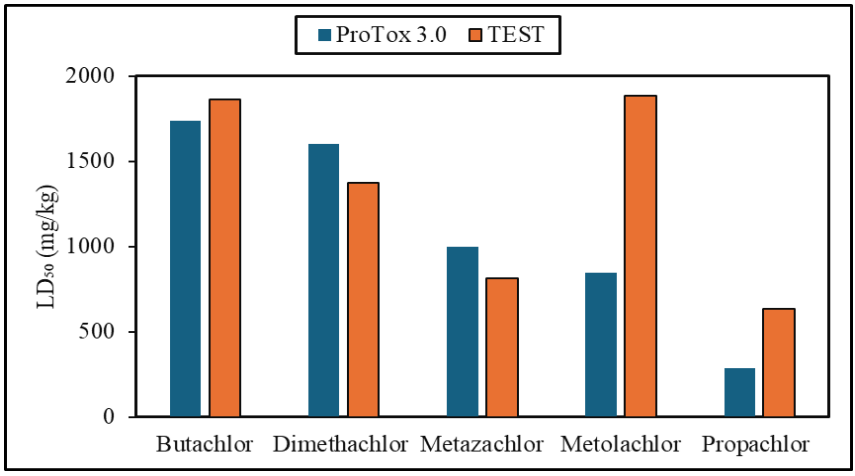

Figure 2. The predicted LD_{50} values of chloroacetanilides using *in silico* tools.

The acute toxicity of butachlor was evaluated using adult earthworms, *Eisenia fetida*, resulting in an LC_{50} value of 0.515 mg kg^{-1} (Gobi & Gunasekaran, 2010). The acute toxicity and stress behavior of butachlor were evaluated on freshwater fish (*Heteropneustes fossilis, Clarias batrachus, Channa punctatus*) and mosquito larvae (*Culex pipiens fatigans*). The LC_{50} values were found to be 2.34 ppm, 3.25 ppm, 2.82 ppm, and 35 ppm for *Heteropneustes fossilis*, *Clarias batrachus*, *Channa punctatus*, and *Culex pipiens fatigans,* respectively (Farah, Ateeq, Ali, Sabir, & Ahmad, 2004). These experimental LC_{50} values for freshwater species were similar to the predicted LC_{50}, 96 h value (2.78 mg/L) exposure to the *Fathead minnow* using the TEST *in silico* platform.

Table 2. The predicted toxicological class of selected chloroacetanilides using the ProTox 3.0.

Chloroacetanilides	**Octanol/water partition coefficient (logP)**	**LD_{50} (mg/kg)**	**Predicted Toxicity Class**
Butachlor	4.16	1740	4
Dimethachlor	2.52	1600	4
Metazachlor	2.73	1000	4
Metolachlor	3.16	849	4
Propachlor	2.67	290	3

Sun et al. reported that pre-exposure to the volatile butachlor, a tobacco cutworm, *Spodoptera litura* larvae, notably decreased susceptibility to the chlorpyrifos. Additionally, exposure to this non-ionic herbicide was

indicated to activate the expression of detoxification enzyme genes (Sun et al., 2021). The acute toxic effect of butachlor, based on LD_{50} values for oral and dermal inhalation routes in rats, was 2620 mg/kg and greater than 5.3 mg/L, respectively. In mice, the estimated LD_{50} (oral) value was 4140 mg/kg, while the LD_{50} (dermal inhalation) value in rabbits was estimated at 13000 mg/kg (Abigail et al., 2015). According to the ProTox 3.0 prediction, the toxicity classification of butachlor chloroacetanilide was found to be class 4, which was an acute oral toxicity LD_{50} value of 1740 mg/kg. The predicted LD_{50} value derived from the TEST software was 1861 mg/kg. The predicted LD_{50} values obtained from two different *in silico* approaches were nearly identical. However, these values were slightly lower than the experimental oral LD_{50} value reported in rats, 2620 mg/kg (Abigail et al., 2015).

Table 3. The predicted toxicological endpoints using the ProTox 3.0 *in silico* platform.

Chloroacetanilides	**Oral rat LD_{50}, 96 h, mg/kg**	***Fathead minnow* LC_{50}, 96 h mg/L**	***Tetrahymena pyriformis* IGC_{50}, 48 h, mg/L**	***Daphnia magna* LC_{50}, 48 h, mg/L**	**Bioconcentration factor**
Butachlor	1861	2.78	3.44	3.48	32.29
Dimethachlor	1373	11.69	28.04	10.21	15.64
Metazachlor	814	2.96	9.56	17.97	39.05
Metolachlor	1884	5.06	13.39	4.90	31.38
Propachlor	635	34.86	48.70	9.98	20.82

The average lethal dose (LD_{50}) of dimethachlor was reported to be 1600 mg/kg, and this medium-toxic pesticide was also defined as extremely harmful to algae and fish (Ćurčić et al., 2022). This value matched the predicted LD_{50} value of 1600 mg/kg from TEST and was also closer to the predicted LD_{50} value of 1373 mg/kg obtained from ProTox 3.0.

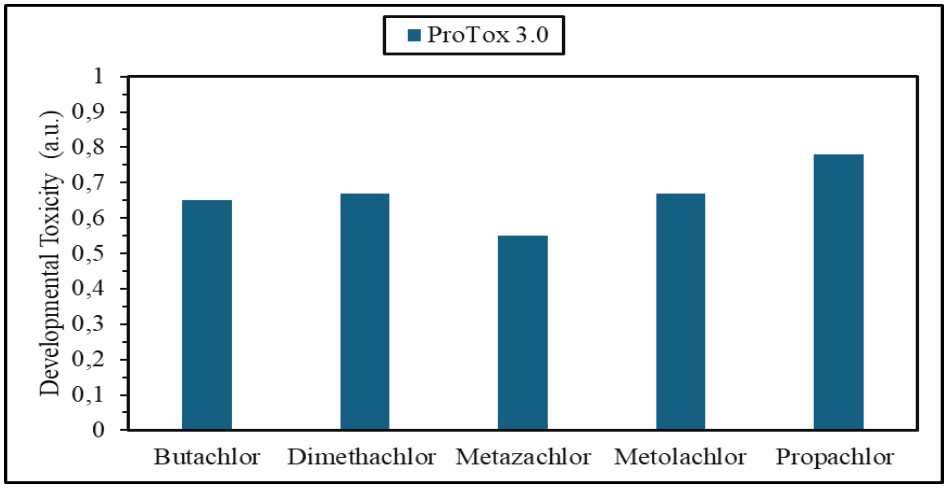

Figure 3. The predicted developmental toxicity values using the TEST method.

The LC_{50} (96h) values of metazachlor reported for rainbow trout (*Oncorhynchus mykiss*), bluegill sunfish (*Lepomis macrochirus*), and common carp (*Cyprinus carpio*) were 4 mg/L, 15 mg/L, and 15 mg/L, respectively, while the EC_{50} (48h) value of 22.3 mg/L was determined for Daphnia magna(FAO, 1999). The predicted LC_{50}, 96 h value of 17.97 mg/L for the *Fathead minnow* was similar to that of the freshwater fish species of *Lepomis macrochirus* (15 mg/L).

Table 4. The predicted toxicological risk assessments using the TEST *in silico* platform.

Chloroacetanilides	**Hepatotoxicity**	**Carcinogenicity**	**Immunotoxicity**	**Mutagenicity**	**Cytotoxicity**
Butachlor	Inactive	Inactive	Active	Active	Inactive
Dimethachlor	Inactive	Active	Inactive	Inactive	Inactive
Metazachlor	Inactive	Active	Inactive	Inactive	Inactive
Metolachlor	Inactive	Inactive	Active	Inactive	Inactive
Propachlor	Inactive	Inactive	Inactive	Inactive	Inactive

The oral LD_{50} values of metolachlor for male and female rats were 3267 and 2577 mg/kg, respectively (Aprea et al., 2016). The metolachlor and its degradation products were investigated using the TEST approach, and it was

determined that all compounds exhibited developmental toxicity (Coffinet et al., 2012). Nicol et al. reported the predicted LD_{50} values of metolachlor and each photoproduct using TEST software, finding that these compounds exhibited higher toxicity than the parent metolachlor compound (Nicol, Genty, Bouchonnet, & Bourcier, 2015). These results were consistent with our toxicity results of metolachlor (Aprea et al., 2016).

ProTox 3.0 results indicate that propachlor was inactive in the toxic parameters of hepatotoxicity, carcinogenicity, immunotoxicity, mutagenicity, and cytotoxicity. Propachlor revealed the lowest predicted LD_{50} values of 290 mg/kg and 635 mg/kg according to the ProTox 3.0 and TEST methods, respectively. This chloroacetanilide was estimated to be toxic, as it belonged to the toxicity class of 3.

CONCLUSION

The predicted toxicity profiles of some selected chloroacetanilides were assessed by using ProTox 3.0 and TEST *in silico* tools. ProTox 3.0 approach stated that butachlor, dimethachlor, metazachlor, and metolachlor compounds were predicted as class 4 (harmful), while propachlor fell in class 3 (toxic). In general, similar results were obtained for most of the chloroacetanilides comparing both ProTox 3.0 and TEXT *in silico* approaches. However, in vivo and/or in vitro biological analysis on chloroacetanilides should be conducted to verify the performance challenge of *in silico* toxicity prediction challenge of these methods.

REFERENCES

Abigail, M. E. A., Samuel, S. M., & Ramalingam, C. (2015). Addressing the environmental impacts of butachlor and the available remediation strategies: a systematic review. *International Journal of Environmental Science and Technology, 12*(12), 4025–4036. doi:10.1007/s13762-015-0866-2

Aprea, M. C., Bosi, A., Manara, M., Mazzocchi, B., Pompini, A., Sormani, F., . . . Sciarra, G. (2016). Assessment of exposure to pesticides during mixing/loading and spraying of tomatoes in the open field. *Journal of*

Occupational and Environmental Hygiene, 13(6), 476–489. doi:10.1080/15459624.2016.1143948

Bamal, D., Duhan, A., Pal, A., Beniwal, R. K., Kumawat, P., Dhanda, S., . . . Yadav, R. (2024). Herbicide risks to non-target species and the environment: A review. *Environmental Chemistry Letters, 22*(6), 2977–3032. doi:10.1007/s10311-024-01773-9

Banerjee, P., Kemmler, E., Dunkel, M., & Preissner, R. (2024). ProTox 3.0: a webserver for the prediction of toxicity of chemicals. *Nucleic Acids Research, 52*(W1), W513–W520.

Bhardwaj, L., Pandey, J., & Dubey, S. K. (2021). Effects of Herbicides on Soil Enzymes and Their Regulatory Factors in Agroecosystem: A Review. In S. K. Dubey & S. K. Verma (Eds.), *Plant, Soil and Microbes in Tropical Ecosystems* (pp. 71–100). Singapore: Springer Singapore.

Cheng, Z., Lu, Z., Shao, Z., Huang, B., Xiong, Y., Fei, H., . . . Lu, Z. (2024). Photodegradation of Propaquizafop in Water Under UV Irradiation: The Identification of Transformation Products and Elucidation of Photodegradation Pathway. *Agronomy, 14*(12), 2959. Retrieved from https://www.mdpi.com/2073-4395/14/12/2959

Coffinet, S., Rifai, A., Genty, C., Souissi, Y., Bourcier, S., Sablier, M., & Bouchonnet, S. (2012). Characterization of the photodegradation products of metolachlor: structural elucidation, potential toxicity and persistence. *Journal of Mass Spectrometry, 47*(12), 1582–1593. doi:https://doi.org/10.1002/jms.3121

Ćurčić, L., Lončar, B., Pezo, L., Stojić, N., Prokić, D., Filipović, V., & Pucarević, M. (2022). Chemometric Approach to Pesticide Residue Analysis in Surface Water. *Water, 14*(24), 4089. Retrieved from https://www.mdpi.com/2073-4441/14/24/4089

Dierickx, P. J. (1999). Glutathione-dependent cytotoxicity of the chloroacetanilide herbicides alachlor, metolachlor, and propachlor in rat and human hepatoma-derived cultured cells. *Cell Biology and Toxicology, 15*(5), 325–332. doi:10.1023/A:1007619919336

FAO. (1999). FAO Specifications And Evaluations For Plant Protection Products.

Farah, M. A., Ateeq, B., Ali, M. N., Sabir, R., & Ahmad, W. (2004). Studies on lethal concentrations and toxicity stress of some xenobiotics on aquatic organisms. *Chemosphere, 55*(2), 257–265. doi:https://doi.org/10.1016/j.chemosphere.2003.10.063

Gobi, M., & Gunasekaran, P. (2010). Effect of Butachlor Herbicide on Earthworm *Eisenia fetida*—Its Histological Perspicuity. *Applied and Environmental Soil Science, 2010*(1), 1–4. doi:10.1155/2010/850758

https://tox.charite.de/protox3/.

https://www.epa.gov/comptox-tools/toxicity-estimation-software-tool-test. (2020). US Environmental Protection Agency, T.E.S.T. (version 5.1) (Toxicity Estimation Software Tool) User's Guide. A Program to Estimate Toxicity from Molecular Structure, USEPA, Washington DC, 2020.

Liu, Y., Yu, Y., Wu, B., Qian, J., Mu, H., Gu, L., . . . Bu, Y. (2024). A comprehensive prediction system for silkworm acute toxicity assessment of environmental and in-silico pesticides. *Ecotoxicology and Environmental Safety, 282*, 116759. doi:https://doi.org/10.1016/j.ecoenv.2024.116759

Mai, H., Gonzalez, P., Pardon, P., Tapie, N., Budzinski, H., Cachot, J., & Morin, B. (2014). Comparative responses of sperm cells and embryos of Pacific oyster (Crassostrea gigas) to exposure to metolachlor and its degradation products. *Aquatic Toxicology, 147*, 48–56. doi:https://doi.org/10.1016/j.aquatox.2013.11.024

Nicol, É., Genty, C., Bouchonnet, S., & Bourcier, S. (2015). Structural elucidation of metolachlor photoproducts by liquid chromatography/high-resolution tandem mass spectrometry. *Rapid Communications in Mass Spectrometry, 29*(23), 2279–2286. doi:https://doi.org/10.1002/rcm.7382

Noga, M., & Jurowski, K. (2025). Reexamining the acute toxicity of chloropicrin: Comprehensive estimation using *in silico* methods. *Toxicology in Vitro, 105*, 106033. doi:https://doi.org/10.1016/j.tiv.2025.106033

Rani, L., Thapa, K., Kanojia, N., Sharma, N., Singh, S., Grewal, A. S., . . . Kaushal, J. (2021). An extensive review on the consequences of chemical pesticides on human health and environment. *Journal of Cleaner Production, 283*, 124657. doi:https://doi.org/10.1016/j.jclepro.2020.124657

Strupp, C., Bomann, W. H., Spézia, F., Gervais, F., Forster, R., Richert, L., & Singh, P. (2018). A human relevance investigation of PPARα-mediated key events in the hepatocarcinogenic mode of action of propaquizafop in rats. *Regulatory Toxicology and Pharmacology, 95*, 348–361. doi:https://doi.org/10.1016/j.yrtph.2018.04.005

Sun, Z., Wang, R., Du, Y., Gao, B., Gui, F., & Lu, K. (2021). Olfactory perception of herbicide butachlor by GOBP2 elicits ecdysone biosynthesis and detoxification enzyme responsible for chlorpyrifos tolerance in *Spodoptera litura*. *Environmental Pollution, 285*, 117409. doi:https://doi.org/10.1016/j.envpol.2021.117409

Velisek, J., Stara, A., Kubec, J., Zuskova, E., Buric, M., & Kouba, A. (2020). Effects of metazachlor and its major metabolite metazachlor OA on early life stages of marbled crayfish. *Scientific Reports, 10*(1), 875. doi:10.1038/s41598-020-57740-1

Wang, Y., Wu, S., Chen, L., Wu, C., Yu, R., Wang, Q., & Zhao, X. (2012). Toxicity assessment of 45 pesticides to the epigeic earthworm *Eisenia fetida*. *Chemosphere, 88*(4), 484–491. doi:https://doi.org/10.1016/j.chemosphere.2012.02.086

Weyrich, A., Joel, M., Lewin, G., Hofmann, T., & Frericks, M. (2022). Review of the state of science and evaluation of currently available *in silico* prediction models for reproductive and developmental toxicity: A case study on pesticides. *Birth Defects Research, 114*(14), 812–842. doi:https://doi.org/10.1002/bdr2.2062

The Historical Development and Efficiency Analysis of Public Libraries in Türkiye: A Quantitative Study on the Period 1945–2022

Ece ÖZGÖREN ÜNLÜ[*]
Cengiz GAZELOĞLU [2]

[1]Department of Statistics, Süleyman Demirel University, Türkiye
[2] Department of Statistics, Süleyman Demirel University, Türkiye
[*](eceozgoren@sdu.edu.tr)

ABSTRACT

This study examines the institutional development of public libraries in Türkiye, the size of their collections, and user demand based on data from the period 1945–2023. The research utilizes statistics published by the Turkish Statistical Institute (TURKSTAT) and compiled from Public Library Directorates. The study first analyzes the distribution characteristics of library, book, and user numbers through descriptive statistics. Time series graphs and annual growth rates are used to reveal long-term trends. To measure the effectiveness of library services, efficiency indicators consisting of user/library, user/book, and book/library ratios were created, and the descriptive statistics and annual changes of these indicators were examined. Furthermore, Pearson correlation analysis was used to test the relationships between variables, revealing that library, book, and user numbers exhibit a high level of positive correlation with each other. The findings reveal that public libraries show continuous growth in the long term, but that the increase in user demand exceeds the growth in the number of libraries and books. This result indicates that library policies should focus not only on quantitative growth but also on strategies for diversity and accessibility in service quality and user needs.

Keywords – Public Libraries, Library Statistics, Efficiency Indicators, User Demand, Correlation Analysis, Türkiye.

INTRODUCTION

Libraries have been among the most fundamental institutions for access to information, cultural transmission, and social development throughout history [1], [2]. Libraries, which contribute to the education, research, and cultural life of societies, are also at the center of democratic participation and lifelong learning [3], [4]. In the modern information society, libraries have evolved beyond being mere repositories of information; they have become dynamic structures that facilitate access to information and respond to users' changing expectations in the digitalization process [5], [6].

The development of public libraries in Türkiye gained acceleration with the proclamation of the Republic and, particularly from the 1940s onwards, underwent a systematic institutionalization process [7], [8]. Public libraries have not only provided books and information services, but have also served as centers for socio-cultural activities, educational activities, and social integration [9]. However, during this process, the increase in the number of users has often outpaced the growth in the number of libraries and books [7], [10].

Nowadays, with the increasing access to digital resources, user expectations have changed significantly, making it necessary for libraries to provide services not only with printed resources but also with digital collections [12],

[13]. In this context, the sustainability and effectiveness of libraries are evaluated not only by the size of their collections but also by the suitability and accessibility of these collections to user needs [14], [15].

Statistics on public libraries in Türkiye indicate a significant growth trend in terms of the number of libraries, books, and users [16]. However, the faster increase in the number of users indicates that the existing infrastructure may sometimes be insufficient in terms of capacity [10], [17]. Studies conducted at the international level also reveal similar trends and emphasize that, especially in developing countries, user demand often exceeds the rate of increase in library resources [18], [19].

This study examines the historical development of public libraries in Türkiye using quantitative data and analyzes trends in the number of libraries, books, and users, particularly during the period 1945–2023. Using descriptive statistics, growth rates, productivity indicators, and correlation analyses, the study reveals the structural transformation of the library system. The findings aim to contribute both to the development of national library policies and to the understanding of the social impact of library services in the international literature.

MATERIALS AND METHOD

Developments in the number of libraries, books, and users in Türkiye between 1945 and 2022 were examined in this study. The data used in the research were obtained from statistics published TURKSTAT, with the original source of the data being the Public Library Directorates [16]. This dataset provides a reliable basis for revealing the long-term trends in the institutional capacities of libraries, the size of their collections, and user demand.

During the analysis process, descriptive statistics were calculated initially, and the mean, standard deviation, minimum, and maximum values of the library, book, and user counts were evaluated [20]. Subsequently, time series graphs were utilized to reveal the development of these variables over the years, examining both the change in absolute values and the annual growth rates [21].

Three key efficiency indicators have been established to evaluate the effectiveness of library services: user/library, user/book, and book/library ratios. Calculations based on these indicators provide an opportunity to assess libraries' capacity to meet user demand and developments in collection size [22].

Correlation analysis was applied to determine the strength and direction of the relationships between variables. Pearson correlation coefficients were calculated, and statistical significance levels were tested. This method reveals whether the number of libraries, the number of books, and the number of users exhibit parallel development [23].

In recent years, data science and machine learning methods have been increasingly used in the social sciences and information management fields; these methods particularly enhance the effectiveness of classification and pattern recognition processes in large datasets [24]. Accordingly, the analysis was performed using the Python programming language; the pandas, matplotlib, seaborn, and statsmodels libraries were used for data processing and visualization.

RESULTS

This section presents and examines in detail the results of the analyses conducted in the study.

Table 1. Presents the descriptive statistics of the core variables: Libraries, Books, and Users.

Index	Count	Mean	Std.	Min.	Max.
Libraries	78,0	665,71	454,73	61,0	1367,0
Books	78,0	7825020,37	6457080,02	702060,0	23091168,0
Users	78,0	11944543,54	9072024,75	465544,0	31451920,0

Table 1 summarizes the descriptive statistics of the three key variables examined in this study: number of libraries, number of books, and number of users. The results obtained provide information about the general distribution and development trend of these indicators during the period under review. As can be seen from the table, the average number of libraries was 665, with the lowest value being 61 and the highest value being 1367. The relatively high standard deviation (≈455) indicates significant fluctuations between years, with rapid increases in some periods and a more stable trend in others.

Number of books is also around 7,8 million on average. The minimum value is 702,000, while the maximum value is over 23 million. The standard deviation being quite high (≈6.45 million) indicates that there are significant differences in book collections over time and that rapid growth occurred during certain periods. Furthermore, the number of users has been identified as the indicator with the highest variability among the three variables. This variable, corresponding to an average of 11,9 million users, has taken values ranging from a minimum of 465,000 to a maximum of around 31 million. The standard deviation exceeding 9 million indicates that the number of users fluctuated significantly over the years and that there were clear upward trends in the public's demand for library services.

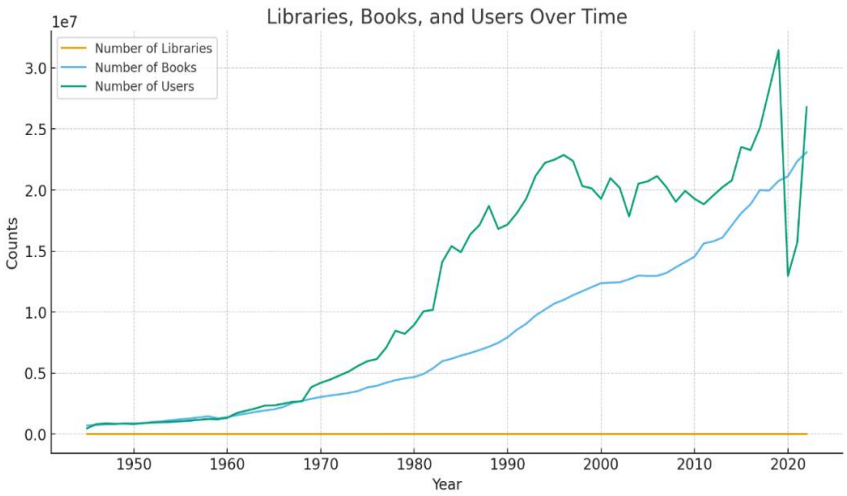

Fig. 1 Libraries, Books and Users (1945-2022)

Figure 1 shows the annual change in the number of libraries, books, and users between 1945 and 2022, revealing that all three variables show an upward trend in the long term. While the number of libraries has remained at relatively low levels and followed a limited growth trend, the number of books has entered a period of rapid growth, particularly since the 1980s. The most notable increase has been in the number of users, with social demand for library services rising significantly after 1980. However, fluctuations in the number of users observed in recent years indicate periodic disruptions and occasional imbalances in demand.

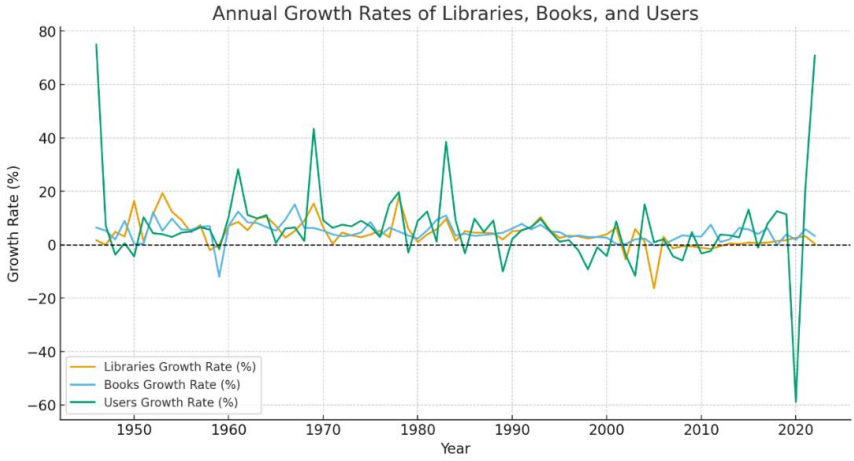

Fig. 2 Annual Growth Rates of Libraries, Books and Users (1945-2022)

Figure 2 reports the annual growth rates of libraries, books, and users, revealing fluctuations in the growth rates of these variables over time. Although the growth rates of all three variables were generally positive, there were notable fluctuations in the number of users; some years saw very high increases, while other periods showed negative growth rates. The growth rate of the number of books has followed a more balanced trend, while the number of libraries has occasionally fallen to negative values, showing a decline in certain periods. These results indicate that the library system is on a continuous growth trend, but that growth rates are not stable, with seasonal fluctuations in user demand being particularly prominent.

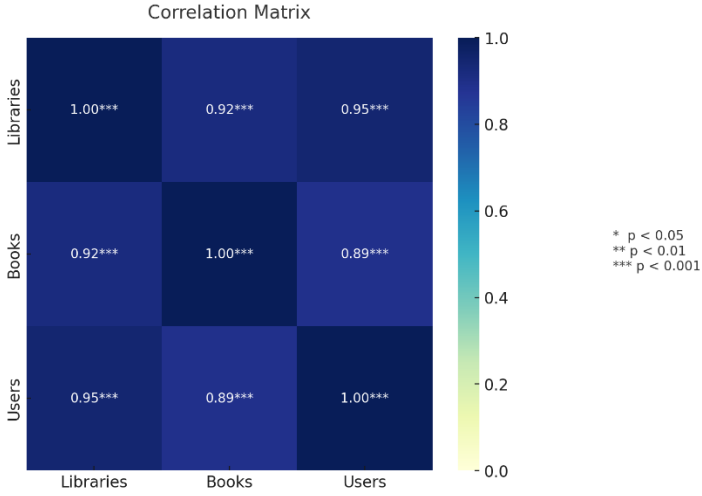

Fig. 3 Correlation Matrix

The correlation matrix showing the relationships between the number of libraries, the number of books, and the number of users is shown in Figure 3. The findings reveal that there are quite strong and positive relationships between the variables. In particular, the correlation coefficient between the number of libraries and the number of users is 0,95, indicating that the expansion of the library infrastructure significantly affects user demand. Similarly, the correlation coefficient between the number of books and the number of libraries is 0,92, while the correlation coefficient between the number of books and the number of users is 0,89. All relationships are statistically highly significant ($p < 0,001$). These results confirm that institutional and content-related developments in the library system directly affect the number of users and that the variables have a parallel growth trend.

Table 2. Presents the descriptive statistics of efficiency indicators.

Index	Count	Mean	Std.	Min.	Max.
Users per Library	78,0	15840,93	4904,92	7631,87	26609,07
Users per Book	78,0	1,48	0,5	0,61	2,61
Books per Library	78,0	11031,84	2538,65	8912,0	18370,06

The descriptive statistics of the three key efficiency indicators created to measure the effectiveness of the library system (user/library, user/book, and book/library ratios) are presented in Table 2. According to the findings, the user/library ratio averages 15,841, ranging from a minimum of 7,632 to a maximum of 26,609; this indicates that libraries are serving an increasing number of users. The user/book ratio averages 1,48, indicating that there are approximately 1,5 users per book; this finding is important in terms of showing the intensity of use of book collections. The book/library ratio is 11,032 on average, ranging from a minimum of 8,912 to a maximum of 18,370, reflecting the expansion of library collections over the years. Overall, productivity indicators reveal that user demand is growing faster than the increase in libraries and books, thus highlighting that libraries are facing increasing social demand.

DISCUSSION

The institutional development, collection size, and user demand of public libraries in Türkiye between 1945 and 2023 were comprehensively examined in this study. The findings reveal that, in the long term, all three variables showed an upward trend, but the increase in the number of users significantly outpaced the increase in the number of libraries and books. This implies that libraries are playing an increasingly critical role in meeting the growing demand for information and services at the societal level. The annual growth rates reveal that seasonal fluctuations in the number of users are more pronounced. These fluctuations suggest that social, economic, or technological changes may directly affect library usage habits. Although the growth in the number of books and libraries follows a more balanced trend, the fact that there have been downward trends in some years is a finding that should be carefully evaluated in terms of the continuity of the library system.

Productivity indicators reveal increasing trends in user/library and user/book ratios over time. This situation demonstrates that libraries are serving an increasing number of users with existing resources, thereby increasing the service load. The long-term growth trend in the book/library ratio indicates that collections are expanding, but this increase might not be entirely sufficient to meet user demand.

According to the results of the correlation analysis, there are strong and positive relationships between the number of libraries, the number of books, and the number of users. In particular, the high correlation coefficient between the number of libraries and the number of users indicates that infrastructure expansion has a direct effect on user demand. Furthermore, it has been observed that trust at the organizational level is a decisive factor in employee loyalty and internal efficiency, and that trust and a sense of belonging play a critical role in the sustainability of service quality [25]. These findings show that library investments are an important tool for creating social impact. Similarly, statistical analyses reveal that social belonging is an important factor that strengthens the interaction power of institutions and the social perception of service quality [26].

CONCLUSION

Study results indicate that public libraries in Türkiye have shown continuous long-term development, but user demand increases at a rate faster than the growth in the number of libraries and books. This situation demonstrates that library policies and investments should focus not only on quantitative growth

but also on service quality and providing a variety of resources that meet user needs.

The strong correlations between the number of libraries, books, and users reveal that these elements are complementary and that the system must be approached holistically. In particular, the rapid increase in the number of users requires libraries to develop more innovative solutions in terms of digitization, accessibility, and new service models.

In conclusion, this study reveals the historical development of public libraries through numerical data, while also providing important insights for future policy development. Considering that libraries are not merely institutions that store books, but centers for access to social knowledge, lifelong learning, and cultural participation, it is necessary to develop sustainable and user-centered strategies. The sustainability of institutional services depends not only on structural and technical capacity but also on the perception of fairness and equality among employees and service recipients; this is seen as a decisive factor in the long-term efficiency of institutions [27].

ACKNOWLEDGMENT

Artificial intelligence programs have been partially utilized to enhance the language accuracy and correct the writing errors in this study.

REFERENCES

[1] M. B. Line, “The information uses and needs of social scientists: An overview of INFROSS,” *Aslib Proceedings*, vol. 23, no. 8, pp. 412–434, 1971.

[2] J. H. Shera, *The Foundations of Education for Librarianship*. Becker and Hayes, 1972.

[3] J. E. Buschman, *Dismantling the Public Sphere: Situating and Sustaining Librarianship in the Age of the New Public Philosophy*. Libraries Unlimited, 2003.

[4] K. Donaldson, L. Bonella, L. Becksford, J. Kubicki, and S. Parramore, “Liaising in the 21st century: The shifting role of the education librarian,” *Education Libraries*, vol. 45, no. 1, 2022.

[5] M. Castells, *The Rise of the Network Society*, 2nd ed. USA: Wiley-Blackwell, 2010.
[6] C. L. Borgman, *From Gutenberg to the Global Information Infrastructure: Access to Information in the Networked World*. MIT Press, 2003.
[7] Ş. Karadeniz and B. Yılmaz, "Türkiye'deki halk kütüphaneleri için ulusal strateji ve eylem planı geliştirme süreci: Durum değerlendirmesi ve bir model önerisi," *Bilgi Dünyası*, vol. 21, no. 2, pp. 299–349, 2020.
[8] M. Avcı, "Cumhuriyet'in ilk yıllarında kütüphanecilik alanında gerçekleştirilen faaliyetler," *Kütüphane, Arşiv ve Müze Araştırmaları Dergisi (Library, Archive and Museum Research Journal)*, vol. 5, no. 2, pp. 192–212, 2024.
[9] A. Ersoy and B. Yılmaz, "Yaşam boyu öğrenme ve Türkiye'de halk kütüphaneleri / Lifelong learning and public libraries in Turkey," *Türk Kütüphaneciliği*, vol. 23, no. 4, pp. 803–834, 2009.
[10] E. Alaca and B. Yılmaz, "Türkiye'de halk kütüphanesi yönetim ve hizmet yapısının yenilikçi örgüt kültürü açısından değerlendirilmesi ve yenilikçi örgüt kültürü stratejisi ve eylem planı önerisi," *Bilgi Yönetimi*, vol. 4, no. 2, pp. 186–221, 2021.
[11] I. Rowlands, D. Nicholas, P. Williams *et al.*, "The Google generation: The information behaviour of the researcher of the future," *Aslib Proceedings*, vol. 60, no. 4, pp. 290–310, 2008.
[12] C. Tenopir, *Use and Users of Electronic Library Resources: An Overview and Analysis of Recent Research Studies*. Washington, D.C.: Council on Library and Information Resources, 2003.
[13] L. S. Connaway and M. L. Radford, *Research Methods in Library and Information Science*, 7th ed. ABC-CLIO, 2021.
[14] International Federation of Library Associations and Institutions (IFLA), *IFLA/UNESCO Public Library Manifesto 1994*. IFLA, 1994. [Online]. Available: https://repository.ifla.org/bitstreams/2c4f3384-67da-4728-8a2e-117f86cbd495/content
[15] American Library Association (ALA), *The State of America's Libraries Report 2020*. USA: American Library Association, 2020. [Online]. Available: https://www.ala.org/sites/default/files/news/content/State-of-Americas-Libraries-2020-web-2.pdf
[16] Türkiye İstatistik Kurumu (TÜİK), *Kütüphane İstatistikleri, 1945–2023*. Kaynak: Halk Kütüphaneleri Müdürlükleri, 2023.
[17] V. Gültekin, "Halk kütüphanesi çalışanlarının dijital yetkinlikleri / Digital competencies of public library staff," *Türk Kütüphaneciliği*, vol. 39, no. 4, 2025.
[18] L. S. Connaway, *The Library in the Life of the User: An Annotated Bibliography of Practical Ideas*. OCLC Online Computer Library Center, 2016.
[19] United Nations Educational, Scientific and Cultural Organization (UNESCO), *Public Library Guidelines*. Paris: UNESCO Publishing, 2019. [Online]. Available: https://unesdoc.unesco.org/ark:/48223/pf0000383205
[20] Ş. Büyüköztürk, *Sosyal Bilimler için Veri Analizi El Kitabı: İstatistik, Araştırma Deseni, SPSS Uygulamaları ve Yorum*. Pegem Akademi, 2016.
[21] D. N. Gujarati and D. C. Porter, *Basic Econometrics*, 5th ed. McGraw-Hill Companies, 2009.
[22] R. Poll, "Measuring impact and outcomes of libraries," *Performance Measurement and Metrics*, vol. 4, no. 1, pp. 5–12, 2008.

[23] A. P. Field, *Discovering Statistics Using IBM SPSS Statistics*, 5th ed. Newbury Park: Sage Publications, 2018.
[24] C. Gazeloğlu and T. Turhan, "Classification of autism spectrum disorder in adult individuals by machine learning methods," in *Recent Studies in Basic Medical Sciences*, İKSAD Publishing House, pp. 19–35, 2022.
[25] C. Gazeloğlu, E. Erkılıç, and E. Aytekin, "The effect of trust in managers on the organizational identification and intention to quit: A research on hospitality business employees," *Journal of Tourism and Gastronomy Studies*, vol. 7, no. 3, pp. 1912–1932, 2019.
[26] C. Gazeloğlu and T. Turhan, "Investigation of the sense of belonging among university students using statistical methods," in *Current Debates on Natural and Engineering Sciences*, vol. 11, pp. 67–76, 1st ed., Ankara: Bidge Publications, 2023.
[27] C. Gazeloğlu, E. Erkılıç, and E. Aytekin, "Determination of the effect of employees' trust perceptions in a manager on their organizational identification behavior: An application on hotel employees," *Journal of Tourism Intelligence and Smartness*, vol. 2, no. 2, pp. 86–109, 2019.

Statistical Optimization of Fungal Enzyme Production in Biotechnological Processes

Derya BERİKTEN

Assoc. Prof. Dr.; Kütahya Health Sciences University, Faculty of Engineering and Natural Sciences, Department of Molecular Biology and Genetics derya.berikten@ksbu.edu.tr ORCID No: 0000-0002-8672-4813

ABSTRACT

Fungal enzymes serve as critical catalysts across a vast array of industrial sectors, including food processing, biofuel production, the paper and pulp industry, and waste management. To enhance production efficiency and reduce costs, the optimization of fermentation conditions is of paramount importance. Because the traditional "one-factor-at-a-time" approach ignores interactions between variables and is time-consuming, powerful statistical and mathematical tools such as Response Surface Methodology have become widespread in modern biotechnology. Through experimental designs such as Central Composite Design and Box-Behnken Design, the individual and interactive effects of critical parameters like temperature, pH, moisture content, incubation time, and nutrient concentration on enzyme yield were analyzed. Previous studies have demonstrated that the application of RSM to fungal enzyme production can result in substantial improvements in yield, in some cases achieving several-fold increases compared to non-optimized conditions. Furthermore, this method supports the sustainable bio-economy by enabling the conversion of agricultural wastes into high-value bio-products. Consequently, Response Surface Methodology stands out as an indispensable strategy for increasing the efficiency, precision, and economic feasibility of fungal enzyme production.

Keywords – Response Surface Method, Fungal Enzyme, Optimization, Industrial Biotechnology.

INTRODUCTION

Enzymes are pivotal catalysts utilized across an expanding range of industrial sectors, including food processing, biofuels, paper and pulp, textiles, detergents, and waste management (Sharma et al., 2001:1; Hasan et al., 2006; Dhaver et al., 2022; Behnam et al., 2019:27). Their importance is underscored by their wide-ranging applications, from biomass degradation and bio-detection to pharmaceutical and medical uses (Mate and Alcalde, 2017; Kudanga et al., 2017; Zhou et al., 2021; Dong et al., 2023; D'Annibale et al., 2006:1586). For instance, proteases alone constitute 60% to 65% of the global enzyme market due to their critical roles in diagnostics, the detergent industry, and food processing (Ben Mefteh et al., 2019). Similarly, lipases are highly valued for their ability to catalyze the hydrolysis, interesterification, and transesterification of lipids, making them essential in industries ranging from food and pharmaceuticals to biodiesel synthesis (Colla et al., 2016:461).

Microbial sources, including bacteria, actinomycetes, and especially fungi, are generally preferred for industrial enzyme production. This preference stems from their ability to grow easily, their simple production processes, and the comparatively low costs involved (Saha and Mazumdar,

2019; Abdullah et al., 2024; Chen et al., 2013:3844). Among these microbes, filamentous fungi, such as Aspergillus species, are widely utilized (Chen et al., 2013:3844; Abdeshahian et al., 2011). Fungi are particularly advantageous over bacteria for degrading complex lignocellulosic biomass, yielding more robust enzymes, especially when cultivated via Solid-State Fermentation (SSF) (Sharma et al., 2025:1).

Enzyme production typically employs two major techniques: Submerged Fermentation (SmF) and SSF (Pandey, 2003). SSF refers to the cultivation of microorganisms on moist solid substrates under conditions of low water activity, closely resembling the natural growth environment of many fungi (Pandey, 2003; Gervais and Molin, 2003; Chen et al., 2013:3844). This method is advantageous as it minimizes the chances of bacterial contamination (Basu et al., 2002; Li et al., 2006). Conversely, SmF is favored in industrial settings because it allows for easier control of parameters (such as temperature and pH) and simplifies downstream enzyme recovery and biomass determination through methods like simple filtration or centrifugation (Colla et al., 2016:461; Coradi et al., 2013).

The primary objectives of optimizing enzyme production are consistently focused on maximizing enzyme yield and reducing production costs, particularly by utilizing low-cost agricultural residues (Lee et al., 2011; Abdeshahian et al., 2011; Ma et al., 2025). However, achieving optimal conditions is complicated because enzyme production is influenced by a multitude of interconnected variables, such as temperature, pH, moisture content, carbon and nitrogen sources, and fermentation time (Chen et al., 2013:3844; Yasmeen et al., 2013:944).

Historically, the conventional optimization approach has been the "one-factor-at-a-time" (OFAT) method, where only one independent variable is altered while all others are held constant (Lotfy et al., 2007). This strategy is now recognized as inherently flawed because it is excessively laborious, costly, time-consuming, and fails entirely to account for the crucial synergistic or antagonistic interactions between the various physiological and nutritional factors (Nor et al., 2017; Ben Mefteh et al., 2019; Granato et al., 2010; Hao et al., 2023; Lotfy et al., 2007; Koç and Kaymak-Ertekin, 2008).

To bypass these limitations and ensure cost-effective, high-yield production, Response Surface Methodology (RSM) has emerged as a robust statistical and mathematical approach (Box and Wilson, 1951; Hao et al., 2023; Koç and Kaymak-Ertekin, 2008). RSM integrates experimental design, mathematical modeling, and statistical analysis, allowing researchers to efficiently model the relationship between multiple input parameters and one or more desired response variables (Koç and Kaymak-Ertekin, 2008; Witek-Krowiak et al., 2014). By facilitating the simultaneous evaluation of numerous variables, RSM significantly reduces the number of experiments required, saving time and resources while substantially enhancing the accuracy of optimization outcomes (Nor et al., 2017; Kolotylo et al., 2023:259). RSM is,

therefore, routinely used to rapidly determine the optimal conditions needed for maximizing microbial metabolites, including fungal enzymes (Chen et al., 2013:3844; Ben Mefteh et al., 2019; D'Annibale et al., 2006:1586).

RESPONSE SURFACE METHODOLOGY (RSM) CONCEPT AND METHODOLOGY

Optimization is the process of holistically considering and applying independent variables, taking into account both their interactions with each other and their effects on the response, in line with predetermined goals (responses) of a process. Generally, an optimization approach aims to maximize or minimize predefined target functions such as product quality, yield, or economic gain. To this end, independent parameters, defined as decision variables, are systematically modified to determine the most suitable conditions (Banga et al., 2003:131).

Response Surface Methodology (RSM) is an approach that integrates statistical and mathematical techniques to analyze, model, and optimize a response affected by multiple variables (Montgomery, 2001). This approach was first developed by Box and Wilson in 1951. RSM is based on fitting polynomial models to data obtained from designed experiments, thereby enabling the prediction of system behavior.

In response surface modeling, while second-degree polynomial equations are often preferred for modeling complex processes, higher-degree polynomials can also be used when necessary. However, since the method is based on statistical models, even the most suitable model cannot fully reflect the real system; the results obtained are an approximate representation of the real system. Nevertheless, although it does not provide absolute accuracy, RSM is considered an effective and applicable optimization approach in solving multivariate problems. The construction of the response surface model is carried out by estimating the β coefficients included in the model using experimental data. The most commonly used method for determining these coefficients is least squares regression, which allows for the statistical calculation of model parameters (Montgomery, 2001).

RSM was initially designed and developed by Box and Wilson (1951) for optimizing chemical reactions and is widely applied today to predict optimal process parameters, ensuring high yield and quality of bioproducts (Box and Wilson, 1951; Hao et al., 2023).

Key Steps and Experimental Designs

Most software packages used in response surface method applications are based on second-order polynomial models. In optimization studies where a single regional minimum is investigated, second-order polynomial models offer both a sufficient and relatively easy-to-implement approach. However, if the response variable or independent variables under investigation do not exhibit behavior suitable for this model, the variables must be transformed or the working ranges of the independent variables must be appropriately rearranged in order for the response to be explained by a second-order polynomial (Baş and Boyacı, 2007:836).

RSM, optimum experimental conditions in complex experimental systems are determined and modeled through different experimental design approaches such as Doehlert matrix (DM), central composite design (CCD), three-level hybrid design, single-factor design, pentagonal design, D-optimal design, factorial design, and Box–Behnken design (BBD) with three-dimensional experimental arrangement (Montgomery, 2001).

Design Models Used for Response Surface Methodology

RSM typically involves defining input parameters (factors) and response values, selecting an experimental design, mathematical modeling, statistical analysis, and optimization (Hao et al., 2023; Witek-Krowiak et al., 2014). The most common experimental designs used in RSM are the Central Composite Design (CCD) and the Box-Behnken Design (BBD) (Hao et al., 2023; Mäkelä, 2017).

RSM is defined as an approach that combines statistical techniques with mathematical expressions for the analysis and modeling of problems where numerous parameters influence the response variable. RSM is widely applied in the development of new product formulations, the improvement of existing product designs, process design, and the optimization and development of processes. The most frequently preferred experimental design models within this method are factorial design, CCD, and BBD with a three-dimensional experimental arrangement. CCD and BBD designs are more commonly used, particularly because they include second-order polynomial models and allow the creation of three-dimensional response surface graphs (Montgomery, 2001; Antony, 2003; Lazic, 2004).

Determining which of these design methods to use is of great importance in terms of the study's requirements and is directly related to the researcher's mastery of the subject matter. For example, the CCD is considered a more advantageous approach in research where the interactions between parameters are significant, as it allows for testing in different regions of the experimental area in addition to the main design points. In contrast, the factorial design method is mostly used to determine the main effects of the parameters and to obtain linear model equations. The BBD is another widely preferred design approach that requires testing only at the main design points.

Among these methods, the most frequently used experimental design model is known as the CCD (Turan and Altundoğan, 2011:11).

Central Composite Design (CCD): Proposed by Box and Wilson, CCD is suitable for multi-factor, multi-level experiments involving continuous variables (Hao et al., 2023; Mäkelä, 2017). CCD is an experimental design approach where the independent variables vary between defined high and low levels. For applicability, the independent variables are generally coded in the range of -1 to +1; the lowest level is defined as -1, the highest as +1, and the middle level as 0. A central composite design includes cube points located at the corner points of the cube defined by the -1 and +1 limits, star (axial) points located at a distance of ±α outside the cube, and central points located at the origin. The value of α is determined depending on the number of factors being examined and some desired statistical properties in the design. CCD is widely used, especially when linear mathematical models are insufficient, to define second-order model equations and to describe the process more accurately. The mathematical model obtained by applying this design transforms into a second-order polynomial structure (Montgomery, 2001; Antony, 2003; Lazic, 2004).

Box-Behnken Design (BBD): BBD is an experimental design approach based on quadratic models. This design allows for the identification of nonlinear relationships between independent variables and the response (output) variable. The experimental results are visualized on the response surface using contour diagrams. In three-factor systems, a cubic surface structure is obtained by connecting the midpoints, and the interactions of the variables can be evaluated through this structure. For models created using BBD, the expected response surfaces can be drawn as three-dimensional graphs, thus allowing for visual analysis of system behavior. Furthermore, this method allows for the observation of experimental errors and the appropriate selection of parameters for the quadratic model (Montgomery, 2001; Antony, 2003; Lazic, 2004). BBD often requires fewer experimental runs and avoids extreme experimental conditions that may be dangerous or impractical, as its design points do not extend beyond the established upper and lower limits (Hao et al., 2023; Mäkelä, 2017; Box and Behnken, 1960). The mathematical modeling typically employs empirical second-order polynomial equations to capture linear, quadratic, and interaction effects between variables (Hao et al., 2023; Koç and Kaymak-Ertekin, 2008).

Statistical Validation

The reliability of the established model is assessed using Analysis of Variance (ANOVA) (Hao et al., 2023). Key metrics include the F-value and P-value (a low P-value, typically ≤0.05, indicates significance), the Coefficient of Determination (R^2), which should be close to 1.0 (ideally > 0.90) for a strong correlation, and the Lack of Fit test (a non-significant P-value, >0.05, confirms the model adequately represents the data) (Koç and

Kaymak-Ertekin, 2008; Hao et al., 2023; Chen et al., 2013:3844; Ramanjaneyulu and Rajasekhar Reddy, 2016).

After estimating the regression model, it is essential to assess how well the resulting equation explains the relationships among the variables and to what extent the predictions derived from it are sensitive and reliable. In addition, the appropriateness of the mathematical form of the selected model—namely, whether it adequately represents the true mean response, which is one of the underlying assumptions—should also be evaluated. For this purpose, various statistical methods are used, such as calculating the coefficient of variation (C.V.), applying general hypothesis tests for regression analysis, testing the individual significance of regression coefficients, determining the coefficient of determination (R^2) and the adjusted coefficient of determination (R^2_adj), calculating the estimated sum of squared residual errors (PRESS), evaluating the adequate precision value, performing a lack of fit test to examine model inappropriateness, and conducting residual analyses (İkiz et al., 2000).

In RSM, data obtained from designed experiments are fitted into regression models, and these models are used to describe system behavior. However, since the created regression model is only an approximate representation of the actual response function, the residuals, which represent the difference between the predicted values and the experimental results, include not only pure experimental error but also error arising from the inadequacy of the model's mathematical form. This error, resulting from the model's mathematical structure not adequately representing the real system, is defined as model lack of fit. Ideally, the model lack of fit should be statistically insignificant, and the regression model should be considered meaningful (Montgomery, 2001; Castillo, 2007).

RESPONSE SURFACE METHODOLOGY APPLICATIONS IN FUNGAL ENZYME PRODUCTION

In process optimization studies, it is often necessary to simultaneously evaluate multiple responses that define the quality criteria of the product or the system performance. Some of these responses may be kept at a maximum level, some at a minimum level, and some may be within a certain target or acceptable range. However, in many cases, improving one response can negatively affect another. Therefore, it becomes necessary to consider all responses defining the system together in the optimization process. On the other hand, increasing the number of responses transforms the optimization

problem into a more complex structure, and various approaches have been developed to explain and solve this situation (Castillo, 2007).

Single-response optimization problems can generally be solved by calculating stationary points. In contrast, multi-response optimization problems are solved using nonlinear programming approaches, superimposing the responses by plotting contour lines, and methods such as the desirability function (Castillo, 2007).

The primary goal in optimizing multi-response systems is to achieve the best possible balance among all responses. However, the nonlinear programming approach cannot always meet this requirement. The method of superimposing the contour lines of the responses is one of the alternative approaches used in solving multi-response optimization problems. In this method, while one independent variable is kept constant, the possible combinations of the other two variables are expressed with contour lines. Depending on the regression coefficients, the shape of the contour lines (circular, elliptical, or saddle point) indicates the presence of maximum, minimum, stagnant peak, or increasing/decreasing peak points. A circular response surface suggests that interactions among the variables are negligible, whereas elliptical or saddle-shaped surfaces indicate the presence of significant interactions. The surface enclosed by the smallest elliptical or circular region corresponds to the maximum or minimum predicted response value (Myers et al., 2004:53). However, this approach loses its practicality when four or more dependent and independent variables are examined simultaneously; Furthermore, the fact that the responses are on different scales makes it difficult to display them together on the same graph (Montgomery, 2001; Castillo, 2007).

Filamentous fungi are commonly used for enzyme production, primarily through Solid-State Fermentation (SSF), where microorganisms grow on moist solid substrates with low water activity (Pandey, 2003; Gervais and Molin, 2003; Chen et al., 2013:3844). SSF mimics the natural habitat of many fungi and is an attractive approach for upgrading lignocellulosic waste biomass, such as agricultural residues, into valuable enzymes (Chen et al., 2013:3844; Yasmeen et al., 2013:944).

RSM has been widely and successfully applied to optimize the critical factors influencing fungal enzyme yields, which include temperature, pH, moisture content, fermentation time, and the concentration/type of carbon and nitrogen sources (Table 1) (Yasmeen et al., 2013:944; Lonsane et al., 1985; Koç and Kaymak-Ertekin, 2008).

Ligninolytic Enzymes (LiP, MnP, Laccase)

Ligninolytic enzymes produced by white-rot fungi (WRF) are essential for degrading lignin (Yang et al., 2011).

Schyzophyllum commune (LiP, MnP, Laccase): RSM using CCD was applied to optimize the production of ligninolytic enzymes by *S. commune*

using corn stover via SSF (Yasmeen et al., 2013:944). Initial screening indicated that *S. commune* yielded higher activities (Lignin Peroxidase (LiP) 1007.39 U/mL, Manganese Peroxidase (MnP) 614.23 U/mL, and Laccase 97.47 U/mL) than *Ganoderma lucidum* (Yasmeen et al., 2013:944). The optimized SSF conditions were determined as pH 4.5, temperature 35°C, inoculum size 4 mL, and moisture content 60% (Yasmeen et al., 2013:944). Under these conditions, the maximal activities achieved were LiP 1270.40 U/mL, MnP 715.08 U/mL, and Laccase 130.80 U/mL (Yasmeen et al., 2013:944). The model showed high reliability, particularly for LiP and MnP, with $R2$ values of 0.9976 and 0.9909, respectively (Yasmeen et al., 2013:944).

Ganoderma lucidum (Laccase Scale-up): RSM (Box-Behnken design) was utilized to optimize laccase production during scale-up to 200 L and 1200 L fermenters (Ma et al., 2025). Critical factors were identified using the Plackett–Burman design as temperature, aeration ratio, and agitation speed (Ma et al., 2025). The optimal conditions were determined as 30°C temperature, 0.66 aeration ratio, and 100 rpm agitation speed, resulting in a maximum laccase activity of 214,185.2 U/L (Ma et al., 2025). The optimum pH for the laccase enzyme activity was determined to be 3.0, characterizing it as an acidic enzyme (Ma et al., 2025).

Cellulolytic and Hemicellulolytic Enzymes

These enzymes are vital for breaking down lignocellulosic biomass (Chen et al., 2013:3844).

Aspergillus terreus K1 (Multi-enzyme): RSM (CCD) was used to optimize the co-production of endoglucanase, mannanase, and xylanase by *A. terreus K1* using palm kernel expeller (PKE) as the substrate (Chen et al., 2013:3844). The four most significant parameters were temperature, moisture, initial pH, and inoculum concentration (Chen et al., 2013:3844). Optimal conditions identified for high multi-enzyme yield were 30.5°C temperature, 62.7% moisture, pH 5.8, and 6% inoculum, yielding maximum xylanase activity of 265.57 U/g DM (predicted 262.01 U/g DM) (Chen et al., 2013:3844).

Aspergillus niger (Cellulase): The production of cellulolytic enzymes (endoglucanase and total cellulase) by *A. niger* using purple mombin residue through SSF was optimized using RSM. The optimization focused on fermentation time (h) and water activity (*Aw*). For endoglucanase, the optimal conditions were determined as an *Aw* of 0.974 and a fermentation time of 93.8 h, yielding 3.21 U/mL. For total cellulase, the optimum was an *Aw* of 0.958 and 79.4 h, yielding 12.1 U/mL. Water activity was found to have the most significant effect on total cellulase activity (Santos et al., 2013:1).

Aspergillus niger (Glucoamylase): Glucoamylase production under SSF conditions was optimized using wheat bran and green gram as substrates. A BBD was applied to evaluate and optimize the effects of substrate concentration, moisture content, sucrose, and tryptone on enzyme yield. The

highest experimental glucoamylase activity reached 313 U/gds, which was in close agreement with the predicted value of 306 U/gds, under optimum conditions consisting of 12 g substrate, 55% moisture, 1 g sucrose, and 0.05 g tryptone. Furthermore, the produced enzyme exhibited good stability, retaining activity up to 60 °C and at pH 5 (Polley and Ghosh, 2020:456).

Fusarium sp. BVKT R2 (Xylanase): RSM (CCD) was applied to optimize the production of xylanase in submerged fermentation (SmF) (Ramanjaneyulu and Rajasekhar Reddy, 2016). The variables optimized were sorbitol concentration, yeast extract (YE), initial pH, temperature, and agitation (Ramanjaneyulu and Rajasekhar Reddy, 2016). Optimal conditions were 1.5% sorbitol, 1.5% yeast extract, pH 5.0, 32.5°C temperature, and 175 rpm agitation, yielding a maximum activity of 4560 U/ml (Ramanjaneyulu and Rajasekhar Reddy, 2016). The model proved reliable with an $R2$ of 0.9821 and an adequate precision ratio of 22.749 (Ramanjaneyulu and Rajasekhar Reddy, 2016).

Trichoderma harzianum (Xylanase): Xylanase production was optimized using a two-step statistical approach: PBD followed by BBD (Dhaver et al., 2022). This optimization resulted in a 4.16-fold increase in xylanase activity (153.80 U/ml) compared to the initial OFAT result (37.01 U/ml) (Dhaver et al., 2022). Optimal conditions were determined as 6 days of fermentation, 70°C incubation temperature, pH 5.0, and 1.2% wheat bran and ammonium sulphate (Dhaver et al., 2022).

Lipase and Protease

Penicillium citrinum (Lipase): Lipase production on olive mill wastewater (OMW) was optimized using CCD (D'Annibale et al., 2006:1586). Ammonium chloride (NH_4Cl) was found to be the most effective nitrogen source, while the addition of vegetable oils did not significantly enhance lipase production (D'Annibale et al., 2006:1586). The optimal combination was 2.7 g dm^{-3} NH_4Cl, 1.1 g dm^{-3} yeast extract, and initial pH 6.15, yielding approximately 1230 U dm^{-3} (D'Annibale et al., 2006:1586).

Aspergillus flavus (Lipase): RSM (CCRD) was used to optimize lipase production (Colla et al., 2016:461). The factors showing significant effects were yeast extract concentration (YEC) and pH (Colla et al., 2016:461). The optimal conditions were 45 g/L YEC and pH 7.15, yielding a maximum activity of 3.04 U (predicted 3.24 U) (Colla et al., 2016:461).

Penicillium bilaiae (Acidic Protease): Production of an acidic protease from this endophytic fungus was optimized using PBD followed by BBD and RSM (Ben Mefteh et al., 2019). The factors significantly affecting the yield were temperature, initial pH, and glucose concentration (Ben Mefteh et al., 2019). Under optimal conditions (temperature 24.5°C, pH 6.26, and 13.75 g/L glucose), a remarkable 1086-fold increase in protease production was achieved (Ben Mefteh et al., 2019).

Fusarium culmorum (Protease): Response surface modeling was applied to optimize protease production, finding that the highest yield correlated with 1.4 g/ml soybean meal concentration and a culture time of 4.5 days. The fungus's growth was found to be dependent on the carbon source concentration, while protease production was influenced by the combined effect of carbon source level and culture time (Rucka et al., 1998:229).

Table 1. Examples of RSM Applications in Enzyme Production in Fungi

Enzyme Type	Microorganism	Substrate/Medium	RSM Design	Optimized Parameters (Example)	Max. Activity/Yield	Citation
Laccase	*G. lucidum*	Tobacco stem (200L/1200L SmF)	BBD	Temp (30°C), Aeration (0.66), Agitation (100 rpm)	214,185.2 U/L	(Ma et al., 2025)
LiP, MnP, Laccase	*S. commune*	Corn Stover (SSF)	CCD	pH (4.5), Temp (35°C), Moisture (60%), Inoculum (4 mL)	1270.40 U/mL (LiP)	(Yasmeen et al., 2013:944)
Lipase	*P. citrinum*	Olive Mill Wastewater (OMW)	CCD	NH_4Cl (2.7 g dm^{-3}), YE (1.1 g dm^{-3}), pH (6.15)	~ 1230 U dm^{-3}	(D'Annibale et al., 2006:1586)
Lipase	*A. flavus*	Wheat/Soybean Bran (SmF)	CCRD	Yeast Extract (45 g/L), pH (7.15)	~ 3.04 U	(Colla et al., 2016:461)
Multi-Enzyme	*A. terreus K1*	Palm Kernel Expeller (SSF)	CCD	Temp (30.5°C), Moisture (62.7%), pH (5.8)	265.57 U/g DM (Xylanase)	(Chen et al., 2013:3844)
Glucoamylase	*A. niger*	Wheat Bran/Green Gram (SSF)	BBD	Substrate (12 gm), Moisture (55%), Sucrose (1 gm)	313 U/gds	(Polley and Ghosh, 2020:456)
Endoglucanase	*A. niger*	Purple Mombin Residue (SSF)	RSM	Aw (0.974), Fermentation time (93.8 h)	3.21 U/mL	(Santos et al., 2013:1)

Xylanase	F. sp. BVKT R2	SmF	CCD	Sorbitol (1.5%), YE (1.5%), pH (5.0), Temp (32.5°C)	4560 U/mL	(Ramanjaneyulu and Rajasekhar Reddy, 2016)
Xylanase	*T. harzianum*	SmF	PBD/BBD	Incubation (6 days), Temp (70°C), pH (5.0), Wheat Bran (1.2%)	153.80 U/mL	(Dhaver et al., 2022)
Acidic Protease	*P. bilaiae*	Glucose, $NaNO_3$	PBD/BBD	Temp (24.5°C), pH (6.26), Glucose (13.75 g/L)	1086.95 U/mL	(Ben Mefteh et al., 2019)
Protease	*F. culmorum*	Soybean Meal (SmF)	RSM	Soybean Meal (1.4 g/ml), Culture time (4.5 days)	Max Yield	(Rucka et al., 1998:229)

RSM is an indispensable tool in optimizing fungal enzyme production processes, offering significant advantages over the conventional OFAT method by considering complex variable interactions (Nor et al., 2017; Hao et al., 2023). Through designs like CCD and BBD, RSM facilitates the efficient screening and fine-tuning of critical factors such as temperature, pH, moisture, and nutrient concentrations (Hao et al., 2023). The industrial relevance of RSM is demonstrated by numerous successful optimizations across various fungal systems—including the large-scale laccase production by *G. lucidum* (Ma et al., 2025), high-yield xylanase production by *Fusarium sp. BVKT R2* (Ramanjaneyulu and Rajasekhar Reddy, 2016), and dramatic fold-increases achieved in acidic protease production by *P. bilaiae* (Ben Mefteh et al., 2019) ultimately ensuring high enzyme activity and supporting cost-effective industrial applications (Yasmeen et al., 2013:944).

CONCLUSION

Fungal enzyme production is a fundamental component of the modern bio-economy, serving diverse sectors ranging from food processing and textiles to biofuel synthesis and waste management. The shift from traditional "one-factor-at-a-time" optimization to RSM represents a significant advancement in bioprocess engineering. RSM provides a robust mathematical and statistical framework that identifies the complex, non-linear interactions between critical variables such as temperature, pH, moisture content, and nutrient concentrations that traditional methods inherently fail to capture.

The strategic application of experimental designs like CCD and BBD has demonstrated that precisely fine-tuning these parameters leads to dramatic enhancements in enzyme activity. As seen across various studies, this approach often results in multi-fold yield increases, sometimes enhancing production by over a thousand times compared to non-optimized conditions. Whether the goal is producing thermostable xylanases for animal feed, high-yield laccases for industrial scale-up, or acidic proteases for pharmaceutical use, RSM ensures that the production process is both efficient and reliable.

Furthermore, the methodology facilitates the successful transition from laboratory-scale research to pilot and industrial-scale fermenters, bridging a critical gap in biotechnological commercialization. By enabling the effective utilization of low-cost agro-industrial residues as primary substrates, RSM-based optimization supports the development of sustainable, cost-effective,

and environmentally friendly processes. Ultimately, this statistical approach serves as an indispensable tool for maximizing microbial potential, reducing operational costs, and advancing the industrial production of high-value fungal metabolites.

REFERENCES

Abdullah, R., Ahmad, S., Nisar, K., Kaleem, A., and Iqtedar, M. (2024). Response surface methodology as an approach for optimization of alpha amylase production by using bacterial consortium under submerged fermentation. Kuwait Journal of Science, 51, 100220. https://doi.org/10.1016/j.kjs.2024.100220

Ahsan, T., Chen, J., Wu, Y., and Irfan, M. (2017). Application of response surface methodology for optimization of medium components for the production of secondary metabolites by Streptomyces diastatochromogenes KX852460. AMB Express, 7, 96. https://doi.org/10.1186/s13568-017-0388-z

Antony, J. (2003). *Design of experiments for engineers and scientists*. Elsevier Science and Technology Books.

Banga, J. R., Balsa-Canto, E., Moles, C. G., and Alonso, A. A. (2003). Improving food processing using modern optimization methods. *Trends in Food Science and Technology, 14*(4), 131–144.

Baş, D., and Boyacı, İ. H. (2007). Modeling and optimization I: Usability of response surface methodology. *Journal of Food Engineering, 78*(3), 836–845.

Behnam, S., Karimi, K., and Khanahmadi, M. (2019). Cellulase production under solid-state fermentation by ethanolic zygomycetes fungi: Application of response surface methodology. Nutrition and Food Sciences Research, 6(1), 27–34.

Ben Mefteh, F., Frikha, F., Daoud, A., Bouket, A. C., Luptakova, L., Alenezi, F. N., Al-Anzi, B. S., Oszako, T., Gharsallah, N., and Belbahri, L. (2019). Response surface methodology optimization of an acidic protease produced by Penicillium bilaiae isolate TDPEF30, a newly recovered endophytic fungus from healthy roots of date palm trees (Phoenix dactylifera L.). Microorganisms, 7(3), 74. https://doi.org/10.3390/microorganisms7030074

Ben Slimene Debez, I., Houmani, H., Mahmoudi, H., Mkadmini, K., Garcia-Caparros, P., Debez, A., Tabbene, O., Djébali, N., and Urdaci, M.-C. (2024). Response surface methodology-based optimization of the chitinolytic activity of Burkholderia contaminans strain 614 exerting biological control against phytopathogenic fungi. Microorganisms, 12(8), 1580. https://doi.org/10.3390/microorganisms12081580

Bhardwaj, K. K., Kumar, R., Bhagta, S., and Gupta, R. (2021). Optimization of culture conditions by response surface methodology for production of extracellular esterase from Serratia sp. EST-4. Journal of King Saud University – Science, 33(8), 101603. https://doi.org/10.1016/j.jksus.2021.101603

Castillo, E. D. (2007). *Process optimization: A statistical approach*. Springer Science + Business Media.

Chen, W. L., Liang, J. B., Jahromi, M. F., Ho, Y. W., and Abdullah, N. (2013). Optimization of Multi-enzyme Production by Fungi Isolated from Palm Kernel Expeller using Response Surface Methodology. BioResources, 8(3), 3844–3858.

Colla, L. M., Primaz, A. L., Benedetti, S., Loss, R. A., de Lima, M., Reinehr, C. O., Bertolin, T. E., and Costa, J. A. V. (2016). Surface response methodology for the optimization of lipase production under submerged fermentation by filamentous fungi. Brazilian Journal of Microbiology, 47(2), 461–467. https://doi.org/10.1016/j.bjm.2016.01.028

D'Annibale, A., Brozzoli, V., Crognale, S., Gallo, A. M., Federici, F., and Petruccioli, M. (2006). Optimisation by response surface methodology of fungal lipase production on olive mill wastewater. Journal of Chemical Technology and Biotechnology, 81(9), 1586–1593. https://doi.org/10.1002/jctb.1554

Dhaver, P., Pletschke, B., Sithole, B., and Govinden, R. (2022). Optimization, purification, and characterization of xylanase production by a newly isolated Trichoderma harzianum strain by a two-step statistical experimental design strategy. Scientific Reports, 12, 22723. https://doi.org/10.1038/s41598-022-22723-x

Hao, B., Xu, D., Wei, Y., Diao, Y., Yang, L., Fan, L., and Guo, Y. (2023). Mathematical models application in optimization of hydrothermal liquefaction of biomass. Fuel Processing Technology, 243, 107673. https://doi.org/10.1016/j.fuproc.2023.107673

İkiz, F., Püskülcü, H., and Eren, Ş. (2000). *İstatistiğe giriş* (6. baskı). Barış Yayınları.

Koç, B., and Kaymak-Ertekin, F. (2009). Yanıt yüzey yöntemi ve gıda işleme uygulamaları [Response surface methodology and food processing applications]. GIDA, 3.

Kolotylo, V., Piwowarek, K., Synowiec, A., and Kieliszek, M. (2025). Optimization of fermentation conditions for microbial transglutaminase production by Streptoverticillium cinnamoneum KKP 1658 using response surface methodology (RSM). Folia Microbiologica, 70, 259–269. https://doi.org/10.1007/s12223-024-01223-7

Lazic, Z. R. (2004). *Design of experiments in chemical engineering*. Wiley-VCH.

Ma, Y., Liu, M., Gu, R., Zhang, R., Ji, X., Zhang, J., Wen, W., and Peng, Z. (2025). Optimization of the scale-up production process for high-yield laccase from white-rot fungi. Frontiers in Bioengineering and Biotechnology, 13, 1631687. https://doi.org/10.3389/fbioe.2025.1631687

Montgomery, D. C. (2001). *Design and analysis of experiments* (5th ed.). John Wiley and Sons.

Myers, R. H., Montgomery, D. C., Vining, G. G., Borror, C. M., and Kowalski, S. M. (2004). Response surface methodology: A retrospective and literature survey. *Journal of Quality Technology, 36*(1), 53–77.

Özdikicierler, O., Eren, İ., Göksungur, Y., Yemişçioğlu, F., and Gümüşkesen, A. S. (2016). Gıda Mühendisliğinde Optimizasyon ve Modelleme Süreçlerinde Cevap Yüzey Metodu Yaklaşımı [Response surface method approach in optimization and modeling processes in food engineering]. Türkiye 12. Gıda Kongresi, Edirne.

Polley, T., and Ghosh, U. (2020). Optimisation of fungal glucoamylase production by Response Surface Methodology and characterisation of the purified

enzyme. Plant Science Today, 7(3), 456–462. https://doi.org/10.14719/pst.2020.7.3.762

Ramanjaneyulu, G., and Rajasekhar Reddy, B. (2016). Optimization of Xylanase Production through Response Surface Methodology by Fusarium sp. BVKT R2 Isolated from Forest Soil and Its Application in Saccharification. Frontiers in Microbiology, 7, 1450. https://doi.org/10.3389/fmicb.2016.01450

Rucka, M., Lamer-Zarawska, E., Maliszewska, I., and Turkiewicz, B. (1998). Optimization of growth and hydrolytic enzymes production by Fusarium culmorum using response surface method. Bioprocess Engineering, 19, 229–232.

Santos, T. C., Abreu Filho, G., Oliveira, A. C., Rocha, T. J. O., Machado, F. P. P., Bonomo, R. C. F., Mota, K. I. A., and Franco, M. (2013). Application of response surface methodology for producing cellulolytic enzymes by solid-state fermentation from the puple mombin (Spondias purpurea L.) residue. Food Science and Biotechnology, 22(1), 1–7. https://doi.org/10.1007/s10068-013-0001-4

Sharma, N., Thakur, C., Ahlawat, Y. K., Mehta, H., Chauhan, V., Sharma, S., and Bisht, K. (2025). Maximizing enzyme production by standardizing process parameters through one factor at a time approach (OFAT) subjected to a statistical technique: Response surface methodology (RSM). Plant Science Today, 12(4), 1–15. https://doi.org/10.14719/pst.8516

Turan, M. D., and Altundoğan, H. S. (2011). Hidrometalurjik araştırmalarda yanıt yüzey yöntemlerinin (YYY) kullanımı. *Madencilik, 50*(3), 11–23.

Yasmeen, Q., Asgher, M., Sheikh, M. A., and Nawaz, H. (2013). Optimization of Ligninolytic Enzymes Production through Response Surface Methodology. BioResources, 8(1), 944–968.

Enhancing Microbial Biogas Production From Agroindustrial Waste Pre-Treated with Filamentous Fungi

Derya BERİKTEN[1]
Gizem ARIK[2]

1- Assoc. Prof. Dr.; Kütahya Health Sciences University, Faculty of Engineering and Natural Sciences, Department of Molecular Biology and Genetics derya.berikten@ksbu.edu.tr ORCID No: 0000-0002-8672-4813
2- Asst. Prof. Dr.; Ankara Medipol University, Faculty of Pharmacy, Department of Pharmaceutical Microbiology gizem.arik@ankaramedipol.edu.tr ORCID No: 0000-0002-3673-3543

ABSTRACT

Lignin is a major barrier to the anaerobic digestion of lignocellulosic biomass, as it limits microbial access to cellulose and hemicellulose. Pretreatment aims to make lignocellulosic biomass more digestible to improve biogas production. Pretreatment methods can be chemical, physical, mechanical or biological. Fungal pretreatment is a low-cost and effective method to increase biogas production from lignocellulosic biomass. In particular, decay fungi produce enzymes that can break down lignin, which increases the digestibility of biomass. Different fungal species have different abilities to break down biomass. Screening studies are needed to select the most effective fungal strains to maximize biogas yield. The effectiveness of fungal pretreatment depends on the fungal strain used, the pretreatment conditions and the type of biomass. Other methods include grinding, irradiation and alkaline or acid treatments. These methods can be effective but may be more expensive or complex to implement than fungal pretreatment. Microorganisms derived from the digestive tracts of animals can be used to degrade biomass and enhance biogas production, and their application through bioaugmentation represents a promising approach. This involves adding specific microorganisms or enzymes that may be deficient. Stable biomass-degrading consortia are economically viable candidates to increase the efficiency of anaerobic digestion of lignocellulose-rich wastes. Biomass composition and pretreatment method affect the quality and quantity of the resulting biogas. The results suggest that fungal pretreatment is a promising technique to increase biogas production from lignocellulosic biomass. However, further research is needed to determine the most effective approach for a specific application.

Keywords – Biogas, Bioaugmentation, Lignin, Fungal Pretreatment, Waste.

INTRODUCTION

With the increase in population and the acceleration of industrialization worldwide, the demand for energy continues to increase. Our traditional energy sources, fossil fuels, are both limited and cause environmental problems. This situation makes the need for renewable energy sources even more critical (Jameel et al., 2024).

Greenhouse gas emissions resulting from the use of fossil fuels are considered one of the main factors of climate change. Therefore, it has become an inevitable necessity to turn to sustainable and environmentally friendly alternatives for energy production. Biogas is a gas mixture consisting of methane (50-70%) and carbon dioxide (30-50%) obtained through the anaerobic digestion of organic waste. Biogas, a renewable

energy source, offers great potential in both waste management and energy production (Das et al., 2023; Jameel et al., 2024).

There are many advantages of biogas production. Energy production; Biogas can be used to produce heat and electricity and can even be upgraded to natural gas quality (highly concentrated biomethane) so that it can be injected into the natural gas grid or used directly in vehicles (Jameel et al., 2024). Waste management; Biogas production offers an effective solution for the management of various organic wastes such as agricultural waste, food waste, animal manure and municipal solid waste. Using these wastes as an energy source instead of disposing of them reduces environmental pollution and contributes to sustainable waste management. Reduction of greenhouse gas emissions; Biogas production plays an important role in combating the greenhouse effect and climate change by preventing the release of methane gas into the atmosphere. Methane, which is released as a result of the decomposition of organic waste in landfills, is a much more powerful greenhouse gas than carbon dioxide. Therefore, reducing methane emissions through biogas production is important for mitigating climate change. Nutrient recovery; Digestate, a by-product of anaerobic digestion, is a nutrient-rich fertilizer that can be used in agriculture. The use of digestate reduces dependence on chemical fertilizers and contributes to the nutrient cycle. Economic benefits; The biogas sector has the potential to create employment, especially in rural areas. In addition, local energy production increases energy independence and contributes to the local economy (Das et al., 2023).

There are also some challenges for the expansion of biogas production: Biogas production technologies are still developing, especially in developing countries. Technological developments are needed to increase efficiency, reduce costs and ensure process stability (Jameel et al., 2024). Appropriate legal regulations are needed for the development and expansion of the biogas sector. Policies that encourage the installation and operation of biogas plants will contribute to the growth of the sector (Jameel et al., 2024). It is important to raise public awareness of biogas technologies and their benefits. Public support for biogas production will facilitate the growth and expansion of the sector.

The resources focus on the importance of microbial communities in biogas production. The anaerobic digestion process is carried out by the interaction of complex microbial communities, and the structure and function of these communities affect the efficiency of biogas production. In this context, biogas production offers a sustainable and environmentally friendly solution in the field of waste management and energy production (Das et al., 2023).

Various strategies are being developed to overcome the challenges faced in biogas production and to increase efficiency. Understanding the sructure and function of microbial communities involved in anaerobic

digestion is important to optimize biogas production. Developing microbial communities that can degrade certain substrates more effectively or are more resistant to harsh environmental conditions can increase the efficiency and stability of biogas production (Das et al., 2023). Some wastes, such as lignocellulosic biomass, are difficult to anaerobic digest. Pretreatment technologies facilitate the anaerobic digestion process by breaking down the structure of these wastes and increase biogas yield. There are chemical, physical and biological pretreatment methods (Rouches et al., 2016:1784). Combined digestion of different types of waste can increase the efficiency of the anaerobic digestion process. For example, co-digestion of carbon-rich wastes with nitrogen-rich wastes optimizes microbial activity and increases biogas yield. Operating the anaerobic digestion process under optimum conditions (temperature, pH, feed rate, etc.) is important to maximize biogas production. Continuous monitoring and control systems help increase process stability and efficiency (Das et al., 2023).

POTENTIAL OF LIGNOCELLULOSIC BIOMASS FOR BIOGAS PRODUCTION

Lignocellulosic biomass is an abundant and renewable resource produced in large quantities worldwide, making it a promising feedstock for biogas production. It can be obtained from various sources such as agricultural residues, grass and wood waste. Lignocellulosic biomass has a complex structure mainly consisting of cellulose, hemicellulose and lignin. Cellulose and hemicellulose sugars are energy-rich components that can be converted into biogas through anaerobic digestion (Govarthanan et al., 2022), (Alexandropoulou et al., 2017:704). However, the presence of lignin poses a major challenge, significantly hindering the anaerobic digestibility of lignocellulosic materials (Govarthanan et al., 2022), (Tuesorn et al., 2013:579).

Lignin forms a complex three-dimensional polymer structure that encases cellulose and hemicellulose, making it difficult for anaerobic microorganisms to access these sugars. Therefore, lignin degradation is crucial for effective biogas production. Key factors affecting the use of lignocellulosic biomass in biogas production are: Sources emphasize that lignin is highly resistant to chemical and enzymatic degradation and is a significant barrier to anaerobic digestion. The higher the lignin percentage, the higher the resistance to chemical and enzymatic degradation, which

affects the biogas production yield. (Govarthanan et al., 2022), (Alexandropoulou et al., 2017:704). Pretreatment is essential for the degradation of lignin, reducing cellulose and hemicellulose crystallinity and making it more suitable for anaerobic digestion. Sources indicate that pretreatment can increase the recovery of fermentable sugars and reduce the number of enzyme inhibitors generated during pretreatment. Various methods are available for pretreatment, including physical, chemical and biological. The choice depends on factors such as the type of biomass, process economics and the desired biogas yield. (Govarthanan et al., 2022), (Alexandropoulou et al., 2017:704). Anaerobic digestion is a complex process and involves a range of microbial communities, including hydrolysis, acidogenesis, acetogenesis, and methanogenesis. The efficiency of these processes is affected by factors such as substrate composition, temperature, pH, and feed rate. (Tuesorn et al., 2013:579), (Govarthanan et al., 2022), (Alexandropoulou et al., 2017:704). The microbial community involved in the anaerobic digestion of lignocellulosic biomass is crucial to the efficiency of the process. There are a variety of bacteria and fungi that can degrade complex lignocellulosic structures and convert them into biogas. (Rouches et al., 2016:1784), (Aryal et al., 2018:359) (Tuesorn et al., 2013:579). Lignocellulosic biomass often exhibits slow hydrolysis rates and low biogas yields when used as a single substrate. To overcome this challenge, combined digestion with other substrates with different C/N ratios has been proposed. For example, lignocellulosic biomass with a high C/N ratio can be combined with manure with a lower C/N ratio, optimizing the overall digestion process. Das et al., 2023, (Govarthanan et al., 2022).

Regarding the potential of lignocellulosic biomass for biogas production, the literature highlights some important developments in this area. One of these is fungal pretreatment. The literature indicates that white-rot fungi are effective in pretreating lignocellulosic biomass due to their ability to secrete lignin-degrading enzymes (Rouches et al., 2016:1784). These enzymes improve the hydrolysis process by breaking down lignin and making it more suitable for anaerobic digestion (Das et al., 2023, Tuesorn et al., 2013:579). Another one is microbial community engineering. The development of microbial communities that can degrade certain substrates more effectively or are more resistant to harsh environmental conditions is a promising strategy to increase biogas production yield and process stability. Advances in genomic techniques such as metagenomics and metatranscriptomics have revolutionized our understanding of the structure and function of microbial communities involved in anaerobic digestion. This information can be used in microbial community engineering to optimize the biogas production process (Das et al., 2023).

Lignin hinders the anaerobic digestion process and reduces biogas yield by making it difficult for anaerobic microorganisms to access the sugars of lignocellulosic biomass. Lignin has a complex three-dimensional

polymer structure, making it highly resistant to both chemical and enzymatic degradation. This complex structure means that enzymes produced by anaerobic microorganisms cannot effectively break down lignin. (Govarthanan et al., 2022), (Tuesorn et al., 2013:579). Lignin is physically and chemically linked to cellulose and hemicellulose, which prevents anaerobic microorganisms from effectively accessing these sugars. As a result, hydrolysis, an important step in anaerobic digestion, is slowed down (Rouches et al., 2016:1784).

High lignin content is directly related to low biogas yield. This is because lignin is inefficiently broken down, making it a poor energy source for biogas production. Furthermore, unbroken lignin can have an inhibitory effect on microorganisms involved in biogas production. (Aryal et al., 2018:359)

In addition, the application of certain pretreatment methods to lignin to degrade lignin may result in the production of inhibitory compounds such as phenolic compounds and furfural, which may negatively affect anaerobic digestion. These inhibitors impair the metabolic activity of anaerobic microorganisms and inhibit biogas production (Taherzadeh and Karimi 2008:1621).

Pretreatment is very important to overcome these difficulties caused by lignin. The aim of pretreatment is to degrade lignin, reduce cellulose and hemicellulose crystallinity, and make lignocellulosic material more suitable for anaerobic digestion. One pretreatment method that is effective in degrading lignin is to use white rot fungi (WRFs) that secrete lignin-degrading enzymes such as lignin peroxidase and laccase. WRFs can also reduce the production of inhibitory compounds that may inhibit anaerobic digestion (Govarthanan et al., 2022), (Tuesorn et al., 2013:579), (Alexandropoulou et al., 2017:704).

Additionally, microbial community engineering is a promising strategy to improve anaerobic digestion of lignin. This approach involves developing microbial communities that can degrade lignocellulosic materials more efficiently or are more resistant to harsh environmental conditions (Ozbayram et al., 2020:489).

FUNGAL PRETREATMENT

Mechanisms of fungal pretreatment

The process of converting lignocellulosic materials into other products with added value requires pretreatment because lignin acts as an inhibitor of enzyme penetration. When comparing different pretreatment procedures, fungal pretreatment is a more environmentally friendly option (Nadir et al., 2019). White rot fungi frequently used in pretreatment studies of various raw materials include *Phanerochaete chrysosporium, Pleurotus ostreatus, Coriolus versicolor, Cyathus stercoreus*, and *Ceriporiopsis subvermispora* (Wan and Li, 2012:1447).

Fungal enzymes involved in lignin degradation

Manganese peroxidase (MnP), laccase, lignin peroxidase (LiP) and versatile peroxidase (VP) are the primary oxidative enzymes that break down lignin (Nadir et al., 2019).

- ***Manganese peroxidase***

The enzyme MnP is a member of the heme-containing oxidoreductases family. The isoenzymes range in molecular weight from 40 to 50 kDa. The enzyme's active site is made up of two Ca^{2+} ions and five disulfide bonds. The active region contains a variety of amino acids, including arginine, histidine, and aspartic acid. It has been demonstrated that one heme propionate, two water molecules, three acidic ligands, and one Mn^{2+} site are present in the substrate binding site (Kumar & Chandra, 2020). The catalytic cycle of MnP is initiated by ferric enzyme and H_2O_2 to generate compound I, an oxo-porphyrin radical complex consisting of Fe^{4+}. On the other hand, monochelated Mn^{2+} ions donate 1 e^- from Mn^{2+} to form Mn^{3+}, so generating compound II. Additionally, the chelated Mn^{3+} ions produced by MnP function as mediators of S–S charge transfer, permitting the oxidation of a variety of phenolic substrates, including amines, simple phenols, phenolic lignin, and a number of dyes (Chowdhary et al., 2019).

- ***Laccase***

Laccases are oxidoreductase enzymes with polyphenol activity. They are in the multicopper oxidase family with ferroxyoxidases and ascorbate oxidases. Three copper atoms transport the electrons to O_2, whereas one of these copper atoms determines which substrates to oxidize based on their redox potential. Fungal laccases are mainly extracellular enzymes that have a molecular weight of 60–70 kDa and are composed of different carbohydrate moieties in varied ratios (10-25%) (Aza & Camarero, 2023).

Laccases become thermostable and are shielded from heat-related deterioration through this glycosylation (Sigoillot et al., 2012:263). Complex substrates cannot be catalyzed by laccase at low redox potential. Thus, in order to sustain the cyclic redox cycle and make the process effective,

natural or artificial mediators are needed. A mediator is a small chemical molecule that the substrate continually reduces and the enzyme continuously oxidizes. The low affinity of the enzyme's active site prevents it from penetrating complex substances like lignocellulose. Oxidizing mediators are therefore employed. Feruloyl esterase, which aids in the dissolution of lignin complexes, is one of the mediators of laccase induction. Mediators are first oxidized in the process. After diffusing from the active site of the enzyme, oxidized mediators enter the plant cell wall through its pores (Kumar & Chandra, 2020).

Fungal laccases have a wide substrate diversity and can catalyze the oxidation of different organic compounds such as aryl amines, N-heterocycles, o-p-substituted phenols and synthetic organic dyes (Aza & Camarero, 2023). The catalytic process varies depending on the type of substrate and reaction. Free radical coupling, which produces dimeric products or polymeric molecules, and oxidative carboxylations are the most common reactions. Oxidation of substrates results in the reduction of molecular oxygen to form two molecules of water. For each reduced oxygen, four molecules of substrate are oxidized and no H_2O_2 is formed as a result of the reaction. Laccases that produce only H_2O as a byproduct are called 'ideal green catalysis' (Rivera-Hoyos et al., 2013:67).

The most well-known biological activity of fungal laccases is their involvement in the biodegradation of lignin, given the fact that they also contain defense mechanisms, pigmentation, and virulence It requires only O_2 for non-specific catalytic activity on lignin polymers and releases water, enabling environmentally friendly applications (Aza & Camarero, 2023).
Phanerochaete chrysosporium, Pleurotus ostreatus, Trametes versicolor, Cerrena maxima, Lentinula edodes, and *Dichomitus squalens* are the major fungal species that are known to produce laccase (Dashora et al., 2023).
Studies on increasing the existing ligninolytic activity of laccase have biotechnological importance. In this context, Kumar et al. produced recombinant laccase enzyme in *Schizophyllum commune* NI-07. In the study where they used Trametes versicolor as a reference, it was reported that the lignin degradation of the purified recombinant laccase increased by 20% (Kumar et al., 2022). The putative laccase gene of *Sordaria macrospora* was expressed heterologously in *Escherichia coli*. It was demonstrated that the new enzyme LacSM enhanced the breakdown of lignin while retaining its oxidative ability at neutral and alkaline pH. These characteristics suggested that this enzyme could be an alternative choice for the lignin-cellulosic biomass lignin breakdown process (Yang et al., 2020:1133).

• ***Lignin Peroxidase***

The first known ligninolytic enzyme, lignin peroxidase, was extracted from the white fungus *Phanerochaete chrysosporium*. It is an extracellular glycosylated heme-containing enzyme that has many isomers with molecular

weights between 37 and 47 kDa. Enzyme activity is reported to be at its peak between 35 and 55 °C and between 2.5 and 3.0 pH levels (Shi et al., 2021:3753).

The two domains in which the enzyme displayed organization were essentially made up of alpha-helices. The center of these two domains is site to LiP's active site, which is made up of a single iron atom with a heme. The nitrogen of a histidine residue and the four nitrogen atoms of the tetrapyrrolic structure are five-coordinated with the iron atom. The three-dimensional structure is stabilized by four disulfide bonds and two calcium ions. Trp171, a hydroxylated residue that is always conserved in LiP sequences, is the product of a post-translational modification that appears to be necessary for the catalytic activity of these enzymes (Sigoillot et al., 2012:263).

There are three phases in the enzyme's catalytic process. The oxo-ferryl intermediate is produced when H_2O_2 oxidizes the ferric enzyme. This is the initial reaction. A substrate reduces the oxo-ferryl intermediate in the second step. The molecule created in the previous stage receives an electron in the last step. The oxidation cycle is so completed (Falade et al., 2017).

The different catalytic reactions of lignin peroxidase can be summarized as follows: aromatic ring cleavage, cleavage of beta-O-4 ether bonds, cleavage of lignin C alpha-C beta bonds, hydroxylation, quinone formation, oxidation of C alpha alcohols to C alpha-oxo compounds (Dashora et al., 2023).

In a study investigating the synergistic effects of LiP and quinone reductase (QR) on the degradation of industrial lignin, QR and LiP genes of Trametes versicolor and *Phanerochaete chrysosporium* were expressed in *Pichia pastoris*. Combined LiP and QR reduced the molecular weight of four different lignin sources. Mostly monomeric degradation products were phenols (Majeke et al., 2021).

• ***Versatile peroxidase***

It is also known as hybrid peroxidase as the molecular combination of manganese peroxidase and lignin peroxidase. With a low to high redox potential, substituted phenol dyes, and Mn^{2+}, VP possesses dual oxidative capabilities. It oxidizes phenolic and non-phenolic and lignin derivatives without the need for Mn^{2+}. VP oxidizes compounds without any mediator. Eleven to twelve helices, four disulfide bridges, two structural Ca^{2+} sites, a heme pocket, and a Mn^{2+}-binding site resembling MnP are all part of the structure of VP. *Pleurotus, Bjerkandera* and *Lipista* genera have been reported to be VP producers (Janusz et al., 2017:941; Kumar & Chandra, 2020).

Fungal pretreatment methods

Fungal pretreatment methods for lignocellulosic biomass offer a more environmentally friendly approach compared to conventional chemical or physical methods. They aim specifically at selectively degrading lignin while preserving cellulose and hemicellulose, which are the main components of the substrate essential for biomethane production (Alexandropoulou et al., 2017:704; Rouches et al., 2016:1784).

- ***Solid State Fermentation (SSF)***

Solid State Fermentation (SSF) is the prevalent and cost-effective process widely preferred for the fungal pretreatment of lignocellulosic biomass. Compared to liquid cultures (submerged fermentation), SSF allows for higher substrate loads, promotes better attachment of fungal enzymes to the substrate surface, and facilitates easier oxygen diffusion within the substrate. Additionally, the costs of SSF are lower than those of liquid culture because it requires less aeration, heating, mixing, and water (Rouches et al., 2016:1784). A study on willow sawdust (WSD) involved preparing SSF batch cultures using White-Rot Fungi (WRF) such as *Leiotrametes menziesii* and *Abortiporus biennis*. In these experiments, the biomass was adjusted to 80% moisture content, a condition optimized for lignin degradation (Alexandropoulou et al., 2017:704).

The main disadvantage of biological pretreatment methods is the long processing time required for sufficient biomass modification (typically ranging from at least one to several weeks). SSF is subject to this long duration, but this constraint can be partially overcome by integrating the process into the material's storage period (Rouches et al., 2016:1784).

- ***Liquid State Fermentation (LSF)***

The sources indicate a tendency toward adopting SSF, especially on an industrial scale, over LSF or submerged cultures, primarily because SSF is considered more efficient and cost-effective for fungal pretreatment. Fungal pretreatments are simpler than enzymatic pretreatments using ligninolytic enzymes, as fungi secrete the enzymes directly while growing on the substrate, eliminating the need for an additional extraction step for enzyme recovery. The use of LSF in fungal pretreatment is generally limited to the objective of mycelium production. For instance, in one study, the *Polyporus brumalis* BRFM 985 strain was cultured in a liquid medium (malt extract broth 20 g/L) to obtain the mycelial biomass necessary for subsequent methane potential tests (Rouches et al., 2016:1784).

- ***Optimization of Pretreatment Conditions***

The success of fungal pretreatment depends on the selective degradation of lignin by the fungal strain and the extent to which it preserves cellulose and hemicellulose—the carbohydrates essential for anaerobic

digestion (AD) (Alexandropoulou et al., 2017:704; Rouches et al., 2016:1784).

The optimal pretreatment duration varies depending on the specific fungal species used and aims to maximize the increase in biochemical methane potential (BMP) (Alexandropoulou et al., 2017:704). For example, in experiments on willow sawdust (WSD), 14 days of cultivation for L. menziesii and 30 days for *A. biennis* resulted in the lowest lignin-to-cellulose ratios, indicating that the optimum duration differs between fungi (Alexandropoulou et al., 2017:704). The efficiency of fungal lignin degradation is closely linked to moisture content. It has been reported that an initial moisture content between 70% and 80% is considered optimal for the lignin degradation and ligninase activities of most White-Rot Fungi (WRF) (Alexandropoulou et al., 2017:704; Reid, 1989).

The introduction of supplemental nutrients (starter solutions), such as glucose and nitrogen, during fungal pretreatment can negatively impact the fungal effect on the substrate's lignin content. Studies have shown that glucose supplementation during pretreatment restricts delignification, leading to a reduction in subsequent methane production from the substrate. High levels of glucose addition increased the insoluble lignin (AIL) content, supporting the hypothesis that glucose inhibits lignin degradation (as clearly observed in a study using the *T. menziesii* BRFM 1369 strain) (Rouches et al., 2016:1784). This effect is believed to be caused by glucose suppressing core ligninolytic enzymes like manganese peroxidase. Lignin degradation is a secondary metabolic process initiated generally in response to carbohydrate depletion, whereas the fungus's primary metabolism focuses on mycelial growth and the consumption of readily available carbohydrates (Rouches et al., 2016:1784; Jeffries et al., 1981; Zadražil, 1977). High glucose levels prolong this initial phase, thereby delaying delignification (Rouches et al., 2016:1784).

For most WRF, delignification is triggered under nitrogen starvation conditions. Consequently, the addition of nitrogen (such as diammonium tartrate) can also impede lignin reduction. The most efficient strategy for enhancing biogas production is to limit the starter solution. Pretreatment using the lowest amount of starter solution (25 mg glucose/g TS straw and 2.5 mg diammonium tartrate/g TS straw) with the *P. brumalis* BRFM 985 strain resulted in a methane increase of up to 21%, even after accounting for mass loss. This indicates that high efficiency can be achieved with low starter input, simultaneously reducing additional costs for industrial applications (Rouches et al., 2016:1784).

ADVANTAGES OF FUNGAL PRETREATMENT COMPARED TO CHEMICAL METHODS FOR LIGNOCELLULOSIC BIOMASS

The effectiveness of fungal pretreatment methods for lignocellulosic biomass, compared to chemical methods, is a crucial topic in maximizing biogas and biomethane production. Biological methods, particularly those employing fungi, are regarded as a highly promising pretreatment strategy alongside alkaline (chemical) methods (Govarthanan et al., 2022). Fungal pretreatment offers distinct advantages over traditional chemical methods, primarily due to its operational environment and specificity. However, chemical methods often excel in speed and sheer bulk removal of components.

Here is a comparison of the effectiveness of fungal pretreatments versus chemical methods based on the sources:

Effectiveness and Advantages of Fungal Pretreatment

Fungal pretreatments are biological methods known for their sustainability and selectivity. Biological pretreatment methods are carried out under mild conditions, require low energy input, and do not release toxic compounds into the environment (Govarthanan et al., 2022; Wei, 2016). The primary limiting factor in the anaerobic digestion (AD) of lignocellulosic biomass is lignin (Govarthanan et al., 2022; Shah and Ullah, 2019:7497). Fungi, specifically White-Rot Fungi (WRF), are the most effective organisms used to break down this complex biomass by selectively degrading lignin (Rouches et al., 2016:1784). Fungal effectiveness in delignification relies on the production of extracellular enzymes such as lignin peroxidases and laccases (Govarthanan et al., 2022). Studies on specific biomass samples show that fungal pretreatments can provide a high level of methane yield increase (Table 1).

Table 1. Comparison of Yields Between Fungal and Chemical Methods

Substrate	Fungal Pretreatment Microorganism	Resulting Yield Increase	Reference
Japanese cedar wood	*Ceriporiopsis subvermispora* (White Rot Fungus)	300% (4-fold) increase in methane	Amirta et al. (2006:71); Govarthanan et al. (2022); Ali and Sun (2015)
Wheat straw	Lignin-degrading fungal culture	5-fold increase in biogas yield	Shah and Ullah (2019); Govarthanan et al. (2022)
Willow Sawdust (WSD)	*Abortiporus biennis* (30 days)	43% increase in Biomethane Potential (BMP)	Alexandropoulou et al. (2017)
Crop waste	*Polyporus brumalis*	75.75% increase in BMP	Das et al. (2023)

Comparison with Chemical Pretreatment Methods

Chemical methods are often faster but can be non-selective and may require harsher conditions, leading to inhibitory byproducts (Taherzadeh and Karimi, 2008:1621). Alkaline pretreatment (e.g., using NaOH) is effective at removing lignin and improving holocellulose solubility (Alexandropoulou et al., 2017:704; Taherzadeh and Karimi, 2008:1621). Treating WSD only with an alkaline solution resulted in a 31.7% removal of lignin (Alexandropoulou et al., 2017:704). Highly effective delignification, up to 65%, was observed in cotton stalks using a 2% NaOH solution at a high temperature (121°C) (Taherzadeh and Karimi, 2008:1621). Dilute acid hydrolysis is highly effective at dissolving hemicellulose, capable of achieving nearly 100% removal; however, it is not efficient for lignin solubilization (Taherzadeh and Karimi, 2008:1621). A combination of 30% acetic acid and 2% nitric acid successfully removed 80% of the lignin from waste newsprints, increasing the biogas production by three times (Taherzadeh and Karimi, 2008:1621).

Combining Fungal and Chemical Treatments

The highest reported efficiencies often arise from combining biological and chemical methods, leveraging the speed and broad effect of chemical treatments with the targeted specificity of fungal degradation. Combining fungal and alkaline pretreatments resulted in significantly enhanced biomethane yields compared to either method used alone. The combined treatment (fungal *A. biennis* followed by alkaline treatment) yielded a maximum BMP increase of 115% compared to untreated raw WSD. This combined strategy resulted in a 12.5% higher methane yield than the alkaline pretreatment alone, and a 50.1% higher yield than the fungal pretreatment alone. The combined treatment was highly effective for lignin removal, achieving 59.8% lignin degradation when using Leiotrametes menziesii and alkali, and 54.2% when using *A. biennis* and alkali. This level of delignification far surpassed that achieved by alkaline treatment alone (31.7%) (Alexandropoulou et al., 2017:704).

Fungal pretreatment is highly effective due to its selective degradation of lignin and its operation under environmentally mild conditions, avoiding the toxic inhibitors often produced by harsh chemical processes (Govarthanan et al., 2022; Taherzadeh and Karimi, 2008:1621). However, the main constraint of fungal methods that limits their application compared to chemical processes is the long pretreatment duration required—typically several weeks—to achieve sufficient biomass modification (Rouches et al., 2016:1784; Shah and Ullah, 2019:7497). Chemical methods, such as combined acid/alkaline treatments, can achieve rapid, high levels of delignification (e.g., 80% lignin removal) and three-fold increases in biogas production in a shorter period (Taherzadeh and Karimi, 2008:1621, citing others). The greatest efficacy for maximum methane yield increase (up to

115% compared to raw material) is achieved when the selective, biological action of fungi is combined with chemical pretreatment, demonstrating a powerful synergistic relationship (Alexandropoulou et al., 2017:704).

PRACTICAL APPLICATIONS OF FUNGAL PRETREATMENT IN ANAEROBIC DIGESTION

Fungal pretreatment, utilizing microorganisms such as White-Rot Fungi (WRF), is recognized as an eco-friendly and advantageous biological method for increasing the efficiency of anaerobic digestion (AD) of recalcitrant lignocellulosic biomass (LCB) (Govarthanan et al., 2022; Alexandropoulou et al., 2017:704). The method selectively degrades lignin, enhancing the accessibility of cellulose and hemicellulose for subsequent methane conversion (Alexandropoulou et al., 2017:704; Rouches et al., 2016:1784).

Examples of Biogas Plants Using Fungal Pretreatment Biomass

The widespread commercial adoption of fungal pretreatment as the primary LCB optimization method remains limited (Rouches et al., 2016:1784). Generally, the research on fungal methods is conducted at the laboratory or pilot scale due to the inherent constraint of prolonged treatment times required for adequate biomass modification (Alexandropoulou et al., 2017:704; Rouches et al., 2016:1784; Paritosh et al., 2021).

Instead of biological pretreatment, most modern, large-scale commercial biogas enhancement strategies focus on rapid physico-chemical methods or gas upgrading technologies:

Hydrogen-Mediated Biogas Upgrading: Commercial plants, such as Microb2Energy – BioPower2Gas (Germany) and Electrochaea (Denmark), rely on biological methanation where H_2 is injected to convert CO_2 in biogas to CH_4 (Aryal et al., 2018:359; Jameel et al., 2024).

Nanomaterial Enhancement: Nanotechnology intervention is an emerging strategy aimed at improving methanogenesis by doping ions or zero-valent metals (e.g., Fe3O4 nanoparticles) into the anaerobic system as powerful catalysts (Govarthanan et al., 2022).

Use of Fungal Pretreatment in Biofortification

Although the term "biofortification" (nutrient enhancement) is not explicitly defined in the context of fungal pretreatment in the sources, the

method contributes significantly to enhancing the utility and safety of the final anaerobic digestate (fertilizer) and increasing resource recovery by performing necessary detoxification:

Detoxification of Inhibitory Compounds: Fungal pretreatment eliminates the release of toxic compounds or inhibitory byproducts (such as furfural or hydroxymethylfurfural) that are commonly generated by harsh chemical or thermochemical methods (Alexandropoulou et al., 2017:704; Taherzadeh and Karimi, 2008:1621; Rouches et al., 2016:1784). White-Rot Fungi have been successfully used to detoxify toxic phenolic compounds found in olive mill wastewater before. Fungal solid-state fermentation (SSF) pretreatment of orange processing wastes has been shown to reduce the level of antimicrobial substances (Rouches et al., 2016:1784; Taherzadeh and Karimi, 2008:1621).

Enhancement of Digestate Quality: The final solid residue (digestate) from anaerobic digestion, which can be valorized as fertilizer, is characterized by its high quality. The anaerobic digestion process, often optimized by pretreatment, improves waste management, enhances the public health level, and contributes to disease control. The produced fertilizer is free of unpleasant odors, easier for plant roots to absorb, and rich in vital nutrients like nitrogen, potassium, and phosphorus (Jameel et al., 2024).

Using Single Fungal Species or Consortia

Both single fungal species and microbial consortia have demonstrated viability for LCB pretreatment, with consortia generally offering broader functional capabilities, leading to potentially higher overall performance (Table 2) (Govarthanan et al., 2022; Tuesorn et al., 2013:579).

Table 2. Using Single Fungal Species or Consortia for lignocellulosic biomass

Strategy	Species / Community Type	Substrate	Key Performance Metric	Reference
Single Species	Abortiporus biennis (WRF)	Willow Sawdust (WSD)	Achieved a 43% BMP increase (30 days cultivation); showed low cellulose uptake, making it attractive for preserving AD substrate	(Alexandropoulou et al., 2017)
	Polyporus brumalis BRFM 985 (WRF)	Wheat Straw	Increased methane production up to 21% per gram of initial total solids (TS) after accounting for mass loss, and up to 43% more methane per gram of pretreated VS	(Rouches et al., 2016:1784)
	Ceriporiopsis subvermispora (WRF)	Japanese Cedar Wood, Yard Trimmings	Biogas increase of 35% in one study and methane yield enhancement up to 54% in another	(Amirta et al., 2006:71; Zhao et al., 2014]
Microbial Consortia	Lignocellulolytic Microbial Consortium (LMC)	Swine Manure (SM)	Increased overall methane yield by 55%; enhanced cellulose degradation by 1.87-fold and hemicellulose degradation by 1.65-fold	(Tuesorn et al., 2013:579)
	Mixed Fungal Consortium (MIX)	Poultry Sludge	Increased biogas yield by 20% and methane yield by 28% compared to the control batch	(Wrońska and Cybulska, 2018:395)
	Microbial Consortium (multiple species)	Corn Straw	Enhanced biomethane yield by over 96.6%	(Govarthanan et al., 2022)

Consortia are frequently considered more suitable for LCB degradation compared to single strains, as they exhibit advantages such as increased adaptability to changing environmental conditions, better consumption of complex substrates, and enhanced microbial diversity related to metabolic functions (Govarthanan et al., 2022; Tuesorn et al., 2013:579).

ECONOMIC AND ENVIRONMENTAL CONSIDERATIONS

Fungal pretreatment offers a sustainable balance between cost and environmental impact, primarily by requiring low operating inputs, although it faces constraints regarding speed and material throughput. Fungal methods are generally considered eco-friendly (Govarthanan et al., 2022). Fungal pretreatment operates under mild conditions with low energy demands, avoiding the high temperatures and pressures common in physicochemical methods (Alexandropoulou et al., 2017:704; Taherzadeh & Karimi, 2008]. Unlike chemical methods, fungal pretreatment does not release toxic compounds or inhibitory byproducts that could negatively affect downstream microbial processes (fermentation or AD) (Alexandropoulou et al., 2017:704; Rouches et al., 2016:1784; Taherzadeh and Karimi, 2008:1621).

Fungal pretreatment offers cost advantages but is hindered by kinetic limitations. The method is generally classified as a less expensive pretreatment option (Shah and Ullah, 2019:7497; Rouches et al., 2016:1784). SSF requires fewer resources, such as water, heating, mixing, and aeration (Rouches et al., 2016:1784). It avoids the substantial expense associated with procuring and extracting purified exogenous enzymes because the fungi secrete the necessary ligninolytic enzymes directly onto the substrate during growth. Limiting the input of rich starter solutions (glucose and nitrogen) maximizes the efficiency of delignification, leading to substantial metanogenesis improvements (up to 21% methane increase) and subsequently reduces operational costs (Rouches et al., 2016:1784). The primary constraint limiting commercial feasibility is the prolonged treatment time required, often spanning at least one to several weeks, for sufficient biomass modification (Alexandropoulou et al., 2017:704; Rouches et al., 2016:1784; Taherzadeh and Karimi, 2008:1621; Paritosh et al., 2021). Fungal growth can lead to unintentional carbohydrate consumption (holocellulose loss), resulting in dry mass loss of the substrate, which can diminish the net methane yield, as observed with *L. menziesii* treatment of willow sawdust (Alexandropoulou et al., 2017:704; Rouches et al., 2016:1784).

FUNGAL PRETREATMENT AS A PROMISING TECHNIQUE TO INCREASE BIOGAS PRODUCTION

Fungal pretreatment, particularly through the use of White-Rot Fungi (WRF), stands as a highly attractive and environmentally sustainable strategy for valorizing lignocellulosic biomass (LCB) into renewable energy sources like methane (Govarthanan et al., 2022; Alexandropoulou et al., 2017:704; Rouches et al., 2016:1784). This method distinguishes itself from conventional chemical and physicochemical pretreatments by operating under mild conditions with low energy demands and without generating toxic compounds that inhibit microbial activity during subsequent anaerobic digestion (AD) (Alexandropoulou et al., 2017:704; Taherzadeh and Karimi, 2008:1621).

The primary success of fungal pretreatment lies in its selective delignification capacity, wherein the lignin barrier is efficiently broken down while preserving the essential carbohydrate polymers (cellulose and hemicellulose) for methanogenic conversion (Alexandropoulou et al., 2017:704; Rouches et al., 2016:1784; Taherzadeh and Karimi, 2008:1621). This selectivity results in substantial improvements in biomethane potential (BMP). For instance, fungal cultures combined with secondary alkaline treatment on willow sawdust yielded a maximum BMP increase of 115% compared to untreated material (Alexandropoulou et al., 2017:704). Moreover, high-performing fungal treatments alone have been shown to increase biogas yields by up to fivefold when applied to wheat straw (Shah and Ullah, 2019:7497). Even when accounting for mass loss due to fungal consumption of substrate, certain strains (*Polyporus brumalis* BRFM 985) demonstrated a net increase of up to 21% in methane per gram of initial total solids, underscoring the promising economic feasibility of this biological route (Rouches et al., 2016:1784). Therefore, fungal pretreatment represents a significant advancement in achieving higher substrate digestibility and maximizing methane production from agricultural and industrial waste feedstocks (Shah and Ullah, 2019:7497).

Future Research Needs

Despite the inherent environmental and selective advantages of fungal pretreatment, its widespread commercial application is currently hindered by several critical limitations, primarily the prolonged treatment duration required, which can span several weeks (Alexandropoulou et al., 2017:704; Rouches et al., 2016:1784; Taherzadeh and Karimi, 2008:1621]. Future research must focus intensely on optimizing operational parameters and increasing cost-effectiveness to bridge the gap between laboratory success and industrial scalability.

Key areas for future investigation include:

1. Optimization of Process Kinetics and Duration: Efforts are needed to significantly shorten the required pretreatment time while maintaining, or enhancing, delignification efficiency, potentially by combining the process with material storage periods to mitigate time constraints (Rouches et al., 2016:1784; Taherzadeh and Karimi, 2008:1621). Research should compare the efficacy of different incubation times to determine the optimum conditions for diverse fungal species and feedstocks (Alexandropoulou et al., 2017:704).
2. Strain Selection and Metabolic Control: Further refinement of microbial culture technology is necessary, focusing on selecting strains with high lignolytic activity and extremely low holocellulose uptake efficiency to minimize dry mass loss that compromises net methane yield (Govarthanan et al., 2022; Alexandropoulou et al., 2017:704; Rouches et al., 2016:1784).
3. Nutrient Management for Cost-Effectiveness: Optimization studies must rigorously quantify and limit the addition of external nutrient sources (like glucose and nitrogen) in starter solutions. Since high nutrient levels inhibit lignin-degrading secondary metabolism and delignification, identifying the minimal effective nutrient input is crucial for simultaneously maximizing methane yield and reducing operational costs (Rouches et al., 2016:1784).
4. Integration with Combined Pretreatment Methods: Further exploration into hybrid strategies, such as combining fungal pretreatment with mild alkaline or other non-inhibitory physical methods, is warranted to replicate and improve upon synergistic effects that have already demonstrated maximum BMP increases (Alexandropoulou et al., 2017:704).

Ultimately, successful optimization across these parameters will solidify fungal pretreatment as a viable, low-cost, and high-efficiency core technology for the sustainable production of biogas (Shah and Ullah, 2019: 7497).

CONCLUSION

Fungal pretreatment, especially through the application of white-rot fungi, represents a promising biological strategy for improving biogas production from lignocellulosic biomass by enhancing substrate accessibility and biomethane potential. Compared to conventional chemical and physicochemical pretreatments, this approach offers clear advantages in terms of environmental sustainability, low energy requirements, and the absence of inhibitory by-products affecting anaerobic digestion. The selective delignification capacity of fungal systems allows for improved

methane yields while preserving fermentable carbohydrates, as demonstrated across various feedstocks and fungal strains. Nevertheless, challenges related to long pretreatment durations, substrate mass losses, and nutrient input costs currently limit large-scale implementation. Overall, existing evidence indicates that targeted optimization of process parameters, strain selection, and integration with mild complementary pretreatment methods could significantly improve the techno-economic feasibility of fungal pretreatment, supporting its potential role in sustainable biogas production and waste valorization.

REFERENCES

Alexandropoulou, M., Antonopoulou, G., Fragkou, E., Ntaikou, I., & Lyberatos, G. (2017). Fungal pretreatment of willow sawdust and its combination with alkaline treatment for enhancing biogas production. Journal of Environmental Management, 203, 704–713. http://dx.doi.org/10.1016/j.jenvman.2016.04.006

Amirta, R., Tanabe, T., Watanabe, T., Honda, Y., Kuwahara, M., & Watanabe, T. (2006). Methane fermentation of Japanese cedar wood pretreated with a white rot fungus, Ceriporiopsis subvermispora. Journal of Biotechnology, 123(1), 71–77. https://doi.org/10.1016/j.jbiotec.2005.10.004

Aryal, N., Kvist, T., Ammam, F., Pant, D., & Ottosen, L. D. M. (2018). An overview of microbial biogas enrichment. Bioresource Technology, 264, 359–369. https://doi.org/10.1016/j.biortech.2018.06.013

Aza, P., & Camarero, S. (2023). Fungal Laccases: Fundamentals, Engineering and Classification Update. In *Biomolecules* (Vol. 13, Issue 12). Multidisciplinary Digital Publishing Institute (MDPI). https://doi.org/10.3390/biom13121716

Chowdhary, P., Shukla, G., Raj, G., Ferreira, L. F. R., & Bharagava, R. N. (2019). Microbial manganese peroxidase: a ligninolytic enzyme and its ample opportunities in research. In *SN Applied Sciences* (Vol. 1, Issue 1). Springer Nature. https://doi.org/10.1007/s42452-018-0046-3

Das, A., Das, S., Das, N., Pandey, P., Ingti, B., Panchenko, V., Bolshev, V., Kovalev, A., & Pandey, P. (2023). Advancements and Innovations in Harnessing Microbial Processes for Enhanced Biogas Production from Waste Materials. Agriculture, 13(9), 1689. https://doi.org/10.3390/agriculture13091689

Dashora, K., Gattupalli, M., Tripathi, G. D., Javed, Z., Singh, S., Tuohy, M., Sarangi, P. K., Diwan, D., Singh, H. B., & Gupta, V. K. (2023). Fungal Assisted Valorisation of Polymeric Lignin: Mechanism, Enzymes and Perspectives. In *Catalysts* (Vol. 13, Issue 1). MDPI. https://doi.org/10.3390/catal13010149

Falade, A. O., Nwodo, U. U., Iweriebor, B. C., Green, E., Mabinya, L. V., & Okoh, A. I. (2017). Lignin peroxidase functionalities and prospective applications. In MicrobiologyOpen (Vol. 6, Issue 1). Blackwell Publishing Ltd. https://doi.org/10.1002/mbo3.394

Govarthanan, M., Manikandan, S., Subbaiya, R., Krishnan, R. Y., Srinivasan, S., Karmegam, N., & Kim, W. (2022). Emerging trends and nanotechnology advances for sustainable biogas production from lignocellulosic waste biomass: A critical review. Fuel, 312, 122928. https://doi.org/10.1016/j.fuel.2021.122928

Jameel, M. K., Mustafa, M. A., Ahmed, H. S., Mohammed, A. J., Ghazy, H., Shakir, M. N., Lawas, A. M., Mohammed, S. K., Idan, A. H., Mahmoud, Z. H., Sayadi, H., & Kianfar, E. (2024). Biogas: Production, properties, applications, economic and challenges: A review. Results in Chemistry, 7, 101549. https://doi.org/10.1016/j.rechem.2024.101549

Janusz, G., Pawlik, A., Sulej, J., Świderska-Burek, U., Jarosz-Wilkolazka, A., & Paszczyński, A. (2017). Lignin degradation: Microorganisms, enzymes involved, genomes analysis and evolution. In FEMS Microbiology Reviews (Vol. 41, Issue 6, pp. 941–962). Oxford University Press. https://doi.org/10.1093/femsre/fux049

Kumar, A., & Chandra, R. (2020). Ligninolytic enzymes and its mechanisms for degradation of lignocellulosic waste in environment. In Heliyon (Vol. 6, Issue 2). Elsevier Ltd. https://doi.org/10.1016/j.heliyon.2020.e03170

Kumar, V. P., Sridhar, M., & Rao, R. G. (2022). Biological depolymerization of lignin using laccase harvested from the autochthonous fungus Schizophyllum commune employing various production methods and its efficacy in augmenting in vitro digestibility in ruminants. Scientific Reports, 12(1). https://doi.org/10.1038/s41598-022-15211-9

Majeke, B. M., Collard, F. X., Tyhoda, L., & Görgens, J. F. (2021). The synergistic application of quinone reductase and lignin peroxidase for the deconstruction of industrial (technical) lignins and analysis of the degraded lignin products. Bioresource Technology, 319. https://doi.org/10.1016/j.biortech.2020.124152

Nadir, N., Liyana Ismail, N., & Shah Hussain, A. (2019). Fungal Pretreatment of Lignocellulosic Materials. In Biomass for Bioenergy - Recent Trends and Future Challenges. IntechOpen. https://doi.org/10.5772/intechopen.84239

Ozbayram, E. G., Kleinsteuber, S., & Nikolausz, M. (2020). Biotechnological utilization of animal gut microbiota for valorization of lignocellulosic biomass. Applied Microbiology and Biotechnology, 104, 489–508. https://doi.org/10.1007/s00253-019-10239-w

Rivera-Hoyos, C. M., Morales-Álvarez, E. D., Poutou-Piñales, R. A., Pedroza-Rodríguez, A. M., RodrÍguez-Vázquez, R., & Delgado-Boada, J. M. (2013). Fungal laccases. In Fungal Biology Reviews (Vol. 27, Issues 3–4, pp. 67–82). https://doi.org/10.1016/j.fbr.2013.07.001

Rouches, A., Zhou, S., Steyer, J. P., & Carrere, H. (2016). White-Rot Fungi pretreatment of lignocellulosic biomass for anaerobic digestion: Impact of glucose supplementation. Process Biochemistry, 51(11), 1784–1792.

Shah, T. A., Ullah, R. (2019). Pretreatment of wheat straw with ligninolytic fungi for increased biogas productivity. International Journal of Environmental Science and Technology (Tehran), 16(11), 7497–7508.

Shi, K., Liu, Y., Chen, P., & Li, Y. (2021). Contribution of Lignin Peroxidase, Manganese Peroxidase, and Laccase in Lignite Degradation by Mixed White-Rot Fungi. Waste and Biomass Valorization, 12(7), 3753–3763. https://doi.org/10.1007/s12649-020-01275-z

Sigoillot, J. C., Berrin, J. G., Bey, M., Lesage-Meessen, L., Levasseur, A., Lomascolo, A., Record, E., & Uzan-Boukhris, E. (2012). Fungal Strategies for Lignin Degradation. In Advances in Botanical Research (Vol. 61, pp. 263–308). Academic Press Inc. https://doi.org/10.1016/B978-0-12-416023-1.00008-2

Taherzadeh, M. J., & Karimi, K. (2008). Pretreatment of Lignocellulosic Wastes to Improve Ethanol and Biogas Production: A Review. International Journal of Molecular Sciences, 9(9), 1621–1651. https://doi.org/10.3390/ijms9091621

Tuesorn, S., Wongwilaiwalin, S., Champreda, V., Leethochawalit, M., Nopharatana, A., Techkarnjanaruk, S., & Chaiprasert, P. (2013). Enhancement of biogas production from swine manure by a lignocellulolytic microbial consortium. Bioresource Technology, 144, 579–586. http://dx.doi.org/10.1016/j.biortech.2013.07.013

Wan, C., & Li, Y. (2012). Fungal pretreatment of lignocellulosic biomass. In Biotechnology Advances (Vol. 30, Issue 6, pp. 1447–1457). https://doi.org/10.1016/j.biotechadv.2012.03.003

Wrońska, I., Cybulska, K. (2018). Quantity and quality of biogas produced from the poultry sludge optimized by filamentous fungi. Ecological Chemistry and Engineering S, 25(3), 395–404. https://doi.org/10.1515/eces-2018-0027

Yang, X., Gu, C., & Lin, Y. (2020). A novel fungal laccase from Sordaria macrospora k-hell: expression, characterization, and application for lignin degradation. Bioprocess and Biosystems Engineering, 43(7), 1133–1139. https://doi.org/10.1007/s00449-020-02309-5

Computational Investigations, Molecular Docking, and ADME Analysis of Naphthylene-Based Hydrazide

Sevgi KANSIZ[1]

1- Asst. Prof.; Samsun University, Faculty of Engineering and Natural Sciences, Department of Fundamental Sciences. sevgi.kansiz@samsun.edu.tr ORCID No: 0000-0002-8433-7975.

ABSTRACT

Naphthalene and hydrazide-based structures are widely explored in medicinal chemistry owing to their aromatic frameworks and favorable interaction potential with biological macromolecules. These features render hydrazone-linked systems promising candidates for in silico drug discovery. Accordingly, the present study focuses on the naphthalene-based hydrazide compound $C_{20}H_{20}N_3O_2$, aiming to elucidate its electronic structure, molecular reactivity, binding affinity, and pharmacokinetic behavior through computational approaches. Density functional theory calculations were employed to investigate the molecular electrostatic potential (MEP) and frontier molecular orbitals (FMOs). The MEP map identified the carbonyl oxygen and hydrazone N–NH group as the primary reactive sites, indicating their potential involvement in ligand–receptor interactions. FMO analysis revealed a moderate HOMO–LUMO gap for the α-spin state, reflecting structural stability, while the β-spin channel exhibited a smaller energy gap, lower hardness, and higher electronegativity, suggesting enhanced chemical reactivity. Molecular docking simulations against antifungal protein (4DRH) showed a favorable binding affinity of –7.209 kcal/mol, stabilized by hydrogen bonding and multiple π-based non-covalent interactions with key amino acid residues. Additionally, SwissADME analysis was conducted to investigate the pharmacokinetic behavior and drug-likeness of the compound, with a focus on absorption, distribution, and key medicinal chemistry parameters. RADAR and BOILED-Egg models were utilized to provide an integrated overview of its physicochemical balance and potential oral bioavailability.

Keywords – Naphthalene, Hydrazide, Molecular Docking, Drug-Likeness, DFT, MEP.

INTRODUCTION

Naphthalene-based scaffolds constitute one of the most versatile classes of polycyclic aromatic systems and have attracted considerable attention due to their broad applications in medicine, materials, and coordination chemistry (Oshi et al., 2017; Jyothi et al., 2024). Structural modifications on the naphthalene ring, particularly through methoxy or alkoxy substitutions, can significantly influence the electronic distribution and conformational preferences of the aromatic core. Such substituents often enhance π–electron delocalization, modulate dipole moments, and improve lipophilicity, features that are crucial for biological membrane permeability and molecular recognition. Methoxynaphthylidene derivatives (Sherif et al., 2021; Liu et al., 2012, Zhou et al., 2009), in particular, have been widely investigated for their photophysical properties, electron-donating behavior, and ability to participate in donor–acceptor interactions, making them attractive building blocks for the design of bioactive and functional organic molecules.

Hydrazones and hydrazide derivatives represent an important class of Schiff base compounds, recognized for their rich coordination chemistry, structural diversity, and broad spectrum of pharmacological activities (Taha et al., 2015; Kansız, 2023; Verma et al., 2014). The presence of the –C(=O)–NH–NH–C=N– linkage confers both nucleophilic and electrophilic sites, enabling these molecules to interact with biological macromolecules through hydrogen bonding, electrostatic interactions, and metal chelation. Numerous studies have highlighted the antimicrobial, anticancer, antioxidant, and enzyme-inhibitory potential of hydrazone and benzohydrazide frameworks, which are often attributed to their tunable electronic properties and ability to adopt multiple tautomeric forms (Korkmaz et al., 2022; Dietl et al., 2015; Murugappan et al., 2024; Kucukoglu et al., 2019). In this context, $C_{20}H_{20}N_3O_2$, containing both an electron-rich naphthalene moiety and a dimethylamino-substituted benzohydrazide fragment, represents a promising candidate for computational studies involving DFT-based electronic structure analysis, molecular docking, and ADME prediction to assess its structural stability and potential biological relevance.

Materials and Method

Density Functional Theory (DFT) calculations were performed using the Gaussian 09W software package (Frisch et al., 2009), and the molecu-lar structures were visualized with GaussView 6.0 (Dennington et al., 2016). Geometry optimization and electronic structure analyses were carried out at the B3LYP/6-31+G(d,p) level of theory (Becke, 1993), which offers a suitable compromise between computational efficiency and accuracy. The optimized structure was subsequently used to evaluate the frontier molecular orbitals (HOMO–LUMO energies) and to generate the Molecular Electrostatic Potential (MEP) map, providing insight into the electrophilic and nucleophilic regions of the molecule. Molecular docking studies for the compound $C_{20}H_{20}N_3O_2$ (Figure 1) were conducted using AutoDock Vina (Trott et al., 2010). Prior to docking, the DFT-optimized structure was converted into PDB and PDBQT formats using Discovery Studio Visualizer 4.0 (https://www.3dsbiovia.com/). The target antifungal protein (März et al., 2013) (PDB ID: 4DRH) was obtained from the RCSB Protein Data Bank (https://www.rcsb.org/), prepared by removing water molecules, adding polar hydrogens, and assigning Kollman charges. In addition, physicochemical descriptors, pharmacokinetic parameters, and drug-likeness properties of the ligand were predicted using the SwissADME online platform (Daina et al., 2017).

RESULTS AND DISCUSSION

Optimization

The optimized geometric parameters of $C_{20}H_{20}N_3O_2$ were obtained at the DFT/B3LYP level, and selected bond lengths and bond angles are summarized in Table 1. The C11–N22 bond length of 1.32 Å is characteristic of a C=N imine linkage, confirming the presence of significant π-electron delocalization along the hydrazone backbone. This observation is further supported by the N22–N23 bond length of 1.41 Å, which lies between typical single and double N–N bonds, indicating partial conjugation within the –C=N–NH– moiety. The C25–N23 bond length (1.40 Å) also reflects partial double-bond character, suggesting effective electron delocalization between the hydrazide nitrogen and the adjacent aromatic system. The C25–O26 bond length of 1.37 Å is shorter than a typical C–O single bond, implying resonance stabilization and conjugation involving the carbonyl oxygen. Additionally, the C14–O21 (1.50 Å) and C17–O21 (1.51 Å) distances are consistent with ether-type C–O single bonds, confirming the integrity of the methoxy substituent. The C–C distances within the aromatic moieties are close to the typical mean value observed for aromatic systems (approximately 1.39 Å). In contrast, variations observed in specific bond lengths and bond angles within the hydrazone/acetyl segment and adjacent linker atoms reflect an extended π-electron delocalization, giving rise to partial double-bond character along the C–N and N–N connectivity. These structural features are consistent with previously reported conjugated hydrazone frameworks (Ilmi et al., 2025; Sert et al., 2014; Gumus et al., 2021; Kansız et al., 2025). Moreover, the aromatic bond parameters show close agreement with literature data for related systems (Chkirate et al., 2019; Ilmi et al., 2023; Gümüş et al., 2025; Cakmak et al., 2022; Gümüş et al., 2022). Bond angle values around the hydrazone core, such as C11–N22–N23 (115°) and C25–N23–N22 (111°), indicate a near-planar arrangement, which facilitates π-conjugation across the molecule. The angles associated with the dimethylamino group (C34–N37–C38 = 109°, C34–N37–C42 = 110°) correspond to a typical sp^3-hybridized nitrogen environment, suggesting localized electron density in this region. The optimized structural parameters confirm a stable, conjugated molecular framework, which is favorable for electronic delocalization and may contribute to the compound's observed chemical reactivity and biological potential.

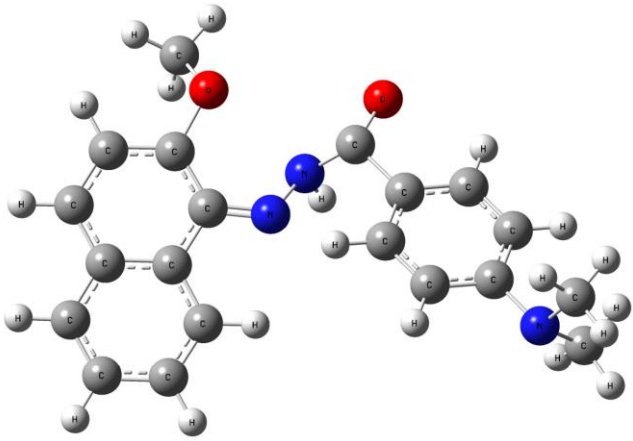

Figure 1: The optimized structure of $C_{20}H_{20}N_3O_2$.

Table 1: Selected bond lengths of $C_{20}H_{20}N_3O_2$.

Bond length	Distance, Å	Bond angle	Value, deg
C11–N22	1.32	C11–N22–N23	115
C25–N23	1.40	C25–N23–N22	111
C34–N37	1.47	C27–C25–N23	114
C38–N37	1.47	C27–C25–O26	112
C42–N37	1.47	N23–C25–O26	110
N22–N23	1.41	C14–O21–C17	110
C25–O26	1.37	C34–N37–C38	109
C14–O21	1.50	C34–N37–C42	110
C17–O21	1.51	C38–N37–C42	109
C25–C27	1.54	C1–C2–C3	120

MEP surface analysis

The intense red region at the carbonyl oxygen identifies it as the most electron-rich site (Al-thamili et al., 2020; Arumugam et al., 2021; Kargar et al., 2025) in the molecule and thus the strongest hydrogen-bond acceptor (Figure 2). This atom is the primary locus for interaction with hydrogen-bond donors on a protein or solvent (for example, backbone NH or side-chain donors). In docking studies, carbonyl O would be expected to form the most favorable and directional hydrogen bonds. The methoxy O showing a shift from yellow to orange indicates a moderately negative potential, it is electron-rich but to a lesser extent than the carbonyl oxygen. Methoxy oxygen can act as a secondary hydrogen-bond acceptor or participate in polar interactions; however, its acceptor strength is weaker than that of the carbonyl O, likely because of electron delocalization into the aromatic system and steric environment.

The yellow coloration over the naphthalene's first aromatic ring indicates a slightly electron-rich π-cloud. Such modest negative potential on

the aromatic face suggests that the naphthyl moiety can engage in π–π stacking, π–cation interactions, or weak polar contacts with electron-deficient protein residues or cofactors. It is unlikely to be a primary hydrogen-bonding site but may contribute to hydrophobic and π-stacking stabilization in the binding pocket. The yellow potential over the benzohydrazide ring and the adjacent nitrogen atom suggests a moderate electron density localized on this aromatic fragment and on the ring-linked N. The presence of the 4-dimethylamino substituent (strongly electron-donating) likely increases electron density on the benzene ring and the adjacent nitrogen, enhancing the ring's nucleophilicity and favoring interactions with electrophilic or polar residues in a receptor. The blue coloration on hydrogen atoms indicates positive electrostatic potential; the particularly pronounced blue at the hydrazide N–NH hydrogen signals it as a strong hydrogen-bond donor. This N–H is therefore a likely site to form directional hydrogen bonds to acceptor atoms in protein active sites (e.g., carbonyl oxygens, carboxylate oxygens, or backbone carbonyls). In docking, this hydrogen often drives specific interactions and can increase binding affinity when complementary acceptors are available.

Taken together, the MEP pattern identifies a classic donor–acceptor pairing within the molecule: a strongly electron-rich carbonyl oxygen (primary acceptor) and a strongly electron-poor N–H (primary donor). These complementary sites make the compound well suited to form hydrogen bonds with biological receptors. Secondary acceptor sites (methoxy O and aromatic π-clouds) and electron-rich aromatic rings (naphthyl and dimethylamino-substituted benzene) can provide additional stabilizing contacts such as π–π stacking, π–cation interactions, and weaker polar contacts. Consequently, in docking studies one should expect the carbonyl O and the N–NH hydrogen to be key players in ligand–receptor hydrogen bonding, with the aromatic surfaces contributing to van der Waals and π-interaction energy terms.

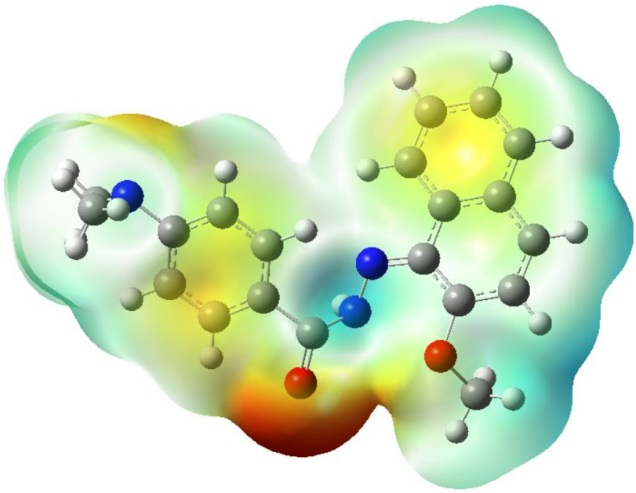

Figure 2: MEP surface of $C_{20}H_{20}N_3O_2$.

Frontier molecular orbitals analysis (FMOs)

FMOs, particularly the highest occupied molecular orbital (HOMO) and the lowest unoccupied molecular orbital (LUMO), play a crucial role in determining the electronic properties, reactivity, and charge-transfer behavior of organic molecules (Sert et al., 2014; Kansiz, 2023). The energy difference between these orbitals, known as the HOMO–LUMO energy gap, is directly related to the molecule's chemical stability, softness, and excitation characteristics. A smaller gap generally indicates higher polarizability and reactivity, whereas a larger gap suggests electronic stability. For the compound $C_{20}H_{20}N_3O_2$, the spatial distribution of the frontier orbitals is illustrated in Figure 3, while the corresponding energetic parameters are summarized in Table 2. The α-spin channel exhibits a HOMO energy of –7.6366 eV and a LUMO energy of –6.0260 eV, yielding a HOMO–LUMO gap of 1.61 eV. This moderate gap indicates a balanced combination of stability and chemical activity. In contrast, the β-spin orbitals display a HOMO at –8.3860 eV and a LUMO at –7.6366 eV, resulting in a significantly smaller energy gap of 0.75 eV. The reduced β-gap suggests that the β-spin electrons require less energy for excitation, implying enhanced reactivity in this spin channel. Global reactivity descriptors derived from these energies (Table 2) further support this interpretation. The β-spin state exhibits higher electronegativity (χ = 8.01 eV) and lower hardness (η = 0.37 eV) compared to the α-spin state (χ = 6.83 eV; η = 0.81 eV). This indicates that the β-spin channel is softer and more chemically responsive, consistent with its smaller HOMO–LUMO gap. Conversely, the α-spin state shows greater hardness and a lower degree of electronic polarizability, reflecting higher stability. The FMO analysis demonstrates that $C_{20}H_{20}N_3O_2$ possesses distinct electronic characteristics across its spin manifolds, with the β-spin

configuration contributing more prominently to the molecule's potential reactivity and electron-transfer behavior.

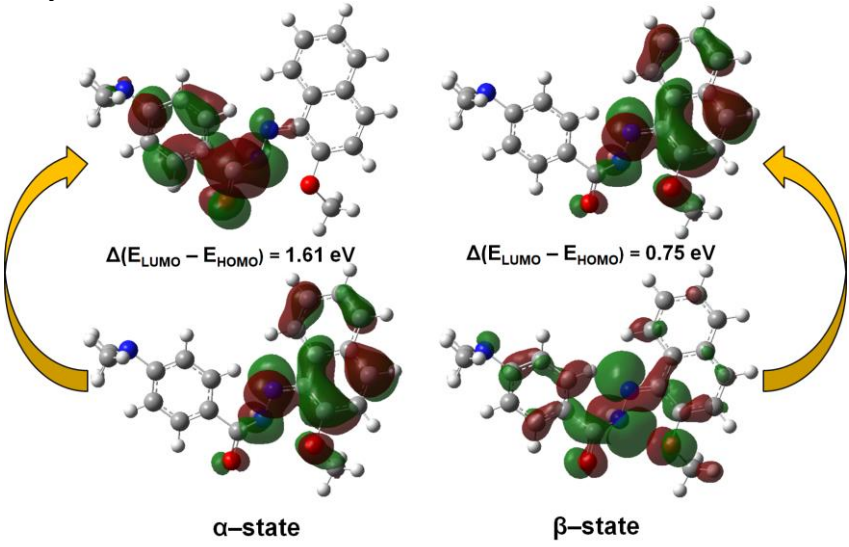

Figure 3: HOMO-LUMO surface of $C_{20}H_{20}N_3O_2$.

Table 2: The energy values of the global reactivity parameters of $C_{20}H_{20}N_3O_2$.

Parameters	α–state values	β–state values
EHOMO (eV)	–7.64	–8.39
ELUMO (eV)	–6.03	–7.64
Energy gap (eV)	1.61	0.75
Ionization potential, $I = -E_{HOMO}$ (eV)	7.64	8.39
Electron affinity, $A = -E_{LUMO}$ (eV)	6.03	7.64
Electronegativity, $\chi = (I + A)/2$ (eV)	6.83	8.01
Hardness, $\eta = (I - A)/2$ (eV)	0.81	0.37
Softness, $S = 1/(2\eta)$ (eV^{-1})	0.62	1.33

Molecular docking analysis

Molecular docking is a widely used computational technique that predicts the preferred orientation, binding mode, and affinity of a ligand when interacting with a biological macromolecule (Bouzian et al., 2021; Eltayeb et al., 2020; OmarAli et al., 2023). By estimating the free energy of binding, docking simulations help identify key non-covalent interactions and assess the potential biological activity of a compound. This method is especially valuable in drug discovery, where understanding ligand–receptor compatibility is essential for designing effective therapeutic candidates. In the present study, the molecular docking of $C_{20}H_{20}N_3O_2$ was performed using AutoDock Vina to investigate its interaction with the target protein (PDB ID: 3ERT). Before docking, the ligand geometry was optimized at the DFT/B3LYP/6-31G(d,p) level using Gaussian 09W to ensure an

energetically stable input structure. The docking grid was centered at x = 14.833, y = 9.444, and z = 8.528, with grid dimensions of 40 × 40 × 40 Å³ and a spacing of 0.375 Å, which provided complete coverage of the active binding region. The docking simulation produced a binding affinity of –7.209 kcal/mol, suggesting a favorable and stable ligand–receptor interaction within the tubulin A binding pocket (Fig. 4 and Table 3). The corresponding interaction profiles (Fig. 5) revealed a diverse array of stabilizing non-covalent contacts, including π–π stacking, π–σ, π–alkyl interactions, and hydrogen bonding. These interactions collectively reinforce the stable accommodation of the ligand inside the active site. A detailed residue-level analysis showed that the ligand interacts with several key amino acids, including GLU323, LEU320, and PRO324. Notably, a single hydrogen bond is established with LEU320, which contributes to the specificity and stability of the binding pose. The combination of aromatic interactions and hydrogen bonding underscores the compound's potential for meaningful biological activity against the antifungal target.

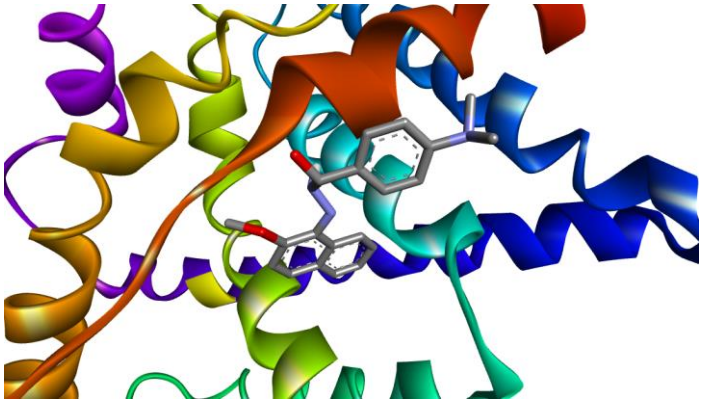

Figure 4: Showing 3D molecular docking results of the ligand+PDB:3ERT.

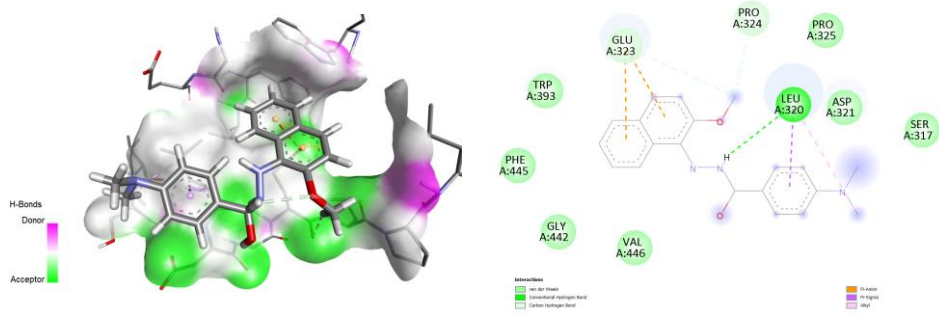

(a) (b)

Figure 5: (a) Showing hydrogen bonds, and (b) 2D molecular docking results of the ligand+PDB:3ERT.

Table 3. The binding affinity and RMSD values.

Mode	Affinity (kcal/mol)	rmsd l.b.	rmsd u.b.
1	-7.209	0.000	0.000
2	-6.823	13.91	16.5
3	-6.720	20.79	22.55
4	-6.717	15.33	16.89
5	-6.523	12.21	14.43
6	-6.440	26.29	28.07
7	-6.428	23.92	25.18
8	-6.379	31.89	33.21
9	-6.349	22.81	25.78

ADME analysis

The SwissADME results (Table 4) indicate that the $C_{20}H_{20}N_3O_2$ compound possesses favorable physicochemical and pharmacokinetic characteristics. The molecular weight (334.40 g/mol), moderate lipophilicity (consensus LogP = 2.80), and relatively low TPSA value (53.93 Å²) suggest good membrane permeability. The compound exhibits high gastrointestinal absorption and satisfies all major drug-likeness filters, including Lipinski, Ghose, Veber, Egan, and Muegge criteria, with no rule violations. Water solubility predictions classify the molecule as moderately soluble to soluble, supporting its suitability for oral administration. In terms of metabolism, the compound is predicted to inhibit CYP2C19, CYP2C9, and CYP3A4 isoenzymes, which should be considered in further pharmacokinetic and drug–drug interaction studies. The absence of PAINS alerts and a reasonable synthetic accessibility score (4.28) further support its potential as a drug-like candidate.

The RADAR plot (Figure 6) provides a visual overview of six key drug-likeness parameters: lipophilicity, size, polarity, solubility, saturation, and molecular flexibility. The red polygon corresponding to the compound largely falls within the optimal pink region, indicating a balanced profile compatible with oral bioavailability. Slight deviations are observed in flexibility and saturation, reflecting the presence of aromatic rings and conjugated systems; however, these features are common in bioactive hydrazone derivatives and do not significantly compromise the overall drug-likeness. Overall, the RADAR analysis confirms that the compound exhibits a well-balanced physicochemical profile.

The BOILED-Egg diagram (Figure 6) shows that the compound is located within the yellow yolk region, indicating a strong likelihood of blood–brain barrier (BBB) permeation, in addition to high human intestinal absorption (HIA). The compound is predicted as P-gp non-substrate (PGP−), suggesting it is not actively effluxed by P-glycoprotein, which favors sustained intracellular concentration and effective distribution. This profile implies that the compound may have potential for central nervous system (CNS) activity, while still maintaining good oral absorption characteristics.

Table 4. ADME analysis results.

Physicochemical Properties		**Lipophilicity**	
Formula	$C_{20}H_{20}N_3O_2$	Log Po/w (iLOGP)	2.82
Molecular weight	334.40 g/mol	Log Po/w (XLOGP3)	3.69
Num. heavy atoms	25	Log Po/w (WLOGP)	3.05
Num. arom. heavy atoms	6	Log Po/w (MLOGP)	2.43
Fraction Csp3	0.20	Log Po/w (SILICOS-IT)	1.99
Num. rotatable bonds	5	Consensus Log Po/w	2.80
Num. H-bond acceptors	3	**Water Solubility**	
Num. H-bond donors	1	Log S (ESOL)	-4.09
Molar Refractivity	100.36	Solubility	2.72e-02 mg/ml; 8.10e-05 mol/l
TPSA	53.93 Å²	Class	Moderately soluble
Pharmacokinetics		Log S (Ali)	-4.51
GI absorption	High	Solubility	1.03e-02 mg/ml; 3.07e-05 mol/l
BBB permeant	Yes	Class	Moderately soluble
P-gp substrate	No	Log S (SILICOS-IT)	-3.75
CYP1A2 inhibitor	No	Solubility	5.95e-02 mg/ml; 1.77e-04 mol/l
CYP2C19 inhibitor	Yes	Class	Soluble
CYP2C9 inhibitor	Yes	**Druglikeness**	
CYP2D6 inhibitor	No	Lipinski	Yes; 0 violation
CYP3A4 inhibitor	Yes	Ghose	Yes
Log Kp (skin permeation)	-5.73 cm/s	Veber	Yes
Medicinal Chemistry		Egan	Yes
PAINS	0 alert	Muegge	Yes
Brenk	1 alert: imine_1	Bioavailability Score	0.55
Leadlikeness	No; 1 violation: XLOGP3>3.5		
Synthetic accessibility	4.28		

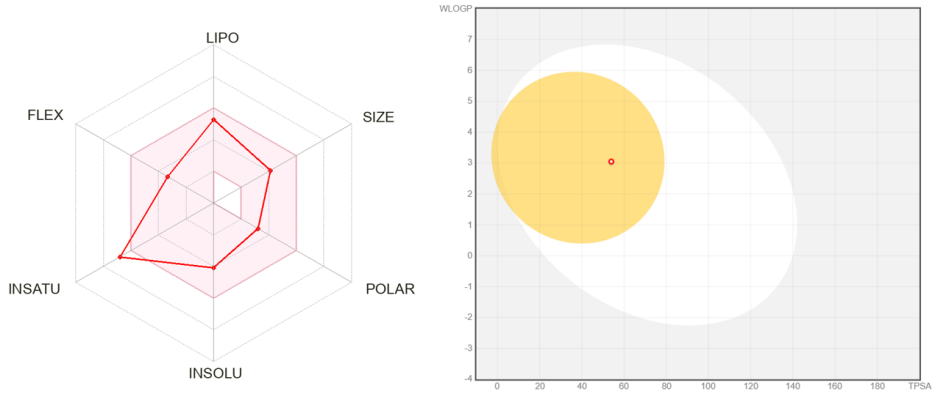

Figure 6: (a) The bioavailability radar, (b) and boiled egg model

CONCLUSION

In this study, a comprehensive theoretical investigation of $C_{20}H_{20}N_3O_2$ was carried out using density functional theory, molecular docking simulations, and in silico ADME predictions. The MEP analysis revealed that the carbonyl oxygen and hydrazone N–NH moiety constitute the most electrophilic and nucleophilic regions of the molecule, highlighting their key role in intermolecular interactions and hydrogen bonding with biological targets. Frontier molecular orbital analysis demonstrated distinct electronic behaviors for the α- and β-spin channels. While the α-spin state exhibited higher hardness and stability, the β-spin channel showed a smaller HOMO–LUMO gap, lower hardness, and higher electronegativity, indicating enhanced chemical reactivity and electron-transfer capability. These findings suggest that the β-spin configuration contributes more significantly to the molecule's reactive character. Molecular docking studies against tubulin A revealed a favorable binding affinity (–7.209 kcal/mol), supported by a combination of π–π stacking, π–alkyl, π–σ interactions, and a stabilizing hydrogen bond with LEU320. The involvement of key residues such as GLU323, LEU320, and PRO324 confirms the stable accommodation of the ligand within the active site and suggests potential antifungal activity. Furthermore, SwissADME analysis indicated that the compound possesses a well-balanced physicochemical and pharmacokinetic profile, with high gastrointestinal absorption, BBB permeability, and compliance with all major drug-likeness rules. The RADAR and BOILED-Egg models further supported its oral bioavailability and favorable distribution properties.

Overall, the combined electronic, docking, and ADME results suggest that $C_{20}H_{20}N_3O_2$ represents a promising drug-like scaffold worthy of further experimental and biological evaluation.

REFERENCES

Al-thamili, D. M., Almansour, A. I., Arumugam, N., Kansız, S., Dege, N., Soliman, S. M., Azam, M., and Kumar, R. S. (2020). Highly functionalized N-1-(2-pyridinylmethyl)-3,5-bis[(E)-arylmethylidene]tetrahydro-4(1H)-pyridinones: Synthesis, characterization, crystal structure and DFT studies. *Journal of Molecular Structure*, *1222*, 128940.

Arumugam, N., Almansour, A. I., Kumar, R. S., Yeswanthkumar, S., Padmanaban, R., Arun, Y., Kansız, S., Dege, N., Manohar, T. S., and Venketesh, S. (2021). Design, stereoselective synthesis, computational studies and cholinesterase inhibitory activity of novel spiropyrrolidinoquinoxaline tethered indole hybrid heterocycle. *Journal of Molecular Structure*, *1225*, 129165.

Becke, A. D. (1993). Density-functional thermochemistry. III. The role of exact exchange. *The Journal of Chemical Physics, 98*(7), 5648–5652.

Bouzian, Y., Sert, Y., Khalid, K., Van Meervelt, L., Chkirate, K., Mahi, L., Ahabchane, N. H., Talbaoui, A., and Essassi, E. M. (2021). Synthesis, spectroscopic characterization, DFT, molecular docking and in vitro antibacterial potential of novel quinoline derivatives. *Journal of Molecular Structure*, *1246*, 131217.

Cakmak, S. Kansiz, S., Azam, M., Ersanlı, C. C., Idil, O., Veyisoglu, A., Yakan, H., Kütük, H., and Chutia, A. (2022). Synthesis, structural investigation, Hirshfeld surface analysis, and biological evaluation of N-(3-Cyanothiophen-2-yl)-2-(thiophen-2-yl) acetamide. *ACS omega*, *7*(13), 11320.

Chkirate, K., Kansiz, S., Karrouchi, K., Mague, J. T., Dege, N., and Essassi, E. M. (2019). Crystal structure and Hirshfeld surface analysis of N-{2-[(E)-(4-methylbenzylidene) amino] phenyl}-2-(5-methyl-1-H-pyrazol-3-yl) acetamide hemihydrate. *Acta Crystallographica Section E, Crystallographic Communications*, *75*(2), 154-158.

Daina, A., Michielin, O., and Zoete, V. (2017). SwissADME: A free web tool to evaluate pharmacokinetics, drug-likeness and medicinal chemistry friendliness of small molecules. *Scientific Reports*, *7*(1), 42717.

Dennington, R., Keith, T. A., and Millam, J. M. (2009). GaussView, Version 5. Semichem Inc., Shawnee Mission, KS.

Dietl, A., Ferousi, C., Maalcke, W. J., Menzel, A., de Vries, S., Keltjens, J. T., Jetten, M. S. M., Kartal, B., and Barends, T. R. (2015). The inner workings of the hydrazine synthase multiprotein complex. *Nature*, *527*(7578), 394–397.

Eltayeb, N. E., Şen, F., Lasri, J., Hussien, M. A., Elsilk, S. E., Babgi, B. A., Gökce, H., and Sert, Y. (2020). Hirshfeld surface analysis, spectroscopic, biological studies and molecular docking of (4E)-4-((naphthalen-2-yl)methyleneamino)-1,2-dihydro-2,3-dimethyl-1-phenylpyrazol-5-one. *Journal of Molecular Structure*, *1202*, 127315.

Frisch, M. J., Trucks, G. W., Schlegel, H. B., Scuseria, G. E., Robb, M. A., Cheeseman, J. R., Scalmani, G., Barone, V., Mennucci, B., and Petersson, G. A. (2009). Gaussian 09, Revision D.01. Gaussian, Inc., Wallingford, CT.

Gumus, M. K., Sen, F., Kansiz, S., Dege, N., and Saif, E. (2021). Crystal structure and Hirshfeld surface analysis of 2-{[(E)-(3-cyclobutyl-1H-1, 2, 4-triazol-5-yl) imino] methyl} phenol. *Acta Crystallographica Section E, Crystallographic Communications*, *77*(12), 1267-1271.

Gümüş, M. K., Kansiz, S., Tulemisova, G. B., Dege, N. and Saif, E. (2022). Crystal structure and Hirshfeld surface analysis of 3-(hydroxymethyl)-3-methyl-2, 6-diphenylpiperidin-4-one. *Acta Crystallographica Section E, Crystallographic Communications*, *78*(1), 29-32.

Gümüş, M. K., Kansız, S., Tulemisova, G. B., and Dege, N. (2025). Synthesis, Crystal Structure, and Hirshfeld Surface Analysis of 4, 4A, 5, 6, 7, 8-Hexahydro-4A-Methyl-2, 5, 7-Triphenyl-2 H-Pyrido [4, 3-d][1, 3] Oxazine. *Journal of Structural Chemistry*, *66*(1), 201-213.

https://www.3dsbiovia.com/.

https://www.rcsb.org/.

Ilmi, R., Kansız, S., Al Rasbi, N. K., Anjum, S., Van Deun, R., and Khan, M. S. (2025). Efficient 0.4–1.6 μm emission from muffin-shaped nine-coordinated ternary samarium(III) and erbium(III) complexes. *Dalton Transactions*, *54*, 10370–10380.

Ilmi, R., Kansız, S., Al Rasbi, N. K., Husband, J., Dege, N., and Khan, M. S. (2023). Synthesis, X-ray crystal structure and determination of non-covalent interactions through Hirshfeld surface analysis of a pure red emitting asymmetrical octacoordinated Sm (III) complex. *Polyhedron*, *246*, 116673.

Jyothi, M. S., Nagarajan, V., and Chandiramouli, R. (2024). Adsorption attributes of methyl naphthalene and naphthalene on P-Germanane sheets–a DFT outlook. *Structural Chemistry*, *35*(5), 1387-1397.

Kansız, S. (2023). Synthesis and Structural Investigations of 1, 2-bis (2-ethoxybenzylidene) hydrazine. *Sakarya University Journal of Science*, *27*(4), 768-780.

Kansız, S., Kaştaş, G., Gümüş, M. K., Dege, N., and Aydın, R. (2025). Synthesis, Structural Characterization, and Supramolecular Assembly of a One-Dimensional Cobalt (II) Coordination Polymer with Succinato and Isonicotinamide Ligands. *Journal of Structural Chemistry*, *66*(4), 722-732.

Kansiz, S. (2023). Investigating the structural and surface properties of copper and nickel complexes fluorine-based salen type Schiff bases. *Journal of Structural Chemistry*, *64*(12), 2295-2310.

Kargar, H., Fallah-Mehrjardi, M., Munawar, K. S., Acar, E., Dege, N., and Kansız, S. (2025). Structural dynamics of a phenoxy-bridged heteronuclear Cu (II)/Hg (II)-Salen complex: synthesis, characterization, DFT insights, and Hirshfeld surface analysis. *Journal of the Iranian Chemical Society*, *22*(4), 769-780.

Korkmaz, I. N., Türkeş, C., Demir, Y., Öztekin, A., Özdemir, H., and Beydemir, Ş. (2022). Biological evaluation and in silico study of benzohydrazide derivatives as paraoxonase 1 inhibitors. *Journal of Biochemical and Molecular Toxicology*, *36*(11), e23180.

Kucukoglu, K., Gul, H. I., Taslimi, P., Gulcin, I., and Supuran, C. T. (2019). Investigation of inhibitory properties of some hydrazone compounds on hCA I, hCA II and AChE enzymes. *Bioorganic Chemistry*, *86*, 316–321.

Liu, S. Y., and Zhang, M. (2012). Crystal structure of N'-(2-methoxynaphthylidene)-4-dimethylamino benzohydrazide, C21H21N3O2. *Zeitschrift für Kristallographie-New Crystal Structures*, *227*(4), 463-464.

März, A. M., Fabian, A. K., Kozany, C., Bracher, A., and Hausch, F. (2013). Large FK506-binding proteins shape the pharmacology of rapamycin. *Molecular and Cellular Biology*, *33*(7), 1357–1367.

Murugappan, S., Dastari, S., Jungare, K., Barve, N. M., and Shankaraiah, N. (2024). Hydrazide-hydrazone/hydrazone as enabling linkers in anti-cancer drug discovery: A comprehensive review. *Journal of Molecular Structure*, *1307*, 138012.

OmarAli, A. A. B., Ahmed, R. K., Al-Karawi, A. J. M., Marah, S., Kansız, S., Sert, Y., Jaafar, M. I., Dege, N., Poyraz, E. B., Ahmed, A. M. A., Ozen, T., Loukil, M., and Jwad, R. S. (2023). Designing of two new cadmium (II) complexes as bio-active materials: Synthesis, X-ray crystal structures, spectroscopic, DFT, and molecular docking studies. *Journal of Molecular Structure*, *1290*, 135974.

Oshi, R., Abdalla, S., and Springborg, M. (2017). Study of the influence of functionalization on the reorganization energy of naphthalene using DFT. *Computational and Theoretical Chemistry*, *1099*, 209-215.

Sert, Y., Balakit, A. A., Öztürk, N., Ucun, F., and El-Hiti, G. A. (2014). Experimental (FT-IR, NMR and UV) and theoretical (M06-2X and DFT) investigation, and frequency estimation analyses on (E)-3-(4-bromo-5-methylthiophen-2-yl) acrylonitrile. *Spectrochimica Acta Part A: Molecular and Biomolecular Spectroscopy*, *131*, 502–511.

Sert, Y., Singer, L. M., Findlater, M., Doğan, H., and Çırak, Ç. (2014). Vibrational frequency analysis, FT-IR, DFT and M06-2X studies on tert-butyl N-(thiophen-2-yl) carbamate. *Spectrochimica Acta Part A: Molecular and Biomolecular Spectroscopy*, *128*, 46–53.

Sherif, E. S. M., and Ahmed, A. H. (2021). Alleviation of Iron Corrosion in Chloride Solution by N, N′-bis [2-Methoxynaphthylidene] amino] oxamide as a Corrosion Inhibitor. *Crystals*, *11*(12), 1516.

Taha, M., Ismail, N. H., Lalani, S., Fatmi, M. Q., Wahab, A., Siddiqui, S., Khan, K. M., Imran, S., and Choudhary, M. I. (2015). Synthesis of novel inhibitors of α-glucosidase based on the benzothiazole skeleton containing benzohydrazide moiety and their molecular docking studies. *European Journal of Medicinal Chemistry*, *92*, 387-400.

Trott, O., and Olson, A. J. (2010). AutoDock Vina: Improving the speed and accuracy of docking with a new scoring function, efficient optimization, and multithreading. *Journal of Computational Chemistry*, *31*(2), 455–461.

Verma, G., Marella, A., Shaquiquzzaman, M., Akhtar, M., Ali, M. R., and Alam, M. M. (2014). A review exploring biological activities of hydrazones. *Journal of Pharmacy and Bioallied Sciences*, *6*(2), 69–80.

Zhou, C., Hou, H., and Yang, T. (2009). Crystal structure of 2-nitro-N′-(2-methoxynaphthylidene)-benzohydrazide, C19H15N3O4. *Zeitschrift für Kristallographie-New Crystal Structures*, *224*(1), 37-38.

Navigating The Nano-Micro Continuum: Kinetic Control and Functional Utility of Biogenic Silver Structures

Alper YARDAN[1]

1- Dr., Balıkesir University, Altınoluk Vocational School, Department of Chemistry and Chemical Processing Technologies, Orcid: 0000-0001-6916-831X

ABSTRACT

For the better part of a decade, green synthesis has enjoyed a reputation as the "sustainable darling" of materials science, largely because it offers a plant-based escape route from the toxic reagents used in conventional chemistry. Yet, despite this popularity, the field remains shackled by a pervasive and somewhat reductionist dogma: the belief that "nano" is the only metric of success. A cursory review of the literature reveals a landscape so heavily biased towards particles below 100 nm that micrometer-sized aggregates are almost universally discarded as experimental failures, rather than being interrogated as legitimate thermodynamic outcomes. This chapter seeks to dismantle that prejudice. We argue that micro-scale aggregation, far from being a stochastic error, is a predictable and thermodynamically inevitable consequence of high-concentration synthesis conditions. By dissecting mechanisms such as "burst" nucleation, Ostwald ripening, and the often-overlooked phytochemical bridging effect, we demonstrate that these larger structures possess intrinsic value—specifically in terms of thermodynamic stability and biocompatibility—that their nano counterparts lack. Consequently, we propose a paradigm shift: rather than treating these micro-structures as waste, we should exploit their slow ion-release kinetics for high-value applications in sustainable agriculture and medicine.

Keywords: Green Synthesis; Silver Microparticles; Burst Nucleation; Ostwald Ripening; Kinetic Control; Phytochemical Bridging.

INTRODUCTION

If one observes the trajectory of materials science in the 21st century, it becomes evident that the discipline is being squeezed by two opposing yet equally urgent pressures. On one flank, there is the desperate global scramble for novel therapeutic agents to hold back the rising tide of antimicrobial resistance (AMR); on the other, there is a strict, non-negotiable environmental imperative to purge toxic effluents from industrial manufacturing (Murray et al., 2022). Entering this breach is "phyto-nanotechnology," a methodology that promises to resolve both issues simultaneously by utilizing benign plant metabolites to replace hazardous reducing agents like sodium borohydride (Iravani, 2011).

However, there is a conceptual blind spot at the heart of this endeavor. The academic community has become so fixated on the fabrication of monodispersed silver nanoparticles (AgNPs)—specifically those with diameters strictly below 100 nm—that it has effectively created a monoculture of thought. This fixation is, to be fair, grounded in theory: the premise that higher specific surface area equates to superior catalytic and biological activity is scientifically sound (Dakal et al., 2016). Yet, this singular focus has

resulted in a publication bias where synthesis protocols are rigidly optimized to arrest particle growth at all costs. The unfortunate side effect is that experimental results yielding micron-sized particles or aggregates are frequently labeled as "failed syntheses," relegated to the laboratory trash bin, and excluded from the scientific record.

We contend that this binary classification—wherein nano represents "success" and micro represents "failure"—is scientifically flawed, primarily inasmuch as it neglects the continuous nature of colloidal growth thermodynamics. When researchers employ potent extracts from endemic flora, particularly at high concentrations, the formation of silver microparticles (AgMPs) is often a reproducible, functional outcome rather than a mistake. This chapter aims to challenge the prevailing nano-obsession. Given the rising toxicological concerns regarding "nano-toxicity"—specifically the potential for ultrafine particles to cross the blood-brain barrier or bioaccumulate in vital organs—the safety profile of larger particles warrants a second look. By exploring how variables like extract concentration influence final morphology, we aim to validate that in scenarios requiring long-term thermodynamic stability or catalyst recycling, the micro-scale may, counter-intuitively, outperform the nano-scale.

1. The Thermodynamic Context: Why "Green" Can Be Chaotic

To truly comprehend why microparticles form, one must first appreciate the messy reality of the reaction medium. Unlike a chemical synthesis performed with purified reagents in a clean room, a crude plant extract is a chaotic, chemically complex soup. It contains a dizzying array of metabolites, from flavonoids to terpenes, each with its own redox potential. Synthesizing silver within this unrefined matrix involves a delicate thermodynamic balancing act, one that is governed not just by temperature or pH, but fundamentally by the precursor-to-extract ratio.

This biological medium is asked to perform two contradictory roles simultaneously. First, it acts as a reducer: specific functional groups, most notably the phenolic –OH groups visible in FTIR analysis, are tasked with stripping electrons from silver ions (Ag^{+}) to reduce them to elemental silver (Ag^{0}). Second, it acts as a stabilizer: bulky organic molecules attempt to envelop the nascent particles, creating a steric barrier intended to prevent aggregation (Ambika & Sundrarajan, 2015; Makarov et al., 2014).

Whether a particle remains kinetically trapped at the nano-size or evolves into a microparticle depends entirely on the race between these two competing functions. Classical nucleation theory, such as the LaMer model, postulates that for monodispersity to occur, the nucleation phase must be separated from the growth phase. However, in high-concentration environments, this separation collapses. Because the reduction rate in these supersaturated scenarios drastically outpaces the diffusion-limited adsorption of capping agents, the system inevitably bypasses the metastable nano-state.

It rushes towards equilibrium, settling into the thermodynamically favored—albeit larger—micro-state.

2. Mechanisms: How the Shift Happens

The transition from discrete nanoparticles to stable microparticles is neither random nor accidental; rather, it is driven by three specific convergent mechanisms that are triggered whenever supersaturation levels become excessive. Understanding these mechanisms is the key to controlling the final material.

2.1. The "Burst" Effect and Coalescence

The primary culprit in aggregation is a phenomenon known as "burst nucleation." When a surplus of reducing agents is introduced instantaneously, the critical energy barrier for nucleation is lowered, causing a massive density of nuclei to form simultaneously throughout the solution (Mittal et al., 2013). In a dilute solution, these nuclei might have time to find a capping agent. But here, the conditions are crowded. The mean free path between nascent particles is so short that they are forced into immediate proximity. Since surface passivation by phytochemicals is a diffusion-limited process that takes time, the naked, high-energy nuclei collide and fuse before they can be effectively capped (Amin et al., 2021). This rapid coalescence is not an error; it is the system's way of rapidly reducing its total surface energy.

2.2. Ostwald Ripening: The Drive for Equilibrium

Following the initial nucleation and coalescence, the system seeks further stabilization through Ostwald ripening. This process is governed by the Gibbs-Thomson effect, which dictates that smaller particles, due to their high surface curvature, possess higher chemical potential and solubility than larger particles.

Consequently, within the complex ionic matrix of the plant extract, smaller particles preferentially dissolve back into ionic species (Ag^{+}). These ions then diffuse through the solution and redeposit onto the surface of larger, energetically stable aggregates (Dolai et al., 2021). Although nanoparticle researchers often view this as a nuisance, in our context, Ostwald ripening is beneficial. It effectively "culls" the unstable nano-population, yielding chemically robust micro-structures that have already reached a state of equilibrium and are less prone to further changes over time.

2.3. The Bridging Effect (Molecular Glue)

Furthermore, we must consider that the role of phytochemicals undergoes a fundamental shift at high concentrations. While they are typically modeled as capping agents that provide steric repulsion, long-chain polyphenols and polysaccharides can act as "molecular glue" through the bridging effect. By adsorbing onto multiple metal nuclei simultaneously—via

hydrogen bonding or chelation—these macromolecules physically tie distinct clusters together (Ghorbani et al., 2017). This creates the rugged, interconnected, and polycrystalline morphologies frequently observed under microscopy, distinguishing biogenic microparticles from simple physical agglomerates formed by drying.

3. Diagnosing the Micro-State: Characterization Signatures

Distinguishing between a "failed" nanoparticle synthesis and the successful formation of stable microparticles requires looking beyond simple visual inspection. One must identify specific instrumental signatures that signal the departure from the quantum confinement regime.

Optical and Spectroscopic Indicators

The most immediate evidence is often found in the optical properties of the suspension. While spherical AgNPs characteristically display a sharp Surface Plasmon Resonance (SPR) peak around 400–450 nm due to the collective oscillation of conduction electrons (El-Nour et al., 2010), microparticles behave as larger scattering centers. According to Mie theory, as the particle size increases beyond the mean free path of the electrons, the plasmon resonance is dampened and broadened. This results in a spectrum where the peak either broadens significantly, loses its intensity, or shifts distinctly towards the UV range (~350 nm) (Paramelle et al., 2014).

My recent experimental work with endemic Turkish flora provided striking confirmation of these spectral signatures. In studies utilizing *Sideritis trojana* Bornm., the synthesized structures did not exhibit the classic plasmon peak expected for nanospheres; instead, they showed a distinct absorption maximum at approximately 362 nm, clearly indicating the presence of larger scattering centers (Yardan, 2025b). Similarly, syntheses mediated by *Origanum sipyleum* L. extract resulted in a hypsochromic shift to roughly 350 nm (Yardan, 2025a). These specific wavelengths were not random artifacts but reproducible indicators that the high phenolic content of these extracts had thermodynamically driven the system toward stable micro-aggregation rather than arresting it at the nanoscale.

Morphological Confirmation

Morphologically, Scanning Electron Microscopy (SEM) reveals the true nature of the material. Unlike discrete, spherical nanoparticles, biogenic microparticles appear jagged, faceted, or fused. The presence of fusion boundaries—where two distinct particles seem to have merged into a single entity—provides physical evidence of the coalescence and ripening processes discussed previously (Mittal et al., 2013).

This bridging phenomenon was particularly evident in the microstructures derived from *Origanum sipyleum* L. Scanning Electron Microscopy (SEM) revealed that the resulting particles were not merely loose

agglomerates but fused, irregular masses with clear grain boundaries, suggesting that phytochemicals acted as a robust molecular glue (Yardan, 2025a). Likewise, the *Sideritis trojana*-mediated synthesis yielded large, polycrystalline clusters that maintained their structural integrity over time, offering physical proof that the transition to the microscale involves a deliberate phytochemical cementing process rather than uncontrolled precipitation (Yardan, 2025b).

Crystallographic and Surface Analysis

For definitive confirmation, X-Ray Diffraction (XRD) is employed to verify the crystalline face-centered cubic (FCC) structure of the silver (Figure 3.1).

If XRD analysis indicates small crystallite sizes (via the Scherrer equation) while SEM imaging shows large micrometer-scale particles, the material is confirmed as a polycrystalline aggregate (Iravani, 2011). Additional verification can be obtained via Energy Dispersive X-Ray Spectroscopy (EDX) to detect carbon signals woven within the silver matrix, which supports the phytochemical bridging theory (Ahmed et al., 2016). Finally, a low Zeta Potential (typically < ±30 mV) serves as the "smoking gun" for kinetic instability, proving that the electrostatic repulsion forces were insufficient to prevent the aggregation driven by the high ionic strength of the concentrated extract (Jeevanandam et al., 2018).

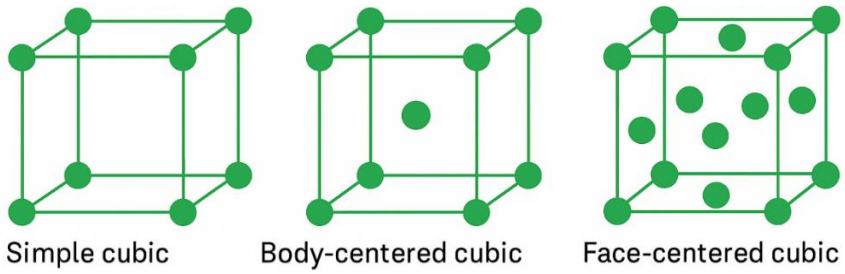

Figure 3.1. This schematic illustrates the Face-Centered Cubic (FCC) lattice structure of metallic silver. The detection of this specific lattice arrangement via XRD confirms the presence of crystalline metallic material, distinguishing the microparticles from amorphous aggregation or organic impurities *(Illustration adapted from Cullity & Stock, 2001)*.

If XRD analysis indicates small crystallite sizes (via the Scherrer equation) while SEM imaging shows large micrometer-scale particles, the material is confirmed as a polycrystalline aggregate (Iravani, 2011). Additional verification can be obtained via Energy Dispersive X-Ray Spectroscopy (EDX) to detect carbon signals woven within the silver matrix,

which supports the phytochemical bridging theory (Ahmed et al., 2016). Finally, a low Zeta Potential (typically < ±30 mV) serves as the "smoking gun" for kinetic instability, proving that the electrostatic repulsion forces were insufficient to prevent the aggregation driven by the high ionic strength of the concentrated extract (Jeevanandam et al., 2018).

Summary of Differences

The physicochemical distinctions between these two states are summarized in Table 3.1 below, highlighting why microparticles should be treated as a distinct class of materials.

Table 3.1. Comparative summary of physicochemical characteristics between biogenic silver nanoparticles and micro aggregates*

Feature	**Nanoparticles (AgNPs)**	**Microparticles / Aggregates (AgMPs)**
Dominant Formation Mechanism	Controlled Nucleation & Capping	Burst Nucleation & Ostwald Ripening
Size Range	1 – 100 nm	> 100 nm (typically 1-10 µm)
Optical Signature (UV-Vis)	Sharp SPR Peak (400–450 nm)	Broadened Peak or Blue Shift (~350 nm)
Thermodynamic State	Metastable (High Surface Energy)	Stable (Lower Surface Energy)
Surface Charge (Zeta)	High (> ±30 mV)	Low (< ±30 mV)
Primary Advantage	High Bioactivity / Surface Area	Long-term Stability / Easy Recovery

**Reference:Data compiled from Mittal et al., 2013; Jeevanandam et al., 2018; Dolai et al., 2021)*

4. Why "Micro" Might Be Better: A Functional Re-evaluation

It is time to challenge the pervasive dogma in nanotechnology that "smaller is always better." We propose that AgMPs are not merely failed nanoparticles but functional materials with unique advantages that make them superior for specific, pragmatic applications.

Thermodynamic Stability and Shelf-Life

Unlike AgNPs, which are thermodynamically metastable and prone to rapid oxidation or aggregation upon exposure to light and air (Jeevanandam et al., 2018), biogenic microparticles have already achieved a low-energy state through the ripening process. This inherent thermodynamic stability allows them to be stored for extended periods without significant degradation or morphological change. For industrial products that require a long shelf-life without the addition of synthetic stabilizers, this is a game-changer.

Safety through Controlled Release

While the "burst" release of silver ions from nanoparticles is highly effective at killing bacteria, it also poses significant cytotoxicity risks to healthy mammalian cells, limiting their use in contact with human tissue (Dolai et al., 2021). Microparticles, due to their lower surface-area-to-volume ratio, act as slow-release reservoirs. They maintain steady, therapeutic levels of silver ions over an extended timeframe. This controlled release profile is ideal for medical coatings that require long-term sterility, such as catheters (Sulaiman et al., 2020), or for agricultural fungicides that need to resist leaching by rain to provide durable crop protection.

Environmental Remediation and Recovery

Moreover, "nano-pollution" presents a significant remediation challenge since nanoparticles are colloquially known to be difficult to filter from water, often passing through conventional treatment systems. In contrast, the larger mass and micrometer dimensions of microparticles allow them to settle naturally or be captured by simple filtration systems. This recoverability positions them as excellent candidates for recyclable heterogeneous catalysts in wastewater treatment, allowing for the degradation of pollutants like azo dyes followed by easy catalyst recovery and reuse (Beydoun et al., 1999).

5. Methodological Conundrums and Standardization

While the functional utility of microparticles is evident, the field of green synthesis faces a unique set of methodological challenges that differ from conventional chemical synthesis. The primary hurdle is the inherent biological variability of the starting material. Since plant extracts are natural products, their phytochemical composition fluctuates based on seasonal changes, soil composition, geographical location, and even the time of harvest. A plant collected in spring may have a different phenolic profile than one collected in autumn, leading to batch-to-batch inconsistencies in the reducing power and subsequent particle size.

This variability necessitates a move away from serendipitous discovery towards "Process Analytical Technology" (PAT). Future research must focus on mapping the precise "tipping points"—such as pH, temperature, and specific extract concentrations—that trigger the switch from nano to

micro. By establishing robust quality control parameters and understanding the kinetic boundaries discussed in this chapter, researchers can transition from "cooking" with plant extracts to "engineering" silver structures of any desired dimension, tailored specifically to the task at hand.

CONCLUSION

This chapter has attempted to peel back the layers of green synthesis to reveal that the interaction between plant extracts and metal ions is not a guaranteed path to nanoparticles, nor should it be. Through a complex interplay of mechanisms like burst nucleation, Ostwald ripening, and phytochemical bridging, nature often favors the formation of the micro-scale. This outcome is not a failure of synthesis but a triumph of thermodynamics. By embracing the full spectrum of particle sizes and understanding the specific advantages of micro-aggregates, we can unlock a new class of safer, more stable, and more recyclable silver materials that address the pressing needs of medicine and industry.

REFERENCES

Ahmed, S., Ahmad, M., Swami, B. L., Ikram, S. (2016). A review on plants extract mediated synthesis of silver nanoparticles. *Journal of Advanced Research*, *7*(1), 17–28.

Ambika, S., Sundrarajan, M. (2015). Green biosynthesis of ZnO nanoparticles using *Vitex negundo* L. extract. *Journal of Photochemistry and Photobiology B: Biology*, *149*, 143-148.

Amin, M., Al-Omair, M. A., Al-Hajji, A. B. (2021). Influence of plant extract concentration on the synthesis of silver nanoparticles. *Arabian Journal of Chemistry*, *14*(3), 103007.

Beydoun, D., Amal, R., Low, G., McEvoy, S. (1999). Role of nanoparticles in photocatalysis. *Journal of Nanoparticle Research*, *1*(4), 439–458.

Cullity, B. D., Stock, S. R. (2001). *Elements of X-Ray Diffraction* (3rd ed.). Prentice Hall.

Dakal, T. C., Kumar, A., Majumdar, R. S., Yadav, V. (2016). Mechanistic basis of antimicrobial actions of silver nanoparticles. *Frontiers in Microbiology*, *7*, 1831.

Dolai, J., Mandal, K., Jana, N. R. (2021). Nanoparticle size effects in biomedical applications. *ACS Applied Nano Materials*, *4*(7), 6471–6496.

El-Nour, K. M., Eftaiha, A. A., Al-Warthan, A., Ammar, R. A. (2010). Synthesis and applications of silver nanoparticles. *Arabian Journal of Chemistry*, *3*(3), 135-140.

Ghorbani, H. R., Safekordi, A. A., Attar, H., Sorkhabadi, S. M. R. (2017). Green synthesis of silver nanoparticles using the extract of fruit of *Tamarindus indica*. *Materials Letters*, *190*, 31-34.

Iravani, S. (2011). Green synthesis of metal nanoparticles using plants. *Green Chemistry*, *13*, 2638–2650.

Jeevanandam, J., Barhoum, A., Chan, Y. S., Dufresne, A., Danquah, M. K. (2018). Review on nanoparticles and nanostructured materials: history, sources, toxicity and regulations. *Beilstein Journal of Nanotechnology*, *9*, 1050–1074.

Makarov, V. V., Love, A. J., Sinitsyna, O. V., Makarova, S. S., Ivanova, A. V., Lafont, F. (2014). "Green" nanotechnologies: Synthesis of metal nanoparticles using plants. *Acta Naturae*, *6*(1), 35–44.

Mittal, A. K., Chisti, Y., Banerjee, U. C. (2013). Synthesis of metallic nanoparticles using plant extracts. *Biotechnology Advances*, *31*(2), 346–356.

Murray, C. J. (2022). Global burden of bacterial antimicrobial resistance in 2019: A systematic analysis. *The Lancet*, *399*(10325), 629-655.

Paramelle, D., Miralles, G., Veyret, B., Pignot-Paintrand, I. (2014). How to play with the surface plasmon resonance of silver nanoparticles for robust and sensitive colorimetric assays. *Analytical Chemistry*, *86*(21), 10756-10764.

Sulaiman, N. S., Hamzah, N., Zakaria, S. F., Che Othman, S. F., Mohamed Suffian, I. F. (2020). Hydrogel-nanoparticle hybrids for biomedical applications: Principles and advantages. *Nanomedicine*, *16*(2), 81-84.

Yardan, A. (2025a). From ions to aggregates: Green synthesis and characterization of silver microparticles using endemic Origanum sipyleum L. extract. *International Journal of Science and Research Archive*, 17(03), 511-515.

Yardan, A. (2025b). Green synthesis of silver microparticles using an aqueous extract of endemic Sideritis trojana Bornm. and their characterization. *Magna Scientia Advanced Research and Reviews*, 15(02), 199-204.

SCAPS-1D Simulation Study of p-CdTe/n-IGZO Thin-Film Solar Cells: Effects of Donor Defect Density, Back Contact Work Function, and Operating Temperature on Photovoltaic Performance

Serap YİĞİT GEZGİN[1]
Hamdi ŞÜKÜR KILIÇ[2]

1- Assoc. Prof. Dr.; Selcuk University Department of Physics, Faculty of Science. serap.gezgin@selcuk.edu.tr ORCID No: 0000-0003-3046-6138
2- Prof. Dr.; Dokuz Eylül University Department of Metallurgically and Materials Engineering, Faculty of Engineering,. hamdisukur.kilic@deu.edu.tr ORCID No: 0000-0002-7546-4243

ABSTRACT

In this study, a p-CdTe/n-IGZO thin-film solar cell was numerically modeled and analyzed using the SCAPS-1D simulation program, a well-established tool for photovoltaic device simulation. Experimentally reported properties of the IGZO thin film, including film thickness, band gap, and absorption coefficient, together with the physical and electrical parameters of each device layer, were used as input parameters. The photovoltaic performance of the solar cell was systematically investigated as a function of the shallow donor density (N_D) in the n-type IGZO layer, the work function of the back contact, and the operating temperature. The results indicate that increasing the shallow donor density enhances carrier concentration and electrical conductivity, leading to improved charge transport, reduced series resistance, and higher short-circuit current density, fill factor, and power conversion efficiency. Furthermore, the back contact work function was found to play a critical role in device performance, where higher work function metals promote favorable band alignment, efficient hole extraction, and reduced recombination losses, resulting in a significant improvement in open-circuit voltage and overall efficiency. In contrast, elevated operating temperatures negatively affect device performance due to increased recombination rates, reduced open-circuit voltage, and degradation of fill factor. Overall, this study demonstrates that careful optimization of IGZO donor density, back contact selection, and operating temperature is essential for achieving high-efficiency p-CdTe/n-IGZO solar cells and provides valuable insights for the design and optimization of IGZO-based photovoltaic devices.

Keywords – IGZO,Thin Film, Work Function, Solar Cell, SCAPS-1D Simulation.

INTRODUCTION

Thin-film solar cells have attracted considerable attention in recent years due to their potential for low-cost fabrication, lightweight structure, and compatibility with large-area deposition techniques. Among various thin-film photovoltaic technologies, Cadmium Telluride (CdTe) based solar cells stand out as one of the most commercially successful systems, owing to their near-optimal band gap, high absorption coefficient, and excellent stability. Despite these advantages, further improvements in device efficiency and performance optimization remain essential to meet the growing demand for high-efficiency and cost-effective photovoltaic technologies (Barbato, Artegiani et al. 2021).

Recently, Transparent Conducting Oxide (TCO) and oxide semiconductor materials have emerged as promising alternatives for electron transport layers in thin-film solar cells. Indium Gallium Zinc Oxide (IGZO) has gained significant interest due to its wide band gap, high electron mobility, good

optical transparency, and excellent electrical tunability(Xu, Hu et al. 2018). These properties make IGZO a strong candidate for use as an n-type semiconductor layer in CdTe-based heterojunction solar cells(Mishra, Anwar et al. 2025). However, the photovoltaic performance of CdTe/IGZO solar cells is strongly dependent on several key material and device parameters, including donor defect density(Samiul Islam, Sobayel et al. 2021), back contact work function(Kumar and Thakur 2018), and operating conditions(Porwal, Paul et al. 2022).

Among these factors, the shallow donor density in the IGZO layer plays a crucial role in controlling charge carrier concentration, electrical conductivity, and transport dynamics, thereby directly influencing charge collection efficiency and overall device performance(Dalal and Sharma 2005). Additionally, the back contact in p-type CdTe solar cells is known to be a critical component, as its work function determines band alignment, carrier extraction efficiency, and recombination behavior at the interface. Improper back contact selection can significantly limit open-circuit voltage and fill factor(Kumar and Thakur 2018, Shi, Wang et al. 2018). Furthermore, operating temperature is an important external parameter that affects carrier recombination, series resistance, and voltage output, ultimately impacting the power conversion efficiency of solar cells(Garain, Basak et al. 2021).

Numerical simulation has proven to be an effective and reliable approach for understanding the complex interplay between material properties and device performance. In this regard, the SCAPS-1D simulation program is widely used for the analysis and optimization of thin-film solar cells, enabling systematic investigation of material parameters and device architectures(Houimi, Gezgin et al. 2021).

In this study, a p-CdTe/n-IGZO solar cell is systematically modeled using SCAPS-1D. The effects of IGZO shallow donor density, back contact work function, and operating temperature on the photovoltaic performance of the device are comprehensively analyzed. The results provide valuable insights into performance-limiting mechanisms and offer clear guidelines for optimizing IGZO-based CdTe solar cells toward higher efficiency and improved device stability.

RESULT AND DISCUSSION

In this study, the back contact/p-CdTe/n-IGZO/i-ZnO/ITO solar cell solar cell has been modelled using the SCAPS-1D program, a significant simulation tool in photovoltaic research. By utilizing the experimental characteristics of the IGZO thin film (such as film thickness, band gap, absorption coefficient) reported in our previous work (Yiğit, Gündoğdu et al. 2021), along with the physical data of the layers provided in the table 1 as input parameters, the photovoltaic performance of the solar cell has been calculated. The performance of the solar cell has been evaluated based on the donor defect density of the IGZO semiconductor, the operating temperature, and the properties of the back contact.

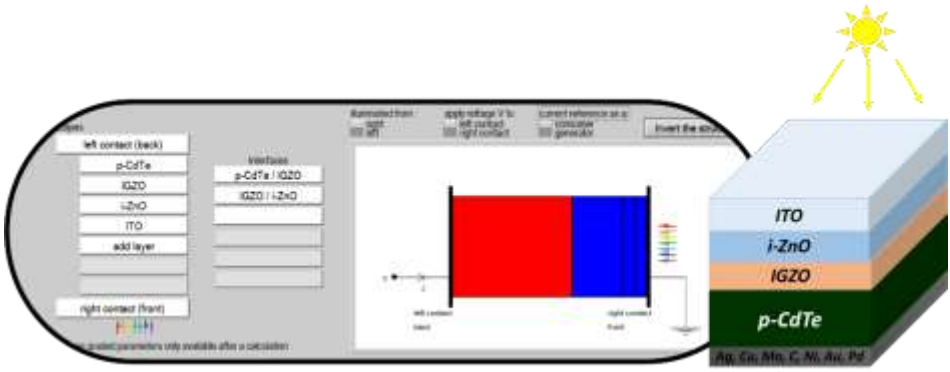

Figure 1: The p-CdTe/n-IGZO solar cell diagram modelled by SCAPS-1D simulation

Table 1: The electrical parameters of semiconductor layers formed Back contact/p-CdTe/n-IGZO/i-ZnO/ITO solar cell

Layers	ITO	i-ZnO	n-IGZO	p-CdTe
Band Gap (eV)	3.6	3.3	3.45	1.45
Electron affinity (eV)	4.6	4.6	4.4	3.9
Dielectric permittivity (relative)	9	9	10	10
CB effective density of states (cm^{-3})	$2.20x10^{18}$	$2.20x10^{18}$	$1.80x10^{18}$	$9.20x10^{17}$
VB effective density of states (cm^{-3})	$1.80x10^{19}$	$1.80x10^{19}$	$2.40x10^{19}$	$5.2x10^{18}$
Electron/Hole thermal velocity (cm/s)	$1.00x10^{7}$	$1.00x10^{7}$	$1.00x10^{7}$	$1.00x10^{7}$
Electron/Hole mobility (cm^2/Vs)	100/25	100/25	100/25	320/40
Shallow donor density (cm^{-3})	$1.00x10^{20}$	$1.00x10^{5}$	*Change*	0
Shallow acceptor density (cm^{-3})	0	0	0	$3x10^{15}$
Thickness (nm)	100	100	420	1000

The Effect of the shallow donor density (N_D) in IGZO on the Performance of p-CdTe/n-IGZO Solar Cells

The shallow donor density in an n-type semiconductor plays a crucial role in enhancing the performance of solar cells by influencing the material's charge carrier dynamics(Kennedy and Frese 1978). Shallow donor impurities introduce energy levels just below the conduction band, making it easier for electrons to be thermally excited into the conduction band, thus increasing the free electron density(Jahandardoost, Walkons et al. 2023).

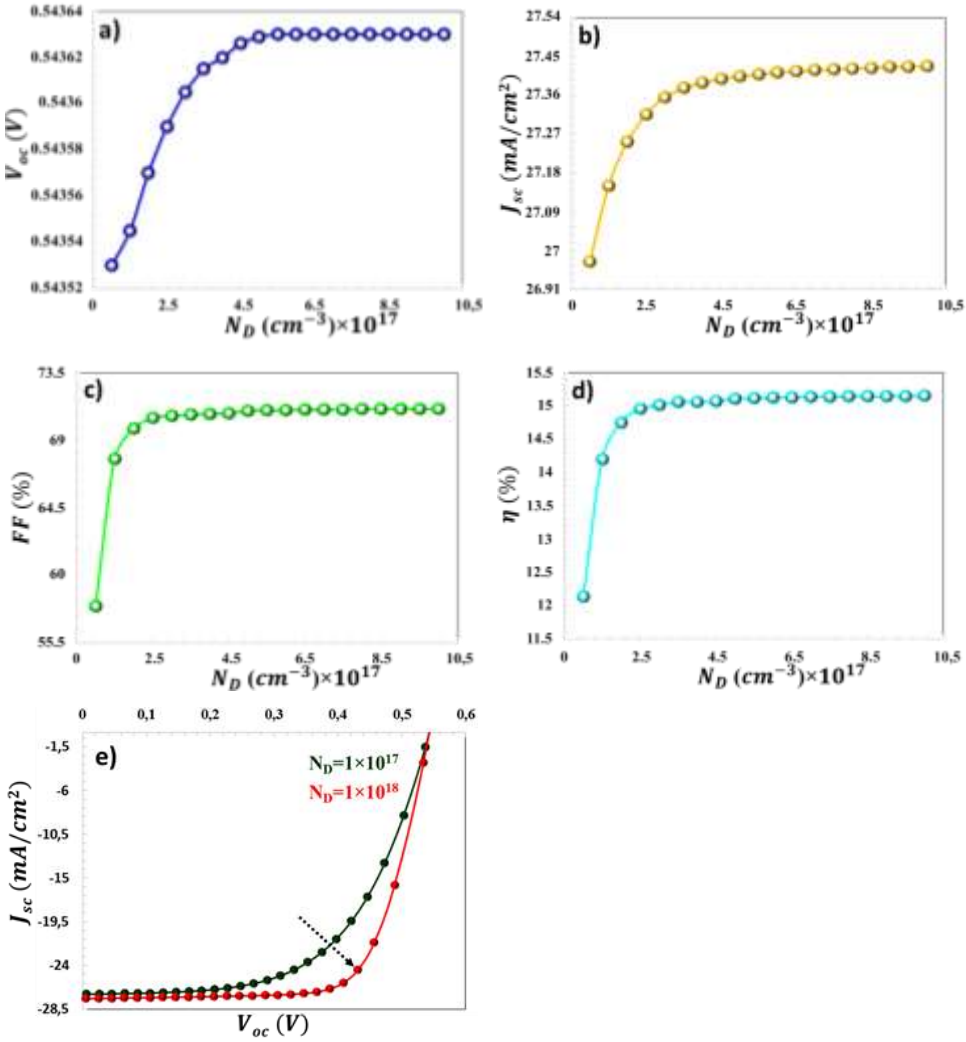

Figure 2: (a-d) The change plots illustrating the effect of N_D on the photovoltaic parameters and e) $J-V$ characteristic of Au/p-CdTe/n-IGZO/i-ZnO/ITO Solar Cell based to N_D Value

An optimized shallow donor density leads to a higher concentration of free electrons in the semiconductor, which improves its electrical conductivity and charge transport properties. This, in turn, enhances the charge collection efficiency of the solar cell, as more electrons are available for movement through the device. With more free carriers, the photo-generated electron-hole pairs are more effectively separated and directed toward the electrodes, resulting in an improvement in the overall power conversion efficiency of the solar cell. The increased carrier concentration due to shallow donors can reduce the series resistance of the solar cell, further

boosting its efficiency(Pathak and Pandey 2020, Jahandardoost, Walkons et al. 2023).

By facilitating more efficient charge separation and transport, a carefully controlled shallow donor density contributes to the solar cell's ability to convert sunlight into electrical energy more effectively. In this study, based on the parameters in the Table 2 and on the plots in Fig 2 and Fig 3, it can be observed that an increase in the shallow donor density (N_D) (1.10^{17} cm^{-3} – 1.10^{18} cm^{-3}) leads to an improvement in the photovoltaic parameters of the solar cell, resulting in enhanced performance (Fig 2 and Fig 3, Table 2).

Table 2: The Photovoltaic Parameters of Au/p-CdTe/n-IGZO/i-ZnO/ITO Solar Cell based to N_D Value

N_D (cm^{-3})	V_{oc} (V)	J_{sc} (mA/cm^2)	FF (%)	η (%)
1.10^{17}	0.54353	26.9743	57.92	12.1322
2.10^{17}	0.54357	27.2519	69.78	14.7513
3.10^{17}	0.54360	27.3553	70.65	15.0102
4.10^{17}	0.54362	27.3893	70.79	15.0588
5.10^{17}	0.54362	27.4040	70.99	15.1087
6.10^{17}	0.54363	27.4125	71.03	15.1233
7.10^{17}	0.54363	27.4182	71.06	15.1330
8.10^{17}	0.54363	27.4223	71.09	15.1400
9.10^{17}	0.54363	27.4255	71.10	15.1452
1.10^{18}	0.54363	27.4281	71.12	15.1492

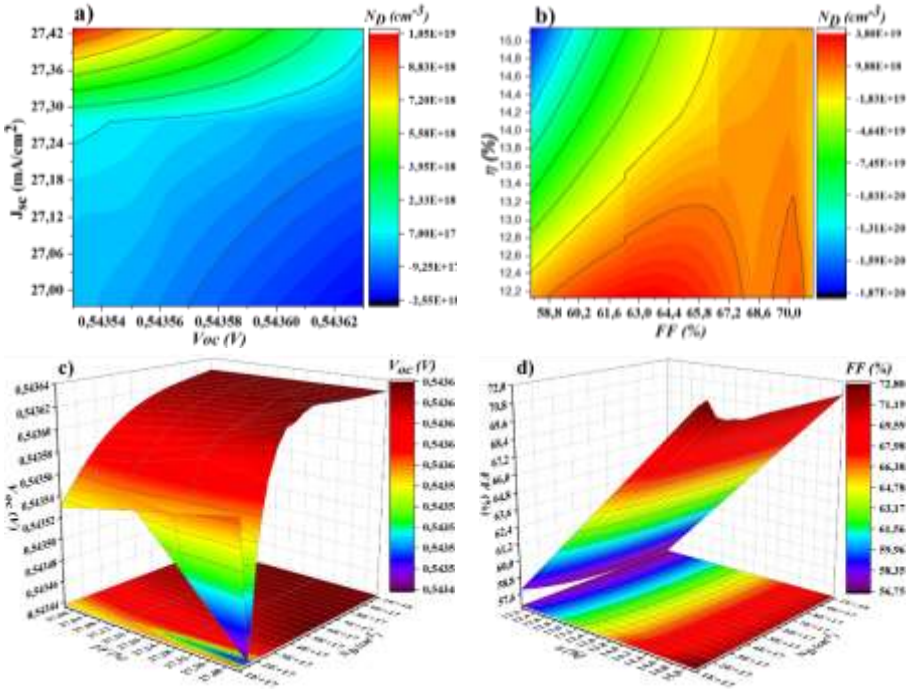

Figure 3: 2D and 3D contour plots of Photovoltaic Parameters of p-CdTe/n-IGZO Solar Cell based to N_D Value

The Effect of the Back Contact on the Performance of p-CdTe/n-IGZO Solar Cells

In p-type semiconductors, the back contact plays a vital role in enhancing the performance of solar cells by facilitating efficient charge carrier collection and minimizing energy losses(Abdul Ameer, Jarad et al. 2024). The characteristics of the back contact, particularly its material properties, work function, and interface quality, can significantly influence key photovoltaic parameters such as open-circuit voltage (V_{oc}), fill factor (FF), and overall power conversion efficiency (PCE)(Ghosh, Porwal et al. 2022).

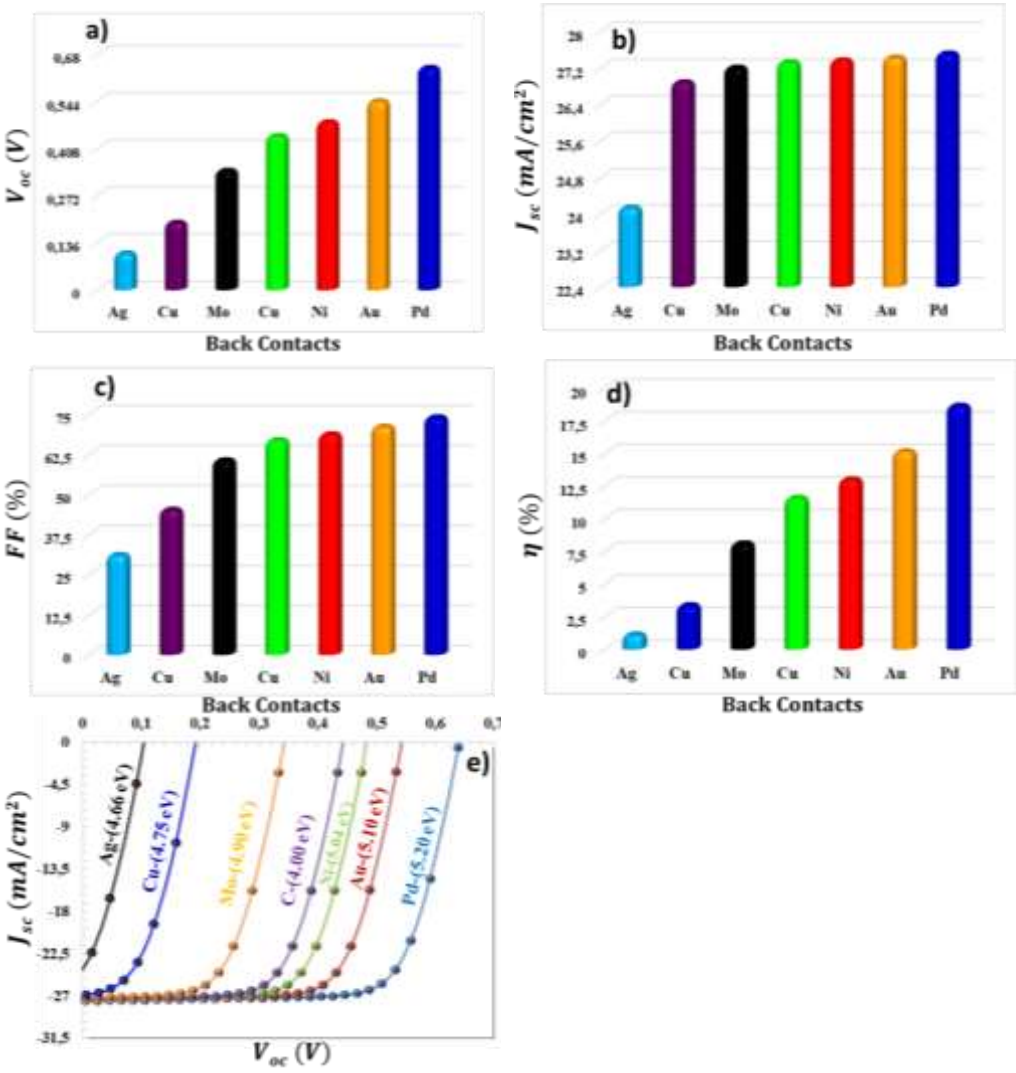

Figure 4: (a-d) The change plots illustrating the effect of the back contact work function on the photovoltaic parameters and e) $J-V$ characteristic of Back Contacts/p-CdTe/n-IGZO/i-ZnO/ITO Solar Cell based to the work function of Back Contacts

A high-quality back contact ensures efficient hole extraction from the p-type semiconductor. By forming a low-resistance, ohmic contact with the p-type material, it reduces energy barriers at the interface, which leads to a reduction in carrier recombination. This, in turn, enhances the charge collection efficiency, allowing more photogenerated carriers to be extracted from the device, resulting in improved photovoltaic performance. A well-designed back contact can directly improve the open-circuit voltage (V_{oc}) of the solar cell. When the back contact has an appropriate work function that

matches or is slightly higher than the p-type material, it ensures minimal energy losses and facilitates efficient hole transport. This helps maintain a higher Voc, which is essential for maximizing the overall efficiency of the solar cell (Fig. 4 and Fig. 5 and Table 3).

In this study, we calculated the photovoltaic parameters based on the work function of the *Ag, Cu, Mo, C, Ni, Au, Pd* metal back contacts (Table 3). The quality of the back contact can significantly reduce carrier recombination at the contact interface. A well-engineered back contact forms a stable interface, reducing the chances of recombination of photogenerated electron-hole pairs. By minimizing recombination losses, the back contact enhances the charge carrier lifetime and boosts the power conversion efficiency of the solar cell. A low-resistance back contact lowers the series resistance (R_s) of the solar cell, which is crucial for improving the fill factor (FF). The reduction in series resistance allows for more efficient current flow through the device, enhancing the overall performance and power output of the solar cell. A well-designed back contact can also contribute to the long-term stability of the solar cell(Abdul Ameer, Jarad et al. 2024). Stable electrical contact between the p-type material and the back electrode ensures consistent performance over time, reducing degradation and improving the device's overall lifetime. As a result, in this study, the increase in the back contact work function (*Ag, Cu, Mo, C, Ni, Au, Pd*) contributes to overall improvements in the electrical performance and efficiency of the solar cell.

Table 3: The Photovoltaic Parameters of Au/p-CdTe/n-IGZO/i-ZnO/ITO Solar Cell based to the work function of Back Contact

Work Function	***V_{oc} (V)***	***J_{sc} (mA/cm^2)***	***FF (%)***	***η (%)***
Ag – (4.66 eV)	0.105	24.1345	31.08	1.126
Cu – (4.75 eV)	0.194	26.8882	45.23	3.370
Mo – (4.90 eV)	0.344	27.2090	60.67	8.109
C – (5.00 eV)	0.443	27.3251	66.89	11.586
Ni – (5.04 eV)	0.484	27.3677	68.76	13.004
Au – (5.1 eV)	0.543	27.4281	71.11	15.149
Pd – (5.2 eV)	0.640	27.5199	74.08	18.657

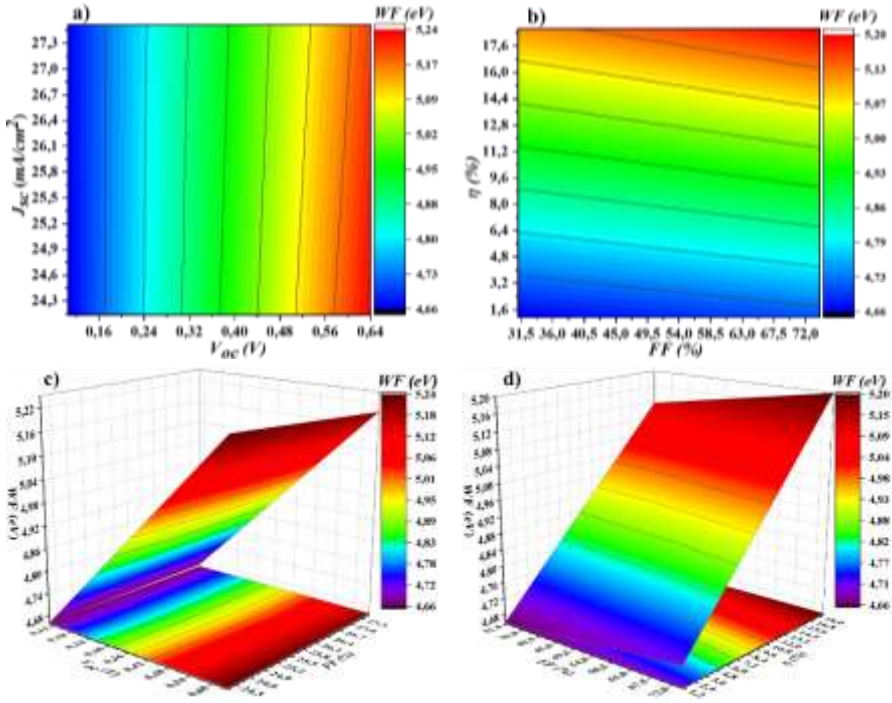

Figure 5: 2D and 3D contour plots of Photovoltaic Parameters of p-CdTe/n-IGZO Solar Cell based to the work function of Back Contacts

The Effect of the Operating Temperature on the Performance of p-CdTe/n-IGZO Solar Cells

In this study, the variation in photovoltaic parameters was investigated by increasing the operating temperature from 300 K to 360 K (Table4). As the temperature rises, the open-circuit voltage (V_{oc}) of the solar cell generally declines(Abdul Ameer, Jarad et al. 2024). This occurs because higher temperatures cause an increase in the intrinsic carrier concentration within the semiconductor material, which can lead to a shift in the energy bandgap. The reduction in V_{oc} lowers the potential difference between the two electrodes, which directly diminishes the overall voltage output of the solar cell. At elevated temperatures, the recombination of electron-hole pairs within the semiconductor increases. The increased thermal energy at higher temperatures enables more electrons to surmount the energy barriers, thereby enhancing the likelihood of recombination events. As a result, fewer free charge carriers are available for current generation, leading to a significant decline in the solar cell's efficiency(Garain, Basak et al. 2021, Talbi, Khaaissa et al. 2022).

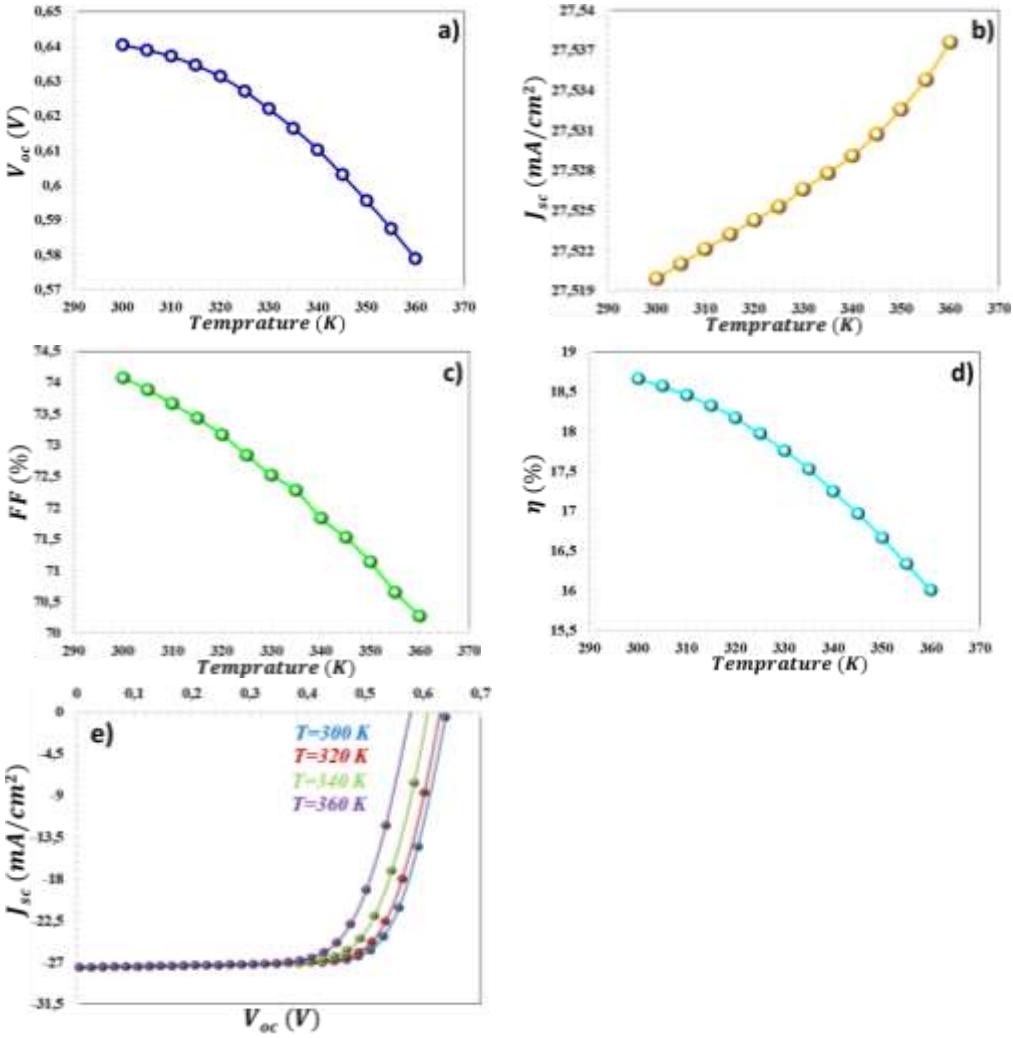

Figure 6: (a-d) The change plots illustrating the effect of operating temperature on the photovoltaic parameters and e) $J-V$ characteristic of Pd/p-CdTe/n-IGZO/i-ZnO/ITO Solar Cell based to the operating temperature

The fill factor (FF), which represents the maximum power output relative to the product of V_{oc}, typically decreases with rising temperatures. This phenomenon is attributed to the combined effects of a decrease in voltage and an increase in series resistance. As the temperature increases, both the resistance of the semiconductor material and the metal contacts rise, which contributes to a reduction in FF, and consequently, a decrease in the overall efficiency of the solar cell. Elevated temperatures lead to an increase in series resistance (R_s), which impedes the current flow through the solar cell. Similarly, shunt resistance decreases as the temperature increases, which can

lead to an increase in leakage current across the device. Both of these factors contribute to a further reduction in efficiency. As a result of the combined effects of reduced V_{oc}, increased recombination, decreased *FF*, the overall power conversion efficiency (*PCE*) of the solar cell is negatively affected by high operating temperatures (Fig 6 and Fig 7 and Table 4). In general, elevated temperatures lead to a reduction in the *PCE*, which is the primary indicator of a solar cell's ability to convert sunlight into electrical energy.

Table 4: The Photovoltaic Parameters of Pd/p-CdTe/n-IGZO/i-ZnO/ITO Solar Cell based to the operating temperature

Temperature (K)	***V_{oc} (V)***	***J_{sc} (mA/cm^2)***	***FF (%)***	***η (%)***
300 K	0.640	27.519	74.08	18.657
310 K	0.637	27.522	73.66	18.456
320 K	0.631	27.524	73.17	18.168
330 K	0.622	27.526	72.52	17.760
340 K	0.610	27.529	71.84	17.245
350 K	0.595	27.532	71.14	16.667
360 K	0.578	27.537	70.28	16.007

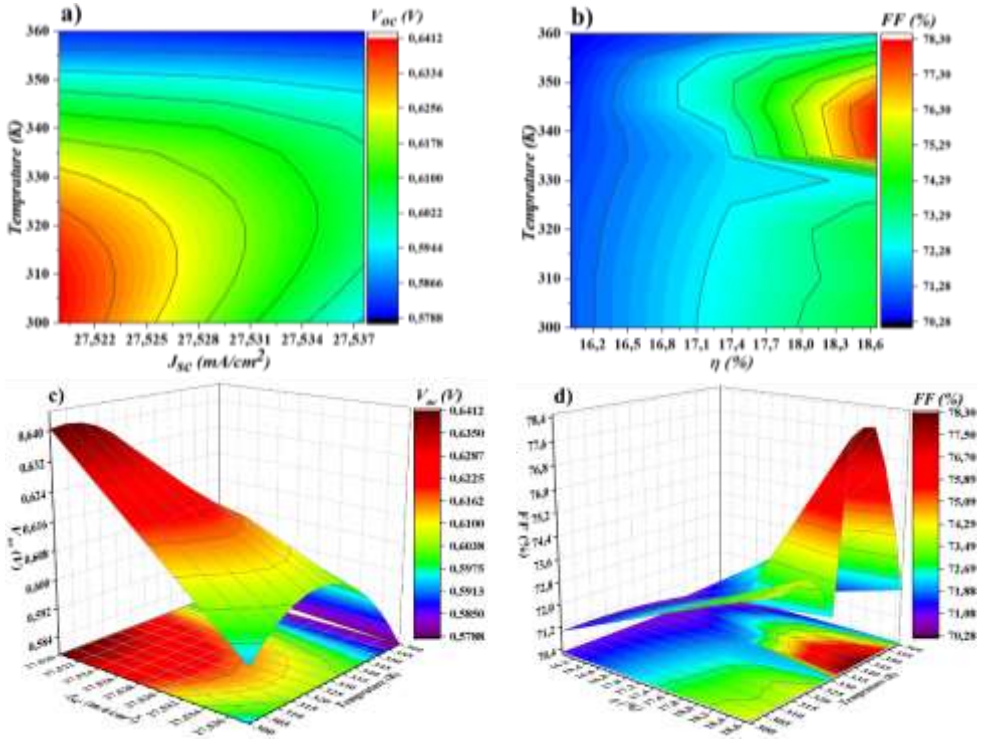

Figure 7: 2D and 3D contour plots of Photovoltaic Parameters of p-CdTe/n-IGZO Solar Cell based to the operating temperature

CONCLUSIONS

In this study, a p-CdTe/n-IGZO thin-film solar cell was numerically modeled and systematically analyzed using the SCAPS-1D simulation program. By incorporating experimentally reported IGZO thin-film properties and realistic material parameters for each device layer, the effects of shallow donor density in the IGZO layer, back contact work function, and operating temperature on the photovoltaic performance of the solar cell were comprehensively investigated. The simulation results demonstrate that the shallow donor density of the n-type IGZO layer plays a crucial role in determining device performance. An increase in donor density leads to enhanced free carrier concentration, improved electrical conductivity, reduced series resistance, and more efficient charge transport. Consequently, significant improvements were observed in key photovoltaic parameters, including short-circuit current density, fill factor, and power conversion efficiency. Furthermore, the work function of the back contact was found to have a pronounced impact on the performance of the p-CdTe/n-IGZO solar cell. Higher work function back contact materials facilitate favorable band alignment and efficient hole extraction while suppressing interfacial recombination losses. As a result, notable enhancements in open-circuit voltage, fill factor, and overall power conversion efficiency were achieved, with the highest efficiency obtained using high–work function metals. Increasing the operating temperature negatively affects device performance. Elevated temperatures lead to increased recombination rates, reduced open-circuit voltage, increased series resistance, and a decline in fill factor, ultimately resulting in a decrease in power conversion efficiency.

ACKNOWLEDGEMENTS

Authors would kindly like to thank to

- Dr. Marc Burgelman's group, University of Gent, Belgium for providing permission for us to use SCAPS-1D simulation program.

REFERENCES

Abdul Ameer, H. R., A. N. Jarad, K. H. Salem, H. S. Hadi, M. A. Alkhafaji, R. S. Zabibah, K. A. Mohammed, K. Kumar Saxena, D. Buddhi and H. Singh (2024). "A role of back contact and temperature on the parameters of CdTe solar cell." Advances in Materials and Processing Technologies **10**(2): 497-505.

Barbato, M., E. Artegiani, M. Bertoncello, M. Meneghini, N. Trivellin, E. Mantoan, A. Romeo, G. Mura, L. Ortolani and E. Zanoni (2021). "CdTe solar cells: technology, operation and reliability." Journal of Physics D: Applied Physics **54**(33): 333002.

Dalal, V. L. and P. Sharma (2005). "Defect density and diffusion length of holes in nanocrystalline silicon devices." Applied Physics Letters **86**(10).

Garain, R., A. Basak and U. P. Singh (2021). "Study of thickness and temperature dependence on the performance of SnS based solar cell by SCAPS-1D." Materials Today: Proceedings **39**: 1833-1837.

Ghosh, S., S. Porwal and T. Singh (2022). "Investigation of the role of back contact work function for hole transporting layer free perovskite solar cells applications." Optik **256**: 168749.

Houimi, A., S. Y. Gezgin, B. Mercimek and H. Ş. Kılıç (2021). "Numerical analysis of CZTS/n-Si solar cells using SCAPS-1D. A comparative study between experimental and calculated outputs." Optical Materials **121**: 111544.

Jahandardoost, M., C. Walkons and S. Bansal (2023). "Degradation behavior of CIGS solar Cells: A parametric analysis." Solar Energy **260**: 61-70.

Kennedy, J. H. and K. W. Frese (1978). "Flatband Potentials and Donor Densities of Polycrystalline α-Fe2 O 3 Determined from Mott-Schottky Plots." Journal of the Electrochemical Society **125**(5): 723.

Kumar, A. and A. D. Thakur (2018). "Role of contact work function, back surface field, and conduction band offset in Cu2ZnSnS4 solar cell." Japanese Journal of Applied Physics **57**(8S3): 08RC05.

Mishra, R., M. Anwar and M. Hasan (2025). "Performance evaluation of CdTe-based heterojunction solar cell with IGZO-based window layer and electron transport layer." Chalcogenide Letters **22**(10): 871-882.

Pathak, C. and S. K. Pandey (2020). "Design, performance, and defect density analysis of efficient eco-friendly perovskite solar cell." IEEE Transactions on Electron Devices **67**(7): 2837-2843.

Porwal, S., M. Paul, H. Dixit, S. Mishra and T. Singh (2022). "Investigation of defects in Cs2SnI6-based double perovskite solar cells via SCAPS-1D." Advanced Theory and Simulations **5**(9): 2200207.

Samiul Islam, M., K. Sobayel, A. Al-Kahtani, M. Islam, G. Muhammad, N. Amin, M. Shahiduzzaman and M. Akhtaruzzaman (2021). "Defect study and modelling of SnX3-based perovskite solar cells with SCAPS-1D." Nanomaterials **11**(5): 1218.

Shi, B., Y. Wang, J. Li, X. Zhang, J. Yan, S. Liu, J. Yang, Y. Pan, H. Zhang and J. Yang (2018). "n-Type Ohmic contact and p-type Schottky contact of monolayer InSe transistors." Physical Chemistry Chemical Physics **20**(38): 24641-24651.

Talbi, A., Y. Khaaissa, K. Nouneh, E. M. Feddi and M. El Haouari (2022). "Effects of temperature, thickness, electron density and defect density on ZnS based solar cells: SCAPS-1D simulation." Materials Today: Proceedings **66**: 116-121.

Xu, W., L. Hu, C. Zhao, L. Zhang, D. Zhu, P. Cao, W. Liu, S. Han, X. Liu and F. Jia (2018). "Low temperature solution-processed IGZO thin-film transistors." Applied Surface Science **455**: 554-560.

Yiğit, S., Y. Gündoğdu and H. Ş. Kılıç (2021). "Electrical Properties of The Heterojunction Diode Produced Based on IGZO Thin Film." Afyon Kocatepe Üniversitesi Fen Ve Mühendislik Bilimleri Dergisi **21**(2): 257-265.

The Effect of MoS_2 BSF Layer on the Efficiency of CIGS Thin-Film Solar Cell Modelled by SCAPS-1D Simulation

Serap YİĞİT GEZGİN[1]
Hamdi ŞÜKÜR KILIÇ[2]

1- Assoc. Prof. Dr.; Selcuk University Department of Physics, Faculty of Science. serap.gezgin@selcuk.edu.tr, ORCID No: 0000-0003-3046-6138
2- Prof. Dr.; Dokuz Eylül University, Department of Metallurgically and Materials Engineering, Faculty of Engineering. hamdisukur.kilic@deu.edu.tr ORCID No: 0000-0002-7546-4243

ABSTRACT

In this study, we modelled a CIGS thin-film solar cell fabricated using Pulsed Laser Deposition (PLD) technique, employing SCAPS-1D simulation software. Solar cell structure consists of a number of layers designed to be Mo/MoS_2/p-CIGS/n-CdS/i-ZnO/AZO, with the physical parameters provided. The photovoltaic performance, including open-circuit voltage (V_{oc}), short-circuit current density (J_{sc}), fill factor (FF), and efficiency (η), was analysed as a function of shallow acceptor density (N_a), interface defect density (N_t), and the thickness of MoS_2 back surface field (BSF) layer. Results indicate that as N_a increas' carrier collection efficiency enhances leading to some improvements in V_{oc}, FF, and the efficiency. In contrast, higher N_t densities reduce device performance by increasing charge carrier recombination at the interface. The thickness of MoS_2 BSF layer was found to positively impact performance, reducing recombination at the back surface. Additionally, the study examined the influence of series resistance (R_s), showing that increased R_s leads to a decrease in the fill factor and overall efficiency, even though V_{oc} and J_{sc} remain stable. These findings emphasize the importance of optimizing N_a, N_t, MoS_2 thickness, and R_s for enhancing the performance of CIGS-based thin-film solar cells.

Keywords – MoS2, BSF, Thin Film, Solar Cell, SCAPS-1D Simulation.

INTRODUCTION

Thin-film solar cells, especially Copper Indium Gallium Selenide (CIGS)-based cells have garnered significant attention in recent years due to their potential for high efficiency, low-cost production, and lightweight properties (Li, Qu et al. 2019). CIGS solar cells are considered one of the most promising candidates for the next generation of photovoltaic technology because of their excellent absorption properties and tunable band gap. However, the efficiency of these cells is heavily influenced by various factors, including material properties, layer interfaces, and defect densities within the solar cell structure (Rau and Schock 2005, Valencia, Conde et al. 2021).

In this study, we investigate the enhancement of performance in CIGS-based thin-film solar cells through the integration of a MoS_2 back surface field (BSF) layer. MoS_2, a two-dimensional (2D) material, has attracted significant attention for its exceptional electronic and optical characteristics, particularly its ability to improve charge carrier collection while minimizing recombination losses (Wang, Li et al. 2018). Due to its high carrier mobility, direct band gap, and the potential for effective energy band alignment with the underlying CIGS absorber, MoS_2 has shown

promise in mitigating back-surface recombination by reflecting minority carriers back into the active region. By systematically varying the thickness of MoS_2 layer, we aim to optimize its role as a BSF, enhancing the device's overall efficiency by minimizing carrier recombination at the back interface. This approach is expected to lead to significant improvements in the power conversion efficiency by reducing energy losses and improving the effective separation and transport of photo-generated charge carriers (Chakma, Islam et al. , Patel, Mishra et al. 2022).

Additionally, we explore the influence of shallow acceptor density (Na) and interface defect density (Nt) on photovoltaic (PV) performance. Shallow acceptors play a crucial role in improving charge carrier balance by enhancing hole transport, while interface defects can act as recombination centers, significantly degrading the performance of solar cell (Teixeira, Vieira et al. 2020).

This work uses SCAPS-1D simulation tool to model the electrical performance of CIGS thin-film solar cell and analyze the effects of various parameters on its efficiency. By examining these key factors, we seek to gain a better understanding of their impact on the overall performance and provide valuable insights for the design of more efficient CIGS-based solar cells.

RESULTS AND DISCUSSION

In this study, we modelled CIGS thin-film solar cell that we previously produced using PLD technique, utilizing SCAPS-1D simulation (Gezgin 2022). The physical parameters of layers *Mo/MoS_2/p-CIGS/n-CdS/i-ZnO/AZO* which constitute the structural components of solar cell, are presented in table 1. These parameters were input into the program, and the simulation was executed. The experimental parameters of CIGS semiconductor have been reported in our previous study. The PV parameters of solar cell have been calculated as a function of the acceptor shallow defect density (N_a), the interface defect density (N_t) and *MoS_2* back surface field (*BSF*) thickness.

Table 1. The electrical parameters of semiconductor layers formed Mo/MoS_2/p-CIGS/n-CdS/i-ZnO/AZO solar cell

Layers	AZO	i-ZnO	n-CdS	CIGS	MoS_2
Band Gap (eV)	3.3	3.3	2.4	1.37	1.70
Electron affinity (eV)	4.6	4.6	4.4	4	3.5
Dielectric permittivity (relative)	9	9	10	13.6	10
CB effective density of states (cm^{-3})	$2.20x10^{18}$	$2.20x10^{18}$	$1.80x10^{18}$	$2.20x10^{18}$	$2.20x10^{18}$
VB effective density of states (cm^{-3})	$1.80x10^{19}$	$1.80x10^{19}$	$2.40x10^{19}$	$1.8x10^{19}$	$1.8x10^{19}$
Electron/Hole thermal velocity (cm/s)	$1.00x10^{7}$	$1.00x10^{7}$	$1.00x10^{7}$	$1.00x10^{7}$	$1.00x10^{7}$
Electron/Hole mobility (cm^2/Vs)	100/25	100/25	100/25	25/40	100/20
Shallow donor density (cm^{-3})	$1.00x10^{20}$	$1.00x10^{5}$	$1.00x10^{18}$	0	0
Shallow acceptor density (cm^{-3})	0	0	0	$3x10^{15}$	$5x10^{15}$
Thickness (nm)	100	100	50	420	20-400

The band diagram of solar cell is provided in the figure 1. The MoS_2 layer acts as a Back Surface Field (BSF), and a spike-like band structure has formed between CIGS and MoS_2 layers. Furthermore, a cliff-like band structure has emerged between CIGS and CdS layers. The presence of a cliff-like band structure in solar cell is crucial because it creates a significant potential barrier that impedes the recombination of charge carriers, particularly electrons. This barrier enhances the efficiency of charge collection by ensuring that the electrons generated in CIGS layer are effectively separated and prevented from recombining with holes in CdS layer. Additionally, the cliff-like band alignment can improve the overall power conversion efficiency by optimizing the interface between the CIGS and CdS layers, minimizing energy losses, and enhancing the performance of solar cell under operational conditions.

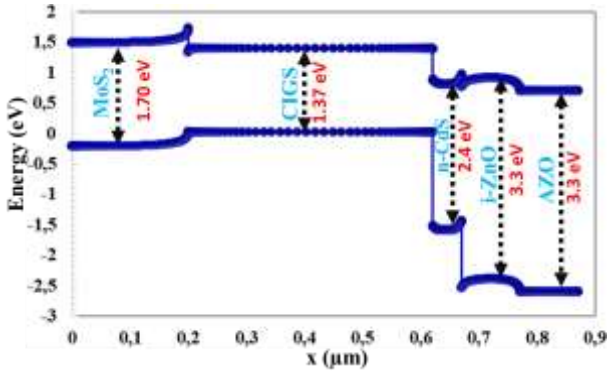

Figure 1: The band diagram of Mo/MoS_2/p-CIGS/n-CdS/i-ZnO/AZO solar cell

The Impact of Shallow Acceptor Density (N_a) on Mo/p-CIGS/n-CdS/i-ZnO/AZO Solar Cell Performance

Shallow acceptor density (N_a) refers to the concentration of shallow acceptor states in a semiconductor material, typically near the valence band. In semiconductors, acceptors are impurity atoms that create energy states just above the valence band when introduced into the material. These acceptor states can accept electrons from the valence band, effectively creating "holes" (the absence of electrons) that act as charge carriers (Meyer, Sann et al. 2005, Kim, Jo et al. 2015).

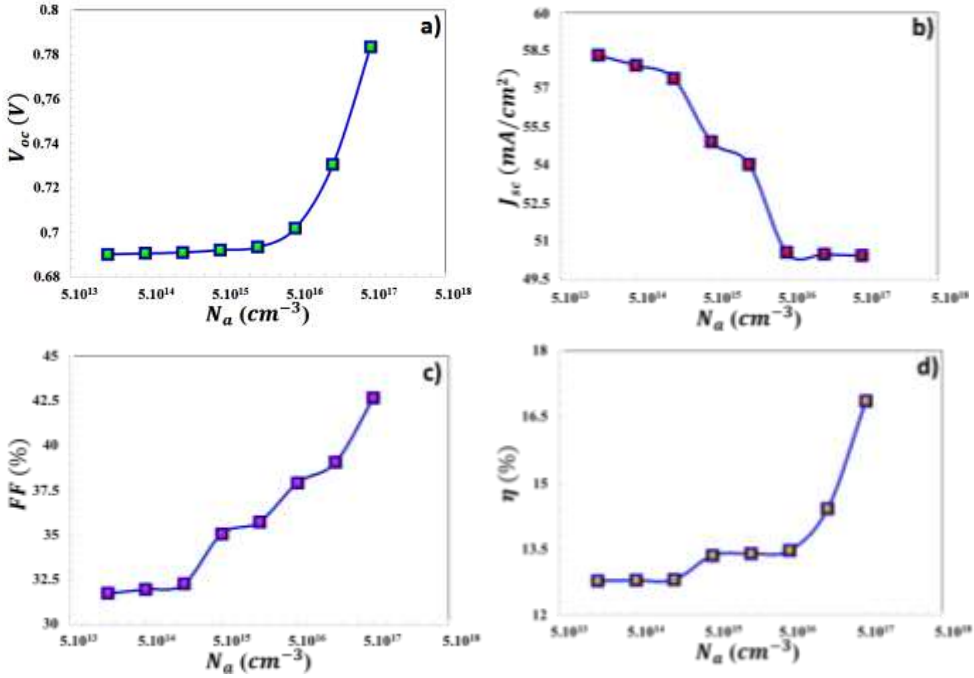

Figure 2: Variation Spectra in PV Parameters of Mo/p-CIGS/n-CdS/i-ZnO/AZO Solar Cell with Respect to N_a Value

As seen in Fig. 2 and 2D and 3D contour plots in Fig.3 and the data presented in Table 1, the parameters of V_{oc}, FF, and efficiency have shown an increase as a function of N_a density. The important effect of shallow acceptor density in a solar cell is that it enhances the overall carrier collection efficiency by effectively controlling the hole concentration near p-n junction. Shallow acceptors introduce energy levels just above the valence band, which facilitates the easy capture of holes, thereby improving hole transport and reducing recombination losses. This leads to higher V_{oc} and overall device performance, as the shallow acceptor states contribute to better charge carrier balance and enhanced electrical conductivity at the junction. Additionally, the controlled doping with shallow acceptors can optimize the carrier dynamics and ensure a more efficient extraction of photogenerated charge carriers in the solar cell (Frisk, Platzer-Björkman et al. 2014).

Table 2: The Variation in PV Parameters of Mo/p-CIGS/n-CdS/i-ZnO/AZO Solar Cell with Respect to Na Value

N_a (cm^{-3})	V_{oc} (V)	J_{sc} (mA/cm^2)	FF (%)	η (%)
1.10^{14}	0.6901	58.3367	31.75	12.7833
5.10^{14}	0.6905	57.9439	31.98	12.7976
1.10^{15}	0.6909	57.4321	32.27	12.8099
5.10^{15}	0.6920	54.9538	35.08	13.3620
1.10^{16}	0.6933	54.0574	35.75	13.4033
5.10^{16}	0.7019	50.5871	37,93	13.4705
1.10^{17}	0,7305	50,5199	39,07	14,4233
5.10^{17}	0.7835	50.4679	42.65	16.8666

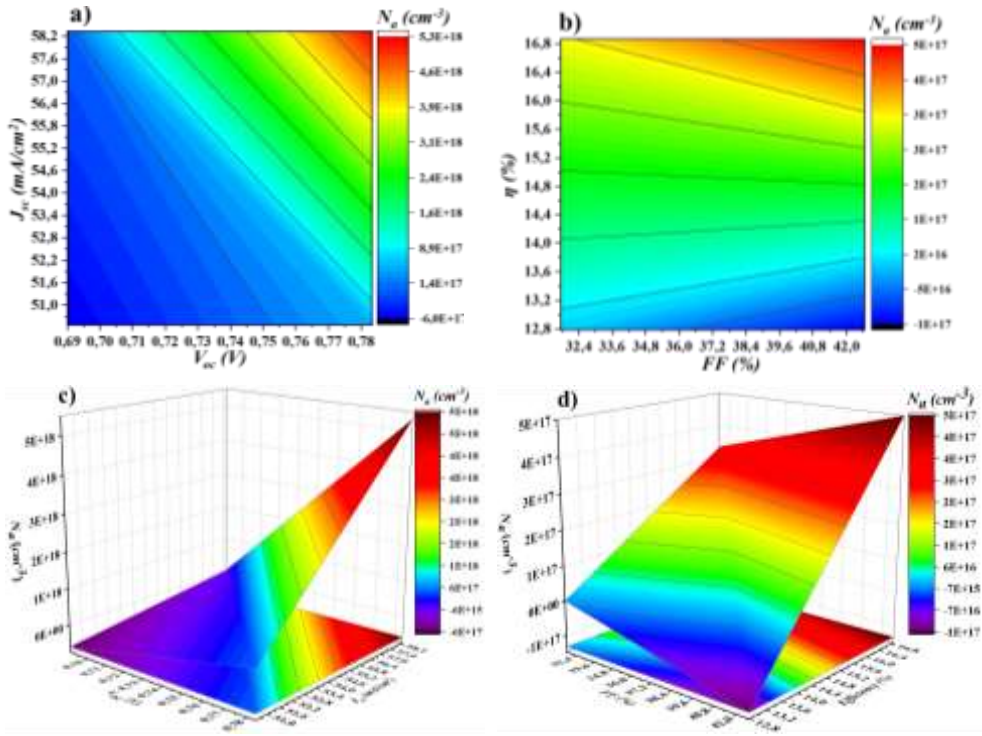

Figure 3: (a-b) 2D and (c-d) 3D countour plots of PV Parameters of Mo/p-CIGS/n-CdS/i-ZnO/AZO Solar Cell depending to N_a Value

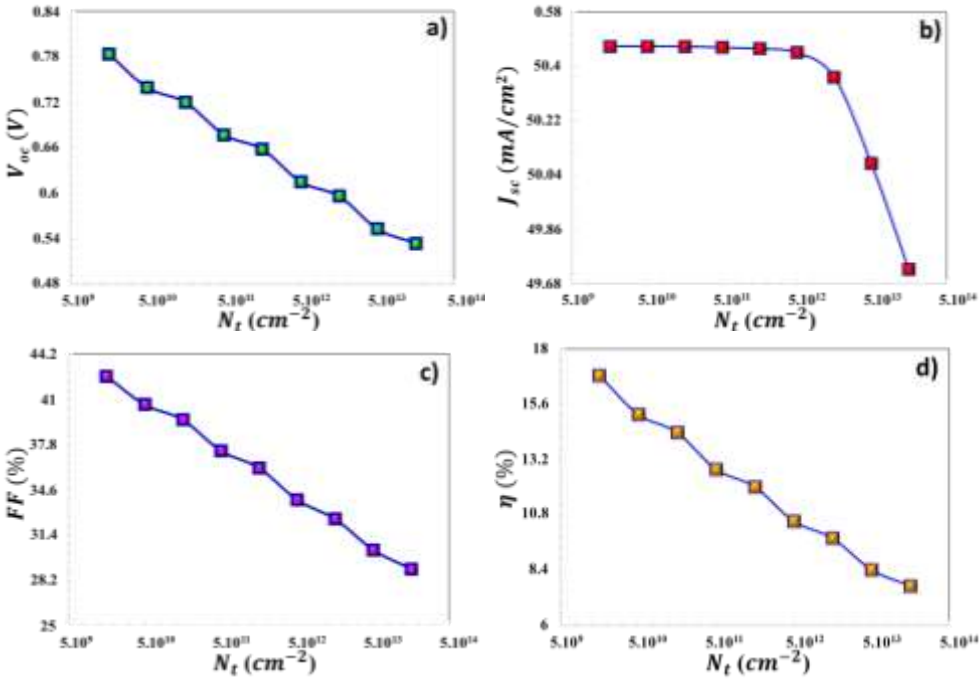

Figure 4: Variation Spectra in PV Parameters of Mo/p-CIGS/n-CdS/i-ZnO/AZO Solar Cell with Respect to N_t Value

As demonstrated in Fig. 4, along with 2D and 3D contour plots in Fig. 5 and the data summarized in Table 3, the parameters of V_{oc}, J_{sc}, FF, and efficiency exhibit a decline with increasing N_t density. Interface defect density (N_t) plays a critical role in determining the device's performance. A high interface defect density at the junction between different materials, such as between the absorber layer and the charge transport layers, can lead to several detrimental effects. These defects act as recombination centers for photo-generated charge carriers (electrons and holes), leading to an increase in carrier recombination rates (Kesavan, Rao et al. 2017). This results in a reduction in the carrier lifetime and a lower charge collection efficiency. Specifically, at the interface of a solar cell, defects can introduce deep states in the band gap, which trap charge carriers before they can contribute to the photocurrent. The presence of these trapped carriers reduces V_{oc} and FF, ultimately lowering the overall power conversion efficiency. Furthermore, these defects can create localized electric fields that hinder the efficient transport of charge carriers, further exacerbating the loss mechanisms. The impact of interface defect density is particularly pronounced in thin-film and

multi-junction solar cells, where the interface quality directly influences the charge transport and recombination dynamics. As a result, minimizing the interface defect density through material optimization, surface passivation, and careful fabrication processes is crucial for enhancing the performance and efficiency of solar cells

Table 3: The Variation in PV Parameters of Mo/p-CIGS/n-CdS/i-ZnO/AZO Solar Cell with Respect to N_t Value

N_t (cm^2)	V_{oc} (V)	J_{sc} (mA/cm^2)	FF (%)	η (%)
1.10^{10}	0.7835	50.4679	42.65	16.8666
5.10^{10}	0.7392	50.4676	40.64	15.1650
1.10^{11}	0.7199	50.4672	39.57	14.3789
5.10^{11}	0.6773	50.4639	37.37	12.7764
1.10^{12}	0.6582	50.4597	36.16	12.0119
5.10^{12}	0.6153	50.4469	33.89	10.5182
1.10^{13}	0.5965	50.3664	32.53	9.7785
5.10^{13}	0.5533	50.0804	30.35	8.4106
1.10^{14}	0.5346	49.7302	29.00	7.7105

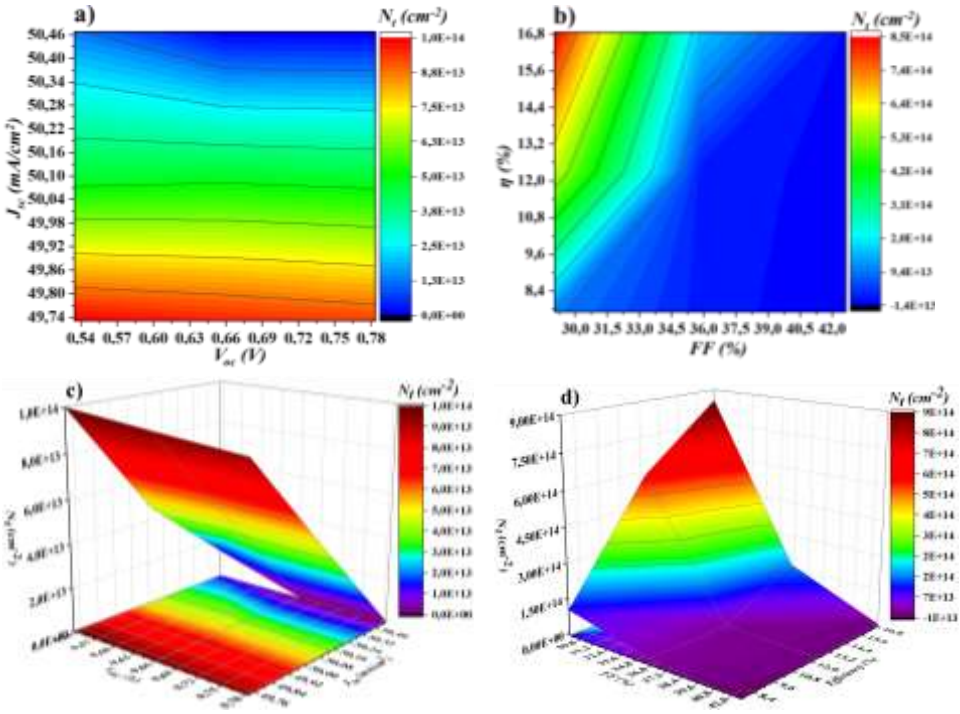

Figure 5: (a-b) 2D and (c-d) 3D countour plots of PV Parameters of Mo/p-CIGS/n-CdS/i-ZnO/AZO Solar Cell depending to N_t Value

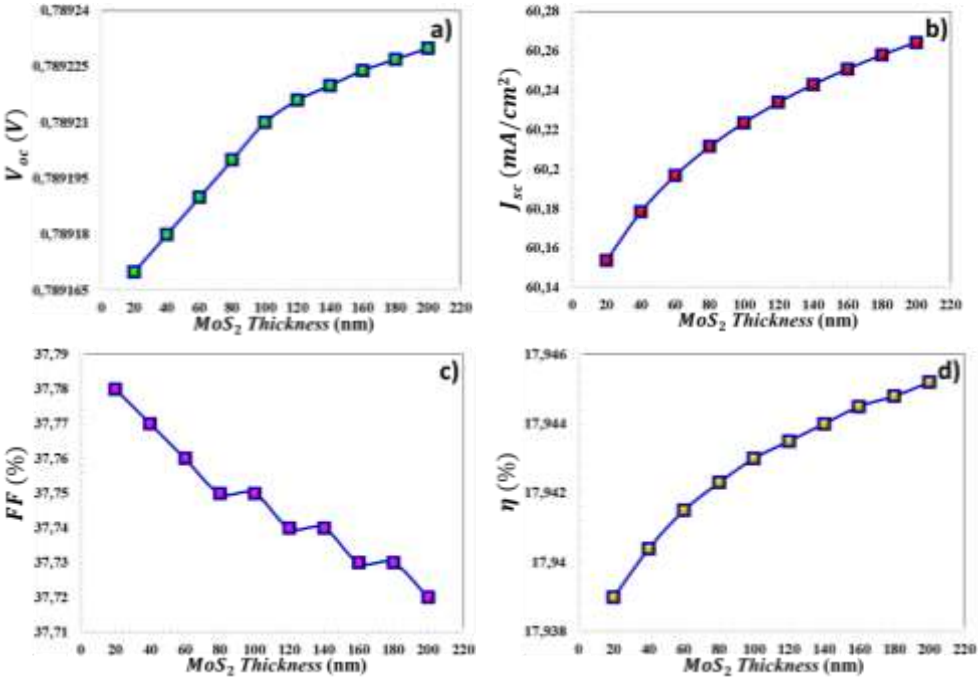

Figure 6: Variation Spectra in PV Parameters of Mo/MoS_2/p-CIGS/n-CdS/i-ZnO/AZO Solar Cell with Respect to MoS_2 thickness

In this study, the thickness of MoS_2 layer used as the Back Surface Field (BSF) in CIGS thin film solar cell was varied from 20 nm to 200 nm, and PV parameters of solar cell were calculated. As illustrated in Figure 6, in conjunction with 2D and 3D contour plots presented in Figure 7, and the data compiled in Table 4, as the thickness of MoS_2 increases, an improvement in the performance of the solar cell has been observed. So, MoS_2 layer is likely used as a back surface field (BSF) layer in solar cell. The purpose of BSF layer is to enhance the efficiency of the device by reducing the recombination of charge carriers (electrons and holes) at the back surface. This effect is crucial for improving the overall device performance.

The graph in Fig. 1 indicates that MoS_2 has an energy band gap of approximately 1.7 eV. MoS_2, being a two-dimensional material, provides excellent electrical properties such as high carrier mobility and low recombination rates. In the diagram, it can be observed that the conduction band of MoS_2 aligns favorably with the other layers (e.g., CIGS, n-CdS, etc.). This favorable band alignment helps in the formation of a barrier that

can reflect minority carriers back into the active region of the device, reducing recombination losses and thus improving the overall performance. This helps in improving V_{oc} and FF, thereby enhancing the overall power conversion efficiency.

Table 4: The Variation in PV Parameters of Mo/MoS_2/p-CIGS/n-CdS/i-ZnO/AZO Solar Cell with Respect to MoS_2 thickness

MoS_2 Thickness (nm)	***V_{oc} (V)***	***J_{sc} (mA/cm²)***	***FF (%)***	***η (%)***
20	0.789171	60.1538	37.78	17.9390
40	0.789182	60.1785	37.77	17.9404
60	0.789190	60.1969	37.76	17.9415
80	0.789202	60.2115	37.75	17.9423
100	0.789210	60.2236	37.75	17.9430
120	0.789216	60.2339	37.74	17.9435
140	0.789223	60.2429	37.74	17.9440
160	0.789224	60.2508	37.73	17.9445
180	0.789227	60.2579	37.73	17.9448
200	0.789231	60.2643	37.72	17.9452

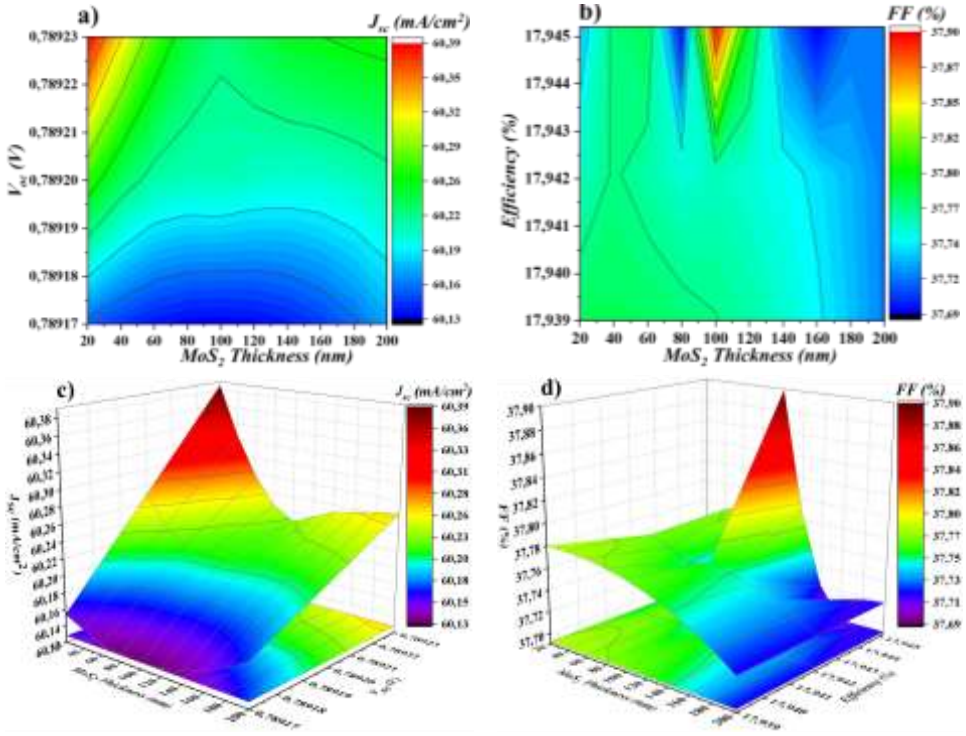

Figure 7: (a-b) 2D and (c-d) 3D countour plots of PV Parameters of Mo/MoS2/p-CIGS/n-CdS/i-ZnO/AZO Solar Cell depending MoS_2 thickness

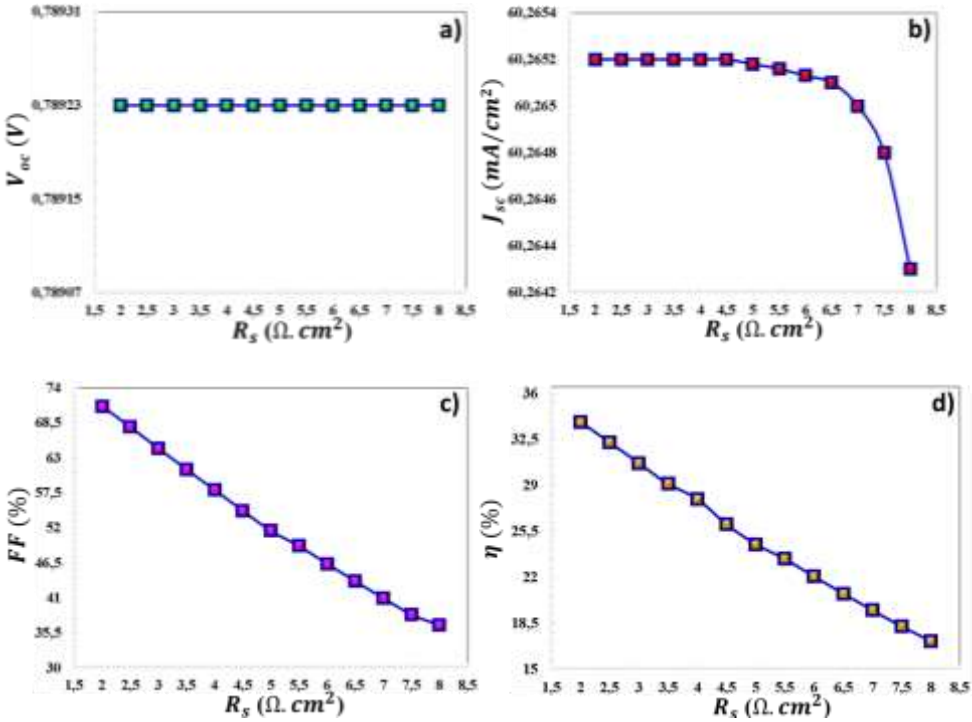

Figure 8: Variation Spectra in PV Parameters of Mo/MoS_2/p-CIGS/n-CdS/i-ZnO/AZO Solar Cell with Respect to (R_s) Serial Resistance

As depicted in Figure 8 and 10, along with the corresponding 2D and 3D contour plots shown in Figure 9 and the data summarized in Table 5 while V_{oc} remained unaffected with increasing series resistance, but other PV parameters exhibited a noticeable decline. Series resistance mainly impacts the fill factor, an essential parameter in assessing the efficiency of solar cells. As the series resistance rises, the fill factor diminishes because of higher voltage losses during current flow. While the V_{oc} and I_{sc} are less directly affected by series resistance, the overall power output is still reduced due to the lower current extracted from the cell under load conditions (Servaites, Yeganeh et al. 2010, Green 2016). V_{oc} and I_{sc} parameters typically remain stable even with an increase in series resistance, particularly in high-quality cells. Nevertheless, the overall power output is still notably impacted due to the decrease in the effective current that can be drawn from the cell. As series resistance rises, the fill factor decreases due to the losses that occur as current passes through the internal resistances of the device. These losses cause a reduction in the voltage at the maximum power point

(V_{max}), which in turn lowers the overall efficiency. In practical terms, an increase in series resistance leads to a more significant drop in current as voltage increases, resulting in a lower fill factor. An increase in series resistance results in some decrease in the maximum power output (P_{max}), mainly due to the reduced fill factor. As the fill factor declines, the overall efficiency of the solar cell is also affected, even if Voc and Isc remain relatively high.

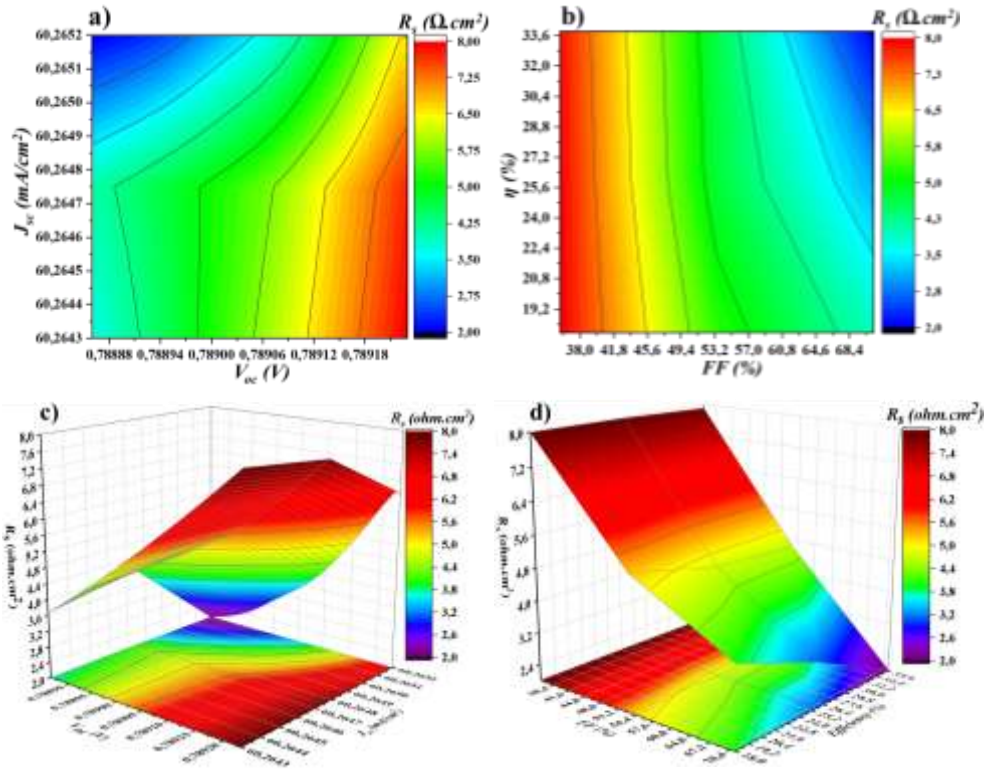

Figure 9: (a-b) 2D and (c-d) 3D countour plots of PV Parameters of Mo/MoS_2/p-CIGS/n-CdS/i-ZnO/AZO Solar Cell dependig to (R_s) Serial Resistance

Table 5: The Variation in PV Parameters of Mo/MoS_2/p-CIGS/n-CdS/i-ZnO/AZO Solar Cell with Respect to (R_s) Serial Resistance

R_s ($\Omega.cm^2$)	V_{oc} (V)	J_{sc} (mA/cm^2)	FF (%)	η (%)
8	0.78923	60.2643	36.72	17.1452
7,5	0.78923	60.2646	38.39	18.2594
7	0.78923	60.2647	40.97	19.4905
6,5	0.78923	60.2648	43.64	20.7567
6	0.78923	60.2649	46.37	22.0578
5,5	0.78923	60,2650	49.18	23.3938
5	0.78923	60,2651	51.55	24.5186
4,5	0.78923	60,2652	54.73	26.0308
4	0.78923	60,2652	57.96	27.9610
3,5	0.78923	60,2652	61.22	29.1152
3	0.78923	60,2652	64.53	30.6862
2,5	0.78923	60,2652	67.88	32.2756
2	0.78923	60,2652	71.15	33.8295

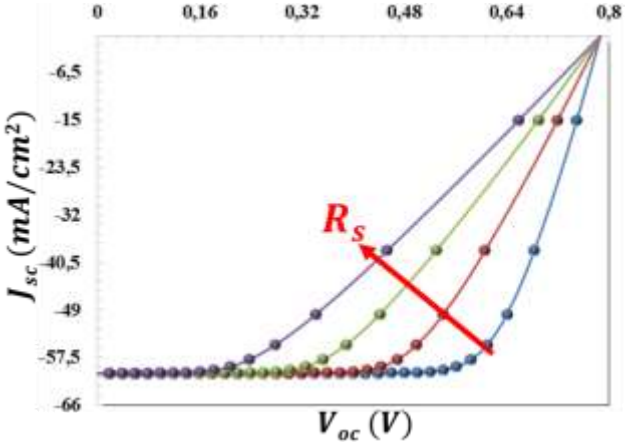

Figure 10: J-V characteristic of Mo/MoS_2/p-CIGS/n-CdS/i-ZnO/AZO Solar Cell dependig to (R_s) Serial Resistance

CONCLUSIONS

This study explores the performance enhancement of CIGS-based thin-film solar cells by incorporating a MoS_2 BSF layer, using SCAPS-1D simulation software. The results show that the integration of a MoS_2 layer can significantly improve PV performance of CIGS solar cells. Specifically, MoS_2 BSF layer reduces recombination at the back surface, enhancing carrier collection efficiency and thereby increasing Voc, FF, and overall power conversion efficiency.

The analysis of shallow acceptor density (N_a) revealed that increasing N_a improves hole transport and reduces recombination, leading to enhanced efficiency. In contrast, a higher interface defect density (N_t) was found to degrade the performance by introducing recombination centers that reduce carrier lifetime and hinder charge transport. Furthermore, the optimization of MoS_2 layer thickness plays a vital role, with thicker layers proving to be more effective in mitigating back-surface recombination and improving efficiency.

The study also examined the effect of series resistance (R_s), which was shown to reduce the fill factor and efficiency as R_s increases, despite minimal effects on Voc and J_{sc}. This highlights the importance of reducing series resistance to achieve optimal performance.

In conclusion, the findings underscore the significant role of MoS_2 as a BSF material in CIGS-based thin-film solar cells. Optimizing parameters such as N_a, N_t, MoS_2 thickness, and R_s is crucial for improving the efficiency of these devices. These insights are valuable for the design and development of high-efficiency thin-film solar cells in the future.

ACKNOWLEDGEMENTS

Authors would kindly like to thank to

- Dr. Marc Burgelman's group, University of Gent, Belgium for providing permission for us to use SCAPS-1D simulation program.
- Selçuk University, Scientific Research Projects Coordination (BAP) Unit for grands via projects with references of 21406007

REFERENCES

Chakma, S. D., S. Islam and M. J. J. Rashid "Parametric Variation in Mose2 Back Surface Layer to Study the Effect of Recombination of a Cigs Solar Cell." Available at SSRN 4985619.

Frisk, C., C. Platzer-Björkman, J. Olsson, P. Szaniawski, J. Wätjen, V. Fjällström, P. Salomé and M. Edoff (2014). "Optimizing Ga-profiles for highly efficient Cu (In, Ga) Se2 thin film solar cells in simple and complex defect models." Journal of Physics D: Applied Physics **47**(48): 485104.

Gezgin, S. Y. (2022). "Modelling and investigation of the electrical properties of CIGS/n-Si heterojunction solar cells." Optical Materials **131**: 112738.

Green, M. A. (2016). "Accurate expressions for solar cell fill factors including series and shunt resistances." Applied physics letters **108**(8).

Kesavan, A. V., A. D. Rao and P. C. Ramamurthy (2017). "Interface electrode morphology effect on carrier concentration and trap defect density in an organic photovoltaic device." ACS Applied Materials & Interfaces **9**(34): 28774-28784.

Kim, G. Y., W. Jo, K. D. Lee, H.-S. Choi, J. Y. Kim, H.-Y. Shin, T. T. T. Nguyen, S. Yoon, B. S. Joo and M. Gu (2015). "Optical and surface probe investigation of secondary phases in Cu2ZnSnS4 films grown by electrochemical deposition." Solar Energy Materials and Solar Cells **139**: 10-18.

Li, H., F. Qu, H. Luo, X. Niu, J. Chen, Y. Zhang, H. Yao, X. Jia, H. Gu and W. Wang (2019). "Engineering CIGS grains qualities to achieve high efficiency in ultrathin Cu (InxGa1− x) Se2 solar cells with a single-gradient band gap profile." Results in Physics **12**: 704-711.

Meyer, B., J. Sann, D. Hofmann, C. Neumann and A. Zeuner (2005). "Shallow donors and acceptors in ZnO." Semiconductor Science and Technology **20**(4): S62.

Patel, A. K., R. Mishra and S. K. Soni (2022). "Performance enhancement of CIGS solar cell with two dimensional MoS2 hole transport layer." Micro and Nanostructures **165**: 207195.

Rau, U. and H.-W. Schock (2005). Cu (In, Ga) Se2 thin-film solar cells. Solar Cells, Elsevier**:** 303-349.

Servaites, J. D., S. Yeganeh, T. J. Marks and M. A. Ratner (2010). "Efficiency enhancement in organic photovoltaic cells: consequences of optimizing series resistance." Advanced Functional Materials **20**(1): 97-104.

Teixeira, J. P., R. B. Vieira, B. P. Falcao, M. Edoff, P. M. Salome and J. P. Leitao (2020). "Recombination channels in Cu (In, Ga) Se2 thin films: impact of the ga-profile." The Journal of Physical Chemistry C **124**(23): 12295-12304.

Valencia, D., J. Conde, A. Ashok, C. Meza-Avendaño, H. Vilchis and S. Velumani (2021). "Optimization of Cu (In, Ga) Se2 (CIGSe) thin film solar cells parameters through numerical simulation and experimental study." Solar Energy **224**: 298-308.

Wang, H., C. Li, P. Fang, Z. Zhang and J. Z. Zhang (2018). "Synthesis, properties, and optoelectronic applications of two-dimensional MoS 2 and MoS 2-based heterostructures." Chemical Society Reviews **47**(16): 6101-6127.

Chalcone Derivates as Antioxidant Agents: Synthesis, Mechanism And Structure–Activity Relationships

Fatma ÇOBAN[1]

1- Assistant Professor (Dr.), Department of Chemistry, Faculty of Arts and Sciences, Burdur Mehmet Akif Ersoy University (MAKÜ), Burdur, Türkiye. fatmaakkus@mehmetakif.edu.tr / ORCID No:0000-0003-4266-211X

ABSTRACT

Chalcones constitute an important class of α, β-unsaturated carbonyl compounds and can be considered open-chain precursors of flavonoids. Their simple synthesis, structural diversity and strong electron delocalization make them attractive scaffolds for the development of antioxidant agents. This chapter provides an overview of chalcone derivatives with antioxidant activity, covering synthetic approaches, mechanisms of action and structure–activity relationships. Classical Claisen–Schmidt condensations and more recent eco-friendly methods, such as microwave-assisted, solvent-free and heterogeneous catalytic routes, are summarized. The main in vitro assay protocols employed to evaluate their antioxidant properties, including DPPH (2,2-diphenyl-1-picrylhydrazyl), ABTS (2,2'-azino-bis(3-ethylbenzothiazoline-6-sulfonic acid)), FRAP (ferric reducing antioxidant power), and CUPRAC (cupric ion reducing antioxidant capacity) assays, metal-chelating and lipid peroxidation assays, are critically discussed. Special emphasis is placed on how the number and position of hydroxyl and methoxy groups, electron-donating, and electron-withdrawing substituents, heteroaromatic rings and extended π-conjugation influence radical scavenging capacity and reducing power. Selected examples from recent literature, together with case studies from our own research, are used to illustrate general trends and to highlight promising lead structures. Finally, current limitations, including solubility, stability, bioavailability and the frequent gap between in vitro and in vivo data, are addressed. Future perspectives for the rational design of multifunctional chalcone-based antioxidants are outlined, with a particular focus on strategies that combine strong radical scavenging ability with suitable pharmacokinetic properties.

Keywords: Chalcone derivatives, Antioxidant activity, Free radical scavenging, Structure–activity relationship (SAR), DPPH and ABTS assays, Reducing power, Flavonoid precursors

---

1. INTRODUCTION

1.1. Chalcones and their place in flavonoid chemistry

Chalcones are a well-known group of open-chain flavonoids characterized by the presence of an α, β-unsaturated carbonyl system connecting two aromatic or heteroaromatic rings (commonly referred to as the A and B rings). Structurally, they can be described by the general formula Ar–CO–CH=CH–Ar', where Ar and Ar' may include various substituents such as hydroxyl, methoxy, halogen, nitro or alkyl groups, as well as heterocycles like thiophene, pyrrole, indole or carbazole (Kaur et al. 2021), (Rudrapal et al.

2021). In biosynthetic pathways, chalcones are key intermediates in the formation of flavanones and other flavonoid subclasses (Adhikari et al. 2025).

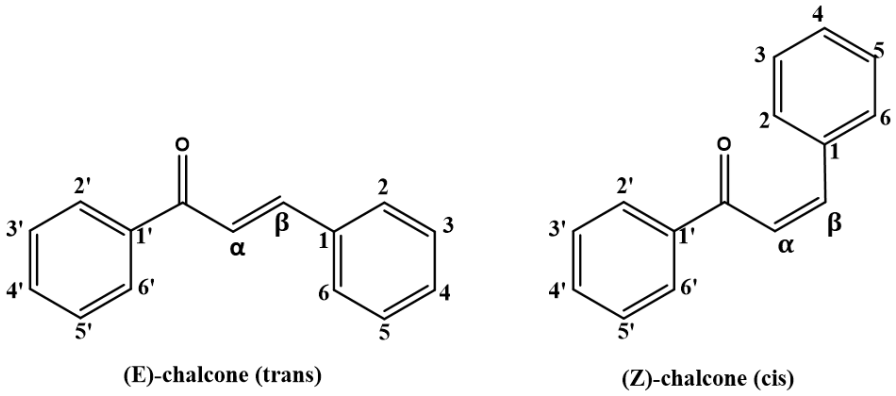

Figure 1. Chemical structures of trans- and cis-chalcone.

Their conjugated enone system provides strong electron delocalization and makes them responsive to subtle structural modifications. As a result, chalcones exhibit a wide range of biological activities, including antioxidant, anti-inflammatory, antimicrobial, antitumor, anti-diabetic, and enzyme inhibitory effects (Goyal and Kaur 2021), (Kaur et al. 2021). Among these, antioxidant activity is one of the most extensively investigated due to the central role of oxidative stress in disease development and aging (Mezgebe, Melaku, and Mulugeta 2023), (Elkanzi et al. 2022).

1.2. Oxidative stress and the relevance of antioxidant agents

Reactive oxygen species (ROS), including hydrogen peroxide (H_2O_2), superoxide anion ($O_2^{\bullet -}$) and hydroxyl radical (•OH), together with reactive nitrogen species (RNS) such as peroxynitrite ($ONOO^-$) and nitric oxide (NO•), are constantly generated in living organisms as side products of normal metabolic processes (Rudrapal et al. 2021). Under physiological conditions, endogenous antioxidant defenses, including enzymatic systems (superoxide dismutase, catalase, glutathione peroxidase) and non-enzymatic molecules (glutathione, uric acid, vitamins C and E), keep ROS/RNS levels under tight control (Hong et al. 2024).

Oxidative stress occurs when this delicate balance is disrupted, either by increased ROS generation or weakened antioxidant defenses. Persistent oxidative stress triggers damage to lipids, proteins, nucleic acids and cellular organelles, ultimately contributing to the initiation and progression of many chronic and degenerative diseases. Therefore, the search for exogenous antioxidant molecules that can complement or restore redox balance remains

a key strategy in medicinal chemistry and pharmacology (Chandimali et al. 2025).

1.3. Advantages of chalcones as antioxidant scaffolds

Chalcones offer several advantages as candidate antioxidant agents:
Ease of synthesis: Simple condensation processes between suitable aldehydes and ketones can typically generate them in good amounts.
High structural tunability: Electron density, solubility, and steric characteristics can be altered by functionalizing the aromatic rings with various substituents (Zhuang et al. 2017).
Conjugated π-system: The prolonged conjugation promotes radical stability and redox activity by facilitating the effective delocalization of unpaired electrons.
Multifunctionality: Additional biological effects like anti-inflammatory or enzyme inhibition are frequently supported by the same structural characteristics that give rise to antioxidant activity, making multifunctional agents possible. These characteristics make chalcones a great starting point for methodical research on the structure-activity link that aims to comprehend and maximize antioxidant function (Goyal and Kaur 2021).

2. SYNTHETIC APPROACHES TO ANTIOXIDANT CHALCONES

2.1. Classical Claisen–Schmidt condensation

The Claisen-Schmidt condensation, which yields the equivalent α,β-unsaturated carbonyl molecule when an aromatic aldehyde and an aromatic ketone react under basic circumstances, is the most popular synthetic route to chalcones. In ethanol, methanol, or aqueous alcoholic environments, a substituted benzaldehyde is usually condensed with an acetophenone derivative when sodium or potassium hydroxide are present. The main products of the reaction are typically E-configured chalcones, which are produced at room temperature or with mild heating (Popatkar et al. 2025), (Erik et al. 2025).
This method's simplicity, affordability, and tolerance to a variety of substituents make it very appealing. The aldehyde and ketone components of antioxidant chalcones are frequently selected to have phenolic hydroxyl groups (such as 4-hydroxybenzaldehyde, 2,4-dihydroxybenzaldehyde, 2-hydroxy-4-methoxybenzaldehyde, 4-hydroxyacetophenone, or related derivatives), which are known to greatly increase the capacity to scavenge radicals (Lahsasni, Al Korbi, and Aljaber 2014).

.

2.2. Solvent-free and green synthesis strategies

In line with green chemistry principles, numerous alternative protocols have been developed for chalcone synthesis. Solvent-free or solid-state reactions, typically accomplished by simple milling or heating, can significantly reduce solvent consumption and chemical waste (Marotta et al. 2022), (Palleros 2004), (K. Saini et al. 2005). Microwave-assisted methods can further accelerate chalcone formation, improving both yield and selectivity (Baqi and Ismail 2025). Additionally, ionic liquids and deep eutectic solvents can function simultaneously as reaction media and catalysts, providing reversible systems in some cases, while heterogeneous catalysts such as basic alumina, zeolites, clays, or metal oxides have been successfully used to promote chalcone formation under milder conditions and with easier processing(Kunde et al. 2009), (Kumar et al. 2021), (Shntaif 2016), (Baqi and Ismail 2025), (Rodica et al. 2022). These environmentally friendly strategies can be easily combined with the addition of functional groups related to antioxidant activity, thus providing an efficient platform for the rapid preparation of various chalcone libraries (Adnan et al. 2020).

2.3. Incorporation of heteroaromatic and functional groups

To enhance antioxidant performance or broaden application areas, chalcones can be designed to incorporate heteroaromatic rings or additional functional parts. For example, heteroaromatic rings such as thiophene, pyrrole, or indole can be added to broaden conjugation and modify electronic properties. Electron-donating groups (e.g., –OH, $–OCH_3$, $–N(CH_3)_2$) are often placed in para or ortho positions to increase electron density and hydrogen-donating ability (Ardiansah 2019), (Sönmez, Gür, and Şahin 2023). Electron-withdrawing groups (e.g., –Cl, $–NO_2$, $–CF_3$) can tune redox potentials and influence radical stabilization patterns (Prabhakar, Iqbal, and Balasubramanian 2016), (Ohkatsu and Satoh 2008). Large substituents or flexible linkers can be used to alter conformational preferences and interactions with biomolecules or membranes. In this context, numerous antioxidant chalcones have been reported, demonstrating how rational synthetic design can direct the electronic and steric environment to support desired redox properties (Mezgebe et al. 2023), (Ardiansah 2019), (Sivakumar, Prabhakar, and Doble 2011).

3. IN VITRO ANTIOXIDANT ASSAYS FOR CHALCONE DERIVATIVES

3.1. Free radical scavenging assays (DPPH, ABTS and related methods)

The antioxidant activity of chalcone derivatives is usually first evaluated using simple in vitro radical scavenging tests. Among these, DPPH and ABTS tests are the most popular due to their ease and reproducibility (Floegel et al. 2011).
DPPH test: The stable 2,2-diphenyl-1-picrylhydrazyl radical (DPPH•) exhibits a dark purple color with a strong absorption band around 517 nm. When it reacts with a hydrogen or electron-donating antioxidant, DPPH• is reduced to the corresponding hydrazine, leading to a decrease in absorption. The degree of this reduction is proportional to the scavenging capacity of the compound being tested. Results are usually expressed as IC50 values (concentration required to reduce absorbance by 50%) or Trolox equivalents (Brand-Williams, Cuvelier, and Berset 1995).
ABTS test: In the ABTS (2'-azinobis-(3-ethylbenzothiazoline-6-sulfonic acid) method, the $ABTS^{\bullet+}$ radical cation is formed (usually via oxidation with potassium persulfate), and a blue-green solution showing absorption around 734 nm is obtained. Antioxidants reduce $ABTS^{\bullet+}$, leading to a spectrophotometrically observable color change. This test is suitable for both hydrophilic and lipophilic antioxidants and is usually expressed in Trolox equivalent antioxidant capacity (TEAC) units (Re et al. 1999).
Depending on the desired mechanistic information, other radical scavenging tests, such as superoxide, hydroxyl, or nitric oxide scavenging tests, can also be applied.

3.2. Reducing power and metal-chelation assays

In addition to direct radical scavenging, chalcones can operate as antioxidants by reducing oxidized species or chelating redox-active metalions. Reducing power tests (e.g., FRAP or CUPRAC) assess a compound's ability to reduce Fe^{3+} to Fe^{2+} or Cu^{2+} to Cu^{+}, resulting in the creation of colored complexes that can be detected spectrophotometrically. Higher absorbance readings suggest a better reduction capacity (Apak et al. 2007).
Metal chelation assays assess chalcones' ability to bind transition metal ions such as Fe^{2+} or Cu^{2+}, which catalyze the formation of hydroxyl radicals via Fenton-type reactions. Chelation can block these activities, indirectly reducing oxidative damage.
Phenolic chalcones with correctly positioned donor atoms (for example, neighboring hydroxyl groups) may exhibit strong metal-binding properties, which contribute to their overall antioxidant profile (Pérez-González et al. 2022).

3.3. Lipid peroxidation and cell-based models

Chalcones are also being tested in lipid peroxidation models and cell-based systems to better simulate biological settings.
Lipid peroxidation assays (e.g., TBARS= thiobarbituric acid reactive substances) measure the generation of secondary oxidation products from polyunsaturated fatty acids, such as malondialdehyde (MDA) (Aguilar Diaz De Leon and Borges 2020). The presence of chalcones reduces MDA production, indicating protection against lipid oxidation.
Cell-based tests may involve measuring intracellular ROS levels, cell viability, mitochondrial activity, or oxidative damage indicators in cultured cells subjected to oxidative stress. These models are more complicated and time-consuming than basic chemical testing, but they yield more physiologically meaningful data (Jomova et al. 2023), (Sikander et al. 2011).

4. STRUCTURE–ACTIVITY RELATIONSHIPS (SAR) IN ANTIOXIDANT CHALCONES

4.1. Effect of hydroxyl and methoxy substitution patterns

One of the most critical determinants of antioxidant activity in chalcones is the presence, number, and position of hydroxyl and methoxy groups on the aromatic rings. Generally:

- Phenolic hydroxyl groups act as hydrogen donors, neutralizing free radicals and forming resonance-stabilized phenoxyl radicals.
- Ortho- and para-dihydroxy patterns can provide additional stabilization via intramolecular hydrogen bonding and extended delocalization.
- Methoxy groups can modulate electron density and lipophilicity; o-methylation of OH groups sometimes reduce hydrogen-donating ability but may improve membrane permeability (Ardiansah 2019).

For many chalcones, derivatives with 4-hydroxy, 3,4-dihydroxy or 2,4-dihydroxy substitution patterns exhibit significantly enhanced radical scavenging and reducing power compared to unsubstituted analogues. However, excessive substitution may decrease stability or complicate synthesis (Erik et al. 2025).

4.2. Influence of electron-donating and electron-withdrawing groups

Electron-donating groups such as –OH, $–OCH_3$ or $–NR_2$ typically increase the electron density of the aromatic ring, lower the dissociation energy of O–H bonds, and promote the formation of stabilized radicals. This often enhances antioxidant activity, particularly in hydrogen atom transfer mechanisms.

Electron-withdrawing groups such as $–NO_2$, $–CF_3$ or halogens can have more complex effects. In some cases, they reduce electron density and hydrogen-donating ability; in others, they stabilize the resulting radical through inductive or resonant effects. For example, chlorine and fluorine can subtly modulate the redox potential without completely suppressing the activity. The final result depends on the precise arrangement of the substituting group and its position relative to the enon system (Ohkatsu and Satoh 2008), (Sönmez et al. 2023).

4.3. Role of heteroaromatic rings and extended conjugation

The addition of heteroaromatic rings (thiophene, pyridine, furan, indole, carbazole, and others) to the chalcone skeleton expands conjugation and introduces additional heteroatoms that can participate in redox processes or non-covalent interactions. Such modifications can: a) alter absorption and emission wavelengths, potentially enabling combined antioxidant and sensing functions (Mahesha, Shetty, and Kulkarni 2025); b) influence bioavailability and localization in biological systems by altering lipophilicity and membrane affinity; c) stabilize oxidized forms of molecules by providing alternative radical delocalization pathways (Wangngae et al. 2021). For example, extended π-conjugation by linking multiple aromatics or heteroaromatic units can further stabilize radical intermediates and enhance overall antioxidant capacity. However, highly conjugated systems can also suffer from poor water solubility, which must be addressed in molecular design.

4.4. Computational insights into antioxidant mechanisms

Computational chemistry, particularly density functional theory (DFT), has become an important tool to rationalize the antioxidant behavior of chalcones (Sivakumar et al. 2011). Calculated parameters such as:
- Bond dissociation enthalpies (BDE) of O–H bonds,
- Ionization potentials (IP),
- Electron affinity (EA),
- HOMO–LUMO energy gaps,
- Spin density distribution in radical species

provide valuable information on the preferred mechanisms (hydrogen atom transfer, single-electron transfer followed by proton transfer, or sequential proton loss–electron transfer) and help identify the most reactive positions within a molecule. By correlating experimental antioxidant data with computed descriptors, researchers can derive predictive SAR models and guide the design of new chalcone derivatives with optimized properties (Sivakumar et al. 2011), (Wang et al. 2015).

5. HIGHLIGHTED EXAMPLES FROM THE LITERATURE

5.1. Phenolic chalcones with enhanced radical scavenging activity

Many studies have demonstrated that chalcones bearing catechol-type moieties (3,4-dihydroxy) or related phenolic patterns display pronounced DPPH and ABTS scavenging activity, often comparable to or exceeding that of reference antioxidants such as Trolox or ascorbic acid. In these molecules, the combination of intramolecular hydrogen bonding, conjugation with the enone system and resonance stabilization of the resulting phenoxyl radicals plays a key role.
Modifying one of the hydroxyl groups to a methoxy substituent may slightly reduce direct radical scavenging but improve lipophilicity and biological membrane penetration, illustrating the delicate balance between intrinsic reactivity and pharmacokinetic properties (Wang et al. 2015).

5.2. Chalcones with Dual Antioxidant and Enzyme Inhibitory Properties

Some chalcone derivatives are designed to function not only as direct antioxidants but also as inhibitors of enzymes associated with oxidative stress and inflammation, such as cyclooxygenases, lipoxygenases, or monoamine oxidases. In these cases, the chalcone skeleton often carries both phenolic functions for radical scavenging and additional substituents to interact with enzyme active sites (Jomova et al. 2023), (Popatkar et al. 2025).
Such dual-functional molecules can provide synergistic benefits by simultaneously reducing ROS levels and modulating key biochemical pathways. They also highlight the potential of chalcones as templates for multi-target drug design (Toublet, Laurent, and Pouget 2025).

5.3. Heteroaromatic Chalcones and Redox-Activated Materials

For example, heteroaromatic chalcones containing thiophene, pyrrole, or carbazole units can exhibit interesting electrochemical and optical properties in addition to antioxidant activity. Redox behaviors can be tuned for potential applications such as electroactive materials, sensors, or organic electronics, where antioxidant properties can help stabilize devices under oxidative conditions (Wang et al. 2015),(Kostopoulou et al. 2021).
These examples demonstrate that antioxidant chalcones are not limited to classical pharmacological fields but can also contribute to functional materials chemistry by bridging the gap between biological activity and advanced material design.

6. FROM PRESENT LIMITATIONS TO FUTURE OPPORTUNITIES: A PATH FORWARD

Despite significant progress in the synthesis and evaluation of antioxidant chalcones, several challenges remain:

- Solubility and stability: Many chalcones are poorly soluble in water and may undergo degradation under physiological pH or light exposure, limiting their practical use.
- Bioavailability and metabolism: Even compounds with excellent in vitro antioxidant profiles may suffer from low oral absorption, rapid metabolism or limited tissue distribution.
- Complex in vivo environment: Antioxidant effects in living systems depend on numerous factors, including localization, interaction with biomolecules, competition with endogenous antioxidants and the dynamic nature of ROS/RNS generation.

To address these issues, future research should focus on:

- Designing chalcones with balanced lipophilicity and polarity to improve absorption and distribution.
- Exploring prodrug strategies or formulation approaches (e.g., nanoparticles, liposomes, inclusion complexes) to enhance stability and bioavailability.
- Developing multifunctional chalcones that combine antioxidant activity with other relevant properties, such as anti-inflammatory or metal-chelating effects.
- Integrating computational modeling and high-throughput screening to accelerate the discovery of optimized lead compounds.
- The combination of synthetic creativity, mechanistic understanding and advanced biological evaluation is expected to yield new chalcone-based antioxidants with genuine therapeutic or technological potential.

7. CONCLUSION

Chalcone derivatives represent a versatile and powerful class of molecules for the development of antioxidant agents. Their simple synthesis, rich structural diversity, and conjugated π-systems offer ample opportunities for fine-tuning their redox properties and exploring multiple mechanisms of action. Systematic studies on substitution patterns, heteroaromatic incorporation, and extended conjugation have revealed clear structure-activity relationships, particularly highlighting the importance of phenolic hydroxyl groups and overall electron distribution.

By combining traditional in vitro experiments with computational investigations and more physiologically relevant models, the field has gained a deeper understanding of how chalcones exhibit antioxidant effects and how

these can be enhanced. Looking to the future, the rational design of multifunctional chalcone-based compounds, supported by modern synthetic and formulation technologies, will open new avenues in both medicinal chemistry and functional materials science.

In summary, chalcones stand out as promising, tunable scaffold structures for next-generation antioxidants, with the potential to make significant contributions to strategies aimed at controlling oxidative stress and its far-reaching biological consequences

REFERENCE

Adhikari, Suman, Priyatosh Nath, Vishal Kumar Deb, Niranjan Das, Antara Banerjee, and Surajit Pathak. 2025. "Pharmacological Potential of Natural Chalcones : A Recent Studies and Future Perspective." *Front. Pharmacol.,* 16:1–51. doi: 10.3389/fphar.2025.1570385.

Adnan, Duha, Bijender Singh, Surinder Kumar Mehta, Vinod Kumar, and Ramesh Kataria. 2020. "Simple and Solvent Free Practical Procedure for Chalcones: An Expeditious, Mild and Greener Approach." *Current Research in Green and Sustainable Chemistry* 3:100041. doi: 10.1016/j.crgsc.2020.100041.

Aguilar Diaz De Leon, Jesús, and Chad R. Borges. 2020. "Evaluation of Oxidative Stress in Biological Samples Using the Thiobarbituric Acid Reactive Substances Assay." *Journal of Visualized Experiments* 2020(159):1–21. doi: 10.3791/61122.

Apak, Reşat, Kubilay Güçlü, Birsen Demirata, Mustafa Özyürek, Saliha Esin Çelik, Burcu Bektaşoğlu, K. Işil Berker, and Dilek Özyurt. 2007. "Comparative Evaluation of Various Total Antioxidant Capacity Assays Applied to Phenolic Compounds with the CUPRAC Assay." *Molecules* 12(7):1496–1547. doi: 10.3390/12071496.

Ardiansah, Bayu. 2019. "Chalcones Bearing N, O, and S-Heterocycles: Recent Notes on Their Biological Significances." *Journal of Applied Pharmaceutical Science* 9(8):117–29. doi: 10.7324/JAPS.2019.90816.

Baqi, Younis, and Ahmed Hussein Ismail. 2025. "Microwave-Assisted Synthesis of Near-Infrared Chalcone Dyes: A Systematic Approach." *ACS Omega* 10(7):7317–26. doi: 10.1021/acsomega.4c11066.

Brand-Williams, W., M. E. Cuvelier, and C. Berset. 1995. "Use of a Free Radical Method to Evaluate Antioxidant Activity." *LWT - Food Science and Technology* 28(1):25–30. doi: 10.1016/S0023-6438(95)80008-5.

Chandimali, Nisansala, Seon Gyeong Bak, Eun Hyun Park, Hyung-jin Lim, Yeong-seon Won, and Eun-kyung Kim. 2025. "Free Radicals and Their Impact on Health and Antioxidant Defenses : A Review." *Cell Death Discovery* 11(19). doi: 10.1038/s41420-024-02278-8.

Elkanzi, Nadia A. A., Hajer Hrichi, Ruba A. Alolayan, Wassila Derafa, Fatin M. Zahou, and Rania B. Bakr. 2022. "Synthesis of Chalcones Derivatives and Their Biological Activities : A Review." *ACS Omega* 7:27769–86. doi: 10.1021/acsomega.2c01779.

Erik, Zeynep, İshak Erik, Can Özgür Yalçin, Sıla Özlem Şener, Şengül Alpay Karaoğlu, Gizem Tatar Yilmaz, Nurettin Yayli, and Rezzan Aliyazicioğlu.

2025. “Evaluation of Synthesized Methoxy Chalcones for Therapeutic Potential through in Vitro and in Silico Methods.” *Journal of Research in Pharmacy* 29(4):1693–1711. doi: 10.12991/jrespharm.1734661.

Floegel, Anna, Dae Ok Kim, Sang Jin Chung, Sung I. Koo, and Ock K. Chun. 2011. “Comparison of ABTS/DPPH Assays to Measure Antioxidant Capacity in Popular Antioxidant-Rich US Foods.” *Journal of Food Composition and Analysis* 24(7):1043–48. doi: 10.1016/j.jfca.2011.01.008.

Goyal, Kamya, and Rajwinder Kaur. 2021. “Chalcones : A Review on Synthesis and Pharmacological Activities.” *Journal of Applied Pharmaceutical Science* 11(Supp 1):1–14. doi: 10.7324/JAPS.2021.11s101.

Hong, Yuhang, Alessandra Boiti, Daniela Vallone, and Nicholas S. Foulkes. 2024. “Reactive Oxygen Species Signaling and Oxidative Stress : Transcriptional Regulation and Evolution.” *Antioxidants* 13:312. doi: https://doi.org/10.3390/antiox13030312.

Jomova, Klaudia, Renata Raptova, Suliman Y. Alomar, Saleh H. Alwasel, Eugenie Nepovimova, Kamil Kuca, and Marian Valko. 2023. *Reactive Oxygen Species, Toxicity, Oxidative Stress, and Antioxidants: Chronic Diseases and Aging*. Vol. 97. Springer Berlin Heidelberg.

K. Saini, K. Rajendra, S. Amit Choudhary, Yogesh. C. Joshi, and P. Joshi. 2005. “Solvent Free Synthesis of Chalcones and Their Antibacterial Activities.” *Journal of Chemistry* 2(4):224–27. doi: 10.1155/2005/294094.

Kaur, Ramanjeet, Lubna Aslam, Shajaat Hussain, Nisha Kapoor, and Ritu Mahajan. 2021. “Flavonoid Biosynthetic Pathway : Genetics and Biochemistry.” *Biosciences Biotechnology Research Asia* 18(2):271–86. doi: http://dx.doi.org/10.13005/bbra/2914 (Received:

Kostopoulou, Ioanna, Andromachi Tzani, Nestor Ioannis Polyzos, Maria Anna Karadendrou, Eftichia Kritsi, Eleni Pontiki, Thalia Liargkova, Dimitra Hadjipavlou-Litina, Panagiotis Zoumpoulakis, and Anastasia Detsi. 2021. “Exploring the 2′-Hydroxy-Chalcone Framework for the Development of Dual Antioxidant and Soybean Lipoxygenase Inhibitory Agents.” *Molecules* 26(9). doi: 10.3390/molecules26092777.

Kumar, Aniket, Lipeeka Rout, L. Satish K. Achary, Sangram Keshari Mohanty, Pratap Sagar Nayak, Bapun Barik, and Priyabrat Dash. 2021. “Solvent Free Synthesis of Chalcones over Graphene Oxide-Supported MnO2 Catalysts Synthesized via Combustion Route.” *Materials Chemistry and Physics* 259:124019. doi: 10.1016/j.matchemphys.2020.124019.

Kunde, Lalita B., Swapna M. Gade, Vishwanath S. Kalyani, and Sunil P. Gupte. 2009. “Catalytic Synthesis of Chalcone and Flavanone Using Zn-Al Hydrotalcite Adhere Ionic Liquid.” *Catalysis Communications* 10(14):1881–88. doi: 10.1016/j.catcom.2009.06.018.

Lahsasni, Siham A., Faeza H. Al Korbi, and Nabilah Abdel Aziz Aljaber. 2014. “Synthesis, Characterization and Evaluation of Antioxidant Activities of Some Novel Chalcones Analogues.” *Chemistry Central Journal* 8(1):1–10. doi: 10.1186/1752-153X-8-32.

Mahesha, Priyanka, Nitinkumar S. Shetty, and Suresh D. Kulkarni. 2025. “Effect of Conjugation Length on the Photophysical Properties of Naphthyl Chalcones: A DFT and Experimental Study.” *Discover Applied Sciences* 7(1102). doi: 10.1007/s42452-025-07076-0.

Marotta, Ludovica, Sara Rossi, Roberta Ibba, Simone Brogi, Vincenzo Calderone, Stefania Butini, Giuseppe Campiani, and Sandra Gemma. 2022. “The Green Chemistry of Chalcones: Valuable Sources of Privileged Core Structures for Drug Discovery.” *Frontiers in Chemistry* 10(988376):1–22. doi: 10.3389/fchem.2022.988376.

Mezgebe, Kibrom, Yadessa Melaku, and Endale Mulugeta. 2023. “Synthesis and Pharmacological Activities of Chalcone and Its Derivatives Bearing N-Heterocyclic Scaffolds: A Review.” *ACS Omega* 8:19194–211. doi: https://doi.org/10.1021/acsomega.3c01035.

Ohkatsu, Yasukazu, and Takuma Satoh. 2008. “Antioxidant and Photo-Antioxidant Activities of Chalcone Derivatives.” *Journal of the Japan Petroleum Institute* 51(5):298–308. doi: 10.1627/jpi.51.298.

Palleros, Daniel R. 2004. “Solvent-Free Synthesis of Chalcones.” *Journal of Chemical Education* 81(9):1345–47. doi: 10.1021/ed081p1345.

Pérez-González, Adriana, Romina Castañeda-Arriaga, Eduardo Gabriel Guzmán-López, Luis Felipe Hernández-Ayala, and Annia Galano. 2022. “Chalcone Derivatives with a High Potential as Multifunctional Antioxidant Neuroprotectors.” *ACS Omega* 7(43):38254–68. doi: 10.1021/acsomega.2c05518.

Popatkar, Bhushan B., Sandeep Yadav, Satish B. Manjare, and Vikas V. Borge. 2025. “Green Methods for the Synthesis of Chalcones: An Overview with Appraisal to Sustainable Development and Bioactive Compounds.” *Organic Communications* 18(2):38–59. doi: 10.25135/acg.oc.189.2504.3495.

Prabhakar, Visakh, Hiba Iqbal, and Ranganathan Balasubramanian. 2016. “Antioxidant Studies on Monosubstituted Chalcone Derivatives-Understanding Substituent Effects.” *Pakistan Journal of Pharmaceutical Sciences* 29(1):165–71.

Re, Roberta, Nicoletta Pellegrini, Anna Proteggente, Ananth Pannala, Min Yang, and Catherine Rice-Evans. 1999. “Antioxidant Activity Applying an Improved ABTS Radical Cation Decolorization Assay.” *Free Radical Biology and Medicine* 26(9–10):1231–37. doi: 10.1016/S0891-5849(98)00315-3.

Rodica, Z., Madalina Tudorache, Vasile I. Parvulescu, Bogdan Cojocaru, and Octavian D. Pavel. 2022. “New MgFeAl-LDH Catalysts for Claisen–Schmidt Condensation.” *Molecules* 27:8391.

Rudrapal, Mithun, Johra Khan, Abdul Aziz, Bin Dukhyil, Randa Mohammed, Ibrahim Ismail, Emmanuel Ifeanyi Attah, Tripti Sharma, Shubham Jagdish Khairnar, and Atul Rupchand Bendale. 2021. “Chalcone Scaffolds , Bioprecursors of Flavonoids : Chemistry, Bioactivities, and Pharmacokinetics.” *Molecules* 26(23):7177. doi: 10.3390/molecules26237177.

Shntaif, Ahmed Hassen. 2016. “Green Synthesis of Chalcones under Microwave Irradiation.” *International Journal of ChemTech Research* 9(2):36–39.

Sikander, Mohammad, Shabnam Malik, Deepak Yadav, Sahabuddin Biswas, Deepshikha Pande Katare, and Swatantar Kumar Jain. 2011. “Cytoprotective Activity of a Trans-Chalcone against Hydrogen Peroxide Induced Toxicity in Hepatocellular Carcinoma (HepG2) Cells.” *Asian Pacific Journal of Cancer Prevention* 12(10):2513–16.

Sivakumar, P. M., P. K. Prabhakar, and M. Doble. 2011. “Synthesis, Antioxidant Evaluation, and Quantitative Structure-Activity Relationship Studies of

Chalcones." *Medicinal Chemistry Research* 20(4):482–92. doi: 10.1007/s00044-010-9342-1.

Sönmez, Fatih, Tuğçe Gür, and Zuhal Şahin. 2023. "Thiophenyl-Chalcone Derivatives: Synthesis, Antioxidant Activity, FMO Energies and Molecular Parameters." *Balıkesir Üniversitesi Fen Bilimleri Enstitüsü Dergisi* 25(1):293–304. doi: 10.25092/baunfbed.1119869.

Toublet, François Xavier, Aurélie Laurent, and Christelle Pouget. 2025. "A Review of Natural and Synthetic Chalcones as Anticancer Agents Targeting Topoisomerase Enzymes." *Molecules* 30(12):2498. doi: 10.3390/molecules30122498.

Wang, Guirong, Yunsheng Xue, Lin An, Youguang Zheng, Yunyan Dou, Ling Zhang, and Yi Liu. 2015. "Theoretical Study on the Structural and Antioxidant Properties of Some Recently Synthesised 2,4,5-Trimethoxy Chalcones." *Food Chemistry* 171:89–97. doi: 10.1016/j.foodchem.2014.08.106.

Wangngae, Sirilak, Kantapat Chansaenpak, Jukkrit Nootem, Utumporn Ngivprom, Sirimongkon Aryamueang, Rung Yi Lai, and Anyanee Kamkaew. 2021. "Photophysical Study and Biological Applications of Synthetic Chalcone-Based Fluorescent Dyes." *Molecules* 26(10):2979. doi: 10.3390/molecules26102979.

Zhuang, Chunlin, Wen Zhang, Chunquan Sheng, Wannian Zhang, Chengguo Xing, and Zhenyuan Miao. 2017. "Chalcone : A Privileged Structure in Medicinal Chemistry." *Chemical Reviews* 117(12):7762–7810. doi: 10.1021/acs.chemrev.7b00020.

Anatomical and Morphological Characteristics of Some Cestode Species

Mehmet Zeynel ELBAY[1]

Mehmet Oğuz ÖZTÜRK[2]

1- Expert Biologist; Afyon Kocatepe University, Faculty of Science and Literature, Department of Molecular Biology and Genetics, Afyonkarahisar, Türkiye zeynelelbay@hotmail.com ORCID No: 0000-0003-3893-571X

2- Prof. Dr.; Afyon Kocatepe University, Faculty of Science and Literature, Department of Molecular Biology and Genetics, Afyonkarahisar, Türkiye oozturk@aku.edu.tr ORCID No: 0000-0001-7263-3585

ABSTRACT

Parasitism is an important factor in shaping the structure of ecological communities in natural environments. One of the parasite groups commonly found in fish populations is cestodes. These parasites can cause weight loss, growth retardation, developmental anomalies, and mortality in their hosts. Therefore, accurate identification of cestode species is essential for the protection of fish health and the control of parasitic infections. In this study, a total of 66 *Squalius recurvirostris* specimens captured from the Düzağaç–Akdeğirmen Dam Lake in Afyonkarahisar were examined for cestode infections. As a result of the study, *Caryophyllaeides fennica* was detected in the intestinal lumen, *Paradilepis scoleciana* in the mesentery of the body cavity, and *Dilepis unilateralis* in the gall bladder. *Caryophyllaeides fennica* is a moderately sized cestode species consisting of a single segment and possesses a tongue-shaped scolex. The posterior lobes of the ovary in this species are convexly fused, and the eggs are oval, thin-shelled, and operculated. The cysticercus of *Paradilepis scoleciana* has an oval body and consists of a scolex bearing four suckers and a hooked rostellum. In this species, the disc-shaped rostellum located at the median-terminal position of the scolex bears two rows of hooks. The hooks in the upper row measured 112–113 µm, while those in the lower row measured 78–80 µm in length. The cysticercus of *Dilepis unilateralis* is conical in shape. The scolex has four lateral suckers located subterminally. A short, conical rostellum bearing two rows of hooks is present at the median-terminal position. The hooks in the upper row measured 25–26 µm, whereas those in the lower row measured 15–16 µm in length. In conclusion, three cestode species were identified in *S. recurvirostris* from the Düzağaç–Akdeğirmen Dam Lake. The anatomical and morphological characteristics of these species were described in detail, and the data obtained from this study aim to contribute to the recognition and knowledge of these cestode parasites.

Keywords – Caryophyllaeides fennica, Dilepis unilateralis, Paradilepis scoleciana, Squalius recurvirostris

---

INTRODUCTION

It is well known that parasitism is one of the factors affecting the structure of populations that constitute communities. One of the taxa commonly observed in fish populations is cestodes. Cestodes can cause weight loss, growth retardation, developmental anomalies, and mortality in host organisms (Mouritsen and Poulin, 2002).

It is emphasized that the similarities and differences among the parasite communities of organisms are influenced by the ecological characteristics of parasite species, host specificity, biotic and abiotic environmental factors, as well as the geographical distance between host populations. In addition, parasites provide up-to-date information on the abiotic characteristics of the aquatic habitats they inhabit and can be used as sensitive biological indicators for monitoring environmental changes (Poulin, 2007).

Accurate identification of the anatomical and morphological structures of parasite species belonging to the taxon *Cestoda* is of great importance for taxonomic classification and epidemiological studies. Detailed examination of the morphological characteristics of species enables the determination of similarities and differences among species and allows for accurate species identification. Moreover, it contributes to a better understanding of host–parasite relationships and to the elucidation of the biological adaptation mechanisms of parasites.

Morphological data also play a crucial role in elucidating the life cycle of parasites. Therefore, the examination of the anatomical and morphological characteristics of cestodes is of great importance for fundamental parasitological research, fish health, and ecosystem management (Bazsalovicsová et al., 2014).

In this study, it was aimed to describe the anatomical and morphological characteristics of cestode species observed in *Squalius recurvirostris*, one of the community members of the Düzağaç–Akdeğirmen Dam Lake (Afyonkarahisar). The results of the study are expected to contribute to the knowledge and recognition of the cestode parasite fauna of *Squalius recurvirostris*.

MATERIALS and METHODS

The Düzağaç–Akdeğirmen Dam Lake is located within the boundaries of Sincanlı district of Afyonkarahisar Province, approximately 2 km northeast of the town of Düzağaç. The dam lake is situated at 38°48′ N latitude and 30°15′ E longitude. The maximum operating water level of Akdeğirmen Dam Lake is 1130 m, the minimum operating water level is 1111 m, and its active storage capacity is 47.367 hm^3 (Anonymous, 2009) (Figure 1).

The *Squalius recurvirostris* specimens examined in this study were collected between 17 February 2012 and 9 March 2013 from approximately 1–2 m depth of Akdeğirmen Dam Lake using trammel nets (Figure 2).

The specimens were transferred into plastic containers filled with dam lake water and transported alive to the research laboratory of Afyon Kocatepe University. Parasitological examinations were carried out within

24–48 hours, during which the fish were maintained in aerated aquarium conditions.

First, the total and fork lengths of the fish specimens were recorded (Figure 3). Subsequently, the fish were longitudinally dissected from the urogenital opening to the level of the pharynx. Organs such as the digestive tract, gonads, liver, spleen, heart, mesentery, and swim bladder were removed and placed into Petri dishes containing physiological saline solution. The tissues and organs were examined under a stereomicroscope equipped with a light source. During the examination, when parasites were encountered, they were separated using dissection needles, pipettes, forceps, or brushes and transferred into physiological saline solution, followed by rinsing with tap water to remove mucus. The locations and numbers of parasites found in tissues and organs were recorded separately for each host fish (Bauer, 1985).

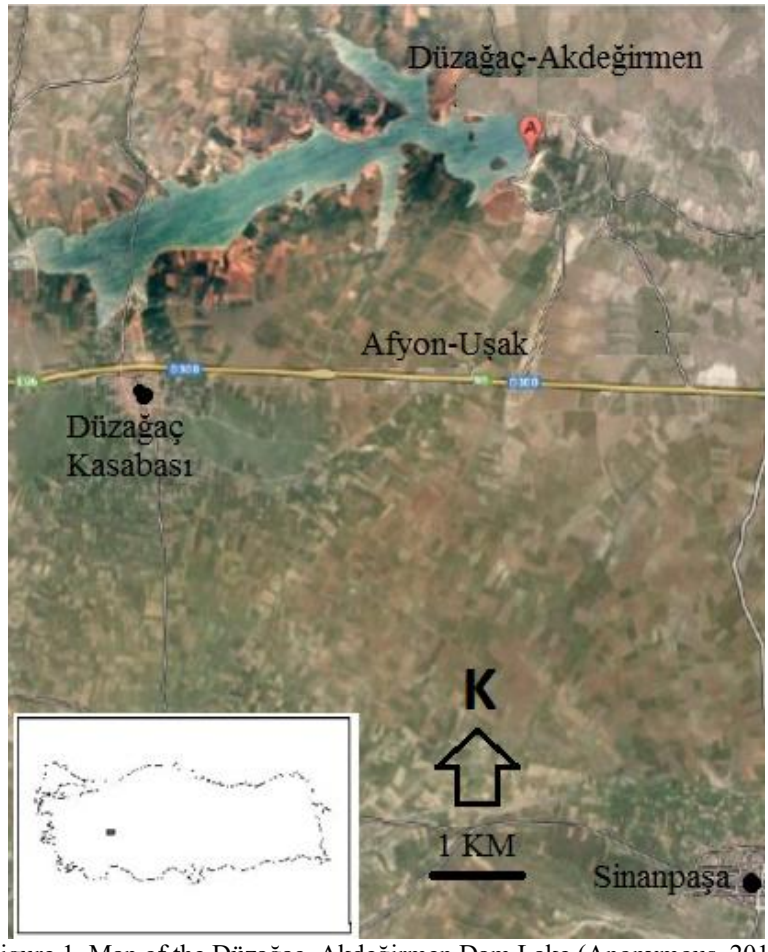

Figure 1. Map of the Düzağaç–Akdeğirmen Dam Lake (Anonymous, 2014)

Figure 2. Capture of *S. recurvirostris* from the Düzağaç–Akdeğirmen Dam Lake using trammel nets (original)

Figure 3. General view of the study specimens, *S. recurvirostris* (original)

The cestodes obtained from the host fish specimens were preserved in 70% ethyl alcohol. Some of these parasites were stained with Mayer's hematoxylin and mounted as permanent preparations in glycerin–gelatin medium. Identification of the cestodes was carried out based on the descriptions provided by Bykhovskaya-Pavlovskaya et al. (1962). Photographs were taken using an Olympus CH20 microscope.

RESULTS

In this study, the cestode parasite fauna of *Squalius recurvirostris* (freshwater chub) inhabiting the Düzağaç–Akdeğirmen Dam Lake was investigated. Among the parasites detected in the host fish, *Caryophyllaeides fennica* (Schneider, 1902) was recorded in the intestinal lumen, *Paradilepis scolecina* (Rudolphi, 1819) in the mesenteric tissue surrounding the liver and gall bladder, and *Dilepis unilateralis* (Rudolphi, 1819) in the gall bladder.

Caryophyllaeides fennica (Schneider 1902)

Caryophyllaeides fennica has a long, ribbon-shaped body consisting of a single segment. The parasite measured 18–24 (23) mm in length and 2.6–3 (2.8) mm in width (Figure 4).

The scolex at the anterior end is simple, slightly swollen, and spatula-like in shape, representing a characteristic morphological feature of this species. Posterior to the scolex lies the body region containing the vitelline glands and testicular lobes.

The genital organs, including the ovary, uterus, and cirrus sac, are located in the posterior part of the body. The testes are arranged as sac-like lobes in the median region, extending from the posterior terminal of the body to the anterior margin near the beginning of the scolex. The testes measured 230–255 (245) µm in length and 180–192 (185) µm in width.

The ovary is situated in the posterior subterminal region of the body and is composed of two arm-shaped structures, the anterior arm being longer than the posterior one, which are connected by a transverse bridge. The posterior extensions of the ovary are convexly fused. The uterus is short and broad, forming several coils posterior to the ovary before extending anteriorly up to the anterior part of the cirrus sac.

The oval-shaped cirrus sac, located in the median region anterior to the ovary, measured 735–1286 (1200) × 615–760 (650) µm. Vitelline glands are arranged as follicular structures extending from the anterior margin of the ovary to the beginning of the scolex and form a small clustered bundle at the posterior end of the body. The vitelline follicles were measured as 210–225 (215) and 163–179 (175) µm. The eggs are oval, thin- and smooth-shelled, and operculated. Eggs were recorded as 50–55 (54) µm and 38–42 (39) µm (Figure 5).

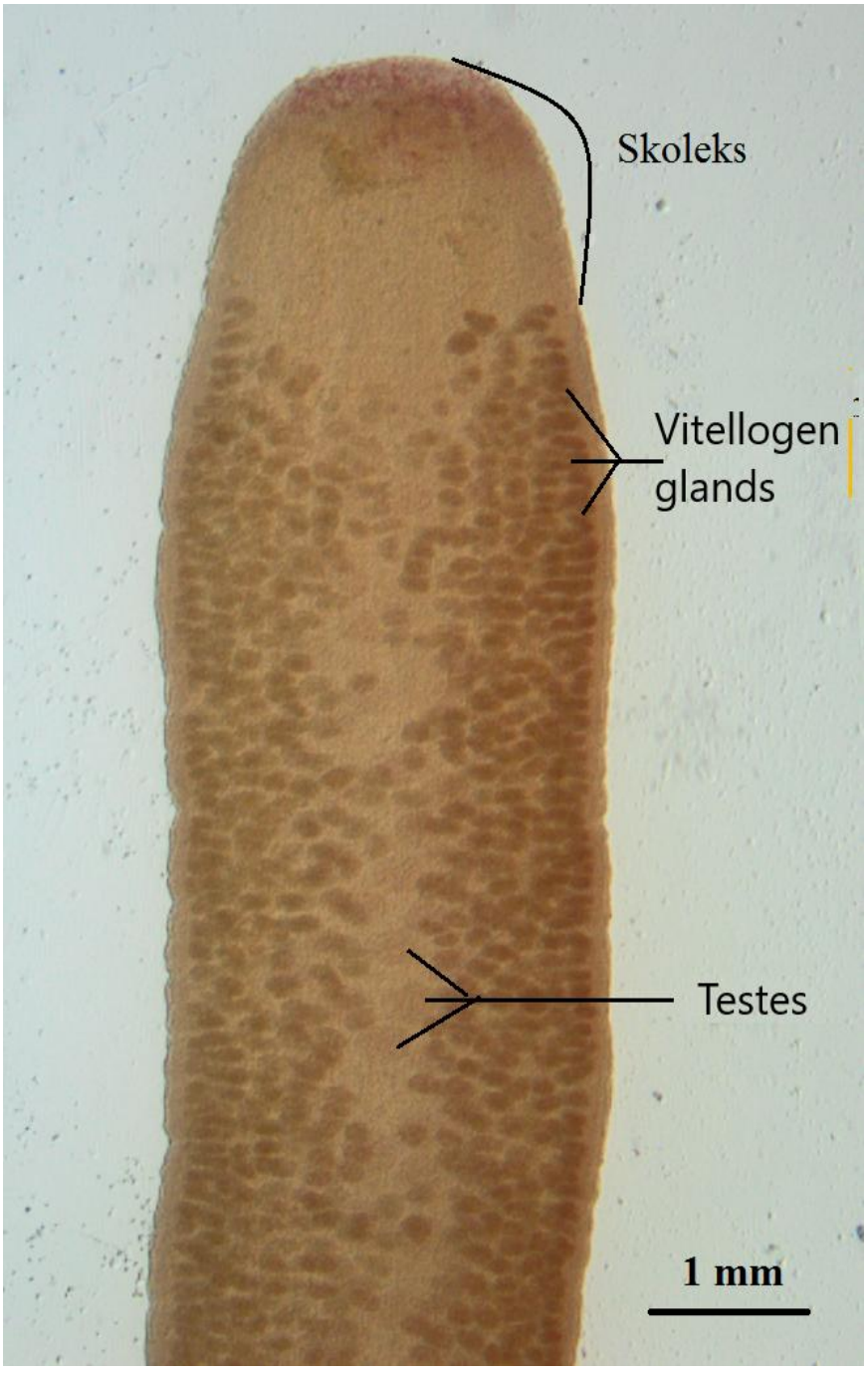

Figure 4. Anterior region of *Caryophyllaeides fennica* (original).

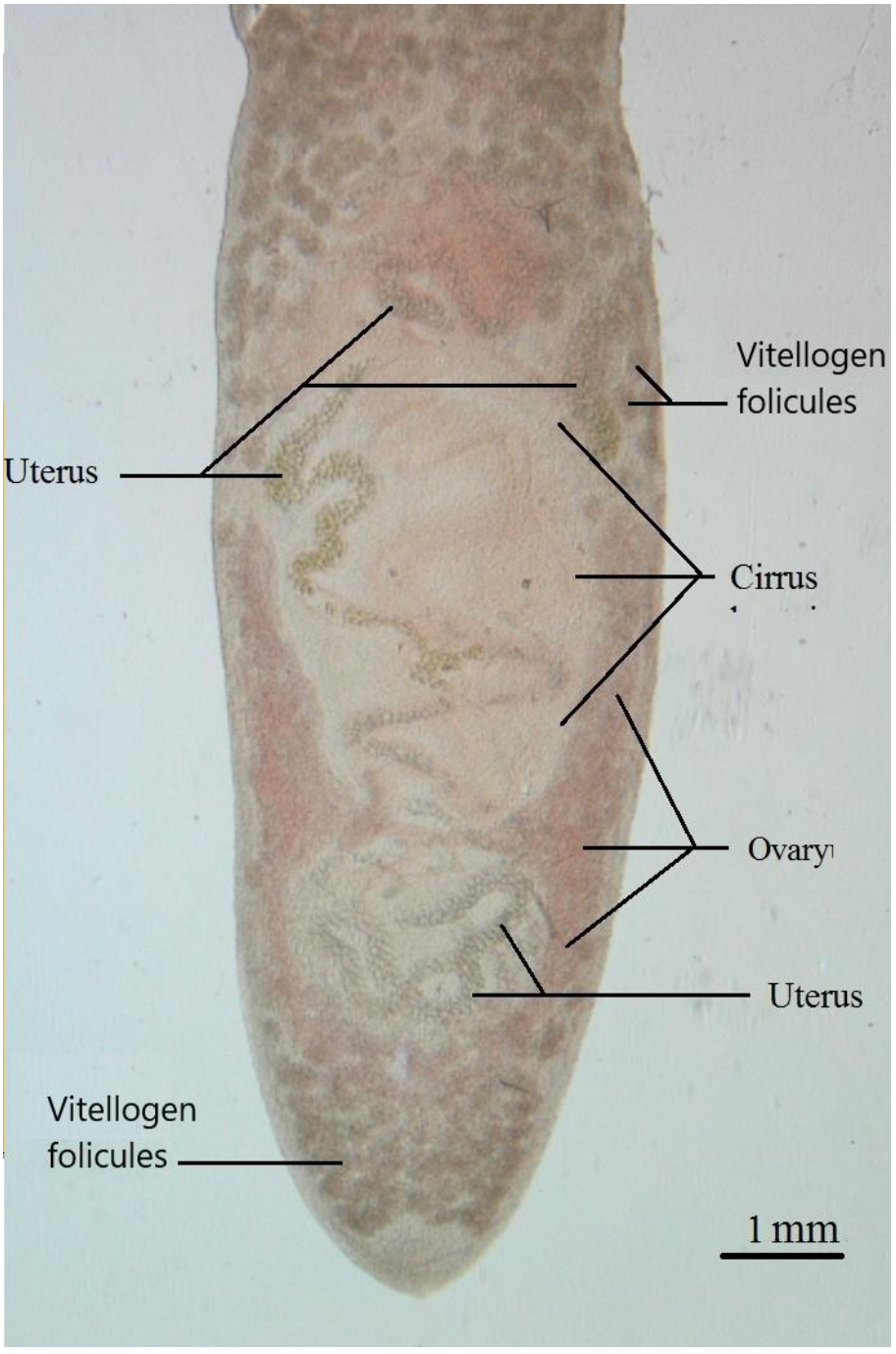

Figure 5. Posterior part of *Caryophyllaeides fennica* (original)

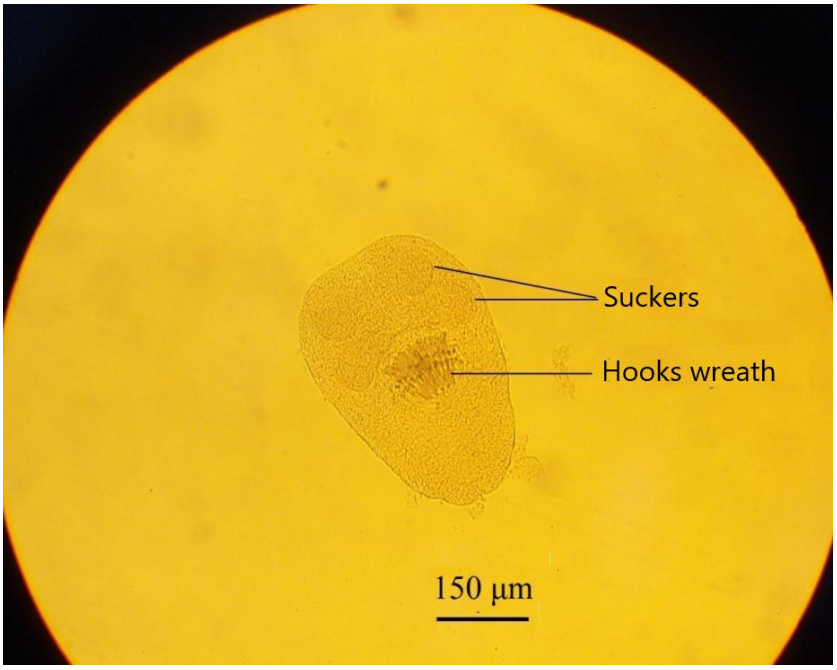

Figure 6. Cysticercus form of Paradilepis scolecina (original)

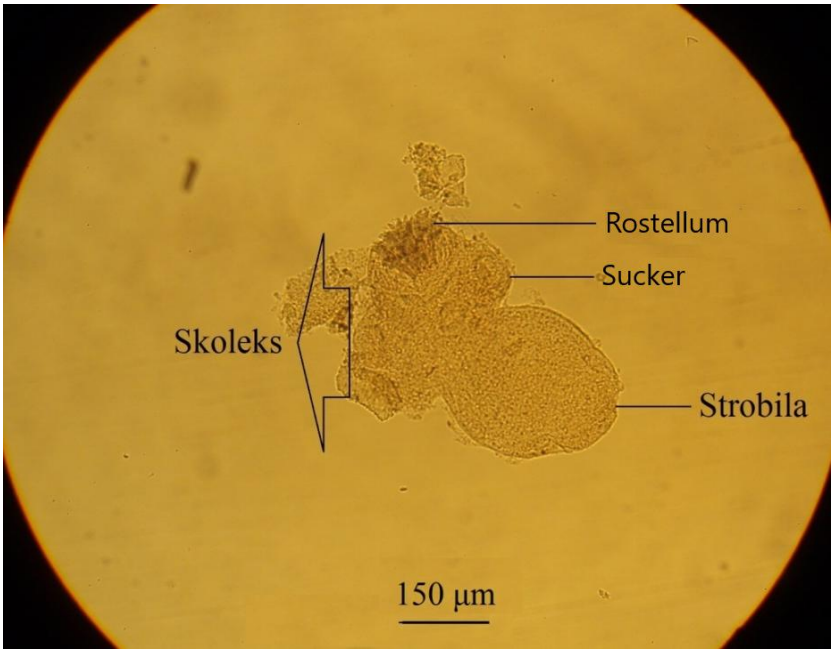

Figure 7. General view of Paradilepis scolecina outside the cysticercus (original)

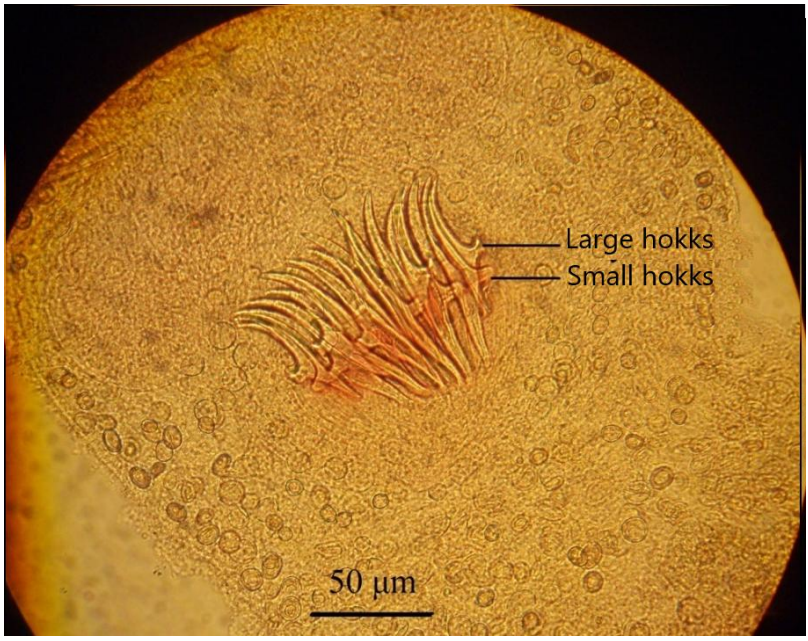

Figure 8. Hook wreath of *Paradilepis scolecina* (original)

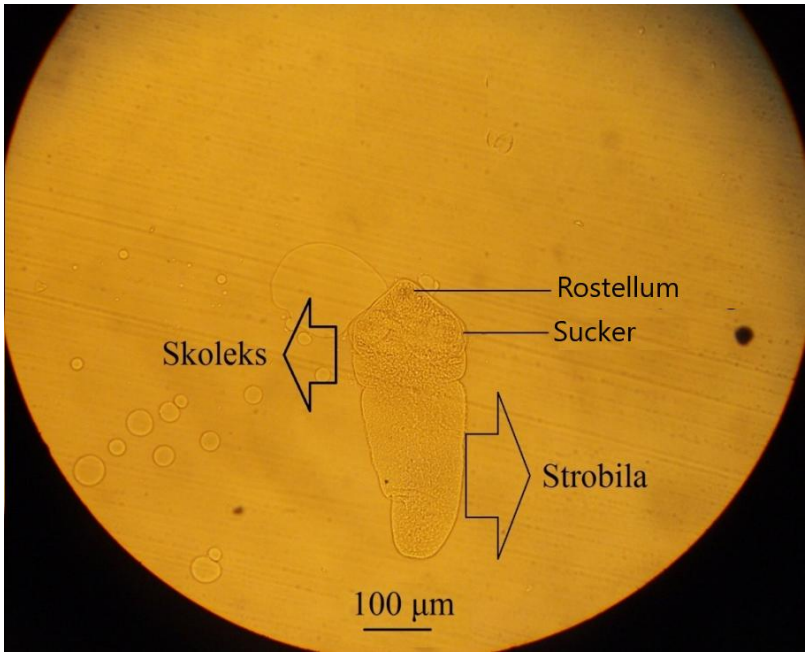

Figure 9. Scolex and hook wreath of *Dilepis unilateralis* (original)

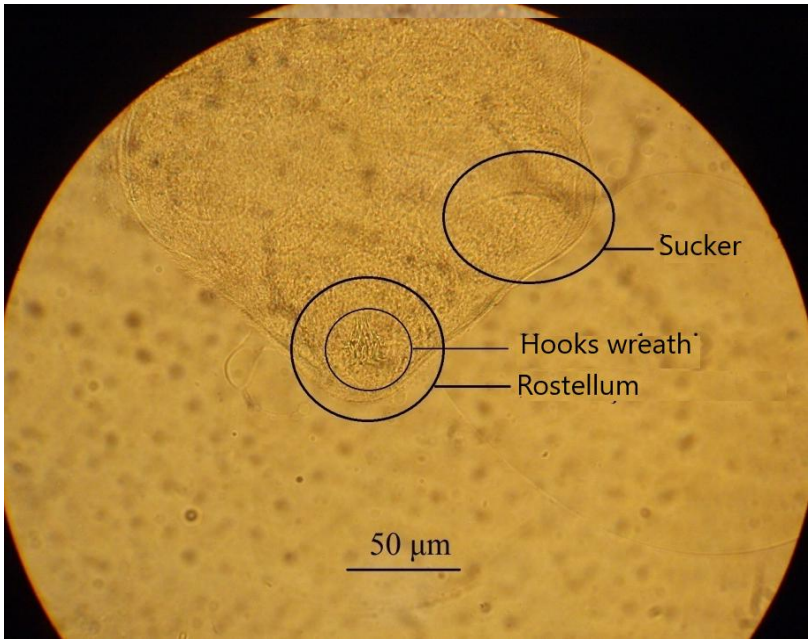

Figure 10. Scolex and parts of the Dilepis unilateralis (original)

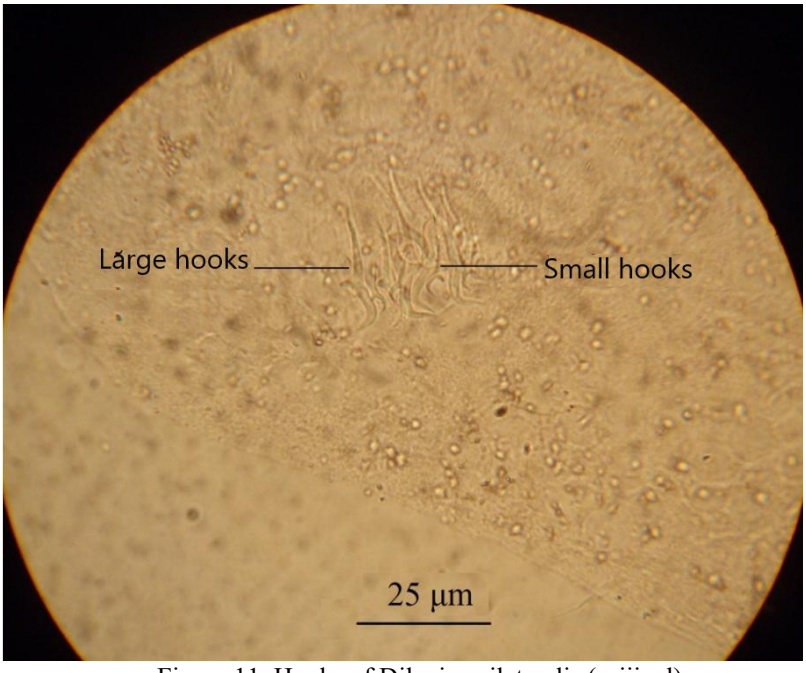

Figure 11. Hooks of Dilepis unilateralis (orijinal)

Cysticercus *Paradilepis scolecina* (Rudolphi, 1819)

The cysticercus of *Paradilepis scolecina*, which has a cystic larval structure, is small and spherical to oval in shape (Figure 6). The cysticercus consists of a scolex bearing suckers and a hook-bearing rostellum, together with a strobila. The length of the parasite, excluding the cysticercus cyst, was measured as 570–650 (585) µm, and its width at the level of the suckers as 320–380 (360) µm (Figure 7). Four strong, disc-shaped muscular suckers are located subterminally on the scolex. These hemispherical suckers measured 87–100 (95) µm in length and 75–100 (93) µm in width. On the median-terminal region of the scolex, the rostellum bears a double row of hook crowns. The shape and number of these hooks are decisive for species identification. The large hooks in the upper row measured 112–113 (112) µm in length, whereas the small hooks in the lower row measured 78–80 (78) µm (Figure 8).

Cysticercus *Dilepis unilateralis* (Rudolphi, 1819)

The cysticercus of *Dilepis unilateralis* is small, spherical, and slightly oval in shape (Figure 9). The length of the cysticercus larva was measured as 480–620 (510) µm, and its width at the level of the suckers as 170–230 (210) µm (Figure 10). Four well-developed, disc-shaped suckers are present subterminally on the scolex. These hemispherical suckers measured 75–82 (80) µm in length and 70–80 (75) µm in width. On the median-terminal region of the scolex, the rostellum bears two rows of hooks arranged as a hook crown. The number and morphology of these hooks are distinctive features for species identification. The large hooks in the upper row measured 25–26 (26) µm in length, whereas the small hooks in the lower row measured 15–16 (15) µm (Figure 11).

DISCUSSIONS

The three cestode species identified in this study belong to the phylum Platyhelminthes (flatworms) due to their dorsoventrally flattened bodies and bilateral symmetry. These parasites are assigned to the class Cestoda based on their flattened body structure, cuticular tegument, and the characteristics of the scolex (Bychowskaya-Pavlovskaya et al., 1962).

Caryophyllaeides fennica, a single-segmented cestode, is a species of medium size. The tongue- to spatula-shaped scolex located at the anterior terminal is a characteristic feature unique to this species. The ovary has a bilobed form, with the anterior part being longer than the posterior, and the two lobes are connected by a transverse bridge. The posterior lobes of the ovary are convex and fused with each other. The oval-shaped cirrus sac is located in the median region anterior to the ovary and is distinguished from those of other species by its dimensions of 735–1286 (1200) × 615–760 (650) µm (Bychowskaya-Pavlovskaya et al., 1962).

The cystic, cysticercus-shaped *Cysticercus Paradilepis scolecina* possesses a small, spherical scolex. In the median-terminal region of the scolex, a disc-shaped hook crown is present on the rostellum, consisting of two rows of hooks. The large hooks in the upper row measure 112–113 (112) µm in length, while the small hooks in the lower row measure 78–80 (78) µm, conferring species-specific diagnostic value (Bychowskaya-Pavlovskaya et al., 1962).

The cystic cestode *Cysticercus Dilepis unilateralis* has a conical body shape. This species is distinguished from others by the presence of a retractile rostellum bearing a double row of hook crowns and by a unilateral genital opening. The hooks located on the short, conical rostellum in the anterior median-terminal region of the scolex measure 25–26 (26) µm in the upper row and 15–16 (15) µm in the lower row. These characteristics represent diagnostic features that distinguish this species from closely related taxa (Bychowskaya-Pavlovskaya et al., 1962).

CONCLUSION

In conclusion, three different cestode species were recorded in the host fish *Squalius recurvirostris* from the Düzağaç–Akdeğirmen Dam Lake in this study. The anatomical and morphological characteristics of these species were described in detail. The data obtained contribute to the recognition and better understanding of the parasites in question.

ACKNOWLEDGEMENTS

This study was produced from a master's thesis. It was supported by Afyon Kocatepe University Scientific Research Projects Unit within the scope of project number 13.Fen.Bil.01.

REFERENCES

Anonymous (2009). Düzağaç-Akdeğirmen Barajı ve sulaması tesis tanıtma föyü. DSİ 183 Şube Müdürlüğü, Afyon.

Anonymous (2014). http://harita.turkcebilgi.com/Afyon_haritasi, 13.05.2014

Bauer, O.N. (1985). Key to parasites of freshwater fishes of the fauna of the USSR. Part II. Nauka, Leningrad.

Bazsalovicsová, E., Králová-Hromadová, I., Brabec, J., Hanzelová, V. & et al. (1962). Key to parasites of freshwater fishes of the USSR. Publ. House of the USSR Acad. Sci.Moscow, Leningrad.

Mouritsen, K. N. and Poulin, R. (2002). Parasitism community structure and biodiversity in intertidal ecosystems. Parasitology, 124: 101-117.

Poulin, R. (2007). The structure of parasite communities in fish hosts: ecology meets geography and climate. *Parassitologia*, 49: 169-172.

The Liverwort Oil Body: Evolutionary Biogenesis, Metabolite Transport, and Intraorganellar Symbiosis

Özcan ŞİMŞEK[1]

[1] Dr.Öğr.Üyesi, Çanakkale Onsekiz Mart Üniv. Yenice MYO, Ormancılık Bölümü. ozcansimsek@comu.edu.tr ORCID No:: 0000-0002-3210-7641

ABSTRACT

The liverwort oil body represents a unique secretory organelle that likely acted as a critical evolutionary adaptation for early embryophytes during the colonization of land. Functioning as a specialized intracellular factory, it sequesters cytotoxic specialized metabolites, particularly sesquiterpenoids and bisbibenzyls, serving dual roles in biotic defense and potential desiccation tolerance. This Viewpoint synthesizes recent molecular breakthroughs, primarily derived from the model species *Marchantia polymorpha*, which demonstrate that organelle biogenesis is driven by the transcription factor *MpERF13*-mediated redirection of the secretory pathway, utilizing specific SNARE and COPI trafficking machineries. Furthermore, the selective accumulation of lipophilic payloads is facilitated by ATP-binding cassette transporters, linking biosynthesis directly to organellar sequestration. Challenging the traditional paradigm of the oil body as a sterile storage depot, recent *in situ* staining studies provide preliminary evidence for the presence of intraorganellar endophytic bacteria. While proposing a novel tripartite symbiosis hypothesis, this work emphasizes the necessity of axenic verification to distinguish obligate mutualism from environmental opportunism. Finally, the potential of liverworts as a model metabolic engineering platform is discussed, alongside critical gaps regarding taxonomic diversity beyond model systems.

Keywords: Liverworts, Chemical defense, Oil body biogenesis, ABC transporters, Endophytes, Synthetic biology.

INTRODUCTION

The liverworts (Marchantiophyta) occupy a pivotal phylogenetic position as the earliest divergent lineage of land plants (Embryophyta). A hallmark feature—a synapomorphy—of this phylum is the oil body (OB), a distinctive membrane-bound organelle present in over 90% of liverwort species. First described by Hübener (1834), the OB has long fascinated botanists; however, its precise biological function and evolutionary origin have only recently begun to be unraveled. While the molecular mechanisms governing OB formation have been extensively characterized in the model species *Marchantia polymorpha*, it is important to acknowledge that this taxon represents a single thalloid lineage. Consequently, extending these mechanistic insights to the broader diversity of leafy liverworts (Jungermanniopsida) necessitates a cautious comparative approach, as species-specific variations in biogenesis may exist.

Origin and Cellular Distinction

The liverwort oil body is structurally and functionally distinct from other plant secretory systems. Unlike the cytosolic lipid droplets (oleosomes) of seed plants, which store neutral lipids solely for energy reserves within a phospholipid monolayer, the oil body is a specialized secretory organelle bounded by a membrane derived from the secretory pathway (Kanazawa et al., 2020). Furthermore, while functionally analogous to the glandular trichomes of vascular plants in terms of terpenoid biosynthesis, oil bodies are strictly intracellular, sequestering cytotoxic metabolites within the cytoplasm rather than secreting them into an extracellular subcuticular space.

Evolutionary Significance

While unique to liverworts, the oil body shares striking functional and developmental parallels with the glandular trichomes of vascular plants. Both structures serve as specialized factories for terpenoid biosynthesis and storage, sequestering bioactive compounds from the plant's own metabolic machinery. However, unlike epidermal trichomes, liverwort oil bodies are intracellular organelles. This distinction raises fundamental evolutionary questions regarding land colonization. As the earliest secretory structure of land plants, the oil body likely provided a selective advantage for the first embryophytes facing the harsh terrestrial environment (Romani et al., 2022). This organelle may have functioned as a critical exaptation, acting as a chemical shield and potentially aiding in desiccation tolerance before the evolution of complex cuticles (Pressel et al., 2009).

In light of paradigm-shifting discoveries—from the redirection of the secretory machinery (Kanazawa et al., 2020) to the identification of intraorganellar bacteria (Young et al., 2025)—a comprehensive synthesis is warranted. This review integrates these findings to challenge the traditional view of the OB as a static storage depot. Specifically, it is hypothesized that the liverwort oil body represents a unique evolutionary convergence of metabolic innovation and microbial symbiosis, functioning as a tripartite interface that facilitated the conquest of land. By evaluating the organelle through these distinct yet interconnected lenses, this article provides a novel functional roadmap for future investigations in evolutionary developmental biology and synthetic biology.

MORPHOLOGY, DISTRIBUTION, AND ECOLOGICAL FUNCTION

Morphological Diversity and Chemosystematics

Oil bodies (OBs) exhibit remarkable structural diversity across the Marchantiophyta, varying significantly in size, shape, number per cell, and internal organization. While the model species *Marchantia polymorpha* possesses specialized idioblasts containing single, large, and spherical oil bodies, the majority of liverwort diversity—particularly within the class Jungermanniopsida—displays complex, segmented, or multiple oil bodies per cell. Morphological classifications traditionally group OBs into distinct types (e.g., Massula-type, Jungermannia-type, Bazzania-type) based on their granularity and homogeneity (Asakawa, 2004).

This morphological variation is not random but correlates strongly with specific terpenoid profiles, facilitating their use as robust chemotaxonomic markers (Table 1). For instance, species such as *Frullania* and *Radula* exhibit oil bodies with granular segmentation, which often coincides with the accumulation of specific sesquiterpene lactones and bibenzyls (Ludwiczuk & Asakawa, 2015). Furthermore, unique pigmentation provides additional diagnostic value; the distinct blue color observed in the OBs of *Calypogeia azurea* is attributed to the localized accumulation of azulene derivatives (Asakawa & Ludwiczuk, 2018). A critical gap in current research is determining whether the molecular machinery characterized in *M. polymorpha*—such as the *MpERF13* regulatory module—is conserved in these morphologically distinct lineages or if leafy liverworts have evolved independent regulatory pathways for oil body biogenesis.

Table 1 Classification of liverwort oil bodies based on morphology and associated dominant chemical constituents.

Oil Body Type	Morphological Description	Representative Genera	Predominant Chemical Class
Massula-type	Homogeneous, glistening, typically small and numerous per cell.	Marsupella, Gymnomitrion	Hydrocarbons, simple sesquiterpenes
Jungermannia-type	Granular/papillose surface, composed of small globules, usually few per cell.	Jungermannia, Scapania	Sesquiterpene lactones, diterpenes
Bazzania-type	Large, homogeneous or faintly segmented, few (2-4) per cell.	Bazzania, Calypogeia	Azulenes (blue-pigmented), bicyclic sesquiterpenes
Marchantia-type	Single, very large organelle occupying most of the cell (idioblast); granular interior.	Marchantia, Conocephalum	Bisbibenzyls (e.g., Marchantins), cuparene-type sesquiterpenes
Frullania-type	Numerous, small, spherical to ellipsoidal, finely segmented.	Frullania, Jubula	Sesquiterpene lactones (highly allergenic)

(Adapted from Asakawa, 2004; Ludwiczuk & Asakawa, 2015).

Cellular Distribution and Defense Role

In the Marchantiopsida class, OBs are strictly confined to scattered secretory cells known as idioblasts, whereas in Jungermanniopsida, they are typically present in all chlorophyllous leaf cells. The primary function of OBs has long been established as a chemical defense mechanism against biotic stress. The sequestered lipophilic compounds, such as plagiochiline A and marchantin A, exhibit potent antifeedant activity against arthropod herbivores (Romani et al., 2020). This defensive role is genetically supported by *MpC1HDZ* loss-of-function mutants in *M. polymorpha*, which lack OBs and consequently suffer significantly higher predation rates.

Beyond biotic interactions, accumulating evidence suggests that OBs play a pivotal role in abiotic stress tolerance, particularly in the context of poikilohydry. Liverworts, as early land colonizers, lack complex vascular systems and true cuticles, making them susceptible to rapid desiccation. In desiccation-tolerant species found in exposed habitats, OBs may function as a crucial physiological buffer. Cytological evidence demonstrates that oil bodies maintain their structural integrity and shape even during severe cytorrhysis (cellular collapse) induced by dehydration, unlike other organelles which may undergo degradation (Pressel et al., 2009). Although the precise biochemical mechanism remains to be fully elucidated, the persistence of these organelles in harsh environments points to an exapted function in environmental adaptation, extending their role beyond mere herbivore deterrence.

MOLECULAR MECHANISMS OF OIL BODY BIOGENESIS

Transcriptional Regulation

The differentiation of oil body cells and the subsequent organelle biogenesis are governed by a hierarchical gene network, primarily characterized in *Marchantia polymorpha*. Genetic analyses demonstrate that the AP2/ERF family transcription factor, *MpERF13*, functions as the master regulator. Loss-of-function mutants (*Mperf13*) completely fail to develop oil bodies, whereas gain-of-function lines (*MpERF13-GOF*) exhibit ectopic oil body formation across the thallus (Kanazawa et al., 2020).

This master regulator operates within a broader transcriptional landscape. The Class I Homeodomain Leucine-Zipper transcription factor *MpC1HDZ* acts upstream of *MpERF13*, controlling the initial determination of oil body cell identity; *Mpc1hdz* mutants lack oil bodies entirely, confirming its essential role in cell fate specification (Romani et al., 2020). Furthermore, recent studies identify the R2R3-MYB transcription factor, *MpMYB02*, as a key modulator of specialized metabolite accumulation, particularly marchantins, linking organelle formation with chemical biosynthesis (Kubo et al., 2024). Conversely, the bZIP transcription factor *MpTGA* has been characterized as a negative regulator, restricting the population of oil body cells to maintain energy balance (Toro Acevedo, 2025).

Membrane Trafficking: Evidence and Models

Unlike cytosolic lipid droplets (oleosomes) found in other land plants, which originate from the ER bilayer, ultrastructural analyses suggest that the liverwort oil body is bounded by a complex membrane structure, proposed to be a phospholipid monolayer/bilayer hybrid derived from the secretory system (Kanazawa et al., 2020). Experimental evidence for this "secretory

redirection" comes from the localization of specific SNARE proteins. The syntaxin *MpSYP12B* is exclusively localized to the oil body membrane and is transcriptionally upregulated by *MpERF13*.

Based on these localization data, the current mechanistic model proposes that Golgi-derived vesicles, rather than fusing with the plasma membrane, are redirected to fuse homotypically, generating the nascent oil body (Figure 1). This model is supported by genetic data involving the COPI (Coat Protein Complex I) machinery. Mutants of *MpSEC28* (an ε-COP ortholog) and other COPI subunits (*MpRET1*, *MpSEC21*) display oil bodies with aberrant, circular morphologies, indicating that retrograde trafficking is essential for maintaining the distinct shape and integrity of the organelle (Kanazawa et al., 2022).

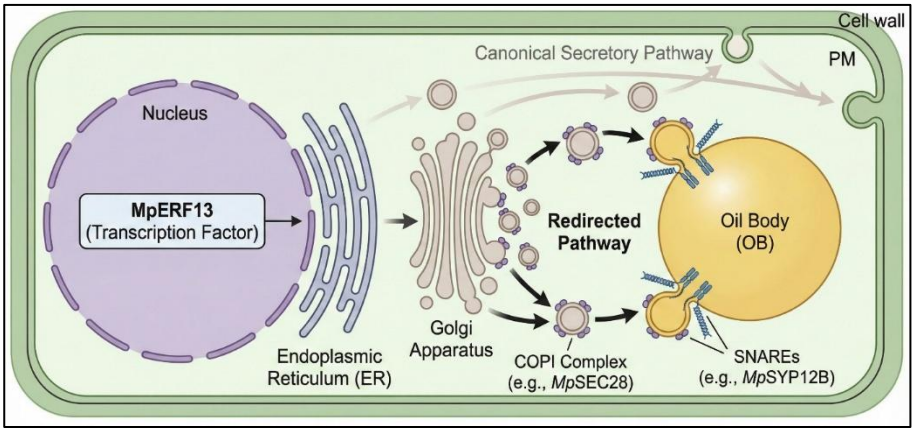

Figure 1. Schematic representation of the redirected secretory pathway in Marchantia polymorpha.

The model illustrates the regulatory role of MpERF13 and the specific functions of SNARE proteins (MpSYP12B) and COPI complexes (MpSEC28) in directing vesicles to form the oil body (Based on Kanazawa et al., 2020).

Comparative Evolutionary Context

It is critical to note that this redirection of the secretory pathway for lipophilic storage appears to be a unique evolutionary innovation of the Marchantiophyta. In contrast, other bryophyte lineages such as mosses (e.g., *Physcomitrium patens*) and hornworts store lipids strictly in cytosolic lipid droplets (LDs) derived directly from the endoplasmic reticulum, utilizing conserved proteins like oleosins and LDAP (Huang, 2018). No evidence

currently exists for a similar "secretory redirection" mechanism in mosses, suggesting that the recruitment of *SYP12B* and *ERF13* homologs for oil body biogenesis represents a lineage-specific exaptation that occurred after the divergence of liverworts from the remaining embryophytes (Robinson et al., 2016).

SPECIALIZED METABOLITE BIOCHEMISTRY AND TRANSPORT

Chemical Constituents

Liverworts are chemically prolific, synthesizing a massive array of specialized metabolites, with over 1600 terpenoids and aromatic compounds reported to date. The oil bodies function as the primary storage sites for these lipophilic constituents. The chemical profile is dominated by sesquiterpenoids—such as thujopsene, chamigrene, β-himachalene, α-gurjunene, and cuparene—which have been isolated directly from the oil bodies of Marchantia polymorpha (Tanaka et al., 2016). Additionally, unique aromatic compounds known as bisbibenzyls, including marchantin A and marchantin C, are abundant. These compounds exhibit potent biological activities; for instance, marchantin A has been reported to induce apoptosis in human MCF-7 breast cancer cells and acts as an antimicrotubular agent, demonstrating synergistic cytotoxic effects when combined with Aurora-A kinase inhibitors (Shi et al., 2009).

Biosynthesis and Transport

The biosynthesis of oil body-associated sesquiterpenoids is primarily linked to the cytosolic mevalonate (MVA) pathway, although metabolic cross-talk with the plastidial MEP pathway cannot be entirely ruled out. Unlike seed plants that typically utilize canonical terpene synthases (TPS), liverworts employ a distinct class of enzymes encoded by Microbial-type Terpene Synthase-Like (MTPSL) genes. For instance, MpFTPSL2 and MpFTPSL3 are co-expressed with oil body markers and are responsible for the core sesquiterpene scaffolds. Functional characterization has provided quantitative insight into their enzymatic efficiency; MpMTPSL3 exhibits the highest specific activity (525.17 ± 14.05 pmol h^{-1} µg^{-1}) using all-trans-FPP, whereas MpMTPSL2 shows a 25-fold substrate preference for neryl diphosphate (NPP) (Kumar et al., 2016).

Phylogenetic analyses of the MpMTPSL gene family suggest a non-canonical origin, pointing to ancient horizontal gene transfer (HGT) events from fungi or bacteria to the ancestral liverwort lineage (Kumar et al., 2016). This acquisition was likely a key evolutionary innovation, enabling land plants to produce volatile terpenes for defense without reinventing the biosynthetic

machinery. However, inferring HGT events requires careful phylogenetic interpretation. While sequence similarity strongly supports the acquisition hypothesis, establishing the directionality of transfer (microbe-to-plant versus plant-to-microbe) and defining rigorous sequence identity thresholds are essential to distinguish true HGT from convergent evolution or potential contamination in transcriptomic datasets.

Following biosynthesis, the sequestration of these cytotoxic metabolites is mediated by specific ATP-binding cassette (ABC) transporters. Recent molecular data indicate that *MpABCG1* and *MpABCG36* are localized to the oil body membrane and are essential for the influx of sesquiterpenoids and bisbibenzyls (Figure 2). Notably, while these transporters have homologs in vascular plants that mediate the secretion of cuticular lipids (e.g., *AtABCG* subfamily in *Arabidopsis*), their recruitment for intracellular organellar loading appears to be specific to liverworts (Kanazawa et al., 2025). Mutant analyses reveal that while the structural formation of the oil body remains intact in *Mpabcg* knockouts, the organelle shows reduced accumulation of lipophilic metabolites, linking biosynthesis directly to organellar transport.

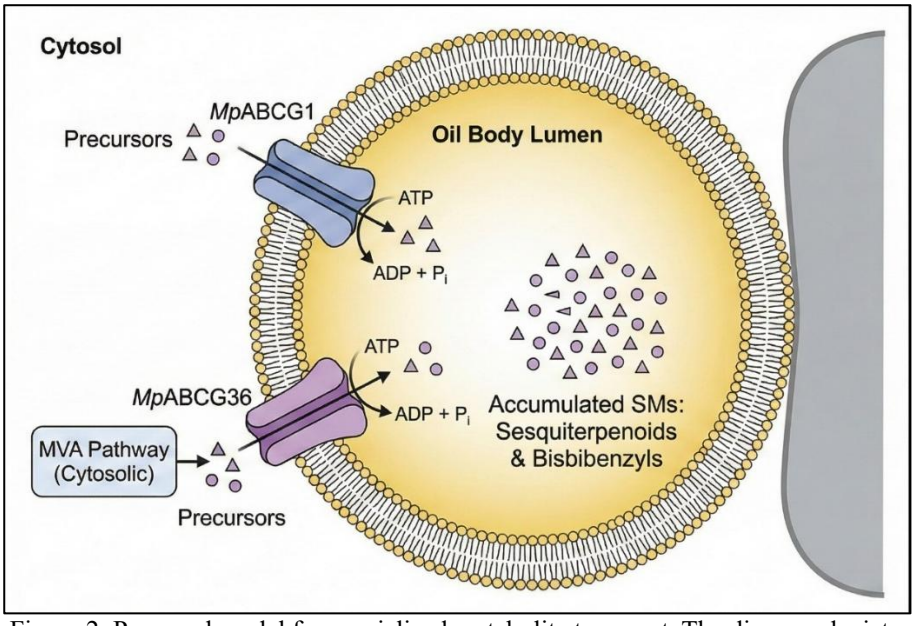

Figure 2. Proposed model for specialized metabolite transport. The diagram depicts the localization of ATP-binding cassette transporters, MpABCG1 and MpABCG36, on the oil body membrane, facilitating the influx of sesquiterpenoids and bisbibenzyls synthesized from the cytosolic mevalonate pathway.

NOVEL STRUCTURAL COMPONENT: INTRAORGANELLAR ENDOPHYTES

Identification and Viability

A recent and potentially paradigm-shifting discovery challenges the established view of the oil body as a sterile secretory organelle. Granular structures within the oil body lumen, previously interpreted in ultrastructural studies as proteinaceous deposits or lipid globules, have been re-identified as intracellular, endophytic bacteria in wild-collected specimens of Marchantia polymorpha and Radula complanata (Young et al., 2025). This re-evaluation relied on advanced in situ fluorescent staining: RADA (a fluorescent D-amino acid) confirmed the presence of peptidoglycans characteristic of active bacterial cell walls, while SYTO-13 validated the presence of nucleic acids (Figure 3).

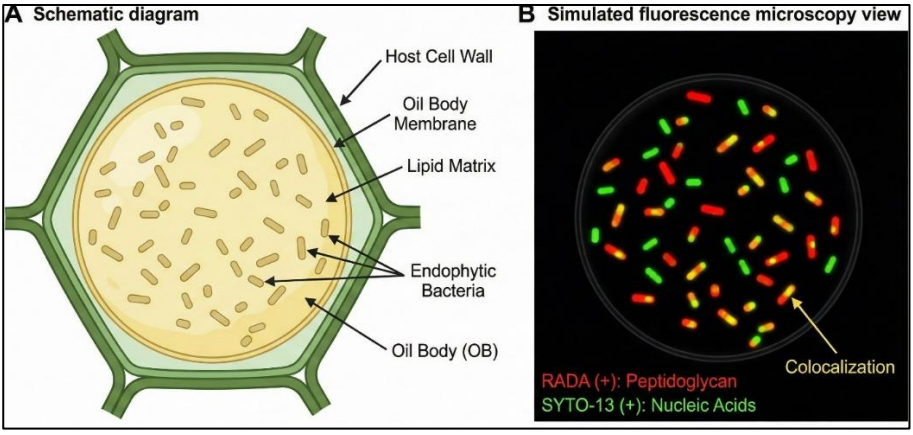

Figure 3. Visualization of intraorganellar endophytes. (A) Schematic representation of the oil body lumen containing granular bacterial structures. (B) Fluorescence microscopy diagram illustrating RADA (peptidoglycan) and SYTO-13 (nucleic acid) positive signals within the oil body, distinguishing endophytes from the surrounding lipid matrix (Based on findings from Young et al., 2025).

Preliminary observations using Gram staining suggest these endophytes are likely Gram-positive (Young et al., 2025). The historical oversight of these structures is likely attributed to methodological limitations; traditional transmission electron microscopy (TEM) fixatives, such as osmium tetroxide, render both bacterial cells and the surrounding lipophilic matrix similarly electron-dense, obscuring the microbial morphology.

Evolutionary Parallels and Hypotheses

If confirmed as a stable biological phenomenon, this intraorganellar association would represent a significant evolutionary convergence with other plant-microbe symbioses. Much like the cyanobacterial colonies housed within the thallus cavities of hornworts (e.g., Anthoceros) or the complex algal-fungal partnership in lichens, the liverwort oil body could function as a specialized micro-habitat that facilitates a tripartite interaction (host–organelle–endophyte). In this hypothetical model, the lipid-rich lumen provides a carbon source and physical protection for the bacteria, while the endophytes might contribute to the chemical defense arsenal of the host via biotransformation of terpenes, a mechanism observed in various endophytic fungi (Young et al., 2025).

Critical Caveats and Future Verification

While these findings are compelling, this review emphasizes that current evidence remains preliminary. The ubiquity of this association across the liverwort lineage has yet to be established. Furthermore, as the reported data are derived exclusively from wild populations, distinguishing between obligate endosymbionts and environmental opportunists (or transient colonization) remains the primary challenge. To validate the "intraorganellar symbiont" hypothesis, future investigations must prioritize the isolation of these bacteria from axenic (sterile) cultures of *M. polymorpha*. Furthermore, applying culture-independent approaches, such as single-cell genomic sequencing of isolated oil bodies or targeted metagenomics, would provide definitive taxonomic identification and metabolic profiling of these putative endophytes. Until functional dependency is demonstrated under controlled conditions—proving that the oil body requires the bacterium for full functionality or vice versa—this model should be viewed as a stimulating framework necessitating rigorous physiological verification.

CONCLUSION AND FUTURE PERSPECTIVES

From Evolutionary Oddity to Bioengineering Chassis

The liverwort oil body represents a unique evolutionary innovation that likely facilitated the terrestrialization of early embryophytes by serving as a specialized chemical factory (Romani et al., 2022). Through the characterization of the *MpERF13* regulatory network and specific SNARE/COPI trafficking systems, the status of the oil body has transitioned from a morphological curiosity to a molecularly defined organelle (Kanazawa et al., 2020; Kanazawa et al., 2022). While these mechanisms are well-established in *Marchantia polymorpha*, they provide a theoretical foundation

for prospective biotechnological applications. By leveraging the streamlined genome of *M. polymorpha* as a "green chassis," transcription factor engineering (e.g., *MpERF13-GOF*) offers a promising, though yet to be fully industrialized, platform for the scalable production of high-value lipophilic terpenoids in cell suspension cultures (Toro Acevedo, 2025).

Multidisciplinary Implications

The functional diversity of oil bodies offers critical insights across biological disciplines:

- **Pharmacology:** Sequestration of potent bisbibenzyls like marchantin A, which exhibits anti-tumor activity (Shi et al., 2009), highlights the potential for metabolic engineering. Understanding transport mechanisms via *MpABCG* proteins is crucial for optimizing the yield of these cytotoxic compounds (Kanazawa et al., 2025).

- **Systematics:** Structural diversity remains a cornerstone for chemotaxonomy. Correlations between oil body types (e.g., segmented vs. homogeneous) and specific terpenoid profiles provide robust markers for resolving phylogenetic ambiguities (Ludwiczuk & Asakawa, 2015).

- **Physiology:** Beyond biotic defense, the persistence of oil bodies in desiccation-tolerant species suggests a critical, under-explored role in abiotic stress tolerance during the water-to-land transition (Pressel et al., 2009).

Limitations and Future Directions

To advance this field from model systems to broader applications, three critical limitations must be addressed:

1. **Taxonomic Bias:** Current molecular models are heavily biased towards the thalloid liverwort *M. polymorpha*. It remains unknown whether the *MpERF13*-mediated redirection of the secretory pathway is conserved in the species-rich leafy liverworts (Jungermanniopsida), which exhibit vastly different oil body morphologies. Comparative genomic studies are urgently needed to test the universality of this mechanism.

2. **The "Tripartite Symbiosis" Hypothesis:** The recent identification of intracellular bacteria within oil bodies (Young et al., 2025) presents

a stimulating hypothesis but not yet an established paradigm. Distinguishing whether these endophytes are obligate symbionts or environmental opportunists requires rigorous verification using axenic cultures.

3. **Secretion Mechanisms:** While influx transporters (*MpABCG1/36*) have been identified, the mechanism of metabolite release from the oil body to the extracellular space remains a "black box." Elucidating this efflux pathway is essential for developing continuous biopharming systems where product extraction does not require biomass destruction.

In conclusion, the liverwort oil body stands as a testament to how evolutionary novelty—the repurposing of a secretory pathway for intracellular defense—can inform modern applications. Unlocking its remaining secrets promises not only a deeper understanding of early plant adaptation but also provides a blueprint for engineering complex metabolic traits in synthetic biology.

REFERENCES

Asakawa, Y. (1995). Chemical Constituents of the Bryophytes. In *Progress in the Chemistry of Organic Natural Products* (Vol. 65, pp. 1–562). Springer Vienna.

Asakawa, Y., & Ludwiczuk, A. (2018). Chemical constituents of bryophytes: structures and biological activity. *Journal of Natural Products*, *81*(3), 641–660.

Asakawa, Y. (2004). Chemosystematics of the hepaticae. *Phytochemistry*, *65*(6), 623–669.

Hübener, J. W. P. (1834). Hepaticologia Germanica: oder Beschreibung der deutschen Lebermoose. Schwan & Götz.

Kanazawa, T., Era, A., Minamino, N., Shikano, Y., Fujimoto, M., Uemura, T., Nishihama, R., Yamato, K. T., Ishizaki, K., Nishiyama, T., Kohchi, T., Nakano, A., & Ueda, T. (2016). SNARE molecules in *Marchantia polymorpha*: unique and conserved features of the membrane fusion machinery. *Plant Cell Physiology*, *57*(2), 307–324.

Kanazawa, T., Kawaguchi, T., Moriwaki, Y., Iwasaki, K., Ueda, T., & Matsui, K. (2025). *ABCG transporters are involved in the accumulation of specialized metabolites in the oil bodies of Marchantia polymorpha*. bioRxiv. **doi:** https://doi.org/10.1101/2025.10.27.684951

Kanazawa, T., Morinaka, H., Ebine, K., Shimada, T. L., Ishida, S., Minamino, N., Yamaguchi, K., Shigenobu, S., Kohchi, T., Nakano, A., & Ueda, T. (2020). The liverwort oil body is formed by redirection of the secretory pathway. *Nature Communications*, *11*(1), 6152.

Kanazawa, T., Nishihama, R., & Ueda, T. (2022). Normal oil body formation in *Marchantia polymorpha* requires functional coat protein complex I proteins. *Frontiers in Plant Science*, *13*, 979066.

Kubo, H., Nozawa, S., Hiwatashi, T., Kondou, Y., Nakabayashi, R., Mori, T., Tanaka, M., Kanazawa, T., & Ishizaki, K. (2018). Biosynthesis of riccionidins and marchantins is regulated by R2R3-MYB transcription factors in *Marchantia polymorpha*. *Journal of Plant Research*, *131*, 849–864.

Kubo, H., Sunhwa, K., Teramori, H., & Takanashi, K. (2024). Mp R2R3-MYB2 is a key regulator of oil body formation in *Marchantia polymorpha*. *Planta*, *260*(3), 68.

Kumar, S., Kempinski, C., Zhuang, X., Norris, A., Mafu, S., Zi, J., Bell, S. A., Nybo, S. E., Kinison, S. E., Jiang, Z., Brown, S. D., Bowman, J. L., Babbitt, P. C., Peters, R. J., Chen, F., & Chappell, J. (2016). Molecular Diversity of Terpene Synthases in the Liverwort *Marchantia polymorpha*. *The Plant Cell*, *28*(10), 2632–2650.

Ludwiczuk, A., & Asakawa, Y. (2015). Chemotaxonomic value of essential oil components in liverwort species. A review. *Flavour and Fragrance Journal*, *30*(3), 189–196.

Pressel, S., Duckett, J. G., Ligrone, R., & Proctor, M. C. F. (2009). Effects of De- and Rehydration in Desiccation-Tolerant Liverworts: A Cytological and Physiological Study. *International Journal of Plant Sciences*, *170*(2), 182–199.

Romani, F., Banić, E., Florent, S. N., Kanazawa, T., Goodger, J. Q. D., Mentink, R. A., Bowman, J. L., & Moreno, J. E. (2020). Oil body formation in *Marchantia polymorpha* Is Controlled by MpC1HDZ and Serves as a Defense against Arthropod Herbivores. *Current Biology*, *30*(14), 2815–2828.e8.

Romani, F., Flores, J. R., Tolopka, J. I., Suarez, G., He, X., & Moreno, J. E. (2022). Liverwort oil bodies: diversity, biochemistry, and molecular cell biology of the earliest secretory structure of land plants. *Journal of Experimental Botany*, *73*(13), 4427–4439.

Shi, Y. Q., Zhu, C. J., Yuan, H. Q., Li, B. Q., Gao, J., Qu, X. J., & Lou, H. X. (2009). Marchantin C, a novel microtubule inhibitor from liverwort with anti-tumor activity both in vivo and in vitro. *Cancer Letters*, *276*(2), 160–170.

Tanaka, M., Esaki, T., Kenmoku, H., Koeduka, T., Kiyoyama, Y., Masujima, T., Asakawa, Y., & Matsui, K. (2016). Direct evidence of specific localization

of sesquiterpenes and marchantin A in oil body cells of *Marchantia polymorpha* L. *Phytochemistry*, *130*, 77–84.

Toro Acevedo, C. A. (2025). *Exploring oil body formation in the liverwort Marchantia polymorpha for biotechnological applications*. (Doctoral dissertation). University of Potsdam.

Young, B. C., Thiers, B., White, J. F., & Struwe, L. (2025). Endophytic bacteria discovered in oil body organelles of the liverworts *Marchantia polymorpha* and *Radula complanata*. *American Journal of Botany*, *112*(3), e70017.

Huang, A. H. (2018). Plant lipid droplets and their associated proteins: Potential for rapid advances. Plant Physiology, 176(3), 1894–1918.

Robinson, D. G., & Pimpl, P. (2014). Receptor-mediated transport of vacuolar proteins: a critical analysis and alternative model. Protoplasma, 251(2), 247-264.

A Study of Some Geometric Properties in the Plane Eqipped with the Generalized Absolute Value Metric

Süheyla EKMEKÇİ[1]

1- Prof. Dr.; Eskişehir Osmangazi University, Department of Mathematics and Computer Science, Faculty of Science, sekmekci@ogu.edu.tr ORCID No: 0000-0003-2820-2096

ABSTRACT

This study investigates fundamental geometric concepts in the plane $\mathbb{R}_g^2$, which is equipped with the generalized absolute value distance d_g. First, the relationship between the distance d_g and the Euclidean distance between two points is expressed in terms of the slope of the line joining the given points, and several related properties are presented. Using this relationship, a formula for the area of a triangle in terms of the d_g-lengths of its base and corresponding height is obtained. Subsequently, the d_g-distance from a point to a given line is introduced. The relationship between this distance and the Euclidean distance from the point to the line is expressed depending on the slope of the line, and several properties are derived. Using this relation, an additional formula for the area of a triangle in terms of d_g-lengths is provided. Furthermore, minimum distance sets and midsets of two given points with respect to the metric d_g are examined and classified.

Keywords – Generalized absolute value metric; Minimum distance set; Midset

INTRODUCTION

Distance functions play a fundamental role in shaping the geometric structure of an analytic plane. When Euclidean distance is replaced by an alternative metric, many classical geometric objects, such as circles and medians, undergo significant changes. Minkowski distance is a family of distances that includes Euclidean and taxicab distances. Many generalizations of distance functions exist in the literature, including the generalized absolute value distance, (Çolakoğlu et al, 2013:123), (Ekmekçi et al, 2015:159), (Ekmekçi et al, 2015:29), (Akça and Nazlı, 2022:128). The generalized absolute value distance is presented in (Kaya et al, 2009:591), (Bayar et al, 2008:1). The plane $\mathbb{R}_g^2$, equipped with the generalized absolute value distance d_g, is a non-Euclidean geometry and provides a rich framework for systematic study. This metric generates an infinite family of distance functions depending on the parameters.

This study examines fundamental geometric structures in the plane $\mathbb{R}_g^2$. By analyzing the concepts of minimum distance sets and midsets between two points, a classification of these sets is provided. Then, the distance between a point and a line is formulated. Furthermore, the relationships between Euclidean and the distance d_g are characterized in terms of the slope

parameter of lines, and these relationship are utilized to derive area formulas for triangles.

PRELIMINARIES ON THE DISTANCE d_g

In this section, some definitions, concepts and theorems used throughout this work are mentioned.

Definition 1. Consider the analytic plane, denoted by $\mathbb{R}^2$, and let $A=(a_1,a_2)$ and $B=(b_1,b_2)$ be any two points in it. For real numbers λ_1 and λ_2 satisfying $\lambda_1 \geq \lambda_2 \geq 0$ and $\lambda_1 \neq 0$, the expression

$$d_g(A,B)=\lambda_1 \max\{|a_1-b_1|,|a_2-b_2|\}+\lambda_2 \min\{|a_1-b_1|,|a_2-b_2|\}$$

defines the generalized absolute value distance d_g between the points A and B, (Kaya et al, 2009:591).

The plane equipped with the distance d_g is represented as $\mathbb{R}_g^2=(\mathbb{R}^2,d_g)$. Different choices of the constants λ_1 and λ_2 yield a family of such distance functions.

The plane $\mathbb{R}_g^2$ shares an identical points and lines with the plane $\mathbb{R}^2$. Angle measurement is also defined and performed analogously in both planes. The differences between the two geometries arise from the definition of distance. Consequently, any geometric property or concept fundamentally reliant on the notion of distance—such as the distance from a point to a line, or the definition of a circle—occurs differently in $\mathbb{R}_g^2$ compared to its Euclidean counterpart.

By Definition 1, each pair of real numbers $\lambda_1,\lambda_2 \in \mathbb{R}$ corresponds to a distinct distance function. This implies that the distances form a family of metrics. Several notable special cases arise for specific parameter choices:

- When both parameters, λ_1 and λ_2, are equal to 1, the distance d_g reduces to the taxicab distance d_T.
- When the parameters λ_1 and λ_2 are equal, the distance d_g is precisely the taxicab metric d_T multiplied by the scalar λ_1.
- When the parameters λ_1 and λ_2 equal 1 and 0, respectively, the distance d_g coincides with the maximum distance d_M.
- When the parameters λ_1 and λ_2 equal 1 and $\sqrt{2}-1$, respectively, the distance d_g coincides with the Chinese Checkers distance d_C.

- When the parameters λ_1 and λ_2 equal 1 and $\sec\alpha-\tan\alpha$, respectively, the distance d_g coincides with the α - distance where $\alpha\in\left[0,\frac{\pi}{2}\right]$.

It can be seen that there is an infinite number of different distance functions depending on the parameters λ_1 and λ_2. In this study, unless otherwise stated, it is assumed that the parameters λ_1 and λ_2 are initially determined and fixed.

It is clear that the d_g distance between the points A and B equals the sum of "λ_1" times the longest Euclidean length and "λ_2" times the shortest Euclidean length of the sides (which are parallel to the coordinate axes) in the right triangle with the hypotenuse AB. The shortest path between the points A and B is the union of a vertical or a horizontal line segment and the line segment with the slope $\pm\frac{2\lambda_1\lambda_2}{\lambda_1^2-\lambda_2^2}$.

Theorem 2. The generalized absolute value distance

$$d_g:\mathbb{R}^2\times\mathbb{R}^2\to[0,\infty)$$

is a metric, (Kaya et al, 2009:591).

Krause classified lines depending on their slope as follows:

Definition 3. Let m be the slope of the line l. The line l is referred to as *the steep line, the gradual line* and *the separator line* in the cases where $|m|>1$, $|m|<1$ and $|m|=1$, respectively. In the special cases that the line l is parallel to the x-axis or the y-axis, it is called *the horizontal line* or *the vertical line*, respectively, (Krause, 1975:31).

The geometric properties of the plane $\mathbb{R}_g^2$ are systematically studied using Krause's classification as an analytical tool in this study.

In $\mathbb{R}_g^2$, a circle is still defined as the set of all points that are the same distance d_g (the radius) from a point (the center), but because of the definition of the distance d_g, the circle is an octagon rather than a smooth curve. In $\mathbb{R}_g^2$, the points on the circle with the center $\mathcal{M}=(m_1,m_2)$ and the radius r satisfy the equation:

$$\lambda_1\max\{|x-m_1|,|y-m_2|\}+\lambda_2\min\{|x-m_1|,|y-m_2|\}=r.$$

The circle has eight vertices that are on the horizontal, the vertical lines and the separator lines passing through the center $\mathcal{M}$. These vertices are $(m_1+\frac{r}{\lambda_1},m_2)$, $(m_1+\frac{r}{\lambda_1+\lambda_2},m_2+\frac{r}{\lambda_1+\lambda_2})$, $(m_1,m_2+\frac{r}{\lambda_1})$, $(m_1-\frac{r}{\lambda_1+\lambda_2},m_2+\frac{r}{\lambda_1+\lambda_2})$, $(m_1-\frac{r}{\lambda_1},m_2)$, $(m_1-\frac{r}{\lambda_1+\lambda_2},m_2-\frac{r}{\lambda_1+\lambda_2})$, $(m_1,m_2-\frac{r}{\lambda_1})$ and

$(m_1+\frac{r}{\lambda_1+\lambda_2}, m_2-\frac{r}{\lambda_1+\lambda_2})$. Thus, it is made up of the line segments connecting these vertices, forming a octagon.

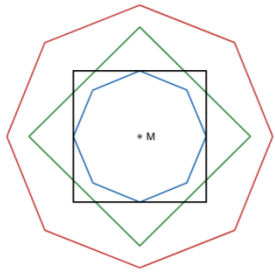

Figure 1 Circles in $\mathbb{R}_g^2$

In the figure, circles with center *M* and radius *r* are given for some values of parameters λ_1 and λ_2.

Theorem 4. All translations of the Euclidean plane are isometries in the plane $\mathbb{R}_g^2$, (Kaya et al, 2009:591).

Theorem 5. The reflections in the line $y=mx$ are isometries in $\mathbb{R}_g^2$ where $m\in\{0,\pm1,\infty\}$ for $\frac{b}{a}\neq\sqrt{2}-1$ and $m\in\{0,\pm1,\pm(\sqrt{2}-1),\pm(\sqrt{2}+1),\infty\}$ for $\frac{b}{a}=\sqrt{2}-1$, (Kaya et al, 2009:591).

Theorem 6. The rotations R_θ about the origin are isometries in $\mathbb{R}_g^2$ where $\theta\in\{0,\frac{\pi}{2},\pi,\frac{3\pi}{2}\}$ for $\frac{b}{a}\neq\sqrt{2}-1$ and $\theta\in\{0,\frac{\pi}{4},\frac{\pi}{2},\frac{3\pi}{4},\pi,\frac{5\pi}{4},\frac{3\pi}{2},\frac{7\pi}{4}\}$ for $\frac{b}{a}=\sqrt{2}-1$, (Kaya et al, 2009:591).

SLOPE-BASED RELATIONSHIP BETWEEN d_E AND d_g DISTANCES

The following theorem characterizes how the Euclidean distance and the distance d_g are related in the analytical plane.

Theorem 7. Let A and B be any two distinct points in $\mathbb{R}_g^2$. The generalized absolute value distance d_g between points A and B satisfies the equality $d_g(A,B)=\rho(m).d_E(A,B)$, where

$$\rho(m)=\begin{cases}\dfrac{\lambda_1+\lambda_2|m|}{\sqrt{1+m^2}}, & |m|\leq 1\\[2ex] \dfrac{\lambda_1|m|+\lambda_2}{\sqrt{1+m^2}}, & |m|\geq 1,\end{cases}$$

and *m* is the slope of the line passing through the points A and B, (Kaya et al, 2009:591).

Proof: Assume the line passing through points $A=(a_1,a_2)$ and $B=(b_1,b_2)$ coincides with the *x*-axis. In this case, the slope $m=0$. The Euclidean distance d_E between points A and B is $d_E(A,B)=|a_1-b_1|$, while the distance d_g is $d_g(A,B)=\lambda_1|a_1-b_1|$. Thus, it follows that:

$$d_g(A,B)=\lambda_1 d_E(A,B).$$

And, when $m=0$, $\rho(m)=\frac{\lambda_1+\lambda_2|m|}{\sqrt{1+m^2}}=\lambda_1$. Then $d_g(A,B)=\rho(m)d_E(A,B)$. The same relationship holds if the line through A and B is a horizontal line.

Now, suppose that the line through A and B is the *y*-axis. Then, $d_E(A,B)=|a_2-b_2|$ and $d_g(A,B)=\lambda_1|a_2-b_2|$, yielding

$$d_g(A,B)=\lambda_1 d_E(A,B).$$

And, since $m\to\infty$, $\lim_{m\to\infty}\frac{\lambda_1|m|+\lambda_2}{\sqrt{1+m^2}}=\lambda_1=\rho(m)$. Then it can be written that $d_g(A,B)=\rho(m)d_E(A,B)$. This result similarly applies when the line is vertical.

Finally, consider the case where the line through A and B is not parallel to either coordinate axis and has a slope *m* satisfying $|m|>1$. Under this assumption,

$$|a_2-b_2|>|a_1-b_1|,$$

so the distance d_g can be expressed as:

$$d_g(A,B)=\lambda_1|a_2-b_2|+\lambda_2|a_1-b_1|=|a_1-b_1|(\lambda_1|m|+\lambda_2).$$

The Euclidean distance between A and B is given by:

$$d_E(A,B)=\sqrt{(a_1-b_1)^2+(a_2-b_2)^2}=|a_1-b_1|\sqrt{1+m^2}.$$

Thus, the ratio of the distance d_g to the distance d_E is

$$\frac{d_g(A,B)}{d_E(A,B)}=\frac{\lambda_1|m|+\lambda_2}{\sqrt{1+m^2}}.$$

Rearranging this relationship, it is obtained

$$d_g(A,B)=\frac{\lambda_1|m|+\lambda_2}{\sqrt{1+m^2}}d_E(A,B).$$

Now, consider the case where $|m|<1$. In this situation:

$$|a_2-b_2|<|a_1-b_1|,$$

which implies

$$d_g(A,B) = \lambda_1 |a_1 - b_1| + \lambda_2 |a_2 - b_2| = |a_1 - b_1|(\lambda_1 + \lambda_2 |m|).$$

The ratio of the distance d_g to the distance d_E is

$$\frac{d_g(A,B)}{d_E(A,B)} = \frac{\lambda_1 + \lambda_2 |m|}{\sqrt{1+m^2}}$$

and consequently,

$$d_g(A,B) = \frac{\lambda_1 + \lambda_2 |m|}{\sqrt{1+m^2}} d_E(A,B).$$

This completes the proof.

Consequently, ρ, defined in terms of the slope, provides a method for converting Euclidean distances to d_g distances. Also, $\rho(m)$ can be generally expressed as the following

$$\rho(m) = \frac{\lambda_1 \max\{1,|m|\} + \lambda_2 \min\{1,|m|\}}{\sqrt{1+m^2}}.$$

The following properties follow immediately from the definition of ρ given in Theorem 7.

Corollary 8. For any nonzero real number *m*, the following identities hold for the relation ρ,

$$\rho(m) = \rho(-m) = \rho(\frac{1}{m}) = \rho(-\frac{1}{m}).$$

Theorem 7 establishes that for any line, the distance d_g is proportional to the distance d_E measured along that line, with a positive constant of proportionality. The subsequent results are direct consequences of this relationship.

Corollary 9. Let A_1, A_2, and A_3 be three collinear points in the analytical plane. Then, $d_E(A_1,A_2) = d_E(A_2,A_3) \Leftrightarrow d_g(A_1,A_2) = d_g(A_2,A_3)$, (Kaya et al, 2009:591).

Corollary 10. Let A_1, A_2, and A_3 be three collinear points in the analytical plane. Then,

$$\frac{d_g(A_1,A_3)}{d_g(A_2,A_3)} = \frac{d_E(A_1,A_3)}{d_E(A_2,A_3)},$$

(Kaya et al, 2009:591).

THE MINIMUM DISTANCE SET

Definition 11. Let $A=(a_1,a_2)$ and $B=(b_1,b_2)$ be two points in $\mathbb{R}_g^2$. The *minimum distance set* between A and B is defined as the set

$$\left\{ X \in \mathbb{R}_g^2 \middle| d_g(A,X)+d_g(X,B)=d_g(A,B) \right\}.$$

This set, denoted by $\overline{AB}$, consists of all points X for which the sum of the distances from A to X and from X to B equals the distance d_g between A and B, (Aylıkçı, D., 2025:54).

It is examined the structure of $\overline{AB}$ based on the relative positions of points A and B as follows. Since translations preserve the distance d_g, assuming point A to be at the origin does not compromise generality.

1) First, consider the case where A and B lie on the *x*-axis. Let $B=(b_1,0)$, where $b_1>0$. Substituting the distance formula in the definition of $\overline{AB}$ yields:

$$\lambda_1 \max\{|x|,|y|\}+\lambda_2 \min\{|x|,|y|\}+\lambda_1 \max\{|x-b_1|,|y|\}+\lambda_2 \min\{|x-b_1|,|y|\}=\lambda_1|b_1|.$$

When this equation is examined, it is seen that the set $\overline{AB}$ is the line segment AB. The same result holds if the line through A and B is horizontal.

2) Consider the case where A and B lie on the *y*-axis. Let $B=(0,b_2)$, where $b_2>0$. Substituting the distance formula in the definition of $\overline{AB}$ yields:

$$\lambda_1 \max\{|x|,|y|\}+\lambda_2 \min\{|x|,|y|\}+\lambda_1 \max\{|x|,|y-b_2|\}+\lambda_2 \min\{|x|,|y-b_2|\}=\lambda_1|b_2|.$$

When this equation is examined, it is seen that the set $\overline{AB}$ is the line segment AB. The same result holds if the line through A and B is vertical.

3) Consider the case where A and B lie on the separator line $y=x$. Let the abscissa of point B be b_1 where $b_1>0$. The minimum distance set $\overline{AB}$ satisfies the equality

$$\lambda_1 \max\{|x|,|y|\}+\lambda_2 \min\{|x|,|y|\}+\lambda_1 \max\{|x-b_1|,|y-b_1|\}+\lambda_2 \min\{|x-b_1|,|y-b_1|\}=(\lambda_1+\lambda_2)|b_1|.$$

When this equation is examined, it is seen that the set $\overline{AB}$ is the line segment AB. The same result holds if the line through A and B is the separator line $y=-x$.

4) Consider the case where A and B lie on a gradual line. Let $B=(b_1,b_2)$, where $b_1>b_2>0$. The minimum distance set $\overset{\square}{AB}$ satisfies the equality $\lambda_1\max\{|x|,|y|\}+\lambda_2\min\{|x|,|y|\}+\lambda_1\max\{|x-b_1|,|y-b_2|\}+\lambda_2\min\{|x-b_1|,|y-b_2|\}=\lambda_1|b_1|+\lambda_2|b_2|.$

From here, it is seen that the set $\overset{\square}{AB}$ is the region bounded by the parallelogram formed by the separator lines with positive slope and horizontal lines passing through points A and B. If line AB has a negative slope, the set $\overset{\square}{AB}$ is the region bounded by the parallelogram formed by the separator lines with negative slope and horizontal lines passing through points A and B.

5) Consider the case where A and B lie on a steep line. Let $B=(b_1,b_2)$, where $b_2>b_1>0$. The minimum distance set $\overset{\square}{AB}$ satisfies the equality $\lambda_1\max\{|x|,|y|\}+\lambda_2\min\{|x|,|y|\}+\lambda_1\max\{|x-b_1|,|y-b_2|\}+\lambda_2\min\{|x-b_1|,|y-b_2|\}=\lambda_1|b_2|+\lambda_2|b_1|.$

And, it is seen that the set $\overset{\square}{AB}$ is the region bounded by the parallelogram formed by the separator lines with positive slope and vertical lines passing through points A and B. If line AB has a negative slope, the set $\overset{\square}{AB}$ is the region bounded by the parallelogram formed by the separator lines with negative slope and vertical lines passing through points A and B.

The minimum distance set plays a role analogous to collinear points with respect tothe triangle inequality: every point X in the minimum distance set satisfies the equality $\left|d_g(A,X)+d_g(X,B)=d_g(A,B)\right.$.

THE MIDSET

Definition 12. Let A and B be any two distinct points in the plane $\mathbb{R}_g^2$. The midset of the points A and B is defined as the locus of points equidistant from A and B with respect to the distance d_g. Formally, the set is given by

$$\left\{X\in\mathbb{R}_g^2 \mid\ d_g(X,A)=d_g(X,B)\right\},$$

(Aylıkçı, D., 2025:54).

The geometric structure of this midset varies depending on the positions of A and B in the plane. In the following, the structure of the midset is classified according to the type of line passing through points A and B.

1) Assume that points A and B share the same coordinate axis. Let this coordinate axis be the *x*-axis. As in the minimum distance set, taking point A to be at the origin will not affect generality. Let the coordinates of point

B be $(b_1,0)$, where $b_1>0$. Then every point $X=(x,y)$ in the midset of A and B satisfies the equality

$$\lambda_1\max\{|x|,|y|\}+\lambda_2\min\{|x|,|y|\}=\lambda_1\max\{|x-b_1|,|y|\}+\lambda_2\min\{|x-b_1|,|y|\}.$$

As a result of examining this equation, it is seen that the midset consists of the vertical line $x=\frac{b_1}{2}$ passing through the midpoint of the points.

In the case where the points are on the *y*-axis, the midset is similarly the horizontal line passing through the midpoint of the points.

2) Assume that points A and B are on the separator line $y=x$. Let the abscissa of point B be b_1. Then, the equation

$$\lambda_1\max\{|x|,|y|\}+\lambda_2\min\{|x|,|y|\}=\lambda_1\max\{|x-b_1|,|y-b_1|\}+\lambda_2\min\{|x-b_1|,|y-b_1|\}$$

holds for the midset of these points. From this equation it is obtained that the midset is the other separator line passing through the midpoint of the given points. This result also holds when the points are on the separator line $y=-x$.

3) When the points A and B are on a horizontal or vertical line, it is clear that the result obtained in (1) remains valid for this case as well, since an appropriate translation reduces the configuration to the previously considered situation.

4) Assume that points A and $B=(b_1,b_2)$ are on a gradual line where $b_1>b_2>0$. Then, the equation

$$\lambda_1\max\{|x|,|y|\}+\lambda_2\min\{|x|,|y|\}=\lambda_1\max\{|x-b_1|,|y-b_2|\}+\lambda_2\min\{|x-b_1|,|y-b_2|\}$$

holds for the midset of these points. Examining this equation yields the followings:

i) If the slope *m* of the gradual line is different from $\pm\frac{\lambda_2}{\lambda_1}$, the midset is formed by the union of two vertical rays and five line segments such that two of the line segments are on vertical lines, the other two are on two steep lines, and one is on the line with slope $\operatorname{sgn}(-m)\frac{\lambda_1}{\lambda_2}$ passing through the midpoint of the points.

ii) If the slope *m* of the gradual line is equal to $\pm\frac{\lambda_2}{\lambda_1}$, the midset is formed by the union of two regions and five line segments such that each region is determined by the vertical line through one of the points and the separator line with slope $\operatorname{sgn}(-m)$ passing through the other and, two of the line segments are on vertical lines, the other two are on two steep lines, and

one is on the line with slope $\operatorname{sgn}(-m)\dfrac{\lambda_1}{\lambda_2}$ passing through the midpoint of the points.

5) Assume that points A and $B=(b_1,b_2)$ are on a steep line where $b_2>b_1>0$. Then, the equation

$$\lambda_1\max\{|x|,|y|\}+\lambda_2\min\{|x|,|y|\}=\lambda_1\max\{|x-b_1|,|y-b_2|\}+\lambda_2\min\{|x-b_1|,|y-b_2|\}$$

holds for the midset of these points. Examining this equation yields the followings:

i) If the slope *m* of the steep line is different from $\pm\dfrac{\lambda_1}{\lambda_2}$, the midset is formed by the union of two horizontal rays and five line segments such that two of the line segments are on horizontal lines, the other two are on two gradual lines, and one is on the line with slope $\operatorname{sgn}(-m)\dfrac{\lambda_2}{\lambda_1}$ passing through the midpoint of the points.

ii) If the slope *m* of the steep line is equal to $\pm\dfrac{\lambda_1}{\lambda_2}$, the midset is formed by the union of two regions and five line segments such that each region is determined by the horizontal line through one of the points and the separator line with slope $\operatorname{sgn}(-m)$ passing through the other and, two of the line segments are on horizontal lines, the other two are on two gradual lines, and one is on the line with slope $\dfrac{\operatorname{sgn}(-m)}{m}$ passing through the midpoint of the points.

THE DISTANCE d_g FROM A POINT TO A LINE

The distance from a point to a line is a fundamental concept in analytic geometry. The distance from a point $P=(p_1,p_2)$ to a line d with the equation $ax+by+c=0$ is defined as the length of the shortest path from point P to line d. In plane $\mathbb{R}_g^2$, the distance d_g from a point P to a line d is defined as the smallest distance d_g from P to any point on the line d. In short,

$$d_g(P,d)=\min_{X\in d}\{d_g(P,X)\}.$$

In the Euclidean plane, this shortest path corresponds to the perpendicular segment dropped from the point to the line. And, it is calculated by the formula

$$d_E(P,d)=\frac{|ap_1+bp_2+c|}{\sqrt{a^2+b^2}}.$$

In non-Euclidean geometries, the distance from a point to a line is computed differently. In such geometries, the "shortest path" may no longer be perpendicular to the line; rather, it depends on the specific definition of the distance in use. In a non-Euclidean geometry, to determine the distance from a point to a line, a circle centered at the given point is constructed. The radius of this circle is then gradually increased. When the circle first touches the line, the corresponding radius is equal to the distance from the point to the line. When this method is applied to examine the distance d_g from a point P to a line d in the plane $\mathbb{R}_g^2$, the following observations are made:

i) If the absolute value of the slope of the line d is greater than or equal to $\frac{\lambda_1}{\lambda_2}$, then the distance d_g from the point P to line d is the d_g length of the line segment between the point P and the point where the line through P parallel to the *x*- axis intersects the line d.

ii) If the absolute value of the slope of the line d is less than or equal to $\frac{\lambda_2}{\lambda_1}$, then the distance d_g from the point P to line d is the d_g length of the line segment between the point P and the point where the line through P parallel to the *y*- axis meets the line d.

iii) If the absolute value of the slope of the line d is between $\frac{\lambda_2}{\lambda_1}$ and $\frac{\lambda_1}{\lambda_2}$, inclusive, then the distance d_g from the point P to line d is the d_g length of the line segment between the point P and the point where the separator line through P meets the line d, (Aylıkçı, D., 2025:54).

Theorem 13. In the plane $\mathbb{R}_g^2$, the distance d_g from a point $P=(p_1,p_2)$ to the line d given by the equation $ax+by+c=0$ is

$$d_g(P,d)=\begin{cases}\dfrac{\lambda_1|ap_1+bp_2+c|}{|b|} & ,|m|\le\dfrac{\lambda_2}{\lambda_1}\\[2ex] \dfrac{(\lambda_1+\lambda_2)|ap_1+bp_2+c|}{|a+\operatorname{sgn}(-m)b|} & ,\dfrac{\lambda_2}{\lambda_1}\le|m|\le\dfrac{\lambda_1}{\lambda_2}\\[2ex] \dfrac{\lambda_1|ap_1+bp_2+c|}{|a|} & ,|m|\ge\dfrac{\lambda_1}{\lambda_2}\end{cases}$$

where *m* denotes the slope of the line d.

Proof: Let circles centered at P be considered.

i) If $|m|$ is less than or equal to $\frac{\lambda_2}{\lambda_1}$, then the line d will touch the circle at one of the antipodal points on the diameter parallel to the y-axis. In

this case, the intersection point of the line $x = p_1$ and the line d is $\left(p_1, \frac{-ap_1 - c}{b}\right)$. Thus, the distance d_g from point P to the line d is obtained as

$$\frac{\lambda_1 |ap_1 + bp_2 + c|}{|b|}.$$

ii) If $|m|$ is greater than or equal to $\frac{\lambda_1}{\lambda_2}$, then the line d will touch the circle at one of the antipodal points on the diameter parallel to the *x*-axis. In this case, the point where the line $y = p_2$ intersects the line d is $\left(\frac{-bp_2 - c}{a}, p_2\right)$. Thus, the distance d_g from point P to the line d is obtained as

$$\frac{\lambda_1 |ap_1 + bp_2 + c|}{|a|}.$$

iii) If $|m|$ is is between $\frac{\lambda_2}{\lambda_1}$ and $\frac{\lambda_1}{\lambda_2}$, inclusive, then the line d will touch the circle at one of the antipodal points of the diameter on the separator line whose the sign of slope is $\text{sgn}(-m)$. In this case, the point that the line $y - p_2 = \text{sgn}(-m)(x - p_1)$ meets the line d is $\left(\frac{b\,\text{sgn}(-m)\,p_1 - bp_2 - c}{a + \text{sgn}(-m)b}, \frac{a(p_2 - \text{sgn}(-m)\,p_1) - \text{sgn}(-m)c}{a + \text{sgn}(-m)b}\right)$. In this case, the distance d_g from point P to the line d is obtained as

$$(\lambda_1 + \lambda_2)\frac{|ap_1 + bp_2 + c|}{|a + sgn(-m)b|}.$$

The proof is completed.

The following theorem provides a general formula for calculating the distance between a point and a line in plane $\mathbb{R}_g^2$:

Theorem 14. Let $P = (p_1, p_2)$ be a point in the plane $\mathbb{R}_g^2$. The shortest distance d_g from point P to the line d given by the equation $ax + by + c = 0$ is

$$d_g(P, d) = \frac{|ap_1 + bp_2 + c|}{\max\left\{\frac{|a|}{\lambda_1}, \frac{|b|}{\lambda_1}, \frac{|a + sgn(-m)b|}{\lambda_1 + \lambda_2}\right\}}.$$

The proof of this theorem is clear from Theorem 13.

Analogously to the ratio of distances between two points, the ratio of the d_E and d_g distances from a point to a line can be expressed in the following way:

$$\frac{d_E(P,d)}{d_g(P,d)} = \frac{\max\left\{\frac{|a|}{\lambda_1}, \frac{|b|}{\lambda_1}, \frac{|a+sgn(-m)b|}{\lambda_1+\lambda_2}\right\}}{\sqrt{a^2+b^2}}.$$

The following theorem establishes a fundamental relationship between the distance d_g and the Euclidean distance d_E from a point to a line:

Theorem 15. Let $P=(p_1,p_2)$ and d be any point and the line given by the equation $ax+by+c=0$ in $\mathbb{R}_g^2$, respectively. The distance d_g from point P to the line d satisfies the equality

$$d_g(P,d) = \delta(m).d_E(P,d),$$

where

$$\delta(m) = \begin{cases} \lambda_1\sqrt{1+m^2}, & |m| \le \frac{\lambda_2}{\lambda_1} \\ \frac{(\lambda_1+\lambda_2)\sqrt{1+m^2}}{|m+\mathrm{sgn}(m)|}, & \frac{\lambda_2}{\lambda_1} \le |m| \le \frac{\lambda_1}{\lambda_2} \\ \frac{\lambda_1\sqrt{1+m^2}}{|m|}, & |m| \ge \frac{\lambda_1}{\lambda_2} \end{cases}$$

and *m* is the slope of the line d.

The following properties follow immediately from the definition of δ given in Theorem 15.

Corollary 16. For any nonzero real number *m*, the following identities hold for the relation δ

$$\delta(m) = \delta(-m) = \delta(\frac{1}{m}) = \delta(-\frac{1}{m}).$$

AREA OF A TRIANGLE IN THE PLANE $\mathbb{R}_g^2$

The area of a triangle is equal to one half of the product of the lengths of a chosen base and the height corresponding to that base. The term base refers to any side of the triangle, while the height is the length of the perpendicular drawn from the vertex opposite the base to the line containing that base. However, this formula does not apply in the non-Euclidean plane, (Kaya, 2006:219), (Çolakoğlu et al., 2013:123). The Euclidean area of a triangle, expressed in terms of the d_g-lengths of its base and height, is examined in the following.

Theorem 17. Let ABC be a triangle with area $\mathcal{A}$ and the side BC be chosen as the base of triangle. Let d_g - length of BC be denoted by a_g and, let d_g - length of the perpendicular from vertex A to the base be denoted by h_g. If the slope of BC is m_{BC}, then the area of the triangle can be expressed in terms of the d_g - lengths and $\rho(m_{BC})$ by

$$\mathcal{A} = \frac{1}{\rho(m_{BC})^2}\frac{a_g h_g}{2}.$$

Proof. The Euclidean and d_g lengths of the base of triangle are $a = d_E(B,C)$ and $a_g = d_g(B,C)$. Similarly, the Euclidean and d_g lengths of the height (perpendicular) corresponding to the base are $h = d_E(A,H)$ and $h_g = d_g(A,H)$, where point H is the foot of the perpendicular drawn from point A to line BC.

If the base BC is on a horizontal line, then $m_{BC} = 0$ and AH is on the vertical line. In this case, the proof of Theorem 7 shows that $a_g = \lambda_1 a$ and $h_g = \lambda_1 h$. Substitution of these in area formula yields

$$\mathcal{A} = \frac{ah}{2} = \frac{1}{\lambda_1^2}\frac{a_g h_g}{2} = \frac{1}{\rho(m_{BC})^2}\frac{a_g h_g}{2}.$$

If the base BC is not on the horizontal line, then $m_{BC} \neq 0$ and $a_g = \rho(m_{BC})a$. Since the slope of the height is $-\frac{1}{m_{BC}}$, it similarly follows that $h_g = \rho(-\frac{1}{m_{BC}})h$. From Corollary 8, it is clear that $\rho(m_{BC}) = \rho(-\frac{1}{m_{BC}})$. When these expressions are substituted in the area formula of the triangle ABC, it is obtained that

$$\mathcal{A} = \frac{ah}{2} = \frac{1}{\rho(m_{BC})^2}\frac{a_g h_g}{2}.$$

This completes the proof.

In the Euclidean plane, the length of the height (perpendicular) from the vertex A to the side BC of triangle ABC is always equal to the Euclidean distance from A to the line BC. However, in the plane $\mathbb{R}_g^2$, d_g-length of the height need not coincide with the distance d_g from the vertex A to the line BC. In the following, the area of triangle ABC is expressed in terms of the length d_g of the side BC and the distance d_g from vertex A to the line BC.

Theorem 18. Let ABC be a triangle with area $\mathcal{A}$ and the side BC be chosen as the base of triangle. Let d_g - length of BC be denoted by a_g and, let the distance d_g from the vertex A to the base be denoted by h_g. If the

slope of the side BC is m_{BC}, then the area of the triangle can be expressed in terms of d_g - lengths, $\rho(m_{BC})$ and $\delta(m_{BC})$ by

$$\mathcal{A} = \frac{1}{\rho(m_{BC})\delta(m_{BC})}\frac{a_g h_g}{2}.$$

Proof. The Euclidean and d_g lengths of the base of triangle are $a = d_E(B,C)$ and $a_g = d_g(B,C)$. Similarly, the Euclidean and d_g distances from the vertex A to the base are $h = d_E(A,BC)$ and $h_g = d_g(A,BC)$.

Assuming that the side BC lies on a horizontal line, then the relations $a_g = \lambda_1 a$ and $h_g = \lambda_1 h$ are valid. Consequently, the area of the triangle is derived in the form

$$\mathcal{A} = \frac{ah}{2} = \frac{1}{\lambda_1^2}\frac{a_g h_g}{2} = \frac{1}{\rho(m_{BC})\delta(m_{BC})}\frac{a_g h_g}{2}.$$

Now, suppose that the side BC lies on a vertical line. In this case as well, the equalities $a_g = \lambda_1 a$ and $h_g = \lambda_1 h$ hold, and the area of the triangle is obtained in the form

$$\mathcal{A} = \frac{ah}{2} = \frac{1}{\lambda_1^2}\frac{a_g h_g}{2} = \frac{1}{\rho(m_{BC})\delta(m_{BC})}\frac{a_g h_g}{2}.$$

Let the side BC lie on neither a horizontal line nor a vertical line. Then it can be on a gradual line, a steep line, or a separator line.

Assume that the side BC is on a gradual line, then $|m_{BC}| < 1$. When $|m_{BC}| \le \frac{\lambda_2}{\lambda_1}$, the equalities $a_g = \frac{\lambda_1 + \lambda_2 |m_{BC}|}{\sqrt{1+m_{BC}^2}} a = \rho(m_{BC})a$ and $h_g = \lambda_1\sqrt{1+m_{BC}^2}\,h = \delta(m_{BC})h$ hold, and the area of the triangle is obtained in the form

$$\mathcal{A} = \frac{ah}{2} = \frac{1}{\lambda_1(\lambda_1 + \lambda_2|m_{BC}|)}\frac{a_g h_g}{2} = \frac{1}{\rho(m_{BC})\delta(m_{BC})}\frac{a_g h_g}{2}.$$

When $\frac{\lambda_2}{\lambda_1} \le |m_{BC}| \le 1$, the equalities $a_g = \frac{\lambda_1 + \lambda_2 |m_{BC}|}{\sqrt{1+m_{BC}^2}} a = \rho(m_{BC})a$ and $h_g = \frac{(\lambda_1+\lambda_2)\sqrt{1+m_{BC}^2}}{|m_{BC} + \operatorname{sgn}(m_{BC})|} h = \delta(m_{BC})h$ hold, and the area of the triangle is obtained in the form

$$\mathcal{A} = \frac{ah}{2} = \frac{|m_{BC} + \operatorname{sgn}(m_{BC})|}{(\lambda_1+\lambda_2)(\lambda_1 + \lambda_2|m_{BC}|)}\frac{a_g h_g}{2} = \frac{1}{\rho(m_{BC})\delta(m_{BC})}\frac{a_g h_g}{2}.$$

In particular, for the case where the slope of the gradual line BC is $\frac{\lambda_2}{\lambda_1}$, the equalities $a_g = \sqrt{\lambda_1^2+\lambda_2^2}a = \rho(m_{BC})a$ and $h_g = \sqrt{\lambda_1^2+\lambda_2^2}h = \delta(m_{BC})h$ hold, and the area of the triangle is obtained in the form

$$\mathcal{A} = \frac{ah}{2} = \frac{1}{\lambda_1^2+\lambda_2^2}\frac{a_g h_g}{2} = \frac{1}{\rho(m_{BC})\delta(m_{BC})}\frac{a_g h_g}{2}.$$

Now, assume that the side BC is on a steep line, $|m_{BC}|>1$. When $|m_{BC}| \geq \frac{\lambda_1}{\lambda_2}$, the equalities $a_g = \frac{\lambda_1|m_{BC}|+\lambda_2}{\sqrt{1+m_{BC}^2}}a = \rho(m_{BC})a$ and $h_g = \frac{\lambda_1}{|m_{BC}|}\sqrt{1+m_{BC}^2}h = \delta(m_{BC})h$ hold, and the area of the triangle is obtained in the form

$$\mathcal{A} = \frac{ah}{2} = \frac{|m_{BC}|}{\lambda_1(\lambda_1|m_{BC}|+\lambda_2)}\frac{a_g h_g}{2} = \frac{1}{\rho(m_{BC})\delta(m_{BC})}\frac{a_g h_g}{2}.$$

When $1 \leq |m_{BC}| \leq \frac{\lambda_1}{\lambda_2}$, the equalities $a_g = \frac{\lambda_1+\lambda_2|m_{BC}|}{\sqrt{1+m_{BC}^2}}a = \rho(m_{BC})a$ and $h_g = \frac{(\lambda_1+\lambda_2)\sqrt{1+m_{BC}^2}}{|m_{BC}+\mathrm{sgn}(m_{BC})|}h = \delta(m_{BC})h$ hold, and the area of the triangle is obtained in the form

$$\mathcal{A} = \frac{ah}{2} = \frac{|m_{BC}+\mathrm{sgn}(m_{BC})|}{(\lambda_1+\lambda_2)(\lambda_1|m_{BC}|+\lambda_2)}\frac{a_g h_g}{2} = \frac{1}{\rho(m_{BC})\delta(m_{BC})}\frac{a_g h_g}{2}.$$

In particular, for the case where the slope of the steep line BC is $\frac{\lambda_1}{\lambda_2}$, the result is the same as that obtained for a gradual line BC with slope $\frac{\lambda_2}{\lambda_1}$.

Finally, assume that side BC is on a separator line. Then $a_g = \frac{\lambda_1+\lambda_2}{\sqrt{2}}a = \rho(m_{BC})a$ and $h_g = \frac{(\lambda_1+\lambda_2)\sqrt{2}}{2}h = \delta(m_{BC})h$. And the area of the triangle is

$$\mathcal{A} = \frac{ah}{2} = \frac{2}{(\lambda_1+\lambda_2)^2}\frac{a_g h_g}{2} = \frac{1}{\rho(m_{BC})\delta(m_{BC})}\frac{a_g h_g}{2}.$$

CONCLUSION

This study systematically investigated fundamental geometric concepts in the plane $\mathbb{R}_g^2$, which is equipped with the generalized absolute value distance d_g. The plane $\mathbb{R}_g^2$ is a non-Euclidean geometry that causes significant changes in the basic objects of Euclidean geometry. The main results obtained are summarized as follows:

- **Relationship Between Distances:** The relationship between the generalized absolute value distance d_g and the Euclidean distance d_E between two points was expressed through a slope-dependent ratio $\rho(m)$, where m is the slope of the line joining the points. This relationship demonstrates that the distance d_g is proportional to the Euclidean distance along the line, with a positive constant of proportionality dependent on the slope.
- **Distance from a Point to a Line:** The distance d_g from a point to a line was introduced and a general formula for calculating this distance was presented. Also, its relationship with the Euclidean distance was established through the slope-dependent ratio.
- **Minimum Distance Sets and Midsets:** The minimum distance set and the midset of two points were examined, and their geometric structures were classified based on the classification of the line passing through the points. The minimum distance set was shown to be either a line segment (on horizontal, vertical and separator lines) or a parallelogram-bounded region (on gradual and steep lines). And, the structure of the midset was revealed to vary depending on the line's slope, ranging from a line (for horizontal, vertical, and separator lines) to the union of two rays and five line segments or the union of two regions and five line segments (for gradual and steep lines).
- **Triangle Area Formulas:** Utilizing the derived distance relationship, two new formulas were obtained to calculate the area of a triangle in terms of its d_g-lengths. The Euclidean area of the triangle was expressed in terms of the d_g-length of its base and the d_g-length of the corresponding height. A second formula was provided using the d_g-length of the base and the d_g-distance from the opposite vertex to the line containing the base.

These findings contribute to the understanding of the geometric structure of the plane $\mathbb{R}_g^2$ and clearly demonstrate the extent to which this plane differs from classical Euclidean plane. This study provides a foundation for future research into other geometric objects in the plane $\mathbb{R}_g^2$.

REFERENCE

Akça, Z., and Nazlı, S. (2022). On the Shortest Distance in the Plane $R_{\pi 3}^2$. New Trends in Mathematical Sciences, 10(4), 128–132.

Aylıkçı, D. (2025). Investigations in the Generalized Absolute Value Plane, MSc, Eskişehir Osmangazi University, Inst. of Sci. and Tech., Turkey.

Bayar, A., Ekmekçi, S., and Akça, Z. (2008). On the Plane Geometry with Generalized Absolute Value Metric. Mathematical Problems in Engineering, 2008, 1–8.

Çolakoğlu, H. B., Gelişgen, Ö., and Kaya, R. (2013). Area formulas for a triangle in the alpha plane. Mathematical Communications, 18(1), 123–132.

Ekmekçi, S., Bayar, A., and Altıntaş, A. (2015). On the Group of Isometries of the Generalized Taxicab Plane. International Journal of Contemporary Mathematical Sciences, 10(4), 159–166.

Ekmekçi, S., Akça, Z., and Altıntaş, A. (2015). On Trigonometric Functions and Norm in the Generalized Taxicab Metric. Mathematical Sciences and Applications E-Notes, 3(2), 27–33.

Kaya, R., (2006). Area Formula of Taxicab Triangles. Pi Mu Epsilon Journal, 12(4), 219–2203.

Kaya, R., Gelişgen, Ö., Ekmekçi, S., and Bayar, A. (2009). On The Group of Isometries of The Plane with Generalized Absolute Value Metric. Rocky Mountain Journal of Mathematics, 39(2), 591–603.

Krause, E. F. (1975). Taxicab geometry. Menlo Park, California: Addison –Wesley Publishing Company.

Some Results On Taxicab Circles

Süheyla EKMEKÇİ[1]

1- Prof. Dr.; Eskişehir Osmangazi University, Department of Mathematics and Computer Science, Faculty of Science, sekmekci@ogu.edu.tr ORCID No: 0000-0003-2820-2096

ABSTRACT

This study examines two fundamental issues in taxicab geometry. One is the relationship between the area of a taxicab circle sector and the taxicab length of its corresponding arc. Similar to the Euclidean formula, this relationship is expressed by the formula $A_{sec} = \frac{r.L}{4}$ where r, L and A_{sec} are the radius of the taxicab circle, the taxicab length of arc and the area of the taxicab circle sector, respectively. The other concerns the conditions under which a taxicab circle cannot pass through given three points. It is observed that a taxicab circle does not pass through three collinear points on a horizontal, vertical, gradual, or steep line; however, if the points are collinear on a separator line, infinitely many taxicab circles exist. It is also seen that if the three lines formed by three noncollinear points are gradual or steep lines, there is no taxicab circle containing these points.

Keywords – Taxicab distance; Taxicab circle; Taxicab circle sector area.

INTRODUCTION

Taxicab geometry, also known as Manhattan geometry, is developed around the concept of the taxicab distance or the taxicab metric. Taxicab geometry is one of the simple non-Euclidean geometries in which the distance between two points is defined as the sum of the absolute differences of their coordinates. Because of its definition, the taxicab metric gives rise to geometric structures that differ significantly from those in Euclidean geometry. In particular, geometric objects that involve the concept of distance exhibit distinctive properties that make taxicab geometry an area of research. (For some references on this subject, see (Kaya et al., 2000:135), (Özcan et al., 2002: 381), (Akça and Kaya, 2004:521), (Akça and Kaya, 2004:491), (Bayar et. al., 2009:17), (Bayar and Ekmekçi, 2015: 58). This geometry offers an alternative distance measurement to Euclidean geometry. While Euclidean geometry measures the shortest distance between two points as a straight line, taxicab geometry measures this distance using only horizontal and vertical movements. One of the well-known differences between Euclidean and taxicab geometry lies in the structure of circles. While a circle in the Euclidean plane is a smooth curve, a taxicab circle is a square whose sides form a 45° angle with the coordinate axes. Consequently, arcs and regions of circular segments in the taxicab plane consist of line segments and polygonal elements

instead of smooth curves. This structural difference makes the re-examination of classical geometric results in the taxicab plane intriguing.

In Euclidean geometry, it is a basic result that the area of a circle sector is equal to one-half of its radius multiplied by the length of the corresponding arc. This relationship, which follows directly from the standard formulas for the area and circumference of a circle, provides a practical alternative to angle-dependent computations when determining sector areas. This formula, which expresses the sector area in terms of arc length and radius, is also similar to the formula for the area of a triangle.

It is another fundamental result in Euclidean geometry that no circle can pass through three distinct collinear points, whereas exactly one circle is determined by three distinct non-collinear points. This naturally leads to the question of whether analogous statements remain valid in taxicab geometry. The validity of these properties in the taxicab plane was first examined by (Tian et al, 1997: 727). Subsequently, (Ekmekçi,2001: 96-113) provided illustrative examples identifying the configurations of three points for which no taxicab circle exists. Later, (Çolakoğlu,2007:67) approached the problem from a synthetic perspective and, by using the notion of bisectors, determined the number of taxicab circles passing through two or three distinct points.

This study is organized as follows. In section 2, basic definitions and results related to taxicab geometry are reviewed. In section 3, the relationship between the area of a taxicab circle sector and the taxicab length of the corresponding arc is established. Section 4 includes the conditions under which a taxicab circle cannot exist for given three points in the taxicab plane.

PRELIMINARIES

In this section, some definitions, concepts and theorems used throughout this work are presented.

Definition 2.1. The taxicab distance between two points $A=(a_1,a_2)$ and $B=(b_1,b_2)$ in the analytical plane is

$$d_T(A,B)=|a_1-b_1|+|a_2-b_2|.$$

It is seen from the definition that the taxicab distance between the points *A* and *B* is equal to the sum of the Euclidean lengths of the sides parallel to the coordinate axes in the right triangle with the hypotenuse *AB*. The taxicab plane is the analytical plane equipped with the taxicab distance d_T and denoted by R_T^2.

Every Euclidean translation preserves the taxicab distance. So, it is an isometry in R_T^2. Reflections in the coordinate axes and the separator lines through the origin are isometries in R_T^2. The set of axes of these isometric

reflections is $\{x=0, y=0, y=x, y=-x\}$. The rotations by θ-angle in the set $\left\{\theta \mid \theta = k\frac{\pi}{2}, k=0,1,2,3\right\}$ are isometries in R_T^2.

In taxicab plane, a circle is still defined as the set of points that are all the same taxicab distance (the radius) from a fixed point (the center), but because of the taxicab distance formula, the figure of the circle becomes a square rather than a smooth curve, with its sides forming a 45° angle with the coordinate axes. The points on the taxicab circle with the center $M = (m_1, m_2)$ and the radius r satisfy the equation: $| x - m_1 | + | y - m_2 | = r$. The taxicab circle has four vertices at points that are on the horizontal and the vertical lines passing through the center. These vertices are $A_1(m_1 + r, m_2)$, $A_2(m_1, m_2 + r)$, $A_3(m_1 - r, m_2)$ and $A_4(m_1, m_2 - r)$.

In the following theorem, the taxicab distance from a point to a line is expressed.

Theorem 2.2. Let a point $P = (x_0, y_0)$ be given in the taxicab plane. The taxicab distance from the point P to the line ℓ with the equation $ax + by + c = 0$ is

$$d_T(P, \ell) = \frac{|ax_0 + by_0 + c|}{\max\{|a|, |b|\}},$$

(Kaya, Akça, Günaltılı and Özcan,2000:136).

Krause classified lines depending on their slope as follows:

Definition 2.3. Let m be the slope of the line ℓ in taxicab plane. The line ℓ is referred to as *the steep line*, *the gradual line* and *the separator line* in the cases where $|m|>1$, $|m|<1$ and $|m|=1$, respectively. In the special cases that the line ℓ is parallel to x-axis or y-axis, it is called *the horizontal line* or *the vertical line*, respectively,(Krause, 1975:31).

Definition 2.4. The minimum distance set (or the shortest distance set) of the points $A_1 = (x_1, y_1)$ and $A_2 = (x_2, y_2)$ in the taxicab plane is the set

$$\left\{X \in \mathbf{R}_T^2 \mid d_T(X, A_1) + d_T(X, A_2) = d_T(A_1, A_2)\right\}$$

This set is a rectangular region determined by the vertical and horizontal lines through the points A_1 and A_2. In the case that these points are on the same horizontal or vertical line, it reduces to the line segment A_1A_2, (Fig. 1).

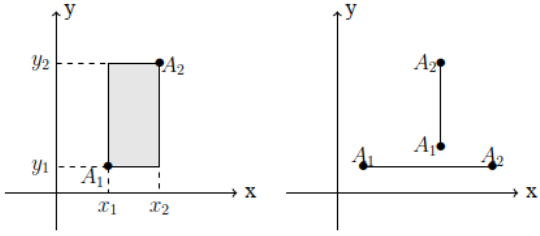

Figure 1. The taxicab minimum distance sets

Definition 2.5. In the taxicab plane, the set of points that are equidistant from any two points A and B in terms of the taxicab distance is called *the taxicab midset*. That is, the taxicab midset is defined as

$$\{ X \in \mathbb{R}^2_T : d_T(A, X) = d_T(X, B) \}.$$

While the midset between two points in Euclidean geometry is a line, in taxicab geometry the midset is formed in different structures, due to the definition of distance. Therefore, the taxicab midsets are characterized according to the positions of the given points as follows:

1) If the points A and B are on a line parallel to the coordinate axis, the taxicab midset of these points is the line passing through the midpoint of the points A, B and perpendicular to the line AB, (Fig.2 b).

2) If the points A and B are on a separator line, the taxicab midset consists of two regions and a line segment connecting these regions. The line segment formed inside the minimum distance set of the points A and B lies on the other separator line passing through the midpoint of them. And, the regions are formed by the horizontal and vertical lines passing through the points A and B, (Fig.2 a).

3) If the points A and B are on a gradual line or a steep line, the taxicab midset consists of two rays and a line segment connecting these rays. The line segment formed inside the minimum distance set of the points A and B lies on the separator line passing through the midpoint of them and having the opposite sign of the slope of the line AB. And, the rays are parallel to the coordinate axis such that the initial points of the rays are the endpoints of the line segment, (Fig.2 c,d).

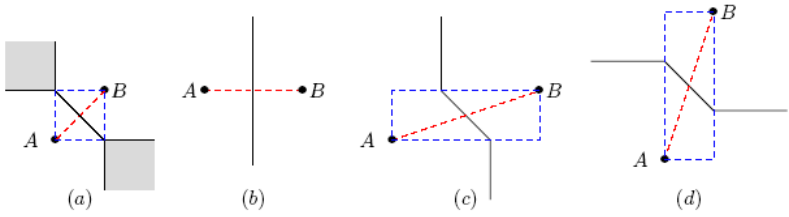

Figure 2. The taxicab midsets

The formula for the area of a triangle in the Euclidean plane is generally not valid in the taxicab plane. If the taxicab lengths of the base and the corresponding altitude of a triangle are known as b_T and h_T, respectively, the Euclidean area of the triangle is given by the following proposition in terms of these taxicab lengths.

Proposition 2.6. Let b_T and h_T denote the taxicab lengths of a given side (base) and the corresponding altitude of a triangle in the taxicab plane. If the slope of the base is m, then the area of the triangle can be calculated by

$$A = \frac{1+m^2}{2\left(1+|m|\right)^2} b_T h_T ,$$

(Kaya,2006:219).

THE AREA OF THE TAXICAB CIRCLE SECTOR

The formula stating that the area of a circle sector of radius *r* in the Euclidean plane is *r/2* times the corresponding arc length is a fundamental result of geometry. This formula is derived from the known formulas for the area and circumference of a circle and often provides a more practical alternative to using the angle when solving circle sector problems. The relationship between the area of a circle sector (A_{sec}) and its corresponding arc length (L) is expressed by the formula $A_{\text{sec}} = \frac{r.L}{2}$ where *r* is the radius of the circle. This formula makes it possible to determine the area of a circle sector without requiring the measure of its central angle. Moreover, the expression closely resembles the area formula of a triangle, where the arc length (L) and the radius (r) serve as the base and the height, respectively.

In the taxicab plane, it is well known that circle arcs are formed as line segments, while circle sectors have polygonal structures. In this section, the variation of the area of a circle sector with respect to the taxicab length of the corresponding arc is examined.

Theorem 3.1. In the taxicab circle with the radius *r*, the taxicab length (*L)* of any arc multipled by one-fourth of the radius *r* is equal to the area (A_{sec}) of the taxicab circle sector corresponding to the arc. That is, the equality

$$A_{\text{sec}} = \frac{r.L}{4}$$

holds.

Proof. Since every translation preserves the taxicab distances, taking the center of the taxicab circle with the radius *r* as the origin does not affect the generality.

Assume that two distinct points $P_1 = (x_1, y_1)$ and $P_2 = (x_2, y_2)$ are on this taxicab circle. The taxicab length of the arc P_1P_2 and the area of the taxicab circle sector corresponding to this arc will now be calculated as the following. Suppose the points P_1 and P_2 are on the same side of the taxicab circle. Let this side be A_1A_2. According to this, the taxicab arc length (L) is

$$L = d_T(P_1, P_2) = 2|x_1 - x_2| .$$

Now, the area $A_{\text{sec}}(OP_1P_2)$ of the taxicab circle sector corresponding to the arc P_1P_2 is the area of the triangle OP_1P_2, i.e. $A_{\text{sec}}(OP_1P_2) = A\ (OP_1P_2)$.

In this triangle, taking the side P_1P_2 as the base and the taxicab distance from the vertex O to this side as the height, it is seen that

$$b_T = d_T(P_1, P_2) \text{ and } h_T = r.$$

From Proposition 2.6, the area of the taxicab circle sector is obtained as

$$A_{\text{sec}}(OP_1P_2) = A\ (OP_1P_2) = \frac{L.r}{4}.$$

The same result is obtained similarly when the points are on A_2A_3, A_3A_4 and A_1A_4.

Assume that the points P_1 and P_2 are on two adjacent sides. First, consider the case where the points P_1 and P_2 are on the sides A_1A_2 and A_2A_3, respectively. Then, the taxicab length of the arc P_1P_2 (formed in the counterclockwise direction) is

$$L = 2\left(|x_1| + |x_2|\right).$$

The area $A_{\text{sec}}(OP_1P_2)$ of the taxicab circle sector corresponding to this arc is found by summing the areas of the taxicab circle sector OP_1A_2 and the taxicab circle sector OA_2P_2 .It is well known that

$$A_{\text{sec}}(OP_1A_2) = A\ (OP_1A_2) = \frac{b_T h_T}{2}$$

where b_T and h_T are the taxicab lengths of the side OA_2 and the height (perpendicular) from the point P_1 to the side OA_2, respectively, (Kaya,2006:219). Since the side OA_2 and the height are horizontal and vertical line segments, respectively, their taxicab lengths are equal to their Euclidean lengths. So,

$$A_{\text{sec}}(OP_1A_2) = A\ (OP_1A_2) = \frac{r|x_1|}{2}.$$

Similarly,

$$A_{\text{sec}}(OA_2P_2) = A\ (OA_2P_2) = \frac{r|x_2|}{2}.$$

Then, the area $A_{\text{sec}}(OP_1P_2)$ is

$$A_{\text{sec}}(OP_1P_2) = \frac{r}{2}(|x_1| + |x_2|) = \frac{r.L}{2}.$$

In the case of being on adjacent sides, let the points P_1 and P_2 be on the sides A_1A_2 and A_1A_4, respectively. Then, the taxicab length of this arc formed in the counterclockwise direction is

$$L = 2\left(2r + |x_1| + |x_2|\right).$$

The area $A_{\text{sec}}(OP_1P_2)$ of the taxicab circle sector corresponding to the arc P_1P_2 is found by summing the areas of the taxicab circle sectors OP_1A_2, $A_2A_3A_4$, OA_4P_2. The areas of these taxicab circle sectors are

$$A_{\text{sec}}(OP_1A_2) = A\ (OP_1A_2) = \frac{r|x_1|}{2},$$

$$A_{\text{sec}}(A_2A_3A_4) = r^2,$$

$$A_{\text{sec}}(OP_2A_4) = \frac{r|x_2|}{2}.$$

Thus, $A_{\text{sec}}(OP_1P_2)$ is found to be

$$A_{\text{sec}}(OP_1P_2) = \frac{r}{2}(2r + |x_1| + |x_2|) = \frac{r.L}{4}.$$

Let the points P_1 and P_2 be on A_2A_3 and A_1A_2, respectively. The taxicab length of arc formed on the taxicab circle from point P_1 to point P_2 in the counterclockwise direction is

$$L = 2\left(2r + |x_1 + r| + |r - x_2|\right).$$

The area $A_{\text{sec}}(OP_1P_2)$ of the taxicab circle sector corresponding to the arc P_1P_2 is calculated as

$$A_{\text{sec}}(OP_1P_2) = r^2 + \frac{|y_1|r}{2} + \frac{|y_2|r}{2} = \frac{r}{2}(2r + |r + x_1| + |r - x_2|) = \frac{r.L}{4}.$$

When the points P_1 and P_2 are on A_2A_3 and A_3A_4, respectively, the taxicab length of arc formed on the taxicab circle from point P_1 to point P_2 is

$$L = 2\left(|x_1 + r| + |r + x_2|\right).$$

The area $A_{\text{sec}}(OP_1P_2)$ of the taxicab circle sector corresponding to the arc P_1P_2 is calculated as

$$A_{\text{sec}}(OP_1P_2) = \frac{r}{2}(|y_1| + |y_2|) = \frac{r}{2}(|r + x_1| + |r + x_2|) = \frac{r.L}{4}.$$

When the points P_1 and P_2 are on A_3A_4 and A_4A_1 , respectively, the taxicab length of arc formed on the taxicab circle from point P_1 to point P_2 is

$$L = 2\left(|x_1| + |x_2|\right).$$

It is clear that the area $A_{\text{sec}}(OP_1P_2)$ of the taxicab circle sector corresponding to the arc P_1P_2 is

$$A_{\text{sec}}(OP_1P_2) = \frac{r.L}{4}.$$

Thus, when the two given points on the taxicab circle are on two adjacent sides, it follows that the area of the corresponding sector is equal to $\frac{r}{4}$ times the taxicab length of the associated arc.

Assume that the points P_1 and P_2 are on two opposite (parallel) sides. First, consider the case where the points P_1 and P_2 are on the sides A_1A_2 and A_3A_4 , respectively. Then, the taxicab length of arc formed on the taxicab circle from the point P_1 to the point P_2 in the counterclockwise direction is

$$L = 2\left(r + |x_1| + |x_2 + r|\right).$$

The area of the taxicab circle sector corresponding to this arc is found as

$$A_{\text{sec}}(OP_1P_2) = \frac{r^2}{2} + \frac{|x_1|r}{2} + \frac{|y_2|r}{2} = \frac{r}{2}(r + |x_1| + |r + x_2|) = \frac{r.L}{4}.$$

If the points P_1 and P_2 are on the sides A_2A_3 and A_1A_4 , respectively, then the taxicab length of arc formed on the taxicab circle from the point P_1 to the point P_2 in the counterclockwise direction is

$$L = 2\left(r + |x_1 + r| + |x_2|\right).$$

The area of the taxicab circle sector corresponding to this arc is found as

$$A_{\text{sec}}(OP_1P_2) = \frac{r^2}{2} + \frac{|y_1|r}{2} + \frac{|x_2|r}{2} = \frac{r}{2}(r + |x_1 + r| + |x_2|) = \frac{r.L}{4}.$$

Thus, for the two distinct points on the taxicab circle, it follows that the area of the corresponding circle sector is equal to the taxicab length of the formed arc multipled by $\frac{r}{4}$.

TAXICAB CIRCLES DETERMINED BY THREE POINTS

It is well known in Euclidean geometry that

- No circle passes through three distinct collinear points,
- One and only one circle passes through three distinct non-collinear points.

This raises the question of whether the same properties hold for taxicab circles. In (Tian et al, 1997: 727), it was investigated whether these propositions were also valid in the Taxicab plane. Then, in (Ekmekçi,2001: 96-113), it is explained with examples in which cases any three given points on the taxicab plane cannot lie the taxicab circle. In (Çolakoğlu,2007:67), the same subject is studied synthetically, and by using the concept of bisector, the number of taxicab circles passing through two or three distinct points is determined. In this section, the cases presented in (Ekmekçi,2001: 96-113) are examined in detail.

In the Taxicab plane, a taxicab circle with the center (h,k) and the radius r is the set of points satisfying the equality

$$|x-h|+|y-k|=r. \tag{1}$$

For given three points $A_i=(x_i,y_i)$, $i=1,2,3$ to be on the taxicab circle in (1), there must exist the point (h,k) and the positive real number *r* such that for each point,

$$|x_i-h|+|y_i-k|=r \tag{2}$$

holds true. From (2), it is reduced to following equalities

$$|x_i-h|+|y_i-k|=|x_j-h|+|y_j-k|,\ i\neq j\ . \tag{3}$$

These implies that the point (h,k) is on the taxicab midset of points A_i and A_j.

The three points A_i can be collinear or non-collinear. If they are collinear, the three points can lie on a horizontal, vertical, gradual, steep, or separator line.

I) Assume that the three points A_i are collinear.

i) Suppose that points A_i are on the *x*-axis. The taxicab midset of points A_1 and A_2 is the vertical line passing through the midpoint of the points A_1 and A_2. Similarly, the taxicab midset of points A_1 and A_3 is the vertical line passing through the midpoint of the points A_1 and A_3 and the taxicab midset of points A_2 and A_3 are the vertical line passing through the midpoints of the points A_2 and A_3. Since these three vertical lines are parallel, they have no

common point. And, there is no point (h,k) that satisfies the equalities in (2) and (3). Thus, there is no taxicab circle passing through these three points. The same result holds when the points are on the *y*-axis, or on a horizontal or vertical line.

Corollary 4.1. If three collinear points lie on a horizontal or vertical line in the taxicab plane, then no taxicab circle passes through these three points.

Example 4.2. Let $A_1=(-2,0)$, $A_2=(0,0)$, and $A_3=(4,0)$ be three collinear points on the *x*-axis in the taxicab plane. Suppose that these points lie on a taxicab circle centered at (h,k) with radius *r*. Then the following equations hold

$$|-2-h|+|k|=r,$$
$$|h|+|k|=r,$$
$$|4-h|+|k|=r.$$

From these equations, it follows that (h,k) must also satisfy the following equalities.

$$|-2-h|=|h|$$
$$|-2-h|=|4-h|$$
$$|h|=|4-h|.$$

These equations show that (h,k) lies on the midsets of the point pairs A_i and A_j. These midsets are the parallel lines $x=-1$, $x=1$, and $x=2$, which have no points in common. Consequently, there is no taxicab circle passing through the given points.

ii) Suppose that points A_i are on the gradual line. The taxicab midset of points A_i and A_j consists of two rays and a line segment connecting these rays. The line segment formed inside the minimum distance set of points is on the separator line passing through the midpoint of points and having the opposite sign of the slope of the line A_iA_j. And, the rays are parallel to the y-axis such that the initial points of the rays are the intersection points of the line segment and the boundary of the minimum distance set. Also, two of minimum distance sets are disjoint. For point pairs with disjoint minimum distance sets, the line segments in their midsets are parallel. Similarly, vertical rays in these midsets, whose initial points are on the boundary of the minimum distance set, are also parallel. And, they have no common point. Therefore, there is no point (h,k) that satisfies the equalities in (2) and (3) and no taxicab

circle passing through these three points. The same result holds when the points are on the steep line.

Corollary 4.3. If three distinct collinear points lie on a gradual line or a steep line in the taxicab plane, then no taxicab circle passes through these three points.

Example 4.4. Let $A_1=(-3,-1)$, $A_2=(0,0)$, and $A_3=(6,2)$ be three collinear points on the line $y=\frac{1}{3}x$ in the taxicab plane.The midsets of the points A_1 and A_2 is

$$\{(x,y): x+y=-2, -3\le x\le 0\}\cup\{(x,y): x=-2, y\ge 0\}\cup\{(x,y): x=-1, y\le -1\}$$

The midsets of the points A_2 and A_3 is

$$\{(x,y): x+y=4, 0\le x\le 6\}\cup\{(x,y): x=2, y\ge 2\}\cup\{(x,y): x=4, y\le 0\}.$$

Since these midsets occur in the regions $\{(x,y): -3<x<0\}$ and $\{(x,y): 0<x<6\}$, they have no points in common. Consequently, there is no taxicab circle passing through the given points.

iii) Suppose that points A_i are on a separator line and $x_1<x_2<x_3$. Taking the separator line $y=x$ does not result in a loss of generality. The taxicab midset of points A_i and A_j consists of two regions and a line segment connecting these regions. The line segment formed inside the minimum distance set of points is on the separator line passing through the midpoint of points and having the opposite sign of the slope of the line A_iA_j. And, each region is determined by the vertical line through one of the points and the horizontal line passing through the other. These midsets are as the following

$$\{(x,y): x+y=x_1+x_2, x_1\le x\le x_2\}\cup\{(x,y): x\le x_1, y\ge x_2\}\cup\{(x,y): x\ge x_2, y\le x_1\},$$

$$\{(x,y): x+y=x_1+x_3, x_1\le x\le x_3\}\cup\{(x,y): x\le x_1, y\ge x_3\}\cup\{(x,y): x\ge x_3, y\le x_1\},$$

$$\{(x,y): x+y=x_2+x_3, x_2\le x\le x_3\}\cup\{(x,y): x\le x_2, y\ge x_3\}\cup\{(x,y): x\ge x_3, y\le x_2\}.$$

Since the intersection of midsets is the set

$$\{(x,y): x\le x_1, y\ge x_3\}\cup\{(x,y): x\ge x_3, y\le x_1\}.$$

For every point (h,k) in this set, there exists a taxicab circle centered at (h,k) with radius *r*, where *r* is the taxicab distance from the point (h,k) to the line containing the points A_i. For example, when $(h,k)=(x_3,x_1)$, the radius $r=|x_3-x_1|$, and the corresponding taxicab circle is given by the equation

$|x-x_3|+|y-x_1|=x_3-x_1$. And, infinitely many taxicab circles pass through the points A_i. Consequently, when the given three points are collinear and lie on a separator line, it is seen that infinitely many taxicab circles pass through these points.

Corollary 4.5. Let A_1, A_2, and A_3 be three collinear points. When the points lie on a separator line, there exist infinitely many taxicab circles passing through them. In all other cases, no such taxicab circle exists.

II) Let the given three points A_i be noncollinear.

i) Suppose that the lines A_iA_j are three gradual lines. The taxicab midset of points A_i and A_j consists of two vertical rays and a line segment connecting these rays. The line segment formed inside the minimum distance set of points is on the separator line passing through the midpoint of points and having the opposite sign of the slope of the line A_iA_j. And, the initial points of the vertical rays are the intersection points of the line segment and the boundary of the minimum distance set.

Let the order between the abscissas of the points be $x_1 < x_2 < x_3$. The minimum distance set of points A_1 and A_2 is the set

$$\{(x,y): x_1 \le x \le x_2, y_1 \le y \le y_2\}.$$

The minimum distance set of points A_2 and A_3 is the set

$$\{(x,y): x_2 \le x \le x_3, y_3 \le y \le y_2\}.$$

The midset of points A_1 and A_2 is contained in the region $\{(x,y): x_1 < x < x_2\}$ and, similarly the midset of points A_2 and A_3 is contained in the region $\{(x,y): x_2 < x < x_3\}$.So, these taxicab midsets do not intersect. Since there is no point (h,k) that satisfies the equations

$$|x_1-h|+|y_1-k|=|x_2-h|+|y_2-k|$$

and

$$|x_2-h|+|y_2-k|=|x_3-h|+|y_3-k|,$$

there is no taxicab circle passing through the points A_i.

The same result holds when the lines A_iA_j are three steep lines.

Corollary 4.6. If three non-collinear points in the taxicab plane are such that all of three lines connecting them pairwise are gradual lines (or steep lines), then no taxicab circle passes through all of three points.

Example 4.7. Let $A_1=(-8,2)$, $A_2=(4,3)$, and $A_3=(15,-2)$ be three points in the taxicab plane. These points determine three gradual lines. Suppose that these points lie on a taxicab circle centered at (h,k) with radius *r*. Then the following equations hold

$$|-8-h|+|2-k|=r,$$
$$|4-h|+|3-k|=r,$$
$$|15-h|+|-2-k|=r.$$

From these equations, it follows that (h,k) must also satisfy the following equalities.

$$|-8-h|+|2-k|=|4-h|+|3-k|$$
$$|4-h|+|3-k|=|15-h|+|-2-k|$$
$$|-8-h|+|2-k|=|15-h|+|-2-k|.$$

The first equality represents the midset of the points A_1 and A_2, which occurs in the region $-8<x<4$. The second equality represents the midset of the points A_2 and A_3, which occurs in the region $5<x<15$. It is clear that these midsets do not intersect. This shows that there exist no values of *h* and *k* satisfying the first two equalities. Consequently, there is no taxicab circle passing through the given points.

CONCLUSION

In this study, two basic results have been obtained in the taxicab plane. First, it is shown that the area of a taxicab circle sector can be expressed directly in terms of the taxicab length of its corresponding arc. In particular, the area of a sector is proportional to the taxicab arc length, and the proportionality constant is one-quarter of the radius. Secondly, given three points in the taxicab plane, the conditions under which a taxicab circle cannot pass through these three points were analyzed. It was observed that no taxicab circle exists when the three collinear points are on horizontal, vertical, gradual, or steep lines. Furthermore, it was observed that no taxicab circle exists when three lines formed by the three non-collinear points are of the gradual or steep line type.

REFERENCES

Akça, Z. and Kaya, R. (2004). On the distance formulae in three dimensional taxicab space. Hadronic J., 27(5), 521–532.

Akça, Z. and Kaya, R. (2004). On the norm in higher dimensional taxicab spaces. Hadronic J. Suppl., 19(4), 491–501.

Bayar, A. and Ekmekçi, S. (2015). On complex numbers and taxicab plane. Mathematical Sciences and Applications E-Notes, 3(1), 58–64.

Bayar, A., Ekmekçi, S. and Özcan, M. (2009). On trigonometric functions and cosine and sine rules in taxicab plane. International Electronic Journal Of Geometry, 2(1), 17–24.

Çolakoğlu, H. B., and Kaya, R. (2007). A synthetic approach to the taxicab circles. Applied Sciences, 9, 67–77.

Ekmekçi, S. (2001). The properties related to the taxicab circles. Doctoral dissertation, Eskişehir Osmangazi University, Institute of Science and Technology, Turkey.

Kaya, R., (2006). Area Formula of Taxicab Triangles. Pi Mu Epsilon Journal, 12(4), 219–220.

Kaya, R., Akça, Z., Özcan, M. and Günaltılı, İ. (2000). General equation for taxicab conics and their classification. Mitt. Math. Ges. Hamburg, 19, 135–148.

Krause, E. F. (1975). Taxicab geometry. Menlo Park, California: Addison–Wesley Publishing Company.

Özcan, M., Ekmekçi, S. and Bayar, A. (2002). A note on the variation of the taxicab lengths under rotations. The Pi Mu Epsilon Journal, 11(7), 381–384.

Tian, S., So, S. S., and Chen, G. (1997). Concerning circles in Taxicab Geometry. Journal of Mathematics Education Science and Technology, 28(3), 727-733.

A New Class of Function Spaces Associated with the Ambiguity Function

Ayşe SANDIKÇI

Doç. Dr.; Ondokuz Mayıs University, Faculty of Science, Department of Mathematics, Samsun, Türkiye.
ayses@omu.edu.tr ORCID No: 0000-0001-5800-5558

ABSTRACT

The ambiguity function represents a cornerstone in time-frequency analysis, serving as an indispensable tool for characterizing radar waveforms. In radar engineering, it provides a comprehensive framework for evaluating critical performance metrics such as time-delay resolution, Doppler resolution, and Doppler-tolerance. These parameters are vital for distinguishing closely spaced targets and accurately measuring their relative velocities. In practical scenarios, ranging from sonar and radar systems to advanced biomedical imaging, chirp signals are typically transmitted to interact with targets. Upon reflection, these signals often manifest as higher-order chirps, carrying complex signatures of the target's physical properties. Consequently, the precise estimation and analysis of reflected signals are paramount for effective signal processing.

In this work, we introduce a new function space, $\mathrm{A}^{a,b}\left(\mathbb{R}^{d}\right)$, as a specific subspace of tempered distributions $\mathrm{S}'\left(\mathbb{R}^{d}\right)$ based on the ambiguity function. This space is defined by the requirement that the ambiguity function, $A(\psi,\phi)$, resides within the Lorentz space $L^{a,b}\left(\mathbb{R}^{2d}\right)$, where ϕ is a fixed, nonzero function. To establish a rigorous analytical structure, we endow $\mathrm{A}^{a,b}\left(\mathbb{R}^{d}\right)$ with a norm derived from the Lorentz space, denoted as $\|\psi\|_{\mathrm{A}^{a,b}} = \|A(\psi,\phi)\|_{ab}$. Our research demonstrates that for the indices $a=b=1$, $a=b=\infty$, or $1<a<\infty$ and $1\le b\le\infty$, the space $\mathrm{A}^{a,b}\left(\mathbb{R}^{d}\right)$ constitutes a Banach space. Furthermore, we explore its structural dynamics, proving its invariance under translation operations and dilation operation. Finally, we show that under specific conditions, $\mathrm{A}^{a,b}\left(\mathbb{R}^{d}\right)$ acts as a Banach module over $L^{1}\left(\mathbb{R}^{d}\right)$.

Keywords – Fourier transform, ambiguity function, Banach algebra, Banach module, Lorentz space

INTRODUCTION

Let M be a normed algebra. A Banach space E is termed a Banach M-bimodule if it is both a left and a right M-module, where the left and right actions, $(y,x)\to y\cdot x$ and $(x,y)\to x\cdot y$ respectively, are linked by the compatibility condition $(y\cdot x)\cdot z=y\cdot(x\cdot z)$ for all $y,z\in M$ and $x\in E$. In terms of its topological structure, these actions must be jointly continuous, meaning there exists a constant $C>0$ such that the inequalities $\|y\cdot x\|\le C\|y\|\|x\|$ and $\|x\cdot y\|\le C\|x\|\|y\|$ hold. This dual interaction allows the Banach space to inherit a rich algebraic structure from M while maintaining the analytic properties of a complete normed space, (Dales, 2000).

Let ψ be a function on $\mathbb{R}^d$. The translation operator of ψ is $T_\eta\psi(u)=\psi(u-\eta)$ for $u\in\mathbb{R}^d$ and the modulation operator of ψ is $M_\gamma\psi(u)=\exp(2\pi i\gamma\cdot u)\psi(u)$ for $u,\gamma\in\mathbb{R}^d$. The dilation operator of ψ is also defined by $\delta^\varepsilon\psi(u)=\psi(\varepsilon u)$, $\varepsilon>0$.

If $a\in[1,\infty)$ the Lebesgue space $L^a(\mathbb{R}^d)$ is the set of all complex-valued measurable functions on $\mathbb{R}^d$ that satisfy

$$\int_{\mathbb{R}^d}|\psi(u)|^a\,du<\infty.$$

If $\psi\in L^a(\mathbb{R}^d)$, the L^a norm of ψ is defined by

$$\|\psi\|_a=\left(\int_{\mathbb{R}^d}|\psi(u)|^a\,du\right)^{1/a}<\infty.$$

The space $L^a(\mathbb{R}^d)$ is complete under the norm $\|\cdot\|_a$.

For two measurable functions ψ, ϕ on $\mathbb{R}^d$, the convolution is defined by

$$(\psi*\phi)(x)=\int_{\mathbb{R}^d}\psi(x-y)\phi(y)\,dy\ ,$$

provided the integral exists. Under this operation, the space $L^1\left(\mathbb{R}^d\right)$ functions as a Banach algebra, as the Young's inequality for $a=1$ ensures that $\|\psi*\phi\|_1 \le \|\psi\|_1 \|\phi\|_1$, thereby satisfying the necessary submultiplicative property. Furthermore, the action of $L^1\left(\mathbb{R}^d\right)$ extends naturally to the $L^a\left(\mathbb{R}^d\right)$ spaces for $a\in[1,\infty)$. Specifically, $L^a\left(\mathbb{R}^d\right)$ constitutes a Banach L^1-module under convolution, where the inequality $\|\psi*\phi\|_p \le \|\psi\|_1 \|\phi\|_p$ establishes the joint continuity of the module action, (Stegeman and Reiter, 2000).

Let $\psi \in L^1\left(\mathbb{R}^d\right)$, let us define $\hat{\psi}$ by

$$\hat{\psi}(\xi)=\int_{\mathbb{R}^d}\exp\left(-2\pi i x\cdot\xi\right)\psi(x)dx\,, \qquad \xi\in\mathbb{R}^d$$

where $x\cdot\xi=\sum_{i=1}^{d}x_i\xi_i$ is the standard dot product. The function $\hat{\psi}$ is called the Fourier transform of the function ψ.

The following definition constitutes the ambiguity function of functionals ψ and ϕ, which are elements of the $L^2\left(\mathbb{R}^d\right)$ space:

$$A(\psi,\phi)(\xi,u)=\int_{\mathbb{R}^d} e^{-2\pi i u\cdot z}\psi\left(z+\frac{\xi}{2}\right)\overline{\phi\left(z-\frac{\xi}{2}\right)}dz\ .$$

If $\psi=\phi$, then we write $A(\psi,\psi)=A(\psi)$,(Gröchenig, 2001), (Debnath and Shah, 2015).

In functional analysis, Lorentz spaces, denoted as $L^{a,b}$ where $a,b\in[1,\infty]$, are generalizations of the standard Lebesgue spaces L^a. They provide a more refined way to measure the "size" of a function by looking at both its height and how its values are spread out. We consider complex-valued measurable functions ψ defined on $\mathbb{R}^d$. To define the Lorentz space $L^{a,b}\left(\mathbb{R}^d\right)$, we first introduce the distribution function $\lambda_\psi(y)$, which measures the "width" of a function at a specific "height" y:

$$\lambda_\psi(y)=\mu\left(\left\{x\in\mathbb{R}^d:|\psi(x)|>y\right\}\right).$$

Using this, we define the decreasing rearrangement $\psi^*(t)$, which is the non-increasing function on $(0,\infty)$ that shares the same distribution as ψ:

$$\psi^*(t) = \inf\left\{y > 0 \middle| \lambda_\psi(y) \le t\right\} = \sup\left\{y > 0 \middle| \lambda_\psi(y) > t\right\}, \quad t > 0.$$

The standard quasinorm for $L^{a,b}(\square^d)$ is defined as:

$$\|\psi\|_{ab}^* = \begin{cases} \left(\frac{b}{a}\int_0^\infty t^{\frac{b}{a}-1}\left[\psi^*(t)\right]^b dt\right)^{1/b}, & 0 < a,b < \infty \\ \sup_{t>0} t^{\frac{1}{a}}\psi^*(t), & 0 < a \le b = \infty. \end{cases}$$

While this expression is widely used, it does not always satisfy the triangle inequality (making it a quasinorm rather than a true norm). To create a true norm, we use the elementary average function $\psi^{**}(t)$, defined as:

$$\psi^{**}(t) = \frac{1}{t}\int_0^t \psi^*(s)\,ds, \quad t > 0.$$

Replacing ψ^* with ψ^{**} in the integral above yields a functional that satisfies the triangle inequality. While the quasinorm and this true norm are equivalent, they are not strictly equal unless specific conditions are met.

When $a = b$, the Lorentz space $L^{a,b}$ is exactly the same as the standard L^a space.

$L^{a,b}(\square^d)$ is also a Banach space under the norm

$$\|\psi\|_{ab} = \begin{cases} \left(\frac{b}{a}\int_0^\infty t^{\frac{b}{a}-1}\psi^{**}(t)\,dt\right)^{1/b}, & 0 < a,b < \infty \\ \sup_{t>0} t^{\frac{1}{a}}\psi^{**}(t), & 0 < a \le b = \infty \end{cases}$$

if $a = b = 1$, $a = b = \infty$, or $1 < a < \infty$ and $1 \le b \le \infty$, (Blozinski, 1972:255), (Chen and Lai, 1975:247), (Edmunds and Evans, 2004), (Hunt, 1966:249), (Yap, 1972:315).

Given a multi-index $\alpha=(\alpha_1,...,\alpha_d)\in\mathbb{N}_+^d$, we write as usual $|\alpha|=\sum_{j=1}^d\alpha_j$, $\omega^\alpha=\prod_{j=1}^d\omega_j^{\alpha_j}$, $D^\alpha=\frac{\partial^{\alpha_1}}{\partial x_1^{\alpha_1}}\cdots\frac{\partial^{\alpha_d}}{\partial x_d^{\alpha_d}}$ for the partial derivative and $X^\alpha\psi(x)=x^\alpha\psi(x)$ for the multiplication operator. Taking Fourier transform we get

$$\left(D^\alpha\psi\right)^{\wedge}(\omega)=(2\pi i\omega)^\alpha\hat{\psi}(\omega)$$

and

$$\left((-2\pi ix)^\alpha\psi\right)^{\wedge}(\omega)=D^\alpha\hat{\psi}(\omega).$$

For suitable test functions, for example, $\psi\in C^\infty(\mathbb{R}^d)$ with compact support, they are easily verified by a direct calculation.

The Schwartz class $\mathrm{S}(\mathbb{R}^d)$ consist of all C^∞ -functions ψ on $\mathbb{R}^d$ such that

$$\sup_{x\in\mathbb{R}^d}\left|D^\alpha X^\beta\psi(x)\right|<\infty$$

for all $\alpha,\beta\in\mathbb{N}_+^d$. Convergence $\psi_n\xrightarrow{\mathrm{S}}\psi$ means that $\left\|D^\alpha X^\beta(\psi-\psi_n)\right\|_\infty\to 0$ for all $\alpha,\beta\in\mathbb{N}_+^d$. Elements in the dual space $\mathrm{S}'(\mathbb{R}^d)$ of $\mathrm{S}(\mathbb{R}^d)$ are called tempered distributions. All L^a functions, $a\in[1,\infty)$, are in $\mathrm{S}'(\mathbb{R}^d)$, (Gröchenig, 2001).

THE FUNCTION SPACE $\mathrm{A}^{a,b}(\mathbb{R}^d)$: DEFINITION AND BASIC PROPERTIES

Definition 1. Let $a,b\in[1,\infty]$ and ϕ be a fixed Schwartz function in $\mathrm{S}(\mathbb{R}^d)$. We denote by $\mathrm{A}^{a,b}(\mathbb{R}^d)$ the functional space comprising all tempered distributions whose ambiguity function resides within the Lorentz

space $L^{a,b}\left(\mathbb{R}^{2d}\right)$. Since $\|.\|_{ab}$ defines a norm on the Lorentz space, the functional $\|\psi\|_{\mathrm{A}^{a,b}} = \|A(\psi,\phi)\|_{ab}$, $\psi \in \mathrm{A}^{a,b}\left(\mathbb{R}^{d}\right)$, is a well-defined norm on the linear space $\mathrm{A}^{a,b}\left(\mathbb{R}^{d}\right)$. Furthermore, because the Lorentz space is a translation-invariant Banach function space, the normed space $\mathrm{A}^{a,b}\left(\mathbb{R}^{d}\right)$ is a complete Banach space if $a=b=1$, $a=b=\infty$, or $1<a<\infty$ and $1\le b\le\infty$. The independence of this space from the choice of the test function ϕ can be established using a method analogous to the proof of Theorem 7 in (Sandıkçı, 2012:263).

Theorem 2. The space $\mathrm{A}^{a,b}\left(\mathbb{R}^{d}\right)$ remains unchanged by time-frequency shifts, provided that $a\in(1,\infty)$ and $b\in[1,\infty)$. In this context, the equality

$$\left\|T_\eta M_\gamma \psi\right\|_{\mathrm{A}^{a,b}} = \|\psi\|_{\mathrm{A}^{a,b}}$$

is satisfied, where $\eta,\gamma\in\mathbb{R}^{d}$.

Proof. If $\psi\in\mathrm{A}^{a,b}\left(\mathbb{R}^{d}\right)$, we write $A(\psi,\phi)\in L^{a,b}\left(\mathbb{R}^{2d}\right)$. For $\eta,\gamma\in\mathbb{R}^{d}$, we write

$$\begin{aligned}
A\left(T_\eta M_\gamma\psi,\phi\right)(\xi,u) &= \int_{\mathbb{R}^d} e^{-2\pi i u\cdot z} T_\eta M_\gamma\psi\left(z+\frac{\xi}{2}\right)\overline{\phi\left(z-\frac{\xi}{2}\right)}dz \\
&= \int_{\mathbb{R}^d} e^{-2\pi i u\cdot z}\psi\left(z-\eta+\frac{\xi}{2}\right)e^{2\pi i\gamma\left(z-\eta+\frac{\xi}{2}\right)}\overline{\phi\left(z-\frac{\xi}{2}\right)}dz \\
&\quad \text{(Applying the substitution } z-\eta+\frac{\xi}{2}=p\text{)} \\
&= \int_{\mathbb{R}^d} e^{-2\pi i u\cdot\left(p+\eta-\frac{\xi}{2}\right)}\psi(p)\,e^{2\pi i\gamma\cdot p}\,\overline{\phi(p+\eta-\xi)}\,dp \\
&= e^{-2\pi i u\cdot\left(\eta-\frac{\xi}{2}\right)}\int_{\mathbb{R}^d} e^{-2\pi i(u-\gamma)\cdot p}\,\psi(p)\,\overline{\phi\left(p-(\xi-\eta)\right)}\,dp\ .
\end{aligned}$$

If we perform the substitution $p=t+\dfrac{\xi-\eta}{2}$, we obtain

$$\begin{aligned}
&A\left(T_\eta M_\gamma\psi,\phi\right)(\xi,u) \\
&= e^{-2\pi i u\cdot\left(\eta-\frac{\xi}{2}\right)}\int_{\mathbb{R}^d} e^{-2\pi i(u-\gamma)\cdot\left(t+\frac{\xi-\eta}{2}\right)}\psi\left(t+\frac{\xi-\eta}{2}\right)\overline{\phi\left(t-\frac{\xi-\eta}{2}\right)}dt
\end{aligned}$$

$$= e^{-2\pi iu\cdot\left(\eta-\frac{\xi}{2}\right)} e^{-2\pi i(u-\gamma)\cdot\left(\frac{\xi-\eta}{2}\right)} \int_{\mathbb{R}^d} e^{-2\pi i(u-\gamma)\cdot t}\, \psi\left(t+\frac{\xi-\eta}{2}\right)\overline{\phi\left(t-\frac{\xi-\eta}{2}\right)}\,dt$$

$$= e^{-2\pi iu\cdot\left(\eta-\frac{\xi}{2}\right)} e^{-2\pi i(u-\gamma)\cdot\left(\frac{\xi-\eta}{2}\right)} A(\psi,\phi)(\xi-\eta,u-\gamma).$$

Leveraging the modulation and translation invariance of Lorentz space, (Chen and Lai, 1975:247), we obtain

$$\left\|T_\eta M_\gamma \psi\right\|_{\mathrm{A}^{a,b}} = \left\|A\left(T_\eta M_\gamma \psi,\phi\right)\right\|_{ab} = \left\|T_{(\eta,\gamma)} A(\psi,\phi)\right\|_{ab}$$

$$= \left\|A(\psi,\phi)\right\|_{ab} = \|\psi\|_{\mathrm{A}^{a,b}}.$$

Thus, the assertion is proved.

Theorem 3. If $\psi \in \mathrm{A}^{a,b}\left(\mathbb{R}^d\right)$, then $\delta^\varepsilon \psi \in \mathrm{A}^{a,b}\left(\mathbb{R}^d\right)$ for all $\varepsilon > 0$.

Proof. Substitute the dilated function $\delta^\varepsilon \psi$ into the integral, we get

$$A\left(\delta^\varepsilon \psi,\phi\right)(\xi,u) = \int_{\mathbb{R}^d} e^{-2\pi iu\cdot z}\, \delta^\varepsilon \psi\left(z+\frac{\xi}{2}\right)\overline{\phi\left(z-\frac{\xi}{2}\right)}\,dz$$

$$= \int_{\mathbb{R}^d} e^{-2\pi iu\cdot z}\, \psi\left(\varepsilon z+\frac{\varepsilon\xi}{2}\right)\overline{\phi\left(z-\frac{\xi}{2}\right)}\,dz$$

(with the change of variables $p = \varepsilon z$)

$$= \varepsilon^{-d} \int_{\mathbb{R}^d} e^{-2\pi iu\cdot\frac{p}{\varepsilon}}\, \psi\left(p+\frac{\varepsilon\xi}{2}\right)\overline{\phi\left(\frac{p}{\varepsilon}-\frac{\xi}{2}\right)}\,dp$$

$$= \varepsilon^{-d} \int_{\mathbb{R}^d} e^{-2\pi iu\cdot\frac{p}{\varepsilon}}\, \psi\left(p+\frac{\varepsilon\xi}{2}\right)\overline{\phi\left(\frac{1}{\varepsilon}\left(p-\frac{\varepsilon\xi}{2}\right)\right)}\,dp$$

$$= \varepsilon^{-d} \int_{\mathbb{R}^d} e^{-2\pi i\frac{u}{\varepsilon}\cdot p}\, \psi\left(p+\frac{\varepsilon\xi}{2}\right)\overline{\delta^{\frac{1}{\varepsilon}}\phi\left(p-\frac{\varepsilon\xi}{2}\right)}\,dp$$

$$= \varepsilon^{-d} A\left(\psi,\delta^{\frac{1}{\varepsilon}}\phi\right)\left(\varepsilon\xi,\frac{u}{\varepsilon}\right). \qquad (0.1)$$

Let us take any function $\psi \in \mathrm{A}^{a,b}\left(\mathbb{R}^d\right)$. By using (0.1), then we write

$$\lambda_{A\left(\delta^\varepsilon\psi,\phi\right)}(y) = \mu\left(\left\{(\xi,u)\in\mathbb{R}^{2d} : \left|A\left(\delta^\varepsilon\psi,\phi\right)(\xi,u)\right| > y\right\}\right)$$

$$= \mu\left(\left\{(\xi,u)\in\mathbb{R}^{2d} : \left|A\left(\psi,\delta^{\frac{1}{\varepsilon}}\phi\right)\left(\varepsilon\xi,\frac{u}{\varepsilon}\right)\right| > \frac{y}{\varepsilon^{-d}}\right\}\right)$$

$$= \mu\left\{\xi \in \mathbb{R}^d : \left|A\left(\psi, \delta^{\frac{1}{\varepsilon}}\phi\right)(\varepsilon\xi, \cdot)\right| > \varepsilon^d y\right\}$$

$$\times\, \mu\left\{u \in \mathbb{R}^d : \left|A\left(\psi, \delta^{\frac{1}{\varepsilon}}\phi\right)\left(\cdot, \frac{u}{\varepsilon}\right)\right| > \varepsilon^d y\right\}.$$

Under the change of variables $\upsilon = \varepsilon\xi$ and $\omega = \frac{u}{\varepsilon}$, the equation becomes

$$\lambda_{A\left(\delta^{\varepsilon}\psi, \phi\right)}(y) = \frac{1}{\varepsilon}\mu\left\{\upsilon \in \mathbb{R}^d : \left|A\left(\psi, \delta^{\frac{1}{\varepsilon}}\phi\right)(\upsilon, \cdot)\right| > \varepsilon^d y\right\}$$

$$\times\varepsilon\ \mu\left\{\omega \in \mathbb{R}^d : \left|A\left(\psi, \delta^{\frac{1}{\varepsilon}}\phi\right)(\cdot, \omega)\right| > \varepsilon^d y\right\}$$

$$= \mu \times \mu\left\{(\upsilon, \omega) \in \mathbb{R}^{2d} : \left|A\left(\psi, \delta^{\frac{1}{\varepsilon}}\phi\right)(\upsilon, \omega)\right| > \varepsilon^d y\right\}$$

$$= \lambda_{A\left(\psi, \delta^{1/\varepsilon}\phi\right)}\left(\varepsilon^d y\right).$$

Then for $t > 0$,

$$A\left(\delta^{\varepsilon}\psi, \phi\right)^*(t) = \inf\left\{y > 0 \middle| \lambda_{A\left(\delta^{\varepsilon}\psi, \phi\right)}(y) \le t\right\}$$

$$= \inf\left\{y > 0 \middle| \lambda_{A\left(\psi, \delta^{1/\varepsilon}\phi\right)}\left(\varepsilon^d y\right) \le t\right\},$$

if we say $s = \varepsilon^d y$

$$A\left(\delta^{\varepsilon}\psi, \phi\right)^*(t) = \inf\left\{\varepsilon^{-d} s \middle| \lambda_{A\left(\psi, \delta^{1/\varepsilon}\phi\right)}(s) \le t\right\}$$

$$= \varepsilon^{-d}\ \inf\left\{s \middle| \lambda_{A\left(\psi, \delta^{1/\varepsilon}\phi\right)}(s) \le t\right\}$$

$$= \varepsilon^{-d}\left(A\left(\psi, \delta^{\frac{1}{\varepsilon}}\phi\right)\right)^*(t).$$

Also, for $x > 0$,

$$\left(A\left(\delta^{\varepsilon}\psi, \phi\right)\right)^{**}(x) = \frac{1}{x}\int_0^x \left(A\left(\delta^{\varepsilon}\psi, \phi\right)\right)^*(t)\,dt$$

$$= \frac{1}{x}\int_0^x \varepsilon^{-d}\left(A\left(\psi, \delta^{\frac{1}{\varepsilon}}\phi\right)\right)^*(t)\,dt$$

$$= \varepsilon^{-d} \left(A\left(\psi, \delta^{\frac{1}{\varepsilon}} \phi \right) \right)^{**} (x).$$

Finally, we have

$$\left\| \delta^{\varepsilon} \psi \right\|_{\mathrm{A}^{a,b}} = \left\| A\left(\delta^{\varepsilon} \psi, \phi \right) \right\|_{ab} = \left(\frac{b}{a} \int_0^{\infty} x^{\frac{b}{a}-1} \left[\left(A\left(\delta^{\varepsilon} \psi, \phi \right) \right)^{**} (x) \right]^b dx \right)^{1/b}$$

$$= \left(\frac{b}{a} \int_0^{\infty} x^{\frac{b}{a}-1} \left[\varepsilon^{-d} \left(A\left(\psi, \delta^{\frac{1}{\varepsilon}} \phi \right) \right)^{**} (x) \right]^b dx \right)^{1/b}$$

$$= \varepsilon^{-d} \left\| A\left(\psi, \delta^{\frac{1}{\varepsilon}} \phi \right) \right\|_{ab}.$$

The fact that ϕ is a Schwartz function implies $\delta^{\frac{1}{\varepsilon}} \phi$ is as well, due to the dilation invariance of $\mathrm{S}\left(\mathbb{R}^d \right)$. Since the space $\mathrm{A}^{a,b}\left(\mathbb{R}^d \right)$ does not depend on the particular ϕ selected, the norms associated with ϕ and its dilated version are equivalent. We thus obtain the estimate:

$$\left\| \delta^{\varepsilon} \psi \right\|_{\mathrm{A}^{a,b}} = \left\| A\left(\delta^{\varepsilon} \psi, \phi \right) \right\|_{ab} = \varepsilon^{-d} \left\| A\left(\psi, \delta^{\frac{1}{\varepsilon}} \phi \right) \right\|_{ab}$$

$$\leq C \varepsilon^{-d} \left\| A\left(\psi, \phi \right) \right\|_{ab} = C \varepsilon^{-d} \left\| \psi \right\|_{\mathrm{A}^{a,b}}.$$

The proof of the assertion is therefore complete.

Teorem 4. The space $\mathrm{A}^{a,b}\left(\mathbb{R}^d \right)$ possesses the structure of a Banach module over the convolution algebra L^1.

Proof. Let $\psi \in \mathrm{A}^{a,b}\left(\mathbb{R}^d \right)$ and $h \in L^1\left(\mathbb{R}^d \right)$. Applying the definition of the ambiguity function for $\psi * h$ and using Fubini's theorem, we obtain

$$A\left(\psi * h, \phi \right)\left(\xi, u \right) = \int_{\mathbb{R}^d} e^{-2\pi i u \cdot z} \left(\psi * h \right)\left(z + \frac{\xi}{2} \right) \overline{\phi\left(z - \frac{\xi}{2} \right)} dz$$

$$= \int_{\mathbb{R}^d} e^{-2\pi i u \cdot z} \left(\int_{\mathbb{R}^d} \psi\left(z + \frac{\xi}{2} - y \right) h(y) dy \right) \overline{\phi\left(z - \frac{\xi}{2} \right)} dz$$

$$= \int_{\mathbb{R}^d} h(y) \left(\int_{\mathbb{R}^d} \psi\left(z + \frac{\xi}{2} - y\right) \overline{\phi\left(z - \frac{\xi}{2}\right)} e^{-2\pi i u \cdot z} \, dz \right) dy .$$

We use the substitution $s = z - \frac{y}{2}$, we have

$$\begin{aligned}
&A(\psi * h, \phi)(\xi, u) \\
&= \int_{\mathbb{R}^d} h(y) \left(\int_{\mathbb{R}^d} \psi\left(s + \frac{\xi - y}{2}\right) \overline{\phi\left(s - \frac{\xi - y}{2}\right)} e^{-2\pi i u \cdot s} \, ds \right) e^{-\pi i u \cdot y} \, dy \\
&= \int_{\mathbb{R}^d} h(y) \, e^{-\pi i u \cdot y} \, A(\psi, \phi)(\xi - y, u) \, dy \\
&= \int_{\mathbb{R}^d} M_{-\frac{u}{2}} h(y) \, A(\psi, \phi)(\xi - y, u) \, dy \\
&= \left(M_{-\frac{u}{2}} h \right) * A(\psi, \phi)(\cdot, u).
\end{aligned}$$

By leveraging the module property of Lorentz spaces with respect to the L^1 algebra and the modulation invariance of L^1, one arrives at the anticipated estimate

$$\begin{aligned}
\|\psi * h\|_{\mathrm{A}^{a,b}} &= \|A(\psi * h, \phi)\|_{ab} = \left\| \left(M_{-\frac{u}{2}} h \right) * A(\psi, \phi) \right\|_{ab} \\
&\leq \left\| M_{-\frac{u}{2}} h \right\|_1 \, \|A(\psi, \phi)\|_{ab} \\
&\leq \|h\|_1 \, \|\psi\|_{\mathrm{A}^{a,b}} .
\end{aligned}$$

Thus, the assertion is proved.

RESULTS AND DISCUSSION

In this study, we introduce a novel function space, denoted as $\mathrm{A}^{a,b}(\mathbb{R}^d)$, constructed as a specialized subspace of tempered distributions $\mathrm{S}'(\mathbb{R}^d)$ through the lens of the ambiguity function. The defining characteristic of $\mathrm{A}^{a,b}(\mathbb{R}^d)$ is the requirement that the ambiguity function, $A(\psi, \phi)$, belongs to the Lorentz space $L^{a,b}(\mathbb{R}^{2d})$, where ϕ serves as a

fixed, non-zero function.To provide this space with a rigorous analytical framework, we equip $\mathrm{A}^{a,b}\left(\square^{d}\right)$ with the norm $\|\psi\|_{\mathrm{A}^{a,b}}=\|A(\psi,\phi)\|_{ab}$. Our analysis confirms that $\left(\mathrm{A}^{a,b}\left(\square^{d}\right),\|\cdot\|_{\mathrm{A}^{a,b}}\right)$ constitutes a complete Banach space, establishing it as a robust environment for further harmonic analysis. A significant portion of our discussion focuses on the structural dynamics and stability of $\mathrm{A}^{a,b}\left(\square^{d}\right)$. We demonstrate its fundamental algebraic properties, specifically proving that the space remains invariant under both translation and dilation operations. These invariance properties are crucial, as they ensure that the space's internal geometry is preserved under standard time-frequency shifts and scaling transformations.Finally, we establish that $\mathrm{A}^{a,b}\left(\square^{d}\right)$ exhibits a sophisticated algebraic structure by acting as a Banach module over $L^{1}\left(\square^{d}\right)$. This modular property suggests that the space is not merely a collection of functions but a structured environment capable of supporting complex operator theoretic frameworks. These findings provide a robust mathematical basis for higher-order signal analysis and the stability of radar waveforms in complex environments.

REFERENCE

Blozinski, A. P. (1972). On a Convolution Theorem for $L(p,q)$ Spaces. American Mathematical Society, 164, 255-265.

Chen, Y. K. and Lai, H. C. (1975). Multipliers of Lorentz spaces. Hokkaido Math. J., 4, 247–260.

Dales, H. G. (2000). *Banach Algebras and Automatic Continuity*. London Math. Soc. Monographs, Vol. 24, Oxford :Clarendon Press.

Debnath, L. and Shah, F. A. (2015). *Wavelet Transforms and Their Applications*. Birkhauser, New York.

Edmunds, D. E. and Evans, W. D. (2004) *Hardy Operators Function Spaces and Embeddings*. Springer Berlin Heidelberg New York.

Gröchenig, K. (2001). *Foundations of Time-Freuquency Analysis*. Birkhauser, Boston.

Hunt, R. A. (1966). On $L(p,q)$ Spaces, Extrait de L'Enseignement Mathematique, T.XII, fasc.4, 249-276.

Sandıkçı, A. (2012). On Lorentz mixed normed modulation spaces, J. Pseudo-Differ. Oper. Appl. 3, 263-281.

Stegeman, J. D., and Reiter, H. (2000). *Classical harmonic analysis and locally compact groups*. (London Mathematical Society Monographs. New Series ed.) Oxford University Press.

Yap, L.Y.H. (1972). On two classes of Subalgebras of $L^1(G)$, Proc. Japan Acad., 48, 315-319.

Weingarten Surfaces: From Theory to Practice

Feray BAYAR[1]

1- Dr. Öğr. Üyesi; Samsun University, Faculty of Engineering and Natural Sciences, Department of Fundamental Sciences, Samsun, Türkiye. feray.bayar@samsun.edu.tr ORCID No: 0009-0000-7646-765X.

ABSTRACT

Weingarten surfaces (W -surfaces) constitute a distinguished class of surfaces in classical differential geometry, characterized by a functional dependence between their mean curvature (H) and Gaussian curvature (K). Originally identified by Julius Weingarten in 1861 in the context of isometric deformations, these surfaces have evolved from theoretical curiosities into fundamental tools for modern computational design and engineering.

This paper provides a detailed mathematical exposition of W -surfaces, deriving the Jacobian condition $\det(\nabla H, \nabla K) = 0$ and analyzing the geometry of parallel surfaces. We present a rigorous classification of Linear Weingarten Surfaces (LWS) and discuss global rigidity theorems, including the seminal works of Liebmann, Chern, and Hartman. Furthermore, we explore the contemporary renaissance of W-surfaces in multidisciplinary fields: from the computational framework for architectural rationalization and mold re-use, to hydrodynamic fairing in naval architecture, and variational modeling of lipid bilayers in biophysics. We conclude by summarizing why W-surfaces serve as a critical bridge between smooth manifold theory and discrete fabrication constraints.

Keywords – Weingarten surfaces, Architectural Geometry, Discrete Differential Geometry, Computational Design, Surface Rationalization

INTRODUCTION

The study of surfaces in Euclidean space $\mathbb{R}^3$ is centrally concerned with the concept of curvature. The local shape of a smooth surface S is completely determined (up to rigid motion) by its first and second fundamental forms. From these, one derives the two principal curvatures, κ_1 and κ_2, which represent the maximum and minimum bending of the surface at a given point (Do Carmo, 1976).

The two most significant invariants derived from the principal curvatures are the Gaussian Curvature (K) and the Mean Curvature (H) :

$$K = \kappa_1 \kappa_2, H = \frac{1}{2}(\kappa_1 + \kappa_2) \quad (1)$$

While elementary geometry focuses on surfaces where these curvatures are constant-such as spheres (H, K constant), planes ($H = K = 0$), and minimal surfaces ($H = 0$)-a much broader and geometrically rich class of surfaces exists where H and K vary but remain coupled.

A surface S is defined as a Weingarten surface (or simply a W - surface) if there exists a non-trivial smooth function $\Phi: \mathbb{R}^2 \to \mathbb{R}$ such that:

$$\Phi(H, K) = 0 \tag{2}$$

at every point on the surface. This condition implies that the principal curvatures are functionally dependent; the state of the surface at any point is constrained to a one-dimensional curve in the (H, K) phase plane.

The importance of Weingarten surfaces cannot be overstated. They serve as a testing ground for global theorems in differential geometry, solutions to non-linear partial differential equations (PDEs), and, recently, as the "Holy Grail" of architectural geometry for their properties related to panelization and manufacturing rationalization.

The theory of W-surfaces dates back to the "Golden Age" of differential geometry in the 19th century, a period dominated by the search for invariants under deformation.

Weingarten's Original Problem (1861)

The German mathematician Julius Weingarten (1836-1910) introduced these surfaces in his seminal paper Über die Oberflächen, für welche einer der beiden Hauptkrümmungshalbmesser eine Function des anderen ist ("On surfaces for which one of the two principal radii of curvature is a function of the other") (Weingarten, 1861).

Weingarten was motivated by the problem of isometric deformation. Specifically, he sought to identify all surfaces that could be mapped isometrically onto a surface of revolution. A surface of revolution possesses rotational symmetry, which implies that its principal curvatures are functions of a single parameter (the arc length of the profile curve). Consequently, a functional relation exists between them.

Weingarten proved a remarkable theorem: If a surface S is isometric to a surface of revolution such that the lines of curvature are preserved under the isometry, then S must satisfy a relation $W(\kappa_1, \kappa_2) = 0$.

The 20th Century: Rigidity

Following Weingarten, the focus shifted to global properties. In 1900, Heinrich Liebmann proved that the only closed, convex surface with

constant mean curvature is the sphere (Liebmann, 1900). This was a precursor to the more general rigidity theorems of the mid-20th century.

Research by Chern (1945) and Hartman and Wintner (1954) utilized the Maximum Principle for elliptic PDEs to generalize Liebmann's result, showing that under convexity conditions, the functional relation $\Phi(H,K)=0$ forces the surface to be a sphere. These results established W -surfaces as a rigid class where local curvature relations dictate global topology.

To understand the mechanics of Weingarten surfaces, we must derive the condition of functional dependence rigorously using differential calculus.

The Jacobian Determinant Condition

Let S be a smooth, oriented surface parameterized by $X: U \subset \mathbb{R}^2 \to \mathbb{R}^3$. Let (u, v) be local coordinates. $H(u,v)$ and $K(u,v)$ are scalar fields on S.

In multivariable calculus, two smooth functions f and g are functionally dependent if and only if their level sets (contour lines) coincide. This geometric condition is equivalent to the requirement that their gradient vectors ∇f and ∇g are parallel everywhere on the domain (Kühnel, 2015).

Mathematically, two vectors in $\mathbb{R}^2$ are parallel if their determinant vanishes. Thus, the necessary and sufficient condition for a surface to be a W -surface is:

Definition (Weingarten Surface). A regular surface S is a Weingarten surface if the Jacobian determinant of the map (H,K) vanishes identically on S :

$$J(H,K)=\frac{\partial(H,K)}{\partial(u,v)}=\det\begin{pmatrix}\frac{\partial H}{\partial u} & \frac{\partial H}{\partial v}\\ \frac{\partial K}{\partial u} & \frac{\partial K}{\partial v}\end{pmatrix}=H_uK_v-H_vK_u=0 \qquad (3)$$

If $J(H,K)\neq 0$ at a point, the Inverse Function Theorem would imply that H and K could serve as independent local coordinates, creating a region where they can vary independently, which contradicts the relation $\Phi(H,K)=0$.

The Theory of Parallel Surfaces

A powerful geometric tool for analyzing W -surfaces is the concept of the Parallel Surface (or Offset Surface). For a surface S with unit normal vector field $\mathbf{N}$, the family of parallel surfaces S_t at distance t is defined by:

$$S_t = \{p + t\mathbf{N}(p) \mid p \in S\} \tag{4}$$

The principal curvatures κ_i^t of the parallel surface S_t are related to the original curvatures κ_i by the formula:

$$\kappa_i^t = \frac{\kappa_i}{1 - t\kappa_i} \tag{5}$$

This transformation is fundamental. It allows us to relate the Mean curvature H_t and Gaussian curvature K_t of the offset surface to those of the base surface:

$$K_t = \frac{K}{1 - 2tH + t^2K} \tag{6}$$

$$H_t = \frac{H - tK}{1 - 2tH + t^2K} \tag{7}$$

Theorem (Offset Characterization). A surface S is a Weingarten surface if and only if there exists a parallel surface $S_t(t \neq 0)$ that has either Constant Mean Curvature (CMC) or Constant Gaussian Curvature (CGC).

Proof. Suppose S_t has constant mean curvature $H_t = c$. Then:

$$\frac{H - tK}{1 - 2tH + t^2K} = c$$

Multiplying through, we get:

$$H - tK = c(1 - 2tH + t^2K)$$
$$H(1 + 2tc) - K(t + ct^2) = c$$

This is a linear relation of the form $aH + bK = d$, which satisfies the Weingarten condition. The converse is also true locally for Linear Weingarten Surfaces.

This theorem is critical for applications: it tells us that complex W -surfaces can be generated by simply offsetting simpler, constant-curvature surfaces.

The class of W -surfaces is vast. To manage it, geometers classify these surfaces based on the specific form of the function $\Phi(H, K)$.

Surfaces of Revolution

Any surface generated by rotating a profile curve around an axis is a W -surface. Consider the parameterization:

$$\mathbf{x}(u, v) = (f(u)\cos\ v, f(u)\sin\ v, g(u))$$

where the profile is parameterized by arc length $((f')^2 + (g')^2 = 1)$. The principal curvatures are:

$$\kappa_1 = f'(u)g''(u) - g'(u)f''(u), \kappa_2 = \frac{g'(u)}{f(u)}$$

Since both depend only on u, the Jacobian $H_u K_v - H_v K_u$ vanishes identically ($K_v = H_v = 0$). Thus, rotational symmetry imposes the W -surface condition.

Linear Weingarten Surfaces (LWS)

The most studied subclass is the Linear Weingarten Surface, defined by:

$$aH + bK = c \tag{8}$$

where a, b, c are real constants $(a^2 + b^2 \neq 0)$. The behavior of LWS depends on the discriminant $\Delta = a^2 + 4bc$:

1. Elliptic Type ($\Delta > 0$): Includes CMC surfaces ($b = 0$) and CGC surfaces ($a = 0$). These surfaces are stable and satisfy strong maximum principles.
2. Hyperbolic Type $(\Delta < 0)$: These relate to surfaces of constant negative curvature. The asymptotic lines on these surfaces form a coordinate system that satisfies the Sine-Gordon equation $(u_{xy} = \sin\ u)$, linking them to soliton theory.
3. Parabolic Type $(\Delta = 0)$: Represents the transition case, often associated with developable surfaces (where $K = 0$).

López (1997) and Gálvez et al. (2003) have provided extensive classifications of complete LWS immersed in $\mathbb{R}^3$, showing that they naturally generalize the classical theory of minimal and constant curvature surfaces.

Tubular Surfaces

A tube (or pipe surface) of constant radius r around a central space curve $\gamma(s)$ is a W surface. One principal curvature is constant, corresponding to the circular cross-section: $\kappa_1 = 1/r$. The other principal curvature κ_2 varies with the curvature of γ. Since κ_1 is constant, the relation is trivial: $\Phi(\kappa_1, \kappa_2) = \kappa_1 - c = 0$.

Global Theory and Rigidity

While local examples of W-surfaces are abundant, the global topology imposes severe constraints. The most famous results concern the rigidity of the sphere.

Can a "bumpy" sphere be a Weingarten surface? Next theorem answers.

Theorem (Chern (1945); Hartman and Wintner (1954)). Let S be a closed (compact without boundary), oriented surface in $\mathbb{R}^3$. Suppose:

1. S is strictly convex ($K > 0$ everywhere).
2. S is a Weingarten surface satisfying a monotonicity condition (e.g., $\frac{\partial \Phi}{\partial H} \neq 0$).

Then S is a sphere.

The proof generalizes the method of the Hopf Differential. For a CMC surface, Hopf defined a quadratic differential that is holomorphic on the surface. For a sphere (genus 0), the only holomorphic quadratic differential is zero. The vanishing of this differential implies $\kappa_1 = \kappa_2$ everywhere (umbilical points). Chern and Hartman extended this to general W -surfaces by constructing a similar quantity satisfying an elliptic differential inequality. By the Maximum Principle, the function relating to the curvatures must be constant, forcing the surface to be totally umbilical, and thus a sphere (Hopf, 1989).

Computational Design

In the 21st century, the study of W -surfaces moved from pure analysis to Computational Design. The driving force is the need to rationalize complex architectural forms, utilizing Discrete Differential Geometry (Bobenko and Suris, 2008).

Architects design freeform "blobs" for aesthetic reasons. However, fabricating these is expensive because every panel has a unique curvature. The question arises: Can we approximate an arbitrary freeform surface with a Weingarten surface?

Pellis et al. (2021) developed an optimization framework to solve this.

1. Curvature Diagram: They analyze the input surface by plotting pairs $(H(p), K(p))$ for all points p. For a generic surface, this plot is a 2D cloud. For a W -surface, it is a 1D curve.
2. Optimization: An algorithm iteratively perturbs the surface vertices to collapse the 2D curvature cloud onto a 1D curve.
3. Result: The implicit relation Φ is not chosen in advance; it emerges from the optimization.

Industrial Rationalization (Mold Re-Use)
Why do this? The answer lies in manufacturing economics.

- Local Congruence: On a W-surface, if two points have the same Mean Curvature H, they also have the same Gaussian Curvature K. This implies the surface patches around these points are (up to second order) congruent.
- Mold Re-Use: If a facade is a W -surface, panels with the same H value can be manufactured using the same physical mold.
- Impact: Instead of 5,000 unique molds for 5,000 panels, a W -surface design might require only 50 molds, drastically reducing costs while maintaining the complex appearance.

The utility of W -surfaces extends far beyond pure mathematics and architecture.

Naval Architecture: Hydrodynamic Fairing
In ship design, "fairing" is the smoothing of the hull surface.

- Flow Physics: Abrupt changes in curvature derivatives can induce flow separation and turbulence.
- W-Surface Smoothing: By constraining the hull to be a W-surface (typically Linear), designers ensure that curvature variation is smooth and predictable. This optimizes hydrodynamic efficiency and simplifies the bending of steel plates (Bruck et al., 2002).

Structural Engineering: Torsion-Free Nodes
Building a glass gridshell requires a steel support structure.

- The Problem: If beams meet at a node at arbitrary angles, the joint requires complex twisting (torsion), which is expensive to manufacture.

- The Solution: Ideally, the beam axes should align with the surface normal. This is only possible if the beams follow the principal curvature lines.
- PQ Meshes: A "Planar Quadrilateral" (PQ) mesh that follows curvature lines and possesses a parallel offset (for the beam depth) is mathematically equivalent to a Discrete Weingarten Surface. Thus, W-surfaces are the "Gold Standard" for buildable glass roofs (Pottmann et al., 2007).

Biophysics: The Ouloid

Nature uses W -surfaces to minimize elastic energy. The shape of lipid bilayers (cell membranes) minimizes the Helfrich Energy:

$$E = \int (H - c_0)^2 + \lambda K dA \qquad (9)$$

The Euler-Lagrange equations for this function define a class of Generalized Weingarten Surfaces. A specific solution, known as the "Ouloid" (Ou-Yang and Helfrich, 1989), replicates the biconcave shape of human red blood cells, demonstrating that biological equilibrium is governed by Weingarten geometry.

RESULTS AND DISCUSSION

Weingarten surfaces represent a profound intersection of local constraints and global form.

- Historically, they solved the problem of isometry classes.
- Theoretically, they provide deep insights into the rigidity of convex shapes and the behavior of elliptic PDEs.
- Practically, they act as a bridge between the continuous world of design and the discrete world of fabrication.

From the rigid spheres of classical geometry to the optimized freeform skins of modern skyscrapers, the functional dependence of H and K remains a guiding principle. As computational power grows, the ability to "search" for W-surfaces in the space of all shapes will likely unlock new possibilities in efficient, sustainable manufacturing across industries.

REFERENCES

Bobenko, A. I., & Suris, Y. B. (2008). Discrete Differential Geometry: Integrable Structure. Graduate Studies in Mathematics, Vol. 98. American Mathematical Society.

Bruck, R., Du, X., & Pottmann, H. (2002). Optimizing the Gaussian curvature of a surface. In Proceedings of the 8th IMA Conference on the Mathematics of Surfaces (pp. 102-116). Springer.

Chern, S. S. (1945). Some new characterizations of the Euclidean sphere. Duke Mathematical Journal, 12(2), 279-290.

Do Carmo, M. P. (1976). Differential Geometry of Curves and Surfaces. Prentice-Hall.

Gálvez, J. A., Martínez, A., & Milán, F. (2003). Linear Weingarten surfaces in $\mathbb{R}^3$. Monatshefte für Mathematik, 138(2), 133-144.

Hartman, P., & Wintner, A. (1954). Umbilical points and W-surfaces. American Journal of Mathematics, 76(3), 502-508.

Hopf, H. (1989). Differential Geometry in the Large. Lecture Notes in Mathematics, Vol. 1000. Springer-Verlag.

Kühnel, W. (2015). Differential Geometry: Curves - Surfaces - Manifolds. Student Mathematical Library, Vol. 77. AMS.

Liebmann, H. (1900). Eine neue Eigenschaft der Kugel. Nachrichten von der Gesellschaft der Wissenschaften zu Göttingen, 51-55.

López, R. (1997). Surfaces of constant mean curvature with boundary in a sphere. Osaka Journal of Mathematics, 34, 625-635.

Ou-Yang, Z., & Helfrich, W. (1989). Bending energy of vesicle membranes: General expressions for the first, second, and third variation of the shape energy and boundary conditions. Physical Review A, 39(10), 5280.

Pellis, D., Kilian, M., Pottmann, H., & Pauly, M. (2021). Computational design of Weingarten surfaces. ACM Transactions on Graphics (SIGGRAPH), 40(4), Article 120.

Pottmann, H., Liu, Y., Wallner, J., Bobenko, A., & Wang, W. (2007). Geometry of Multilayer Freeform Structures for Architecture. ACM Transactions on Graphics, 26(3), 65.

Weingarten, J. (1861). Über die Oberfächen, für welche einer der beiden Hauptkrümmungshalbmesser eine Function des anderen ist. Journal für die reine und angewandte Mathematik (Crelle's Journal), 59, 296-302.

Recent Developments in Glycoanalytical Technologies

Hacı Mehmet KAYILI[1]

1- Assoc.Prof. Dr. Karabuk University, Faculty of Engineering and Natural Sciences, Biomedical Engineering Department, h.mehmetkayili@karabuk.edu.tr ORCID No: 0000-0002-6740-0645

ABSTRACT

This book chapter discusses the latest sample preparation methods in glycomic analysis and the powerful innovations focused on speed/automation in this stage in recent years. Rapid workflows supported by PNGase F-based but adapted to formats such as 96-well filters are prominent in N-glycans, while in O-glycans, optimized β-elimination and stable isotope approaches that reduce sialic acid loss, along with site-specific enzymatic options, stand out. In the enrichment of glycosylated species, alongside multiple lectin strategies, methods such as boronate/boric acid chemistry (especially stronger dendrimer-based binding), glycoblotting, and HILIC have become essential tools to expand the scope of analysis. Finally, it is emphasized that in derivatization/labeling, RapiFluor-MS (RFMS) and similar rapid labels (InstantPC; procainamide as a cost-effective alternative) increase both FLD and MS sensitivity and shorten preparation time, supporting high-throughput analyses.

Keywords – Glycomics*, Glycan sample preparation, PNGase F (N-glycan release), O-glycan release (β-elimination), Glycopeptide enrichment (HILIC / lectin affinity / boronate chemistry)*

INTRODUCTION

Glycans (carbohydrate chains) are structures found almost everywhere in the world of biomolecules; in humans, they comprise more than half of proteins and bind to numerous lipids, dramatically influencing their properties(Bielik & Zaia, 2010). Glycosylation is the covalent binding of glycans to biomolecules via enzymes. It is a crucial post-translational modification affecting protein folding, stability, intracellular/extracellular transport, and cellular signal transduction(Onigbinde et al., 2025). Unlike DNA and proteins, glycans are not synthesized directly according to a genetic template. Instead, they possess a highly diverse structural variation, arising through complex biosynthetic pathways and branched architectures. This diversity gives glycans a wide range of functions. For example, they regulate recognition by the immune system and often serve as the first point of interaction in cell-pathogen interactions(Varki, 2017).

Abnormal glycosylation is considered one of the features that can be used in the recognition of many pathologies, including cancer, inflammatory diseases, and neurodegenerative disorders(Krištić, Lauc, & Pezer, 2022; Yue, Huang, Lan, Xiao, & Luo, 2023). Therefore, comprehensive and systematic study of glycans is gaining increasing interest in terms of biomarker discovery

and therapeutic development. However, the analysis of "glycome" (the sum of all glycans in a cell or organism) presents significant analytical challenges due to factors such as glycan heterogeneity, isomerism, and often low abundance(Kayili & Salih, 2021). Traditional glycoanalysis approaches rely mostly on labour-intensive chemical derivatization steps, chromatographic separations, and mass spectrometry (MS)-based methods to elucidate glycan composition and structure(Reyes et al., 2022).

Recent advances in instrumentation and methodology have significantly changed this picture. High-sensitivity MS/MS fragmentation techniques and high-performance liquid chromatography (HPLC) and capillary electrophoresis (CE)-based separation methods enable glycan profiling at previously unattainable levels of detail. In parallel, new computational workflows and databases supporting the processing and interpretation of glycoanalytic data have been developed(Polasky, Yu, Teo, & Nesvizhskii, 2020).

This section provides a comprehensive framework for emerging glycoanalytic technologies and their applications. First, it summarizes the historical development of glycoanalysis techniques. In this context, it highlights current innovations in sample preparation, separation, and detection steps, as well as the latest advances in glycoinformatics. Finally, it addresses the new application areas these developments open up in biomedicine and biotechnology.

History of Glycoanalytical Technologies

Early studies in the field of glycanalysis relied on classical biochemical methods. Periodic acid-Schiff staining and lectin agglutination tests provided the first evidence of glycans on cell surfaces. The identification of ABO blood groups occurred in this way. By the mid-20th century, analytical breakthroughs such as paper chromatography and gas-liquid chromatography enabled the analysis of the basic monosaccharide composition of glycans(Pan, Chen, Aebersold, & Brentnall, 2011). Developments in mass spectrometry in the 1980s and 1990s had a dramatic impact on shaping the field. In particular, matrix-assisted laser desorption/ionization (MALDI) and electrospray ionization (ESI) enabled direct mass profiling of glycans and glycopeptides, while collision-induced dissociation (CID) in MS/MS provided structural information. These fundamental techniques formed the core glycomic

workflow of release, separation, and MS detection, which is still used today. Over the last decade, advances in glycoanalytical technologies have greatly accelerated the pace of glycan analysis(Bielik & Zaia, 2010).

The demand for high-throughput and more precise glycan profiling has increased in systems biology and clinical studies. This demand has enabled the development of automated ultra-high-throughput platforms, allowing for the parallel processing of hundreds to thousands of samples for *N*-glycan profiling. One example is the development of 96-well plate workflows combining rapid PNGase F glycan release, fluorescent labeling, and UPLC-MS analysis, which has significantly accelerated glycan biomarker studies(Reusch et al., 2015). Similarly, work on the Human Glycome Project has highlighted a broader demand for addressing population-scale glycomic assays, such as faster solid-phase extractions and robotic sample preparation(Habazin et al., 2021). On the identification side, MS instruments have advanced with higher resolution and improved ion mobility spectrometry (IMS) integration, enabling the separation of glycan isomers previously impossible to resolve. Novel fragmentation methods (e.g., electron-based dissociation and ultraviolet photodissociation) provide richer structural fingerprints for complex glycans. Complementing MS, glycan microarray technology, which emerged in the 2000s and matured in the last decade, has enabled high-throughput profiling of glycan-protein interactions(Kayili & Salih, 2022). All these developments signal a shift from low-throughput, expert-focused assays to more automated, sensitive, and comprehensive glycomic profiling approaches. The evolution of glycoanalysis, thus reflecting other "omics" fields, is progressing from single-target measurements to global and integrative analyses.

Emerging Sample Preparation and Enrichment Strategies

Efficient glycoanalysis is highly dependent on sample preparation. Prior to glycan analysis, glycans must be released or captured from complex biological matrices, enriched, and appropriately derivatized for detection. Significant innovations have emerged in these preparation steps in recent years(Donohoo et al., 2022).

Glycan release methods have been developed for both N- and O-linked glycans. PNGase F remains the primary enzyme in N-glycan

analysis(Turnbull & Field, 2007). However, faster and more easily automated protocols have become widespread. For example, filter-assisted rapid N-glycan release workflows have been introduced, utilizing ultrafiltration membranes to combine protein denaturation, PNGase F digestion, and glycan capture in a single process, enabling high-throughput processing in a 96-well format(Habazin et al., 2021). O-glycans, which are difficult to release enzymatically, can now be released more safely using optimized β-elimination chemistries that reduce sialic acid cleavage. Wang et al. The O-glycan release approach developed by (2017) with stable isotopic labeling enables quantitative O-glycomic analysis from small sample volumes. Similarly, novel endoglycosidases facilitate site-specific O-glycan analysis by enzymatically cleaving O-glycans from specific regions(Wilkinson & Saldova, 2020).

Enrichment and purification of glycosylated species is another important area of progress. Traditional lectin affinity methods based on carbohydrate-binding proteins have been developed to capture glycoproteins and glycopeptides. The biggest disadvantage of lectin affinity methods is their focus on specific types of glycans. For broader glycoform coverage, multiple lectin approaches using multiple lectins with different specificities have been adopted(Madera, Mechref, Klouckova, & Novotny, 2007). However, lectin-based capture, by its nature, cannot cover the entire glycan diversity. Therefore, chemical enrichment strategies have also come to the fore. One of the significant breakthroughs in this field is the use of boric acid/boronate chemistry for glycopeptide capture. While simple boronate affinity can miss low-abundance species due to weak binding, demonstrated that polyvalent benzoboroxol dendrimers form stronger and more synergistic interactions with cis-diol groups in glycans. This dendrimer-based approach has significantly increased the scope of the glycoproteome, contributing to the identification of thousands of glycopeptides, including low-abundance species. Other chemical strategies, such as “glycoblotting” based on hydrazide binding to oxidized glycans, have also been miniaturized and integrated into micro-scale devices for higher throughput(Liu et al., 2022). In parallel, hydrophilic interaction liquid chromatography (HILIC) has become one of the fundamental methods for enriching released glycans and glycopeptides according to their hydrophilicity. HILIC has published studies systematically

comparing porous graphitized carbon (PGC) and boronic chemistry. It has presented methods for selecting the appropriate method or combining methods for maximum coverage(Melmer, Stangler, Premstaller, & Lindner, 2011).

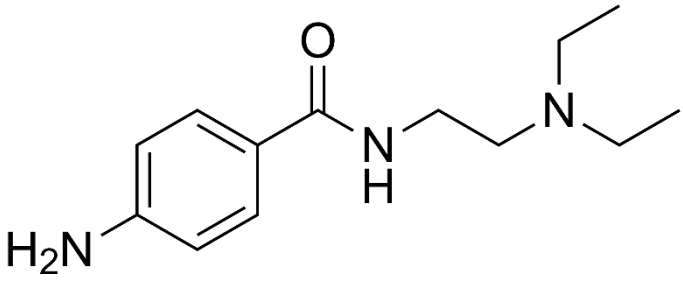

Figure 1. The structure of procainamide tag.

Derivative and labeling strategies are another rapidly advancing area. Labeling glycans with chromophore or fluorophore not only facilitates optical detection but can also increase MS sensitivity by enhancing ionization. The introduction of RapiFluor-MS (RFMS) in 2015 was a milestone in this regard. RFMS reacts with released glycans within minutes, generating derivatives that significantly enhance the MS signal(Zhang, Reed, Birdsall, Yu, & Chen, 2020). Similar rapid labels (e.g., InstantPC) support high-throughput glycan profiling in clinical laboratories by increasing sensitivity while shortening sample preparation time. Recently, the procainamide tag (Figure 1) has been presented as the most cost-effective alternative to these tags, and its ability to generate strong FLD and MS signals has been demonstrated in various studies(Kayili, 2020).

REFERENCES

Bielik, A. M., & Zaia, J. (2010). Historical overview of glycoanalysis. *Methods Mol Biol, 600*, 9-30. doi:10.1007/978-1-60761-454-8_2

Donohoo, K. B., Wang, J., Goli, M., Yu, A., Peng, W., Hakim, M. A., & Mechref, Y. (2022). Advances in mass spectrometry-based glycomics-An update covering the period 2017-2021. *Electrophoresis, 43*(1-2), 119-142. doi:10.1002/elps.202100199

Habazin, S., Mlinarević, D., Balog, M., Bardak, A., Gaspar, R., Szűcs, K. F., . . . Heffer, M. (2021). High-throughput rat immunoglobulin G N-glycosylation profiling revealed subclass-specific changes associated with chronic stress. *J Proteomics, 245*, 104293. doi:https://doi.org/10.1016/j.jprot.2021.104293

Kayili, H. M. (2020). Identification of bisecting N-glycans in tandem mass spectra using a procainamide labeling approach for in-depth N-glycan profiling of biological samples. *International Journal of Mass Spectrometry, 457*. doi:10.1016/j.ijms.2020.116412

Kayili, H. M., & Salih, B. (2021). N-glycan Profiling of Glycoproteins by Hydrophilic Interaction Liquid Chromatography with Fluorescence and Mass Spectrometric Detection. *Jove-Journal of Visualized Experiments*(175). doi:10.3791/62751

Kayili, H. M., & Salih, B. (2022). Site-specific N-glycosylation analysis of human thyroid thyroglobulin by mass spectrometry-based Glyco-analytical strategies. *J Proteomics, 267*. doi:10.1016/j.jprot.2022.104700

Krištić, J., Lauc, G., & Pezer, M. (2022). Immunoglobulin G glycans - Biomarkers and molecular effectors of aging. *Clin Chim Acta, 535*, 30-45. doi:10.1016/j.cca.2022.08.006

Liu, Z. L., Xu, M. M., Zhang, W. Q., Miao, X. Y., Wang, P. G., Li, S. W., & Yang, S. (2022). Recent development in hydrophilic interaction liquid chromatography stationary materials for glycopeptide analysis. *Analytical Methods, 14*(44), 4437-4448. doi:10.1039/d2ay01369j

Madera, M., Mechref, Y., Klouckova, I., & Novotny, M. V. (2007). High-sensitivity profiling of glycoproteins from human blood serum through multiple-lectin affinity chromatography and liquid chromatography/tandem mass spectrometry. *J Chromatogr B Analyt Technol Biomed Life Sci, 845*(1), 121-137. doi:10.1016/j.jchromb.2006.07.067

Melmer, M., Stangler, T., Premstaller, A., & Lindner, W. (2011). Comparison of hydrophilic-interaction, reversed-phase and porous graphitic carbon chromatography for glycan analysis. *J Chromatogr A, 1218*(1), 118-123. doi:10.1016/j.chroma.2010.10.122

Onigbinde, S., Adeniyi, M., Daramola, O., Chukwubueze, F., Bhuiyan, M. M. A. A., Nwaiwu, J., . . . Mechref, Y. (2025). Glycomics in Human Diseases and Its Emerging Role in Biomarker Discovery. *Biomedicines, 13*(8), 2034. Retrieved from https://www.mdpi.com/2227-9059/13/8/2034

Pan, S., Chen, R., Aebersold, R., & Brentnall, T. A. (2011). Mass spectrometry based glycoproteomics--from a proteomics perspective. *Mol Cell Proteomics, 10*(1), R110.003251. doi:10.1074/mcp.R110.003251

Polasky, D. A., Yu, F., Teo, G. C., & Nesvizhskii, A. I. (2020). Fast and comprehensive N- and O-glycoproteomics analysis with MSFragger-Glyco. *Nat Methods, 17*(11), 1125-1132. doi:10.1038/s41592-020-0967-9

Reusch, D., Haberger, M., Maier, B., Maier, M., Kloseck, R., Zimmermann, B., . . . Wuhrer, M. (2015). Comparison of methods for the analysis of therapeutic

immunoglobulin G Fc-glycosylation profiles--part 1: separation-based methods. *MAbs, 7*(1), 167-179. doi:10.4161/19420862.2014.986000

Reyes, C. D. G., Hakim, M. A., Atashi, M., Goli, M., Gautam, S., Wang, J., . . . Mechref, Y. (2022). LC-MS/MS Isomeric Profiling of N-Glycans Derived from Low-Abundant Serum Glycoproteins in Mild Cognitive Impairment Patients. *Biomolecules, 12*(11), 1657. Retrieved from https://www.mdpi.com/2218-273X/12/11/1657

Turnbull, J. E., & Field, R. A. (2007). Emerging glycomics technologies. *Nat Chem Biol, 3*(2), 74-77. doi:10.1038/nchembio0207-74

Varki, A. (2017). Biological roles of glycans. *Glycobiology, 27*(1), 3-49. doi:10.1093/glycob/cww086

Wilkinson, H., & Saldova, R. (2020). Current Methods for the Characterization of O-Glycans. *Journal of Proteome Research, 19*(10), 3890-3905. doi:10.1021/acs.jproteome.0c00435

Yue, J., Huang, R. J., Lan, Z. H., Xiao, B., & Luo, Z. H. (2023). Abnormal glycosylation in glioma: related changes in biology, biomarkers and targeted therapy. *Biomarker Research, 11*(1). doi:10.1186/s40364-023-00491-8

Zhang, X., Reed, C. E., Birdsall, R. E., Yu, Y. Q., & Chen, W. (2020). High-Throughput Analysis of Fluorescently Labeled N-Glycans Derived from Biotherapeutics Using an Automated LC-MS-Based Solution. *SLAS Technol, 25*(4), 380-387. doi:10.1177/2472630320922803

Integrated Glycomics and Glycoproteomics Workflows for *N*-Glycosylation Analysis

Hacı Mehmet KAYILI[1]

1- Assoc.Prof. Dr. Karabuk University, Faculty of Engineering and Natural Sciences, Biomedical Engineering Department, h.mehmetkayili@karabuk.edu.tr ORCID No: 0000-0002-6740-0645

ABSTRACT

Glycosylation is one of the most common and functionally important post-translational modifications affecting protein stability, biological activity, and disease-related processes. Advances in mass spectrometry enable detailed characterization of glycans and glycoproteins. However, due to the inherent structural complexity of glycans, analyses of glycan-containing molecules require well-designed analytical workflows and specialized bioinformatics tools. This book chapter provides a clear and practical overview of integrated glycomic and glycoproteomic workflows for *N*-glycosylation analysis. Released N-glycan-based glycomic workflows are described, including enzymatic glycan release, labeling strategies, chromatographic separation, mass spectrometric analysis, structural annotation, and relative quantification. In parallel, site-specific glycoproteomic workflows focusing on protein digestion, glycopeptide enrichment, LC-MS/MS analysis, database-driven identification, and reliable assignment of glycosylation sites and glycoforms are briefly summarized. This section highlights how the glycomic approach, which provides a global glycan repertoire, and the glycoproteomic approach, which performs protein and site-based glycosylation mapping, complement each other. By offering simplified yet robust workflows, this section aims to guide researchers in selecting and implementing appropriate strategies for N-glycosylation analysis in complex biological samples, including serum and biopharmaceutical products.

Keywords – Glycomics; Glycoproteomics; N-glycosylation; Mass spectrometry, Glycan profiling

INTRODUCTION

Glycomics and glycoproteomics are complementary fields aimed at characterizing the structure and function of glycans. Glycomics is generally defined as the comprehensive study of the glycome—the entirety of glycans produced by a cell or organism under specific conditions(Apweiler, Hermjakob, & Sharon, 1999; Campbell et al., 2011). Glycoproteomics, on the other hand, examines these glycans in the context of proteins, determines which proteins are glycosylated, and identifies the locations and structures of linked glycans. Glycosylation is known to be one of the most common post-translational modifications in nature. It is estimated that more than half of mammalian proteins and the vast majority of secreted and membrane proteins are glycosylated(Cao, 2024). These carbohydrate modifications play critical

roles in biological processes such as intercellular communication, immune recognition, and protein stability, and changes in glycosylation patterns have been associated with many diseases(Cooper, Gasteiger, & Packer, 2001). Furthermore, glycosylation can alter the efficacy and safety of biotherapeutics, highlighting the importance of glycan analysis in biopharmaceutical development(Cummings & Pierce, 2014). Despite their importance, glycans are difficult structures to analyze due to their immense structural complexity. Unlike linear DNA or protein polymers, glycans are branched with various monosaccharide building blocks, linkages, and modifications. A single glycoprotein can be found in numerous glycoforms, and each glycosylation site may be partially occupied(Damerell et al., 2012). This complexity means that the glycome cannot be directly inferred from genomic or proteomic data, and structures need to be determined experimentally(Zeng et al., 2016). Advances in mass spectrometry (MS) have played a key role in advancing the fields of glycomics and glycoproteomics, enabling the efficient detection of glycans and glycopeptides in complex samples(MacLean et al., 2010). However, the interpretation of MS data for glycan structures or glycopeptides is a process requiring specialized software and databases(Mereiter, Balmaña, Campos, Gomes, & Reis, 2019). In recent years, a range of bioinformatics tools have emerged to aid in glycomic and glycoproteomic data analysis, from the identification of glycan compositions to the mapping of site-specific glycosylation on proteins. This section provides an overview of these tools, including their functions, usage workflows, and an evaluation of their strengths, limitations, and recent developments.

Glycomics Workflow Example – Released Glycan Analysis

When a researcher wants to profile *N*-linked glycans in an antibody drug or cell culture supernatant, the first goal is to reliably determine the structures in which glycans are present and their relative abundances in the sample. For this purpose, the process usually begins with a controlled sample preparation step, followed by MS-based measurement, composition/structure determination, quantification, and biological interpretation. In the first step, glycans are enzymatically released from glycoproteins using PNGase F(H. M. Kayili & Salih, 2021). The released glycans are often labeled with a fluorescent tag (e.g., 2-AB or 2-AA) to facilitate detection and quantification. After labeling, the sample undergoes a cleanup step to remove proteins, salts, and other matrix components that could interfere with the measurement. This

results in a more consistent input material in terms of both chromatographic separation and MS signal quality. The labeled glycans are then separated, usually by a chromatographic method suitable for glycans such as HILIC, and fed into mass spectrometry (e.g., ESI-QTOF or MALDI-TOF for profiling; different platforms in the context of LC-MS)(H. Mehmet Kayili, Atakay, Hayatu, & Salih, 2022). The main output of this step is the MS1 spectra showing the molecular ions of the glycans. Each glycan is seen as a peak at a specific m/z value; the mass of the glycan can be recalculated back to its "unlabeled equivalent" mass, considering the mass of the label and possible mass/charge states. Alongside MS1, the MS/MS spectra obtained for the selected glycan ions provide critical information for structural verification. Fragmentation patterns (especially B/Y ions and in some cases cross-ring fragments) provide clues about the composition of the antennas, branching characteristics, and partly about linkage/isomer possibilities. Although a single MS/MS condition may not definitively separate every isomer, the appropriate fragments are powerful in narrowing down structural hypotheses.

These fragments are then separated using a chromatographic method suitable for glycans, such as HILIC, and fed into mass spectrometry (e.g., ESI-QTOF or MALDI-TOF for profiling; different platforms in the context of LC-MS). The first practical step in data processing is the compositional identification of the glycan peaks observed in MS1. This is where tools like GlycoMod come into play: the observed mass(s) are entered, and the software lists possible composition candidates such as Hex/HexNAc/Fuc/NeuAc for each mass. For example, an observation corresponding to a labeled mass might match a common N-glycan composition such as $Hex_5HexNAc_4$ among the candidates. The researcher can narrow the candidate list to a more realistic range by applying constraints based on the biological context of the sample (e.g., limiting the number of fucos in a mammalian sample). If the sample is a well-characterized system (e.g., human IgG), many compositions can be quickly associated with forms such as G0F, G1F, G2F in IgG glycan notation. Once compositional candidates are identified, the researcher cross-references them with databases such as UniCarbKB or GlyTouCan to match them with known glycan structures. For example, the composition $Hex_3HexNAc_2Fuc_1NeuAc_1$ might match a sialylated complex biantennary structure (with abbreviations like A1F) in a database query. Such databases

often provide information on possible connections and sometimes even examples of sources where the structure has been reported.

To more robustly validate the structures, the MS/MS spectrum of each glycan is described in detail. Software like GlycoWorkbench is quite useful at this point: the researcher draws one or more candidate structures for each composition using GlycanBuilder and uploads them to the software. GlycoWorkbench generates theoretical fragments for these structures and matches them with the observed MS/MS peaks; thus, a semi-automatic annotation can be performed by highlighting peaks that correspond to B/Y ions. For example, the spectrum of a biantennary glycan might show fragments corresponding to a single antenna; in cases where two antennas carry different decorations (e.g., one branch is sialylated, the other is not), this difference can be reflected in the fragment pattern(H. M. Kayili, 2020). However, some uncertainties may remain (e.g., Galβ1-4 to Galβ1-3 linkage or isomer discrimination); in this case, multiple hypothesis annotations are evaluated side-by-side to select the most consistent explanation. In the quantification phase, if glycans are fluorescently labeled, relative abundances can be estimated via the fluorescence signal, or alternatively via the MS signal. For automated/semi-automated reporting, tools such as the GRITS Toolbox can take MS data, assign peaks to structures using a glycan database, and generate a glycan profile report (e.g., 20% G0F, 50% G1F variants, 20% G2F, 10% sialylated forms, etc.). Furthermore, side-by-side comparison of profiles between samples can more quickly identify batch differences, cell line/condition effects, or product quality trends. Without GRITS, researchers can manually integrate LC peaks or use vendor software to retrieve domains, combine composition/structure assignments with GlycoMod and MS/MS validation, and calculate percentages (Figure 1).

Glycoproteomic Workflow Example – Glycopeptide Analysis

A glycoproteomic workflow can be implemented to map *N*-glycosylation sites in the serum proteome and to see how the glycans carried in each site differ between disease-control and disease-control. Because serum is a very complex matrix (many proteins and many peptides), the approach needs to be highly throughput and selective. In the first step, serum proteins are denatured, disulfide bonds are reduced, and after alkylation, the proteins are digested with trypsin(Wuhrer, Catalina, Deelder, & Hokke, 2007). An

additional protease can be used to increase digestion efficiency(Pan, Chen, Aebersold, & Brentnall, 2011). The post-digestion mixture contains thousands of peptides, only a small fraction of which are glycopeptides. Therefore, enrichment is essential to highlight the glycopeptides(Xiao, Chen, Smeekens, & Wu, 2018). Common options are affinity enrichment with lectins that bind to N-glycans or HILIC-based enrichment. This process results in a significantly enriched sample of glycopeptides, but it is not completely purified; some unglycosylated peptides may remain in the medium. The enriched glycopeptides are then analyzed by LC-MS/MS. Data collection can be performed in DDA or DIA format. CID or HCD is most commonly used for fragmentation. This produces both peptide fragments (b/y ions) and glycan fragments (oxonium ions and Y ions) within the same spectrum. For more robust site validation or to complement glycan-peptide information, methods such as EThcD can be applied in addition to HCD. Characteristic oxonium ions indicating the presence of glycans are frequently seen in glycopeptide spectra; for example, peaks such as m/z 204.086 (HexNAc) and m/z 366.14 (Hex-HexNAc) are strong indicators that the spectrum is of glycopeptide origin.

After MS/MS data is obtained, glycoproteomic search engines are used for identification. To increase coverage and confidence, two search engines, such as Byonic and MSFragger-Glyco, can be run in parallel(Kong, Leprevost, Avtonomov, Mellacheruvu, & Nesvizhskii, 2017). A protein sequence database (human FASTA or a subset of the target protein) is selected for the search. Additionally, an allowed list of glycan compositions for N-glycans is defined; this list can be derived from a glycomic catalog previously obtained from the same samples. When both software programs are run with the appropriate settings, they produce result lists containing glycopeptide spectrum matches (PSMs) and their scores. Results are generally filtered at the PSM and/or glycopeptide level with 1% FDR, and reliable matches are reported. In a typical output example, the N residue in the peptide “SWPAVGNYR” is marked as glycosylated, and it is stated that this peptide carries a specific glycan composition (e.g., Hex5HexNAc4Fuc1). This assignment is supported by two types of evidence: Y/oxonium ions confirming the glycan mass and b/y ions confirming the peptide sequence and glycosylation site. Thus, both “which protein/peptide” and “which N-glycan composition” are determined simultaneously (Figure 1).

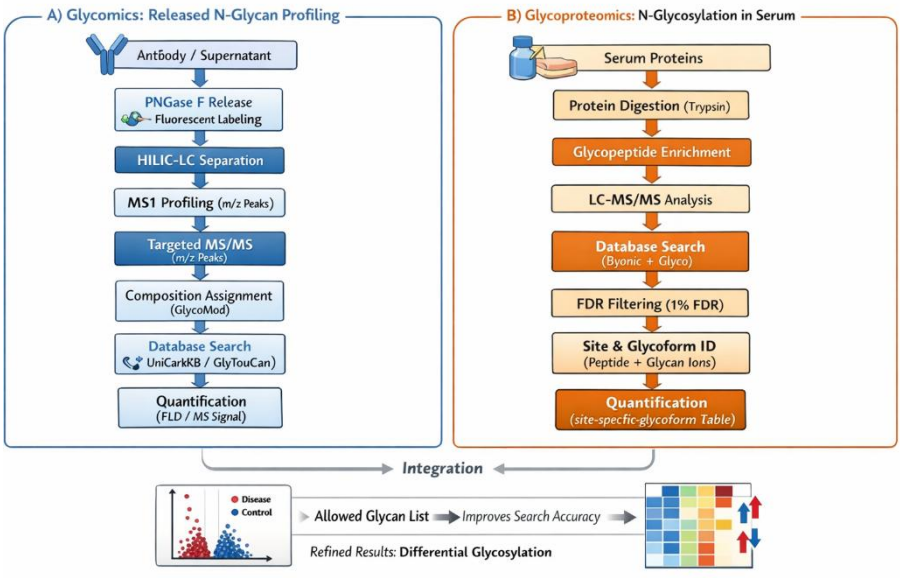

Figure 1. Integrated glycomics and glycoproteomics workflows for N-glycosylation analysis.

REFERENCES

Apweiler, R., Hermjakob, H., & Sharon, N. (1999). On the frequency of protein glycosylation, as deduced from analysis of the SWISS-PROT database. *Biochimica Et Biophysica Acta-General Subjects, 1473*(1), 4-8. doi:10.1016/s0304-4165(99)00165-8

Campbell, M. P., Hayes, C. A., Struwe, W. B., Wilkins, M. R., Aoki-Kinoshita, K. F., Harvey, D. J., . . . Packer, N. H. (2011). UniCarbKB: Putting the pieces together for glycomics research. *PROTEOMICS, 11*(21), 4117-4121. doi:10.1002/pmic.201100302

Cao, W. (2024). Advancing mass spectrometry–based glycoproteomic software tools for comprehensive site-specific glycoproteome analysis. *Current Opinion in Chemical Biology, 80*, 102442. doi:10.1016/j.cbpa.2024.102442

Cooper, C. A., Gasteiger, E., & Packer, N. H. (2001). GlycoMod – A software tool for determining glycosylation compositions from mass spectrometric data. *PROTEOMICS, 1*(2), 340-349. doi:10.1002/1615-9861(200102)1:2<340::aid-prot340>3.3.co;2-2

Cummings, Richard D., & Pierce, J. M. (2014). The Challenge and Promise of Glycomics. *Chemistry & Biology, 21*(1), 1-15. doi:10.1016/j.chembiol.2013.12.010

Damerell, D., Ceroni, A., Maass, K., Ranzinger, R., Dell, A., & Haslam, S. M. (2012). The GlycanBuilder and GlycoWorkbench glycoinformatics tools: updates and new developments. *bchm, 393*(11), 1357-1362. doi:10.1515/hsz-2012-0135

Kayili, H. M. (2020). Identification of bisecting N-glycans in tandem mass spectra using a procainamide labeling approach for in-depth N-glycan profiling of biological samples. *International Journal of Mass Spectrometry, 457*. doi:10.1016/j.ijms.2020.116412

Kayili, H. M., Atakay, M., Hayatu, A., & Salih, B. (2022). Sample preparation methods for N-glycomics. *Advances in Sample Preparation, 4*, 100042. doi:https://doi.org/10.1016/j.sampre.2022.100042

Kayili, H. M., & Salih, B. (2021). N-glycan Profiling of Glycoproteins by Hydrophilic Interaction Liquid Chromatography with Fluorescence and Mass Spectrometric Detection. *Jove-Journal of Visualized Experiments*(175). doi:10.3791/62751

Kong, A. T., Leprevost, F. V., Avtonomov, D. M., Mellacheruvu, D., & Nesvizhskii, A. I. (2017). MSFragger: ultrafast and comprehensive peptide identification in mass spectrometry-based proteomics. *Nat Methods, 14*(5), 513-520. doi:10.1038/nmeth.4256

MacLean, B., Tomazela, D. M., Shulman, N., Chambers, M., Finney, G. L., Frewen, B., . . . MacCoss, M. J. (2010). Skyline: an open source document editor for creating and analyzing targeted proteomics experiments. *Bioinformatics, 26*(7), 966-968. doi:10.1093/bioinformatics/btq054

Mereiter, S., Balmaña, M., Campos, D., Gomes, J., & Reis, C. A. (2019). Glycosylation in the Era of Cancer-Targeted Therapy: Where Are We Heading? *Cancer Cell, 36*(1), 6-16. doi:10.1016/j.ccell.2019.06.006

Pan, S., Chen, R., Aebersold, R., & Brentnall, T. A. (2011). Mass spectrometry based glycoproteomics--from a proteomics perspective. *Mol Cell Proteomics, 10*(1), R110.003251. doi:10.1074/mcp.R110.003251

Wuhrer, M., Catalina, M. I., Deelder, A. M., & Hokke, C. H. (2007). Glycoproteomics based on tandem mass spectrometry of glycopeptides. *Journal of Chromatography B-Analytical Technologies in the Biomedical and Life Sciences, 849*(1-2), 115-128. doi:10.1016/j.jchromb.2006.09.041

Xiao, H., Chen, W., Smeekens, J. M., & Wu, R. (2018). An enrichment method based on synergistic and reversible covalent interactions for large-scale analysis of glycoproteins. *Nature Communications, 9*(1), 1692. doi:10.1038/s41467-018-04081-3

Zeng, W.-F., Liu, M.-Q., Zhang, Y., Wu, J.-Q., Fang, P., Peng, C., . . . Yang, P. (2016). pGlyco: a pipeline for the identification of intact N-glycopeptides by using HCD- and CID-MS/MS and MS3. *Scientific Reports, 6*(1). doi:10.1038/srep25102

Ostrowski Type Fractional İnequalities for Functions Whose Higher-Order Partial Derivatives Are Convex With Respect to the Coordinates

Samet ERDEN[1]

Sueda ALTINDAĞ[2]

Zehra Nur AĞIR[3]

1- Assoc. Prof..; Bartın University, Faculty of Science, Depertmant of Mathematics. erdensmt@gmail.com ORCID No: 0000-0001-8430-7533

2- UG Student ; Bartın University, Faculty of Science, Depertmant of Mathematics. altindagsueda@gmail.com ORCID No: 0009-0006-4631-5739

3- UG Student ; Bartın University, Faculty of Science, Depertmant of Mathematics. Zehranuragir04@gmail.com ORCID No: 0009-0006-1352-0664

ABSTRACT

The primary aim of this study is to establish new double integral inequalities for functions whose higher-order partial derivatives are convex with respect to the coordinates. By employing a fractional integral identity introduced in a previously published work, we derive Ostrowski-type inequalities for double integrals associated with mappings whose higher-order partial derivatives, in absolute value, exhibit coordinated convexity. Also, an Ostrowski type inequality of double integrals for mappings whose powers of higher-order partial derivatives in modulus are co-ordinated convex funtions are obtained by using a same fractional integral identity. Furthermore, the connections between the inequalities presented in this work and similar inequalities previously introduced in the literature are presented.

.

Keywords –Fractional integrals, Co-ordinated convex functions, Ostrowski type inequalities, Double integrals
MSC2020–26D15, 26A33, 26D10, 26A51

INTRODUCTION

The Ostrowski inequality, first introduced by Alexander Markovich Ostrowski in 1938 (Ostrowski, 1938), is regarded as one of the most fundamental integral inequalities in mathematical analysis. This classical inequality can be stated in the form of the following theorem.

Theorem 1. *Let* $f:[a,b]\to R$ *be a differentiable mapping on* (a,b) *whose derivative* $f':(a,b)\to R$ *is bounded on* (a,b), *i.e.,* $\|f'\|_\infty = \sup_{t\in(a,b)} |f'(t)| < \infty$. *Then, the inequality holds:*

$$\left|f(x)-\frac{1}{b-a}\int_a^b f(t)dt\right| \le \left[\frac{1}{4}+\frac{(x-\frac{a+b}{2})^2}{(b-a)^2}\right](b-a)\|f'\|_\infty \quad (1)$$

for all $x\in[a,b]$. *The constant* $\frac{1}{4}$ *is the best possible.*

The Ostrowski inequality (1) is widely acknowledged as a fundamental result with extensive applications across various branches of mathematical analysis, particularly in numerical integration and the theory of special means. It serves as an essential tool for deriving error estimates

associated with a variety of quadrature formulas, including the midpoint, trapezoidal, Simpson, and related rules. In many classical treatments, the establishment of such error bounds for specific quadrature formulas is commonly based on the Peano kernel method. These traditional analyses typically assume that the functions under consideration admit bounded derivatives of order higher than one, an assumption that guarantees both the validity and precision of the resulting estimates.

We now proceed by recalling the definitions of the fractional integral operators that are essential for the development of our main results.

Definition 1. (Kilbas, 2006) *Let* $f \in L_1[a,b]$. *The Riemann-Liouville integrals* $J_{a+}^{\alpha}f$ *and* $J_{b-}^{\alpha}f$ *of order* $\alpha > 0$ *with* $a \geq 0$ *are defined by*

$$J_{a+}^{\alpha}f(x) = \frac{1}{\Gamma(\alpha)}\int_a^x (x-t)^{\alpha-1}f(t)dt, \quad x > a$$

and

$$J_{b-}^{\alpha}f(x) = \frac{1}{\Gamma(\alpha)}\int_x^b (t-x)^{\alpha-1}f(t)dt, \quad x < b$$

respectively. Here, $\Gamma(\alpha)$ *is the Gamma function and* $J_{a+}^{0}f(x) = J_{b-}^{0}f(x) = f(x)$.

The definitions of the Riemann-Liouville fractional integrals for two-variable functions are now provided as follows.

Definition 2. (Sarıkaya, 2014) *Let* $f \in L_1([a,b]\times[c,d])$. *The Riemann-Liouville fractional integrals* $J_{a+,c+}^{\alpha,\beta}$, $J_{a+,d-}^{\alpha,\beta}$, $J_{b-,c+}^{\alpha,\beta}$ *and* $J_{b-,d-}^{\alpha,\beta}$ *are defined by*

$$J_{a+,c+}^{\alpha,\beta}f(x,y) = \frac{1}{\Gamma(\alpha)\Gamma(\beta)}\int_a^x\int_c^y (x-t)^{\alpha-1}(y-s)^{\beta-1}f(t,s)\,dsdt, \quad x > a, y > c,$$

$$J_{a+,d-}^{\alpha,\beta}f(x,y) = \frac{1}{\Gamma(\alpha)\Gamma(\beta)}\int_a^x\int_y^d (x-t)^{\alpha-1}(s-y)^{\beta-1}f(t,s)\,dsdt, \quad x > a, y < d,$$

$$J_{b-,c+}^{\alpha,\beta}f(x,y) = \frac{1}{\Gamma(\alpha)\Gamma(\beta)}\int_x^b\int_c^y (t-x)^{\alpha-1}(y-s)^{\beta-1}f(t,s)\,dsdt, \quad x < b, y > c,$$

and

$$J_{b-,d-}^{\alpha,\beta} f(x,y) = \frac{1}{\Gamma(\alpha)\Gamma(\beta)} \int_x^b \int_y^d (t-x)^{\alpha-1}(s-y)^{\beta-1} f(t,s)\, dsdt,$$

$$x < b, y < d.$$

Finally, the concept of co-ordinates convex, which will be used in this article, will be mentioned. Let us now consider a bidimensional interval $\Delta =: [a,b] \times [c,d]$ in R^2 with $a < b$ and $c < d$. A mapping $f: \Delta \to R$ is said to be convex on Δ if the following inequality:

$$f(tx + (1-t)z, ty + (1-t)w) \leq tf(x,y) + (1-t)f(z,w)$$

holds, for all $(x,y),(z,w) \in \Delta$ and $t \in [0,1]$. A function $f : \Delta \to R$ is said to be on the co-ordinates on Δ if the partial mappings $f_y: [a,b] \to R$, $f_y(u) = f(u,y)$ and $f_x: [c,d] \to R$, $f_x(v) = f(x,v)$ are convex where defined for all $x \in [a,b]$ and $y \in [c,d]$ (Dragomir, 2001).

A formal definition for co-ordinated convex function may be stated as follows:

Definition 3. *A function $f: \Delta \to R$ will be called co-ordinated canvex on Δ, for all $t,s \in [0,1]$ and $(x,y),(u,v) \in \Delta$, if the following inequality holds:*

$$f(tx + (1-t)y, su + (1-s)v)$$
$$\leq tsf(x,u) + s(1-t)f(y,u) + t(1-s)f(x,v) + (1-t)(1-s)f(y,v).$$

Clearly, every convex function is co-ordinated convex. Furthermore, there exist co-ordinated convex function which is not convex, (Dragomir, 2001).

In his important works (Dragomir, 2017a; Dragomir, 2017b), Dragomir established a series of Ostrowski-type inequalities by utilizing novel integral identities derived from the sum of right- and left-sided Riemann-Liouville integrals. This methodology yielded significant error bounds for various classes of functions, including those of bounded variation, Hölder continuous functions, Lipschitzian functions, and absolutely continuous functions in Lebesgue norm spaces. Furthermore, several other significant contributions to this topic include studies in which Hermite-Hadamard and Ostrowski inequalities were established for fractional integrals of functions of two variables in (Sarikaya, 2014) and (Latif et. al, 2012), respectively. Recently, Erden et al. (2020a) provided some Ostrowski type inequalities including Riemann-Liouville fractional

integrals for functions in class of functions L_p, L_∞ and L_1, respectively. Moreover, Erden et al. (2020b) established new double fractional Ostrowski-type inequalities for functions of bounded variation in two variables. Researchers who wish to pursue a more detailed investigation on these topics may also consult the sources listed in the references (Anastassiou et. al, 2009; Sarıkaya and Filiz, 2014; Sarikaya, 2010; Yaldız, 2017).

In many branches of analysis and applied mathematics, one frequently encounters problems that require the consideration of derivatives of arbitrary order, extending beyond the classical first- and second-order cases. This observation naturally motivates the investigation of Ostrowski-type inequalities for functions possessing higher-order derivatives. Accordingly, considerable attention has been directed toward the development of such inequalities involving higher-order derivatives, underscoring their importance in both theoretical analysis and a broad spectrum of practical applications. For foundational works that present results concerning single-variable functions with higher-order derivatives and two-variable functions with higher-order partial derivatives, the reader may consult the references in (Anastassiou, 1995; Cerone et. al, 1999; Sofo, 2002; Wang and Zhao, 2009; Changjian, and Cheung, 2010; Hanna, 2002; Ujević, 2003). It is also important to highlight the inequalities involving Riemann--Liouville fractional integrals of functions of two variables. Ostrowski-type inequalities involving Riemann--Liouville fractional integrals for various classes of functions of two variables have been investigated extensively in the literature. For results obtained within this framework, the reader may consult the references in (Erden et. al, 2024; Erden and Uyanık, 2025; Latif and Hussain, 2012; Sarıkaya, 2023).

For Ostrowski-type inequalities involving Riemann--Liouville fractional integrals obtained under the assumption that the partial derivatives are co-ordinated convex, the interested reader is referred to references (Erden and Altun, 2024; Erden and Özdemir, 2025a; Erden, 2025, Erden and Özdemir, 2025b). These works develop several generalized forms of the Ostrowski inequality by incorporating fractional integral operators and exploiting the convexity properties of the involved partial derivatives, thereby extending the classical results to a broader analytical framework. Motivated by the aforementioned studies, this paper establishes new Ostrowski-type inequalities involving Riemann-Liouville fractional integrals for functions whose higher-order partial derivatives are convex with respect to each coordinate. New Ostrowski-type results are also presented for functions whose powers of the absolute values of higher-order partial derivatives are convex with respect to the coordinates. It should also be emphasized that the inequalities presented herein represent generalizations of the inequalities established in references (Erden, 2025) and (Erden and Özdemir, 2025b), applicable to partial derivatives of arbitrary order

FRACTIONAL DOUBLE INTEGRAL INEQUALITIES

In this section, we introduce the fundamental identities that form the basis for the derivation of the main results. As integrals involving higher-order partial derivatives are generally difficult to evaluate and express in closed form, we adopt suitable notation to facilitate a clearer and more concise presentation of the identities that follow.

$$J(f;x,y) = (-1)^{n+m} J^{\alpha,\beta}_{x-,y-} f(a,c) + (-1)^{n} J^{\alpha,\beta}_{x-,y+} f(a,d) + (-1)^{m} J^{\alpha,\beta}_{x+,y-} f(b,c) + J^{\alpha,\beta}_{x+,y+} f(b,d), \tag{2}$$

$$F_1(f;x,y;n,m) = \left(\frac{(x-a)^{n+\alpha} + (b-x)^{n+\alpha}}{\Gamma(n+\alpha+1)}\right)\left[J^{\beta}_{y+}\frac{\partial^n f(x,d)}{\partial x^n} + (-1)^m J^{\beta}_{y-}\frac{\partial^n f(x,c)}{\partial x^n}\right] + \left(\frac{(y-c)^{m+\beta} + (d-y)^{m+\beta}}{\Gamma(m+\beta+1)}\right)\left[J^{\alpha}_{x+}\frac{\partial^m f(b,y)}{\partial y^m} + (-1)^n J^{\alpha}_{x-}\frac{\partial^m f(a,y)}{\partial y^m}\right] \tag{3}$$

$$F_2(f;x,y;n,m) = \frac{[(x-a)^{n+\alpha} + (b-x)^{n+\alpha}]\left[(y-c)^{m+\beta} + (d-y)^{m+\beta}\right]}{\Gamma(n+\alpha+1)\Gamma(m+\beta+1)}\frac{\partial^{n+m} f(x,y)}{\partial x^n \partial y^m}, \tag{4}$$

$$\begin{aligned} S_1(f;x,y;n,m) &= \sum_{k=0}^{n-1}\sum_{j=0}^{m-1}\frac{[(-1)^{n+k}(x-a)^{\alpha+k} + (b-x)^{\alpha+k}]}{\Gamma(\alpha+k+1)} \times \frac{\left[(-1)^{m+j}(y-c)^{\beta+j} + (d-y)^{\beta+j}\right]}{\Gamma(\beta+j+1)}\frac{\partial^{k+j} f(x,y)}{\partial x^k \partial y^j} \\ &- \sum_{k=0}^{n-1}\frac{(-1)^{n+k}(x-a)^{\alpha+k} + (b-x)^{\alpha+k}}{\Gamma(\alpha+k+1)} \times \left[(-1)^m J^{\beta}_{y-}\frac{\partial^k f(x,c)}{\partial x^k} + J^{\beta}_{y+}\frac{\partial^k f(x,d)}{\partial x^k}\right] \\ &- \sum_{j=0}^{m-1}\frac{(-1)^{m+j}(y-c)^{\beta+j} + (d-y)^{\beta+j}}{\Gamma(\beta+j+1)} \times \left[(-1)^n J^{\alpha}_{x-}\frac{\partial^j f(a,y)}{\partial y^j} + J^{\alpha}_{x+}\frac{\partial^j f(b,y)}{\partial y^j}\right], \end{aligned} \tag{5}$$

$$S_2(f;x,y;n,m) = \frac{(x-a)^{n+\alpha} + (b-x)^{n+\alpha}}{\Gamma(n+\alpha+1)} \tag{6}$$

$$\times \sum_{j=0}^{m-1} \frac{\left[(-1)^{m+j}(y-c)^{\beta+j}+(d-y)^{\beta+j}\right]}{\Gamma(\beta+j+1)} \frac{\partial^{n+j} f(x,y)}{\partial x^n \partial y^j}$$
$$+\frac{(y-c)^{m+\beta}+(d-y)^{m+\beta}}{\Gamma(m+\beta+1)}$$
$$\times \sum_{k=0}^{n-1} \frac{\left[(-1)^{n+k}(x-a)^{\alpha+k}+(b-x)^{\alpha+k}\right]}{\Gamma(\alpha+k+1)} \frac{\partial^{k+m} f(x,y)}{\partial x^k \partial y^m},$$

The following equality involving fractional integrals of functions of two variables are established by Erden and Uyanık (2025).

Lemma 1. *Suppose that* $f:[a,b]\times[c,d]=:\Delta\subset R^2\to R$ *is an absolutely continuous function such that the partial derivatives* $\frac{\partial^{k+j} f(t,s)}{\partial t^k \partial s^j}$ *exists and are continuous on* Δ *for* $k=0,1,2,\ldots,n,\ j=0,1,2,\ldots,m$ *with* $n,m\in N^+$. *Then, for any* $(x,y)\in\Delta$, *one has*

$$\frac{1}{\Gamma(n+\alpha)\Gamma(m+\beta)}\int_a^b\int_c^d \Omega(t,s)\left(\int_x^t\int_y^s \frac{\partial^{n+m+2} f(u,v)}{\partial u^{n+1}\partial v^{m+1}}dvdu\right)dsdt \quad (7)$$
$$= J(f;x,y)+S_4(f;x,y;n,m)+S_5(f;x,y;n,m)$$
$$-F_3(f;x,y;n,m)+F_2(f;x,y;n,m)$$

where $\Omega(t,s)$ is defined by

$$\Omega(t,s) := \begin{cases} (t-a)^{n+\alpha-1}(s-c)^{m+\beta-1}, & a\le t<x \text{ and } c\le s<y \\ (t-a)^{n+\alpha-1}(d-s)^{m+\beta-1}, & a\le t<x \text{ and } y\le s\le d \\ (b-t)^{n+\alpha-1}(s-c)^{m+\beta-1}, & x\le t\le b \text{ and } c\le s<y \\ (b-t)^{n+\alpha-1}(d-s)^{m+\beta-1}, & x\le t\le b \text{ and } y\le s\le d, \end{cases}$$

and the expressions $J(f;x,y)$, $F_1(f;x,y;n,m)$, $F_2(f;x,y;n,m)$, $S_1(f;x,y;n,m)$ and $S_2(f;x,y;n,m)$ are as defined in (2)-(6), respectively.

Now, we observe some double integral inequalities involving Riemann-Liouville fractional expressions by considering the above identity and co-ordinated convex functions.

Theorem 2. *Suppose that* $f:[a,b]\times[c,d]=:\Delta\subset R^2\to R$ *is an absolutely continuous function such that the partial derivatives* $\frac{\partial^{k+j} f(t,s)}{\partial t^k \partial s^j}$ *exists and are continuous on* Δ *for* $k=0,1,2,\ldots,n,\ j=0,1,2,\ldots,m$ *with* $n,m\in N^+$. *If* $\left|\frac{\partial^{n+m+2} f(u,v)}{\partial u^{n+1}\partial v^{m+1}}\right|$ *is a convex function on the co-ordinates on* Δ, *then we have the Riemann-Liouville fractional inequality*

$$
\begin{aligned}
&|J(f;x,y)+S_4(f;x,y;n,m)+S_5(f;x,y;n,m) \qquad (8)\\
&-F_3(f;x,y;n,m)+F_2(f;x,y;n,m)|\\
&\le \frac{(x-a)^{n+\alpha+1}(y-c)^{m+\beta+1}}{4\Gamma(n+\alpha+1)\Gamma(m+\beta+1)}\\
&\times\left[\left|\frac{\partial^{n+m+2}f(a,c)}{\partial u^{n+1}\partial v^{m+1}}\right|+\left|\frac{\partial^{n+m+2}f(a,y)}{\partial u^{n+1}\partial y^{m+1}}\right|+\left|\frac{\partial^{n+m+2}f(x,c)}{\partial x^{n+1}\partial v^{m+1}}\right|+\left|\frac{\partial^{n+m+2}f(x,y)}{\partial x^{n+1}\partial y^{m+1}}\right|\right]\\
&+\frac{(x-a)^{n+\alpha+1}(d-y)^{m+\beta+1}}{4\Gamma(n+\alpha+1)\Gamma(m+\beta+1)}\\
&\times\left[\left|\frac{\partial^{n+m+2}f(a,y)}{\partial u^{n+1}\partial y^{m+1}}\right|+\left|\frac{\partial^{n+m+2}f(a,d)}{\partial u^{n+1}\partial v^{m+1}}\right|+\left|\frac{\partial^{n+m+2}f(x,y)}{\partial x^{n+1}\partial y^{m+1}}\right|+\left|\frac{\partial^{n+m+2}f(x,d)}{\partial x^{n+1}\partial v^{m+1}}\right|\right]\\
&+\frac{(b-x)^{n+\alpha+1}(y-c)^{m+\beta+1}}{4\Gamma(n+\alpha+1)\Gamma(m+\beta+1)}\\
&\times\left[\left|\frac{\partial^{n+m+2}f(x,c)}{\partial x^{n+1}\partial v^{m+1}}\right|+\left|\frac{\partial^{n+m+2}f(x,y)}{\partial x^{n+1}\partial y^{m+1}}\right|+\left|\frac{\partial^{n+m+2}f(b,c)}{\partial u^{n+1}\partial v^{m+1}}\right|+\left|\frac{\partial^{n+m+2}f(b,y)}{\partial u^{n+1}\partial y^{m+1}}\right|\right]\\
&+\frac{(b-x)^{n+\alpha+1}(d-y)^{m+\beta+1}}{4\Gamma(n+\alpha+1)\Gamma(m+\beta+1)}\\
&\times\left[\left|\frac{\partial^{n+m+2}f(x,y)}{\partial x^{n+1}\partial y^{m+1}}\right|+\left|\frac{\partial^{n+m+2}f(x,d)}{\partial x^{n+1}\partial v^{m+1}}\right|+\left|\frac{\partial^{n+m+2}f(b,y)}{\partial u^{n+1}\partial y^{m+1}}\right|+\left|\frac{\partial^{n+m+2}f(b,d)}{\partial u^{n+1}\partial v^{m+1}}\right|\right]
\end{aligned}
$$

for all $(x,y)\in\Delta$ *and* $\alpha,\beta>0$.

Proof. Taking absolute value of both sides of the equality (7), because of the definition of $\Omega(t,s)$, it follows that

$$
\begin{aligned}
&|J(f;x,y)+S_4(f;x,y;n,m)+S_5(f;x,y;n,m) \qquad (9)\\
&-F_3(f;x,y;n,m)+F_2(f;x,y;n,m)|\\
&\le \frac{1}{\Gamma(n+\alpha)\Gamma(m+\beta)}\int_a^x\int_c^y (t-a)^{n+\alpha-1}(s-c)^{m+\beta-1}\\
&\times\left|\int_x^t\int_y^s \frac{\partial^{n+m+2}f(u,v)}{\partial u^{n+1}\partial v^{m+1}}dvdu\right|dsdt\\
&+\frac{1}{\Gamma(n+\alpha)\Gamma(m+\beta)}\int_a^x\int_y^d (t-a)^{n+\alpha-1}(d-s)^{m+\beta-1}\\
&\times\left|\int_x^t\int_y^s \frac{\partial^{n+m+2}f(u,v)}{\partial u^{n+1}\partial v^{m+1}}dvdu\right|dsdt\\
&+\frac{1}{\Gamma(n+\alpha)\Gamma(m+\beta)}\int_x^b\int_c^y (b-t)^{n+\alpha-1}(s-c)^{m+\beta-1}\\
&\times\left|\int_x^t\int_y^s \frac{\partial^{n+m+2}f(u,v)}{\partial u^{n+1}\partial v^{m+1}}dvdu\right|dsdt\\
&+\frac{1}{\Gamma(n+\alpha)\Gamma(m+\beta)}\int_x^b\int_y^d (b-t)^{n+\alpha-1}(d-s)^{m+\beta-1}
\end{aligned}
$$

$$\times \left| \int_x^t \int_y^s \frac{\partial^{n+m+2} f(u,v)}{\partial u^{n+1} \partial v^{m+1}} dvdu \right| dsdt.$$

Since $\left| \frac{\partial^{n+m+2} f(u,v)}{\partial u^{n+1} \partial v^{m+1}} \right|$ is a convex function on the co-ordinates on $(u,v) \in [a,x] \times [c,y]$, we have

$$\left| \frac{\partial^{n+m+2} f}{\partial u^{n+1} \partial v^{m+1}} \left(\frac{x-u}{x-a} a + \frac{u-a}{x-a} x, \frac{y-v}{y-c} c + \frac{v-c}{y-c} y \right) \right| \tag{10}$$
$$\leq \frac{(x-u)(y-v)}{(x-a)(y-c)} \left| \frac{\partial^{n+m+2} f(a,c)}{\partial u^{n+1} \partial v^{m+1}} \right| + \frac{(x-u)(v-c)}{(x-a)(y-c)} \left| \frac{\partial^{n+m+2} f(a,y)}{\partial u^{n+1} \partial y^{m+1}} \right|$$
$$+ \frac{(u-a)(y-v)}{(x-a)(y-c)} \left| \frac{\partial^{n+m+2} f(x,c)}{\partial x^{n+1} \partial v^{m+1}} \right| + \frac{(u-a)(v-c)}{(x-a)(y-c)} \left| \frac{\partial^{n+m+2} f(x,y)}{\partial x^{n+1} \partial y^{m+1}} \right|.$$

Therefore, from the inequality (10), it is clear that

$$\left| \int_x^t \int_y^s \frac{\partial^{n+m+2} f(u,v)}{\partial u^{n+1} \partial v^{m+1}} dvdu \right| \leq \int_a^x \int_c^y \left| \frac{\partial^{n+m+2} f(u,v)}{\partial u^{n+1} \partial v^{m+1}} \right| dvdu$$
$$\leq \frac{(x-a)(y-c)}{4} \left[\left| \frac{\partial^{n+m+2} f(a,c)}{\partial u^{n+1} \partial v^{m+1}} \right| + \left| \frac{\partial^{n+m+2} f(a,y)}{\partial u^{n+1} \partial y^{m+1}} \right| \right.$$
$$\left. + \left| \frac{\partial^{n+m+2} f(x,c)}{\partial x^{n+1} \partial v^{m+1}} \right| + \left| \frac{\partial^{n+m+2} f(x,y)}{\partial x^{n+1} \partial y^{m+1}} \right| \right].$$

Then, it follows that

$$\frac{1}{\Gamma(n+\alpha)\Gamma(m+\beta)} \int_a^x \int_c^y (t-a)^{n+\alpha-1} (s-c)^{m+\beta-1}$$
$$\times \left| \int_x^t \int_y^s \frac{\partial^{n+m+2} f(u,v)}{\partial u^{n+1} \partial v^{m+1}} dvdu \right| dsdt$$
$$\leq \frac{(x-a)(y-c)}{4\Gamma(n+\alpha)\Gamma(m+\beta)} \left[\left| \frac{\partial^{n+m+2} f(a,c)}{\partial u^{n+1} \partial v^{m+1}} \right| + \left| \frac{\partial^{n+m+2} f(a,y)}{\partial u^{n+1} \partial y^{m+1}} \right| \right.$$
$$\left. + \left| \frac{\partial^{n+m+2} f(x,c)}{\partial x^{n+1} \partial v^{m+1}} \right| + \left| \frac{\partial^{n+m+2} f(x,y)}{\partial x^{n+1} \partial y^{m+1}} \right| \right]$$
$$\times \int_a^x \int_c^y (t-a)^{n+\alpha-1} (s-c)^{m+\beta-1} dsdt$$
$$= \frac{(x-a)^{n+\alpha+1} (y-c)^{m+\beta+1}}{4\Gamma(n+\alpha+1)\Gamma(m+\beta+1)} \left[\left| \frac{\partial^{n+m+2} f(a,c)}{\partial u^{n+1} \partial v^{m+1}} \right| + \left| \frac{\partial^{n+m+2} f(a,y)}{\partial u^{n+1} \partial y^{m+1}} \right| \right.$$
$$\left. + \left| \frac{\partial^{n+m+2} f(x,c)}{\partial x^{n+1} \partial v^{m+1}} \right| + \left| \frac{\partial^{n+m+2} f(x,y)}{\partial x^{n+1} \partial y^{m+1}} \right| \right].$$

Similarly, since $\left|\frac{\partial^{n+m+2} f(u,v)}{\partial u^{n+1}\partial v^{m+1}}\right|$ is a convex function on the co-ordinates on $(u,v) \in [a,x] \times [y,d]$, one has

$$\begin{aligned}
&\frac{1}{\Gamma(n+\alpha)\Gamma(m+\beta)}\int_a^x \int_y^d (t-a)^{n+\alpha-1}(d-s)^{m+\beta-1} \\
&\times \left|\int_x^t \int_y^s \frac{\partial^{n+m+2} f(u,v)}{\partial u^{n+1}\partial v^{m+1}} dvdu\right| dsdt \\
&\leq \frac{(x-a)^{n+\alpha+1}(d-y)^{m+\beta+1}}{4\Gamma(n+\alpha+1)\Gamma(m+\beta+1)}\left[\left|\frac{\partial^{n+m+2} f(a,y)}{\partial u^{n+1}\partial y^{m+1}}\right| + \left|\frac{\partial^{n+m+2} f(a,d)}{\partial u^{n+1}\partial v^{m+1}}\right|\right. \\
&\left. + \left|\frac{\partial^{n+m+2} f(x,y)}{\partial x^{n+1}\partial y^{m+1}}\right| + \left|\frac{\partial^{n+m+2} f(x,d)}{\partial x^{n+1}\partial v^{m+1}}\right|\right].
\end{aligned}$$

Since $\left|\frac{\partial^{n+m+2} f(u,v)}{\partial u^{n+1}\partial v^{m+1}}\right|$ is a convex function on the co-ordinates on $(u,v) \in [x,b] \times [c,y]$, we have

$$\begin{aligned}
&\frac{1}{\Gamma(n+\alpha)\Gamma(m+\beta)}\int_x^b \int_c^y (b-t)^{n+\alpha-1}(s-c)^{m+\beta-1} \\
&\times \left|\int_x^t \int_y^s \frac{\partial^{n+m+2} f(u,v)}{\partial u^{n+1}\partial v^{m+1}} dvdu\right| dsdt \\
&\leq \frac{(b-x)^{n+\alpha+1}(y-c)^{m+\beta+1}}{4\Gamma(n+\alpha+1)\Gamma(m+\beta+1)}\left[\left|\frac{\partial^{n+m+2} f(x,c)}{\partial x^{n+1}\partial v^{m+1}}\right| + \left|\frac{\partial^{n+m+2} f(x,y)}{\partial x^{n+1}\partial y^{m+1}}\right|\right. \\
&\left. + \left|\frac{\partial^{n+m+2} f(b,c)}{\partial u^{n+1}\partial v^{m+1}}\right| + \left|\frac{\partial^{n+m+2} f(b,y)}{\partial u^{n+1}\partial y^{m+1}}\right|\right]
\end{aligned}$$

and since $\left|\frac{\partial^{n+m+2} f(u,v)}{\partial u^{n+1}\partial v^{m+1}}\right|$ is a convex function on the co-ordinates on $(u,v) \in [x,b] \times [y,d]$, we have

$$\begin{aligned}
&\frac{1}{\Gamma(n+\alpha)\Gamma(m+\beta)}\int_x^b \int_y^d (b-t)^{n+\alpha-1}(d-s)^{m+\beta-1} \\
&\left|\int_x^t \int_y^s \frac{\partial^{n+m+2} f(u,v)}{\partial u^{n+1}\partial v^{m+1}} dvdu\right| dsdt \\
&\leq \frac{(b-x)^{n+\alpha+1}(d-y)^{m+\beta+1}}{4\Gamma(n+\alpha+1)\Gamma(m+\beta+1)}\left[\left|\frac{\partial^{n+m+2} f(x,y)}{\partial x^{n+1}\partial y^{m+1}}\right| + \left|\frac{\partial^{n+m+2} f(x,d)}{\partial x^{n+1}\partial v^{m+1}}\right|\right. \\
&\left. + \left|\frac{\partial^{n+m+2} f(b,y)}{\partial u^{n+1}\partial y^{m+1}}\right| + \left|\frac{\partial^{n+m+2} f(b,d)}{\partial u^{n+1}\partial v^{m+1}}\right|\right]
\end{aligned}$$

If the above four results are substituted in right hand side of (9) inequality, the desired inequality (8) can be obtained.

Remark 1. *With* $n = m = 0$ *and the same assumption of Teorem 2, the sum symbols disappear and* 0 *is substituted insted of* n *and* m *in the remaining expressions, one possesses the inequalities*

$$\begin{aligned}
&\Big|J^{\alpha,\beta}_{x+,y+}f(b,d) + J^{\alpha,\beta}_{x+,y-}f(b,c) + J^{\alpha,\beta}_{x-,y+}f(a,d) + J^{\alpha,\beta}_{x-,y-}f(a,c) \\
&-\frac{(d-y)^{\beta}+(y-c)^{\beta}}{\Gamma(\beta+1)}\left[J^{\alpha}_{x+}f(b,y) + J^{\alpha}_{x-}f(a,y)\right] \\
&-\frac{(b-x)^{\alpha}+(x-a)^{\alpha}}{\Gamma(\alpha+1)}\left[J^{\beta}_{y+,}f(x,d) + J^{\beta}_{y-,}f(x,c)\right] \\
&+\frac{[(b-x)^{\alpha}+(x-a)^{\alpha}]\left[(d-y)^{\beta}+(y-c)^{\beta}\right]}{\Gamma(\alpha+1)\Gamma(\beta+1)}f(x,y)\Big| \\
\leq\ &\frac{(x-a)^{\alpha+1}(y-c)^{\beta+1}}{4\Gamma(\alpha+1)\Gamma(\beta+1)}\left[\left|\frac{\partial^2 f(a,c)}{\partial u\partial v}\right| + \left|\frac{\partial^2 f(a,y)}{\partial u\partial y}\right| + \left|\frac{\partial^2 f(x,c)}{\partial x\partial v}\right| + \left|\frac{\partial^2 f(x,y)}{\partial x\partial y}\right|\right] \\
&+\frac{(x-a)^{\alpha+1}(d-y)^{\beta+1}}{4\Gamma(\alpha+1)\Gamma(\beta+1)}\left[\left|\frac{\partial^2 f(a,y)}{\partial u\partial y}\right| + \left|\frac{\partial^2 f(a,d)}{\partial u\partial v}\right| + \left|\frac{\partial^2 f(x,y)}{\partial x\partial y}\right| + \left|\frac{\partial^2 f(x,d)}{\partial x\partial v}\right|\right] \\
&+\frac{(b-x)^{\alpha+1}(y-c)^{\beta+1}}{4\Gamma(\alpha+1)\Gamma(\beta+1)}\left[\left|\frac{\partial^2 f(x,c)}{\partial x\partial v}\right| + \left|\frac{\partial^2 f(x,y)}{\partial x\partial y}\right| + \left|\frac{\partial^2 f(b,c)}{\partial u\partial v}\right| + \left|\frac{\partial^2 f(b,y)}{\partial u\partial y}\right|\right] \\
&+\frac{(b-x)^{\alpha+1}(d-y)^{\beta+1}}{4\Gamma(\alpha+1)\Gamma(\beta+1)}\left[\left|\frac{\partial^2 f(x,y)}{\partial x\partial y}\right| + \left|\frac{\partial^2 f(x,d)}{\partial x\partial v}\right| + \left|\frac{\partial^2 f(b,y)}{\partial u\partial y}\right| + \left|\frac{\partial^2 f(b,d)}{\partial u\partial v}\right|\right]
\end{aligned}$$

which was provided by Erden (2025).

Now, we observe some double integral inequalities involving Riemann-Liouville fractional expressions by considering the above identity and co-ordinated convex functions.

Theorem 3. *Suppose that* $f : [a,b]\times[c,d] =: \Delta \subset R^2 \to R$ *is an absolutely continuous function such that the partial derivatives* $\frac{\partial^{k+j} f(t,s)}{\partial t^k \partial s^j}$ *exists and are continuous on* Δ *for* $k = 0,1,2,\dots,n,\ \ j = 0,1,2,\dots,m$ *with* $n,m \in N^+$ *. If* $\left|\frac{\partial^{n+m+2} f(u,v)}{\partial u^{n+1}\partial v^{m+1}}\right|^q$ *is a convex function on the co-ordinates on* Δ *for* $p,q > 1$ *with* $\frac{1}{p}+\frac{1}{q} = 1,$ *then we have the Riemann-Liouville fractional inequality*

$$\begin{aligned}
&|J(f;x,y) + S_4(f;x,y;n,m) + S_5(f;x,y;n,m) \\
&-F_3(f;x,y;n,m) + F_2(f;x,y;n,m)| \qquad (11)\\
\leq\ &\frac{\Gamma\left(1+\frac{1}{p}\right)\Gamma\left(1+\frac{1}{p}\right)}{4^{\frac{1}{q}}\Gamma\left(n+\alpha+1+\frac{1}{p}\right)\Gamma\left(m+\beta+1+\frac{1}{p}\right)} \\
&\times\left\{(x-a)^{n+\alpha+1}(y-c)^{m+\beta+1}\left[\left|\frac{\partial^{n+m+2} f(a,c)}{\partial u^{n+1}\partial v^{m+1}}\right|^q + \left|\frac{\partial^{n+m+2} f(a,y)}{\partial u^{n+1}\partial y^{m+1}}\right|^q\right.\right.
\end{aligned}$$

$$+\left|\frac{\partial^{n+m+2}f(x,c)}{\partial x^{n+1}\partial v^{m+1}}\right|^q+\left|\frac{\partial^{n+m+2}f(x,y)}{\partial x^{n+1}\partial y^{m+1}}\right|^q\Bigg]^{\frac{1}{q}}$$

$$+(x-a)^{n+\alpha+1}(d-y)^{m+\beta+1}\left[\left|\frac{\partial^{n+m+2}f(a,y)}{\partial u^{n+1}\partial y^{m+1}}\right|^q+\left|\frac{\partial^{n+m+2}f(a,d)}{\partial u^{n+1}\partial v^{m+1}}\right|^q\right.$$

$$\left.+\left|\frac{\partial^{n+m+2}f(x,y)}{\partial x^{n+1}\partial y^{m+1}}\right|^q+\left|\frac{\partial^{n+m+2}f(x,d)}{\partial x^{n+1}\partial v^{m+1}}\right|^q\right]^{\frac{1}{q}}$$

$$+(b-x)^{n+\alpha+1}(y-c)^{m+\beta+1}\left[\left|\frac{\partial^{n+m+2}f(x,c)}{\partial x^{n+1}\partial v^{m+1}}\right|^q+\left|\frac{\partial^{n+m+2}f(x,y)}{\partial x^{n+1}\partial y^{m+1}}\right|^q\right.$$

$$\left.+\left|\frac{\partial^{n+m+2}f(b,c)}{\partial u^{n+1}\partial v^{m+1}}\right|^q+\left|\frac{\partial^{n+m+2}f(b,y)}{\partial u^{n+1}\partial y^{m+1}}\right|^q\right]^{\frac{1}{q}}$$

$$+(b-x)^{n+\alpha+1}(d-y)^{m+\beta+1}\left[\left|\frac{\partial^{n+m+2}f(x,y)}{\partial x^{n+1}\partial y^{m+1}}\right|^q+\left|\frac{\partial^{n+m+2}f(x,d)}{\partial x^{n+1}\partial v^{m+1}}\right|^q\right.$$

$$\left.+\left|\frac{\partial^{n+m+2}f(b,y)}{\partial u^{n+1}\partial y^{m+1}}\right|^q+\left|\frac{\partial^{n+m+2}f(b,d)}{\partial u^{n+1}\partial v^{m+1}}\right|^q\right]^{\frac{1}{q}}\Bigg\}$$

for all $(x,y)\in\Delta$ *and* $\alpha,\beta>0$.

Proof. Taking absolute value of both sides of the equality (7), because of the definition of $\Omega(t,s)$, it follows that

$$\begin{aligned}&|J(f;x,y)+S_4(f;x,y;n,m)+S_5(f;x,y;n,m)\\&-F_3(f;x,y;n,m)+F_2(f;x,y;n,m)|\\&\leq\frac{1}{\Gamma(n+\alpha)\Gamma(m+\beta)}\int_a^x\int_c^y(t-a)^{n+\alpha-1}(s-c)^{m+\beta-1}\\&\times\left|\int_x^t\int_y^s\frac{\partial^{n+m+2}f(u,v)}{\partial u^{n+1}\partial v^{m+1}}dvdu\right|dsdt\\&+\frac{1}{\Gamma(n+\alpha)\Gamma(m+\beta)}\int_a^x\int_y^d(t-a)^{n+\alpha-1}(d-s)^{m+\beta-1}\\&\times\left|\int_x^t\int_y^s\frac{\partial^{n+m+2}f(u,v)}{\partial u^{n+1}\partial v^{m+1}}dvdu\right|dsdt\\&+\frac{1}{\Gamma(n+\alpha)\Gamma(m+\beta)}\int_x^b\int_c^y(b-t)^{n+\alpha-1}(s-c)^{m+\beta-1}\end{aligned}\tag{12}$$

$$\times \left| \int_x^t \int_y^s \frac{\partial^{n+m+2} f(u,v)}{\partial u^{n+1} \partial v^{m+1}} dvdu \right| dsdt$$

$$+ \frac{1}{\Gamma(n+\alpha)\Gamma(m+\beta)} \int_x^b \int_y^d (b-t)^{n+\alpha-1} (d-s)^{m+\beta-1}$$

$$\times \left| \int_x^t \int_y^s \frac{\partial^{n+m+2} f(u,v)}{\partial u^{n+1} \partial v^{m+1}} dvdu \right| dsdt.$$

Since $\left| \frac{\partial^{n+m+2} f(u,v)}{\partial u^{n+1} \partial v^{m+1}} \right|^q$ is a convex function on the co-ordinates on $(u,v) \in [a,x] \times [c,y]$, we have

$$\left| \frac{\partial^{n+m+2} f}{\partial u^{n+1} \partial v^{m+1}} \left(\frac{x-u}{x-a} a + \frac{u-a}{x-a} x, \frac{y-v}{y-c} c + \frac{v-c}{y-c} y \right) \right|^q$$

$$\leq \frac{(x-u)(y-v)}{(x-a)(y-c)} \left| \frac{\partial^{n+m+2} f(a,c)}{\partial u^{n+1} \partial v^{m+1}} \right|^q + \frac{(x-u)(v-c)}{(x-a)(y-c)} \left| \frac{\partial^{n+m+2} f(a,y)}{\partial u^{n+1} \partial y^{m+1}} \right|^q$$

$$+ \frac{(u-a)(y-v)}{(x-a)(y-c)} \left| \frac{\partial^{n+m+2} f(x,c)}{\partial x^{n+1} \partial v^{m+1}} \right|^q + \frac{(u-a)(v-c)}{(x-a)(y-c)} \left| \frac{\partial^{n+m+2} f(x,y)}{\partial x^{n+1} \partial y^{m+1}} \right|^q.$$

Using the above inequality, which was obtained for a function whosepowers of the absolute value of the partial derivatives in moduls is convex on the coordinates, together with the use of Hölder's inequality, it is clear that

$$\left| \int_x^t \int_y^s \frac{\partial^{n+m+2} f(u,v)}{\partial u^{n+1} \partial v^{m+1}} dvdu \right| \leq \int_x^t \int_y^s \left| \frac{\partial^{n+m+2} f(u,v)}{\partial u^{n+1} \partial v^{m+1}} \right| dvdu$$

$$\leq \left(\int_x^t \int_y^s dvdu \right)^{\frac{1}{p}} \left(\int_x^t \int_y^s \left| \frac{\partial^{n+m+2} f(u,v)}{\partial u^{n+1} \partial v^{m+1}} \right|^q dvdu \right)^{\frac{1}{q}}$$

$$= (x-t)^{\frac{1}{p}} (y-s)^{\frac{1}{p}} \left(\frac{(x-a)(y-c)}{4} \right)^{\frac{1}{q}} \left[\left| \frac{\partial^{n+m+2} f(a,c)}{\partial u^{n+1} \partial v^{m+1}} \right|^q \right.$$

$$\left. + \left| \frac{\partial^{n+m+2} f(a,y)}{\partial u^{n+1} \partial y^{m+1}} \right|^q + \left| \frac{\partial^{n+m+2} f(x,c)}{\partial x^{n+1} \partial v^{m+1}} \right|^q + \left| \frac{\partial^{n+m+2} f(x,y)}{\partial x^{n+1} \partial y^{m+1}} \right|^q \right]^{\frac{1}{q}}.$$

Then, it is found that

$$\frac{1}{\Gamma(n+\alpha)\Gamma(m+\beta)} \int_a^x \int_c^y (t-a)^{n+\alpha-1} (s-c)^{m+\beta-1} \qquad (13)$$

$$\times \left| \int_x^t \int_y^s \frac{\partial^{n+m+2} f(u,v)}{\partial u^{n+1} \partial v^{m+1}} dvdu \right| dsdt$$

$$\leq \left[\left| \frac{\partial^{n+m+2} f(a,c)}{\partial u^{n+1} \partial v^{m+1}} \right|^q + \left| \frac{\partial^{n+m+2} f(a,y)}{\partial u^{n+1} \partial y^{m+1}} \right|^q + \left| \frac{\partial^{n+m+2} f(x,c)}{\partial x^{n+1} \partial v^{m+1}} \right|^q \right.$$

$$\left. + \left| \frac{\partial^{n+m+2} f(x,y)}{\partial x^{n+1} \partial y^{m+1}} \right|^q \right]^{\frac{1}{q}}$$

$$\times \frac{(x-a)^{\frac{1}{q}} (y-c)^{\frac{1}{q}}}{4^{\frac{1}{q}} \Gamma(n+\alpha)\Gamma(m+\beta)} \int_a^x (t-a)^{n+\alpha-1} (x-t)^{\frac{1}{p}} dt$$

$$\times \int_c^y (s-c)^{m+\beta-1} (y-s)^{\frac{1}{p}} ds$$

To complete the proof, we must calculate two integrals in the right side of the result (13). Applying the change of the variable $\frac{t-a}{x-a} = u$ and $dt = (x-a)du$ for the first integral, it is found that

$$\int_a^x (t-a)^{n+\alpha-1} (x-t)^{\frac{1}{p}} dt$$

$$= \int_a^x (t-a)^{n+\alpha-1} (x-a-(t-a))^{\frac{1}{p}} dt$$

$$= (x-a)^{n+\alpha+\frac{1}{p}} \int_0^1 u^{n+\alpha-1} (1-u)^{\frac{1}{p}} du$$

$$= (x-a)^{n+\alpha+\frac{1}{p}} B\left(n+\alpha, 1+\frac{1}{p}\right).$$

And similarly, we have

$$\int_c^y (s-c)^{m+\beta-1} (y-s)^{\frac{1}{p}} ds$$

$$= (y-c)^{m+\beta+\frac{1}{p}} B\left(m+\beta, 1+\frac{1}{p}\right).$$

Then, it is clear that

$$\frac{1}{\Gamma(n+\alpha)\Gamma(m+\beta)} \int_a^x \int_c^y (t-a)^{n+\alpha-1} (s-c)^{m+\beta-1}$$

$$\times \left| \int_x^t \int_y^s \frac{\partial^{n+m+2} f(u,v)}{\partial u^{n+1} \partial v^{m+1}} dvdu \right| dsdt$$

$$\leq \frac{(x-a)^{n+\alpha+1}(y-c)^{m+\beta+1}}{4^{\frac{1}{q}} \Gamma(n+\alpha)\Gamma(m+\beta)} B\left(n+\alpha, 1+\frac{1}{p}\right) B\left(m+\beta, 1+\frac{1}{p}\right)$$

$$\times \left[\left| \frac{\partial^{n+m+2} f(a,c)}{\partial u^{n+1} \partial v^{m+1}} \right|^q + \left| \frac{\partial^{n+m+2} f(a,y)}{\partial u^{n+1} \partial y^{m+1}} \right|^q + \left| \frac{\partial^{n+m+2} f(x,c)}{\partial x^{n+1} \partial v^{m+1}} \right|^q \right.$$

$$\left. + \left| \frac{\partial^{n+m+2} f(x,y)}{\partial x^{n+1} \partial y^{m+1}} \right|^q \right]^{\frac{1}{q}}.$$

To complete the proof of the theorem, the results of the remaining three integrals on the right-hand side of inequality (12) must be obtained. We first present the basic integrals required for this computation. Applying the change of the variable $\frac{b-t}{b-x} = v$ and $dt = (x-b)dv$ for the second integral, it is found that

$$\int_x^b (b-t)^{n+\alpha-1}(t-x)^{\frac{1}{p}} dt$$

$$= \int_x^b (b-t)^{n+\alpha-1}(b-x-(b-t))^{\frac{1}{p}} dt$$

$$= (b-x)^{n+\alpha+\frac{1}{p}} B\left(n+\alpha, 1+\frac{1}{p}\right).$$

,and one has

$$\int_y^d (d-s)^{m+\beta-1}(s-y)^{\frac{1}{p}} ds$$

$$= (d-y)^{m+\beta+\frac{1}{p}} B\left(m+\beta, 1+\frac{1}{p}\right)$$

Then, since $\left| \frac{\partial^{n+m+2} f(u,v)}{\partial u^{n+1} \partial v^{m+1}} \right|^q$ is a convex function on the co-ordinates on $(u,v) \in [a,x] \times [y,d]$, one has

$$\frac{1}{\Gamma(n+\alpha)\Gamma(m+\beta)} \int_a^x \int_y^d (t-a)^{n+\alpha-1}(d-s)^{m+\beta-1}$$

$$\times \left| \int_x^t \int_y^s \frac{\partial^{n+m+2} f(u,v)}{\partial u^{n+1} \partial v^{m+1}} dvdu \right| dsdt$$

$$\leq \frac{(x-a)^{n+\alpha+1}(d-y)^{m+\beta+1}}{4^{\frac{1}{q}} \Gamma(n+\alpha)\Gamma(m+\beta)} B\left(m+\beta, 1+\frac{1}{p}\right) B\left(n+\alpha, 1+\frac{1}{p}\right)$$

$$\times \left[\left| \frac{\partial^{n+m+2} f(a,y)}{\partial u^{n+1} \partial y^{m+1}} \right|^q + \left| \frac{\partial^{n+m+2} f(a,d)}{\partial u^{n+1} \partial v^{m+1}} \right|^q + \left| \frac{\partial^{n+m+2} f(x,y)}{\partial x^{n+1} \partial y^{m+1}} \right|^q \right.$$

$$\left. + \left| \frac{\partial^{n+m+2} f(x,d)}{\partial x^{n+1} \partial v^{m+1}} \right|^q \right]^{\frac{1}{q}}.$$

Since $\left| \frac{\partial^{n+m+2} f(u,v)}{\partial u^{n+1} \partial v^{m+1}} \right|^q$ is a convex function on the co-ordinates on $(u,v) \in [x,b] \times [c,y]$, we have

$$\frac{1}{\Gamma(n+\alpha)\Gamma(m+\beta)} \int_x^b \int_c^y (b-t)^{n+\alpha-1} (s-c)^{m+\beta-1} \left| \int_x^t \int_y^s \frac{\partial^{n+m+2} f(u,v)}{\partial u^{n+1} \partial v^{m+1}} dvdu \right| dsdt$$

$$\leq \frac{(b-x)^{n+\alpha+1}(y-c)^{m+\beta+1}}{4^{\frac{1}{q}} \Gamma(n+\alpha)\Gamma(m+\beta)} B\left(m+\beta, 1+\frac{1}{p}\right) B\left(n+\alpha, 1+\frac{1}{p}\right)$$

$$\times \left[\left| \frac{\partial^{n+m+2} f(x,c)}{\partial x^{n+1} \partial v^{m+1}} \right|^q + \left| \frac{\partial^{n+m+2} f(x,y)}{\partial x^{n+1} \partial y^{m+1}} \right|^q + \left| \frac{\partial^{n+m+2} f(b,c)}{\partial u^{n+1} \partial v^{m+1}} \right|^q \right.$$

$$\left. + \left| \frac{\partial^{n+m+2} f(b,y)}{\partial u^{n+1} \partial y^{m+1}} \right|^q \right]^{\frac{1}{q}}$$

and since $\left| \frac{\partial^{n+m+2} f(u,v)}{\partial u^{n+1} \partial v^{m+1}} \right|^q$ is a convex function on the co-ordinates on $(u,v) \in [x,b] \times [y,d]$, we have

$$\frac{1}{\Gamma(n+\alpha)\Gamma(m+\beta)} \int_x^b \int_y^d (b-t)^{n+\alpha-1} (d-s)^{m+\beta-1} \times \left| \int_x^t \int_y^s \frac{\partial^{n+m+2} f(u,v)}{\partial u^{n+1} \partial v^{m+1}} dvdu \right| dsdt$$

$$\leq \frac{(b-x)^{n+\alpha+1}(d-y)^{m+\beta+1}}{4^{\frac{1}{q}} \Gamma(n+\alpha)\Gamma(m+\beta)} B\left(m+\beta, 1+\frac{1}{p}\right) B\left(n+\alpha, 1+\frac{1}{p}\right)$$

$$\times \left[\left| \frac{\partial^{n+m+2} f(x,y)}{\partial x^{n+1} \partial y^{m+1}} \right|^q + \left| \frac{\partial^{n+m+2} f(x,d)}{\partial x^{n+1} \partial v^{m+1}} \right|^q + \left| \frac{\partial^{n+m+2} f(b,y)}{\partial u^{n+1} \partial y^{m+1}} \right|^q \right.$$

$$\left. + \left| \frac{\partial^{n+m+2} f(b,d)}{\partial u^{n+1} \partial v^{m+1}} \right|^q \right]^{\frac{1}{q}}$$

If the above four results are substituted in right hand side of (12) inequality, the desired inequality (11) can be obtained.

Remark *With* $n = m = 0$ *and the same assumption of Teorem t1, the sum symbols disappear and* 0 *is substituted insted of* n *and* m *in the remaining expressions, one possesses the inequalities*

$$\begin{aligned}
&\left|J^{\alpha,\beta}_{x+,y+}f(b,d)+J^{\alpha,\beta}_{x+,y-}f(b,c)+J^{\alpha,\beta}_{x-,y+}f(a,d)+J^{\alpha,\beta}_{x-,y-}f(a,c)\right.\\
&\quad-\frac{(d-y)^{\beta}+(y-c)^{\beta}}{\Gamma(\beta+1)}\left[J^{\alpha}_{x+}f(b,y)+J^{\alpha}_{x-}f(a,y)\right]\\
&\quad-\frac{(b-x)^{\alpha}+(x-a)^{\alpha}}{\Gamma(\alpha+1)}\left[J^{\beta}_{y+,}f(x,d)+J^{\beta}_{y-,}f(x,c)\right]\\
&\quad\left.+\frac{[(b-x)^{\alpha}+(x-a)^{\alpha}]\left[(d-y)^{\beta}+(y-c)^{\beta}\right]}{\Gamma(\alpha+1)\Gamma(\beta+1)}f(x,y)\right|\\
&\quad\leq\frac{\Gamma\left(1+\frac{1}{p}\right)\Gamma\left(1+\frac{1}{p}\right)}{4^{\frac{1}{q}}\Gamma\left(\alpha+1+\frac{1}{p}\right)\Gamma\left(\beta+1+\frac{1}{p}\right)}\\
&\times\left\{(x-a)^{\alpha+1}(y-c)^{\beta+1}\left[\left|\frac{\partial^2 f(a,c)}{\partial u\partial v}\right|^q+\left|\frac{\partial^2 f(a,y)}{\partial u\partial y}\right|^q+\left|\frac{\partial^2 f(x,c)}{\partial x\partial v}\right|^q\right.\right.\\
&\quad\left.+\left|\frac{\partial^2 f(x,y)}{\partial x\partial y}\right|^q\right]^{\frac{1}{q}}\\
&+(x-a)^{\alpha+1}(d-y)^{\beta+1}\left[\left|\frac{\partial^2 f(a,y)}{\partial u\partial y}\right|^q+\left|\frac{\partial^2 f(a,d)}{\partial u\partial v}\right|^q+\left|\frac{\partial^2 f(x,y)}{\partial x\partial y}\right|^q\right.\\
&\quad\left.+\left|\frac{\partial^2 f(x,d)}{\partial x\partial v}\right|^q\right]^{\frac{1}{q}}\\
&+(b-x)^{\alpha+1}(y-c)^{\beta+1}\left[\left|\frac{\partial^2 f(x,c)}{\partial x\partial v}\right|^q+\left|\frac{\partial^2 f(x,y)}{\partial x\partial y}\right|^q+\left|\frac{\partial^2 f(b,c)}{\partial u\partial v}\right|^q\right.\\
&\quad\left.+\left|\frac{\partial^2 f(b,y)}{\partial u\partial y}\right|^q\right]^{\frac{1}{q}}\\
&+(b-x)^{\alpha+1}(d-y)^{\beta+1}\left[\left|\frac{\partial^2 f(x,y)}{\partial x\partial y}\right|^q+\left|\frac{\partial^2 f(x,d)}{\partial x\partial v}\right|^q+\left|\frac{\partial^2 f(b,y)}{\partial u\partial y}\right|^q\right.\\
&\quad\left.\left.+\left|\frac{\partial^2 f(b,d)}{\partial u\partial v}\right|^q\right]^{\frac{1}{q}}\right\}
\end{aligned}$$

which was provided by Erden and Özdemir (2025b).

REFERENCE

Anastassiou, G., Hooshmandasl, M. R., Ghasemi, A., and Moftakharzadeh, F. (2009). Montgomery identities for fractional integrals and related fractional inequalities, J. Inequal. in Pure and Appl. Math, 10(4), Art. 97, 6 pp.

Anastassiou, G., (1995). Ostrowski type inequalities, Proc. of the American Math. Soc., 123 (12), 3775-378.

Cerone, P., Dragomir, S. S., and Roumeliotis, J. (1998). Some Ostrowski type inequalities for n-time differentiable mappings and applications. *RGMIA research report collection*, *1*(1).

Changjian, Z., and Cheung, W. S. (2010). On Ostrowski-type inequalities for heigher-order partial derivatives, Journal of Ineqaulities and Applications, Article ID 960672, 1-8.

Dragomir, S. S. (2001). On Hadamard's inequality for convex functions on the co-ordinates in a rectangle from the plane, Taiwanese Journal of Mathematics, 4, 775-788.

Dragomir, S. S. (2017a). Ostrowski Type inequalities for riemann-Liouville fractional integrals of absolutely continuous functions in terms of $\infty -$ norms, RGMIA Research Report Collection, 20, Article 49.

Dragomir, S. S. (2017b). Ostrowski Type inequalities for riemann-Liouville fractional integrals of absolutely continuous functions in terms of $p -$ norms, RGMIA Research Report Collection, 20, Article 50.

Dragomir, S. S., Barmett N. S., and Cerone, P. (2003), An Ostrowski type inequality for double integrals in terms of Lp-norms and applications in numerical integration, Anal. Num. Theor. Approx., 32 (2), 161-169.

Erden, S., Özdemir, B. G., Kılıçer, S., & Demır, C. (2024). Ostrowski type inequalities including Riemann-Liouville fractional integrals for two variable functions. Konuralp Journal of Mathematics, 12(1), 62-73.

Erden, S., Budak, H., Sarikaya, M. Z., Iftikhar, S. and Kumam, P. (2020). Fractional Ostrowski type inequalities for bounded functions. Journal of Inequalities and Applications, 123, 1-11.

Erden, S., Budak, H., and Sarikaya, M. Z. (2020). Fractional Ostrowski type inequalities for functions of bounded variaton with two variables. Miskolc Mathematical Notes, 21(1), 171-188.

Erden, S., and Uyanik, N. (2025). Fractional inequalities involving double integrals of Riemann-Liouville for higher-order partial differential functions. Thermal Science, 29(4 Part B), 3013-3022.

Erden, S., and Altun, E. (2024). Fractional Ostrowski type inequalities of double integrals for co-ordinated convex functions, 4.th ICFAR, December 13-14, Konya, Turkey.

Erden, S., and Gökkurt Özdemir, B. (2025a). Fractional inequalities of double integrals for functions whose powers are convex on the coordinates, 4.th ICMAR, Nowember 06-07, Konya, Turkey.

Erden, S. (2025). New Fractional Ostrowski Type Inequalities for Functions of Two Variables with Co-ordinated Convexity, 3rd International Conference on Recent and Innovative Results in Engineering and Technology, November 15-16, Konya, Turkey.

Erden, S., and Gökkurt Özdemir, B. (2025b). Double Fractional integral inequalities for co-ordinated convex functions, 2nd Kocaeli SCcience Congress (KOSC-2025), November 19-21, İzmit, Kocaeli, Türkiye.

Hanna, G., Dragomir, S. S., & Cerone, P. (2002). A general Ostrowski type inequality for double integrals. Tamkang Journal of Mathematics, *33*(4), 319-334..

Kilbas, A. A. (2006). Theory and applications of fractional differential equations. *North-Holland Mathematics Studies*, *204*.

Latif, M. A., Dragomir S. S. and Matouk, A. E. (2012). New inequalities of Ostrowski type for co-ordinated convex functions via fractional integrals, J. Fract. Calc. Appl, 2(1).

Latif M. A., Hussain, S. (2012). New inequalities of Ostrowski type for co-ordinated convex functions via fractional integrals, J Fractional Calc Appl., 2 (9), 1-15.

Ostrowski, A. (1938). Über die Absolutabweichung einer differentiierbaren funktion von ihrem integralmittelwert, Comment. Math. Helv., **10**, 226-227.

Sarikaya, M. Z. (2014). On the Hermite-Hadamard-type inequalities for co-ordinated convex function via fractional integrals, Integral Transforms and Special Functions, 25(2), 134-147.

Sarikaya, M. Z. and Filiz, H. (2014). Note on the Ostrowski type inequalities for fractional integrals, Vietnam J. Math., **42** (2), 187-190.

Sarikaya, M. Z. (2010). On the Ostrowski type integral inequality, Acta Math. Univ. Comenianae, Vol. LXXIX, 1, 129-134.

Sarikaya, M. Z. (2014). On the Hermite-Hadamard-type inequalities for co-ordinated convex function via fractional integrals, Integral Transforms and Special Functions, Vol. 25(2), 134-147.

Sarikaya, M. Z. (2015). Some inequalities for differentiable co-ordinated convex mappings, Asian-European Journal of Mathematics, Vol: 08, 1550058, 21 pages.

Sarkaya, M. Z. (2023). On the generalized Ostrowski type inequalities for co-ordinated convex functions, Filomat, 37, 22, 7351-7366.

Sofo, A. (2022) Integral inequalities for n- times differentiable mappings, with multiple branches,on the L_p norm, Soochow Journal of Mathematics, 28 (2), 179-221.

Ujević, N. (2003). Ostrowski-Grüss type inequalities in two dimensional, J. of Ineq. in Pure and Appl. Math., 4 (5), article 101.

Wang M. and Zhao, X. (2009). Ostrowski type inequalities for higher-order derivatives, J. of Inequalities and App., Vol. 2009, Article ID 162689, 1-8.

Yaldiz, H., Sarkaya M. Z. and Dahmani, Z. (2017). On the Hermite-Hadamard-Fejer-type inequalities for co-ordinated convex functions via fractional integrals, International Journal of Optimization and Control: Theories & Applications (IJOCTA), 7(2), 205-215.

A TREASURE TROVE OF HEALING: *Rosmarinus officinalis*

Handan KARAOĞLU[1]

Fatih SEYİS[2]

1- Dr. Öğretim Üyesi.; Recep Tayyip Erdoğan Üniversitesi Ziraat Fakültesi Tarla Bİtkileri Bölümü. Handan.karaoglu@erdogan.edu.tr ORCID No: 0000-0001-6838-1856

2- Prof. Dr.; Recep Tayyip Erdoğan Üniversitesi Ziraat Fakültesi Tarla Bİtkileri Bölümü.. fatih.seyis@erdogan.edu.tr ORCID No: 0000-0001-9714-370X

ABSTRACT

Because they are a rich source of naturally occurring bioactive chemicals, medicinal plants have been essential to healthcare throughout history. Furthermore, these plants and their volatile oils have played a crucial role in traditional medicine and still have a lot of potential for use in the food, cosmetic, and pharmaceutical industries today. Rosemary, or Rosmarinus offi cinalis, is a common household plant that is grown all over the world and is a member of the Lamiaceae family. It is a woody, perennial herb with white, pink, purple, or blue flowers and aromatic, evergreen, needle-like leaves. Bitter principle, resin, tannic acid, volatile oils, and flavonoids are among the chemical components. Borneol, bornyl acetate, camphene, cineol, pinene, and camphor make up the volatile oil. It is applied to issues pertaining to the central nervous system, cardiovascular system, genito-urinary disorders, liver therapies, reproductive system, and respiratory system. The plant's volatile oil is used in lotions and oils to treat a variety of conditions, including gout, arthritis, neuralgia, muscle soreness, and wounds. It is also rubbed into hair to stimulate new activity in the hair bulbs and prevent premature baldness. A brief review will be given including taxonomy, distribution, chemical composition and biological activities of Rosmarinus officinalis.

Keywords – Lamiaceae, chemical composition, biological activity, medicinal plant, volatile oil

INTRODUCTION

Rosemary, or Rosmarinus officinalis L., is a fragrant, medicinal shrub in the Lamiaceae family. Although the plant has a large cultural range today, it only grows in Mediterranean nations (Allegra et al., 2020:24; Andrade et al., 2018:4). Salvia rosmarinus Schleid. and Rosmarinus angustifolius Mill. are reported synonyms for the plant *R. officinalis* (Borges et al., 2019:16; Heinrich et al., 2006:4). It is recognised in the literature as belonging to the Lamiales order, Asteridae subclass, and Magnoliopsida class based on scientific categorisation (Begum et al., 2013:13). Scientific research has demonstrated that there are numerous variations of *R. officinalis*, which are distinguished by morphological distinctions such as leaf size, calyx, and corolla variances (Zaouali et al., 2010:8)

Botany

Taxonomical position [22]:

Clade: Angiosperms

Order: Lamiales

Family: Lamiaceae or Labiatae

Genus: Rosmarinus

Number of species: Five

Accepted name: *Rosmarinus officinalis* L. (*Salvia rosmarinus* Scheid.)

Synonyms: 21 (*R. angustifolius*, *R. latifolius*, *R. tenuifolius*, etc.)

Common name (some European countries): Romero (Spanish), alecrim (Portuguese), rosemary (English), rosmarin (French and German), rosmarino (Italian), and δενδρολίβανο (Greek).

Commercial varieties:

22 different cultivars, the most common varieties being: "Arp", "Hill1" (synonymous "Hill Hardy"), "Albus", "Bendenen Blue", "Goodwin Creek", "Herb Cottage", "Logee's Light Blue", "Jessup's Upright", "Russian River" and "Salem" (Begum et al., 2013:13). Morales indicates that there are more than 100 varieties in the world (Morales, 2010:4).

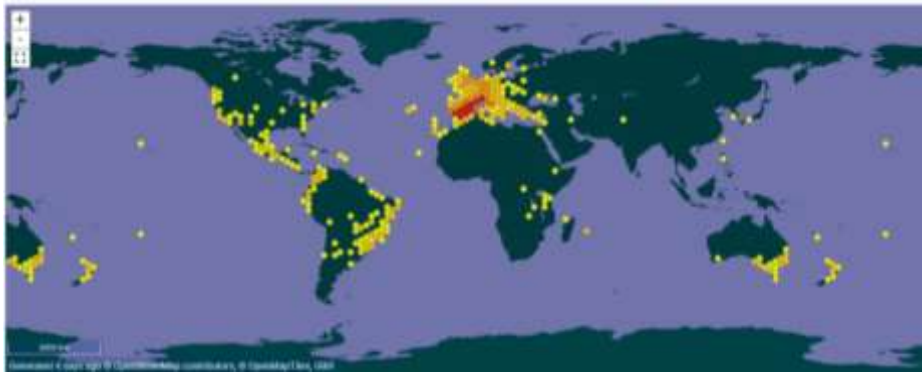

Fig. 1: Geographic distribution of *Rosmarinus officinalis* according to the Global Biodiversity Information Facility (GBIF, 2025).

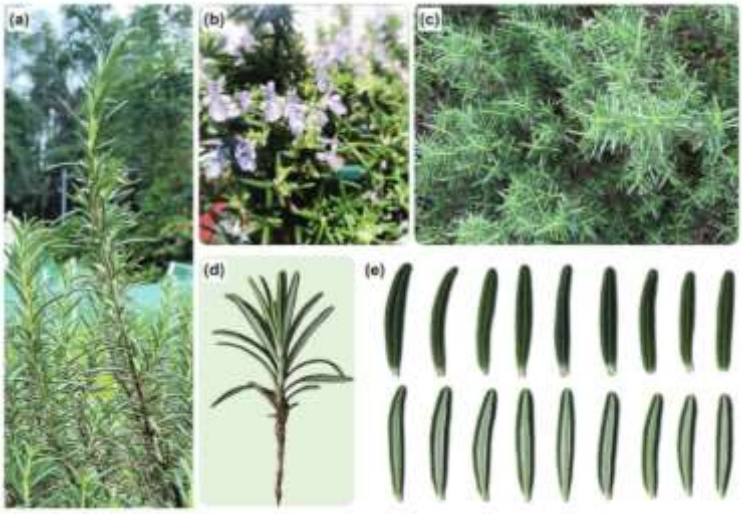

Fig.2. The pictures of Rosmarinus officinalis L. (a) The plants with side view; (b) flowers; (c) the plants with top view; (d) twig; (e)leaf with dorsal view above and ventral below (Qiu et al., 2024:12).

Distribution and cultivation of R. officinalis

Rosmarinus officinalis, also known as rosemary in Turkish, is a valuable essential oil and spice plant belonging to the Lamiaceae family. This plant is a perennial, semi-shrub or shrub-like plant. Rosemary (*R. officinalis*) is one of the characteristic plants of the Mediterranean (Hussain et al., 2010:8; Borrás-Linares et al., 2014:21). It grows naturally in countries bordering the Mediterranean, especially on the coasts and mountain slopes facing the coast.

Rosemary eventually made its way to the West Indies and was seen as invasive in Cuba (Acevedo-Rodríguez and Strong, 2012:1192). It can flourish in a variety of soil types, including poor, dry, sandy, and rocky soil forms, and it can tolerate dry spells and warm weather (Mesoamericana, 2014:6). The Mediterranean region is home to both wild and cultivated *R. officinalis.*

The most important cultivated rosemary species is *R. officinalis*. In Türkiye, this species is distributed from the Mediterranean and Aegean coasts up to altitudes of 1000 m. However, economically, it is mostly

produced in Mersin and Adana provinces, collected wild from the coasts and mountain slopes facing the coast at altitudes of 100-250 m (Arıhan, 2003:226; Gülbaba and Özkurt, 2004:8; Baydar, 2009; 347).

Rosemary is an evergreen, perennial, shrub-like plant with a strong main root, a plant height of 50-100 cm, needle-shaped leaves, and pale blue flowers, and it is cross-pollinating (Malaylıoğlu, 2010:8).

This plant, which can grow up to 2m in height, has aromatic, leathery leaves that contain volatile oils in their characteristic shield-shaped, full glandular hairs (Marin et al., 2006:4). Due to its rich metabolites, it has a wide range of uses in many sectors such as food, pharmacology, and cosmetics (Begum et al., 2013: 13; Kulak, 2019:24; Aziz et al., 2022:15; González-Minero et al., 2020:17). *R. officinalis* L. exhibits many biological activities, including anticancer, antimicrobial, insecticidal, antioxidant, and neuroprotective effects, due to the secondary metabolites it contains (Bai et al., 2010:4; Hussain et al., 2010:8).

These plant species are now grown as decorative and fragrant plants in numerous agricultural areas throughout the world (Kadri et al., 2011:5; Alavi et al., 2021:15). In Europe, rosemary has adapted to a variety of growing environments and is primarily grown in areas with a warm climate. Additionally, it thrives on a variety of land types, including rock hills in Bermuda (Erkan et al., 2020:7), arid valleys in Bolivia (Jørgensen et al., 2014:74), and lower mountain and/or wet forests in Colombia.

Application in the Food Industry

Plant-derived essential oils (EO) exhibit strong antimicrobial properties (Lahmar et al., 2018:8). It simultaneously activates the enzyme system linked to cellular respiration and enhances the permeability of the cell membrane (Witwit, 2018:8). Minas Frescal cheese's microencapsulated rosemary essential oil inhibits the growth of mesophilic bacteria. There are no preservatives and a high moisture level in the Minas Frescal cheese. According to Fernandes et al. (2017:9), rosemary essential oil prolongs the shelf life of Minas Frescal cheese by preventing microbiological development. The bacterial growth that causes mozzarella cheese to deteriorate can be inhibited by rosemary essential oil (Fig. 1)

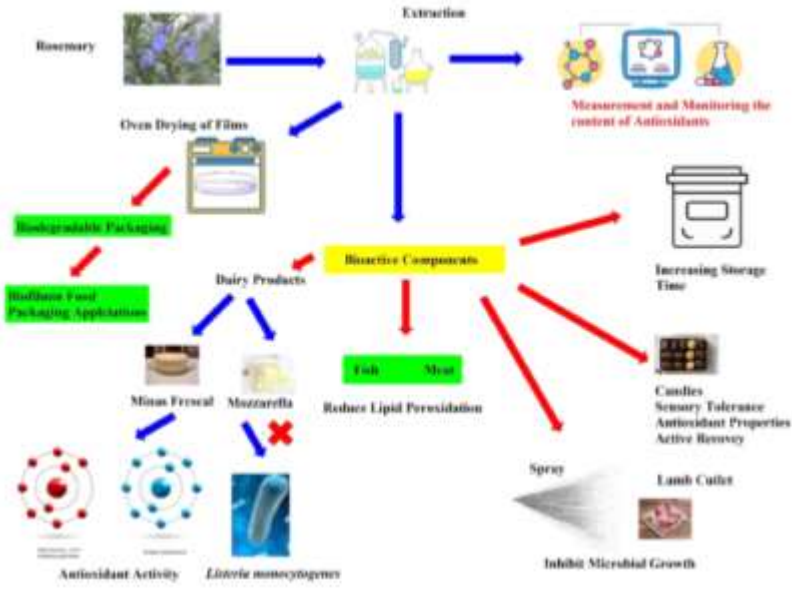

Figure 3. Rosemary potential application in the food industry (Aziz et al., 2022:15).

By neutralising free radicals and preventing the oxidation of unsaturated fatty acids, rosemary essential oil functions as an antibacterial agent in mozzarella cheese, protecting it from Listeria monocytogenes (WitWit, 2018:8). Foods can be stored for longer thanks to the essential oil of rosemary (Baj et al., 2018:9). In order to improve product quality, rosemary essential oil (EO) lowers lipid peroxidation in meals like meat and fish items kept in refrigeration (Wang et al., 2018:11). A variety of goods, including fresh sausages, burgers, and chicken breasts with a longer shelf life, were used to evaluate the rosemary essential oil.

It stops the production of aldehyde, which is necessary for effectively keeping meat, by preventing the growth of bacteria (Al-Hijazeen and Rawashdeh, 2017:8). Because of the active oxygen packaging, the study on lamb cutlets found that the sprayable EO shields the entire meat muscle food from oxidation and inhibits microbiological growth (Pesavento et al., 2015:9; Lahmar et al., 2018:8).

R. officinalis is used in cooking and is a strong antioxidant (Andrade et al., 2018:4). In order to preserve the freshness of packaged prawns and provide a longer shelf life of up to four days, low-density polyethylene-based active

packaging film is made using rosemary essential oil (Dong et al., 2018:8; Moczkowska et al., 2020;14).

While fresh silver carp are coated with 0.5% EO to extend the shelf life of fish fillets by changing their chemical properties, the coating solution with EO contains 4.7% protein powder in a water and ethyl alcohol mixture in the ratio [3:1, v/v] (Abdeldaiem et al., 2018:11).

Together with the low pH or other specific components of the apple juice, the rosemary extracts (V20, V40) inhibit the formation of Alicyclobacillus spores and decrease their vegetative cells (Piskernik et al., 2016:9).

Components, extraction methods, and potential applications of *Rosmarinus officinalis* L.

Addittionaly to Fig. 1 components, extraction methods, and potential applications of *Rosmarinus officinalis* L. are given in Fig. 2.

Minerals, Volatile and non volatile components etc. obtained from different parts of this plants, their extraction methods are given.

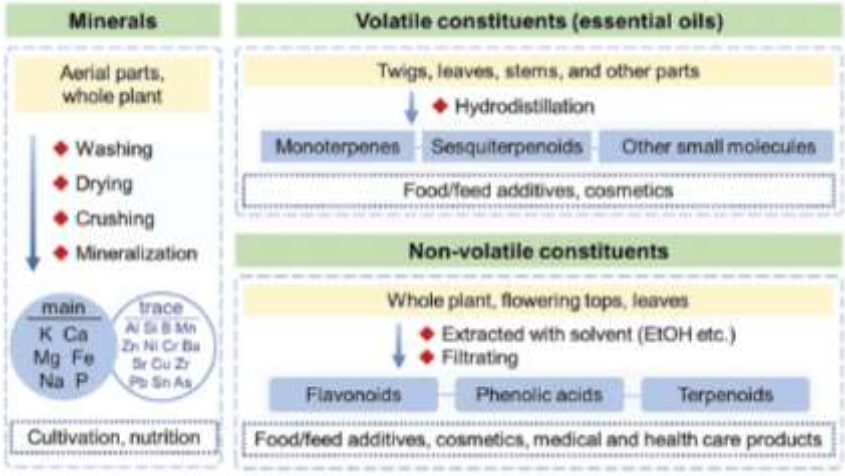

Fig. 4: Components, extraction methods, and potential applications of *Rosmarinus officinalis* L. (Quiu et al., 2024:12)

Mineral components of *Rosmarinus officinalis* L.

The roots of rosemary can absorb trace mineral elements from the soil, or the leaves can directly absorb these elements from the air. A few noteworthy

research and composition assessments on the mineral components of rosemary have been conducted due to its unique nutritional value; the reported total minerals of rosemary are summarised as indicated in Table 1.

Table 2: Mineral components of *R. officinalis* L.

	K	Ca	Mg	Fe	Na	P	Al	Si
Aerial parts [1]	198.2	178.8	34.2	45.0	11.6	35.6	24.6	1.4
Leaves [1]	141.5	83.5	13.7	23.8	7.3	32.8	17.2	3.1
Stems [1]	272.3	301.1	62.3	42.1	9.2	56.5	15.8	5.0
Conc. (mg/100g)	2035.5	1246.4	45.9	45.3	92.3	477.3	/	/
Proportion (%)	73 %	15%	9%	2%	1%	/	/	/

Reference: changed based on Ouknin et al. (2021:8) Ali et al. (2021:15) Tahri et al. (2013:7) **[1]mg/kg**

As can be seen in Table 2, aerial parts, leaves and stems of *R. officinalis* are containing high amounts of K, Ca and Mg. We can see also remarkable amounts of Fe, Na, P, Al and Si in *R. officinalis*.

Essential oils

Nearly all plants, particularly medicinal plants, contain Essetial oils (EOs) primarily in their flowers, leaves, and other sections (Elyemni et al., 2019:6).

The production of essential oil, which is widely utilised in the cosmetics industry and has garnered growing interest for its culinary applications, is one of the most significant usage aspects in the industrial potential of R. officinalis. Steam distillation is typically used to extract R. officinalis essential oil due to its cost-effectiveness and operational safety (Salamon et al., 2019:5).

The most important essentail oils present in *R. officinalis* are given in Fig. 5.

α- and β-pinene:

Pinene (C10H16) is a terpenoid hydrocarbon with two bicyclic bonds (Winnacker et al., 2018). Two isomers, α- and β-pinene, are present in nature, such as in essential oils (EOs) from pine (coniferous trees). They are among the most well-known members of a large class of monoterpenes.

Due to their varied biological activity, these two phytochemicals have a wide range of applications and functions, including fungicidal agents, flavours, perfumes, and antiviral and antibacterial agents (da Silva et al., 2012). Moreover, renal and hepatic medications contain α- and β-pinene Sybilska et al. (1994). Additionally, because of their harmful effects on membranes, α- and β-pinene are utilised as antibacterials (Alma et al., 2004). Furthermore, leukaemia and breast cancer have been demonstrated to be inhibited by α- and β-pinene (You et al., 2004). The use of pinenes extends beyond natural medicine; for example, it has been demonstrated that they are highly versatile in the synthesis of polymers (Winnacker et al., 2018:16; Kamagaito et al., 2017:45; Thomsett et al., 2019:7; Manfredi, 2007:214), and polymers made from pinenes are superior to other polymers (Satoh et al., 2014:8).

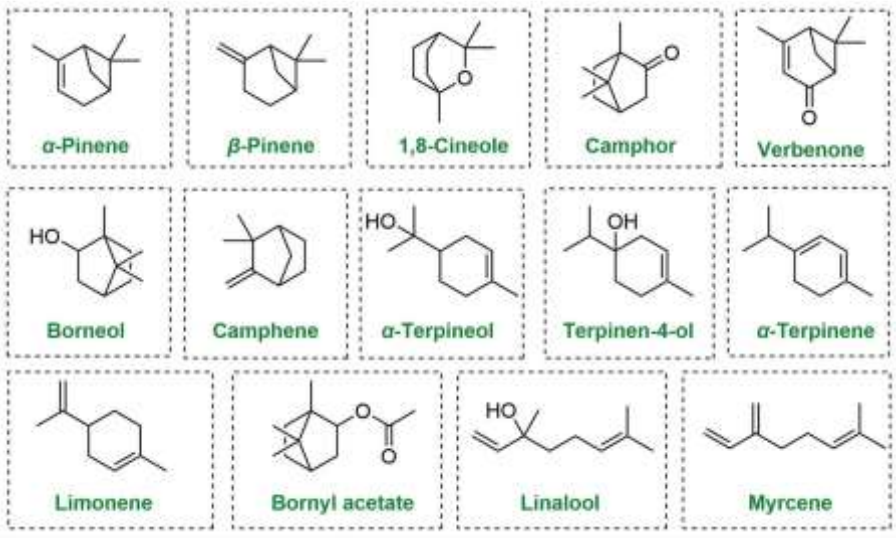

Fig. 5: Structures of the main monoterpenes in rosemary essential oil (Quiu et al, 2024:12)

1,8 Cineole (Eucalyptol):

Eucalyptol, also known by its synonym cajeputol, is a natural compound with the formula $C_{10}H_{18}O$ and is generally considered safe. Eucalyptol can easily cross the blood-brain barrier and directly act on enzymes and receptors in the brain (Seol and Kim, 2016:9; Moss and Oliver, 2012:10).

Studies in the literature have documented the pharmacological effects of 1,8-cineole, which is a common component of essential oils (Murata et al., 2013:5). The essential oils of several plants, including eucalyptus, rosemary, thyme, and sage, include 1,8 cineol (eucalyptol), which has a number of benefits, including anti-inflammatory, antioxidant, antibacterial, analgesic, and anticancer effects (Hoch et al., 2023:16). Cytotoxicity studies involving colon (Murata et al., 2013:5), lung (Rodenak-Kladniew et al., 2020:13), ovarian (Abdalla et al., 2020:12), skin (Sampath et al., 2018:11), and liver (Rodenak-Kladniew et al., 2020:13) have demonstrated the anticancer properties of 1,8 cineole.

Camphor

Camphor is a bicyclic monoterpene ketone and is known as a naturally occurring monoterpenoid. It is one of the most important secondary metabolites. Its chemical formula is $C_{10}H_{16}O$.

It is a key ingredient in many essential oils used in cosmetics and medicine. Its insect repellent and insecticidal properties have been widely confirmed. It has been used topically for various symptoms, such as redness, as an antiseptic, and as an antipruritic. It plays a key role in ointments used to relieve redness, reduce irritation, have mild analgesic properties, and alleviate neuralgia and similar conditions. It has also been reported to possess antiviral, antimicrobial, anticancer, antitussive (cough suppressant), antimutagenic, immunomodulatory, antiproliferative, hypoglycemic, antihyphal, and antibiofilm activity (Altınöz, 2023:25).

Verbenone:

Verbenone (trimethyl-bicyclo-heptenone) is a natural bicyclic ketone mono-terpene found in *D. carota* and other medicinal plants, including Rosmarinus officinalis. It can also be produced through the oxida tion of α-pinene from turpentine oil (Hu et al., 2017). This colourless, minty liquid is

only soluble in non-polar solvents. It is employed as an anti-aggregation pheromone to control insects, a cough suppressant, and in aromatherapy for its pleasant scent. Other investigations have revealed its anticancer, anti-inflammatory, hemolytic, bronchodialat ing, antiviral, and antioxidant properties (Ju et al., 2013; Mander et al., 2019).

Borneol:

Borneol, a highly lipid-soluble bicyclic terpene derived primarily from plants, is an example of monoterpenoids. Modern medicine has discovered that borneol has a variety of pharmacological properties and is used to treat a variety of disorders, mainly cardiovascular and cerebrovascular diseases. The critical function in boosting drug delivery and increasing bioavailability has received a lot of attention. In addition, borneol is frequently used in the food, everyday chemicals, fragrance, and flavour sectors (Hu et al., 2024:24).

Camphene:

Camphene ($C_{10}H_{16}$), also known as 2,2-dimethyl-3-methylidenebicyclo[2.2.1] heptane, is a volatile chemical from the terpenoid family, specifically monoterpene hydrocarbons. It is found as a secondary metabolite in a variety of aromatic and medicinal plants, particularly in the Thymus, Origanum, and Salvia genera, and is regarded a primary component of their essential oils (Hachlafi et al., 2023). Numerous in vitro and in vivo studies have demonstrated camphene's biological capabilities, which include antibacterial, antifungal, anticancer, antioxidant, antiparasitic, antidiabetic, anti-inflammatory, and hypolipidemic activity. Furthermore, camphene has been shown to have anti-leishmanial, hepatoprotective, antiviral, and anti-acetylcholinesterase actions (Chen et al., 2023:14).

α-Terpineol:

Many plant essential oils contain α-terpineol, a monocyclic monoterpenoid tertiary alcohol with a lilac-like scent. α-terpineol has numerous biological actions, including antioxidant, anti-inflammatory, antibacterial, anticancer, analgesic, gastroprotective, cardioprotective, neuroprotective, and antidiarrheal properties. α-terpineol's positive effects, unique aroma, and safety make it suitable for use in various industries,

including food, cosmetics, medicine, agriculture, and chemicals(Chen et al., 2023:14).

Terpinen-4-ol:

Terpinen-4-ol (T-4-ol), a bioactive monoterpene alcohol and the primary component of tea tree oil (TTO), has made its way into translational research. This compound possesses a wide range of pharmacological activities, including antibacterial, antivirulent, antioxidant, anti-inflammatory, antihypertensive, and anti-cancer actions (Prerna et al., 2024:12).

α-Terpinene:

Essential oils contain the monoterpene α-terpinene, which is used as a scent component. It is one of the components that contribute to tea tree oil's antioxidant properties. α-Terpinene, like other monoterpenes like limonene, undergoes autoxidation and forms allergenic chemicals when exposed to air (Rudbäck et al., 2012:8).

Limonene:

Limonene (C10H16) is an olefinic hydrocarbon that exists as a colourless liquid at ambient temperature. Its chemical formula is 1-methyl-4-(1-methylethenyl) cyclohexane3. Limonene has a wide range of medicinal and non-therapeutic applications. Traditionally, it has been employed in the manufacturing of soaps and perfumes, as it has the characteristic odour of lemons, as well as the production of insecticides and insect repellents (Devi et al., 2025:27).

Bornyl acetate:

Bornyl acetate (BA), a bicyclic monoterpene, is an active volatile component found in a wide range of plants worldwide. BA is commonly employed as an essence and food flavouring agent, as well as in perfumes and food additives (Zhao et al., 2025:15).

Linalool:

Linalool ($C_{10}H_{18}O$, 3,7-dimethyl-1,6-octadien-3-ol) is a monoterpene acyclic tertiary alcohol. As a fragrance chemical, it has a wide range of

applications, including perfumes, lotions, soaps, and shampoos, as well as non-cosmetic household items like detergents and cleansers (Mazka et al., 2022:19).

Myrcene:

Myrcene (β-myrcene) is a common monoterpene found in many plant species, including hops and cannabis. It is a common flavouring and fragrance agent (food additive) used in the production of foods and beverages. β-myrcene is known for its anxiolytic, antioxidant, anti-aging, anti-inflammatory, and analgesic activities (Surendran et al., 2021:14).

RESULTS AND DISCUSSION

R. officinalis, an ancient plant in the European Pharmacopoeia, is used medicinally. Throughout history, it has been widely utilised to treat many diseases. Scientific evidence of the plant's medical advantages has been established through in vitro, in vivo, and human studies during the past decades. Phytotherapy, which uses plant materials such phytocompounds, extracts, essential oils, and tinctures, has been shown to be effective in alternative or complementary medicine.

Rosemary essential oil has acquired popularity due to its numerous pharmacological characteristics and applications in medicine, cosmetics, and gastronomy. Despite its expanding importance, there is still a lack of information about how extraction processes influence the chemical makeup and medicinal efficacy of essential oils.

CONCLUSION

Advances in molecular biology, genetics, and high-accuracy analytical techniques have made it possible to isolate plant compounds that are present in microscopic levels. These developments have made it possible to study their chemical composition and therapeutic potential, which enables the molecule to be modified to produce new, more focused medicinal medicines. Due to in vitro and in vivo study on a range of biological qualities, including as analgesic, anti-inflammatory, and antioxidant qualities previously documented in ethnobotanicals studies, rosemary has gained increased interest since the 1990s for its potential therapeutic benefits.

R. officinalis has a bright future in medicine, particularly in the treatment and prevention of viral diseases, a variety of malignancies, and newly developing conditions like depression, Parkinson's disease, and Alzheimer's disease. The safety and effectiveness of many herbal treatments are still

questionable, with insufficient or inconsistent methodology, thus these research into herbal remedies should be given more weight. In light of this, more trustworthy studies are required in the future to assess the safety and effectiveness of *R. officinalis* active phytocompounds in treating various pathological disorders.

REFERENCES

Abdalla, A.N., Shaheen, U., Abdallah, Q.M., Flamini, G., Bkhaitan, M.M., Abdelhady, M.I., ve Bader, A. (2020). Proapoptotic activity of Achillea membranacea essential oil and its major constituent 1, 8-cineole against A2780 ovarian cancer cells. Molecules, 25(7), 1582.

Abdeldaiem, M.H., Mohammad, H.G., ve Ramadan, M.F. (2018). Improving the quality of silver carp fish fillets by gamma irradiation and coatings containing rosemary oil. Journal of Aquatic Food Product Technology 27 (5), 568–579.

Alavi, M.S., Fanoudi, S., Ghasemzadeh Rahbardar, M., Mehri, S., ve Hosseinzadeh, H. (2021). An updated review of protective effects of rosemary and its active constituents against natural and chemical toxicities. Phototherapy Research 35, 1313–1328.

Ali, H. I., Dey, M., Alzubaidi, A. K., Alneamah, S. J. A., Altemimi, A. B., ve Pratap-Singh, A. (2021). Effect of rosemary (Rosmarinus officinalis L.) supplementation on probiotic yoghurt: Physicochemical properties, microbial content, and sensory attributes. Foods, 10(10), 2393.

Al-Hijazeen, M., ve Al-Rawashdeh, M. (2017). Preservative effects of rosemary extract (Rosmarinus officinalis L.) on quality and storage stability of chicken meat patties. Food Science and Technology 201700.

Allegra, A., Tonacci, A., Pioggia, G., Musolino, C., ve Gangemi, S. (2020). Anticancer activity of Rosmarinus officinalis L.: mechanisms of action and therapeutic potentials. Nutrients. 12(6)

Alma, M.H., Nitz, S., Kollmannsberger, H., Digrak, M., Efe, F.T., ve Yilmaz, N. (2004). Chemical composition and antimicrobial activity of the essential oils from the gum of Turkish pistachio (Pistacia vera L.). J. Agric. Food Chem. 52, 3911–3914.

Altınöz, A. (2023). Aromaterapeutic and therapeutic effects of the Rosmarine (Rrosmarinus officinalis) Plant. In: International Work in Health Sciences, June 2023. Edts. Gerçeker, F.Ö., Akgül, H., Selamoğlu Z. Chapter 13, 199-224.

Andrade, J.M., Faustino, C., Garcia, C., Ladeiras, D., Reis, C.P., ve Rijo, P. (2018). Rosmarinus officinalis L.: an update review of its phytochemistry and biological activity. Future Sci OA. 4(4):FSO283.

Arıhan, S.K. (2003). Antik Dönemde Tıp ve Bitkisel Tedavi. Ankara Üniversitesi Sosyal Bilimler Enstitüsü Arkeoloji Bölümü Klasik Arkeoloji Anabilim dalı, Yüksek lisans Tezi.

Acevedo-Rodríguez, P., ve Strong, M.T. (2012). Catalogue of seed plants of the West Indies. Mithsonian Contributions to Botany.

Aziz, E., Batool, R., Akhtar, W., Shahzad, T., Malik, A., Shah, M.A., Iqbal, S., Rauf, A., Zengin, G., Bouyahya, A., Rebezov, M., Dutta, N., Khan, M.U., Khayrullin, M., Babaeva, M., Goncharov, A., Shariati, M.A. ve Thiruvengadam, M. (2022). Salvia rosmarinus species: A review of phytochemicals, bioactivities and industrial applications. South Afr. J. Botany 151, 3–18.

Baj, T., Baryluk, A., ve Sieniawska, E. (2018). Application of mixture design for optimum antioxidant activity of mixtures of essential oils from Ocimum basilicum L. Origanum majorana L. and Rosmarinus officinalis L. Industrial Crops and Products 115, 52–61.

Bai, N., He, K., Roller, M., Lai, C. S., Shao, X., ve Pan, M. H. (2010). Flavonoids and phenolic compounds from Rosmarinus officinalis L. Journal of Agricultural and Food Chemistry, 58(9), 5363-5367.

Baj, T., Baryluk, A., ve Sieniawska, E. (2018). Application of mixture design for optimum antioxidant activity of mixtures of essential oils from Ocimum basilicum L., Origanum majorana L. And Rosmarinus officinalis L. Ind. Crops Prod. 115, 52–61.

Baydar, H. (2009). Tıbbi ve aromatic bitkiler bilimi ve teknolojisi (Genişletilmiş 3. Baskı). Süleyman Demirel Üniversitesi Yayın No: 51 (ISBN: 975 7929--79-4), pp. 1-347.

Begum, A.,Sandhya, S., Vinod, K. R., Reddy, S., ve Banji, D. (2013). An in-depthreview on themedicinal flora Rosmarinus officinalis (Lamiaceae). Acta scientiarum polonorumTechnologia alimentaria, 12(1), 61-74.

Borges, R.S., Ortiz, B.L.S., Pereira, A.C.M., Keita, H., ve Carvalho, J.C.T. (2019). Rosmarinus officinalis essential oil: a review of its phytochemistry, anti-inflammatory activity, and mechanisms of action involved. J Ethnopharmacol. 229:29–45.

Borrás-LinaresStojanović, Isabel., Z., Quirantes-Piné, R., ve Arráez-Román, D. (2014). Rosmarinus Officinalis Leaves as a Natural Source of Bioactive Compounds‖, International Journal of Molecular Sciences, 15, no. 11, pp. 20585-20606.

Chen, Y., Zhang, L. L., Wang, W., ve Wang, G. (2023). Recent updates on bioactive properties of α-terpineol. *Journal of Essential Oil Research*, *35*(3), 274–288. https://doi.org/10.1080/10412905.2023.2196515

da Silva, A.C., Lopes, P.M., de Azevedo, M.M., Costa, D.C., Alviano, C.S., ve Alviano, D.S. (2012). Biological activities of alpha-pinene and beta-pinene enantiomers. Molecules, 17, 6305–6316.

Devi, S., Bhattacharya, N., Sharma, B., Singh, A., Kumar, I., Huanbutta, P., ve Sangnim, K. (2025). From Citrus to Clinic: Limonene's Journey Through Preclinical Research, Clinical Trials, and Formulation Innovations. *Int J Nanomedicine*. 20:4433-4460.

Dong, X., Zhang, J., Yang, F., Wu, J., Cai, R., Wang, T., ve Zhang, J. (2018). Effect of luteolin on the methylation status of the OPCML gene and cell growth in breast cancer cells. Experimental and Therapeutic Medicine 16 (4), 3186–3194.

Elyemni, M., Louaste, B., Nechad, I., Elkamli, T., Bouia,A., Taleb, M., Chaouch,M., ve Eloutassi, N. (2019). Extraction of essential oils of Rosmarinus officinalis L. by two different methods: Hydrodistillation andmicrowave assisted hydrodistillation. The ScientificWorld Journal, 2019, 3659432.

Erkan, I.E., (2020). Studies on Antimicrobial, Antifungal and Antioxidant Properties of Rosemary: A Review. Turkish Journal of Agriculture-Food Science and Technology 8 (12), 2708–2715.

Fernandes, R.V.D.B., Guimaraes, I.C., Ferreira, C.L.R., Botrel, D.A., Borges, S.V., ve Souza, A.U. (2017). Microencapsulated rosemary (Rosmarinus officinalis) essential oil as a biopreservative in Minas Frescal cheese. Journal of Food Processing and Preservation 41 (1), e12759.

GBIF (2025). Global Biodiversity Information Facility—. Available online: https://www.gbif.org/ (accessed 23 November 2025).

Gülbaba, A.G., ve Özkurt, N. (2004). Adana ve Mersin yöresi doğal biberiye (Rosmarinus officinalis L.) populasyonlarının alan, yaprak ve yağ verimlerinin belirlenmesi, 14. Bitkisel İlaç Hammaddeleri Toplantısı, 29-31 Mayıs, Eskişehir.

González-Minero, F.J., Bravo-Díaz, L., ve Ayala-Gómez A. (2020). Rosmarinus officinalis L. (Rosemary): an ancient plant with uses in personal healthcare and cosmetics. Cosmetics. 7(4).

Hachlafi, N. E., Aanniz, T., Menyiy, N. E., Baaboua, A. E., Omari, N. E., Balahbib, A., ve Bouyahya, A. (2023). *In Vitro* and *in Vivo* Biological Investigations of Camphene and Its Mechanism Insights: A Review. *Food Reviews International*, *39*(4), 1799–1826.

Heinrich, M., Kufer, J., Leonti, M., ve Pardo-de-Santayana, M. (2006). Ethnobotany and ethnopharmacology – interdisciplinary links with the historical sciences. J. Ethnopharmacol. 107(2):157–60.

Hoch, C. C., Petry, J., Griesbaum, L., Weiser, T., Werner, K., Ploch, M., ve Wollenberg, B. (2023). 1, 8-cineole (eucalyptol): A versatile phytochemical with therapeutic applications across multiple diseases. Biomedicine & Pharmacotherapy, 167, 115467.

Hu, Q., Lin, G-S., Duan, W-G., Huang, M., ve Lei F-H (2017). Synthesis and biologi cal activity of novel (z)- and (e)- verbenone oxime exters. Molecules 22(10):1678.

Hu, X., Yan, Y., Liu, W., Liu, J., Fan, T., Deng, H., ve Cai, Y. (2024). Advances and perspectives on pharmacological activities and mechanisms of the monoterpene borneol, Phytomedicine, Volume 132, 2024, 155848.

Hussain, A., Anwar, F., ve Jabbar, A. (2010). Rosmarinus officinalis essential oil: antiproliferative, antioxidant and antibacterial‖, Brazilian Journal of Microbiology, cilt 41, no. 4, pp. 1070-1078.

Jørgensen, P., Nee, M., ve Beck, S. (2014). Catalogue of the vascular plants of Bolivia. Catalogue of the vascular plants of Bolivia.

Ju, C., Song, S., Hwang, S., Kim, C., Kim, M., Gu, J., Oh, Y.K., Lee, K., Kwon, J., Lee, K., Kim, W.K., ve Choi Y (2013) Discovery of novel (1S)-(-)-verbenone derivatives with anti-oxidant and anti-ischemic effects. Bioorg Med Chem Lett 23(19):5421–5425

Kadri, A., Zarai, Z., Ben Chobba, I., Bekir, A., Gharsallah, N., Damak, M., Gdoura, R. (2011). Chemical constituents and antioxidant properties of Rosmarinus officinalis L. essential oil cultivated from South-Western Tunisia. Journal of Medicinal Plants Research 5, 5999–6004.

Kamagaito, M. ve Satoh, K. (2017). Sustainable vinyl polymers via controlled polymerization of terpenes. In *Sustainable Polymers from Biomass*; Tang, C., Ryu, C.Y., Eds.; Wiley: Hoboken, NJ, USA, pp. 55–90.

Kulak, M. (2019). A time-coursestudy on essential oil of rosemary (Rosmarinus officinalis) under drought stress. Adıyaman Üniversitesi Fen Bilimleri Dergisi, 9(1), 165-189.

Lahmar, A., Morcuende, D., Andrade, M.J., Chekir-Ghedira, L., ve Estevez, M. (2018). Prolonging shelf life of lamb cutlets packed under high-oxygen modified atmosphere by spraying essential oils from north-African plants. Meat Science 139, 56–64

Mączka, W., ve Duda-Madej, A., Grabarczyk, M., & Wińska, K. (2022). Natural Compounds in the Battle against Microorganisms—Linalool. *Molecules*, *27*(20), 6928.

Malaylıoğlu, H.B. (2010). Biberiyenin (Rosmarinus officinalis L.) antioksidan etkisi. Hayvansal Üretim, 51(2), 59-67.

Mander, S., Kim, D.H., Nguyen, H.T., Yong, H.J., Pahk, K., Kim, E.Y., Lee, K., Seong, J.Y., Kim, W-K., ve Hwang, J-I. (2019) SP-8356, a (IS)-(-)-verbenone derivative, exerts in-vitro and in-vivo anti-breast cancer effects by inhibiting nf-ŋb signaling. Sci Rep 9(6595):1–12

Manfredi, K.P. (2007). Terpenes. Flavors, Fragrances, Pharmaca, Pheromones By Eberhard Breitmaier (University of Bonn). J. Nat. Prod. 2007, 70, 711.

Marin, M., Koko, V., Duletić-Laušević, S., Marin, P.D., Rančić, D., Dajic-Stevanovic, Z. (2006). Glandular trichomes on the leaves of Rosmarinus officinalis: Morphology, stereology and histochemistry, South African Journal of Botany, 72, 3, 378-382.

Mesoamericana, F. (2010). Flora Mesoamericana. Missouri Botanical Garden, St. Louis, Missouri, USA. Morales, R. Flora Ibérica; CSIC: Madrid, Spain, Volume 12, pp. 321–327.

Moss, M., ve Oliver, L. (2012). Plasma 1,8-cineole correlates with cognitive performance following exposure to rosemary essential oil aroma. Therapeutic Advances in Psychopharmacology, 2(3), 103–113.

Murata, S., Shiragami, R., Kosugi, C., Tezuka, T., Yamazaki, M., Hirano, A., ve Ohkohchi, N. (2013). Antitumor effect of 1, 8-cineole against colon cancer. Oncology reports, 30(6), 2647-2652.

Moczkowska, M., Karp, S., Horbanczuk, O.K., Hanula, M., Wyrwisz, J., Kurek, ve M.A. (2020). Effect of rosemary extract addition on oxidative stability and quality of hemp seed oil. Food and Bioproducts Processing 124, 33–47.

Ouknin, M., Aghraz, A., Chibane, M., Boumezzourh, A., Costa, J., ve Majidi, L. (2021). Enzyme inhibitory, antioxidant activity and phytochemical analysis of essential oil from cultivated Rosmarinus officinalis. Journal of Food Measurement andCharacterization, 15(4), 3782–3790.

Pesavento, G., Calonico, C., Bilia, A.R., Barnabei, M., Calesini, F., Addona, R., ve Nostro, A.L. (2015). Anti-bacterial activity of Oregano, Rosmarinus and Thymus essential oils against Staphylococcus aureus and Listeria monocytogenes in beef meatballs. Food Control 54, 188–199.

Piskernik, S., Klancnik, A., Demsar, L., Mozina, S.S., ve Jersek, B. (2016). Control of Alicyclobacillus spp. vegetative cells and spores in apple juice with rosemary extracts. Food Control 60, 205–214.

Prerna, J.C., Lavanya, K., Umang, M., ve Kusum, H. (2024). A comprehensive review on the pharmacological prospects of Terpinen-4-ol: From nature to medicine and beyond, Fitoterapia, Volume 176, 2024, 106051

Qiu, K., Wang, S., Duan, F., Sang, Z., Wei, S., Liu, H., ve Tan, H. (2024). Rosemary: Unrevealing an old aromatic crop as a new source of promising functional food additive—A review. Comprehensive Reviews in Food Science and Food Safety. 23. 1-38.

Rodenak-Kladniew, B., Castro, A., Stärkel, P., Galle, M., ve Crespo, R. (2020). 1, 8-Cineole promotes G0/G1 cell cycle arrest and oxidative stress-induced senescence in HepG2 cells and sensitizes cells to anti-senescence drugs. Life sciences, 243, 117271.

Rudbäck, J., Bergström, M.A., Börje, A., Nilsson, U., ve Karlberg, A.T. (2012). α-Terpinene, an antioxidant in tea tree oil, autoxidizes rapidly to skin allergens on air exposure. Chem Res Toxicol. 19;25(3):713-21.

Sampath, S., Subramani, S., Janardhanam, S., Subramani, P., Yuvaraj, A., ve Chellan, R. (2018). Bioactive compound 1, 8-Cineole selectively induces G2/M arrest in A431 cells through the upregulation of the p53 signaling pathway and molecular docking studies. Phytomedicine, 46, 57-68.

Salamon, I., Kryvtsova, M., Bucko, D., ve Tarawneh, A. H. (2019). Chemical characterization and antimicrobial activity of some essential oils after their industrial large-scale distillation. Journal of Microbiology, Biotechnology and Food Sciences, 8(4), 984–988.

Satoh, K., Nakahara, A., Mukunoki, K., Sugiyama, H., Saito, H., ve Kamigaito, M. (2014). Sustainable cycloolefin polymer from pine tree oil for optoelectronics material: Living cationic polymerization of β-pinene and catalytic hydrogenation of high-molecular-weight hydrogenated poly(β-pinene). Polym. Chem. 5, 3222–3230.

Seol, G. H., ve Kim, K. Y. (2016). Eucalyptol and Its Role in Chronic Diseases. In:S. C. Gupta, S. Prasad, & B. B. Aggarwal (Ed.), *Drug Discovery from Mother Nature* (ss. 389–398). Switzerland: Springer.

Surendran, S., Qassadi, F., Surendran, G., Lilley, D., ve Heinrich M. (2021). Myrcene-What Are the Potential Health Benefits of This Flavouring and Aroma Agent? Front Nutr. 19; 8: 699666.

Sybilska, D., Kowalczyk, J., Asztemborska, M., Ochocka, R.J., ve Lamparczyk, H. (1994). Chromatographic studies of the enantiomeric composition of some therapeutic compositions applied in the treatment of liver and kidney diseases. J. Chromatogr. A 665, 67–73.

Tahri, M., Imelouane, B., Aouinti, F., Amhamdi, H., ve Elbachiri, A. (2013). The organic and mineral compounds of the medicinal aromatics, Rosmarinus tournefortii and Rosmarinus officinalis, growing in eastern Morocco. Research on Chemical Intermediates, 40(8), 2651–2658.

Thomsett, M.R., Moore, J.C., Buchard, A., Stockman, R.A., ve Howdle, S.M. (2019). New renewably-sourced polyesters from limonene-derived monomers. Green Chem. 21, 149–156.

Wang, L.C., Wei, W.H., Zhang, X.W., Liu, D., Zeng, K.W., ve Tu, P.F. (2018). An integrated proteomics and bioinformatics approach reveals the anti-inflammatory mechanism of carnosic acid. Frontiers in Pharmacology 9, 370.

Winnacker, M., ve Rieger, B. (2015). Recent progress in sustainable polymers obtained from cyclic terpenes: Synthesis, properties, and application potential. Chem. Sus. Chem. 8, 2455–2471.

Winnacker, M. (2018). Pinenes: Abundant and Renewable Building Blocks for a Variety of Sustainable Polymers. Angew. Chem. Int. Ed. 2018, 57, 14362–14371.

Witwit, N.M. (2018). Potential effectiveness of essential oil as natural food preservatives compared with chemical. Journal of Global Pharma Technology 10 (3), 462–470.

Zaouali, Y., Bouzaine, T., ve Boussaid M. (2010). Essential oils composition in two *Rosmarinus officinalis* L. varieties and incidence for antimicrobial and antioxidant activities. Food Chem Toxicol. 48(11):3144–52.

Zhao, Z.J., Sun, Y.L., ve Ruan, X.F.. (2023). Bornyl acetate: A promising agent in phytomedicine for inflammation and immune modulation. Phytomedicine. 114:154781.

Zhou, J.Y., Tang, F.D., Mao, G.G., ve Bian, R.L. (2004). Effect of alpha-pinene on nuclear translocation of NF-kappa B in THP-1 cells. *Acta Pharmacol. Sin.*, *25*, 480–484.

Anatomic and Morphologic Characteristics of Medicinal Leech, *Hirudo verbana* (Carena, 1820)

Al-Hussein Hameed Hussein OKBI[1]

Mehmet Oğuz ÖZTÜRK[2]

1- Expert Biologist; Afyon Kocatepe University, Science and Literature Faculty, Department of Molecular Biology and Genetics, Afyonkarahisar, Turkey alhusseinalagabi@gmail.com ORCID No: 0000-0002-0083-4676

2- Prof. Dr.; Afyon Kocatepe University, Science and Literature Faculty, Department of Molecular Biology and Genetics, Afyonkarahisar, Turkey oozturk@aku.edu.tr ORCID No: 0000-0001-7263-3585

ABSTRACT

Hirudinean organisms are characterized by a particular emphasis on ectoparasitic taxa that feed on vertebrate blood. Ectoparasitic medicinal leech species belonging to the class Hirudinea have been used for therapeutic purposes throughout human history. The aim of this study was to describe the anatomical and morphological characteristics of *Hirudo verbana* specimens collected from Lake Karamık. The specimens were collected from Lake Karamık. In total, 16 *Hirudo verbana* specimens were examined. The leech specimens exhibited reddish-orange, rosary-like or narrow black mottled stripes on the dorsal surface. The paramedian lines of *H. verbana* were broad and orange. The ventral surface displayed yellowish-green pigmentation with black or dark brown stripes. Between these two dark bands, a light-colored region without spots was observed. *Hirudo verbana* specimens possessed oval suckers at both the anterior and posterior ends. The caudal sucker was larger than the anterior sucker but did not exceed the maximum body width. Five pairs of eyes appeared as black dots on the anterior-dorsal terminal region. Three keratinized jaws were located approximately 2–3 mm from the anterior sucker, and the jaws bore evenly distributed fine teeth along their edges. This study characterized the anatomical and morphological features of *Hirudo verbana* obtained from Lake Karamık and contributes to the understanding of the geographical distribution and evolutionary homogeneity of this species.

Anahtar Kelimeler – Anatomy, *Hirudo verbana*, *Lake Karamık*, *Morphology*

INTRODUCTION

Hirudinean organisms are characterized by a particular emphasis on ectoparasitic taxa that feed on vertebrate blood. Ectoparasitic medicinal leech species belonging to the class Hirudinea have been used for therapeutic purposes throughout human history (Živić et al. 2015). Among these species, *Hirudo medicinalis* and *Hirudo verbana* were historically grouped under the name *Hirudo medicinalis* due to insufficient knowledge of their biology and reproductive systems (Kutschera and Elliott 2014). Consequently, detailed taxonomic studies were conducted in subsequent years, which demonstrated that the majority of medicinal leeches in Türkiye belong to *Hirudo verbana* (Apakupakul et al. 1999; Sağlam 2011; Sağlam et al. 2016, 2018; Sağlam 2019).

In this study, the anatomical and morphological features of *Hirudo verbana* specimens collected from Lake Karamık are described for the first

time. The findings of this study will contribute to a better understanding of the species *Hirudo verbana*.

MATERIALS and METHODS

Study Area

Lake Karamık is located in the Aegean Region of Türkiye (Figure 1). The study area is situated in the southern part of a tectonic depression extending in a north–south direction, east of the Sultandağları Mountains and west of Kükürt Mountain. Lake Karamık lies at an elevation of 1002 m above sea level and has a surface area of approximately 56 km². The drainage basin covers an area of 342 km² (Figure 2). Lake Karamık is a shallow and eutrophic lake, with a water depth ranging between 2 and 3 m (Hasbek and Arı 2018).

Collecting of Hirudo verbana Samples

In this study, *Hirudo verbana* specimens were collected from Lake Karamık. To attract the leeches, disturbances were created in the water, prompting them to move toward the area of activity. The specimens were then captured using a plastic scoop and transferred into plastic bottles containing lake water (Figure 3). The collected specimens were transported to the research laboratory, where they were fixed at 37 °C in 70% ethanol and subsequently stored in 95% ethanol for anatomical and morphological investigations (Figure 4-6).

The specimens were identified based on their anatomical and morphological characteristics using an Olympus SZ30 stereomicroscope, an Olympus CH20 light microscope, and a ZEISS Axio Imager microscope, following the identification criteria described by Neubert and Nesemann (1999).

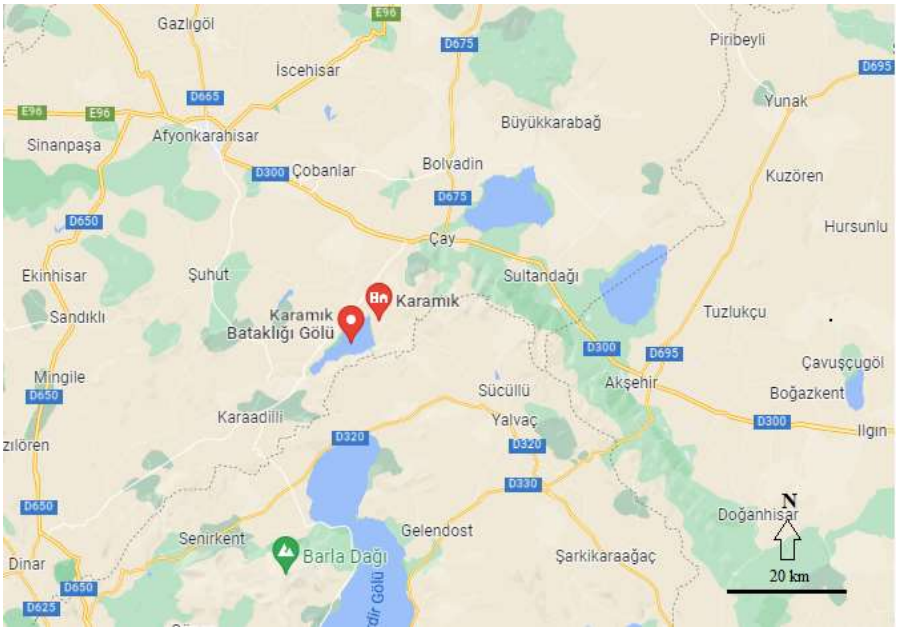

Figure 1. Location of Lake Karamık (Anonymous 2023).

Figure 2. Koçbeyli district from Lake Karamık (original).

Figure 3. Collecting activity of *Hirudo verbana* samples from Lake Karamık (original).

Figure 4. Relaxing and fixation of the samples in warmish ethanol medium (original).

Figure 5. *Hirudo verbana* samples flattened from dorso-ventral side (original).

Figure 6. Samples of *Hirudo verbana* preserved in ethanol medium (original).

RESULTS

Anatomic and Morphologic Features of Hirudo verbana Samples

In this study, a total of 16 *Hirudo verbana* specimens were examined. The largest specimen measured 10.3 cm in length and weighed 6.80 g, whereas the smallest specimen measured 3.8 cm in length and weighed 0.26 g (Table 1).

Anatomical and morphological characteristics of the specimens were determined as follows.

The body of *H. verbana* is slightly dorsoventrally flattened and consists of segments, or metamers. The leech specimens exhibited reddish-orange, rosary-like or narrow black mottled stripes on the dorsal surface. The paramedian lines of *H. verbana* were broad and orange. The ventral surface showed yellowish-green pigmentation with black or dark brown stripes. Between these two dark bands, a light-colored region without spots was observed (Figures 7, 8).

Hirudo verbana specimens possess oval suckers at both the anterior and posterior ends. The caudal sucker is larger than the anterior sucker but does not exceed the maximum body width (Figures 9, 10).

Five pairs of eyes appear as black dots on the anterior-dorsal terminal region. Each pair of eyes is located within the same annulus, and the eyes are arranged in an arc-shaped symmetrical pattern (Figure 11).

The mouth is situated at the center of the anterior sucker, and the muscular pharynx is well developed. Three keratinized jaws are located approximately 2–3 mm from the anterior sucker, and the jaws bear uniformly fine teeth along their edges (Figures 12, 13).

The stomach, or mid-intestine, constitutes the largest part of the digestive system and is a wide, thin-walled tubular structure. Eleven pairs of gastric caeca are present along the stomach. The hindgut is short, and the anus is located dorsally, just anterior to the posterior sucker (Figure 14).

Genital pores are located in the clitellar region on the XI and XII metamers. The male genital opening is situated in the groove between the fourth and fifth annuli of segment XI, whereas the female genital pore is located between the fourth and fifth annuli of segment XII (Figure 15).

Epididymis is small, and the ejaculatory (discharge) bulb is elongated. The penis sheath is long and well developed, and the vagina is tubular in form. The specimens possess ten pairs of oval-shaped testicular sacs (Figure 16).

Table 1. Body measurement values of *Hirudo verbana* samples.

Collected Date	Location	Samples No	Length (cm)	Width (cm)	Weight (gr)
13. 09. 2021	Karamık Lake, Koçbeyli location	Hv-1	10.3	1.90	6.80
		Hv-2	9.0	1.55	4.20
		Hv-3	8.4	1.80	2.82
		Hv-4	8.4	1.50	3.00
		Hv-5	8.3	1.65	2.90
		Hv-6	7.5	1.60	2.17
		Hv-7	7.4	1.20	1.86
		Hv-8	6.9	1.20	1.86
		Hv-9	6.4	1.55	1.58
		Hv-10	6.3	0.90	1.30
		Hv-11	6.1	0.95	1.10
		Hv-12	5.4	0.85	0.56
		Hv-13	4.9	0.70	0.78
		Hv-14	4.0	0.60	0.42
		Hv-15	4.0	0.55	0.38
		Hv-16	3.8	0.45	0.26

Figure 7. General view of *Hirudo verbana* specimens from dorsal and ventral (original).

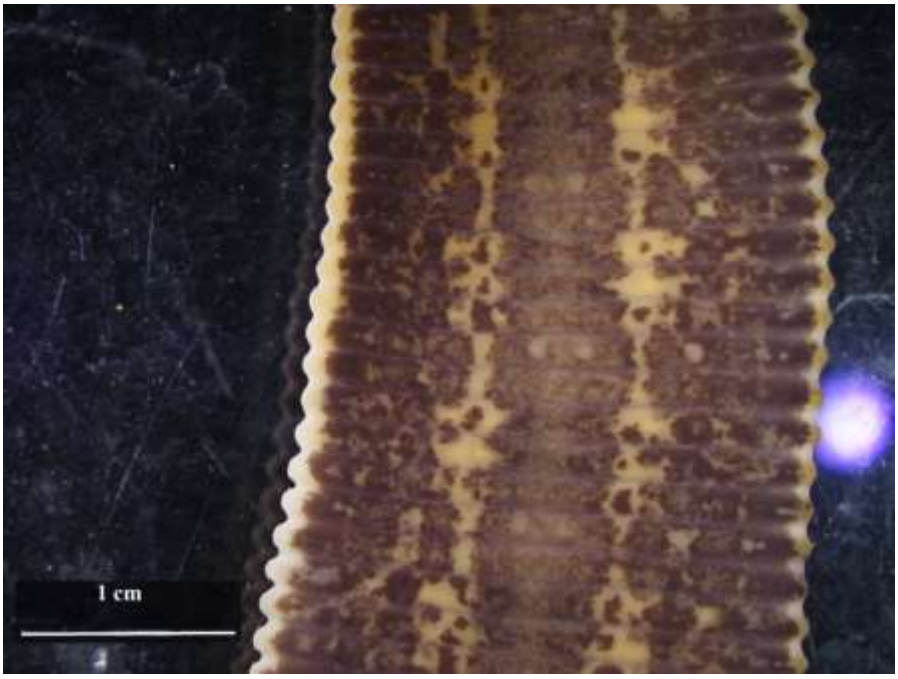

Figure 8. Dorsal view of *Hirudo verbana* (original).

Figure 9. Ventral view of mouth sucker of *Hirudo verbana* (original).

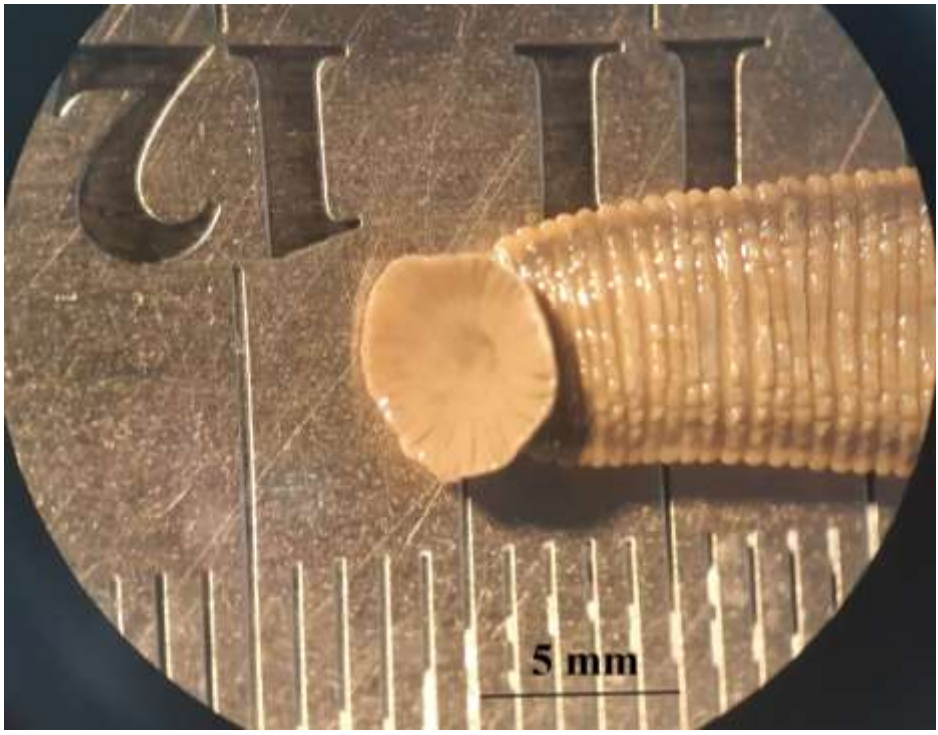

Figure 10. Ventral view of posterior sucker of *Hirudo verbana* (original).

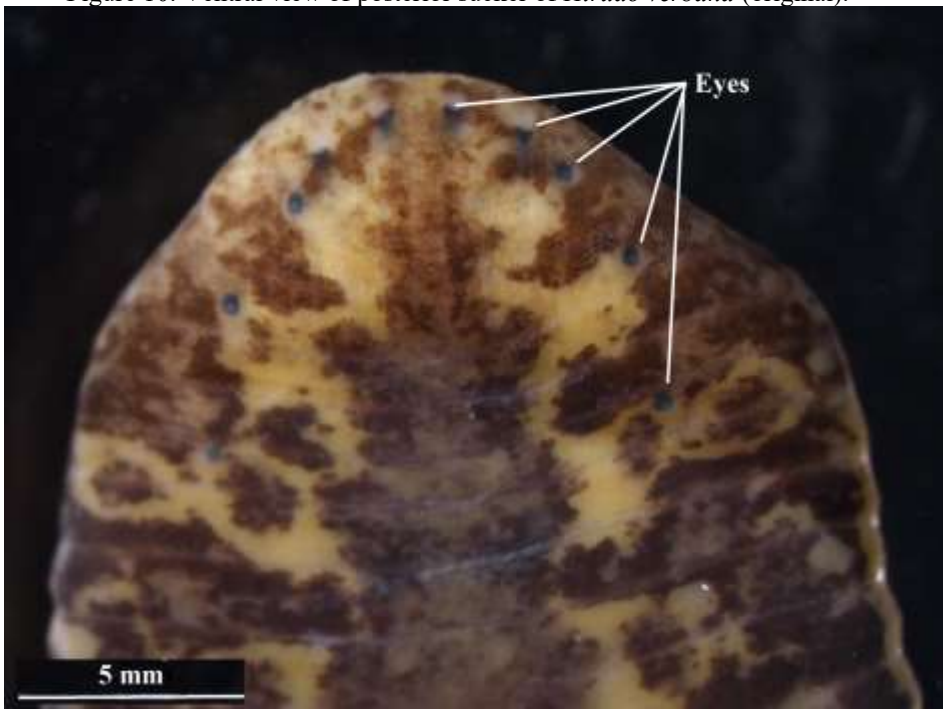

Figure 11. Eye spots from the anterior dorsal side of *Hirudo verbana* (original).

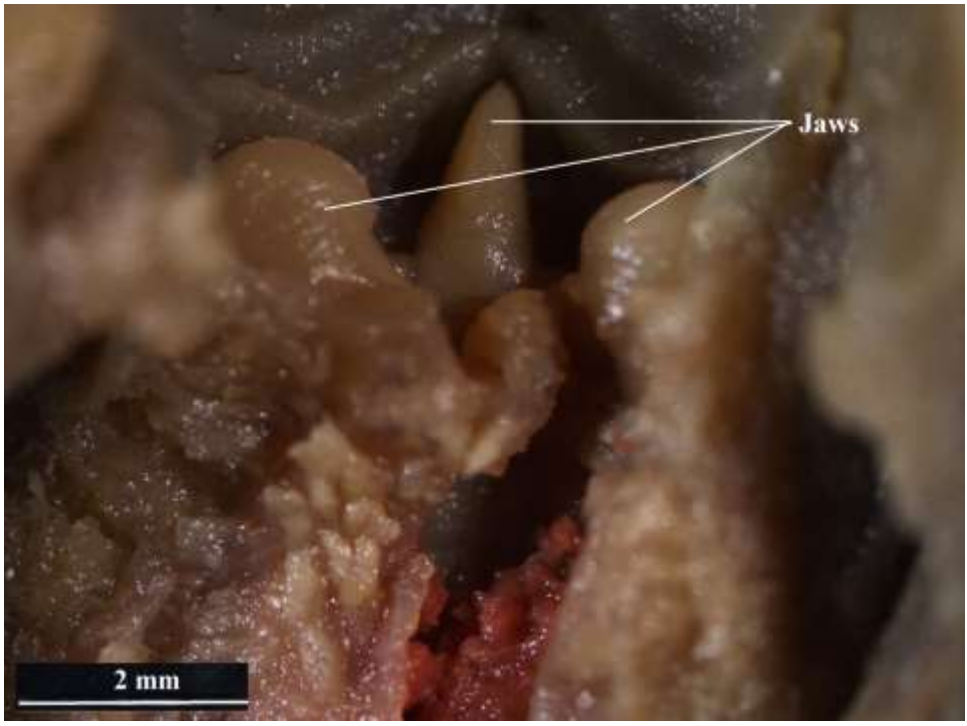

Figure 12. Position of jaws of *Hirudo verbana* (original).

Figure 13. Ridges of teeth on jaws of *Hirudo verbana* (original).

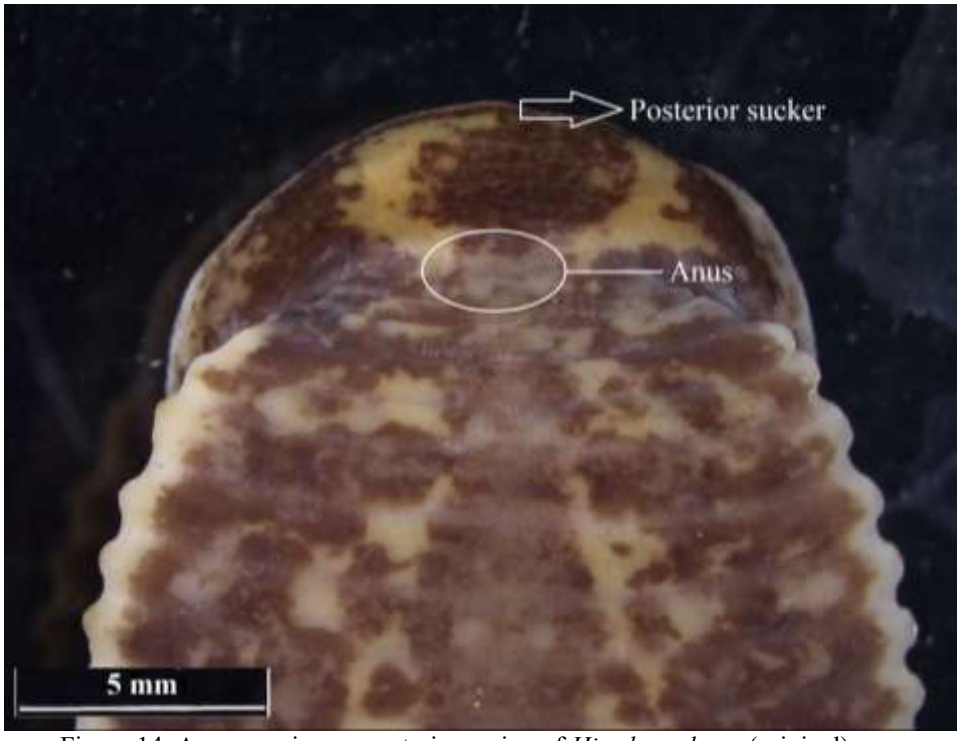

Figure 14. Anus opening on posterior region of *Hirudo verbana* (original).

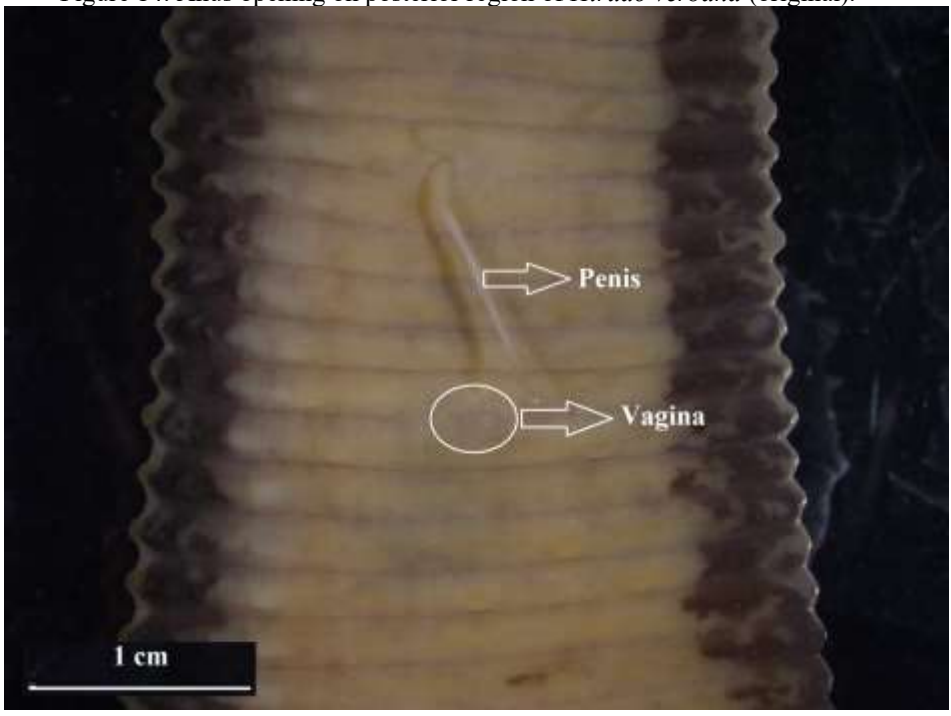

Figure 15. Position of genital organs of *Hirudo verbana* (original).

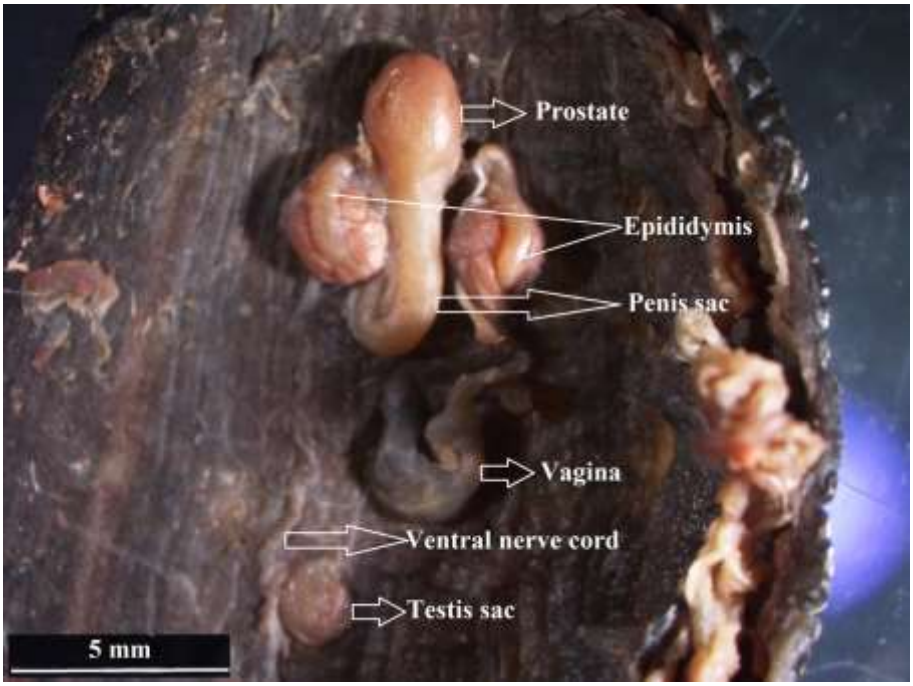

Figure 16. Position of genital organs in body cavity of Hirudo verbana (original).

DISCUSSION and CONCLUSION

Today, medicinal leeches are used effectively in the treatment of many diseases in numerous countries. They are the primary hematophagous organisms employed in the management of post-operative sites in humans and various animals, including cats, dogs, horses, and birds, as well as in the treatment of inflammatory conditions, edema, and painful areas. Among the bioactive substances present in medicinal leech saliva, hirudin is the most potent anticoagulant and exhibits an effect similar to that of heparin. Hirudin has also been reported to have beneficial effects in mitigating diabetic complications and in the treatment of blood-related disorders such as intravascular coagulation syndrome and polycythemia (Abdisa 2018).

When medicinal leeches are used directly in postoperative procedures, bacteria present in their digestive systems may cause secondary bacterial or viral infections. The bacterial and viral flora of medicinal leeches varies among species as a result of their symbiotic ecology. Therefore, accurate and reliable identification of the taxonomic status of medicinal leech species is one of the essential prerequisites for safe (Baskova et al. 2008).

Within the taxon Hirudinea, three species of medicinal leeches (*Hirudo medicinalis*, *Hirudo verbana*, and *Hirudo troctina*) are widely

distributed across Eurasia (Utevsky et al. 2010). Until recent years, *H. medicinalis* and *H. verbana* were collectively referred to as *Hirudo medicinalis* due to insufficient knowledge of their biology, a distinction that was only definitively resolved through molecular analyses (Siddall et al. 2007).

In recent years, the distribution range of *Hirudo medicinalis* has been defined more accurately through extensive taxonomic and molecular studies (Utevsky et al. 2008; Westendorff et al. 2008; Utevsky et al. 2010; Elliott et al. 2011; Živić et al. 2015). Moreover, it has been demonstrated that the majority of medicinal leech populations in Türkiye belong to *Hirudo verbana* rather than *H. medicinalis* (Apakupakul et al. 1999; Siddall and Burreson 1998; Sağlam 2011; Sağlam et al. 2018; Ceylan et al. 2019; Sağlam 2019; Ceylan and Çetinkaya 2021).

Anatomical and morphological features observed in this study are typical of medicinal leeches and clearly distinguish this species from other European leeches of the genus *Hirudo* (Trontelj and Utevsky 2005; Siddall et al. 2007; Utevsky et al. 2008, 2010; Elliott and Kutschera 2011; Trontelj and Utevsky 2012; Kutschera and Elliott 2014). The similar coloration and consistent dorsal and ventral patterning observed among the examined specimens indicate that all medicinal leeches studied belong to a single species, *Hirudo verbana*. These findings support existing knowledge that *Hirudo verbana* is widely distributed throughout Anatolia.

Ceylan et al. (2015) reported that the smallest individual among *Hirudo verbana* specimens collected from Lake Eğirdir weighed 1.85 g. Wilkin and Scofield (1991) recorded that the minimum weight of mature medicinal leeches decreased from 3.07 g to 1.30 g. The weight values of the smallest mature *Hirudo verbana* specimens examined in the present study are consistent with those reported by previous researchers. The *H. verbana* population in Lake Karamık also exhibits similar bio-ecological characteristics. Understanding these bio-ecological characteristics is essential for assessing the population dynamics of medicinal leeches collected from their natural habitats for medical use and for ensuring the sustainable conservation of their populations (Karataş and Dernekbaşı 2018).

CONCLUSION

In conclusion, this study provides a detailed description of the anatomical and morphological characteristics of *Hirudo verbana* specimens collected from Lake Karamık and reliably confirms their taxonomic identity based on diagnostic morphological traits. The findings contribute to a more precise understanding of the geographical distribution of *H. verbana* in Anatolia and support previous reports indicating that this species represents the dominant medicinal leech taxon in Türkiye. Accurate species identification is of particular importance for the safe and effective clinical use of medicinal leeches, as species-specific biological and symbiotic

characteristics may influence therapeutic outcomes and infection risks. Moreover, the bio-ecological information obtained in this study may serve as a baseline for future population monitoring and conservation strategies, supporting the sustainable use and protection of natural *H. verbana* populations. Further studies integrating molecular analyses and ecological assessments are recommended to better understand population structure, genetic diversity, and long-term conservation status of this medically important species.

ACKNOWLEDGEMENTS

This study was produced from a master's thesis. It was supported by Afyon Kocatepe University Scientific Research Projects Unit within the scope of project number 21.Fen.Bil.01.

REFERENCES

Anonymous (2023). www.google.com.tr/maps/

Abdisa T. (2018). Therapeutic Importance of Leech and Impact of Leech in Domestic Animals, MOJ Drug Des Develop Ther, 2 (6), 235–242. Doi: 10.15406/mojddt.2018.02.00068

Apakupakul K & Siddall M E, Burreson E M. (1999). Higher level relationships of leeches (Annelida:
Clitellata: Euhirudinea) based on morphology and gene sequences, Mol. Phylog. Evol, 12, 350-359.

Baskova I P, Kostrjukova E S, Vlasova M A, Kharitonova O V, Levitskiy S A, Zavalova L L, Moshkovskii S A, & Lazarev V N. (2008). Proteins and peptides of the salivary gland secretion of medicinal leeches *Hirudo verbana*, *H.medicinalis*, and *H.orientalis,* Biochemistry-Moscow, 73, 315-320.

Ceylan M & Çetinkaya O. (2021). Size and structure of the Mediterranean Medicinal Leech, *Hirudo verbana* Populations Inhabiting Wetlands Around Lake Eğirdir, Turkey, Ege Journal of Fisheries and Aquatic Sciences, 38, 437-447. Doi.org/10.12714/egejfas.38.4.05

Ceylan M, Çetinkaya O, Küçükkara R & Akçimen U. (2015). Reproduction Efficiency of the Medicinal Leech *Hirudo verbana* Carena, 1820. Turkish journal of fisheries and aquatic sciences, 15, 411-418. Doi.org/10.4194/1303-2712-v15_2_27

Ceylan M, Küçükkara R & Akçimen U. (2019). Effects of Broodstock Density on Reproduction Efficiency and Survival of Southern Medicinal Leech, *Hirudo verbana* Carena, 1820, Aquaculture, 498, 279-284.

Elliott J M & Kutschera U. (2011). Medicinal Leeches: Historical Use, Ecology, Genetics, and Conservation, Freshwater Reviews, 4 (1), 21-41.

Hasbek M & Ari Y. (2018). Bizim Gölümüzü Bize Vermeyecekler: Karamik Gölü'nün Kültürel ve Politik Ekolojisi, Doğu Coğrafya Dergisi, 23 (40), 37-60.

Karataş E & Dernekbaşı S. (2018). A Research on the Culture of Medicinal Leech (*Hirudo verbana* Carena, 1820) in Aquarium Conditions, Gaziosmanpasa

Journal of Scientific Research, 7 (2), 27-37.
Kutschera U & Elliott J M. (2014). The European Medicinal Leech *Hirudo medicinalis* L.: Morphology and Occurrence of an Endangered Species, Zoosyst. Evol, 91 (2), 271–280. Doi 10.3897/zse.90.8715
Neubert E & Nesemann H. (1999). Annelida, Clitellata: Branchiobdella, Acanthobdellea, Hirudinea Sübwasser Fauna von Mitteleuropa 6/2, Spektrum Akademischer Verlag, Heidelberg, 178p.
Saglam N. (2011). Protection and Sustainability, Exportation of Some Species of Medicinal Leeches (*Hirudo medicinalis* L., 1758 And *Hirudo verbana* Carena, 1820), Journal of Fisheries Sciences, 5 (1), 1-15.
Saglam N, Saunders R, Lang S A & Shain D H. (2016). A New Species of *Hirudo* (Annelida: Hirudinidae): Historical Biogeography of Eurasian Medicinal Leeches, BMC Zoology, 1(5), 2-12.
Sağlam N. (2019). Internal and External Morphological Characteristics of the Medicinal Leech Species *Hirudo sulukii* and *Hirudo verbana,* Turkiye Parazitol Derg, 43 (4), 204-209.
Sağlam N, Özbay Ö, Demir T, Balcı M, Pala A & Kılıç A. (2018). Effect of Water Quality on Monthly Density Variation of the Endangered Southern Medicinal Leech *Hirudo verbana* Carena, 1820 (Hirudinea: Arhynchobdellida: Hirudinidae), Acta Zool Bulg, 70 (3), 433-441.
Siddall M E. & Burreson E M. (1998). Phylogeny of leeches (Hirudinea) based on mitochondrial cytochrome c oxidase subunit I, Mol Phylog Evol, 9, 156-162.
Siddall M E, Trontelj P, Utevsky S Y, Nkamany M & Macdonald K S. (2007). Diverse Molecular Data Demonstrate that Commercially Available Medicinal Leeches are not *Hirudo medicinalis*, Proceedings of the Royal Society B, 274, 1481–1487. Doi: 10.1098/ rspb.2007.0248
Trontelj P & Utevsky S Y. (2005). Celebrity With a Neglected Taxonomy: Molecular Systematics of the Medicinal Leech (Genus *Hirudo*), Mol Phylogenet Evol, 34, 616–624. Doi:10.1016/j.ympev.2004.10.012.
Trontelj P & Utevsky S Y. (2012). Phylogeny and Phylogeography of Medicinal Leeches (Genus *Hirudo*): Fast Dispersal and Shallow Genetic Structure, Molecular Phylogenetics and Evolution, 63, 475–485. Doi:10.1016/j.ympev.2012.01.022
Utevsky S Y, Zinenko A I, Atemasov A A, Huseynov M A, Utevska O M & Utevsky A Y. (2008). New Information on the Distribution of the Medicinal Leech (Genus *Hirudo*) in the Iberian Peninsula, the Caucasus and Central Asia, Lauterbornia, 65,119–130.
Utevsky S, Zagmajster M, Atemasov A, Zinenko O, Utevska O, Utevsky A & Trontelj P. (2010). Distribution and status of medicinal leeches (genus *Hirudo*) in the western palaearctic: anthropogenic, ecological, or historical effects? Aquatic Conservation, 20, 198–210. Doi:10.1002/aqc.1071.
Westendorff M, Kalettka T & Jueg U. (2008). Occurrence of Leeches (Hirudinea) in Different Types of Water Bodies in Northeast Germany (Brandenburg), Lauterbornia, 65, 153–162.
Wilkin P J & Scofield, A M. (1991). Growth of the Medicinal Leech, *Hirudo medicinalis*, under Natural and Laboratory Conditions, Freshwater Biology, 25, 547-553.
Živić I, Radosavljević T, Stojanović K & Petrović A. (2015). The First Molecular

Characterization of the Genus *Hirudo* on the Territory of Serbia: Estimation of Endangerment, Aquat Ecol, 49 (1), 81–90.